21th Numerical Towing Tank Symposium

30 September – 2 October 2018

Cortona/Italy

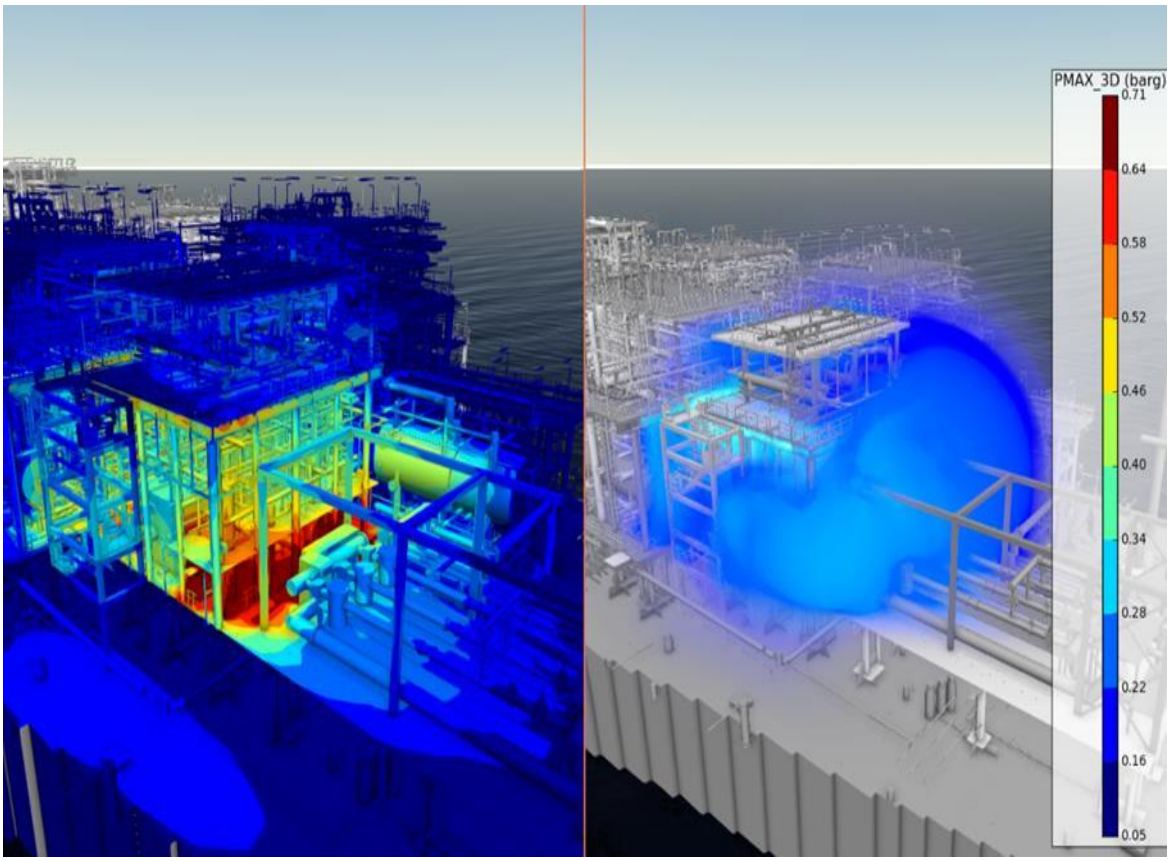

Volker Bertram (Ed.)

TuTech
TUHH Technologie GmbH

Sponsored by

Numeca

www.numeca.com

Cover image source: Bo Wen (DNV GL)

Index of Papers

Simon Beelen, Martijn van Rijsbergen
Bubble screening in lifting flows

Manuel Cerro, Hans Vreugdenhil, Alex Kruijswijk
CFD analysis of performance new design bow thruster tunnel

Antonio Coppedè, Stefano Gaggero, Giuliano Vernengo, Diego Villa
Surrogate Model for Ship Resistance: A Sensitivity Analysis of Shape Deformation

Griet Decorte, Jaak Monbaliu
A Review on the Application of OpenFOAM's Mesh Motion Techniques to Wave-Structure Interaction Problems

Toon Demeester, E. Harald van Brummeleny, Joris Degroote
An Iterative Fitting Method for 2D Supercritical Steady Free Surface Flow

Mahesh Dhone, Nikolai Kornev
Tracking of Tip Vortices Arising from Marine Structures

Pranav Doijode Sumanth, Stefan Hickel, Tom van Terwisga
On the Design of Experiments for propellers - Getting to design variables that matter and design points that are important

Luis Eça, Guilherme Vaz, Martin Hoekstra
On the Role of Iterative Errors in Unsteady Flow Simulations

Arash Eslamdoost, Jennie Andersson, Rickard Bensow
Including Energy Equation for Analyzing Propulsor-Hull Interaction Effects

Inno Gatin, Shengnan Liub, Nikola Vladimira, Hrvoje Jasaka
Compressible Two–phase flow model with the Ghost Fluid Method for Marine Hydrodynamics

Ebrahim Ghahramani, Rickard Bensow
Numerical study of cavitating flow around a cylindrical bluff body

John Martin K. Godø, Jarle V. Kramer, Sverre Steen (NTNU), Luca Savio (SINTEF Ocean)
Unsteady forces on hydrofoil vessels in waves - validation of a dynamic lifting line using CFD

Nobuhiro Hasuike, Kohei Himei
Cavitation simulation on composite marine propellers

Adam Higgens, Philipp Joseph, Stephen Turnock
Improvements in the Methodology for Identifying Noise Sources in Ducted Marine Propellers

Qiu Jin, Dominic Hudson, Pandeli Temarel
Simulation of Non-breaking and Breaking Waves with OpenFOAM

Maarten Klapwijk, Thomas Lloyd, Guilherme Vaz, Tom van Terwisga
Channel flow at Re_τ = 395: LES is more (turbulent than PANS)

Jarle V. Kramer, John Martin K. Godø, Sverre Steen
Hydrofoil simulations – non-linear lifting line vs CFD

Benoît LeBlanc, Hamn-Ching Cheny, Christiaan Klaijz
Evaluation of a Coupled Level Set and Volume of Fluid Method for Unstructured Grids

Sebastien Lemaire, Guilherme Vaz, Stephen Turnock
Implementation and Verification of an Explicit Overset Grid Method

Rui Lopes, Luis Eça, Guilherme Vaz
Assessment of RANS Transition Models

Stefano Lovato, Geert Keetels, Guilherme Vaz, Serge Toxopeus
Verification of a CFD code for laminar viscoplastic fluid flow

Nicholas McCaw, Stephen Turnock, William Batten
An Investigation of the Vortex Shedding Frequency and Natural Frequency of a Ship Propeller

João Muralha, Luis Eça, Christiaan Klaijy
Application of the SIMPLE Algorithm to a Manufactured Subsonic Flow

Milovan Perić
On the Estimation of Discretization and Modeling Errors and their Interaction

Robinson Perić, Moustafa Abdel-Maksoud
Influence of Choice of Boundary Treatment for 3D Flow Simulations with Free-Surface Waves

Gem Rotte, Florian Charruault, Maarten Kerkvliet, Tom van Terwisga
An Investigation on the Set-up of Air Cavity Simulations using a Scale Resolving Method

Simone Saettone, Bhushan Taskar, Pelle Bo Regener, Poul Andersen
Unsteady propeller forces and hull pressure pulses in waves

Yuki Saito, Takanori Hino
Development of Propeller Shape Optimization System Using CFD Analysis

Nobuaki Sakamoto, Kunihide Ohashi
Implementation of THINC-type VoF Advection Scheme on Structured FVM Solver

Lars-Uve Schrader, Jan-Patrick Voß, Erik Leenders, John Nicholson
Aerodynamics of Britain's new polar research ship

Keun Woo Shin
Simplified CFD Approach for Simulating Propeller Flows in Ship Wake Fields

Simon Törnros, Olof Klerebrant Klasson
Demonstration of Propeller Blade Optimization using BEM and CFD

Arthur E.P. Veldman, Henk Seubers, Matin Hosseini Zahraei, Peter van der Plas, Peter Wellens
Strong quasi-simultaneous coupling for fluid-structure interaction in offshore applications

Kevin Vidal, Benoit Mallol, Charles Hirsch
Weighted trade-off optimization of a self-propelled passenger ferry using efficient design space analysis techniques and adaptive grid refinement

JeroenWackers, Charles-Edouard Jeanson, Patrick Queutey, Michel Visonneau, Riccardo Pellegrini, Andrea Serani, Matteo Diez
Hull shape optimisation using multi-fidelity metamodels and adaptive grid refinement

Michał Wawrzusiszyn, Marek Kraskowski, Przemysław Król, Tomasz Bugalski
Experimental and Numerical Hydrodynamic Analysis of Propulsion Factors On R/V Nawigator XXI with a Pre-Swirl Stator Device

Bubble screening in lifting flows and its effect on cavitation inception

Simon Beelen*, **Martijn van Rijsbergen***
*MARIN, Wageningen/Netherlands simonbeelen@hotmail.com

1 Introduction

Cavitation inception on foils and propellers is often initiated by free-stream micro-bubbles (van Rijsbergen and van Terwisga, 2010). However, dependent on their size and relative position, bubbles can be pushed away by the high pressure region, preventing them from reaching the low pressure region. This is designated as the screening effect by (Johnson and Hsieh, 1966), who made a quasi-steady evaluation of this effect for a headform. A more realistic approach is to couple the equation of motion of the bubble with a bubble dynamics equation. Such a coupled method can be used to study the mechanisms of and scale effects on cavitation inception. In this paper this method is presented and applied to 2D symmetric and asymmetric (lifting) potential flows. Screening limits in terms of initial bubble radius and initial bubble position are derived.

2 Methodology

The 2D equation of motion for potential flow is based on a force balance, which is given below:

$$\boldsymbol{F}_m = \boldsymbol{F}_I + \boldsymbol{F}_D + \boldsymbol{F}_p + \boldsymbol{F}_g + \boldsymbol{F}_H \tag{1}$$

The terms from left to right are:

- The force due to the acceleration of the bubble: $\boldsymbol{F}_m = \rho_b \frac{4}{3}\pi R_0^3 \frac{d\boldsymbol{w}_b}{dt}$, where ρ_b is the density of the bubble, R_0 is the initial bubble radius and $\boldsymbol{w}_b$ is the velocity vector of the bubble.

- The forces related to the Kelvin impulse: $\boldsymbol{F}_I = -C_{am}\rho_l \frac{4}{3}\pi R^3 \frac{d\boldsymbol{w}_b}{dt} + C_{am}\rho_l 4\pi R^2 \frac{dR}{dt}(\boldsymbol{w} - \boldsymbol{w}_b)$. C_{am} is the added mass coefficient, set at $\frac{1}{2}$, ρ_l is the liquid density, R is the bubble radius and $\boldsymbol{w}$ is the liquid velocity vector.
  The Kelvin impulse is primarily known to describe the behaviour of a collapsing bubble near a boundary (Blake, 1988). Conservation of the Kelvin impulse in the equation of motion yields a decreasing magnitude of the relative velocity for growing bubbles (Ohl et al., 2003) and an increasing magnitude of the relative velocity for shrinking bubbles (Blake, 1988).

- The drag force: $\boldsymbol{F}_D = \frac{1}{2}\rho_l C_D R^2 (\boldsymbol{w} - \boldsymbol{w}_b)|\boldsymbol{w} - \boldsymbol{w}_b|$, where C_D is the drag coefficient. The drag coefficient for bubbles depends amongst others on the amount of surfactant in the surrounding liquid. Surfactants cause a no-slip boundary condition at the bubble interface via the Marangoni effect (Takagi and Matsumoto, 2011), which leads to a boundary layer similar to that around a solid sphere. For typical applications such as a ship propeller it can be assumed that the flow is contaminated by surfactants, leading to a drag coefficient of a solid sphere:
  $C_D = \frac{24}{\mathrm{Re}_b}\left(1 + 0.197\mathrm{Re}_b^{0.63} + 2.6 \cdot 10^{-4}\mathrm{Re}_b^{1.38}\right)$ (Johnson and Hsieh, 1966). The bubble Reynolds number is defined as: $\mathrm{Re}_b = \frac{2R|\boldsymbol{w}-\boldsymbol{w}_b|}{\nu_l}$, where ν_l is the kinematic liquid viscosity.

- The pressure gradient force: $\boldsymbol{F}_p = -(1 + C_{am})\frac{4}{3}\pi R^3 \boldsymbol{\nabla} p$, where $\boldsymbol{\nabla} p$ is the pressure gradient. The added mass coefficient which appears in the forces related to the Kelvin impulse is included in this force.

- The gravitational force: $\boldsymbol{F}_g = \frac{4}{3}\pi \boldsymbol{g}\left(R_0^3\rho_b - R^3\rho_l\right)$, where $\boldsymbol{g}$ is the gravitational acceleration vector.

- The history force for steady flow: $\boldsymbol{F}_H = -6\pi R\rho_l\nu_l \int_{-\infty}^{t} K(t,\tau)\left(\frac{d\boldsymbol{w}_b}{d\tau} - (\boldsymbol{w}_b(\tau)\cdot\boldsymbol{\nabla})\boldsymbol{w}(\tau)\right)d\tau$, with the history force integration kernel K, and integration variable τ.
  The history force is a consequence of the lagging build-up of the boundary layer, and can be interpreted as the unsteady part of the drag force. The decay of the history kernel is crucial for a

relevant implementation; in general the distant past should be less influential than the near past. The used kernel is:

$$K(t,\tau) = \frac{K_{Bas}(t,\tau)}{\left(1 + \left[\frac{1}{16\pi f_H}\left(\frac{\mathrm{Re}_b(t)}{K_{Bas}(t,\tau)}\right)^3\right]^{\frac{1}{c_1}}\right)^{c_1}}$$

with $f_H = (0.75 + c_2\mathrm{Re}_b(t))^3$, and the Basset kernel: $K_{Bas}(t,\tau) = \frac{1}{\sqrt{4\pi}}\frac{1}{\sqrt{T_H(t,\tau)}}$, the history time $T_H(t,\tau) = \frac{t-\tau}{\tau_d}$ with the diffusive time scale of the bubble $\tau_d = \frac{4R^2}{\nu_l}$. The constants $c_1 = 2.5$ and $c_2 = 0.2$ are taken from (Loth and Dorgan, 2009).

A simple impact model is implemented which lets a bubble follow the local streamline if it is in contact with the surface of the object. This impact model is therefore not based on an equation of motion.

The bubble dynamics is described by the Keller-Miksis equation (Prosperetti and Lezzi, 1986). This variant of the Rayleigh-Plesset equation is derived for a compressible liquid, which results in a more realistic damped behaviour of the bubble at high collapse velocities.

$$\left(1 - \frac{\frac{dR}{dt}}{c}\right)\rho_l R\frac{d^2R}{dt^2} + \frac{3}{2}\left(\frac{dR}{dt}\right)^2\rho_l\left(1 - \frac{1}{3}\frac{\frac{dR}{dt}}{c}\right) = \left(1 + \frac{\frac{dR}{dt}}{c}\right)\left[p_v - p + p_g(t)\right] + \frac{R}{c}\frac{dp_g(t)}{dt} - 4\rho_l\nu_l\frac{\frac{dR}{dt}}{R} - \frac{2\gamma}{R} \quad (2)$$

Where c is the speed of sound, p_v is the vapour pressure, p is the local pressure, p_g is the partial gas pressure and γ is the surface tension. The terms $\frac{\frac{dR}{dt}}{c}$ and $\frac{R}{c}\frac{dp_g(t)}{dt}$ show that the damping depends on the collapse velocity of the bubble.

The potential flow field is constructed using a Kármán-Trefftz transformation (Halsey, 1979). This method transforms the potential flow solution around a 2D cylinder to the flow around a 2D foil.

The equation of motion and the bubble dynamics equation form a set of second-order ordinary differential equations, which can be written as a set of first-order ordinary differential equations. A fourth-order accurate Runge-Kutta integration scheme with variable time stepping is used to solve the set of equations. The history force is integrated at every time step using the trapezoidal rule. It is assumed that prior to the initial time no relative accelerations have occurred. During the last time step, which should be small, the Basset kernel is used with a constant relative acceleration.

3 Results

3.1 Symmetrical screening

Symmetrical screening is investigated using the flow around a Rankine half body in one of the conditions used in Johnson and Hsieh (1966). The leading edge of the half body with some streamlines and limits is shown in Fig. 1(a). In constant flow conditions with a constant x_0 position, the bubble behaviour is dependent on the initial vertical position, y_0, and the initial bubble radius, R_0. The (R_0, y_0) parameter space, designated as a screening plot, is shown in Fig. 1(b). The used equation of motion excludes the history force to reduce computational costs. Gravity is excluded because of its asymmetrical effect. Fig. 1(b) is thus symmetrical around $y_0 = 0$.

In the screening plot three categories are distinguished: A bubble reaches its critical radius (red asterisks), a bubble reaches its critical radius whilst hitting the surface in the region below the vapour pressure (black square), and a bubble hits the surface in the region below the vapour pressure (green asterisks). The first category can also be designated as bubble cavitation. Bubbles in the second and third category can induce sheet cavitation, dependent on the surface and boundary layer characteristics (van Rijsbergen, 2016).

The cavitation number is defined as: $\sigma_v = \frac{p_0 - p_v}{\frac{1}{2}\rho_l U_0^2}$, where U_0 is the linear free stream velocity and p_0 is the initial surrounding pressure.

Four limits can be approximated for the screening plot, see Fig 1. Two dynamical limits (a) and (b), and

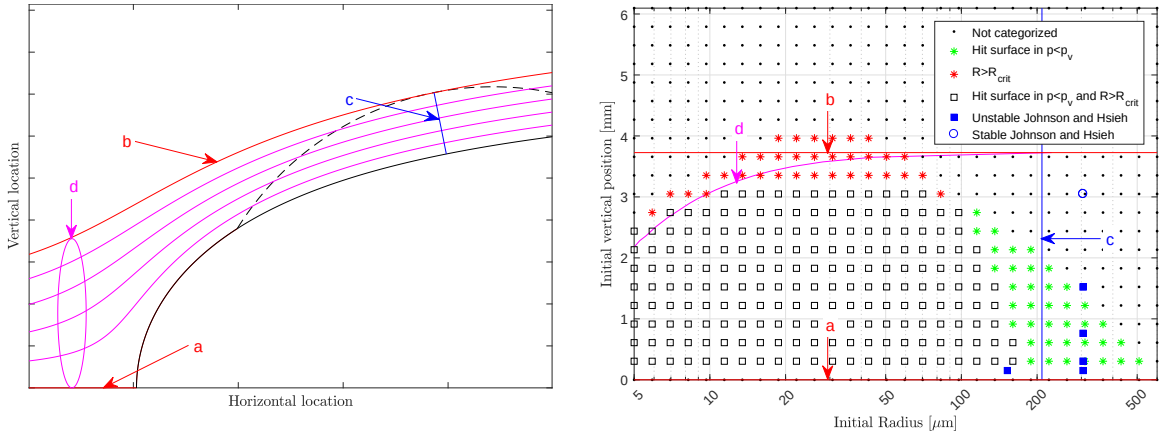

(a) Leading edge of half body with the given limits, note that the initial condition is not shown.

(b) Limits in the screening plot given by a, b, c and d.

Fig. 1: Screening plot for one of the conditions in Johnson and Hsieh (1966), $h = 15.24\,\mathrm{mm}$ (half ultimate body width), $U_0 = 15.24\,\mathrm{ms}^{-1}$, $x_0 = -76.2\,\mathrm{mm}$, $\sigma_v = 0.4$ (cavitation number).

two quasi-static limits (c) and (d).
Limit (a) is the dividing streamline and limit (b) is the streamline tangent to the contour of the vapour pressure. Bubbles need to end up in between both limits in order to encounter pressures below the vapour pressure. In Fig. 1(a) both limits are shown, in Fig. 1(b) these limits are represented by their initial vertical position.
Limit (c) depends on the maximum height of the region where the pressure is below the vapour pressure, D_{p_v}. If the pressure experienced by the bubble is taken in the centre of the bubble whilst remaining spherical, the critical radius of the bubble, $R_{\mathrm{crit}} = R_0\sqrt{3\left(\frac{\rho_l U_0^2 R_0 \sigma_v}{4\gamma} + 1\right)}$, should be smaller than D_{p_v}. Solving $D_{p_v} = R_{\mathrm{crit}}$ gives limit (c). For large bubbles the Laplace pressure is much smaller than the experienced pressure differences, the maximum initial radius can thus be approximated by:

$$R_{0,\max} = \left(\frac{4}{3}\frac{\gamma}{\rho_l U_0^2 \sigma_v}\right)^{\frac{1}{3}} D_{p_v}^{\frac{2}{3}} \tag{3}$$

Limit (d) is based on the minimum pressure along streamlines between the two bounding streamlines, and will form an approximate lower limit. For small bubbles deviations from the streamline are small, so if bubbles remain stable they approximately experience the lowest pressure along their initial streamline. A bubble remains stable if it is smaller than the minimum radius found by the Blake threshold (Johnson and Hsieh, 1966):

$$C_{p,\min}(y_0) + \sigma_v = -\sqrt{\frac{4}{27}}\sigma_v \frac{\left(\frac{4\gamma}{R_{0,\min}\rho_l U_0^2 \sigma_v}\right)^{\frac{3}{2}}}{\left(1 + \frac{4\gamma}{R_{0,\min}\rho_l U_0^2 \sigma_v}\right)^{\frac{1}{2}}} \tag{4}$$

Solving this equation for $R_{0,\min}$ couples the initial condition of a small bubble with its dynamical behaviour, and gives limit (d).

If $-C_{p,\min} \ll \sigma_v$ the minimum radius can be approximated by:

$$R_{0,\min} = \sqrt{\frac{16}{27}}\frac{2\gamma}{\rho_l U_0^2(-\sigma_v - C_{p,\min})} \tag{5}$$

The screening plot shows that a number of bubbles do reach their critical radius in the dynamic simulations which are beyond the limits (b) and (d). Limit (c) corresponds well with the results from the dy-

namic simulations. However, in our model, the 300 μm bubbles do not reach their critical radius whereas in Johnson and Hsieh's model they do, see the blue filled squares in Fig. 1(b).

3.2 Asymmetrical screening

Most cavitating conditions are asymmetric flow conditions. The effect of the history force on the trajectory and radius of a bubble is shown in Fig. 2(a). The history force counteracts deviation from the initial streamline, which confirms its designation as the unsteady part of the drag force. In this case the effect of the history force on a bubble's trajectory and growth is obvious. However, in this 2D situation, its effect can also be interpreted as a shift in initial vertical position. Therefore, the screening plot is made without the history force.

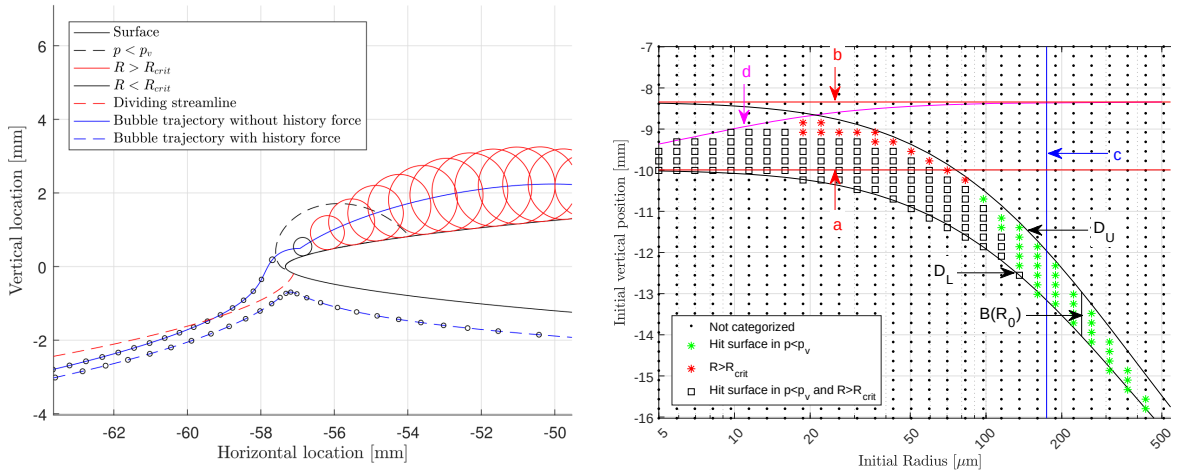

(a) Trajectories with and without the history force of bubbles with the same initial conditions.

(b) Screening plot including limits a, b, c and d without history force.

Fig. 2: Results for a blade section of the propeller model as used in (van Rijsbergen and van Terwisga, 2010) at 60% of the blade radius, transformed to a 2D situation. $c = 115$ mm (chord length), $t_{max} = 4.7$ mm (maximum thickness), $\alpha = 2.5°$ (angle of attack), $U_0 = 6.55\,\mathrm{ms}^{-1}$, $R_0 = 70\,\mu$m, $(x_0, y_0) = (-146, -11.2)$ mm (the origin is the middle of the blade section), $\sigma_v = 0.59$.

The screening plot of the non-symmetric situation, shown in Fig. 2(a), is given in Fig. 2(b). In the screening plot two black lines are plotted, these are a continuous approximation of the vertical starting position per bubble. The deviation from the initial streamline as a function of the radius for small bubbles should look like $D \sim R_0^2$, neglecting the influence of the free stream velocity (Liu and Brennen, 1998). Assuming the same reasoning, as used in the derivation of small bubble deviation, is valid for large bubbles yields a fully dominant pressure gradient force. At a distance D_∞ below the dividing streamline the pressure gradient has no component directed towards the dividing streamline, meaning that the suction side can not be reached by any bubble. In reality, however, inertia of the added mass will play a role for large bubbles. It is assumed that a distance below the dividing streamline, D_{eff}, can be found which is the effective limiting distance below the dividing streamline. D_∞ and D_{eff} depend on the initial horizontal position and on the asymmetry in the flow. A function is proposed which fulfils both small and large bubble behaviour:

$$D = \frac{D_{\mathrm{eff}} R_0^2}{R_0^2 + R_a R_0 + R_b^2} \tag{6}$$

The proposed function for the deviation can be applied for both the lower limit deviation (D_L) and the upper limit deviation (D_U):

$$D_L = \frac{D_{\mathrm{eff}} R_0^2}{R_0^2 + R_a R_0 + R_b^2}, \quad D_U = \frac{(D_{\mathrm{ds}} + D_{\mathrm{eff}})\, R_0^2}{R_0^2 + R_a R_0 + R_b^2} \tag{7}$$

D_L is the lower limit and the distance below the dividing streamline. D_U is the upper limit and the distance below the streamline tangent to the vapour pressure contour, see Fig. 2(b). The upper limit assumes that the bubbles are subject to the same repulsive pressure gradients as for the lower limit. D_{ds} is the vertical distance between limit (a) and limit (b). R_a, R_b and D_{eff} are constants depending on the effect of the adverse pressure gradients on the bubble trajectory and can therefore most accurately be found using the dividing streamline as reference. The initial vertical positions of three bubbles with significantly different R_0 who just reach the suction side are used to calculate R_a, R_b and D_{eff}.
The range of vertical positions where bubbles can start to pass the region where the pressure is below the vapour pressure, B, see Fig. 2(b), is defined accordingly:

$$B = D_{\mathrm{ds}} \left(1 - \frac{R_0^2}{R_0^2 + R_a R_0 + R_b^2} \right) \tag{8}$$

B is thus independent of D_{eff}. If R_a is large compared to the bubble spectrum, the relevant part of B can be approximated by D_{ds}.
For the conditions of Fig. 2(b) $D_\infty = 84.9\,\mathrm{mm}$, $D_{\mathrm{eff}} = 11.6\,\mathrm{mm}$, $D_{\mathrm{ds}} = 1.65\,\mathrm{mm}$, $R_a = 411\,\mu\mathrm{m}$ and $R_b = 97.3\,\mu\mathrm{m}$.

The applicability of these limits will be shown for two parameter variations with respect to the situation in Fig. 2.

- In Fig. 3(a) the cavitation number is increased to $\sigma_v = 1.1$. Obviously the dividing streamline will not change, but because the region where the pressure is below the vapour pressure is smaller, the range of initial vertical positions is smaller. The maximum bubble radius available for bubble cavitation inception will decrease due to the same decreased area below the vapour pressure. The overall minimum pressure will be higher as to increase the cavitation number the surrounding pressure must increase, leading to larger stable bubbles.
- In Fig. 3(b) the free stream velocity is increased to $U_0 = 13.1\,\mathrm{ms}^{-1}$. Again the dividing streamline remains the same. With a constant cavitation number, the streamline tangent to the vapour pressure contour will also remain the same. Higher velocities will lead to a lower upper limit on the bubble size, see equation 3. The increased velocity will lead to a decreased minimum radius approximation as can be seen from equation 4.

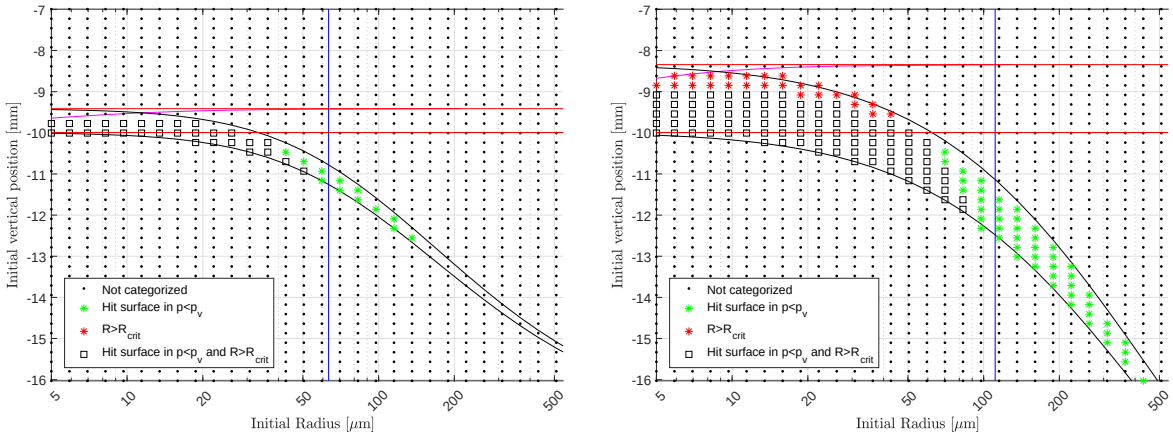

(a) Increased cavitation number, $\sigma_v = 1.1$

(b) Increased free stream velocity, $U_0 = 13.1\,\mathrm{ms}^{-1}$

Fig. 3: Varying σ_v and U_0 whilst keeping the other variables as given in Fig. 2.

As can be seen in Fig. 3 the limits do indeed follow the trend of the dynamical simulations accurately.

4 Discussion

The combination of the impact model and the bubble growth model determine the maximum initial bubble radius that can reach its critical radius. Limit (c) in Fig. 1(b) indicates that in a quasi-static model,

bubbles with a maximum initial radius of approximately 200 μm can reach their critical radius. In the dynamic simulations, however, these bubbles do not reach their critical radius, due to the inertia of the water around the bubble. Both the quasi-static limit and the dynamic simulations use an impact model where the minimum distance between the centre of the bubble and the surface of the object is equal to the bubble radius. This couples the maximum radius of the bubble to the maximum height of the region where the pressure is below the vapour pressure. A larger bubble will experience a higher pressure as a result of the impact model and will therefore be limited in its growth. The model of Johnson and Hsieh, however, allows the centre of the bubble to hit the surface of the body. This leads to lower experienced pressures and no limit to the initial bubble radius, so even bubbles with an initial radius of 300 μm can reach their critical radius.
In reality, bubbles will deform to a spherical cap when hitting the surface. The effective pressure experienced by the bubble can be approximated by the value at the centre of mass of the bubble. For a hemispherical shape, this pressure will be lower than that of a sphere, and higher than the pressure at the surface. Therefore, an impact model with bubble deformation is expected to give more realistic results.
The definition of the screening effect as discussed by Johnson and Hsieh, where large bubbles do not cause cavitation inception because they are pushed over the low pressure region, is not sufficient in lifting flows. For lifting flows larger bubbles can still reach the low pressure region if they start at a particular location below the dividing streamline. The range of vertical positions where bubbles can start, however, decreases with increasing bubble radius. Therefore the screening effect in general can be seen as a selection effect on the initial position.

5 Concluding remarks

- The history force is important for the trajectory of a single bubble with a fixed initial position. In terms of the bandwidth however the history force is less relevant.
- Quasi-static limits are able to represent the contours of dynamic simulations quite well.
- The impact model of choice should be related to the expected bubble deformation.
- To predict the sheet cavitation inception behaviour on a foil in realistic conditions knowledge of the available bubble spectrum is vital.

References

Blake, J. R. (1988). The kelvin impulse: application to cavitation bubble dynamics. *The Journal of the Australian Mathematical Society. Series B. Applied Mathematics*, 30(2):127–146.

Halsey, N. (1979). Potential flow analysis of multielement airfoils using conformal mapping. *AIAA Journal*, 17(12):1281–1288.

Johnson, V. and Hsieh, T. (1966). The influence of the trajectories of gas nuclei on cavitation inception. In *6th Symposium on Naval Hydrodynamics, 1966*, pages 163–179. National Academy Press.

Liu, Z. and Brennen, C. E. (1998). Cavitation nuclei population and event rates. *Journal of fluids engineering*, 120(4):728–737.

Loth, E. and Dorgan, A. J. (2009). An equation of motion for particles of finite reynolds number and size. *Environmental Fluid Mechanics*, 9(2):187–206.

Ohl, C. D., Tijink, A., and Prosperetti, A. (2003). The added mass of an expanding bubble. *Journal of Fluid Mechanics*, 482:271–290.

Prosperetti, A. and Lezzi, A. (1986). Bubble dynamics in a compressible liquid. part 1. first-order theory. *Journal of Fluid Mechanics*, 168:457–478.

Takagi, S. and Matsumoto, Y. (2011). Surfactant effects on bubble motion and bubbly flows. *Annual Review of Fluid Mechanics*, 43:615–636.

van Rijsbergen, M. X. (2016). A review of sheet cavitation inception mechanisms. In *International Symposium on Transport Phenomena and Dynamics of Rotating Machinery*, Honolulu, Hawaii.

van Rijsbergen, M. X. and van Terwisga, T. J. (2010). Water quality effects on sheet cavitation inception on a ship propeller model. In *7th International Conference on Multiphase Flow*.

CFD analysis of performance new design bow thruster tunnel

Manuel Cerro*, Hans Vreugdenhil* and Alex Kruijswijk*
*Royal IHC, Kinderdijk/the Netherlands
Ab.kruijswijk@royalihc.com

1. Introduction

Royal IHC is a shipbuilding company that builds vessels and equipment for the offshore and dredging industry. This paper focusses on the performance of bow tunnel thrusters on trailing suction hopper dredger (TSHD). A TSHD typically operates in harbors, rivers and other narrow waterways. The maneuverability is very important with respect to safety and operating performance. It is known from theory and practice that the performance of a bow tunnel thruster is decreasing in slow forward condition (vs = 1-5 knots) with respect to zero forward speed of the ship [2],[3]. At higher ship speeds the bow thruster is not effective any more (approx. vs > 5-6 kn). The slow forward situation occurs for a TSHD when dredging and maneuvering, also taking into account current. A new design tunnel with a wing shaped cross-section is developed to improve the performance of the tunnel thruster. In CFD it is compared with a traditional circular shape. The performance of the tunnel thruster is also tested full-scale. A full-scale comparison between similar ships is made, one with circular and the other with wing shape. First results showed that the wing shape has better turning rate performance in slow forward condition.

Fig. 1: Example of wing shaped cross section for bow thruster tunnel.

Fig. 2: Example of TSHD in dredging condition.

2. Ship maneuvering

The software used for this CFD study is FineMARINE. Which is capable of solving the flow and motions of a free floating body in 6 DOF. In order to reduce computation time, the hydrodynamic forces and moments acting on the ship are solved with partial imposed motions. In the setup the forward motion is imposed and the yaw motion is solved. The roll motion is not considered in this study. The positive x-axis is from aftship to foreship, the positive y-axis points towards portside of the ship and the z-axis is positive upward.

Sea trails measuring method bow thrusters

During sea trials the bow thruster capabilities are measured with two type of tests. The first one is the rate of turn of the vessel at initial zero forward speed. The measurement continues until the rate of turn is constant (IMO 2.6.1).
The second test is on slow forward speed. The initial speed is zero, the bow thruster is set to full power. After the turn rate is constant the main propellers are set to full ahead. The ship speed and course are measured until the course is constant (IMO 2.6.2). See a typical measurement in figure 4. Higher final heading, means better performance of the bow thruster. After a certain speed the bow thruster is not effective anymore resulting in a constant heading, typically above 5 or 6 knots.

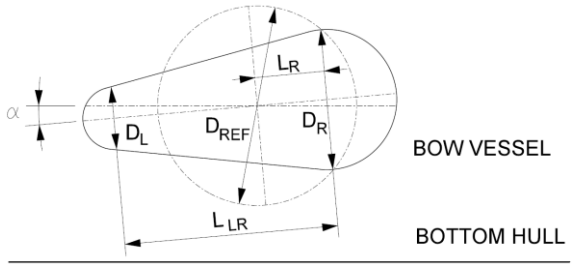

Fig. 3: Schematic overview of wing shape tunnel.

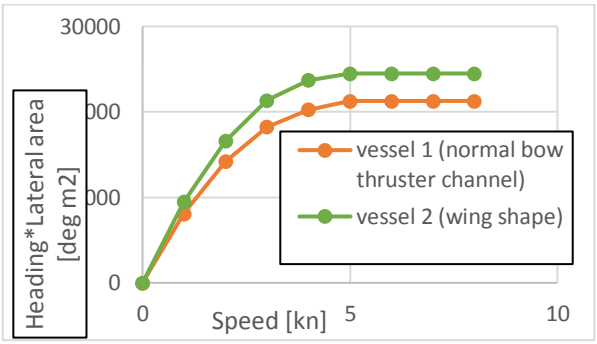

Fig. 4: Example of IMO 2.6.2 full-scale bow thruster capability test with increasing forward speed with normal and wing shape tunnel.

3. Model setup and mesh

A TSHD is typically a twin-screw ship with high block coefficient with two main propellers, having nozzles and rudders behind the nozzles. Some TSHD have a bulb fitted for better wave making resistance. In the aft a skeg is fitted at the centerline for course keeping ability. TSHD ships have low L/B [4.0-5.5] and high B/T [2.5-4.0] ratios.

Geometry

Since we are interested in the turning moment around the z-axis the whole ship is modelled instead of half ship as in resistance prediction. This model contains an headbox, tunnel, gondola, skeg, nozzle and rudder at the aftship, other recesses below the waterline are not taken into account. Their effect on the turning ability of the ship is assumed to be negligible. The grid bars at the bow tunnel openings and the hub of the thruster are not modelled. Although they will have an impact on the turning performance, the comparison between tunnel shapes is focusing on the turning rate and improved pressure field around the tunnel openings.

The inlet and outlet of the new bow tunnel design have a wing shape cross section. This wing shape is defined by 5 parameters, see figure 3. The parameters are used to vary in wing shape cross section and compare performance of different wing shapes. The diameters D_L and D_R are varied. All wing shapes have equal area, which is also the area of the circular shape, and this results in L_{LR}. The center of area is taken similar as the center of area of the circular shape, resulting in L_R. The total length is limited to fit in three web frames of the vessel.

The bow thruster tunnel is modelled with a beveled edge (figure 6: yellow). At the centerline of the ship, the profile of the tunnel is circular, an envelope to the end shape (normal or wing) is made.

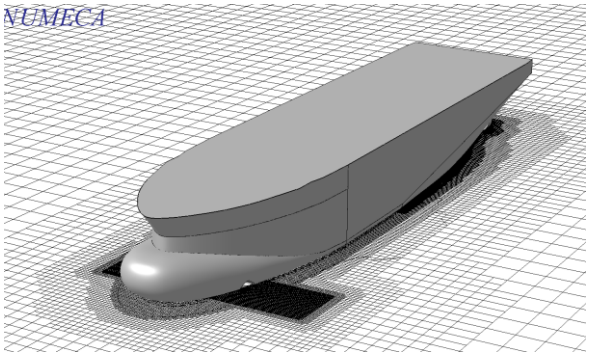

Fig 5: Cut-plane of mesh at centerline bow tunnel in z-direction.

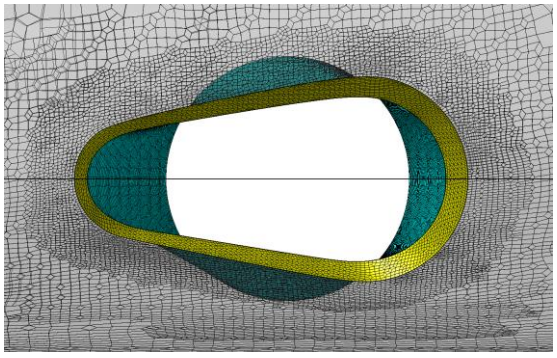

Fig 6: Detail of bow tunnel with beveled edge.

Domain size

With the whole body modelled the domain size is chosen. Relative low speeds of vessel, global mesh moves with ship coordinate system. The length of the domain is taken at 6L (1.5 L before vessel), the width 4L and the height 2L (1.5 L water and 0.5 L air), this is in line with [1].

Mesh setting
Mesh refinement is applied by surface refinement on the ship surfaces, refinement box around the bow tunnel area and free surface refinement. Free surface refinement is done with standard diffusion setting but with limited min(dz) because the maximum change in wave height is very limited (max(|dz|)/T = 0.046).

Grid Study with AGR
A mesh convergence study is done with adaptive grid refinement (AGR) and with the pressure Hessian refinement criterion. The refinement sector is set to the entire hull below the waterline. In the study the target cell size and the threshold are varied for finer meshes. The initial mesh has 6M cells and final number of cells are limited to <20M. The wall function is used in the boundary layer and only refinement in tangential direction is allowed [4].
In preliminary computations it was noted that for vs=4knots the circular shape was converging most difficult. So this case is taken in the grid study.

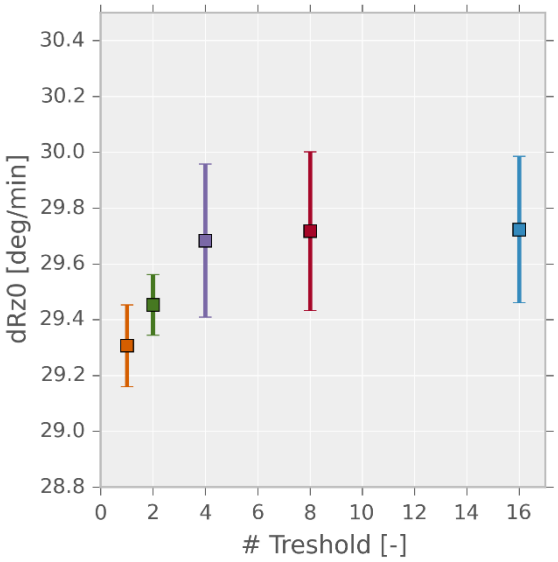

Fig 7: Errorbar presents St.Dev.(dRz0). The minimum cell size is 0.10 m.

Grid triplet	p	GCI
1-2-16	0.921	5.86
1-2-8	1.279	4.47
1-2-4	2.608	2.66
1-4-16	-2.78	
1-4-8	-2.41	
1-8-16	-4.54	
2-4-8	-6.39	
2-4-16	-6.78	
2-8-16	-8.84	
4-8-16	-13.53	

Table 1: Order of convergence for grid triplets based on treshold

We want a uniform refinement ratio between the grid triplet used in the Richardson Extrapolation. Which is not the case in most triplets, and *p* is negative. Grid triplet 1-2-8 has best uniform ratio and this lead to order of convergence of 0.921 and GCI=4.47% with safety factor Fs=3.0. Grid triplet 1-2-16 is second best (close to 1-2-8) and leads to GCI=5.86.
The time step is based on ship and tunnel parameters, dt = 0.4 sec. This is a compromise in order to get reasonable solved yaw rate within computational limits. Solely based on flow behavior in tunnel and tunnel length, dt = 0.06-0.10 sec. Time steps have been varied but showed no significant change in the turning rate (dRz0) for smaller time steps.
Total numerical uncertainty is defined by round-off error, iteration error and discretization error. From the unsteady simulation an error arises which now is defined by the standard deviation of the last 10% of the result. For this study the numerical uncertainty is calculated with the spatial discretization error and the unsteady error.

Wall function
The viscous forces on the body are calculated with the wall function. The application of the first layer thickness is split in two parts: 1) the ship surface itself (Lref = Lpp, vref=vx), 2) tunnel (Ltunnel, v_max tunnel). V_max in tunnel is estimated from earlier computations.

Turbulence model
In this study the k-w SST Menter model is used and results are time averaged for engineering purposes. The flow in and out of the tunnel is perpendicular to the forward motion of the vessel and it is expected that there is a significant amount of turbulence.

4. Computational setup and strategy

A computation strategy is applied which ensures reasonable computation times. In order to do more parametric variations of the tunnel shape, most of the computation will be done without AGR. These results are calculated with base case settings and from the most promising shapes the AGR will be applied and plotted with the estimated uncertainty.
The measured points of the IMO 2.6.2 bow thruster capability (see Fig. 4) test show the heading of the vessel. However, these are no steady-state conditions, since the vessel is still accelerating. To do a comparable analysis between different tunnel geometries, in CFD the forward speed is taken constant and the heading and rotational speed are calculated until it converges to a constant rotational speed (dRz0) of the vessel. This is repeated for different forward speeds.
Global axis are defined for the domain, the ship turns around the z-axis. In order to impose the forward motion of the vessel a dynamic library is applied which relates the forward motion of the vessel in the global axis. In the tunnel an Actuator Disk is set at the center plane (y=0) for bow thrust towards portside of the ship.

5. CFD results

For the parametric variation computations the forces and motions are evaluated from the converged part of the computation. The mean value of the last 10% of dRz0 is plotted.
From figures 8 and 9 the shapes which are most promising are wing08000800 with equal diameters and wing07000850 and wing06000950 with unequal diameters. These shapes perform better than the circular shape at slow forward speed.

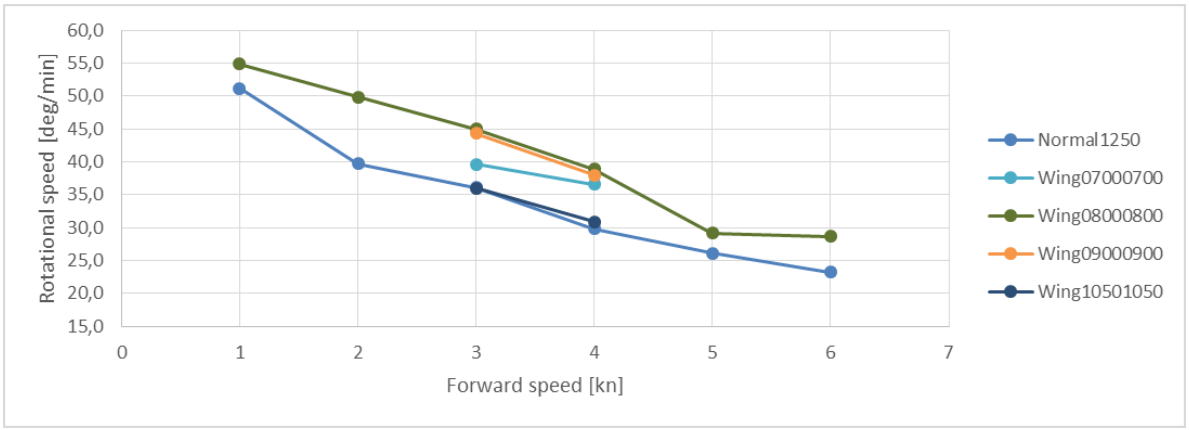

Fig 8: Dr=Dl, parametric variation of wing shape

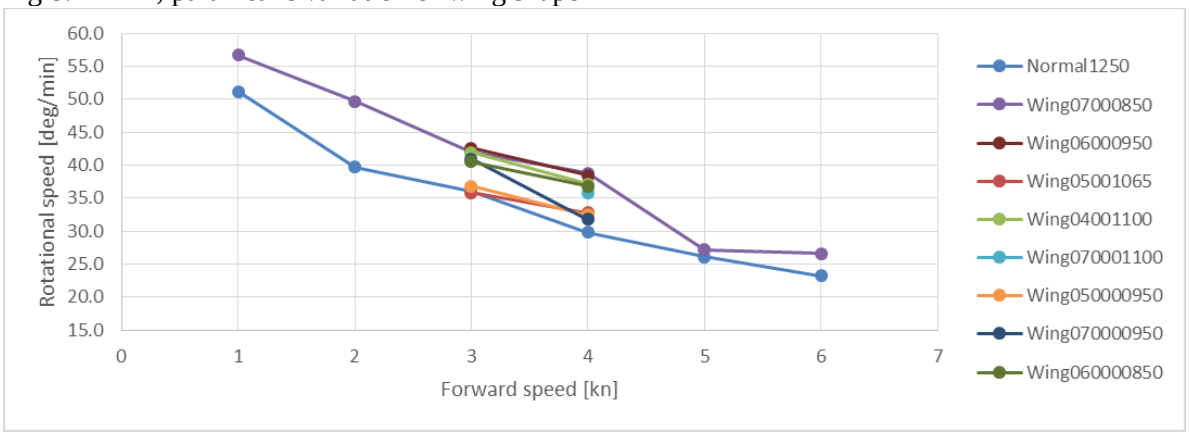

Fig 9: Dr<> Dl, parametric variation of wing shape

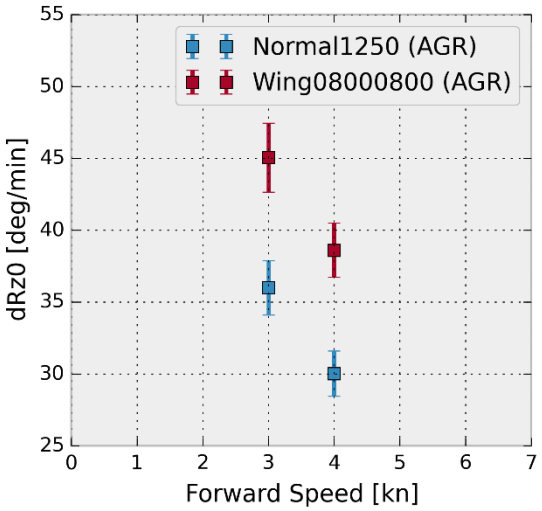

Fig 10: Errorbar indicates the spatial discretization error and the unsteady error.

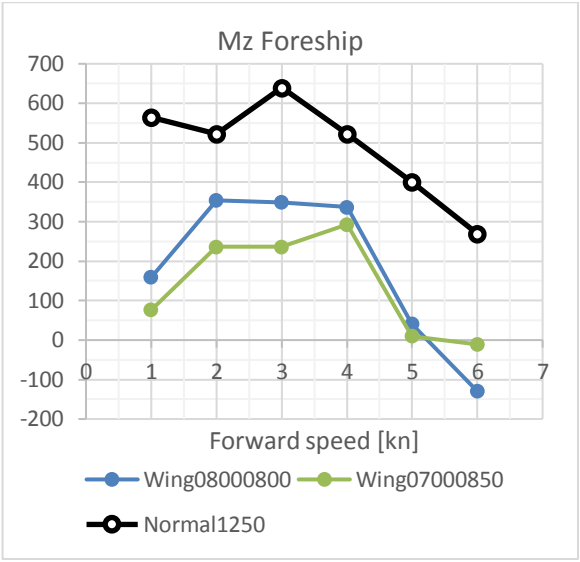

Fig 11: Moment around z-axis caused by forces on foreship. Positive moment is resistance for dRz0 in this setup.

In figure 10 the errorbars are plotted for the circular and one of the best wing shapes. Although the uncertainty is relatively high the difference between performance for 3-4 knots is big enough to see that the wing shape is performing better than circular shape.

The total moment on the ship around Lpp/2 is constant over the speed range. There is an equilibrium with the force from the actuator disk in the bow channel. In this case a positive moment on the foreship is felt as resistance for the yaw motion. The moments on the foreship for wing shapes are significant lower than for the circular shape (fig.11). The highest Mz(foreship) are found at 2-4 knots.

The moment on the foreship consists of a viscous part and a pressure part. The latter has a significant part in the moment around z-axis and is important around the openings [2],[3]. A negative pressure peak near the tunnel outlet has an opposed force to the turning motion dRz0. The idea of the wing shape is to reduce the negative pressure peak and thus improving turning ability in slow forward condition. For the wing shape with equal diameter (fig. 13) the negative pressure behind the outlet is much lower than for the circular shape (fig.12).

The viscous force in the tunnel are higher for wing shapes. This is caused by the increased wetted area and the higher velocities in the tunnel for the wing shape.

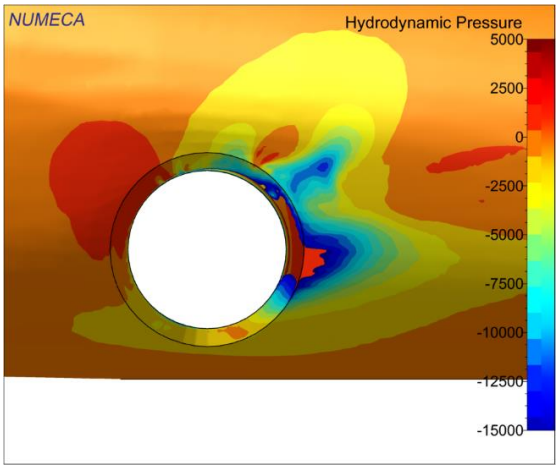

Fig 12: Outlet of circular shape (vs=4kn). Negative pressure is resistance for dRz0.

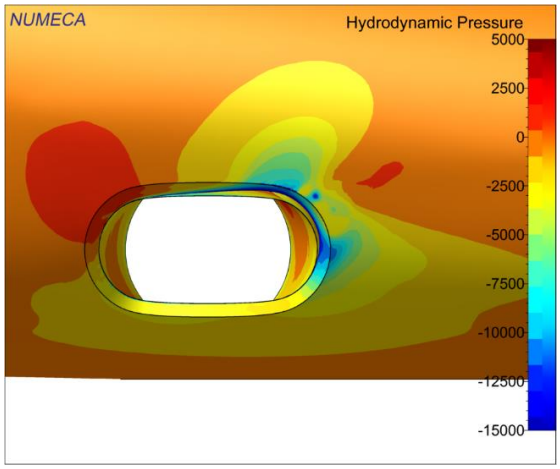

Fig 13: Outlet of wing shape (vs=4kn).

The strong negative pressure can also influence the suction of air when the openings of the bow tunnel are near the free-surface. Which is common for a TSHD in empty condition. Reducing the pressure can reduce the change of suction of air in to the tunnel.

For two shapes the fluxes are calculated through a plane (figure 15) which is defined perpendicular to the y-axis and is shifted along the y-axis. The forward speed and the thrust settings are the same for both shapes. In figure 14 it can be seen that the wing shape has a stronger flux along the y-axis. The flow out of the wing shape is more concentrated and is less affected by the cross flow due to the forward motion of the ship.

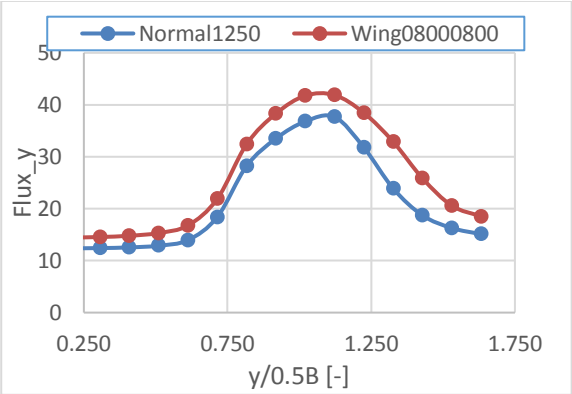

Fig 14: Flux through plane perpendicular to y-axis at outlet of tunnel (portside).

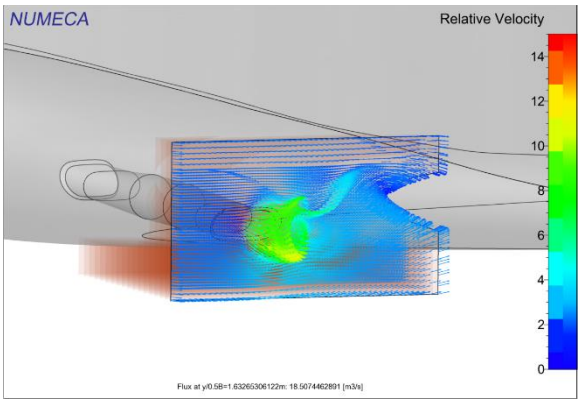

Fig 15: Vertical cut-plane with relative velocity vectors.

6. Conclusions and future work

A full-scale CFD comparison is made between a circular and other wing shape bow thruster tunnel. The wing shape tunnel showed improved performance at slow forward speed compared to the normal circular shape. Reduced negative pressure peak aft of the tunnel outlet is found for the wing shape. Results also show an increased flux through the tunnel and out of the tunnel for the wing shape compared to the circular shape. The diameters of the wing shapes have been varied. Best results are found with wing diameters of approx. 60-70% of original circular tunnel diameter for this trailing suction hopper dredger. Additional research would focus on the angle of the tunnel outlet, computations with 2 bow tunnels and the influence on the forward speed resistance. And other operating conditions like shallow water and empty condition are also of interest. In order to get a better understanding of the quantative results an unsteady setup would be interesting for comparison with steady results. And modelling of the hub and grid bars and actual geometry of propeller, so cavitation and suction of air into the tunnel can be investigated.

7. References

[1] International Towing Tank Conference (2017). “Recommended Procedures and Guidelines – Guideline un Use of RANS Tools for Manoeuvring Prediction”

[2] U. Nienhuis (1992). Analysis of thruster effectivity for dynamic positioning and low speed manoeuvring. Ph.D. thesis. Delft University of Technology, Delft, the Netherlands

[3] T. Schaap (2015). Changing the cross-sectional geometry of a bow tunnel thruster - Effects on the performance of the thruster at slow forward motion using CFD. Master Thesis. Delft University of Technology, Faculty of Mechanical, Maritime and Materials Engineering

[4] G. Deng, A. Leroyer, E. Guilmineau, P. Queutey, M. Visonneau, J. Wackers (2016) .Unstructured Grid Convergence Study. Journal of Applied Mathematics and Physics.

Surrogate Model for Ship Resistance: a Sensitivity Analysis of Shape Deformation

Antonio Coppedè*, Stefano Gaggero*, Giuliano Vernengo* and Diego Villa*
*Dept. of Electric, Electronic, Telecommunication Engineering and Naval Architecture (DITEN), University of Genova, 16145, Italy
antoniocoppede@gmail.com, stefano.gaggero@unige.it, giuliano.vernengo@unige.it, diego.villa@unige.it

1 Introduction

Shape optimization and sensitivity can now be considered a standard to design efficient ships and new unconventional hull forms. There might be very different strategies to achieve such a process, depending on many circumstances, both operational (e.g. available time windows for computations) and methodological (e.g. available numerical methods). As in most of the engineering cases, the best trade-off between accuracy of the solution and the time required to achieve it is searched. When using medium-fidelity methods e.g. Boundary Element Methods (BEMs) for wave resistance and seakeeping, population based optimization algorithm can still be a viable way to achieve a design solution (see e.g. Vernengo et al., 2015 or Vernengo and Brizzolara, 2017). However, when the solution of the quantity of interest becomes more demanding, alternative methods of searching through the design space are needed. In this perspective, a surrogate model based approach for hull form sensitivity analysis is presented. The method relies on the features of a Kriging response surface (see for instance Forrester et al., 2008) to interpolate few computed solutions and to predict the same solution over the whole explored domain. The sensitivity analysis focuses on the effect of hull form variations with respect to calm water resistance at a given forward speed. The total ship resistance is computed by means of a high-fidelity viscous solver based on the *openFOAM* libraries (Jasak et al., 2007). The shape variations are achieved by a combined approach specifically developed to preserve the fairness of the hull surface based on *Subdivision Surface* and *Free Form Deformation* (FFD) (Coppedé et al., 2018).
The hydrodynamic solver has been preliminary validated by comparison against available experimental measurements on the KRISO Container Ship (KCS) hull. The variation of the Kriging response surface performance with respect to different sizes of the initial sampling have been studied and possible optimum hull shape have been detected and compared in terms of calm water resistance, wave patterns and pressure on the surface.

2 Framework

The three main tools on which the framework for calm water resistance surrogate model generation relies on are described in the following sections.

2.1 Hull shape generation and variation

According to the combined approach proposed by Coppedé et al., 2018, the hull surface has been first generated by using the *QuadTri* Subdivision Surface algorithm (Stam and Loop, 2003). Based on an initial control polygon, made of both triangular and quadratic elements, this algorithm provides a smooth surface by a recursive subdivision of the initial control polygon itself. The final surface mesh is represented by a unique watertight patch. As a first result, this surface can be easily linked to numerical solvers avoiding conversion that might cause further unwanted geometric deviations. However, for complex hull forms e.g. with bulbows bow and stern skeg, such a surface is typically generated by using a relatively large number of control points. Since variations are in principle obtained by changing the three cartesian coordinates of those control points, this usually results in too many free parameters to be managed in the context of an optimization/exploration problem. Similarly to what have been proposed by Peri and Campana, 2003, in order to overcome this issue, FFD transformations (see Sederberg and Parry, 1986) have been applied to the control points of the Subdivision Surface rather than directly on the hull surface. Such an approach ensures the limit surface of the hull to be recreated by the *QuadTri* algorithm after each shape variation, hence excluding possible discontinuities or excessive

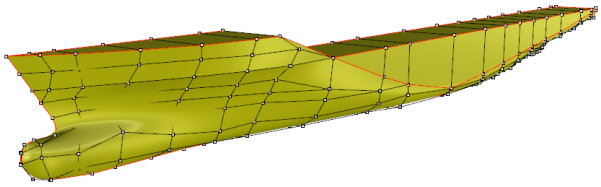

Fig. 1: KCS hull with Subdivsion Surface control polygon, where the red line describes the crease edges.

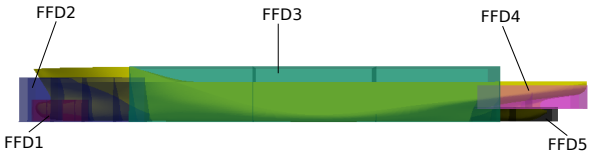

Fig. 2: Original Hull of the Kriso Container Ship (KCS) with five Free Form Deformation control volumes.

deformations of the patches. Moreover, by following this method the number of free parameters controlling the shape is drastically reduced, being the FFD transformations themselves the free variables of the optimization process.
The original KCS hull with its control polygon is represented in Figure 1 while the created FFD boxes are shown in Figure 2. This five boxes are designed to achieve both local and global shape variations. The FFD1 and FFD5 are designed for local variations of the bulbous bow and of the skeg, respectively. The FFD2 transformation acts on the bow hull shape while the FFD4 is defined over the upper stern rise. The FFD3 is instead used to modify a relatively long longitudinal part of the hull by moving afterward and forward the volume of the parallel body in a Lackemby's transformation fashion (Lackenby, 1950). In order to further simplify the deformation process the number of free parameters is reduced to seven by using analytic functions for FFD points variations. Hence, some selected control points of each FFD volume are modified at the same time according to the laws imposed by these mathematical functions.

2.2 High-fidelity CFD resistance computation

An open source viscous based RANS solver has been used to compute the calm water resistance of the ship. By using such a high-fidelity solver the influence on resistance of both global and local shape variations can be taken into account. The selected solver has already been proven to ensure reliable predictions of the KCS resistance (see among the other Gaggero et al., 2017, Villa et al., 2011 and Larsson et al., 2015). Results of the validation in terms of comparison between experimental and numerical total resistance coefficient C_T, sinkage and trim, respectively, are reported in Table 1. The hull surface and the domain have been discretized by using about 1.5 ML cells with specific refinements of the free surface close to the hull over a region where the wave field is supposed to propagate.
The comparison shows that the numerical prediction of the total resistance is in good agreement with the experimental measurements, especially in the range of higher speeds ($F_N > 0.2$) for which the relative error is less than 2%. At lower speeds ($F_N < 0.2$), the agreement is still very good but the error rise up to 5%. In all the tested cases such a relative error is lower than the experimental uncertainty, as shown in Figure 3. Running attitude of the ship are also well predicted as displayed in the comparison of the drafts at the aft and forward perpendicular, respectively.
Since each simulation run for about 30 hours on a 24 cores work-station a mesh coarsening analysis has been carried out in order to check the feasibility of using a lower number of elements, i.e. to reduce the computational burden while keeping a good accuracy of the solution. So other two coarsening levels have been considered, namely the Coarse L_1 mesh having 0.8 ML cells and the Coarse L_2 made of 0.4 ML cells. The CPU time required for the solution with the coarser mesh is five time lower compared to that needed with the finer mesh. Rather than an usual mesh sensitivity analysis based on the reference KCS hull, figure 4 displays the variation of the computed resistance obtained by using the three meshes

on 30 hull variations achieved by the combined approach above described. Since the design by optimization is focused on local shape variations it is crucial to verify the monotonicity of predictions at different discretization levels, being optimization designs based on reliable comparative analyses more than on absolute results. Each simulation has been performed at the same displacement, ensuring the static equilibrium condition (i.e. both longitudinal and vertical equilibrium) by proper rotation and translation of the hull. Except for two cases, the predicted values of the resistance are bounded within a small range of variation.

In addition the wave profiles at $y/L_{PP} = 0.2$ for the original hull computed by using the three meshes are shown in Figure 5. Throws and crests are predicted in the same location showing minor differences in terms of wave amplitude. This is a further confirmation that the coarser mesh can be used for the proposed sensitivity study since the analysis is mainly focused on the comparison of the solutions.

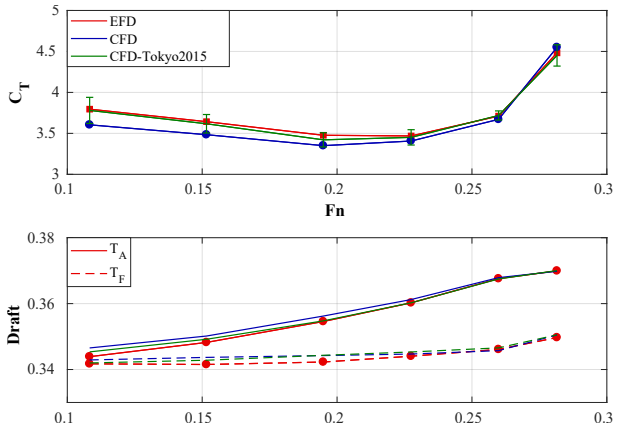

Fig. 3: Comparison of present CFD predictions (blue line) among EFD measurements (red line) and average CFD prediction reported in the Tokyo 2015 workshop (green line).

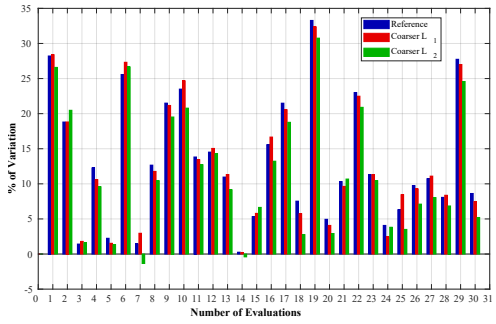

Fig. 4: Comparison of the hull drag trend (% of reference case) for 30 hull shape variations for reference (blue), Coarse L1 (red) and Coarse L2 (green) mesh densities.

Table 1: Comparison between experimental measurements (EFD) and numerical results (CFD) for the KCS test case

Model test		EFD			CFD		
Speed [m/s]	Fn	$C_T \cdot 10^3$	Sink [cm]	Trim [deg]	$C_T \cdot 10^3$	Sink [cm]	Trim [deg]
0.915	0.108	3.795	-0.089	-0.017	3.604	-0.274	-0.028
1.281	0.152	3.643	-0.273	-0.053	3.484	-0.478	-0.051
1.647	0.195	3.477	-0.599	-0.097	3.350	-0.781	-0.094
1.922	0.228	3.469	-0.950	-0.127	3.406	-1.031	-0.130
2.196	0.260	3.711	-1.394	-0.169	3.671	-1.386	-0.174
2.379	0.282	4.483	-1.698	-0.159	4.550	-1.736	-0.152

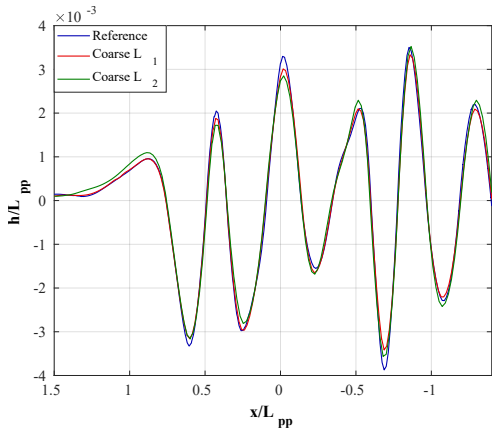

Fig. 5: Non-dimensional wave elevation for a longitudinal profile at y/L_{PP}=0.2.

3 Sensitivity analysis by Kriging response surface

The analysis of the size of the sampling on the performance of the Kriging response surface has been performed by using three sets of designs, made of 30, 60 and 120 geometries respectively. Two Cross-Validation methods have been applied to evaluate the prediction capabilities of the three surrogate models, namely the so-called *Leave-One-Out* (LOO) and the *k-fold* (see for instance Forrester et al., 2008). According to the *K-fold* model the DoE in divided into k subset. Each subset is then discarded from the generation of the surrogate model and the prediction error is evaluated by comparing the value obtained by the model with respect to the original value. This process is repeated for all the k subsets and the mean error of all k is finally computed. The LOO method can be considered as a particular case of a *k-fold* with $k = 1$, i.e. one design at the time is discard from the initial sampling. For both methods, the correlation coefficient and the Root Mean Squared Error (RMSE) are computed according to Eq. (1) and Eq. (2), respectively:

$$R^2 = \left(\frac{cov\left(\mathbf{r}, \widehat{\mathbf{r}}\right)}{\sqrt{var(\mathbf{r}) var(\widehat{\mathbf{r}})}} \right)^2 \tag{1}$$

$$RMSE = \sqrt{\frac{\sum_{i=1}^{n} \left(r_i - \widehat{r_i}\right)^2}{n}} \tag{2}$$

Results of this cross-validation are reported in Table 2. All the three surrogate models show good prediction capabilities having $R^2 > 0.8$ and $RMSE < 10\%$, respectively. As indicated by the increase of the R^2 and by the corresponding decrease of the $RMSE$, the accuracy of the Kriging model is increased for larger sampling.

The global *minima* of the three models have been searched by means of a classic genetic algorithm (GA) in order to avoid possible local optimal designs. Compared to the original KCS hull, the three designs achieve resistance reductions in the extent of 5.9%, 6.1% and 6.3% for the model with the lowest sampling size up to that with the larger one, respectively. Figure 6 displays the location of the three optimal designs on sub-spaces of the Kriging model based on the larger sampling (120 designs). Each sub-space is defined in the plane of two of the seven parameters at a time. The other five parameters are kept at

Table 2: Results of the LOO and *k-fold* cross validations of the three Kriging models.

Parameter	$KR_{\#30}$	$KR_{\#60}$	$KR_{\#120}$
R^2_{LOO}	0.947	0.948	0.973
$RMSE_{LOO}$	0.0887	0.0846	0.0462
R^2_{k-fold}	0.871	0.898	0.965
$RMSE_{k-fold}$	0.0838	0.0817	0.0542

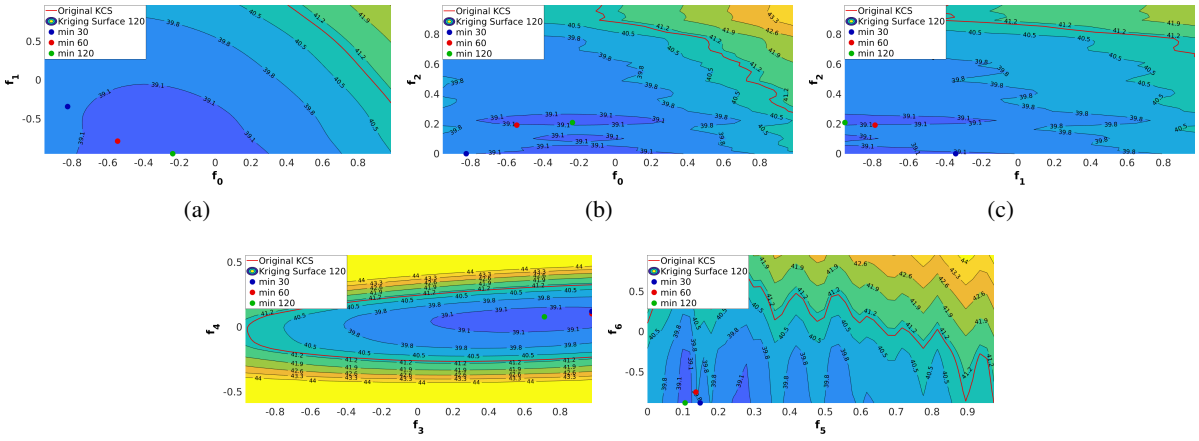

Fig. 6: Kriging surface generated with 120 design, the red contour of the original KCS and the projection of the three minimum obtained for all three model

the value corresponding to the optimum design of the Kriging with the largest sampling size. It is worth noting that the optimum designs for the first two surrogate models do not exactly lay on the presented planes, since they belong to different surfaces, hence to different combinations of the parameters. The three Kriging surrogate model provides different optimum designs since the three points are locate at different positions on each sub-space. The wave patterns of the three selected hull surfaces are compared to those of the original KCS hull in Figure 7 while Figure 8 displays the pressures over the three optimum hulls from the corresponding surrogate models. As expected both the wave patterns and the pressure distributions are very close one to the other. This is mainly due to the fact that neither the length at the design waterline of the ship or the length of the bulb have been significantly changed. Despite this, a common trend can be detected for all the three designed hulls. In particular, the wave pattern is slightly anticipated. The first divergent wave generated by the bulb of the optimized shape (red contours) propagates away from the hull with a higher local crest. It decays faster moving backwards towards the hull forward shoulder. In turn, also the divergent waves created at the forward shoulder is anticipated. This phase lag is kept in the far field wave pattern too. The optimized hulls produces lower waves aft of the transom stern. Those little variations are partially seen also on the dynamic pressures on the hulls.

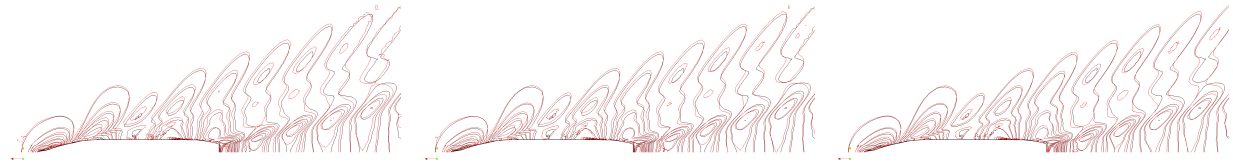

Fig. 7: Comparison of the wave patterns generated by the three selected hulls. Black one corresponds to the original KCS hull.

4 Conclusions

A surrogate model based sensitivity analysis of hull shape variations with respect to total resistance has been presented. A Kriging response surface has been used to predict the calm water resistance of the KCS hull subject to several geometric changes. The hull form variations have been achieved by means of a combined approach based on Subdivision Surface and Free Form Deformation. The effect of the size of the initial sampling on the performance of the surrogate model has been studied. Three sampling sizes

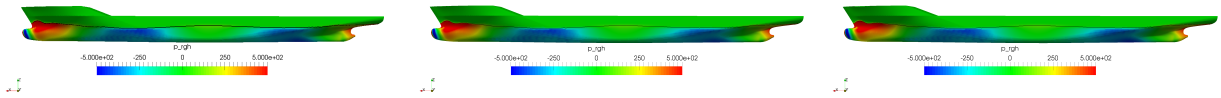

(a) (b) (c)

Fig. 8: Comparison of the dynamic pressures on the three selected hulls.

have been considered, namely 30, 60 and 120 designs.
Cross-validation on the three surrogate models shows that all the response surfaces have good prediction capabilities. However, the three optimum points on each surface have different combination of the design parameters. This highlight the fact that the size of the initial sampling affect the shape of the surrogate model and, in turn, the choice of the final best solution.
Further studies on ad-hoc infilling strategies will be performed since there is not a clear trend of the increase of the sampling size with respect to the accuracy of the solution.

References

Coppedé, A., Vernengo, G., and Villa, D. (2018). A combined approach based on subdivision surface and free form deformation for smart ship hull form design and variation. *Ships and Offshore Structures*.

Forrester, A., Keane, A., et al. (2008). *Engineering design via surrogate modelling: a practical guide*. John Wiley & Sons.

Gaggero, S., Villa, D., and Viviani, M. (2017). An extensive analysis of numerical ship self-propulsion prediction via a coupled bem/rans approach. *Applied Ocean Research*, 66:55–78.

Jasak, H., Jemcov, A., and Tukovic, Z. (2007). Openfoam: A c++ library for complex physics simulations. In *International workshop on coupled methods in numerical dynamics*, volume 1000, pages 1–20. IUC Dubrovnik, Croatia.

Lackenby, H. (1950). On the systematic geometrical variation of ship forms. *Trans INA*, 92:289–316.

Larsson, L., Stern, F., Visonneau, M., Hirata, N., Hino, T., and Kim, J. (2015). Tokyo 2015: A workshop on cfd in ship hydrodynamics. In *Proceedings of the Tokio 2015 Workshop - A Workshop on CFD in Ship Hydrodynamics*, volume 2, pages 1–1.

Peri, D. and Campana, E. F. (2003). Multidisciplinary design optimization of a naval surface combatant. *Journal of Ship Research*, 47(1):1–12.

Sederberg, T. W. and Parry, S. R. (1986). Free-form deformation of solid geometric models. *ACM SIGGRAPH computer graphics*, 20(4):151–160.

Stam, J. and Loop, C. (2003). Quad/triangle subdivision. In *Computer Graphics Forum*, volume 22, pages 79–85. Wiley Online Library.

Vernengo, G. and Brizzolara, S. (2017). Numerical investigation on the hydrodynamic performance of fast swaths with optimum canted struts arrangements. *Applied Ocean Research*, 63:76–89.

Vernengo, G., Brizzolara, S., Bruzzone, D., et al. (2015). Resistance and seakeeping optimization of a fast multihull passenger ferry. *International Journal of Offshore and Polar Engineering*, 25(01):26–34.

Villa, D., Gaggero, S., and Brizzolara, S. (2011). Simulation of ship in self propulsion with different CFD methods: From actuator disk to potential flow/RANS coupled solvers. In *RINA, Royal Institution of Naval Architects - Developments in Marine CFD, Papers*, pages 1–12.

A Review on the Application of OpenFOAM's Mesh Motion Techniques to Wave-Structure Interaction Problems

Griet Decorte and Jaak Monbaliu
KU Leuven, Department of Civil Engineering, Kasteelpark Arenberg 40, 3001 Heverlee, Belgium
(griet.decorte@kuleuven.be, jaak.monbaliu@kuleuven.be)

1 Introduction

Mesh motion is of key importance in assuring adequate CFD modelling of wave-structure interaction problems, such as wave impact on floating offshore wind turbines and seakeeping of ships. Not seldomly wave forcing leads to large displacements of the (floating) structures the waves are interacting with. As a consequence, the fluid domain boundaries need to move in order to accommodate for these wave-induced displacements. The mesh quality needs to be preserved at all times to guarantee accurate and stable results for the solid body displacements as well as for the fluid variables. The fluid domain mesh needs to adapt to its deforming boundaries. Because the displacements of the fluid-structure interfaces are a priori unknown and as such a result of the solution itself, the mesh motion needs to be done automatically.
The literature dealing with automatic mesh motion handling is extensive. During the last decade, some of these methods have been implemented in the powerful open-source CFD toolbox OpenFOAM. This paper attempts to give a comprehensive overview of these methods as implemented in OpenFOAM as well as highlights their advantages and shortcomings concerning excessive mesh motion and extreme wave modelling through comparison for a free decay reference case and an extreme wave loading case.

2 Short literature review: automatic mesh motion handling in OpenFOAM

Based on their implementation in OpenFOAM, these automatic mesh motion handling techniques can be roughly divided into three main categories; Arbitrary Lagrangian-Eulerian (ALE) methods, overset (Chimera) methods and immersed boundary method. A comprehensive scheme is shown in Figure 1.

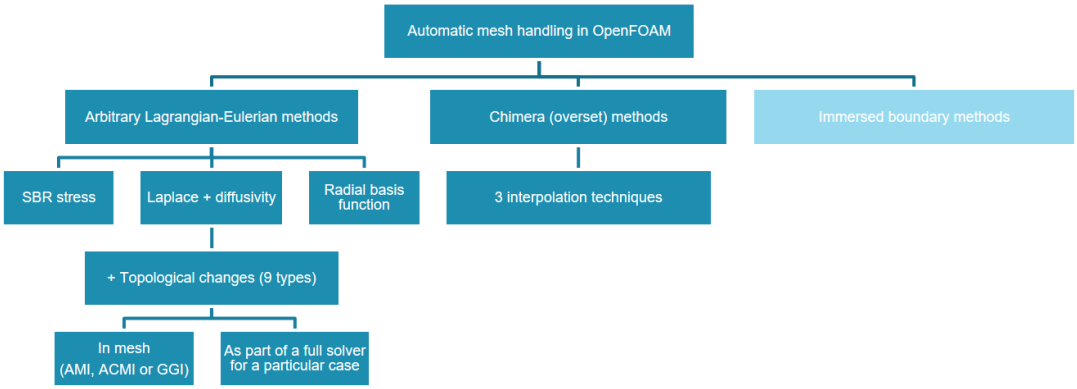

Fig. 1: A comprehensive oversight of mesh motion handling in OpenFOAM.

The most obvious way of dealing with mesh motion is through an *Arbitrary Lagrangian-Eulerian method*. In order to accurately describe the boundary motion as well as allowing for the fluid motion on the (fixed) internal grid, an Arbitrary Lagrangian-Eulerian (ALE) form of the conservation equations in combination with a Space Conservation Law (SCL) is adopted. It prevents creating an extra source term and thus generating large errors. (Demirdžić and Perić, 1988, 1990). By doing so, essentially, a Lagrangian approach is applied at the moving boundary, while the internal domain is described by an Eulerian approach.
ALE necessitates an automatic mesh displacement algorithm to get the (fluid) grid velocities well-suited to the problem under consideration. Ideally, this is done through potential type equations or interpolations (Donea et al., 2004). As shown in Figure 1, three methods are currently implemented in OpenFOAM: the solid-body rotational stress method (SBR-stress), which adopts a pseudo-solid approach and assumes

static equilibrium for small deformations of a linear elastic solid with solid body rotation added, the radial basis function method (RBF), which allows for large rotations through a local radial basis and the Laplacian with an expression for the diffusivity depending on a chosen diffusivity model and distance from the moving boundary (Bos, 2009)(OpenCFD, 2018).
Because of its high accuracy and its discretisation error being comparible to static meshes, ALE methods are the go-to option for small displacements. Unfortunately, in the case of large boundary deformation, the mesh deteriorates, giving rise to stability problems and loss of accuracy. Note that the RBF technique by Bos (2009) mentioned earlier, allows for large rotations, but ultimately also leads to distorted meshes. In case of large displacements, it might be more appropriate to also apply topological changes.
Topological changes are used to change the mesh resolution and connectivity, using sliding interfaces, cell layering and similar techniques. In OpenFOAM, nine operations exist of which a full list can be found in OpenCFD (2018). For the sake of consistency, these operations are ideally bundled, either as part of a specific topology changing solver, either as part of a boundary patch, e.g. cyclicA(C)MI in OpenFOAM or GGI in Foam-Extend.
When confronted with excessive mesh motion, *Chimera (overset) methods* are by far the most versatile technique. In this technique, two meshes are created initially. A fixed mesh is used for the background, while the overset mesh, which is allowed to move relatively to the background mesh, is connected to the moving object. The conservation equations on the background mesh are written in Eulerian description. At each time step, the fluid forces are calculated and the body motion is updated. Based on this body motion, the overset mesh is moved and the new addressing, i.e. which cells are calculated, interpolated or blocked in the upcoming interpolation, is determined. Subsequently, the moved object is mapped onto the background mesh. Finally, the fluid variables are computed on both meshes. This method can even be combined with a deforming mesh method in the overlapping mesh. This is interesting in case the structure consists of a flexible part. The rigid body motion can be dealt with by the overset method, while the deformation is dealt with by deformation in the moving mesh only. Although this method has merits, non-conservative mapping leads to large mapping errors and thus necessitates high resolution meshes. Also, the currently three implemented mapping methods are extremely slow.
The last method is the *immersed boundary method*. In this method, the grid is fixed in space and covers both the fluid and the moving structure, which is allowed to move with respect to the fixed grid (Dooms, 2009). In the immersed boundary method, a Dirac delta function is introduced as a body force in the Eulerian formulated conservation equations. This body force only differs from one at the fluid-structure interface. As the structure moves, the fluid elements covering the structure continuously change. This method has already been applied as part of OpenFOAM's PISO loop by Constant et al. (2017). Because this method does not allow for mesh refinement close to the structure and thus not allows for accurate boundary layer simulation, this method is often not well-suited for the considered applications. It was added for completeness and will not be discussed further.

3 Model Description

The fluid motion is described by the Navier-Stokes equations, which are solved by a PIMPLE algorithm (in PISO form). In order to deal with the two-phase water-air nature of the considered problem, the fluid solver has been supplied with a volume-of-fluid (VoF) method. This is readily available within OpenFOAM's native interFoam solver. In order to solve for rigid body motion and its corresponding mesh motion, the interFoam solver has been extended with the sixDoFMotionSolver to interDyMFoam (OpenCFD, 2018) for the ALE method and overInterDyMFoam for the overset method. The program lay-out is shown in Figure 2.
Owing to the discussed problem, waves will have to be adequately generated and absorbed. To this end, interDyMFoam and overInterDyMFoam have been extended by the wave generation/absorption toolbox olaFoam, which is an evolution of the IHFOAM toolbox developed by Higuera et al. (2013), to respectively olaDyMFoam and overOlaDyMFoam. This toolbox adopts an active wave generation/absorption approach, which is closely related to the way waves are generated in state-of-the-art waves basins as well as computationally efficient compared to the similar approaches based on numerical sponge layers.

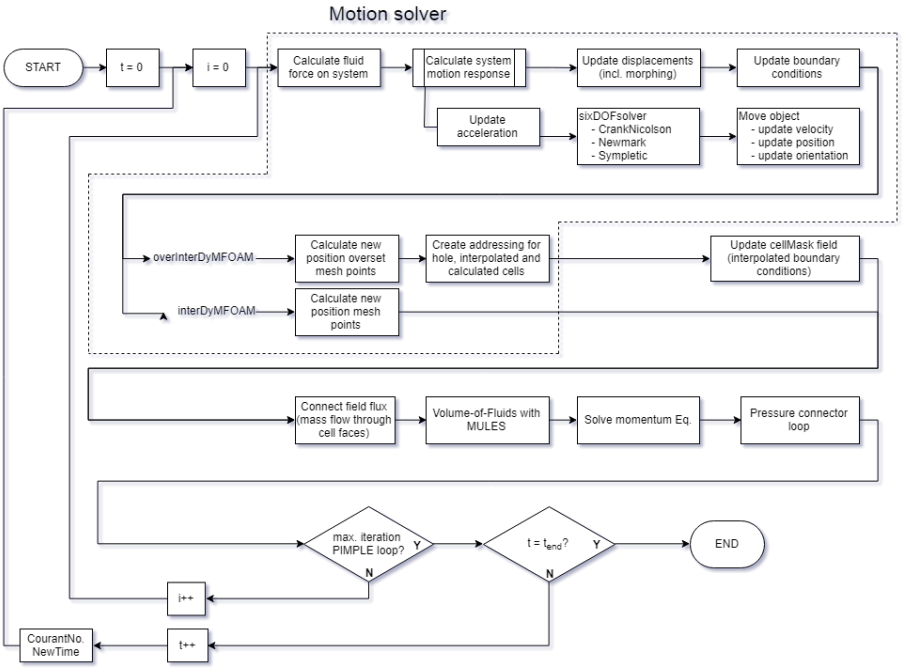

Fig. 2: Program lay-out for olaDyMFoam and overOlaDyMFoam.

4 Test cases

In order to assess the suitability of the previously mentioned approaches, two numerical examples will be simulated.
Firstly, the reference case for a freely heaving horizontal cylinder by Maskell and Ursell (1970) will be used to validate the solvers and make a first comparison. In Figure 3, the 2-D meshes used for this case are shown. The maximum cell size about the waterline of the 2-D meshes amounts to $D/20$. The cylinder has a diameter D of 0.1524m and has been displaced by 0.00615m above the water line. Reflection of the radiated waves at the left and right boundary is prevented by applying the 2-D active absorption boundary condition included in the olaFOAM toolbox by Higuera et al. (2013).

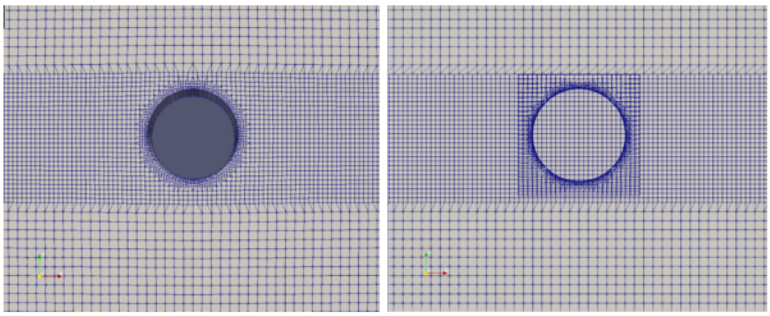

Fig. 3: 2-D meshes for the Maskell and Ursell (1970) reference case (left: ALE, right: Overset).

Next, both approaches will be used to simulate the response of a vertical cylinder to a 2nd order Stokes wave and as such assess the ability of both solvers to deal with large motion and extreme waves. As can be seen in Figure 4, only half of the cylinder (and the fluid domain) has been modelled in order to save up on computation time.

The diameter of the cylinder is again 0.1524m and the cell sizes around the water line are respectively $L/100$ in the x-direction and $H/100$ in the y-direction as determined by a convergence study. At the inlet, the wave generation/absorption boundary condition by Higuera et al. (2013), which generates a 2nd order

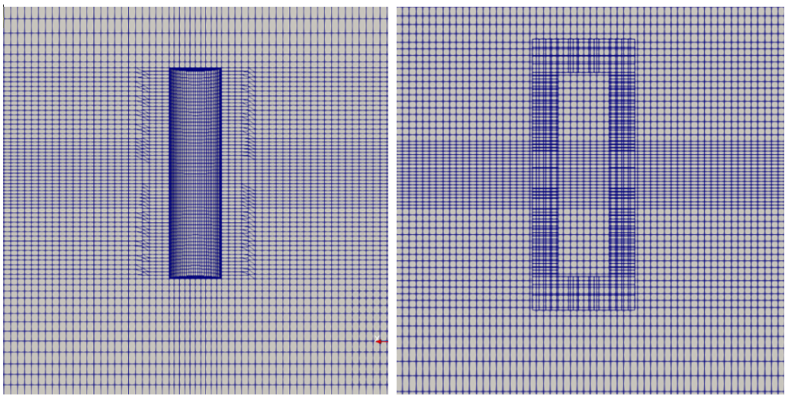

Fig. 4: 3-D meshes for the 2nd order Stokes wave case (left: ALE, right: Overset).

Stokes wave with a wave height H of 0.1m, a wave period T of 1.2s and a wave length L of 2.24m, has been applied, while at the outlet the 2-D active absorption boundary condition is used to reduce reflection.

5 Results and Discussion

The results for the free decay case are shown in Figure 5. In this figure, the heave Z normalized by the initial displacement Z_0 is depicted as a function of the normalized time $t\sqrt{g/a}$, where g is the gravitational acceleration and a is the cylinder radius, and shown on the left. On the right, the corresponding acceleration is also shown as a function of the normalized time.

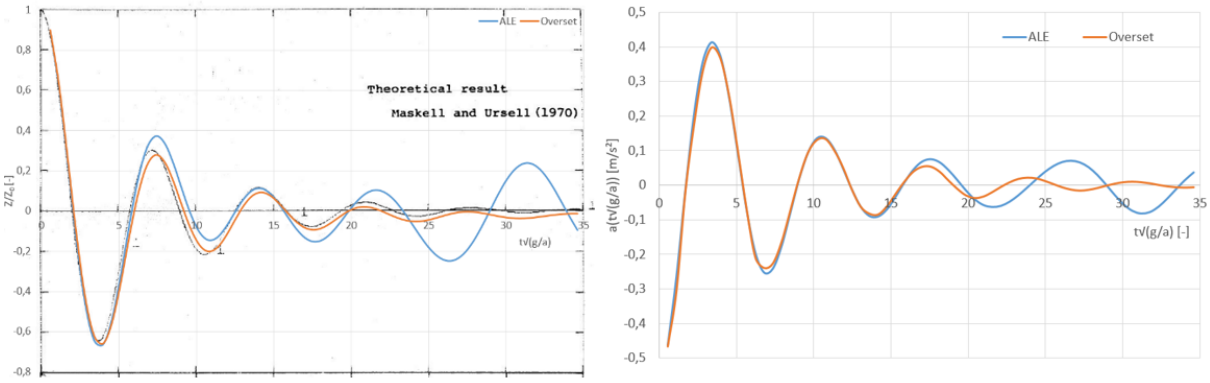

Fig. 5: Results for the Maskell and Ursell (1970) reference case (left: relative vertical position Z/Z_0, right: acceleration a).

As can be seen from the left figure, notwithstanding a small offset with respect to the rest position of the cylinder, the overset approach seems to perform better than the ALE strategy. The order of magnitude of this offset is comparable to the cell size and can be attributed to the interpolation of the body motion on the background mesh.
The ALE mesh motion approach seems to perform reasonably well until time step 15, after which the solution diverges from the numerical result by Maskell and Ursell (1970). This was originally thought to be due to the weakly coupled partitioned fluid/6DoF-solver applied herein. Causin et al. (2005) and Förster et al. (2006) state that the loosely coupled partitioned fluid/6DoF-solver implemented in OpenFOAM introduces an artificial added mass into the solution independent of the used discretization scheme.
In order to nihilate the effect of this non-physical added mass, late OpenFOAM implementations adapt an under-relaxation technique as part of their acceleration update in their 6DoF-solver. Also, several discretization schemes have been made available in order to solve the 6DoF motion, e.g. a CrankNicolson-scheme, a Newmark scheme and a symplectic scheme. In the under-relaxation method and the sixDoFsolver, two new parameters have to be chosen, an acceleration damping, a fixed reduction on the

acceleration in the velocity update, and an acceleration relaxation. Both are recommended by the OpenFOAM documentation to be in the range 0.9-1.0 (OpenCFD, 2018).
When looking at the expressions of the under-relaxation technique in Equation1, this actually means that almost no relaxation is applied.

$$a_i = a_{relax}.a_i + (1 - a_{relax}) .a_{i-1} \tag{1}$$

Therefore, a smaller acceleration relaxation of 0.5 was adopted. Unfortunately, this change in acceleration relaxation did not show a significant improvement compared to the original results with an acceleration relaxation of 0.95. Only a change of mesh resolved the issue in the end. The stability of the ALE method seems to be strongly dependent on the mesh. This is a logical result, as mesh deformation leads to poor meshes.
Although the overset simulation was done with the same original value for the acceleration relaxation and a similar mesh, the result complied well with the results by Maskell and Ursell (1970). The reason probably lies within the overset strategy itself. After each motion update, the dynamic overset mesh solver determines the new position of the overset mesh as well as identifies the addressing of the calculated, interpolated and hole, i.e. blocked by the presence of the structure, cells. The displaced cells of the overset mesh are subsequently interpolated onto the background mesh. This interpolation, inverseDistance, is non-conservative, thus introducing conservation errors strongly dependent on the adopted mesh resolution (Völkner et al., 2017). Notwithstanding these conservation errors, which are here rather small due to the fine mesh resolution, the overset seems to be more robust towards mesh choice as the mesh is not distorted.
This can also been seen in the case where a vertical cylinder underwent wave forcing by a 2nd order Stokes wave. In Figure 6, the results for both approaches are shown.

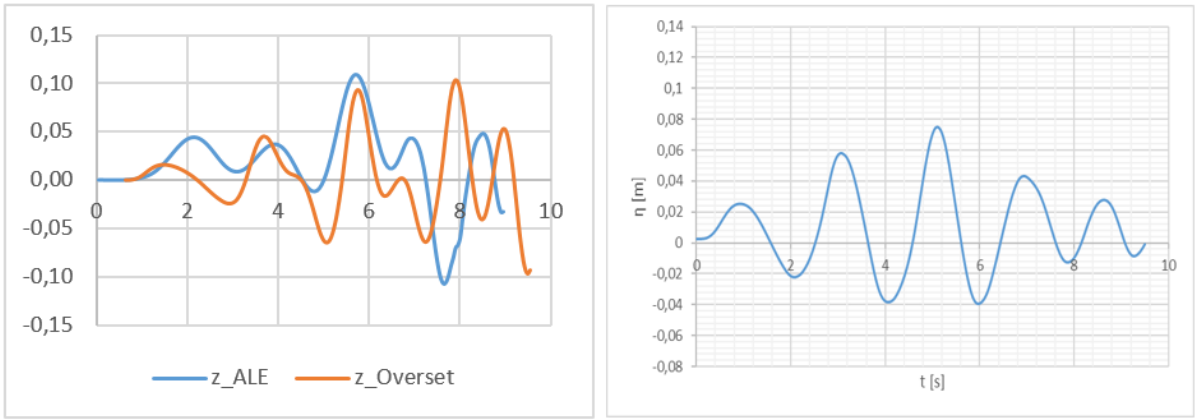

Fig. 6: Results for the 2nd Order wave case (left: heave motion, right: wave captured at 3m before the cylinder.

Notwithstanding the small oscillations during the first time steps, probably due to the large wave components introduced by initiating the 2nd-Order Stokes wave, the response by the overset approach seems to be physically sound. The wave period of the Stokes wave (1.2s) was chosen slightly smaller the eigenfrequency of the vertical cylinder (1.25s). When the wave approaches, the cylinder follows the wave up and the cylinder is displaced from its equilibrium. Because the peaks are sharper and the troughs are longer, the cylinder tries to carry out its free decay motion in between peaks, hence the peak followed by a bump. The ALE approach does not simulate this well, but for one wave period. Due to the large displacement, the mesh becomes too distorted for the ALE approach to simulate the body motion well.

6 Conclusion and further work

Based on the two test cases, the ALE approach seems to be extremely sensitive to mesh distortion and thus mesh choice. New cases need to be systematically validated.

When using a fine resolution, overset meshes perform well, even capturing extreme wave events, such as the 2nd order wave response. Unfortunately, in this simulation, the computation time for the overset method was about 10 times higher compared to the ALE method due to its costly interpolation, therefore rendering it quite expensive for long runs.
It would be interesting to find out if the ALE approach combined with a strong coupling for the body motion/fluid solver as done by Dunbar et al. (2015) and/or topological changes such as sliders, would be less costly than the overset approach and more robust than the original ALE strategy.

Acknowledgements

The Research Foundation - Flanders, Belgium (FWO) is gratefully acknowledged for the funding grant.

References

Bos, F. (2009). *Numerical simulation of flapping foil and wing aerodynamics: Mesh deformation using radial basis functions*. PhD thesis, Technical University Delft.

Causin, P., Gerbeau, J.-F., and Nobile, F. (2005). Added-mass effect in the design of partitioned algorithms for fluid–structure problems. *Computer methods in applied mechanics and engineering*, 194(42-44):4506–4527.

Constant, E., Favier, J., Meldi, M., Meliga, P., and Serre, E. (2017). An immersed boundary method in openfoam: Verification and validation. *Computers & Fluids*, 157:55–72.

Demirdžić, I. and Perić, M. (1988). Space conservation law in finite volume calculations of fluid flow. *International journal for numerical methods in fluids*, 8(9):1037–1050.

Demirdžić, I. and Perić, M. (1990). Finite volume method for prediction of fluid flow in arbitrarily shaped domains with moving boundaries. *International Journal for Numerical Methods in Fluids*, 10(7):771–790.

Donea, J., Huerta, A., Ponthot, J.-P., and Rodriguez-Ferran, A. (2004). Encyclopedia of computational mechanics vol. 1: Fundamentals., chapter 14: Arbitrary lagrangian-eulerian methods.

Dooms, D. (2009). Fluid-structure interaction applied to flexible silo constructions. *Katholieke universiteit Leuven.*, pages 17–33.

Dunbar, A. J., Craven, B. A., and Paterson, E. G. (2015). Development and validation of a tightly coupled cfd/6-dof solver for simulating floating offshore wind turbine platforms. *Ocean Engineering*, 110:98–105.

Förster, C., Wall, W. A., and Ramm, E. (2006). The artificial added mass effect in sequential staggered fluid-structure interaction algorithms. In *ECCOMAS CFD 2006: Proceedings of the European Conference on Computational Fluid Dynamics, Egmond aan Zee, The Netherlands, September 5-8, 2006*. Delft University of Technology; European Community on Computational Methods in Applied Sciences (ECCOMAS).

Higuera, P., Lara, J. L., and Losada, I. J. (2013). Realistic wave generation and active wave absorption for navier–stokes models: Application to openfoam®. *Coastal Engineering*, 71:102–118.

Maskell, S. and Ursell, F. (1970). The transient motion of a floating body. *Journal of Fluid Mechanics*, 44(2):303–313.

OpenCFD (2018). Openfoam user guide.

Völkner, S., Brunswig, J., and Rung, T. (2017). Analysis of non-conservative interpolation techniques in overset grid finite-volume methods. *Computers & Fluids*, 148:39–55.

An Iterative Fitting Method for 2D Supercritical Steady Free Surface Flow

Toon Demeester[*], **E. Harald van Brummelen**[†], **Joris Degroote**[*,‡]
[*]Ghent University, Belgium
[†]Eindhoven University of Technology, the Netherlands
[‡]Flanders Make, Belgium
toon.demeester@ugent.be

1 Introduction

Computational methods to simulate incompressible, viscous water-air flows around ships can be divided in two categories: surface capturing and surface fitting methods. Capturing methods reconstruct the position of the free surface. An example is the volume-of-fluid method. In fitting methods the mesh lies along the free surface and deforms with it, so that its position is always known exactly. The air phase is often neglected, leading to one phase flow with free surface boundary conditions. The dynamic boundary condition (DBC) requires continuity of the stresses, but it is often assumed that the shear stresses are zero so that the DBC reduces to a condition of constant pressure at the free surface. The kinetic boundary condition (KBC) requires that the free surface is impermeable. For steady flows this means that the velocity must be parallel to the surface.

It is not possible to apply both these conditions to the free surface simultaneously. For this reason fitting methods are iterative techniques consisting of two steps: first the flow field is calculated with a fixed free surface position and suitable boundary conditions, then the free surface position is updated. These steps are repeated until the KBC and DBC are met to the required precision. For steady free surface flows, two clearly different fitting methodologies can be found in literature. The first one uses the DBC in the first step and the KBC in the second (Tzabiras (1997); Muzaferija and Perić (1997)). Using the KBC for updating the surface results in a time-stepping method, which is not efficient for steady cases due to the large number of time steps before transient phenomena disappear. The second methodology uses a combined boundary condition (KBC + DBC) in the flow solver and the DBC for the surface update. This *steady iterative* method by van Brummelen et al. (2001) is efficient but requires a dedicated coupled flow solver, making it less flexible.

This paper proposes a 2D fitting method which combines a steady iterative approach with a black-box flow solver. This requires that the boundary conditions in the flow solver are easy to implement (only KBC) and that the update procedure is time-independent (only DBC). Section 2 describes the theory, Section 3 the numerical results and Section 4 the conclusion.

2 Theory

Some notations are first introduced. Arrays are distinguished from scalars by the use of bold symbols ($\boldsymbol{z}$ versus z). A superscript (usually k) is used to denote the iteration index of the fitting method. Differences between values from consecutive iterations are written as $\Delta \boldsymbol{z}^k = \boldsymbol{z}^{k+1} - \boldsymbol{z}^k$.

2.1 Perturbation analysis

Before deriving the new fitting method, a basic free surface flow is investigated to better comprehend the nature of the problem at hand. The solution of an inviscid flow over a horizontal plate (see Fig. 1) is a flat free surface: for any depth h, the free surface pressure $\boldsymbol{p}$ will be constant (DBC) and the streamlines parallel to the surface (KBC). If the height $\boldsymbol{y}$ of the surface is perturbed with an arbitrary $\Delta \boldsymbol{y}$, the pressure will change with a certain $\Delta \boldsymbol{p}$. The relation between these two was derived by Demeester et al. (2017) for small perturbations. The conclusions are summarized here.

The free surface height is perturbed with

$$\Delta \boldsymbol{y} = a \sin\left(k\boldsymbol{x} + \theta\right) \tag{1}$$

where $k = 2\pi/\lambda$ is the wavenumber, θ an arbitrary phase angle and the amplitude a small relative to λ

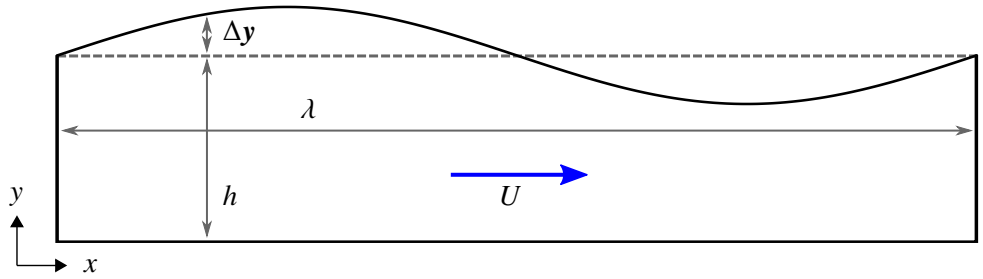

Fig. 1: Flow over a horizontal plate with perturbation $\Delta \boldsymbol{y}$.

and h. The pressure perturbation $\Delta \boldsymbol{p}$ then follows from a proportional relation:

$$\Delta \boldsymbol{p} = L\, \Delta \boldsymbol{y} \qquad \text{with} \qquad L = \rho g \left(\mathrm{Fr}^2 \frac{kh}{\tanh kh} - 1 \right). \tag{2}$$

ρ is the fluid density, g the gravitational acceleration and $\mathrm{Fr} = U/\sqrt{gh}$ the Froude number based on the depth h and the average flow velocity U. Eq. (2) is graphically shown in Fig. 2 as a function of the dimensionless groups kh and Fr. For clarity $1/L$ is plotted instead of L. An asymptote splits the domain in a region where gravitational forces dominate the flow (lower left corner) and a region where inertial forces dominate. At the asymptote (where $1/L \to \pm\infty$ or $L \to 0$), the opposing effects of gravity and inertia on $\Delta \boldsymbol{p}$ balance each outer out. If L is set to zero in Eq. (2), the dispersion relation for gravitational waves is found (neglecting surface tension, Johnson (1997)). As a consequence, waves with $L = 0$ have their phase velocity equal to the average flow velocity U, so that they appear stationary. These so-called *steady gravity waves* are solutions of the linearized free surface problem and have $\Delta \boldsymbol{p} = 0$ for a non-zero $\Delta \boldsymbol{y}$. L can be zero only if the flow is subcritical ($\mathrm{Fr} < 1$). In that case no unique $\boldsymbol{y}$ exists for a given $\boldsymbol{p}$. As this complicates the construction of a free surface fitting method, only supercritical flow ($\mathrm{Fr} > 1$) is treated in this paper.

2.2 Surrogate model

The free surface flow over a horizontal plate as described in Section 2.1 can also be simulated with a CFD solver, returning the free surface pressure perturbation $\Delta \boldsymbol{p}$ for an arbitrary height perturbation $\Delta \boldsymbol{y}$. In this section, a surrogate model will be constructed which approximates the behavior of this CFD solver.

Consider a numerical simulation where the free surface is discretized in the x-direction with n equidistant points, with the y-values collected in an array $\boldsymbol{y} \in \mathbb{R}^{n,1}$. It is assumed that these points are ordered from inlet to outlet, i.e. $\boldsymbol{y}(0)$ and $\boldsymbol{y}(n-1)$ are respectively the free surface heights at inlet and outlet of the domain. The height $\boldsymbol{y}$ is now perturbed with an arbitrary (not necessarily small) $\Delta \boldsymbol{y}$, which can be decomposed into n Fourier modes: a constant mode, `floor(n/2)` cosine modes and `floor((n-1)/2)` sine modes. It is assumed that for each[1] mode Eq. (2) is approximately valid, so that the corresponding $\Delta \boldsymbol{p} \in \mathbb{R}^{n,1}$ can be estimated. This operation can be written in matrix form as

$$\Delta \boldsymbol{p} = \boldsymbol{F}\, \Delta \boldsymbol{y} = \sum_{j=0}^{n-1} L_j\, \boldsymbol{\Phi}_j\, \Delta \boldsymbol{y} \qquad \text{with} \qquad \boldsymbol{\Phi}_j = \phi_j\, \phi_j^T \tag{3}$$

where ϕ_j is the normalized basis vector for Fourier mode j and L_j the corresponding factor from Eq. (2).

If there is a difference between inlet and outlet height, erroneous high frequency components appear in the Fourier decomposition. The solution is to subtract a sawtooth wave such that inlet and outlet heights become equal. The sawtooth is considered to have frequency zero (it is multiplied with L_0), instead of being decomposed into a spectrum of low and high frequencies. The sawtooth is identified by

[1] For the constant mode it is assumed that $\lambda \to \infty$ or $k \to 0$ so that $L_0 = \lim_{k \to 0} L = \rho g \left(\mathrm{Fr}^2 - 1 \right)$.

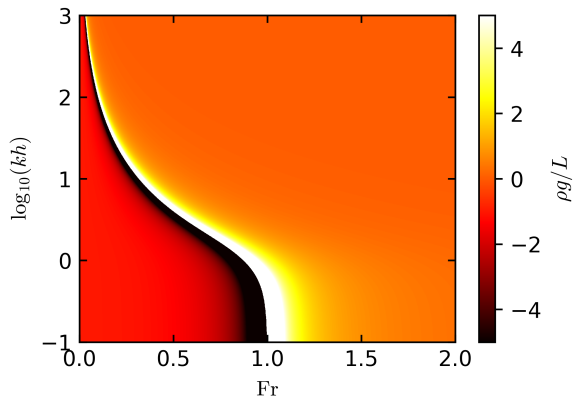

Fig. 2: $1/L$ as a function of Fr and kh.

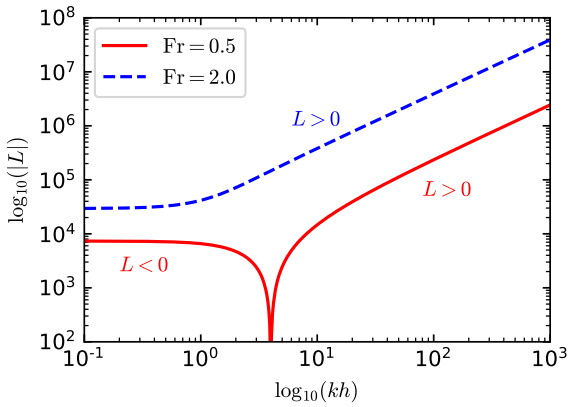

Fig. 3: $|L|$ as a function of kh for Fr = 0.5 (subcritical) and Fr = 2.0 (supercritical).

multiplying $\Delta \boldsymbol{y}$ with the matrix

$$\boldsymbol{\Phi}_t = \begin{bmatrix} \frac{1}{2} & 0 & \cdots & 0 & -\frac{1}{2} \\ \vdots & \vdots & & \vdots & \vdots \\ \frac{1}{2} - \frac{i}{n-1} & 0 & & 0 & \frac{i}{n-1} - \frac{1}{2} \\ \vdots & \vdots & & \vdots & \vdots \\ -\frac{1}{2} & 0 & \cdots & 0 & \frac{1}{2} \end{bmatrix} \tag{4}$$

where $\boldsymbol{\Phi}_t \in \mathbb{R}^{n,n}$ and i is the row index. Eq. (3) is accordingly adapted to

$$\Delta \boldsymbol{p} = \boldsymbol{F}_t \, \Delta \boldsymbol{y} \qquad \text{with} \qquad \boldsymbol{F}_t = L_0 \, \boldsymbol{\Phi}_t + \boldsymbol{F} \, (\boldsymbol{I}_n - \boldsymbol{\Phi}_t) \, . \tag{5}$$

The matrix $\boldsymbol{F}_t$ serves as a surrogate model for simulations of flow over a horizontal plate. Assuming perturbations of any 2D free surface flow behave similarly to those of flow over a horizontal plate, $\boldsymbol{F}_t$ can be used as a surrogate model for a variety of cases, although it will likely be less accurate then.

2.3 Free surface fitting method

The free surface problem is now stated more precisely, using the same free surface discretization as in the previous section ($\boldsymbol{y}, \boldsymbol{p} \in \mathbb{R}^{n,1}$ and uniformly distributed):

> given a black-box flow solver $\boldsymbol{\mathcal{G}}(\boldsymbol{y}) = \boldsymbol{p}$ which fulfills the KBC,
> find $\boldsymbol{y}$ so that $\boldsymbol{p} = p_{cst}\mathbf{1}$ and $\boldsymbol{y}(0) = y_0$.

The KBC is fulfilled by using a free-slip wall in the flow solver. It is assumed that the function $\boldsymbol{\mathcal{G}}$ is a bijection[2], i.e. with each $\boldsymbol{y}$ corresponds a unique $\boldsymbol{p}$ and vice-versa. As $\boldsymbol{p}$ can be equal to an arbitrary constant p_{cst} ($\mathbf{1}$ is the all-ones array), a condition on the inlet $\boldsymbol{y}(0)$ has to be added to close the system and assure uniqueness of the solution $\boldsymbol{y}$. The value of p_{cst} is not of interest and can be removed from the problem by filtering out the constant mode (average value). With $\boldsymbol{p}_\emptyset = (\boldsymbol{I}_n - \boldsymbol{\Phi}_0) \, \boldsymbol{p}$ and $\boldsymbol{\mathcal{F}} = (\boldsymbol{I}_n - \boldsymbol{\Phi}_0) \, \boldsymbol{\mathcal{G}}$ the free surface problem becomes:

> given a black-box flow solver $\boldsymbol{\mathcal{F}}(\boldsymbol{y}) = \boldsymbol{p}_\emptyset$ which fulfills the KBC,
> find $\boldsymbol{y}$ so that $\boldsymbol{p}_\emptyset = 0$ and $\boldsymbol{y}(0) = y_0$.

This problem has to be solved iteratively: in each iteration k the flowfield is solved by calling $\boldsymbol{\mathcal{F}}$, then the new position $\boldsymbol{y}^{k+1} = \boldsymbol{y}^k + \Delta \boldsymbol{y}^k$ is calculated and the mesh updated accordingly. Newton's method can be used to calculated $\Delta \boldsymbol{y}^k$ as

$$\boldsymbol{\mathcal{F}}' \, \Delta \boldsymbol{y}^k = -\boldsymbol{p}_\emptyset^k \tag{6}$$

[2]There is no strict proof that the non-linear black-box $\boldsymbol{\mathcal{G}}$ is bijective, but the linear model for an inviscid flow clearly is for Fr > 1 (see Eq. 3 and Fig. 3)

with $\mathcal{F}'$ the Jacobian of $\mathcal{F}$. As the flow solver is a black-box, its Jacobian is not known, but an approximation $\widehat{\mathcal{F}'}$ can be used. Rewriting the inlet condition, a linear system emerges to calculate $\Delta \boldsymbol{y}^k$:

$$\begin{cases} \widehat{\mathcal{F}'} \Delta \boldsymbol{y}^k = -\boldsymbol{p}_\emptyset^k \\ \Delta \boldsymbol{y}^k(0) = y_0 - \boldsymbol{y}^k(0) \end{cases} \tag{7}$$

The surrogate model $\boldsymbol{F}_t$ from Eq. (5) is used in a first approximation to $\mathcal{F}'$:

$$\widehat{\mathcal{F}'_{pert}} = (\boldsymbol{I}_n - \Phi_0)\boldsymbol{F}_t \tag{8}$$

To stabilize and accelerate the iterations, a second approximation for $\mathcal{F}'$ is constructed using the IQN-ILS algorithm by Degroote et al. (2009). This is used in fluid-structure-interaction to improve convergence of coupling iterations. The idea is to use known input-output pairs of a black-box system to construct a better approximation of its Jacobian than is available at that moment. In this case, the input of the black-box $\mathcal{F}$ is $\boldsymbol{y}$, the output $\boldsymbol{p}_\emptyset$. Differences between consecutive iterations are stored in the matrices

$$\boldsymbol{V}^k = \begin{bmatrix} \Delta \boldsymbol{y}^{k-1} & \cdots & \Delta \boldsymbol{y}^0 \end{bmatrix}, \tag{9}$$

$$\boldsymbol{W}^k = \begin{bmatrix} \Delta \boldsymbol{p}_\emptyset^{k-1} & \cdots & \Delta \boldsymbol{p}_\emptyset^0 \end{bmatrix} \tag{10}$$

from which an approximate Jacobian is constructed as

$$\widehat{\mathcal{F}'}_{IQN}^k = \boldsymbol{W}^k \boldsymbol{R}^{k-1} \boldsymbol{Q}^{kT} \qquad \text{with} \qquad \boldsymbol{V}^k = \boldsymbol{Q}^k \boldsymbol{R}^k \quad \text{(economy-size QR-decomposition).} \tag{11}$$

There are now two approximations of the Jacobian, which have to be combined. The Jacobian based on the perturbation analysis (Eq. (8)) is constant, the one based on IQN-ILS (Eq. (11)) changes in each iteration as the matrices $\boldsymbol{V}^k$ and $\boldsymbol{W}^k$ grow bigger. $\widehat{\mathcal{F}'_{IQN}}$ only affects the part of $\Delta \boldsymbol{y} \in \text{span}(\boldsymbol{V})$, which is extracted as $\boldsymbol{Q}^k \boldsymbol{Q}^{kT} \Delta \boldsymbol{y}$. $\widehat{\mathcal{F}'_{pert}}$ is used for the remaining part of $\Delta \boldsymbol{y}$.

The linear system to calculate $\Delta \boldsymbol{y}^k$ is

$$\begin{cases} \widehat{\mathcal{F}'}^k \Delta \boldsymbol{y}^k = -\boldsymbol{p}_\emptyset^k \\ \Delta \boldsymbol{y}^k(0) = y_0 - \boldsymbol{y}^k(0) \end{cases} \tag{12}$$

with

$$\widehat{\mathcal{F}'}^k = \widehat{\mathcal{F}'}_{IQN}^k \boldsymbol{Q}^k \boldsymbol{Q}^{kT} + \widehat{\mathcal{F}'_{pert}} \left(\boldsymbol{I}_n - \boldsymbol{Q}^k \boldsymbol{Q}^{kT} \right) \tag{13}$$

$$= \boldsymbol{W}^k \boldsymbol{R}^{k-1} \boldsymbol{Q}^{kT} + (\boldsymbol{I}_n - \boldsymbol{\Phi_0}) \boldsymbol{F}_t \left(\boldsymbol{I}_n - \boldsymbol{Q}^k \boldsymbol{Q}^{kT} \right). \tag{14}$$

The Jacobian approximation $\widehat{\mathcal{F}'}$ has rank $n - 1$, because the constant mode is not part of its column space. By adding the inlet condition, the system in Eq. (12) with n unknowns becomes rank n and has a unique solution. However, as it has $n + 1$ equations for n unknowns it must be solved with a least-squares method.

Algorithm 1 outlines the fitting method. For compactness the left-hand side matrix and right-hand side array of Eq. (12) are denoted respectively by $\boldsymbol{A}^k \in \mathbb{R}^{n+1,n}$ and $\boldsymbol{b}^k \in \mathbb{R}^{n+1,1}$, so that the system can be written in the form $\boldsymbol{A}^k \Delta \boldsymbol{y}^k = \boldsymbol{b}^k$.

3 Numerical experiments

The new method is tested on the academic test case of 2D flow over an obstacle as shown in Fig. 4 (flow from left to right). The experimental data was acquired by Cahouet (1984) and has been used in several papers for evaluating surface fitting methods (Tzabiras (1997); van Brummelen et al. (2001)). The shape of the obstacle is described by

$$y_{obst}(x) = \frac{27}{4} \frac{H}{L^3} x(x - L)^2 \qquad \text{for} \qquad 0 \leq x \leq L \tag{15}$$

Algorithm 1 Free surface fitting method.

$k = 0$
$\boldsymbol{p}_\emptyset^0 = \mathcal{F}\left(\boldsymbol{y}^0\right)$ ▷ $\mathcal{F} = (\boldsymbol{I}_n - \boldsymbol{\Phi}_0)\,\mathcal{G}$
while $\left\|\boldsymbol{p}_\emptyset^k\right\|_2 > \varepsilon$ **do**
  if $k > 0$ **then**
    construct $\boldsymbol{V}^k$, $\boldsymbol{W}^k$
    calculate QR-decomposition $\boldsymbol{V}^k = \boldsymbol{Q}^k \boldsymbol{R}^k$
  end if
  construct $\boldsymbol{A}^k$ and $\boldsymbol{b}^k$ ▷ $\boldsymbol{A}^k$ and $\boldsymbol{b}^k$ from Eq. (12)
  solve $\boldsymbol{A}^k \Delta \boldsymbol{y}^k = \boldsymbol{b}^k$ with least-squares
  $\boldsymbol{y}^{k+1} = \boldsymbol{y}^k + \Delta \boldsymbol{y}^k$
  $k = k + 1$
  $\boldsymbol{p}_\emptyset^k = \mathcal{F}\left(\boldsymbol{y}^k\right)$
end while

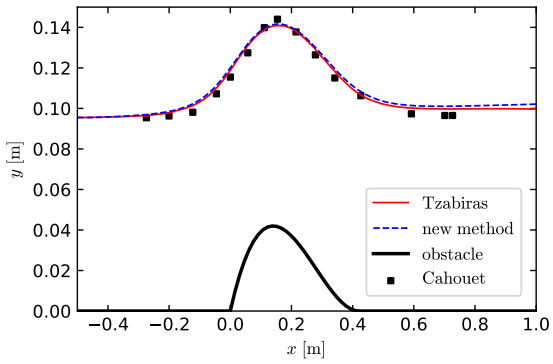

Fig. 4: Free surface height compared to experimental data from Cahouet (1984) and numerical data from Tzabiras (1997).

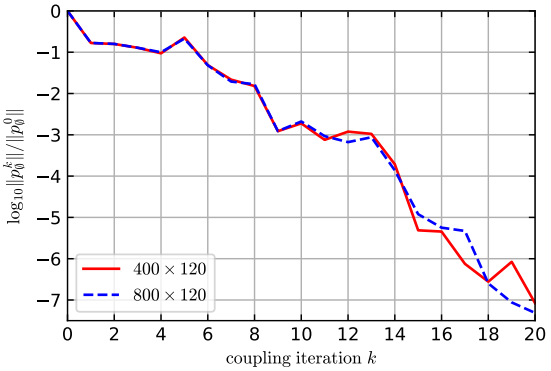

Fig. 5: Relative norm of free surface pressure $\boldsymbol{p}_\emptyset^k$ for two meshes.

where $H = 0.042$m is the height and $L = 0.42$m the length of the obstacle. The inlet water depth is 0.09545m, the Froude number is 2.05. From these two, the inlet velocity can be determined. Boundary conditions are a uniform inlet velocity, a hydrostatic pressure outlet, a free-slip wall at the free surface and a no-slip wall at the bottom. A structured mesh of 400×120 cells ($x \times y$) is used. Exponential growth is used at the bottom to resolve the boundary layer, giving $1 < y^+ < 5$. The standard $k - \epsilon$ model is used for turbulence modeling. To assess convergence of the fitting method, the pressure $\boldsymbol{p}_\emptyset$ at the free surface is monitored. The initial height $\boldsymbol{y}^0$ is a horizontal free surface.

Fig. 4 compares the new method to the experimental results by Cahouet (1984) and to the simulations by Tzabiras (1997), all results agree well. Fig. 5 shows the decrease of the free surface pressure $\boldsymbol{p}_\emptyset$ during the coupling iterations for the original mesh and for a mesh which is refined in the x-direction. Both converge 7 orders of magnitude in 20 iterations. No influence of the number of Fourier modes (i.e. the mesh size) can be seen.

The new method cannot easily be compared to the time-stepping method of Tzabiras (1997) in terms of speed due to a lack of data. The number of coupling iterations (i.e. surface updates) for a certain decrease in residual can be compared, but it must be kept in mind that the residual's definition is very different[3]. For a similar setup, the time-stepping method needed ~500 coupling iterations for the residual to decrease by one order of magnitude, compared to 20 iterations for 7 orders with the new method.

[3]In Tzabiras (1997), the DBC is used in the flow solver, so the residual is based on the KBC, i.e. the mass flow rate through the free surface.

4 Conclusion

A novel fitting method is introduced for 2D supercritical steady free surface flows, based on a perturbation analysis of the free surface. The method successfully combines a steady iterative approach with a black-box flow solver. The IQN-ILS technique is added to improve stability and accelerate convergence.

The method is compared to both experimental and numerical reference data and shows good correspondence. Convergence is reached in a small number of iterations and seems to be independent of mesh size. Currently the method is being extended to subcritical flows, after which it will be generalized to 3D.

References

Cahouet, J. (1984). *Etude numérique et expérimentale du problème bidimensionnel de la résistance de vagues non-linéaire*. Ecole nationale supérieure de techniques avançées.

Degroote, J., Bathe, K.-J., and Vierendeels, J. (2009). Performance of a new partitioned procedure versus a monolithic procedure in fluid–structure interaction. *Computers & Structures*, 87(11):793–801.

Demeester, T., Degroote, J., and Vierendeels, J. (2017). Stability analysis of a partitioned iterative method for steady free surface flow. *Journal of Computational Physics*.

Johnson, R. S. (1997). *A modern introduction to the mathematical theory of water waves*, volume 19. Cambridge University Press.

Muzaferija, S. and Perić, M. (1997). Computation of free-surface flows using the finite-volume method and moving grids. *Numerical Heat Transfer*, 32(4):369–384.

Tzabiras, G. (1997). A numerical investigation of 2D, steady free surface flows. *International Journal for Numerical Methods in Fluids*, 25(5):567–598.

van Brummelen, E., Raven, H., and Koren, B. (2001). Efficient numerical solution of steady free-surface Navier–Stokes flow. *Journal of Computational Physics*, 174(1):120–137.

TRACKING OF TIP VORTICES ARISING FROM MARINE STRUCTURES

Mahesh Dhone[1], Nikolai Kornev[1]
[1] *Faculty of Mechanical Engineering and Marine Technology, University of Rostock, Albert Einstein Str.-2, Rostock, 18059, Germany*
Email*: mahesh.dhone2@uni-rostock.de*

1. Introduction

The resolution of tip vortices by CFD is a huge challenge because of inherent numerical dissipation effects which lead to an unphysical strong decay of the vortices. In real world, these vortices stay for a longer time and distance until they are dissipated into the fluid. The tip vortices play a major role in marine engineering structures like propeller hydrodynamics. Tip vortices arising from ship and submarine propellers lead to cavitation which can generate noise and lead to erosion of surface of the rudder. It can even influence the forces acting on the rudder thereby disturbing the control dynamics of the ships. In CFD, the numerical errors are of mainly two types - discretisation errors and modeling errors. The accuracy of prediction of vortex resolution is also limited due to presence of imperfections in available mathematical models.

This work is focused on grid based methods and vortex methods for tracking the tip vortices in the far downstream until they decay. It is confirmed from the experimental investigation that the tip vortex sustain for a longer distance in the far wake which is a benchmark test conducted by Devenport et. al [1]. Several grid based refinement techniques and modeling approaches were applied using OpenFOAM code based on Finite Volume Method. Alternatively solution was obtained using domain decomposition approach by coupling of grid based and vortex methods. Results obtained are validated for tracking of the tip vortex in far downstream with the experimental data.

2. Experimental case

The experiment referred to is conducted by Devenport at Re 5.3 x 10^5 [1]. The experiment investigates the trailing of tip vortex shedding from a NACA0012 wing (A.R 8.66 and chord 0.2 m) at 5 deg angle of attack until far downstream i.e. 30 chords. The data is presented in the form of turbulence properties and tangential and axial velocities in the region of the vortex core. This experiment provides superior quality of data because it tracks the vortex in far wake and takes into account, the effect of vortex core wandering caused due to possible wing vibrations or instability.

3. Numerical Setup

3.1 Geometry Modeling

The computations were conducted using OpenFOAM - a Finite Volume based C++ code. The co-ordinate system and the computational domain is constructed to match the geometry of tunnel as in the experiment with the NACA0012 wing located at 1/3rd distance from the inlet and the origin at the leading edge of airfoil as seen from the Figure 1.

3.2 High Re number and Low Re number grid

In order to save computational effort, the domain is constructed using symmetric properties of the wing. There are two types of grid computed, high Re-number grid generated by ANSYS ICEM and low Re-number grid generated by SnappyHexMesh tool. The high Re-number grid starts with coarse 2.7 million grid cells which has finer resolution near the wing. By applying a special routine, the grid has been refined statically in the region in the vortex core by using two boxes. Every grid cell in the first box is subdivided into two cells until x/c 10, while in the second box into four cells until x/c 20 respectively. This arises to 7.2 million grid cells in total. (See Figure 1) Further refinement of the 7.2 million grid with same technique gives 42.2 million grid cells in total. The high Re-number grid has its $5 < Y+ < 30$ lying in the logarithmic region with the application of wallfunctions while low Re-number grid has its $Y+ < 5$, with the near wall region well resolved using a special routine with the application of geometric progression for the growth of layers along the wall normal direction. The low Re-number grid also is refined in the far field using static refinement technique arising to 7.1 million grid cells in total.

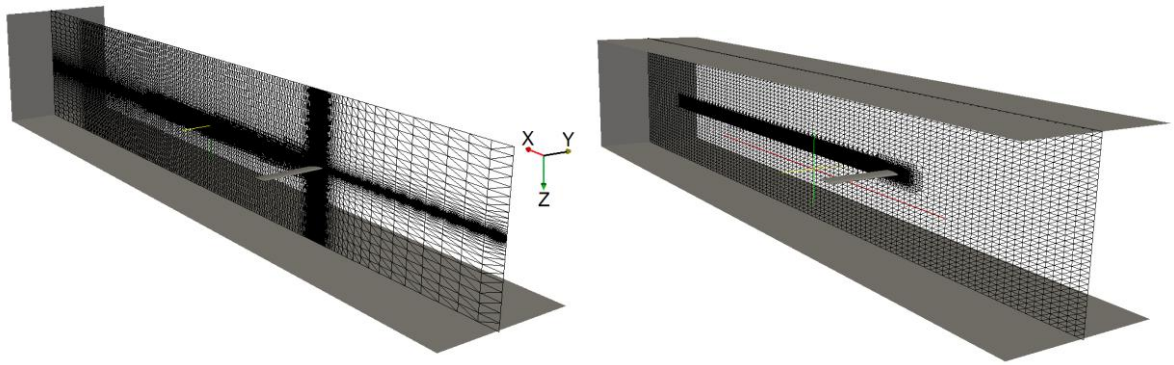

Figure 1: Computational domain with high-Re mesh (left) and low-Re mesh (right) refinements

3.3 Adaptive Mesh Refinement AMR

Adaptive mesh Refinement is a technique which dynamically controls resolution of the grid in simulation run time. Here, we implemented this technique to control the resolution of vortex core which is adapted in each time step. Buffering of the mesh was also introduced which takes into account the refinement layers of the neighbors of the cells which are set for refinement. AMR is one measure to analyze the influence of the numerical error due to the domain discretisation which leads to an increased numerical dissipation of tip vortices. The author proposed the idea of using infrequent refinement by introducing a factor 'n' which is the total number of refinements required. n = Total time = (deltaT /refineInterval).

3.4 Turbulence Modeling and Boundary conditions

The various turbulence models applied here are as follows -

Model	**Origin**	**Abbreviation**
1 - equation Spalart Allmaras	Spalart and Allmaras (1994) [6]	SA
1 - equation Spalart Allmaras with curvature correction	Shur et al. (2000) [4]	SA-CC
2 - equation k-ω-SST	Menter et al. (2003a) [3] [7]	SST
2 - equation k-ω-SST with curvature correction	Smirnov and Menter (2009) [5]	SST-CC
Launder-Reece-Rodi Reynolds stress	Launder et.al (termed LRR) [8]	LRR
w/o turbulence model	-	w/o Turb.
Large Eddy Simulation dynamic Smagarinsky model	-	LES

Curvature correction considers the effects of streamline curvature of the vortex by introducing an emperical function for correction of curvature which is used to modify the source term in the RANS equations. The discretization of convection, diffusion and unsteady terms are solved with second order accuracy. For w/o Turb., the PISO algorithm is applied for unsteady case with 4 times pressure correction loops and maximum Courant number of 10 for 42.2 million grid. For LES, PIMPLE algorithm was applied with 2 times pressure correction and maximum Courant number of 93 for the 42.2 million grid. The flow was made to pass two times the full domain upto 60 chord lengths for better convergence before the averaged data was extracted in all unsteady cases with time step as 1e-5.

3.5 Grid free Vortex Method

Grid based method approaches are very efficient to resolve the flow layers close to the body whereas the particle based approaches have difficulties with formulation of boundary conditions and smooth representation of thin near wall flows. And so, there are not so many applications of vortex methods for the real 3D problems with high Re number flows. On the other hand, grid based approach shows strong numerical dissipation in the far downstream. Therefore, to overcome disadvantages of both the approaches, domain decomposition method is applied. Grid based method is applied close to the body whereas far from the body, vortex method is applied.

In this paper we use the domain decomposition procedure originally developed by Cottet's group (see [2], sec. 8.3.2) to improve the resolution of tip vortices in 3D by coupling the vortex method and OpenFoam. The domain is decomposed into the upstream (zone A) and downstream (zone B) sub-domains (Figure 2). In the domain A, OpenFoam is used, whereas in the domain B vortex method is used. The outlet conditions for the A-domain solution are taken from the B-domain by direct calculation of velocities induced by vortex elements. The

strength and the position of vortex elements flowing into B-domain from A are calculated using the following conditions:

- A vortex element is generated on the face at $x = x_1$ if the vorticity magnitude ω_{OF} calculated from the OpenFoam solution, is larger than some threshold $|\omega_{OF}| > \omega_{tr}$.
- The vortex element strength is set as $\gamma_j = \omega_{OF}(x_j)\, Vol_j$, where $\omega_{OF}(x_j)$ is the vorticity of the grid simulation at point x_j and $Vol_j = \Delta^3$ is the volume of cell within which the vorticity is replaced by the j - th vortex element.
- The irrotational and rotational components of velocity induced by the sub-domain A (induced by the wing and the part of the tip vortex in A) in sub-domain B are taken by the Poincare identity into account.
- The Schwartz alternating algorithm is applied to match the solutions in A and B at the interface $x = x_1$.

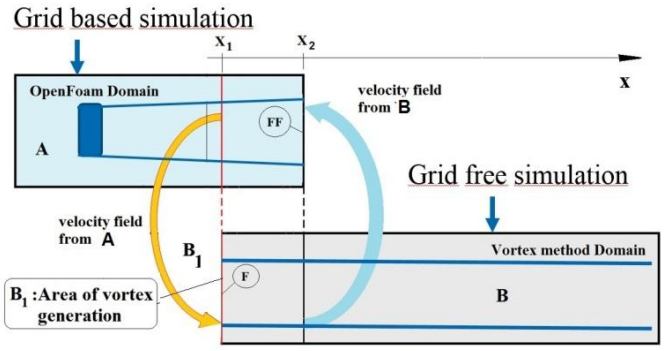

Figure 2: Domain-decomposition method for tip vortex problem

4. Results

Figure 3 illustrates the normalized mean tangential velocity profiles for different models and resolutions of high Re number grid at the x/c 5. Mean velocity profiles are obtained by averaging the maximum tangential velocities in circumferential direction along 32 different radial lines passing through the vortex core which is identified using λ2 criteria.

Improvement of accuracy is observed with the application of curvature correction when SST and SST-CC curves are compared for 7.2 million grid. Grid independence study showed that convergence is attained on the grid with 7.2 million cells for curvature correction models. Improvement in accuracy is also seen with increase in resolution of high Re number grid. Confinement in vortex core is observed due to application of curvature correction.

LRR yields better result overall when compared to rest of the turbulence models. Confinement in the vortex core is also observed which occurs due to inclusion of rotation term in the equations of LRR model. But LRR has strong instability at higher resolutions, which is typical known behavior of this model and it is observed here for 42.2 million grid. The most promising results were obtained by use of dynamic Smagarinsky LES and w/o Turb. (without any subgrid models or as an under resolved direct numerical simulation) with 42.2 mio grid showing best agreement with the experimental data. The w/o Turb. analysis tends to DNS which is formulation when laminar flow is solved. This simulation supports the conclusion of Devenport et al. (1996) [1] that "flow in the core is laminar and that velocity fluctuations experienced here are inactive motions produced as the core is buffeted by turbulence from the surrounding wake".

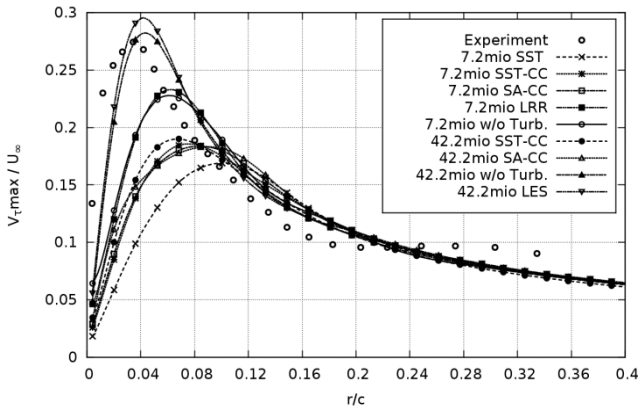

Figure 3: Influence of different turbulence modelling, CC and grid refinement on mean tangential velocity profiles at x/c = 5 for high Re number grid

It was observed that adaptive mesh refinement shows its potential by local refining in the vortex core dynamically with significant improvement in accuracy at x/c 1.5 and x/c 5. See Figure 4

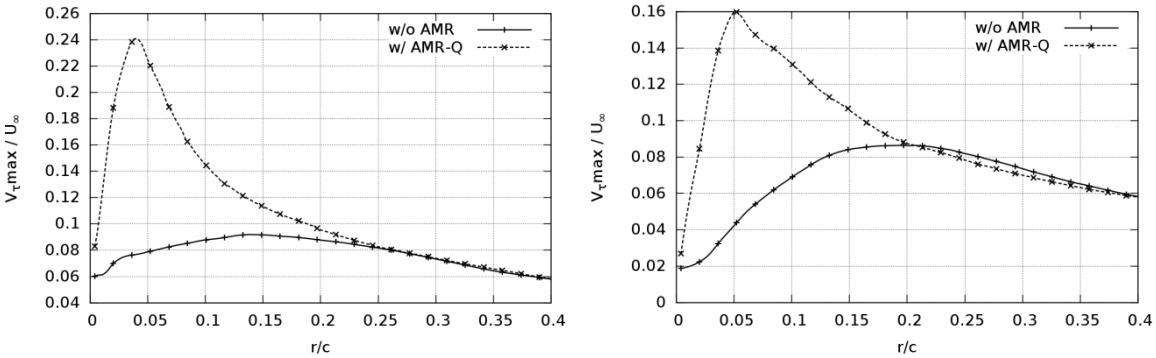

Figure 4: Influence of AMR on mean tangential velocity at x/c 1.5 (left) and x/c 5 (right)

As seen from Figure 5, the strength of vortex decays very slowly in the far field in experiment. In the numerical analysis, minimum rate of decay is observed with w/o Turb. model which is upto 50 percent by the end of domain i.e. x/c 30, followed by the rest turbulence models. Vortex strength decays faster in the far field after x/c = 20 due to coarsening of the grid after x/c > 20. Also, the vortex core grows upto twice the size in simulation by the end of the domain as compared to experiment where it almost remains constant.

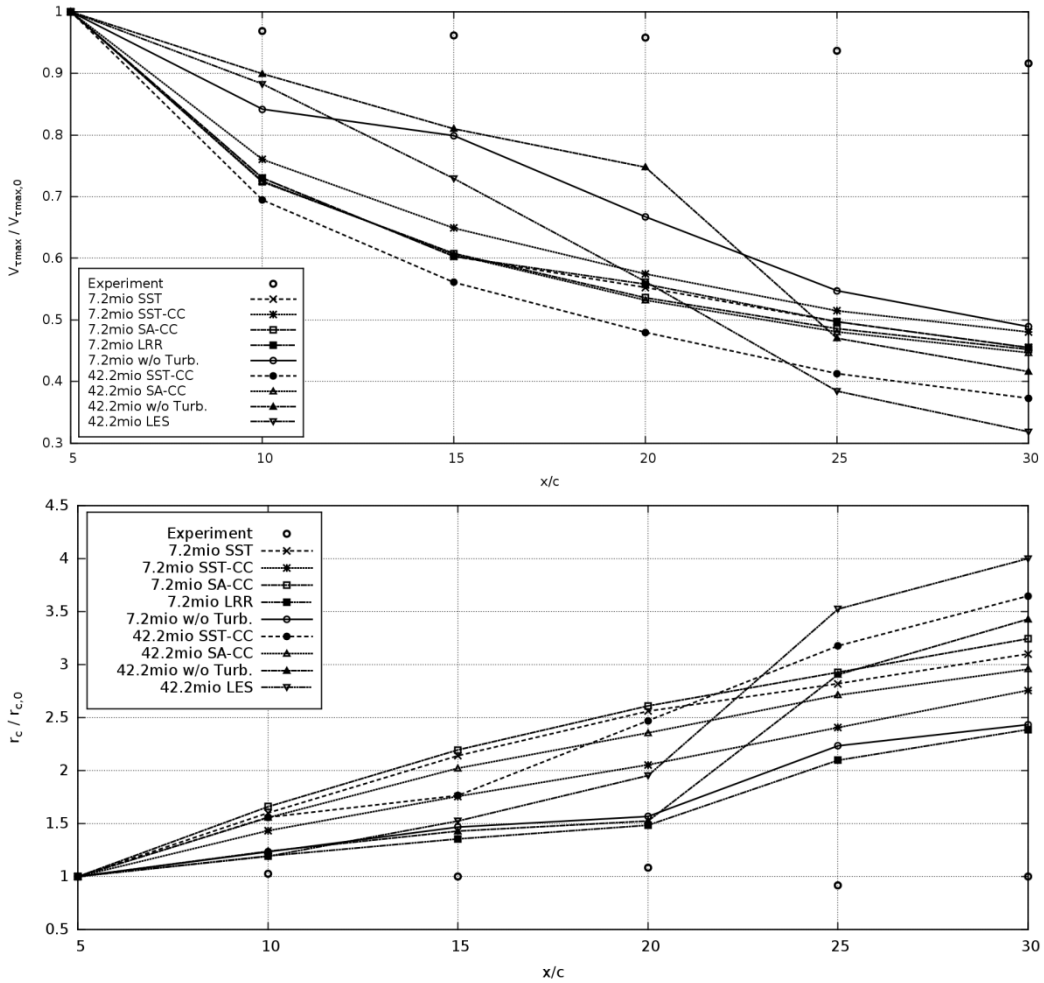

Figure 5: Influence of various turbulence modelling and grid on the vortex core parameters for high Re grid.

The influence of a high Re-number grid and a low Re-number grid on the rate of decay of strength of vortex is shown in Figure 6. A low Re-number grid has the near wall region well resolved as compared to high Re-number grid. It is observed that with increase in the wall refinement, the decay of strength of vortex is strictly

controlled as seen in SST-CC and w/o Turb. with 7.1 million grid. With the w/o Turb. and well resolved near wall flow, the loss in the strength of vortex in far field is reduced down to 25 percent (compared to high Re grid where loss was 50 percent), and growth of vortex radius is also controlled upto 1.6 times the size.

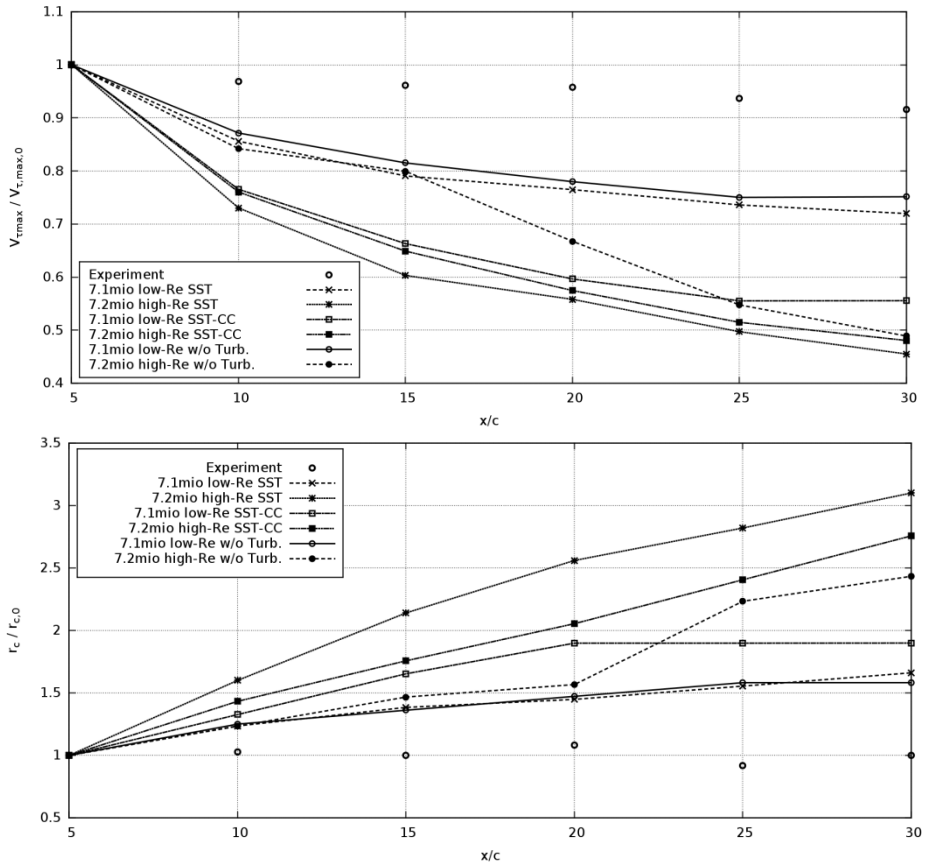

Figure 6: Influence of various turbulence modelling and grid on the vortex core parameters for low Re grid.

The best numerical result obtained till now is with the use of vortex method and domain decomposition approach coupled with grid methods. See Figure 7

5. Conclusions

The most promising results among grid based methods were obtained using the approach without turbulence modelling which also supports experimental conclusion. It exactly matches with the experimental data at x/c 5, further shows decay of maximum tangential velocity decrease by twenty five percent at the end of the domain due to effects of artificial dissipation. As seen from the Figure 7, with the vortex method approach the maximum tangential velocity decreases only by seven percent at the end of the domain. This is the best numerical solution obtained so far matching close to experiment. It shows a strong potential of the vortex method to radically improve the quality of numerical simulation of the tip vortex flow. Further development of the vortex method and their coupling with the grid based methods seem to be a very promising way for a radical improvement of the accuracy of tip vortex dynamics prediction in marine structures.

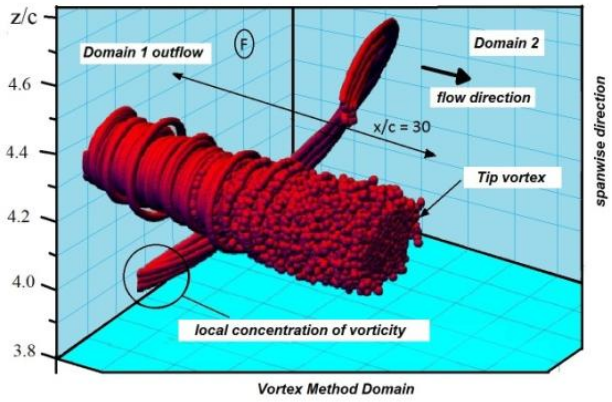

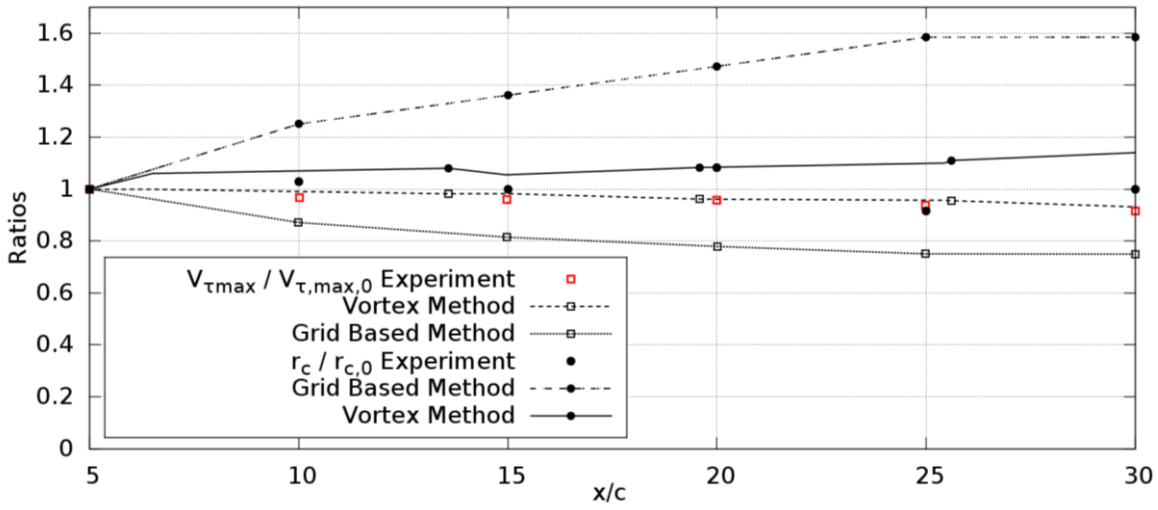

Figure 7: Up - Instantaneous distribution of 86,500 vortex elements in vortex domain Below - Maximum tangential velocity decay downstream. (domain decomposition result)

6. References

[1] W. J. Devenport, M.C. Rife, S. I. Liapis, and G. J. Follin (1996) The structure and development of a wing tip vortex. *J. Fluid Mech.*, Vol. 312, 67-106.

[2] G. H. Cottet and P. D. Koumoutsakos (2000) Vortex Methods : Theory and Practice, Cambridge University Press, New York.

[3] Menter, F., Ferreira, J. C., Esch, T., Konno, B. and Germany, A. C., 2003. "The SST turbulence model with improved wall treatment for heat transfer predictions in gas turbines," *Proceedings of the international gas turbine congress*, 2003, pp. 2–7.

[4] Shur, M. L., Strelets, M. K., Travin, A. K., Spalart, P. R. "Turbulence Modeling in Rotating and Curved Channels: Assessing the Spalart-Shur Correction" AIAA Journal Vol. 38, No. 5, 2000, pp. 784-792.

[5] Menter F.R. Smirnov P.E. "Sensitization of the sst turbulence model to rotation and curvature by applying the spalart–shur correction term" Journ. of Turbomachinery, 131(4), 2009.

[6] Spalart, P. R, Allmaras S.R, "A one equation turbulence model for aerodynamic flows", 30th AIAA Aerospace Sciences Meeting and Exhibit, 1994.

[7] Menter, F., Kuntz, M. and Langtry. R. "Ten years of Industrial Experience with the SST Turbulence Model" ,Turbulence, Heat and Mass Transfer 4. 2003.

[8] Launder, B. E., Reece, G. J., Rodi, W., 1975. Progress in the development of a Reynolds-stress turbulence closure. Journal of fluid mechanics 68 (3), 537-566.

[9] G. Winckelmans and A. Leonard (1993) Contributions to vortex particle methods for the computation of three dimensional incompressible unsteady flows, J. Comput. Phys., Vol. 109, 247-273.

On the Design of Experiments for propellers - Getting to design variables that matter and design points that are important

Pranav Doijode Sumanth[a], **Tom van Terwisga** [a,b], **Stefan Hickel**[c]
[a] Department of Maritime & Transport Technology, Delft University of Technology, The Netherlands
[b] Maritime Research Institute Netherlands (MARIN), Wageningen, The Netherlands,
[c] Chair of Aerodynamics, Faculty of Aerospace Engineering, Delft University of Technology, The Netherlands
Corresponding author email: p.doijodesumanth@tudelft.nl

1 Introduction

Design and Optimisation (D&O) of propellers can be cost effective if lucrative regions in the design space are explored efficiently. This requires insight into the sensitivities of performance w.r.t design variables in all regions of the design space. Using the sensitivities it is possible to reduce the number of design variables and/or number of samples required to explore the design space thus reducing the cost of D&O. These sensitivities are estimated via analysis (computational or experimental) which can be the most expensive steps of D&O routines. Thus, it would be a good advantage to gain insight into sensitivities with very few design point evaluations or in an a-priori manner i.e. without analysis. As the variations in performance correlate with variations in geometry of the propeller, such an a-priori insight into the magnitude of sensitivities could be gained by investigating variations in propeller geometry. As a pre-requisite to such an investigation, the variations in propeller geometry need to be quantified. This paper explores the applicability of Singular Value Decomposition (SVD) to quantify the relevance of geometric and performance variations.

2 Singular Value Decomposition

Singular Value Decomposition or SVD (Weisstein, 2002) of a real matrix $A_{m\times n}$ is defined as $A_{m\times n} = U_{m\times m}\Sigma_{m\times n}V^T_{n\times n}$, where U and V are left and right singular vectors of A respectively. U is a collection of orthonormal vectors (*basis*) and can be interpreted as the principal dimensions of the data in A. Σ is a diagonal matrix which stores the singular values σ_i. They can be interpreted as the magnitude of each dimension. V can be interpreted as the rotation matrix for the data set.

The matrix that we factorize is populated with data that reasonably represent geometric variations. Firstly, we generate a spline surface from classical design variables such as Diameter (D) and radial distributions of Pitch (p), Skew (s), Rake (r), Chord length (c)(Arribas and Fernández, 2018). The surface can be probed in the spline's parametric space where the coordinates $u, v \in [0.0, 1.0]$ represent the same point on the surface for all designs. In the Cartesian space, probed points $\vec{P_i}(u, v)$ and the local gradients $\nabla\vec{P_i}(u, v)$ are extracted from spline parameters. The difference between probed points and local gradients of the i-th design and baseline design are used to quantifying geometric variation. Thus, our data matrix (also referred to later as *geometry probe data matrix*) becomes $X_{N\times n} = \{\vec{X_1}, \vec{X_2}...\vec{X_N}\}$, where

$$\begin{aligned}\vec{X_i} = \{&\vec{P_i}(u_0, v_0) - \vec{P}_{ref}(u_0, v_0), \nabla\vec{P_i}(u_0, v_0) - \nabla\vec{P}_{ref}(u_0, v_0)... \\ &\vec{P_i}(u_{n'}, v_{n'}) - \vec{P}_{ref}(u_{n'}, v_{n'}), \nabla\vec{P_i}(u_{n'}, v_{n'}) - \nabla\vec{P}_{ref}(u_{n'}, v_{n'})\}\end{aligned} \tag{1}$$

The sum of singular values $\lambda = \sum_{i=1}^{n}\sigma_i$ can be a measure of the total variance of the data. When data corresponding to a particular design is removed from X, the new sum of singular values λ' is lower than λ. The magnitude of difference $|\lambda - \lambda'|$ indicates the reduction in total variance. $\vec{X_i}$ can also be defined as the design vector of classical variables making X the *design*

matrix.

For the geometry probe data matrix, $\Delta\lambda_i$ indicates the magnitude of similarity between the i-th design (G_i) and the reference design (G_0). A low value of $\Delta\lambda$ indicates that G_i is very similar to the reference design and a high value of $\Delta\lambda$ indicates that G_i varies significantly from G_0. This information can then be used to identify design variables which significantly influence design as well as choose geometries which represent high, mid and low variance design clusters.

3 Test Cases

Two cases are considered to test the viability of using SVD. The first is a propeller blade geometry and the second is a NACA4412 airfoil. The goal of this exercise is to investigate whether it is possible to classify classical design variables based on the magnitude of influence on the geometry and/or reduce the number of sample points required to explore the design space.

3.1 Propeller Blade

The baseline geometry is initialized from coordinates of a reference propeller. Six hydrofoil cross-sections are defined and the blade is then lofted through them. Figure 1 illustrates the generated blade geometry. To study the geometric variation, design variables listed in Table 1 are varied within the specified bounds. The suffix i indicates the section which is modified. The suffix sf indicates that the design variable is a scaling factor. For this case, it is important to note that variation in classical design variables are not proportional to variations in the geometry. For example, both $\Delta s_i, \Delta p_i \in [-0.056, 0.056]$ however, their influence on the geometry may be quite different. The test for the proposed method is to distinguish between the influence of these design variables.

Design Variables	**Units**	**Lower Bounds**	**Upper Bounds**
ΔD	mm	-300.00	+400.00
Δs_4	rad	-0.056	+0.56
Δs_4	rad	-0.056	+0.56
$c_{sf,2}$	-	0.8	1.2
$c_{sf,3}$	-	0.8	1.2
$c_{sf,4}$	-	0.8	1.2
$c_{sf,5}$	-	0.8	1.2
Δp_1	rad	-0.056	+0.56
Δp_2	rad	-0.056	+0.56
Δp_3	rad	-0.056	+0.56
Δp_4	rad	-0.056	+0.56
Δp_5	rad	-0.056	+0.56
thk_dist$_{sf,1}$	-	-0.04	0.04
thk_dist$_{sf,2}$	-	-0.04	0.04
thik_dist$_{sf,5}$	-	-0.04	0.04

Table 1: Design Variables and Bounds

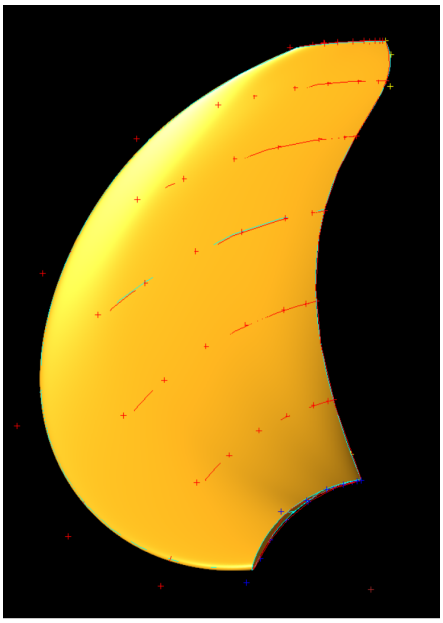

Fig. 2: Generated Blade Geometry

3.2 NACA 4412

The NACA4412 airfoil's camberline is parametrized with two control points $\vec{P}_1, \vec{P}_2$ as illustrated in Figure 3. The design variables are the ordinates of the control points. In this case, both design variables y_{cp1}, y_{cp2} are varied within the bounds $[-4.5e-2, 1.0e-5]$. The setup is such that it is not possible to reduce the number of design variables as both influence the geometry in comparable magnitudes. The goal thus is to investigate whether the number of samples required to map the design space can be reduced. To achieve this goal, trends in Coefficient of Lift (CL),

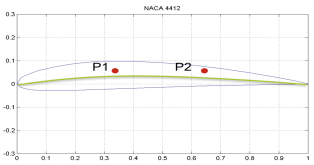

Fig. 3: NACA4412 parametrisation

ω_{SPLmax} and Sound Pressure Level (SPL)(ω) predicted from the *reduced sample set* must lead to minima and maxima which are in close proximity to that predicted by the unreduced sample set.

CL is predicted with XFOIL (Drela, 1989) and broadband turbulence noise is estimated with NAFNoise (Moriarty, 2005). NAFNoise is a semi-empirical method developed to estimate the broadband frequency spectrum due to turbulent boundary layer of a 2D airfoil (Moriarty and Migliore, 2003). The underlying models correlate the thickness of the boundary layer, shear stresses within the boundary layer and freestream velocity to estimate amplitude and frequency of surface pressure fluctuations. While the absolute uncertainties in SPL prediction for broadband frequencies is high, NAFNoise claims to have low relative uncertainty in prediction for NACA0012 at moderate angles of attack with a laminar boundary layer. The authors recognize that in our case, high uncertainties are expected in the prediction of SPL(ω).

Both CL and SPL(ω) are predicted for a flow assumed to be at Mach number $(M) = 0.2$, $Re = 5.4e5$ with an Angle of Attack (α) of 0^o.

4 Results

4.1 Propeller Blade

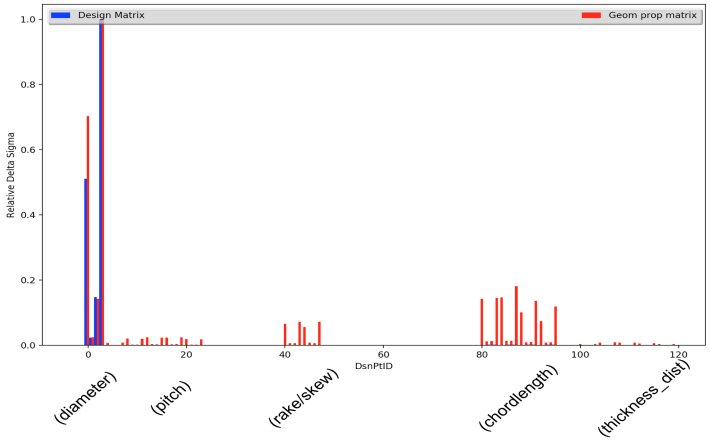

Fig. 4: Propeller Blade $\Delta\lambda/\lambda$ vs design variables

Figure 4 compares $\Delta\lambda_i/\lambda$ when data for the i-th design is removed from the design matrix and geometry probe data matrix. The histogram shows clustered bars and each cluster corresponds to a design variable. The leftmost bar in the cluster corresponds to the design when $x_i = lb_i$ and the right most bar in the cluster corresponds to $x_i = ub_i$.

SVD of the *design matrix* indicates that D has the highest influence on the geometry. This is because the magnitude of ΔD is highest among design variables. Given that the bounds for Δs_i and Δp_i are the same, corresponding $\Delta\lambda/\lambda$ are also the same. Thus, no inference can be drawn about the influence of each design variable on the geometry. However, SVD of the *geometry probe data matrix* makes a distinction between the influence of the two design variables. Furthermore,

it also gives insight into sensitivities of the geometry w.r.t design variables allowing them to be classified. This classification can be beneficial in multi-stage D&O routines where variables which influence geometry significantly can be investigated in the preliminary design stages and finer modifications in the detailed design phases.

4.2 NACA 4412

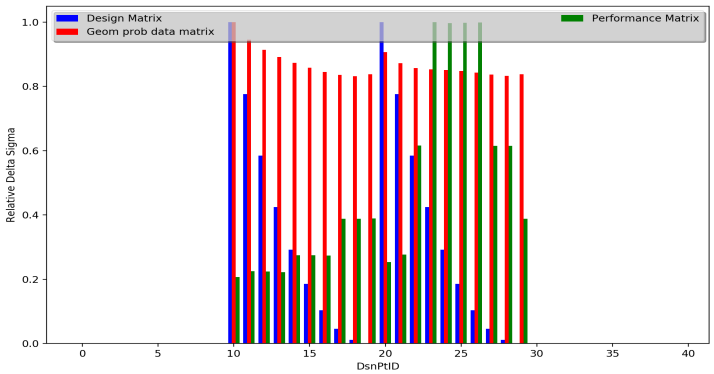

Fig. 5: NACA 4412 $\Delta\lambda/\lambda$ vs design variables

Figure 5 compares $\Delta\lambda_i/\lambda$ when data for the i-th design is removed from the design matrix and geometry probe data matrix. The performance matrix $X_{N\times 3}$ has CL in the first column, ω_{SPLmax} in the second column and the corresponding SPL(ω_{maxSPL}) in the third column. The histogram shows clustered bars and each cluster corresponds to a design variable. As in the case of the propeller, the design variables are systematically changed one at a time. The leftmost bar in the cluster corresponds to the design vector when $x_i = lb_i$ and the right most bar in the cluster corresponds to $x_i = ub_i$.

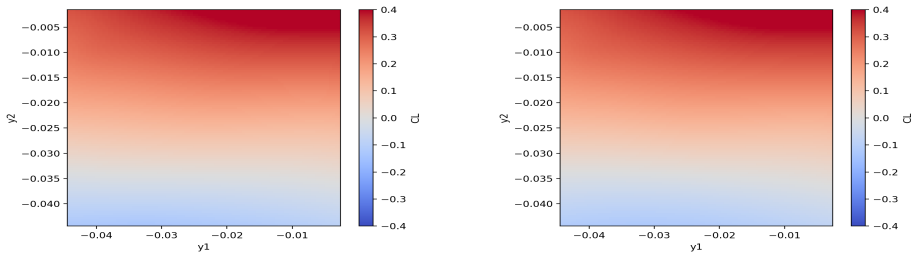

(a) Response Surface (RS) for CL generated from all samples

(a) RS for CL generated from 50% of original samples

Fig. 6: CL Response Surfaces

From Figure 5 it can be observed that the geometry is comparably sensitive to both the design variables. Thus, it is not possible to reduce the number of design variables in the current stage of design. While design variables cannot be classified, the designs can be clustered to significantly reduce the number of designs required to map the design space.

To make a-priori design selections for analysis, $\Delta\lambda_i$ from SVD analysis of the geometry probe data matrix is used to classify designs into high, mid and low variance categories. From each category, half the samples are selected. For the selected subset the performance predictions are made with XFOIL and NAFNoise. A Radial Basis Function (RBF) RS is built to correlate the design vector with performance predictions. Figure 6 - 8 illustrate the response surfaces built

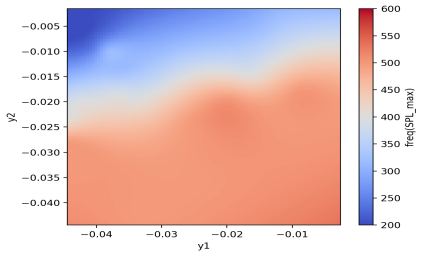

(a) RS for ω_{SPLmax} generated from all samples

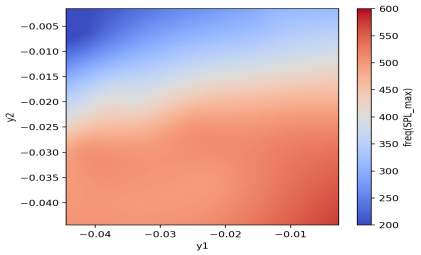

(a) RS for ω_{SPLmax} generated from 50% of original samples

Fig. 7: ω_{maxSPL} Response Surfaces

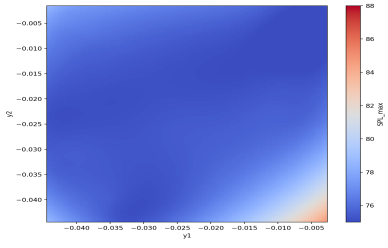

(a) RS for SPL(ω_{SPLmax}) generated from all samples

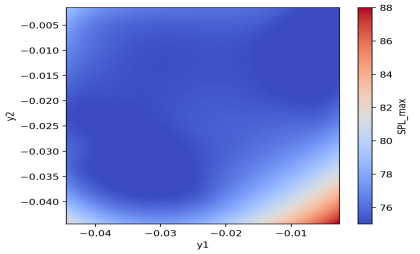

(a) RS for SPL(ω_{SPLmax}) generated from 50% of original samples

Fig. 8: SPL(ω_{SPLmax})Response Surfaces

from the original design matrix ($N = 38$) and the reduced design matrix ($N = 19$) for CL, ω_{SPLmax} and $SPL(\omega_{SPLmax})$. It is observed that there is reasonable agreement between the RS built with the unreduced sample set (RS1) and the reduced sample set (RS2). The RSs are searched with a constrained Sequential Least SQuares Programming (SLSQP) algorithm to find the minima. The results are listed in Table 4.2. It is observed that for CL and ω_{SPLmax}, the minima predicted by RS1 and RS2 are close. However, for $SPL(\omega_{SPLmax})$ the minima are quite far apart. This is because, there are two possible minima as shown in Figure 8 and one of them was not included in the reduced sample set. This issue can be addressed with adaptive sampling where ever a lucrative trough is located on the RS.

	RS1	**RS2**
Num Training Samples	38	19
CL_{min}	-0.14	-0.12
$\vec{X}_{sol,CL}$	[-0.033, -0.045]	[-0.032, -0.045]
$min(\omega_{SPLmax})$	179.95	174.36
$\vec{X}_{sol,min(\omega_{SPLmax})}$	[-4.50e-02, 1.00e-05]	[-4.50e-02, 1.00e-05]
$min(\text{SPL}_{max})$	74.48	74.29
$\vec{X}_{sol,SPL}$	[-0.0058, -0.0067]	[-0.033, -0.033]

Table 2: Minima

5 Conclusion

SVD seems to be a promising technique to (a) reduce the number of samples in Design of Ex-

periments (DoE) and, (b) classify design variables based on their magnitude of influence on the geometry. For the method to be applicable, data populating the factorized matrix must represent geometric variations reliably. Thus, data such as probed points and local gradients are more useful to quantify geometric variation as opposed to design vectors with classical design variables. This is because, the magnitude of change in geometry is not always proportional to the magnitude of change in classical design variables all the time.

In the propeller blade case, SVD of the geometry probe data matrix enabled the classification of variables based on the magnitude of influence on the geometry. To gain insight into the sensitivities of performance w.r.t design variables, analysis of specific design points is required. The jacobians of performance data w.r.t design variables may be appended to the data matrix for analysis. The hypothesis is that the method may require fewer design point evaluations compared to classical methods to provide necessary insight into global sensitivities of performance parameters.

In the case of the airfoil, it was possible to identify from SVD of the geom probe data matrix that classification of variables is not viable. Furthermore, it was also possible to reduce the number of sample points by 50% while still capturing the performance trends globally in the design space. However, it is noted that the reducing the initial sample set may lead to exclusion of one or more local minima. This can be addressed by adaptively refining the RS in regions where a trough is observed and a local minima is expected.

Also, for the 2D airfoil case, the use of lower-fidelity methods leads to monotonic or convex trends in performance. But the use of higher fidelity methods could lead to more complex performance trends. Under such circumstances, SVD's applicability is yet to be investigated. This concern mainly arises from studies which drop all smaller modes/dimensions of the data. However, these smaller modes may be necessary to preserve dynamics within the data. Our methods preserve some of the smaller dimensions/modes, but they need to be demonstrated for cases with complex performance trends.

6 Acknowledgment

The authors would like to whole heartedly thank Evert-Jan Foeth for thoughts and comments on the research. We also thank Erik Rotteveel, Thomas Scholcz and Bart Schuiling at MARIN for interesting exchange of ideas on design and optimisation.

References

Arribas, F. P. and Fernández, R. P. (2018). A b-spline design model for propeller blades. *Advances in Engineering Software*, 118:35 – 44.

Drela, M. (1989). Xfoil: An analysis and design system for low reynolds number airfoils. In Mueller, T. J., editor, *Low Reynolds Number Aerodynamics*, pages 1–12, Berlin, Heidelberg. Springer Berlin Heidelberg.

Moriarty, P. (2005). Nafnoise user's guide. *National Wind Technology Center, National Renewable Energy Laboratory.*

Moriarty, P. and Migliore, P. (2003). Semi-empirical aeroacoustic noise prediction code for wind turbines.

Weisstein, E. W. (2002). Singular value decomposition. from mathworld–a wolfram web resource. Accessed: 2018-06-27.

On the Role of Iterative Errors in Unsteady Flow Simulations

Luís Eça*, Guilherme Vaz† and Martin Hoekstra+
*IST Técnico Lisboa, Lisbon/Portugal, †MARIN Maritime Research Institute Netherlands,
Wageningen/The Netherlands, + Consultant
luis.eca@tecnico.ulisboa.pt

1 Introduction

Simulation of (statistically) unsteady flows is no longer an exceptional task in Engineering applications. For wall-bounded (turbulent) flows at high Reynolds numbers it is usual to apply implicit techniques for time integration[1], i.e. a non-linear system of partial differential equations must be solved at each time step. This means that a convergence tolerance is needed to decide on when having solved this non-linear system well enough. Any iterative error propagates to the next time step and so the numerical error of a given solution may not be dominated by the numerical error inherent to the space and time discretization.

In the last two years, two Workshops dedicated to Iterative Errors in Unsteady Flow Simulations were held at the ASME V&V Symposiums of 2017 and 2018, Workshop (2017), Workshop (2018). The main goal of these Workshops was to create awareness to the problem and to confirm that different flow solvers, including ANSYS Fluent, ANSYS CFX, OpenFoam, ReFRESCO, SATURNE and STAR-CCM+, exhibited the same trends. The simple two-dimensional, laminar flow of a single-phase, incompressible, Newtonian fluid around a circular cylinder at the Reynolds number of 100 is sufficient to illustrate the challenges posed by iterative errors in unsteady flow simulations.

This paper presents a brief illustration of the outcome of the two Workshops on Iterative Errors in Unsteady Flow Simulations. However, our main goal is to answer the following questions:

- How far do we need to converge at each time step to guarantee a negligible iterative error?
- How do we estimate iterative errors for the quantities of interest?
- What is the impact of the iterative error on the estimation of the discretization error?

2 Test Case

The selected test case is the laminar flow around a circular cylinder at Reynolds numbers ($Re = \frac{V_\infty D}{\nu}$) based on the incoming velocity V_∞, cylinder diameter D and kinematic viscosity of the fluid ν of $Re = 100$. It was suggested to assume that the fluid is incompressible.[2]

The flow is two-dimensional and the calculation domain is a rectangle with the distances of the boundaries to the cylinder centre equal to $20D$ upstream for the inlet, $80D$ downstream for the outlet and $40D$ for top and bottom boundaries. The Cartesian (x, y) coordinate system adopted has the origin at the centre of the cylinder and the x axis aligned with V_∞. Boundary conditions are: no-slip condition at the cylinder surface ($\sqrt{x^2 + y^2} = D/2$) and normal derivative of the pressure set equal to zero ($\nabla p \cdot \vec{n} = 0$); uniform flow at the inlet boundary ($x = -20D$) with horizontal velocity component $V_x = V_\infty$ and vertical velocity component $V_y = 0$; pressure imposed at the outlet boundary ($x = 80D$) and derivatives of the two velocity components in the streamwise direction (x) equal to zero ($\frac{\partial V_x}{\partial x} = \frac{\partial V_y}{\partial x} = 0$); free-slip at the top and bottom boundaries ($y = \pm 40D$), i.e. normal velocity component equal to zero ($V_y = 0$) and derivatives of the velocity component in the horizontal direction and pressure in the normal direction equal to zero ($\frac{\partial V_x}{\partial y} = \frac{\partial p}{\partial y} = 0$).

There are four geometrically similar multi-block structured grids available, which are illustrated in Fig. 1. The grids have clustering of grid nodes in the block of the near-wake. As a consequence, there

[1] If the fluid is incompressible a system of equations must be solved even for explicit time integration.

[2] In the 2018 edition, there was a submission for a compressible flow solver (Mach number of the incoming flow equal to 0.2) with explicit time integration using a dual time step technique.

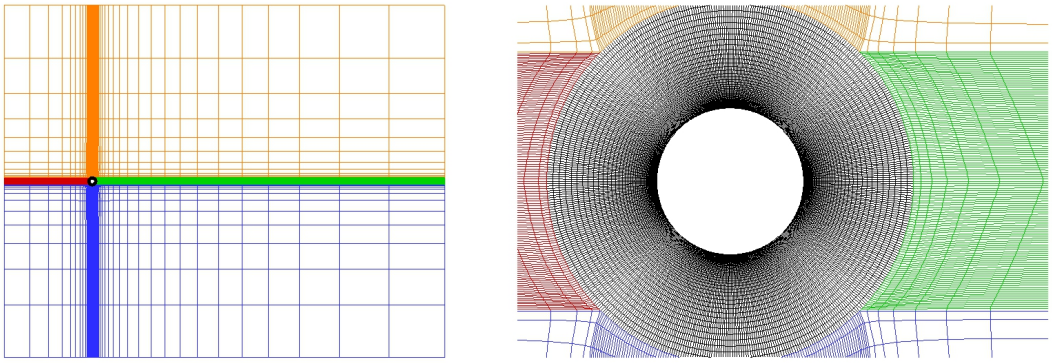

Fig. 1: Illustration of the grids for the calculation domain of the flow around a circular cylinder.

is a sudden change of cell size at the edge of the inner block, but several preliminary tests were done to guarantee that these grids are suitable for the determination of the quantities of interest. Furthermore, these tests showed that it was important to include a significant increase of the cell-size at the outlet, top and bottom boundaries to avoid pressure reflections. Table 1 presents the total number of cells, the number of faces on the cylinder surface and the grid and time refinement ratios $r_i = h_i/h_1 = \Delta t_i/\Delta t_1$ of the 4 grids and the dimensionless time steps with the corresponding maximum values of the Courant number $\mathrm{C_{max}}$.

Table 1: Grids available for the Workshops on Iterative Errors in Unsteady Flow Simulations and recommended time steps.

Grid	Number of Cells	Number of Faces on Cylinder Surface	r_i	Dimensionless time step, $\Delta t_i V_\infty / D$			
				$\mathrm{C_{max}}$=0.8	$\mathrm{C_{max}}$=1.6	$\mathrm{C_{max}}$=6.2	$\mathrm{C_{max}}$=15
4	125910	960	2	0.0025	0.005	0.02	0.05
3	196266	1200	1.6	0.002	0.004	0.016	0.04
2	282174	1440	1.3(3)	0.0016(6)	0.003(3)	0.013(3)	1.3(3)
1	503640	1920	1.	0.00125	0.0025	0.01	0.025

The complete list of the selected quantities of interest is available at available at Workshop (2017), Workshop (2018). In this paper, we will restrict ourselves to two quantities: time-averaged drag coefficient $(C_D)_{\mathrm{avg}}$ and maximum lift coefficient $(C_L)_{\mathrm{max}}$.

3 Overview of Results

The participants of the two Workshops were asked to perform simulations of the selected test case using different iterative convergence criteria for the solution at each time step. The selected criteria ranged from maximum and root mean squared values of normalized residuals[3] to number of non-linear iterations performed at each time step. Nonetheless, participants using the latter option also reported values of the residuals obtained at each time step. Therefore, the selected flow quantities are plotted as a function of the ratio between the loosest residual and the different values of the residuals tested, designated by ε[4]. It should be mentioned that simulated time of all submissions was sufficient to achieve statistical convergence, i.e. differences between consecutive cycles were significantly smaller than iterative convergence criteria at each time step.

[3] As expected, normalization of the residuals is not the same for all participants

[4] This means that the largest value of ε is 1. However, this choice does not guarantee that the differences between the criteria selected by the different participants are correctly captured.

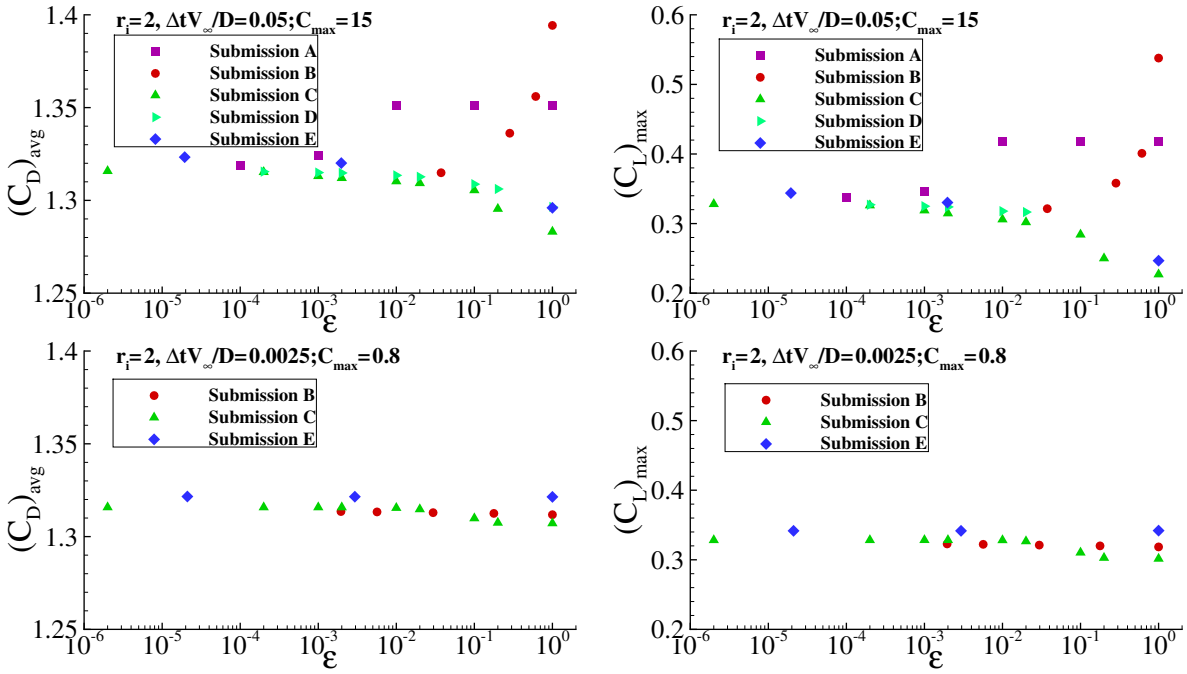

Fig. 2: Time-averaged drag coefficient $(C_D)_{\text{avg}}$ and maximum lift coefficient $(C_L)_{\text{max}}$ as a function of the iterative convergence criteria applied at each time step. Results from five different submissions obtained in the coarsest grid ($r_i = 2$) with the largest (top) and smallest (bottom) time steps. Flow around a circular cylinder with Reynolds number of 100.

Figure 2 presents $(C_D)_{\text{avg}}$ and $(C_L)_{\text{max}}$ from five different submissions[5] using second-order accurate time and space discretization techniques. Results were obtained in the coarsest grid ($r_i = 2$) with the largest and smallest time steps.

The data obtained with the different flow solvers confirm that insufficient iterative convergence at each time step can lead to significant iterative errors even for (integral) force coefficients. Nonetheless, as mentioned above, all simulations performed with the different iterative convergence criteria tested achieved statistical convergence, i.e. it was possible to obtain a (converged) periodical time history of the force coefficients. On the other hand, monotonic iterative convergence is obtained with the different flow solvers[6], which is strongly dependent on the selected time step (Courant number) and on the selected quantity of interest. In the present test case, iterative convergence has a stronger effect on the lift coefficient than on the drag coefficient. As expected, the influence of iterative convergence criteria decreases with the reduction of the time step, because solution changes between consecutive time step diminish.

4 Handling iterative errors

4.1 Estimation of iterative errors

The results presented in the previous section show that the selection of a reliable iterative convergence criterion that does not lead to unnecessarily large computational time is not straightforward, because it depends on grid density, time step (Courant number) and selected quantity of interest. Therefore, it is of practical interest to estimate iterative errors without converging the solution (almost) to machine accuracy at each time step.

A method similar to that proposed in Eça and Hoekstra (2014) for the estimation of discretization errors is proposed for the estimation of the contribution of iterative errors to the numerical uncertainty.

[5] Results were obtained using four different flow solvers using segregated and/or coupled solutions procedures at each time step.

[6] However, in some cases the change with ε shows opposite signs for different submissions.

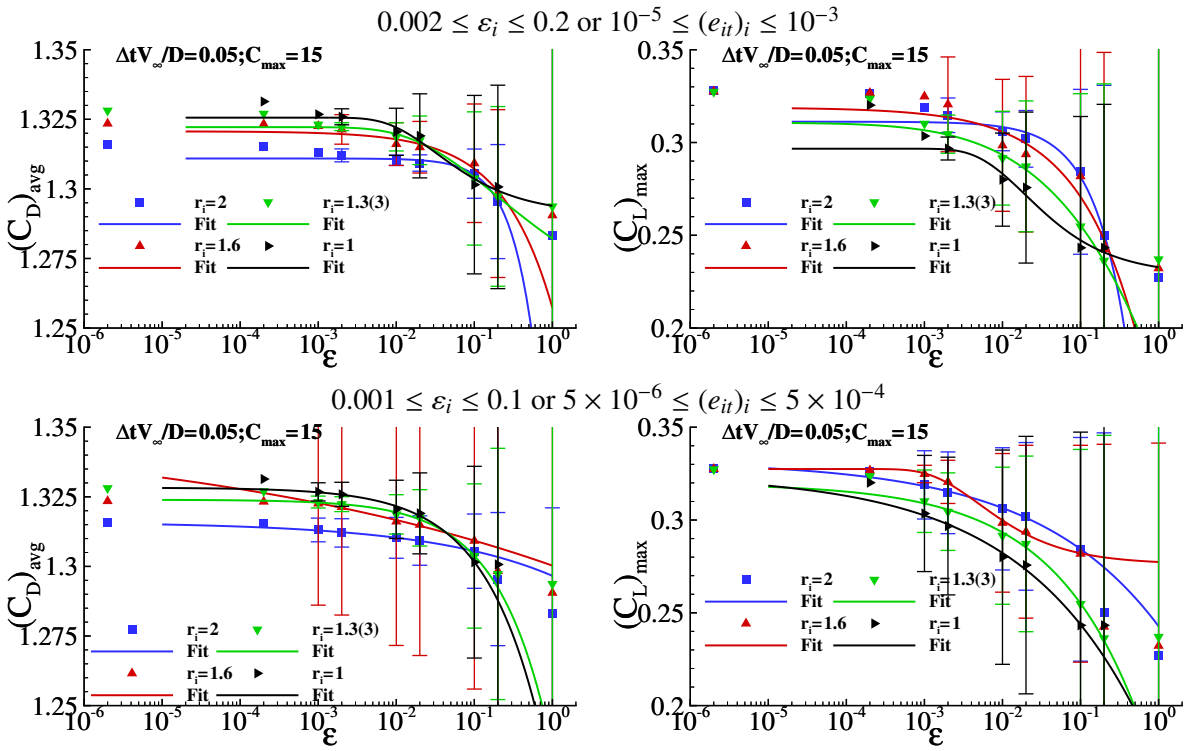

Fig. 3: Estimation of the iterative error of the time-averaged drag coefficient $(C_D)_{\text{avg}}$ and maximum lift coefficient $(C_L)_{\text{max}}$ as a function of the iterative convergence criteria applied at each time step. Error bars estimated with the data between $0.002 \leq \varepsilon \leq 0.2$ (top) and (bottom) for the four grids ($r_i = 2$) using the largest time steps. Flow around a circular cylinder with Reynolds number of 100.

Compared to the method for discretization errors, there are three main changes: the typical cell size h_i is replaced by ε_i that quantifies the level of the residuals achieved at each time step[7]; the least-squares line fits are performed without weights; the error equation is defined by

$$\phi(\varepsilon_i) - \phi_o = \alpha \exp^{F(\varepsilon_i)\beta} \, . \tag{1}$$

The estimate of the iterative error at convergence level ε_i ($\phi(\varepsilon_i) - \phi_o$) depends on the estimate of the exact numerical solution[8] ϕ_o and on the constants α and β . The function $F(\varepsilon_i)$ must go to minus infinity when ε_i goes to zero and two alternatives are tested[9]: $F = \ln(\varepsilon_i)$ and $F = -1/\varepsilon_i^p$. As for the discretization error estimation, equation (1) is solved in the least-squares sense to determine ϕ_o, α and β and the standard deviation of the fit is used to select $F(\varepsilon_i)$. At this stage, the exponent p is not determined in the fit. Fixed values between 0.1 and 3 with $\Delta p = 0.1$ are tested.

An example of the application of the procedure described above is presented in figure 3 for the $(C_D)_{\text{avg}}$ and $(C_L)_{\text{max}}$ results of submission C obtained in the four available grids with the largest time step. In this submission, iterative errors are controlled by the maximum normalized residual of all equations solved at each time step, e_{it}. Calculations were performed with $10^{-8} \leq (e_{it})_i \leq 5 \times 10^{-3}$, which leads to $2 \times 10^{-6} \leq \varepsilon_i \leq 1$. Two different error estimates using five different data points are depicted in figure 3: in the top plots $0.002 \leq \varepsilon_i \leq 0.2$ (or $10^{-5} \leq (e_{it})_i \leq 10^{-3}$), whereas the error bars of the bottom plots were obtained with $0.001 \leq \varepsilon_i \leq 0.1$ (or $5 \times 10^{-6} \leq (e_{it})_i \leq 5 \times 10^{-4}$).

In general, the fits exhibit a good agreement with the selected data. However, not all the error bars contain the result obtained with the smallest value of ϵ_i (or $(e_{it})_i$). Nonetheless, these nonconservative

[7]For example, for a method that uses the residual e_{it} as the convergence criteria at each time step $\varepsilon_i = (e_{it})_i/(e_{it})_{\text{max}}$).

[8]This corresponds to the exact numerical solution for a given grid and time step and not to the exact solution of the system of partial differential equations.

[9]The first option corresponds to a power series expansion with a single term. Only restriction applied is $\beta > 0$ for all cases.

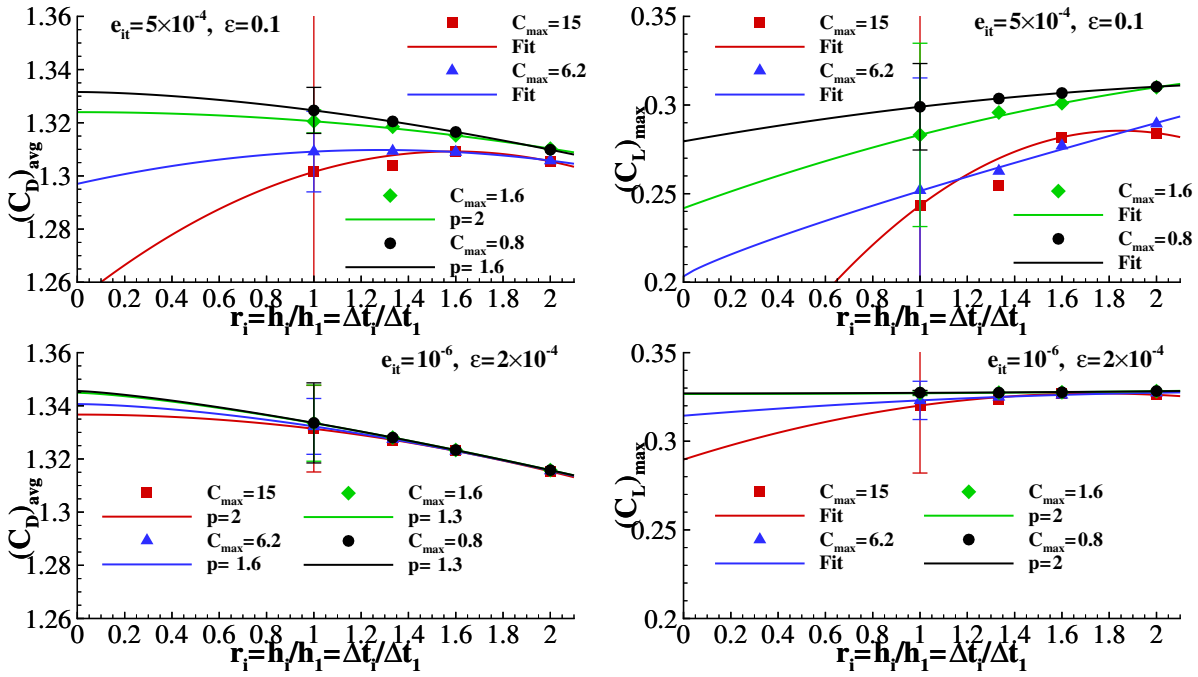

Fig. 4: Estimation of the discretization error of the time-averaged drag coefficient $(C_D)_{\text{avg}}$ and maximum lift coefficient $(C_L)_{\text{max}}$ for different iterative convergence criteria applied at each time step. Flow around a circular cylinder with Reynolds number of 100.

uncertainty estimates occur mainly for the variable with the smallest influence of ε_i ($(C_D)_{\text{avg}}$) when data points with the least demanding iterative criteria are used (top left plot). Bearing in mind that the calculations with $e_{it} = 10^{-8}$ required on average 200 ($r_i = 2$) to 800 ($r_i = 1$) iterations per time step, the present procedure is a valuable tool for the estimation of iterative error contributions to the numerical uncertainty of unsteady flow simulations.

4.2 Influence of iterative errors on the discretization error estimation

Discretization errors are often considered the dominant contribution to the numerical uncertainty. Such assumption requires that iterative errors are negligible when compared to the discretization error. If that is not achievable, it might be useless to refine the grid and/or reduce the time step because the numerical uncertainty may become dominated by the iterative error contribution. On the other hand, there is no guarantee that iterative and discretization errors are independent and so discretization errors estimated with data contaminated by iterative errors may lead to misleading results.

An example of the influence of iterative errors on the estimation of discretization errors is presented in figure 4 using again the data of submission C. Calculations were performed for the four grids with all the time steps given in table 1, which guarantee that the Courant number remains approximately constant because the grid refinement ratio h_i/h_1 is equal to the time step ratio $\Delta t_i/\Delta t_1$, i.e. $r_i = h_i/h_1 = \Delta t_i/\Delta t_1$. In these conditions it is possible to apply the procedure proposed in Eça and Hoekstra (2014) to estimate the discretization error using the data obtained for each Courant number. The top plots were obtained with the results of the calculations performed with $e_{it} = 5 \times 10^{-4}$ ($\varepsilon = 0.1$), whereas the bottom plots corresponds to the data obtained with $e_{it} = 10^{-6}$ ($\varepsilon = 2 \times 10^4$).

There is a significant influence of the iterative convergence criterion e_{it} on the estimated discretization errors, especially for $(C_L)_{\text{max}}$ that does not exhibit monotonic convergence with r_i for any of the four Courant numbers when $e_{it} = 5 \times 10^{-4}$. For the maximum lift coefficient, the effect of the iterative error is to increase the discretization error estimate making it too conservative. However, the most misleading result obtained with the loosest iterative convergence criterion ($e_{it} = 5 \times 10^{-4}$) is the (discretization) error bar for $(C_D)_{\text{avg}}$ with $C_{\text{max}} = 1.6$. The estimate is based on an observed order of grid/time convergence

of 2, but the error bar does not contain the extrapolated solution for the same $C_{\max}$ determined with $e_{it} = 10^{-6}$. This means that it is possible to obtain (apparent) statistical (periodic solution) and monotonic grid/time convergence with solutions contaminated by iterative errors. In that case, ignoring iterative errors may lead to a significant under-estimation of the numerical uncertainty.

5 Conclusions

The two Workshops dedicated to Iterative Errors in Unsteady Flow Simulations have demonstrated that it is important to estimate iterative errors in simulations based on implicit time integration. The simple two-dimensional, laminar flow ($Re = 100$) of an incompressible, single-phase Newtonian fluid around a circular cylinder is sufficient to illustrate the influence of iterative errors using several flow solvers. The results show that the selection of a reliable iterative convergence criterion at each time step is not trivial, because it depends on the grid density, time step (Courant number) and selected quantity of interest.

Bearing in mind that in practical unsteady flow simulations converging each time step to machine accuracy is not affordable, it is important to develop practical procedures for the assessment of iterative errors in unsteady flow simulations. A simple procedure that uses solutions obtained with different residuals achieved at each time step is successfully applied to the Workshops data. Although it was not possible to obtain a conservative estimate of the iterative error for all the cases tested, the proposed procedure gives a more reliable estimate of the iterative error than assuming that it is equal to the order of the residuals required by the iterative convergence criterion.

The selected examples also showed that insufficient iterative convergence can lead to a significant deterioration of the estimation of discretization errors, which does not always mean too conservative estimates. On the other hand, when iterative errors dominate it is possible to obtain an apparent smooth grid/time convergence but to the wrong solution. Finally, it is not to be expected that the effects of iterative errors will become less important for practical applications dealing with wall-bounded turbulent flows at high Reynolds numbers.

Acknowledgements

The authors would like to thank all the participants of the two Workshops on Iterative Errors for Unsteady Flow Simulations. The authors acknowledge the Laboratory for Advanced Computing at University of Coimbra (http://www.uc.pt/lca) for providing computing resources to perform this work.

References

Workshop (2017) http://web.tecnico.ulisboa.pt/ist12278/Workshop_iterative_2017.htm

Workshop (2018) http://web.tecnico.ulisboa.pt/ist12278/Workshop_iterative_2018/Workshop_iterative_2018.htm

ANSYS Fluent http://www.ansys.com/Products/Fluids/ANSYS-Fluent

ANSYS CFX http://www.ansys.com/Products/Fluids/ANSYS-CFX

OpenFoam http://www.openfoam.com/

ReFRESCO http://www.refresco.org/

SATURNE http://code-saturne.org/cms/

STAR-CCM+ https://mdx.plm.automation.siemens.com/star-ccm-plus

Eça L. and Hoekstra M. (2014), *A procedure for the estimation of the numerical uncertainty of CFD calculations based on grid refinement studies*. Journal of Computational Physics, **262**:104-130.

Including Energy Equation for Analyzing Propulsor-Hull Interaction Effects

Arash Eslamdoost
Department of Mechanics and Maritime Sciences, Chalmers University of Technology, Gothenburg, Sweden
arash.eslamdoost@chalmers.se

1 INTRODUCTION

The interaction effects between propeller and hull are important design factors. The performance of the entire system can be improved noticeably by considering the interaction effects during the propeller and hull design process. These effects are most commonly described using a well-established terminology, including thrust deduction, wake fraction, propulsive efficiency etc. Such a description has an important drawback since it is based on experimental rather than theoretical considerations. This can imply limitations both in redesign and optimization of existing propulsion concepts. Limitations of the classical methods for analyzing the interaction effects are even more pronounced when distinctive designs with less understood physics are considered.

We believe that computational fluid dynamics (CFD) has reached a degree of maturity which can be used to extract more detail and precise data of the flow around self-propelled craft, even in full scale. Such information can aid us to understand the interaction effects deeper rather than through assessment of a few global values such as wake fraction and thrust deduction.

Several attempts have been made to develop methods and guidelines based on CFD or analytical approaches for analyzing the interaction effects. Dyne and Jonsson (1989) and Dyne (1995), by means of splitting a self-propelled system into a bare hull and an open-water propeller, proposed a method to study the propulsive efficiency based on wake losses and gains. This method is mostly derived based on potential flow assumptions, which implies that it is not correct to apply it for analyzing viscous flow simulation results. In order to achieve a better system efficiency, Dang et al. (2012, 2015) studied the dimensionless kinetic energy evaluated in the wake for two different applications. The method is easily applicable for analyzing CFD results. Although this approach does not take all the energy components into account, it has been used successfully for comparing the axial and transverse kinetic energy losses. Van Terwisga (2013) evaluated the propulsion power based on wake losses downstream of self-propelled hull. Schuiling et al. (2016) also presented a method based on energy balance over a control volume for analyzing a propeller in open water. The energy equation was not solved in this work and viscous losses were obtained through volume integrals of dissipation term inside the control volume. Similar to the marine sector, propulsor-hull interaction has been in focus of research in aircraft industry. For instance, Drela (2009) and Capitao-Patrrao et al. (2016) kept track of energy fluxes through control volumes which they used around their studied cases. More recently Eslamdoost et al. (2017) and Andersson et al. (2018 (a)); (2018 (b)); (2018 (c)) have presented a CFD based method grounded on balancing energy fluxes through control volumes around self-propelled vessels for tracking the shaft power into different energy components inside the flow field. In these series of articles, the authors have shown the practicality of the proposed method for marine applications. However, those studies were carried out in the absence of free-surface. The current paper is a summary of an in-progress research with the objective to study numerical implications of including free-surface in the energy balance model. To this end, a self-propelled axisymmetric body, the DARPA Suboff (1992) is used as a test case in this paper.

2 CONTROL VOLUME APPROACH FOR ENERGY ANALYSIS

We can keep track of the total energy delivered to the system (propeller work) through the energy components and their conversion from one form to another. This can be done with the aid of the Reynolds Transport Theorem. This theorem states that for a steady state system, the change of any quantity (here total energy, E) plus the production of that quantity within a control volume enclosing a system is equal to the sum of the flux of that quantity over the surfaces of the control volume. A sample control volume around the case studies in this paper is shown in Figure 1.

In a steady state flow where no body force is acting on the system, the Reynolds Transport theorem for energy per unit mass e, for a control volume simplifies as follows,

$$\int_{CS} e\rho(\vec{u}\cdot\vec{n})\,dS = \int_{CS} (-p\cdot\vec{n}+\vec{\tau})\cdot\vec{u}\,dS, \tag{1}$$

where the fluid velocity vector and density are denoted by $\vec{u}$ and ρ, respectively. The surfaces which enclose the control volume are denoted by CS with their unit normal vector, $\vec{n}$, pointing out of the control volume. The

right-hand side is the integrand of force×velocity on control surfaces and represents the work done by the pressure and shear forces on the control volume. The pressure and the surface shear stress vector are shown by p and $\bar{\tau}$, respectively.

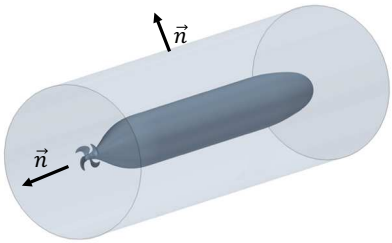

Figure 1. A sample cylindrical control volume around the axisymmetric body and the propeller.

The right-hand side of Equation (1) can be split into the pressure and shear stress work acting on the material surfaces, CS_{MS} (hull and propeller), and on the virtual surfaces, CS_{VS} (outer enclosing surfaces), of the control volume. The former component for the test case used in this study is the propeller work,

$$P_D = 2\pi nQ, \tag{2}$$

where n is the shaft revolution per second and Q is the shaft torque.

The force work surface integral (RHS of Equation (1)) on CS_{VS} can be simplified. Provided that the control surfaces are located far from the studied self-propelled object or normal to the local flow direction, we can neglect the shear stresses acting on CS_{VS} and just consider the pressure force contribution.

In order to evaluate the energy distribution inside the control volume, e can be decomposed to four different components: (1) kinetic energy in the axial direction (2) kinetic energy in the transverse directions (3) turbulence kinetic energy and (4) internal energy. Since, the flow cannot penetrate CS_{MS}, LHS of Equation (1) simplifies to a surface integral just on CS_{VS}.

Considering the assumptions and divisions explained above, Equation (1) can be simplified as follows;

$$P_D = \int_{CS} \frac{1}{2} u_x^2 \rho(\vec{u}\cdot\vec{n})\,dS + \int_{CS} \frac{1}{2}\left(u_r^2 + u_\theta^2\right)\rho(\vec{u}\cdot\vec{n})\,dS + \int_{CS} k\rho(\vec{u}\cdot\vec{n})\,dS + \int_{CS} \hat{u}\rho(\vec{u}\cdot\vec{n})\,dS + \int_{CS} p(\vec{u}\cdot\vec{n})\,dS, \tag{3}$$

where k is the turbulent kinetic energy and u_x, u_r and u_θ are the axial, the radial and the tangential velocity components, respectively.

The first four terms on the right-hand side are the axial kinetic energy, the transverse kinetic energy, the turbulent kinetic energy and the internal kinetic energy fluxes, respectively. The fifth term represents the work done by pressure forces on CS_{VS}. The internal energy change within the control volume (the fourth term on the RHS), can be obtained through,

$$\hat{u} = c_p T, \tag{4}$$

where c_p is the specific heat of water and T is temperature.

In summary, the addressed energy balance method shows that the propeller shaft power of a self-propelled vessel is balanced with a set of different energy flux components through the surfaces of a deliberate control volume enclosing the system.

3 COMPUTATIONAL METHOD, DOMAIN AND MESH

We have employed the commercial CFD package STAR-CCM+13.02.013, a finite volume method solver, in this study. The code solves the conservation equations for momentum, mass, turbulence quantities as well as energy using a segregated solver based on the SIMPLE-algorithm. A 2nd order upwind discretization scheme in space was used. We have also solved the energy equation, to be able to measure the dissipation of kinetic energy and turbulent kinetic energy in the form of temperature (Equation (4)). Since the wake into the propeller is circumferentially symmetric, the Moving Reference Frame (MRF) technique was used to model propeller rotation. The turbulence was modeled using a RANS approach and the k-ω SST model. The tracing of free-surface is done using the Volume of Fluid method (VOF) in combination with the High-Resolution Interface Capturing (HRIC) scheme to discretise the convective term of the volume fraction transport equation (Muzaferija and Perić 1999). This scheme is suitable for tracking sharp interphase of an immiscible phase mixture and resolves the free-surface within typically one cell. All the aforementioned equations were solved employing an implicit unsteady solver.

The DARPA Suboff model is $L = 4.356$ m long and has a maximum dimeter of 0.508 m. In the employed computational domain of this study, the inlet boundary with a constant inlet velocity was located 4L in front of the hull. The inlet velocity was set to $2.0\ m/s$, equivalent to $Re = 7.9 \times 10^6$(fresh water as the operating medium and L as the reference length). The outlet boundary was placed 10L downstream of the hull. A pressure outlet boundary condition was used on this boundary. A cylinder with a diameter of $D = 7L$ was used as the surrounding boundary and a symmetry boundary condition was imposed on it.

Different mesh types have been used in different part of the computational domain. Trimmed hexahedral grids were used around the hull as well in the far field region but the computational grid for the propeller domain consists of polyhedral cells due to the complex geometry with high curvatures in this region. Prism layers along walls are used to create the boundary layer mesh. Due to dissimilar boundary layer thickness on the hull and the propeller blades, different prism layer thicknesses are used for each of these surfaces and thus the number of prism layers were adjusted accordingly. The number of prism layers were set to 35 and 20 on the hull and propeller blades, respectively. In order to resolve the boundary layer down to the wall, the near wall cell's height was adjusted to obtain $y^+ \approx 1$. The grid distribution inside the computational domain as well as the hull and propeller surface are shown in Figure 2. As seen in this figure, the finest mesh region is around the propeller and the mesh gradually becomes coarser further away from the propeller and hull. The total number of cells is 29 million cells of which about 1 million of that is dedicated to the propeller region. Almost 75% of the grids are packed in the vicinity of the undisturbed free-surface to enable a more accurate prediction of the free-surface.

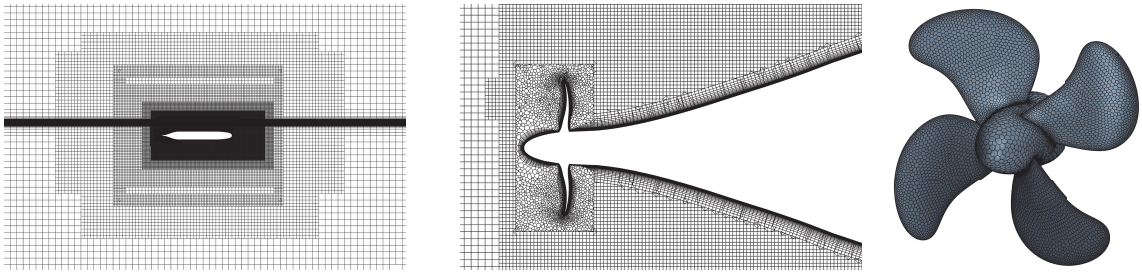

Figure 2. Grid distribution near field region (left), aft part boundary layer prism layer and propeller region mesh (middle) and propeller surface mesh (right).

The propeller revolution rate is iteratively modified until the thrust and the resistance of the propeller and hull are in balance.

4 RESULTS AND DISCUSSION

Several control volumes of different sizes are employed in the process of post-processing the results. The smallest control volume is a cylinder which only surrounds the propeller. The other control volumes are much larger and contain the entire propeller-hull system. Figure 3 depicts these control volumes.

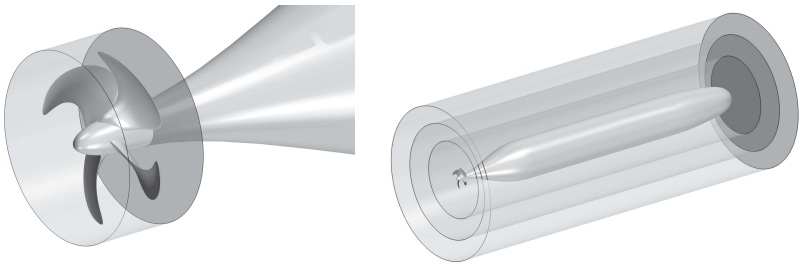

Figure 3. Different control volumes which are used in this study. The left figure shows a small cylindrical control volume around the propeller (CV_{Prop}) and the right figure depicts three cylindrical control volume around the entire system. The smallest control volume is CV1, the middle size control volume is CV2 and the largest one is CV3.

4.1 ENERGY BALANCE METHOD IN ABSENCE OF FREE-SURFACE

Based on the theory presented in Section 2, two methods are used for computing the power consumption in self-propulsion. The first method is a well-established explicit approach through direct computation of the propeller torque (Equation (2)) and the second method was based on the control volume energy balance method (Equation (3)). The results obtained from these two methods are presented in Table 1. The same data is

visualized in Figure 4. In the rest of this paper, the contribution from axial kinetic energy, transversal kinetic energy, pressure work, internal energy and turbulent kinetic energy are abbreviated as Ux, Urt, P, u and k, respectively. Deviation of the sum of all energy flux components with the explicitly obtained shaft power (last column of Table 1) verifies that the energy balance method can well capture the shaft power conversion to different energy components in the flow, almost with the same order of accuracy for all the studied control volumes. Among these control volumes, the energy flux sum obtained from the smallest control volume, CV_{Prop}, has the largest deviation from the propeller delivered power, about 0.30%. Shear stresses acting on the control volume surfaces might be the reason for such a deviation. In this work, we have assumed that shear stress contribution is negligible and has not be taken into account. However, since the control surfaces of CV_{Prop} (especially the lateral surface of the control volume) are subject to large velocity gradient in the vicinity of the propeller, shear stress contribution might be better to consider.

Table 1. Energy fluxes split for different control volumes without free-surface.

	Ux	Urt	P	u	k	sum	Shaft Power	deviation %
CV_{Prop}	44.56	6.19	26.23	15.15	0.12	92.24	91.97	0.30
CV 1	129.70	-2.07	-117.35	80.64	1.10	92.02	91.97	0.05
CV 2	120.23	2.73	-114.26	82.31	1.02	92.02	91.97	0.05
CV 3	104.57	4.54	-101.07	83.12	0.99	92.14	91.97	0.18

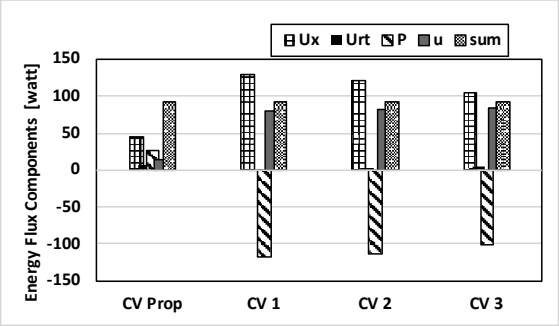

Figure 4. Energy flux components through 4 different control volumes without free-surface.

As mentioned in Introduction section, the current system energy balance method has already been successfully employed by the authors to a series of different marine application such as investigating propeller performance in open water, studying two different ducted and open propeller configurations as well as propeller diameter optimization in behind condition. All the aforementioned studies have been carried out without taking the influence of free-surface into account. In the rest of this paper we will evaluate the effect of free-surface inclusion in the system energy balance method.

4.1 ENERGY BALANCE METHOD IN PRESENCE OF FREE-SURFACE

In the forthcoming computations DARPA is set to be $1.5D_0$ below the undisturbed free-surface. The wave pattern induced by the self-propelled DARPA is shown in Figure 5. In comparison to the previous simulations which were performed in the absence of free-surface, the propeller revolution rate has been increased by about 7.7% to compensate for the increased resistance due to wave making resistance. This results in about 33% increased shaft delivered power. All the control volumes are located below the free-surface, except CV3. As shown in Figure 6, this control volume extends above the free-surface

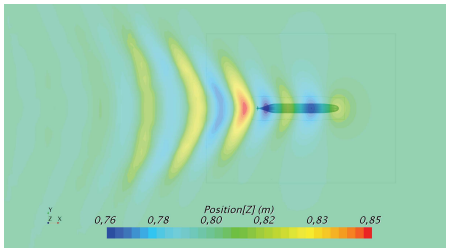

Figure 5. Induced wave pattern by DARPA. The contours indicate the wave height.

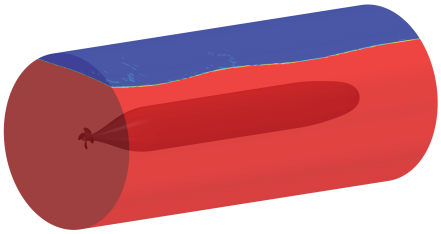

Figure 6. Control volume CV3 and volume fraction contour on the surfaces of this control volume. The red color represents volume fraction 1 (water) the blue represents volume fraction 0 (air).

The energy flux components for all the studied control volumes in presence of free-surface are presented in Table 2. The sum of energy flux components for CV_{Prop} is 2% larger than the explicitly computed shaft delivered power, however shows that this control volume is capable of capturing the conversion of shaft power to different energy components within this control volume. Despite the different absolute values of energy fluxes through CV_{Prop} with and without free-surface(Table 2 and Table 1), the shares of each component from the sum have remained almost unchanged (see Figure 7).

Table 2. Energy flux split for different control volumes with free-surface.

	Ux	Urt	P	u	k	sum	Shaft Power	deviation %
CV_{Prop}	58.58	8.93	36.94	21.62	0.43	126.50	123.99	2.02
CV 1	149.43	2.6	-152.52	97.48	1.45	98.44	123.99	-20.61
CV 2	133.34	1.77	-218.52	98.34	1.47	16.40	123.99	-86.77
CV 3	30.33	19.43	-255.19	96.73	1.57	-107.13	123.99	-186.40

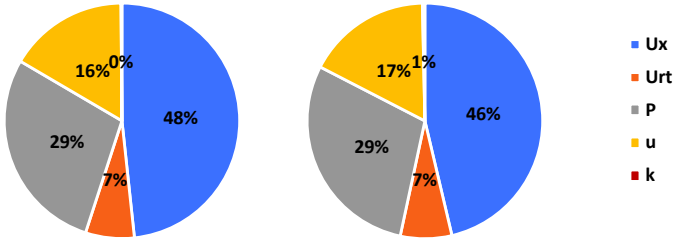

Figure 7. Energy flux split for CV_{Prop} without free-surface (left) and with free-surface (right).

The contour plot of energy flux components through the downstream surface of CV_{Prop} for the case with and without free-surface are shown in Figure 8. Except for the pressure work contribution contours, the lower and upper limit of respective color bars are set to the same values for both of the cases. This enables a direct comparison between the two conditions. Because of the larger required thrust for the self-propelled DARPA in presence of free-surface, the flow needs to be accelerated more to generate the required thrust. The larger axial kinetic energy flux for the DARPA with free-surface is associated with this requirement. Because of the faster rotational speed of the propeller as well as presence of a stronger hub vortex the transversal kinetic energy flux through the downstream boundary of CV_{Prop} is larger for the case with free-surface. Moreover, because of the faster propeller rotational speed, the viscous losses and thus the internal energy flux are larger for the case with free-surface. The associated flux due to pressure work is one order of magnitude larger for the case with free-surface in comparison to the case without free-surface. However, the total contribution from the pressure work has the same order of magnitude for both of the cases. Of course, the total pressure level can be very different between the cases since one takes the gravity into account and the other ignores that. However, the total contribution from each of these energy components is calculated through summation of these fluxes over all the surfaces of the control volume. Therefore, despite the very different absolute values for the fluxes associated with pressure work between the cases with and without free-surface, the total contributions still have the same order of magnitudes (i.e. 26.23 watt versus 36.94 watt).

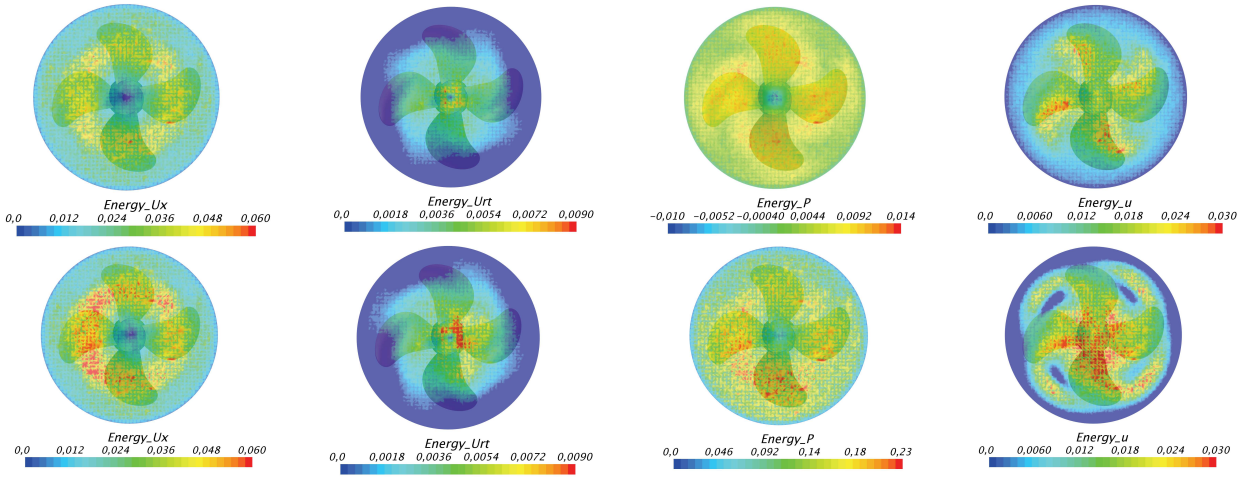

Figure 8. Energy flux components through downstream boundary of CV_{Prop} without free-surface (top row) and with free-surface (bottom row).

According to the time history of the computed variables for CV_{Prop}, the energy fluxes converge rather quickly. However, the convergence of the energy fluxes behaves differently for the larger control volumes. As the control volume becomes larger it takes longer time to have the flow field oscillations stabilized. These oscillations are weaker for the contribution from transversal energy flux and internal energy flux in comparison to the contribution from pressure work as well as the axial kinetic energy flux. The contribution from turbulent kinetic energy is always small and thus negligible. It can be noted that the sum of energy fluxes deviates from the explicitly computed shaft delivered power (123.99 watt) as the control volume becomes larger. Through comparison of the components with and without free-surface (see Table 2 and Table 1), it can be seen that the variation trend of internal energy flux and turbulent energy flux from one control volume to another almost follows the same trend. Moreover, considering the 33% larger delivered power to the self-propelled DARPA in presence of free-surface, the absolute values of these two energy fluxes are comparable to each other. However, the contribution from the pressure work as well as the axial and transversal kinetic energy fluxes for CV1, CV2 and CV3 follow different trends than what was detected and verified earlier for the case without free-surface.

For better understanding of causes for the distinct behaviors of the velocity and pressure fields when the VOF solver is used, a series of simpler computations are carried out with bare hull DARPA with and without free-surface (VOF solver). In these set of computations, the same control volumes are used, however for studying the momentum fluxes and pressure force acting on the control volumes rather than the energy fluxes. Figure 9 shows the non-dimensional axial-velocity distribution around the bare hull with and without free-surface together with the overlaid control volumes.

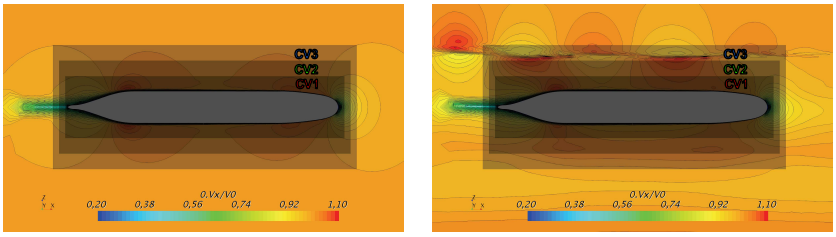

Figure 9. Velocity distribution around DARPA bare hull without free-surface (left) and with free-surface (right). The gray zones show three different control volumes around DARPA.

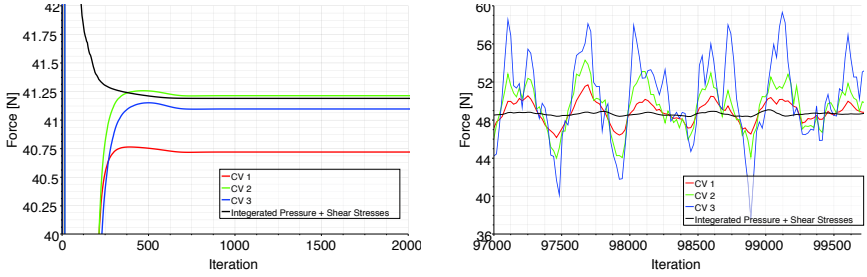

Figure 10. Sum of the momentum flux plus pressure contribution to the forces acting on different control volumes for DARPA bare hull without free-surface (left) and with free-surface (right). The black line indicates the bare hull resistance.

The sum of pressure forces acting on one of the depicted control volumes in the axial direction and the axial momentum flux change through that control volume represents the total force acting on the control volume, provided that frictional forces acting on the control volume are negligible. This total force should be as large the resistance of the bare hull. The convergence history of the sum of axial momentum flux through each of these control volumes plus pressure forces in the axial direction together with the hull resistance are presented for the case with and without free-surface in Figure 10. In case of a single-phase simulations all the contributing terms show a smooth and fast converge trend. The forces acting on the control volumes are quite similar to the resistance of the bare hull. The largest deviation is computed by CV1 (1.2% difference) which most possibly originates from the fact that the shear stress acting on the control has been neglected. The forces computed from the other two control volumes, which their control surfaces are located a bit farther, show a better match with the bare hull resistance (less than 0.1% deviation). However, the convergence history is quite different when the VOF solver is considered. As seen in Figure 10 (right), the oscillation amplitude of the integral force acting on the control volume grows larger as the control volume increases in size and gets closer to the free-surface. The mean values of the computed integral forces also deviate more and more from the bare hull resistance. This momentum flux analysis indicates that the imbalance between the shaft delivered power and

Compressible Two–phase flow model with the Ghost Fluid Method for Marine Hydrodynamics

Inno Gatin*[a], Shengnan Liu[b], Nikola Vladimir[a], Hrvoje Jasak[a]
[a]University of Zagreb, Zagreb/Croatia,
[b]University of Stavanger, Stavanger/Norway
inno.gatin@fsb.hr, shengnan.liu@uis.no, nikola.vladimir@fsb.hr, hrvoje.jasak@fsb.hr

1 Introduction

A Finite Volume (FV) based two–phase flow model where air (gas) is modelled as an ideal gas undergoing adiabatic process, while water (liquid) is assumed to be incompressible, is presented in this paper. The model employs the Ghost Fluid Method (GFM) to discretise numerical operators across the free surface, where the sharp change in fluid compressibility is taken into account along with the jump of other properties (density and consequential pressure gradient). The numerical method is based on the two–phase incompressible flow model which utilises the GFM [Vukčević et al., 2017]. The sharp treatment of compressibility properties and the pressure–based formulation, along with the ideal adiabatic gas assumption, proved to result in a very efficient and robust numerical method due to the fact that the equations reduce to incompressible form when the compressibility effects are absent. Thus, realistic every–day simulations including complex geometries can be simulated on large grids where compressibility effects may or may not happen, without additional computational cost with respect to the equivalent incompressible method.

There are several important phenomena in marine hydrodynamics that require gas to be modelled as a compressible gas. These phenomena are not related to dynamic compressibility effects (e.g. supersonic flows), but to volumetric compression of gas by the liquid. Breaking wave impacts with trapped air are one of these phenomena, where the air compression can change the way the energy is being transferred to the structure, often causing higher structural response due to the prolongation of high pressure acting on the surface, and by increasing the surface on which it acts [Obhrai et al., 2004, Bullock et al., 2007]. Breaking wave impacts can be present in coastal engineering, sloshing, and green water events. Compartment flooding can also be influenced by the compressibility of air, where air trapped by the incoming water and the structure can change the rate of flooding, and consequently the damaged ship's stability dynamics. Another important phenomenon where compressibility plays an important role is slamming, where small volume of air can be trapped in the rapidly changing geometry of the free–surface–structure intersection, changing the pressure loads.

In this work the present approach is used to simulate a breaking wave impact with compressibility effects and green water event of an Ultra Large Container Ship (ULCS) in an irregular wave train. The breaking wave impact pressure force is compared to experimental measurements showing good correspondence. A basic, oscillating water column validation is shown first to prove the accuracy of the model.

The mathematical and numerical formulation of the methodology is briefly outlined, followed by the simple water column test case. Next, the compressible wave impact test case is presented with experimental comparison. Finally, the green water load calculation of an ULCS is shown as a representative realistic industrial case.

2 Compressible Two–phase Flow Model

The momentum conservation equation for two–phase flow where liquid is considered incompressible and the gas compressible states:

$$\frac{\partial \mathbf{u}}{\partial t} + \nabla\cdot(\mathbf{u}\mathbf{u}) - \nabla\cdot(\mathbf{R}) = \\ -\frac{1}{\rho}\nabla p_d - \left(\frac{1}{\rho}\nabla\rho\mathbf{g}\cdot\mathbf{x} - \mathbf{u}\nabla\cdot\mathbf{u}\right), \tag{1}$$

where $\mathbf{u}$ denotes the velocity field, $\mathbf{R}$ is the Reynolds stress tensor, while ρ is the density field with a discontinuity across the interface. p_d stands for the dynamics pressure expressed as $p_d = p - \rho\mathbf{g}\cdot\mathbf{x}$, p

being the static pressure field, **g** the gravity acceleration and **x** the radii vector. The continuity equation reads:

$$\nabla\cdot\mathbf{u} = -\frac{1}{\rho}\frac{\partial\rho}{\partial p}\left(\frac{\partial p_d}{\partial t} + \nabla\cdot(p_d\mathbf{u}) - p_d\nabla\cdot\mathbf{u} + \frac{\partial(\rho\mathbf{g}\cdot\mathbf{x})}{\partial t} + \mathbf{u}\cdot\nabla\rho\mathbf{g}\cdot\mathbf{x}\right). \tag{2}$$

Note that above equations reduce to incompressible flow if $\partial\rho/\partial p = 0$ and $\nabla\rho = 0$, giving numerically stable equation set. Due to GFM employed to discretise numerical operators, the change of $\partial\rho/\partial p$ and $\nabla\rho$ across the interface is sharp instead of gradual, giving physically correct physical properties of both phases near the interface. The gas phase in this study is modelled with isentropic ideal gas assumption, where:

$$\frac{\partial\rho}{\partial p} = \frac{1}{a_c\gamma}\frac{p}{a_c}^{\frac{1-\gamma}{\gamma}}, \tag{3}$$

where γ stands for the constant specific heats ratio, and a_c stands for the isentropic constant.

The GFM enforces the sharp changes in fluid properties to be accounted for during the discretisation of Eqns. 2 and 3. The sharp changes, or jump conditions, arise from different properties of the two fluids, and also from the free surface boundary conditions. The kinematic free surface boundary conditions states that the velocity is continuous across the interface, while the dynamic free surface boundary condition results in:

$$[p_d] = -[\rho]\,\mathbf{g}\cdot\mathbf{x}, \tag{4}$$

which ensures that the jump in dynamic pressure equals the jump of hydrostatic pressure to ensure a continuous pressure field. Operator $[\cdot]$ denotes the difference between the value infinitesimally close to the interface on the side of the liquid and gas side. Apart from the free surface boundary conditions, the governing equation also give rise to jump conditions that need to be satisfied ([Desjardins et al., 2008, Huang et al., 2007, Queutey and Visonneau, 2007]). For the two–phase flow where gas is considered compressible, the jump condition arising from the momentum equation (Eqn. 1) states:

$$\left[\frac{1}{\rho}\nabla p_d\right] = \left[-\nabla\cdot(\mathbf{uu}) + \mathbf{u}\nabla\cdot\mathbf{u} - \frac{1}{\rho}\nabla\rho\mathbf{g}\cdot\mathbf{x}\right], \tag{5}$$

that prescribes the jump in dynamic pressure gradient over density as being proportional to compressibility effects on the air side. In the case when compressibility effects are negligible Eqn. 5 reduces to zero jump condition corresponding to the incompressible flow model [Vukčević et al., 2017].

3 Liquid Piston

In this test case the basic capability of the model to capture volumetric compressibility effects is tested. A one–dimensional vertical grid is generated, where a layer of water is suspended by two pockets of air. The geometry of the case is shown in Fig. 1, where α_I denotes the Volume of Fluid fraction, where 1 stands for liquid and 0 for gas. At time zero equal atmospheric pressure of 1 bar is initialised in both air pockets, causing the water column to oscillate under the influence of gravity causing the interchange between kinematic and gas compression energy. The domain is discretized with 60 cells equidistantly spaced in the vertical direction, while a time–step of 0.01 s was used. Both air and water are inviscid, while no energy transfer exists through the domain boundaries Thus, the energy should remain conserved indefinitely. Fig. 2 shows the comparison of pressure in time at the top and bottom boundary with the solution published by [Ma et al., 2014]. The pressure corresponds well to the referent solution, while no energy loss is evident showing good energy conservation of the model.

4 Compressible Breaking Wave Impact

A breaking wave impact simulation is carried out based on the large–scale experimental measurements conducted by [Bullock et al., 2007] in the Grosser Wellenkanal at the Forschungszentrum Küste in Hannover, Germany. Regular incident waves are imposed that break in front of a vertical concrete wall, with

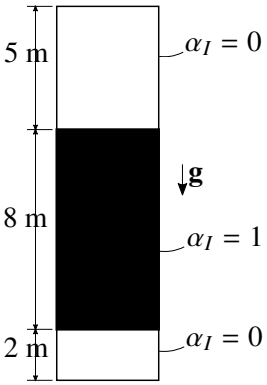

Fig. 1: A schematic representation of a one–dimensional liquid piston case.

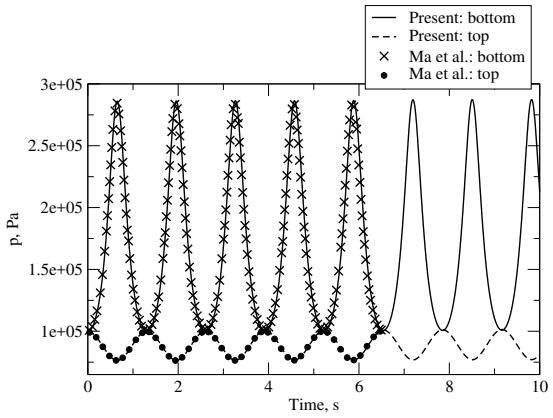

Fig. 2: Comparison of pressure at the bottom and top boundary of the liquid piston case during 10 seconds.

air compressibility effects. Incident wave height is $H = 1.25$ m while the period is $T = 8$ s. The computational domain is presented in Fig. 3, which is discretised using 127 120 cells, while the simulation is carried out in two dimensions. Fig. 4 shows the initial condition where the free surface elevation is visible in front and behind the vertical wall. The compared item is the integrated pressure horizontal force acting on the wall on the side of the oncoming waves (the back of the wall is not taken into account), where the pressure is integrated based on measurements taken on a vertical sequence of pressure sensors used in the experiment and in the simulation.

The comparison of pressure force signal is presented in Fig. 5, where good agreement of the first force peak and through can be observed. After the first force oscillation, the force damps quickly in the experiment, while in the simulation the oscillations are continued significantly longer. Thus, there seems to be larger energy loss of the oscillating air bubble in the experiment. One of the possible reasons are holes that are bored through the vertical wall in the experiment to permit the water level on both sides of the wall to level. Same holes permit air escape from the compressed air bubble diminishing the oscillations. Another reason could be the significant structural response of the wall and the wave flume walls during the impact, which is not accounted for in the simulation. Fig. 6 shows a photograph of the vertical wall used in the experiment, where the holes can be seen. Fig. 7 shows the free surface, velocity and pressure evolution during the wave impact against the vertical wall.

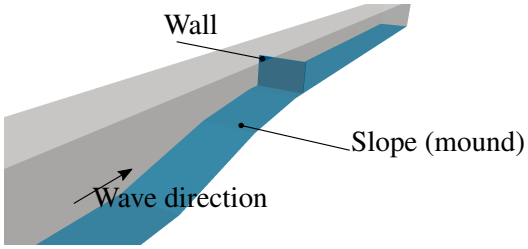

Fig. 3: Numerical domain for the wave impact test case. The vertical wall is placed on a two–segment inclined slope which is covered with gravel in the experiment.

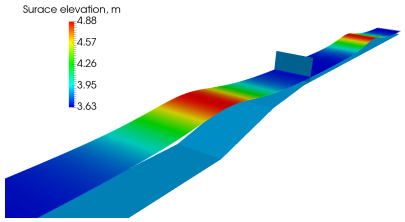

Fig. 4: Initial condition of the free surface elevation in the wave impact case.

5 ULCS Green Water Loads

A long term statistical analysis using linear spectral–domain methods is carried for an ULCS, where the relative wave elevation is used as the dominant loading parameter. Using the results from the long term response, a Response Conditioned Wave (RCW) is defined [Hauteclocque et al., 2012], which is an

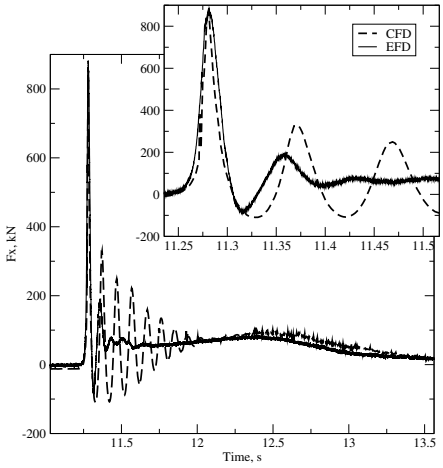

Fig. 5: Force signal comparison for the breaking wave case.

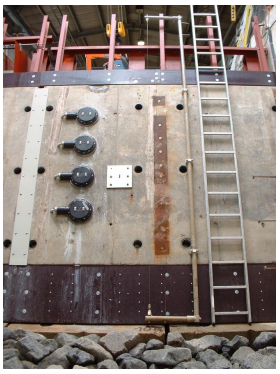

Fig. 6: Photograph of the vertical wall from the breaking wave impact experiment [Bullock et al., 2007].

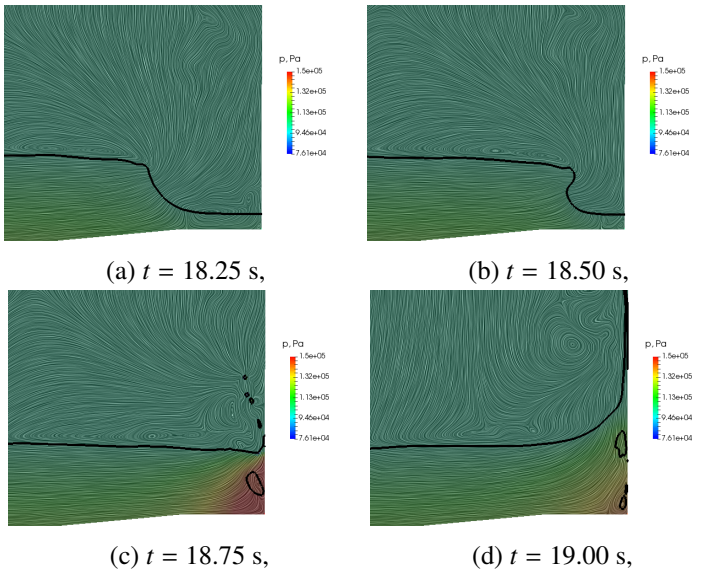

(a) t = 18.25 s, (b) t = 18.50 s,

(c) t = 18.75 s, (d) t = 19.00 s,

Fig. 7: Evolution of the interface, velocity and pressure field in breaking wave impact event with trapped air.

irregular focused wave that is related to the extreme response of the relative wave elevation. The wave condition is based on the Pierson–Moskowitz sea spectrum with the significant wave height H_s = 14.5 m and peak period of T_p = 16.2 s. The simulation is carried out in full scale, Table 8 shows the main ship particulars. In the simulation, the velocity is reduced to 5 kt which conforms with class rules in heavy weather. Pressure loads acting on a breakwater mounted on the bow of the ship are measured, which can be used for structural design purposes. The layout of the computational domain can be seen on Fig. 9, where the relaxation zones used to force the wave field into the CFD domain are denoted. The mesh has 2 374 416 cells generated with the automatic meshing software `cfMesh`. Fig. 10 shows the surface mesh of the ship at the bow where the refinements near the breakwater are visible. The simulation is initialised at t = 30 s to reduce the computational time. Fig. 11 shows the initial condition of the free surface.

As predicted by the liner spectral–domain method, the green water does occur in the event, as can be seen in Fig. 12. The pressure loads exerted on the breakwater in time in the longitudinal direction are shown in Fig. 13. The simulation took 17.2 hours to calculate on a desktop PC with an Intel i5-3570K processor. In the simulation no significant compressibility effects are present, proving that the present numerical method is general. Furthermore, relatively low computational time required to perform

the simulation, on very modest CPU resources, suggests that it is efficient as well and can be used in industrial applications.

Fig. 8: General ship characteristics of the ULCS.

L_{OA}, m	400.0
L_{PP}, m	383.0
B, m	58.6
H, m	30.5
T, m	14.5
Δ, t	212913.0
V, kt	23.0

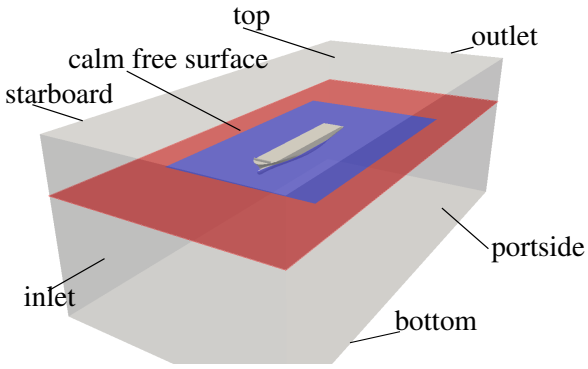

Fig. 9: View of the CFD compuational domain. The relaxation zones are indicated with red colour on the calm free surface. The blue colour indicates undisturbed CFD solution region.

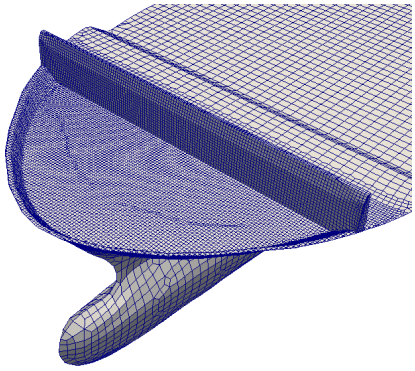

Fig. 10: Surface mesh of the bow and the breakwater used in the simulation.

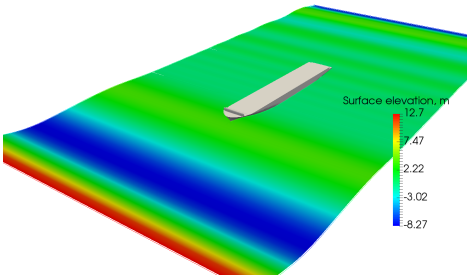

Fig. 11: Initial condition in the Response Conditioned Wave simulation, t = 30.0 s.

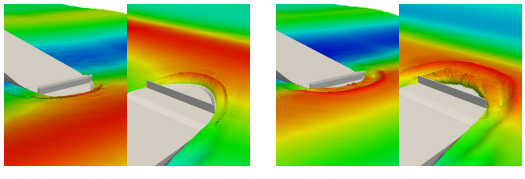

(a) t = 56.4 s, (b) t = 58.0 s,

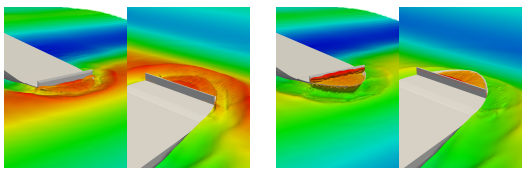

(c) t = 58.8 s, (d) t = 59.6 s,

Fig. 12: The green sea event from the Response Conditioned Wave simulation.

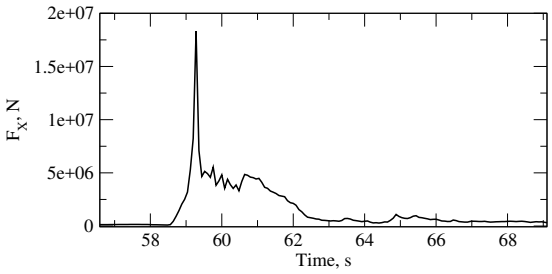

Fig. 13: Longitudinal force acting on the breakwater in the Response Conditioned Wave simulation.

6 Conclusion

The presented numerical model enables performing general marine hydrodynamics simulations where air compressibility may have an important influence on the phenomenon. The model is based on FV methodology, where GFM is employed to discretise numerical operators across the free surface, providing a sharp two–phase, compressible/incompressible flow model.

The numerical framework is first tested on a simple 1D problem of the oscillating water column, proving the basic capability of accounting for the volumetric compression of the gas phase, and showing good energy conservation abilities. In the second case the model is used to simulate a breaking wave impact with trapped air pocket causing oscillatory pressure load on the vertical structure. The results show good correspondence with the experimental measurements. Finally, the versatility, efficiency and generality of the method is shown on the simulation of a green water event on board a ULCS, where pressure loads on a breakwater are measured.

The presented method is capable of simulating phenomena that have volumetric compressibility effects, while it is also effective when air compressibility is absent, providing a single general method for problems in marine hydrodynamics where compressibility may occur, such as green water loads or slamming. At the same time, the inclusion of gas compressibility does increase the computational cost of the approach.

References

Bullock, G. N., Obhrai, C., Peregrine, D. H., and Bredmose, H. (2007). Violent breaking wave impacts . Part 1 : Results from large-scale regular wave tests on vertical and sloping walls. *Coastal Engineering*, 54:602–617.

Desjardins, O., Moureau, V., and Pitsch, H. (2008). An accurate conservative level set/ghost fluid method for simulating turbulent atomization. *J. Comput. Phys.*, 227(18):8395–8416.

Hauteclocque, G. D., Derbanne, Q., and El-gharbaoui, A. (2012). Comparison of Different Equivalent Design Waves with Spectral Analysis. *31st International Conference on Ocean, Offshore and Arctic Engineering*, pages 1–9.

Huang, J., Carrica, P. M., and Stern, F. (2007). Coupled ghost fluid/two–phase level set method for curvilinear body–fitted grids. *Int. J. Numer. Meth. Fluids*, 44:867–897.

Ma, Z. H., Causon, D. M., Qian, L., Mingham, C. G., Gu, H. B., and Ferrer, P. M. (2014). A compressible multiphase flow model for violent aerated wave impact problems. *Proceedings of the Royal Society A: Mathematical, Physical and Engineering Sciences*, 470(2172):20140542–20140542.

Obhrai, C., Bullock, G., Wolters, G., Muller, G., Peregrine, H., Bredmose, H., and Grune, J. (2004). Violent Wave Impacts on Vertical and Inclined Walls: Large Scale Model Tests. *Coastal Engineering*, pages 4075–4086.

Queutey, P. and Visonneau, M. (2007). An interface capturing method for free–surface hydrodynamic flows. *Comput. Fluids*, 36:1481–1510.

Vukčević, V., Jasak, H., and Gatin, I. (2017). Implementation of the Ghost Fluid Method for free surface flows in polyhedral Finite Volume framework . *Computers & Fluids*, 153:1 – 19.

Numerical study of cavitating flow around a surface mounted cylindrical bluff body

Ebrahim Ghahramani, and Rickard E. Bensow
Chalmers University of Technology, Gothenburg/Sweden
ebrahim.ghahramani@chalmers.se

1 Introduction

Cavitation is in many cases an undesirable and unavoidable occurrence in industrial hydraulic systems, such as marine propulsion systems and fuel injectors. Cavitation erosion is believed to be the result of violent collapses of the flowing micro-bubbles. Also, cavitation has significant effects on performance and efficiency of the system. Generated cavities in a hydraulic device can have different patterns and characteristics which are functions of flow field properties. To have a betters understanding of the cavity behaviour, usually the cavitating flows are studied over simpler test cases such as hydrofoils and bluff bodies or inside converging-diverging nozzels.

Although cavitation on lifting bodies has been extensively studied (e.g. Laberteaux & Ceccio, 2001; Asnaghi et al., 2017), fewer studies exist for bluff bodies. Cavitation behind bluff bodies can be categorized into three types (Gnanaskandan & Mahesh, 2016): cyclic, fixed and transitional cavitation. Periodically shedding cavities from the body are know as cyclic cavities, and when a major part of the vapour structure remains attached to the body, it is called fixed cavities. A transitional cavity displays a mix of these phenomena.

Several studies about the wake flows of cylindrical obstacles can be found in literature; however, only a few of them concerned the two-phase cavitation regimes. The main objectives of such studies have been the understanding of the generated noise, measuring the shedding frequency and cavity length, calculating the impulse pressures and determining the erosive cavity collapses and flow conditions. Among the numerical studies, for example, Seo at al. (2008) used direct numerical simulation (DNS) approach to compute the generated sound in a cavitating flow over a cylinder at low Reynolds number and found that the cavity collapse is the main source of noise in the flow. Also, Gnanaskandan & Mahesh (2016) investigated the near-wake characteristics of cavitating flow over a cylinder and found that cavitation significantly influences the evolution of pressure, boundary layer and loads on the cylinder surface. They also observed that cavitation suppresses turbulence in the near wake and delays three-dimensional breakdown of the vortices.

In this study, the cavitating flow around a surface mounted half-circular cylinder is studied numerically. Due to the flat frontal side of the cylinder in this study, no boundary layer is formed in front of the body and more pressure drop is expected behind the cylinder with more aggressive vortices, as compared to earlier studies with (fully) circular cylinders. The numerical simulation is performed using the incompressible homogeneous mixture model in which the cavity generation and transport is modelled by solving a scalar transport equation based on the liquid volume fraction.

In the following sections, the flow geometry and boundary conditions are described first. Then, the numerical model is explained and finally the cavity pattern behind the cylinder is analysed in the result section.

2 Geometry and boundary conditions

The half-circular cylinder has a diameter of 5 mm and a length of 9.65 mm, and is put vertically in a channel as a bluff body. To have a larger pressure drop and higher local velocities, which augments cavitation, the channel has a converging-diverging rectangular cross-section around the cylinder. The upper side of the channel has a curved profile while the lower wall is raised at a constant slope. The cylinder is put at the end of the lower slope just before the the diverging part of the nozzle, Figure 1. The flat side of the half-cylinder is facing upstream.

The channel sides and the cylinder are considered as rigid walls with no-slip boundary condition. A constant volume flow rate of 0.04 m^3/s is set at the inlet and the constant pressure is set as the outlet boundary condition. The outlet pressure is set equal to 297 kPa.

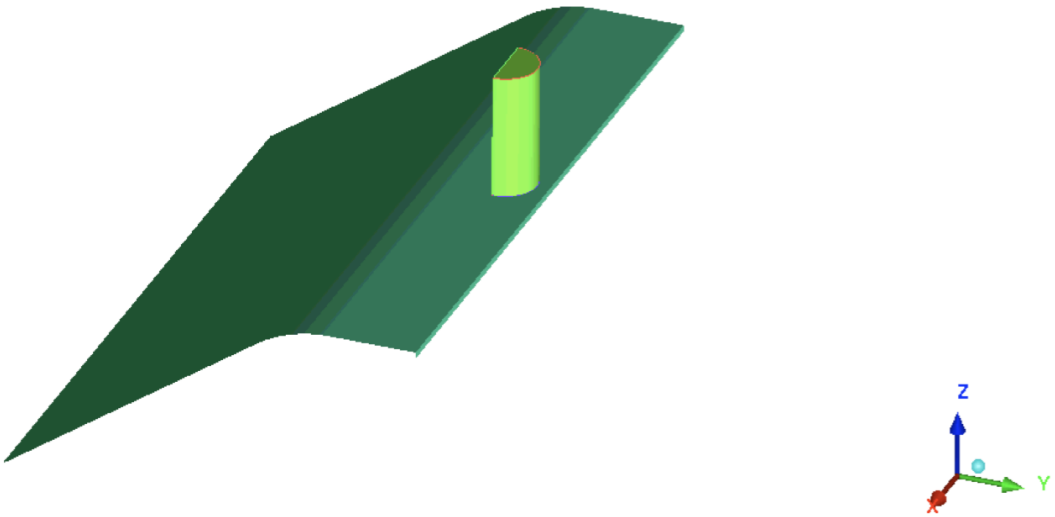

Fig. 1: Cylindrical bluff body. The flow direction is from left to right

3 Numerical method

In this study, the incompressible homogeneous mixture model is used to model the generation and transport of vapour cavities. In this model, the vapour and liquid phases are treated as a single mixture fluid, and the continuity equation and one set of momentum equations for the mixture are solved. The continuity equation is then given by

$$\frac{\partial u_i}{\partial x_i} = (\frac{1}{\rho_l} - \frac{1}{\rho_v})\dot{m}. \tag{1}$$

The RHS term is the effect of vaporization and condensation, where $\dot{m}$ is the rate of mass transfer between phases, ρ_l is the liquid density and ρ_v is the vapour density. Further, the Navier-Stokes equations are

$$\frac{\partial (\rho_m u_i)}{\partial t} + \frac{\partial \left(\rho_m u_i u_j\right)}{\partial x_j} = \frac{\partial \tau_{ij}}{\partial x_j} + \rho_m g_i. \tag{2}$$

Here, ρ_m and τ_{ij} are the mixture density and the stress tensor, respectively, which are defined as

$$\rho_m = \alpha\rho_l + (1-\alpha)\rho_v, \tag{3}$$

$$\tau_{ij} = -p\delta_{ij} + \mu_m\left(\frac{\partial u_i}{\partial x_j} + \frac{\partial u_j}{\partial x_i} - \frac{2}{3}\frac{\partial u_k}{\partial x_k}\delta_{ij}\right), \tag{4}$$

where μ_m is the the mixture dynamic viscosity, given by

$$\mu_m = \alpha\mu_l + (1-\alpha)\mu_v, \tag{5}$$

and α is the liquid volume fraction which specifies the relative amount of liquid in a given volume, e.g. a computational cell. In this approach, the evolution of the volume fraction is calculated by solving a scalar transport equation given as

$$\frac{\partial \alpha}{\partial t} + \frac{\partial (\alpha u_i)}{\partial x_i} = \frac{\dot{m}}{\rho_l}. \tag{6}$$

To close the above set of equations the mass transfer rate, $\dot{m}$ should be determined. There are many numerical models in literature to estimate this term and most of them are based on a simplified form

of the well-known Rayleigh-Plesset equation. In this study, the Schnerr-Sauer (Schnerr & Sauer, 2001) model is used. The vaporization and condensation rates are then given by

$$\begin{aligned} \dot{m}_c &= C_c \alpha(1-\alpha)\frac{3\rho_l\rho_v}{\rho_m R_B}\sqrt{\frac{2}{3\rho_l|p-p_{threshold}|}}\max(p-p_{threshold},0), \\ \dot{m}_v &= C_v \alpha(1+\alpha_{Nuc}-\alpha)\frac{3\rho_l\rho_v}{\rho_m R_B}\sqrt{\frac{2}{3\rho_l|p-p_{threshold}|}}\min(p-p_{threshold},0), \end{aligned} \tag{7}$$

where $\dot{m}_c$ and $\dot{m}_v$ are the rates of condensation and vaporization, respectively. In the above equations, R_B and α_{Nuc} are user defined model parameters corresponding to generic radius and volume fraction of bubble nucleis in the liquid. Also, $p_{threshold}$ is a threshold pressure at which the phase change is assumed to happen, usually considered as the vapour pressure of the fluid. This model is available in the open source C++ package OpenFOAM as the InterPhaseChangeFOAM solver. In equation 7, C_c and C_v are the empirical condensation and vaporization coefficients implemented in OpenFOAM, respectively. These parameters are set to 1 in the following simulation. R_B and ρ_m are functions of liquid volume fraction and are updated at each time step. In this study, the liquid and vapor densities are 1000 kg/m3 0.01389 kg/m3, saturation pressure is 2320 kg/ms2 and α_{Nuc} is set to 5×10^{-5} by assuming 10^8 nuclei/m3 with initial diameter of 0.1 mm. It should also be noted that the flow turbulence is modelled using the Implicit LES approach (Bensow & Bark, 2010).

4 Results

In Figure 2 the cavity patterns around the cylinder is shown for 5 different time steps. Here the cavity shape is plotted using isovolume of liquid volume fraction with $0 < \alpha < 0.9$, which means that each grid cell that has a liquid volume fraction of 0.9 or less is considered as a vapour cell. The flat side of the cylinder is marked with black colour in the plots. The volumes are coloured based on the axial velocity value, U_y. As can be seen from the figure, the cavity length behind the cylinder changes with time and some small structures are shed both at the trailing edge and at the sides of the fixed cavity. Also, two sheet cavities are generated on the lower wall of the channel at both sides of the cylinder. From the negative velocity values (blue areas), some re-entrant jet flows are seen below these side structures. Also, based on Gnanaskandan & Mahesh (2016) categorization for bluff body cavity structures, in this case we have a fixed cavity pattern.

In Figure 3 the cavity patterns around the cylinder are shown at the same time steps but with isovolume of liquid volume fraction with $0 < \alpha < 0.5$. As the liquid volume fraction has higher values at the cavity interface, and it decreases in the innner part of the cavity, in the new volumes with $\alpha < 0.5$, inner regions of the cavities are depicted. Here, we see that while in Figure 2 the axial component of the velocity at the cavity boundary is almost positive and in the same direction as the main flow, it has negative values at some regions inside the cavity, which means that a reverse flow occurs in the cavitating region. From the figures it can also be inferred that the reverse flow starts at the cavity closure area and moves toward the cylinder and as it moves upstream, it disturbs the cavity interface behind itself, which is seen in Figures 3 (c)-(d) and Figures 2 (c)-(d).

Another point that can be detected from the figures is the vapour string at the end of the developed fixed cavity area, Figure 2c. Due to pressure variations in the wake area and the cavity dynamics in the closure line, some vapour strings are randomly generated with a later collapse at this zone.

In future, the simulations will be performed with different grid resolutions and solution parameters and at various flow conditions to have a more comprehensive investigation about the cavitation dynamics in the wake region that can be deterministic in the erosion estimation behind bluff bodies. Also, the results will be verified with experimental tests and will be compared with earlier studies for fully cylindrical and triangular (2D wedge) test cases.

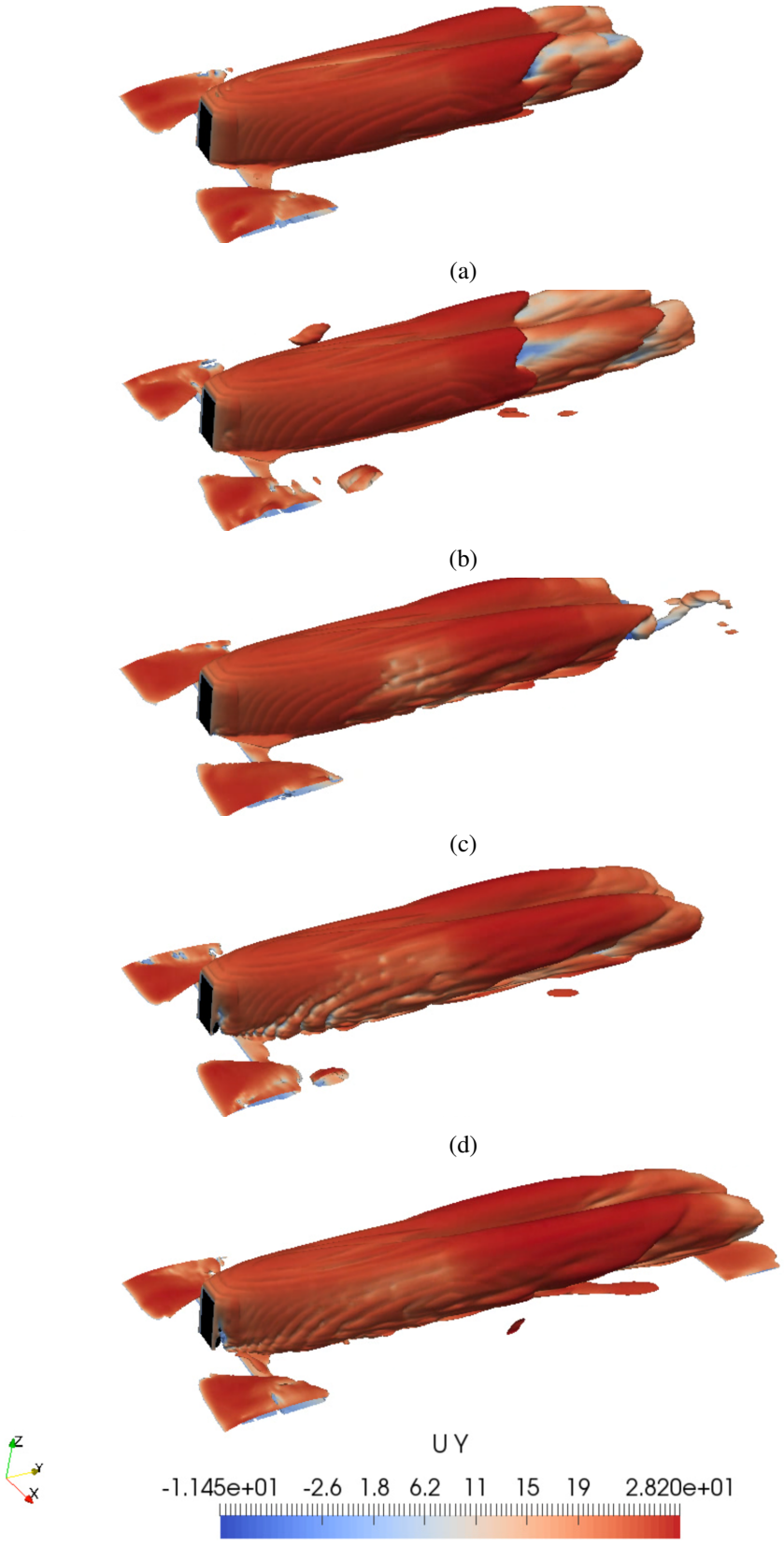

Fig. 2: Cavity patterns with $0 < \alpha < 0.9$; (a) $t = t_0$, (b) $t = t_0 + 0.003$ s, (c) $t = t_0 + 0.007$ s, (d) $t = t_0 + 0.009$ s, (e) $t = t_0 + 0.011$ s

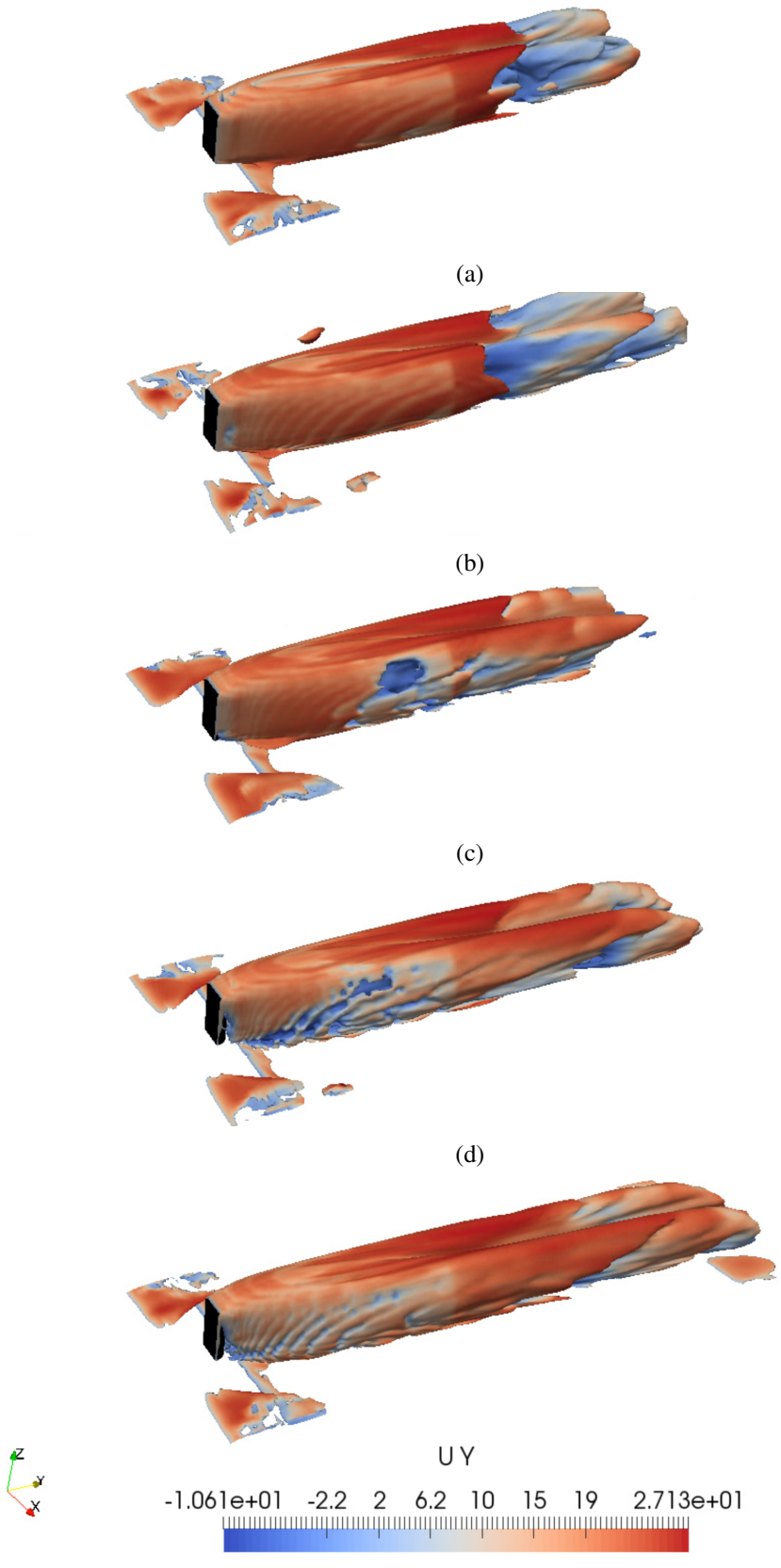

Fig. 3: Cavity patterns with $0 < \alpha < 0.5$; (a) $t = t_0$, (b) $t = t_0 + 0.003$ s, (c) $t = t_0 + 0.007$ s, (d) $t = t_0 + 0.009$ s, (e) $t = t_0 + 0.011$ s

Acknowledgements

This work is funded through the EU H2020 project CaFE, a Marie Skłodowska-Curie Action Innovative Training Network project, grant number 642536. Also, the computations were performed on resources at Chalmers Centre for Computational Sciences and Engineering (C3SE) provided by the Swedish National Infrastructure for Computing (SNIC).

References

K. R. Laberteaux, S. L. Ceccio (2001) Partial cavity flows. Part 1. Cavities forming on models without spanwise variation. *Journal of Fluid Mechanics*. 431, 1-41.

A. Asnaghi, R. E Bensow, U. Svennberg (2017), Implicit Large Eddy Simulation of Tip Vortex on an Elliptical Foil, *Fifth International Symposium on Marine Propulsion*, SMP 17 , Espoo, Finland

A. Gnanaskandan, K. Mahesh (2016), Numerical investigation of near-wake characteristics of cavitating flow over a circular cylinder, *Journal of Fluid Mechanics*, 790, 453-491

J. H. Seo, Y.J. Moon, B.R. Shin,(2008) Prediction of cavitating flow noise by direct numerical simulation. *Journal of Computational Physics*, 227 (13), 6511-6531.

G. H. Schnerr and J. Sauer, Physical and numerical modeling of unsteady cavitation dynamics, *Fourth international conference on multiphase flow*, New Orleans, USA, vol. 1, 2001.

R.E. Bensow, G. Bark (2010) Implicit LES predictions of the cavitating flow on a propeller. *Journal of Fluids Engineering*, 132(4), 041302

Unsteady forces on hydrofoil vessels in waves - validation of a dynamic lifting line using CFD

John Martin K. Godø[1], Jarle V. Kramer[1], Sverre Steen[1], Luca Savio[2]
[1]Norwegian University of Science and Technology, Trondheim, Norway
[2]SINTEF Ocean, Trondheim, Norway
john.martin@ntnu.no

Introduction

The principle of using hydrofoils for lift and thereby reducing resistance at high speed is gaining popularity in a broad spectrum of waterborne vessels, ranging from small hydrofoil surfboards to large commercial passenger ferries. For the larger classes of vessels, it is of interest to be able to properly model the forces acting on the hydrofoil system when running in waves. These forces determine both the seakeeping abilities and the added resistance. Documenting behaviour in a seaway typically involves running a set of 20-minute real-time simulations at a series of incoming wave directions for each relevant sea state. 3D RANS analyses are currently too computationally expensive for a direct approach in this kind of analysis. It is therefore of interest to develop simplified approaches which yield sufficient accuracy for engineering judgement, while being computationally efficient. Such a tool has been developed, based on dynamic lifting line theory, and current work aims to quantify its accuracy. In short:

The current study investigates the accuracy of a dynamic lifting line code by using 3D unsteady RANS simulations as validation results.

Test case

A hydrofoil vessel - with several lifting surfaces, struts, control surfaces, a propulsion system and a free surface interacting in a complex incoming flow created by irregular seas - is a challenging task to fully model. If attempting to model the whole problem, it might also be difficult to separate errors originating from different assumptions and modelling approaches. In the current work the problem is therefore simplified into a single wing of rectangular planform, oscillating in undisturbed water. Oscillation frequency is set so that it represents typical encounter frequencies and the amplitude is tuned so that the maximum inflow angle is equal to what can be expected when running a hydrofoil vessel in waves. Free surface effects, horizontal wave-induced velocities, cavitation and potential ventilation phenomena are neglected. This serves as a starting point for validation of the dynamic lifting line (DLL), isolating the question of whether the effect of induced velocities from a 3D dynamic wake is properly captured. Fully submerged hydrofoil systems typically have an aspect ratio of 4-10 (Van Walree, 1999). Under the assumption that emerging hydrofoil design companies aim to minimize resistance, an aspect ratio in the upper end of this range is judged as most relevant for future hydrofoil vessels. We therefore set the aspect ratio to 10 in the current work. For simplicity and generalization, the planform is set to be rectangular and the foil profile is chosen as Eppler E-817.

Having determined the geometry, the next question is how to oscillate the wing so that dynamic lift effects are representative for those encountered by a hydrofoil vessel running in a seaway. The empirical formulae in equations (1) and (2) (Tucker & Pitt, 2001) have been used for estimating significant wave height and peak period H_s and T_p in relevant sea states. Here f is the fetch distance in kilometers and U_w is the wind speed in m/s.

$$H_s = 0.0163\, f^{0.5 U_w} \tag{1}$$

$$T_p = 0.566\, f^{0.3\, U_w^{0.4}} \tag{2}$$

$$\dot{z}_{a,2m} = \omega_p z_a = \omega_p H_s e^{kz} = \omega_p H_s e^{\frac{\omega_p^2 z}{g}} = 1.14\, m/s \tag{3}$$

In the current study we have assumed a wind speed of 10.7 m/s, which is at the limit between a fresh and a strong breeze on the Beaufort scale. Fetch distance is set to 50 km, corresponding to a typical value for the most densely fast-ferry operated area of the world, the Pearl River Delta between Hong Kong and China. This gives $H_s = 1.23\, m$, $T_p = 4.72\, s \leftrightarrow \omega_p = 1.33\, rad/s$. We assume the wing to be submerged by 2 meters and estimate a representative vertical water speed amplitude at this depth, $\dot{z}_{a,2m}$, by the assumption of linear wave

theory through equation (3). Now the inflow angle amplitude when running in the given seaway, β, can be estimated by trigonometric considerations. Assuming a forward speed of 35 knots we get $\beta = 3.63°$.

Upper and lower limits for the most relevant frequencies of oscillation are found from calculating the encounter frequency ω_e in head and following seas by equation (4) (Faltinsen, 2005). Here γ represents the horizontal incoming wave direction in the vessel coordinate system, U_s is the vessel speed and ω_0 is the wave frequency, which is here set equal to the peak frequency in the sea state spectrum. The upper and lower encounter frequency limits were found to be 4.6 rad/s and 1.9 rad/s respectively. For generalisation we transform these numbers into dimensionless parameters, by the definition of reduced frequency k given in equation (5). c symbolises wing chord length, which is assumed to be 1 m. This is within the range of typical values for hydrofoil vessels (Van Walree, 1999). Inserting numbers, the upper and lower reduced frequency limits are identified as k = 0.13 and k = 0.05 respectively. In the current study we choose to investigate k values between 0.05 and 0.25, covering the range of probable encounter frequencies in addition to frequencies nearly twice as high as the identified upper limit. For all cases we adjust the heave amplitude so that the quasi-static angle of attack amplitude equals 4°, which is slightly higher than the representative inflow angle calculated above.

$$\omega_e = \omega_0 + \omega_0^2 U_s cos(\gamma) \tag{4}$$

$$k = \frac{\omega c}{2U_s} \tag{5}$$

The expected dynamic effect on oscillatory lift amplitudes can be found for 2D conditions from the Theodorsen function (Theodorsen, 1935). The magnitude of this parameter gives the expected ratio of dynamic lift amplitude to the amplitude calculated by a quasi-steady approach. A plot of the Theodorsen function is shown in Figure 1, indicating that a 25-30% lift reduction due to dynamic effects can be expected in the upper frequency range of the current study. The chosen cases are hence suitable for testing the ability of the code to capture dynamic lift effects. Geometry and motion pattern parameters are summed up in Table 1.

Table 1: Geometry and motion pattern

Parameter	*Value*
Aspect ratio	10
Chord length	1 m
Foil profile	Eppler E-817
Planform	Rectangular
Motion pattern	Harmonic heave
Angle of attack amplitude	4 degrees
Reduced frequencies	0, 0.05, 0.075, 0.15, 0.20 and 0.25

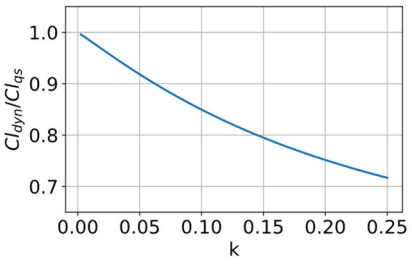

Figure 1: Theodorsen function values at reduced frequencies from 0 to 0.25

When evaluating hydrofoil seakeeping we believe that the most interesting output parameters are vessel accelerations and the resistance when running in waves. The former dictates passenger comfort and the latter gives input for dimensioning of machinery. In the evaluation of the accuracy of the DLL code we have therefore chosen to monitor two parameters: The RMS value of the dynamic part of lift $C_{L,dyn,RMS}$, and the mean value of drag, $C_{D,mean}$.

RANS setup

Solver and boundary conditions

The open-source CFD software OpenFOAM and the dynamic overset mesh solver overPimpleDyMFoam has been used for all RANS simulations. A k-ω SST turbulence model was used together with wall functions. For convective terms discretisation was done with a linear upwind scheme, turbulent quantities were discretised with the Gauss limitedLinear scheme and a limiting coefficient of 1, while a Gauss linear scheme was used for all other quantities. For the overset interpolation we used the inverseDistance method in OpenFOAM, and an Euler scheme was used for time discretisation.

Mesh

The OpenFOAM programs blockMesh and snappyHexMesh were used for creating both the inner and outer meshes, with the routine mergeMeshes used for combining the two into a mesh suitable for the overset mesh

solver. The mesh used in presented simulations had properties as shown in Table 2. The case is assumed symmetric about mid-span of the wing, hence only half the physical geometry was meshed.

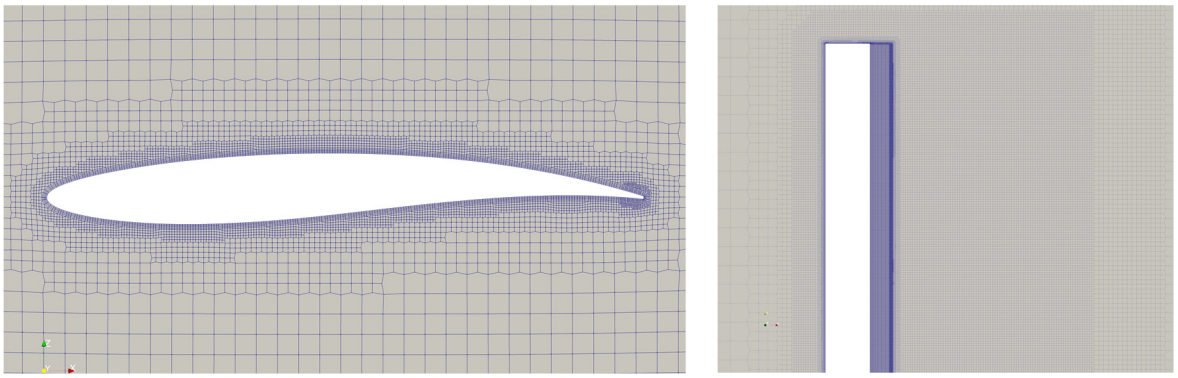

Figure 2: Close-up view of mesh around foil section and top view of inner mesh.

All simulations were done at a Reynolds number of 3e6. This is relatively low compared to what one would have for a full-scale hydrofoil vessel, but the reduction of Reynolds number was viewed as necessary to get a reasonable cell count for running at the available computing resources. Current settings give a mesh of 7.9 million cells for the final mesh. Time step adjustment was done during run time so that the maximum CFL number in the simulation was 20. This yielded approximately 1550 time steps per motion cycle at the highest oscillation frequency.

Table 2: Final mesh properties

Property	*Value*
yPlus	90
Inner cell size [chords]	0.0022
Number of layers	5
Layer expansion ratio	1.11
Outer cell size [chords]	0.282
Cells between levels	4
LxWxH [chords]	35x15x20
Wake refinement length [chords]	2.5
Wake cell size [chords]	0.025

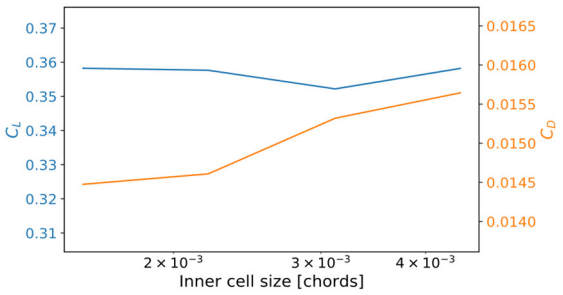

Figure 3: Cell size refinement study, performed in steady-state conditions.

Spatial and temporal refinement

A mesh refinement study was performed, scaling all mesh dimensional quantities by a factor of $\sqrt{2}$. Mesh scaling included the y^+ value, yielding equal number of layers and layer expansion ratio between meshes. For reasons of computational power limitations this was done in steady-state conditions. Results can be seen in Figure 3, where $C_{L,mean}$ and $C_{D,mean}$ are plotted as functions of cell size scaling factor. The final mesh has inner cell size of 2.2e-3, yielding approximately 0.2% and 0.9% inaccuracy in lift and drag as compared to the finest mesh in the refinement study.

Dynamic lifting line

A non-linear dynamic lifting line code (DLL) has been developed, based on the non-linear lifting line by (Kramer, et al., 2018). Extension to dynamic conditions was done by the addition of a panelised wake, methods for updating, truncating and calculating induced velocities from the wake, and the addition of support for moving line elements and dynamic foil section forces.

The lifting line code builds on the assumption that the problem of a lifting surface and its wake can be split into a three-dimensional outer domain, constituted by a set of straight vortex lines of constant vorticity strength, and a set of inner domains of 2D foil cross-sections exposed to uniform inflow velocity. The inner and outer domains are illustrated in Figure 4 and Figure 5 respectively. The two domains are connected by a set of equations, relating inner domain foil section lift to outer domain line vorticity.

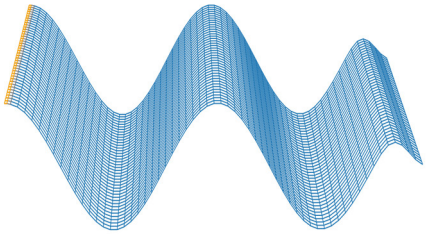

Figure 4: Outer domain. Bound vorticity lines and horseshoe vortices are marked by orange colour. Wake vorticity lines from previous time steps are marked by blue colour.

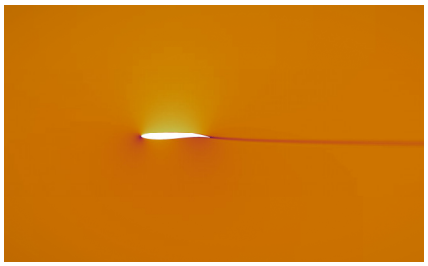

Figure 5: Inner domain constituted by RANS generated static profile data corrected for dynamic effects. Flat plate added mass and $\frac{\delta\Gamma}{\delta t}$terms are added according to formulae below.

All calculations of vortex induced velocity are based on the Biot-Savart law, in a form valid for straight vortex lines of constant strength given in Equation (6) (Phillips & Snyder, 2000). Here $\boldsymbol{r_1}$ and $\boldsymbol{r_2}$ denote the vectors from the ends of the vortex line to the evaluation point, Γ denotes line vorticity and **V** denotes the resulting 3-dimensional velocity vector. The latter is set to zero if the denominator of (6) is zero.

$$\boldsymbol{V} = \frac{\Gamma}{4\pi}\frac{(|\boldsymbol{r_1}| + |\boldsymbol{r_2}|)(\boldsymbol{r_1} \times \boldsymbol{r_2})}{|\boldsymbol{r_1}||\boldsymbol{r_2}|\,(|\boldsymbol{r_1}||\boldsymbol{r_2}| + \boldsymbol{r_1} \cdot \boldsymbol{r_2})} \tag{6}$$

The set of equations which is solved at each time step is on the form $\boldsymbol{A\Gamma} = \boldsymbol{b}$. The left-hand side constitutes the outer domain. The diagonal of the **A** matrix contains lift on a vortex line segment of constant strength, as found by the Kutta-Jukowski theorem. Adding terms to account for lift due to the time derivative of bound vorticity, one can express this as in Equation (7) (Katz & Plotkin, 2001). $\boldsymbol{dl}$ symbolises the vector from one end of the line element to the other. All entries in **A** also contains a term equal to $-\frac{\delta C_l}{\delta \alpha}U_{ij}$, where U_{ij} is the induced velocity on element i per unit bound vorticity at element j. This includes both the effect of bound vorticity in the line and the effect of a horseshoe vortex stretching downstream from one end of the bound line to the trailing edge, along the trailing edge and back upstream to the other end of the bound line. Each horseshoe vortex is assumed to have the same strength as the bound vorticity line element at the current spanwise position. **b** symbolises the inner domain and contains foil section lift due to camber, inflow angle of attack and pitch rate. Static foil section lift data are found through 2D RANS simulations. In the current study these have the same mesh sizing properties as the 3D simulations. When solved, the set of equations gives a **Γ** vector which balances local foil section lift with induced velocities due to bound, horseshoe and wake vorticity.

$$\boldsymbol{dF} = \rho(\Gamma + \frac{\delta\Gamma}{\delta t}\frac{c}{|\boldsymbol{V} \times \boldsymbol{dl}|})(\boldsymbol{V} \times \boldsymbol{dl}) \tag{7}$$

When **Γ** is found, the remaining step is to calculate forces on the wing. This is done by summing forces due to circulation as found from Equation (7) and oscillating flat plate added mass force as expressed in Equation (8) modified from (Leishman, 2006). Here u_n and u_t symbolises normal and tangential relative water velocity respectively, θ is the foil pitch angle, x_{rot} is the chordwise centre of rotation measured in chord lengths and with positive direction towards the trailing edge. $\boldsymbol{n}$ is the chord normal vector and dotted parameters symbolise time derivatives.

$$\boldsymbol{dF_{AM}} = \frac{\pi c^2}{4}\left(-\dot{u}_n + u_t\dot{\theta} + (0.75 - x_{rot})c\ddot{\theta}\right)\frac{\boldsymbol{n}}{|\boldsymbol{n}|}|\boldsymbol{dl}| \tag{8}$$

In short, the solution process at each time step consists of the following steps:

1. Calculate wake induced velocity and add wing motion to get elementwise inflow velocity
2. Construct induced velocity matrix from bound vorticity lines and horseshoe vortices
3. Run solver until convergence
   a. Calculate induced velocity from previous Gamma and linearize 2D lift model about relevant angle of attack
   b. Construct set of equations and solve
4. Calculate forces.
5. Move wing, shed new upstream wake panels and remove downstream wake panels

A convergence study has been performed, both with respect to the number of spanwise elements, the number of iterations per oscillation period and the streamwise length of the saved wake. Convergence of $C_{L,rms}$ and $C_{D,mean}$ can be seen in Figure 6, Figure 7 and Figure 8. All results used when comparing with RANS simulations were obtained with 80 spanwise elements, 100 iterations per oscillation and a saved wake length of $1.25 * TU$.

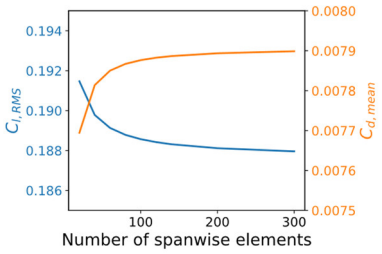

Figure 6: Lifting line convergence with respect to number of spanwise elements

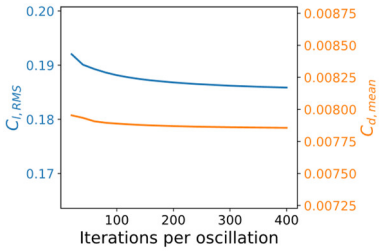

Figure 7: Lifting line convergence with respect to number of iterations per oscillation period

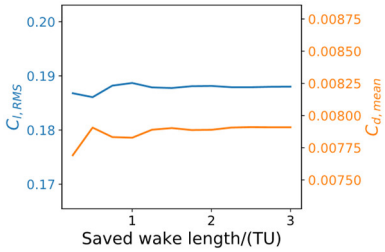

Figure 8: Lifting line convergence with respect to saved wake length normalised by distance travelled per oscillation period

Results

Figure 9 and Figure 10 show time series of C_L and C_D obtained from RANS simulations together with those obtained by the dynamic lifting line code for a reduced frequency of k = 0.075. $C_{L,mean}$+/- $C_{L,dyn,RMS}$ and $C_{D,mean}$ are marked by dashed lines. It is seen that the DLL code can capture the qualitative shape of both time series very well. Except for a start-up transient the time series of C_L is captured close to perfectly, and both mean lift and $C_{L,dyn,RMS}$ correspond within 2.5%. The shape of the C_D curve is also very well captured, but numerical values deviate slightly close to time instants of minimum drag, corresponding to time instants of maximum lift. Lift rms and mean drag deviate by 1.6% and 8.4% respectively in the current case.

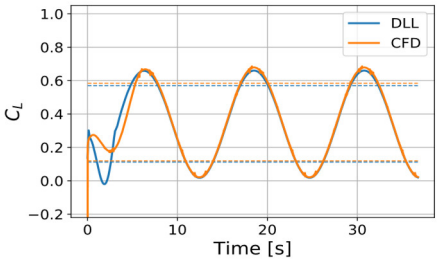

Figure 9: Cl time series from DLL and RANS, k = 0.075. Dashed lines show $C_{L,mean}$+/- $C_{L,dyn,,RMS}$.

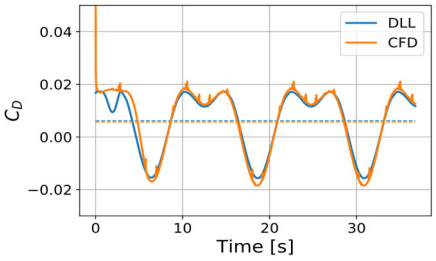

Figure 10: Cd time series from DLL and RANS, k = 0.075. Dashed lines show $C_{d,mean}$

Figure 11 and Figure 12 show acceleration and resistance results from a range of frequency values. To make the numbers intuitively meaningful we have plotted vertical acceleration rms instead of $C_{L,dyn,RMS}$ directly. In the conversion the vessel mass is assumed to correspond to the weight support by the wing in steady conditions. Accelerations are seen to be well captured at the lower oscillation frequencies up to and including k = 0.15, with less than 2% deviation between DLL and CFD. Mean drag is well described by the DLL at all tested oscillation frequencies. Except for the frequencies of k = 0.05 and k = 0.075, where drag deviates by approximately 8.4%, the DLL and CFD drag values correspond to within 2.5%. Having a steady-state drag reference it is possible to calculate the added resistance in waves, in the form of mean drag in dynamic conditions divided by mean drag in static conditions. With this approach the largest deviation between DLL and CFD constitutes 4.0 percentage points of added resistance. Figure 13 shows mean lift as a function of reduced frequency. The largest mean lift deviation in dynamic cases is 3.3%. For the static case the DLL under predicts lift and drag relative to the 3D RANS simulation by 2.2 % and 1.7% respectively.

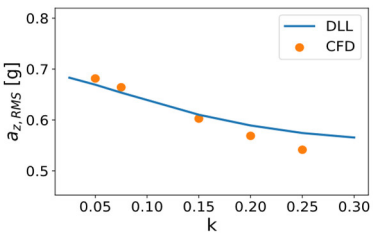

Figure 11: Vertical acceleration rms plotted as a function of dimensionless frequency of encounter.

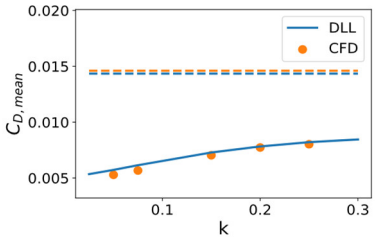

Figure 12: Mean drag plotted as a function of dimensionless frequency of encounter. Dashed lines show steady-state values.

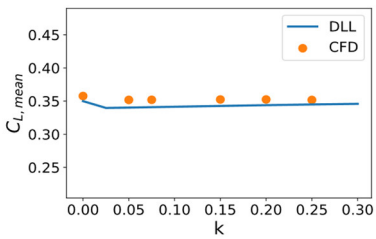

Figure 13: $C_{L,mean}$ plotted as a function of dimensionless frequency of encounter

Conclusions

Current results indicate that a dynamic lifting line code can capture unsteady lift variations and mean drag on a wing oscillating with frequencies corresponding to relevant encounter frequencies for hydrofoil vessels, to an accuracy of 2.0 % and 8.4 % respectively. If evaluating added resistance instead of mean drag, the deviation between DLL and CFD is 4.0 percentage points. This is judged as sufficiently accurate for analyses of hydrofoil seakeeping and added resistance in waves. The fact that the time series of lift is replicated with very little phase lag also makes the DLL suitable for stability analyses of closed-loop flight control systems. It is encouraging that good correspondence between CFD and DLL is found at a relatively low Reynolds number. Wake vorticity dissipates more slowly at higher Reynolds numbers, and since the DLL assumes zero wake vorticity decay it is expected that DLL-CFD correspondence will be better when running simulations in full scale.

The reason why drag estimates are less accurate than lift estimates is currently not completely understood. Parts of the difference might be argued to originate from the low total drag in dynamic cases, making it increasingly hard to reduce percentage errors as drag falls to less than half its static value in some dynamic cases. The applied 2D static model for drag might also be inaccurate for certain angles of attack, or dynamic boundary layer effects may play a role in the 3D simulation. The current lift and drag models were produced from 2D static CFD analyses with angle of attack steps of 0.5 degrees. A finer angular resolution might be required to capture drag variations, especially at higher lift coefficients, where Figure 10 indicates the largest DLL-CFD discrepancy. The largest lift and drag deviations happen at the same time instant, which supports the hypothesis that an error in the 2D data at a specific angle of attack might explain both discrepancies. Lift forces are at least an order of magnitude larger than drag forces, and since local foil lift is decomposed into the streamwise direction when calculating net drag, a small error in the lift curve might yield a percentage wise large drag error.

An interesting fact evident from current results is that mean drag is reduced by a factor of 60% and 49 % from the steady case in the dynamic cases at $k = 0.05$ and $k = 0.15$ respectively. Mean lift is practically unchanged. This indicates that one might experience negative added resistance when running a hydrofoil vessel head on into large waves. It is judged likely that the negative added resistance originates from energy being extracted from the relative vertical velocity of the surrounding water with respect to the wing, as is the case when a ship operating in waves gets thrust from Wavefoils (Bøckmann, 2015). The resistance reduction might be smaller when accounting for increased drag due to wetted hull parts and control surface action required in rough seas. The relative change of resistance will also be smaller when adding resistance from struts and air resistance. Still, the high relative drag reduction on the main wing found in the current study might indicate that significant net negative added resistance on a hydrofoil vessel operating in waves is possible.

The current study is simplified in the manner that the relative water velocity is assumed harmonic and purely vertical, and by the exclusion of free surface effects, wing-strut interaction and added resistance from control surface deflections. Results serve as a validation of the basic ability of the DLL to capture dynamic lift and drag on wings. The code is intended for implementation in a simulator which models an active control system and vessel motions, with the hydrodynamics module preferably including free surface effects and a full wing geometry with struts. (Kramer, et al., 2018) has shown that a non-linear steady lifting line performs well for analyses of wings under a free surface and of wings with high winglets resembling struts. Further validation remains before one might conclude that the DLL code can accurately model the full problem of a hydrofoil vessel operating in waves.

References

Bøckmann, E., 2015. *Wave Propulsion of Ships, PhD Thesis.* s.l.:s.n.

Faltinsen, O. M., 2005. *Hydrodynamics of High-Speed Marine Vehicles.* 1. red. s.l.:Cambridge University Press.

Katz, J. & Plotkin, A., 2001. *Low-Speed Aerodynamics.* 2. red. s.l.:Cambridge University Press.

Kramer, J. V., Godø, J. M. K. & Steen, S., 2018. *Hydrofoil simulations - non-linear lifting line vs CFD.* s.l., Numerical Towing Tank Symposium.

Leishman, G. J., 2006. *Principles of Helicopter Aerodynamics.* 2. red. s.l.:Cambridge University Press.

Phillips, W. & Snyder, D., 2000. Modern Adaptation of Prandtl's Classic Lifting-Line Theory. *Journal of Aircraft*, pp. 662-670.

Theodorsen, T., 1935. *General Theory of Aerodynamic Instability and the Mechanism of Flutter,* s.l.: NACA Technical Report 496.

Tucker, M. & Pitt, E., 2001. *Waves in Ocean Engineering.* 1 red. s.l.:Elsevier Science.

Van Walree, F., 1999. *Computational Methods for Hydrofoil Craft in Steady and Unsteady Flow.* s.l.:s.n.

Cavitation simulation on composite marine propellers

Nobuhiro Hasuike[1] and Kohei Himei[2]
Nakashima Propeller Co., Ltd., Okayama/Japan, web page: http://www.nakashima.co.jp/
E-mail: [1]nobuhiro@nakashima.co.jp, [2]k-himei@nakashima.co.jp

1 Introduction

In composite propellers design, deformation of blades affects to cavitation performance. Therefore, design tool considering fluid-structure interaction (FSI in short) is necessary. Several commercial CFD software implements the FSI method. However, multiphase unsteady flow simulation is time consuming and instable. Coupling of unsteady cavitation simulation with FSI simulation is still difficult. This research discussed practical simulation tool based on coupling of unsteady cavitation simulation with quasi steady structural analysis. Simulation results were compared with model test.

2 Numerical simulation of cavitation performance of composite propellers

Concept of cavitation simulation on composite marine propellers

Cavitation simulation of marine propellers is typically aimed at assessment of pressure pulse level, cavitation erosion risk and propeller noise issue operating in ship wake flow. For these targets, cavitation pattern including tip vortex cavitation should be simulated. This means use of large number of grid elements is inevitable. In view of deformation, changing amount of pitch, camber and rake distribution are essential for the cavitation performance of composite propellers. In case of commercial CFD software, flow simulation and structural analysis is iteratively calculated at each time step. However, cavitation flow simulation often arise unexpected illogical pressure value at each time step in comparison with non-cavitation flow simulation.
If this unexpected illogical pressure is used for the structural analysis, it causes illogical structural deformation. As a result, it is very difficult to be converged. To avoid this unexpected pressure value, time step and deformation amount per each time step should be very small. These are the reasons for unpractical time consumption by FSI simulation implemented in commercial CFD software. Thereby, some practical idea of exclusion of unrealistic pressure value and minimizing of iteration between flow simulation and structure is necessary. In this research, practical simulation concept was suggested as daily design tool. Simulation concept is based on following concepts;

i) Smoothed time history of deformation in one rotation (0deg. to 360deg.) is used.
ii) Number of iteration between flow and structural simulation are minimized.
iii) Conversion of FSI is based on maximum deformation amount in one rotation.

Flow chart is illustrated in Fig. 1. By using smoothed time history of deformation, unexpected pressure is excluded. Minimizing of iteration between flow and structural simulation realized stable simulation and shorter computing time.
On the other hand, structural damping and additional water mass are neglected in this research.

In this research, transitional flow around propeller was simulated using SOFTWARE CRADLE SC/Tetra V13 software, which was based on a finite volume method with an unstructured grid. 3-equations realizable k-ε model was selected based on the previous research (Hasuike et al.[1] 2015). The full Cavitation model (Singhal et al.) was used in the calculation. NCG was set to 1ppm and the empirical constants Ce and Cc were set to 0.02 and 0.01 respectively.

Numerical Grids

The computational domain was composed of the inner rotational part including the propeller and the outer stationary part (Fig.1). Unsteady propeller simulation in the wake uses the sliding mesh methodology. The numerical mesh was an unstructured grid, and basic cells were tetrahedral and prismatic cells were applied to near the blade surface for resolving the boundary layer (Fig. 2). The first layer thickness of the prism layer was set to a non-dimensional wall distance for a wall-bounded flow (y+ in short) =50. The second order accuracy of the convective term was adapted. The axial wake distributions are given as an inlet boundary condition.

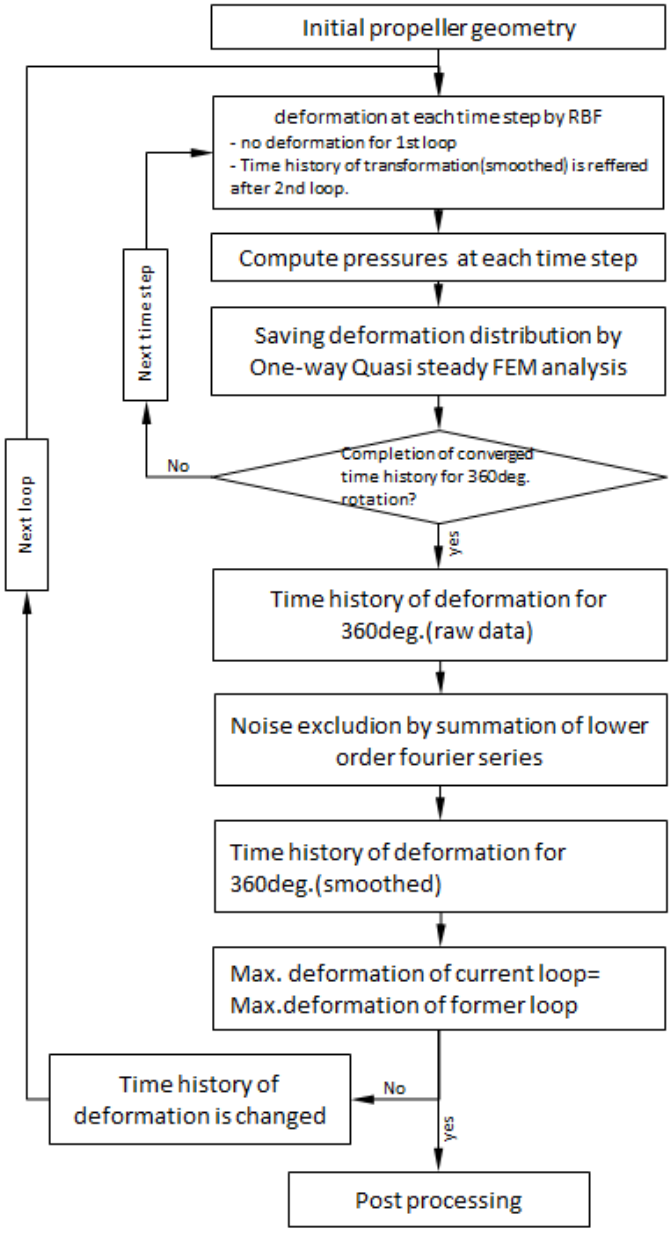

Figure 1: Flow chart of cavitation simulation on composite propellers

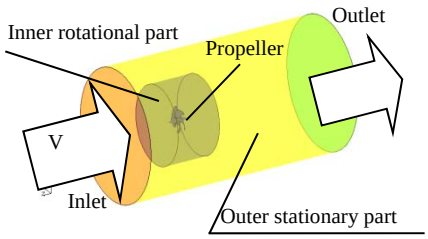

Figure 2: Computational domain

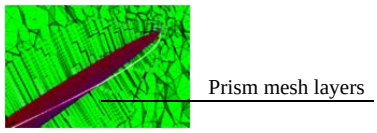

Figure 3: Prism mesh arrangement near blade surface

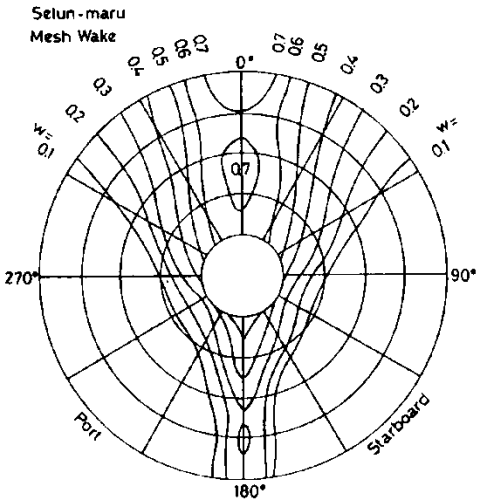

Figure 4: Ship wake distribution

3 Cavitation performance of composite propellers

Propeller models and open water characteristics

Propeller model made by fiber reinforced plastic (PPS G40) was used for model tests. Young's modulus is 6.2GPa. Propeller model made by normal metal was also tested for comparison Table 1 and Figure 5 show principal particulars of propeller models and photos respectively. Diameters of both propeller models are 0.25m. Blade geometry of PPS model and metal model are slightly different. The pitch ratio of PPS was slightly higher to achieve almost same thrust as the metal model Pitch ratio of PPS model was decided with consideration of deformation (decrease) amount of pitch by steady deformation amount at the design point in uniform flow. Propeller open water test at Rn(Kempf)=6×10^5 was conducted. POT results are shown in Figure 6. Propeller torque at J=0.76 were almost same, which means initial assumption of pitch deformation was successfully considered for pitch determination. Propeller open efficiency of PPS G40 was slightly higher at over all range of advance coefficient J.

Table 1: Principal particulars of propellers and test condition

	PPS	Metal
Diameter(m)	0.25	0.25
Pitch ratio(0.7R)	1.0842	1.0649
Expanded area ratio	0.650	0.650

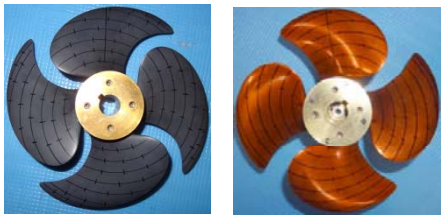

Figure 5: Photos(left: PPS, right: metal)

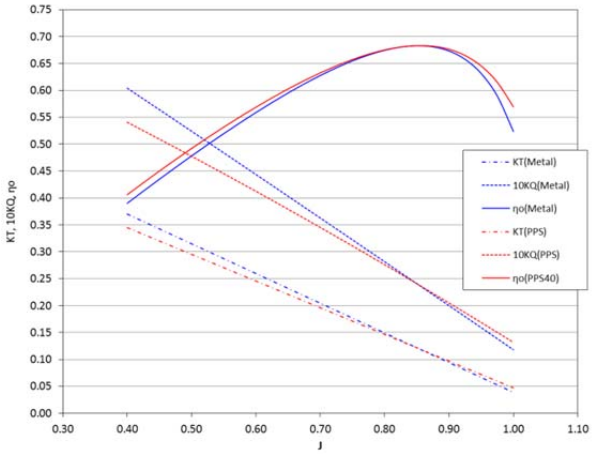

Figure 6: POT results(Rn(Kempf)=6×10^5)

Cavitation test

Cavitation performance of PPS model was compared with the metal model. Cavitation test was conducted at Mitsui Akishima Labo.. Test condition is shown in Table 2. Thrust coefficient kT was set to 0.1763 and cavitation number was set to 4.0 for both propellers. Ship wake distribution was shown in Figure 4. Wake distribution was simulated by wire mesh. Cavitation patterns were observed by high speed video. Pressure pulses were also measured.

Pressure pulse measurement

Measured pressure pulses are shown in Figure 7. The first and second order blade frequency components of pressure amplitude were compared. PPS propeller model showed smaller pressure amplitude. This preferable tendency may be explained by cavitation observation result.

Cavitation pattern observation

Cavitation patterns of PPS model and the metal model were compared in Figure 8. Sheet cavitation was incepted at 330deg. on the metal model and at 320deg. on the PPS model. Inception positions were both leading edge at around 0.6R for both propellers. The difference of blade angle of inception was caused by slightly higher pitch ratio of PPS model. In case of the metal propeller model, sheet cavitation was developed and stably maintained from leading edge. On the other hand, sheet cavitation was partially disappeared at leading edge in case of PPS model. Tip vortex intensity of the PPS propeller model was weaker than that of metal propeller model. Sheet cavitation was maintained in wider range of blade angle position in case of PPS propeller model. This was explained as followings;

- The model shape was almost same as original form at blade position of cavitation inception
- Pitch at blade tip was decreased at highest wake region by highest loading.
- Pitch was recovered to original shape at the stage of cavitation disappearance.

Through this deformation process, maximum cavitation volume at high wake region was decreased. At the stage of inception and disappearance, cavitation is easily maintained. This contributes to decrease time derivative of cavity volume, which enables to reduce the pressure pulse amplitude.

Table 2: Model test condition

	PPS	Metal
Ship wake	Seiun-Maru	Seiun-Maru
Rotation speed(rps)	22.0	22.0
KT	0.1763	0.1763
σ_n	4.0	4.0
Tip clearance(%Dp)	25	25

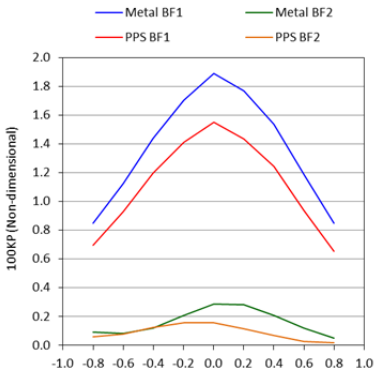

Figure 7: Pressure pulse measurement result

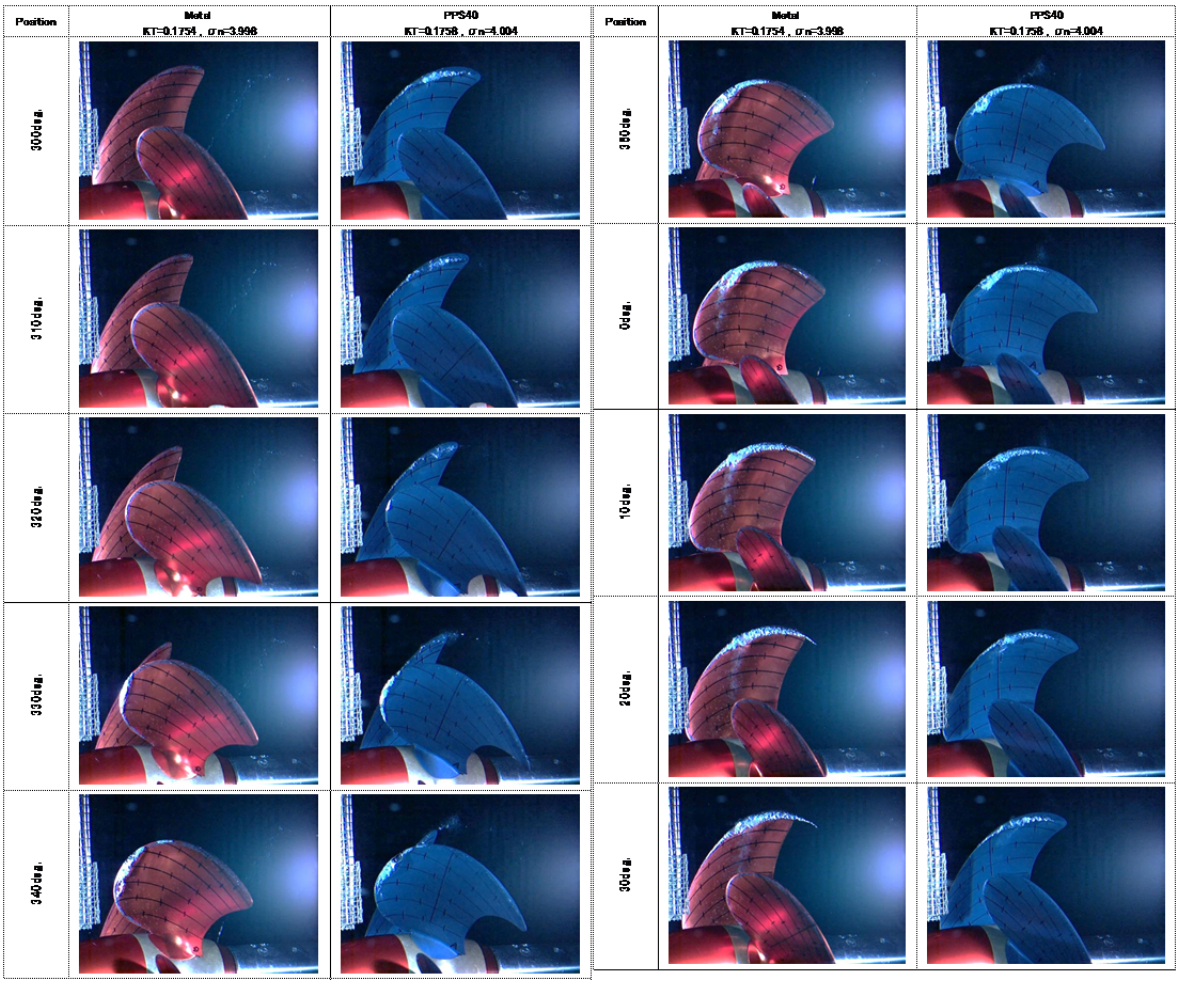

Figure 8: Cavitation pattern observed by highe speed video.

4 Numerical simulation of cavitation performance of PPS propeller model

Cavitation pattern of PPS model was simulated based on flow chart in Figure 1. Total number of grid elements was17.9 million for fluid analysis. Total number of elements for structural analysis was 57836. Time step was 1deg. /cycle. Convection term was set to second order. For smoothing of time history of deformation, Fourier series from 1st to 20th order were summed up. 5 rotations (1800 cycles) were necessary for conversion of flow field for each loop (See flow chat in Figure 1). 3 loops (5400 cycles) were necessary for conversion of maximum deformation.

This means 3 candidates of time history of deformation were tried and successfully converged. Converged maximum deformation amount was 9mm at high wake region.

Simulation results are shown in Figure 9. Snap shot was taken at blade angle 30deg. Deformation amount at high wake zone was greater than side and bottom position (See right contours).

Deformation amount at trailing edge side was greater than leading edge from 0.9R to tip. This means blade shape at tip region deforms to tip unloading mode. Pressure distribution and cavitation pattern are shown in middle and left contour respectively. From the simulation result, pressure at leading edge at 0.9R was recovered and cavitation disappeared at leading edge. This tendency was well captured as well as model test. Cavitation pattern of w/ and w/o condition were compared in Figure 10. Stable sheet cavitation was located from leading edge in case of w/o deformation. This tendency may be similar as the model test results of the metal propeller model. These results encourage the possibility of this simulation concept as practical design tool. For the validation, comparison with measurement of detail deformation and time history of blade loading are necessary.

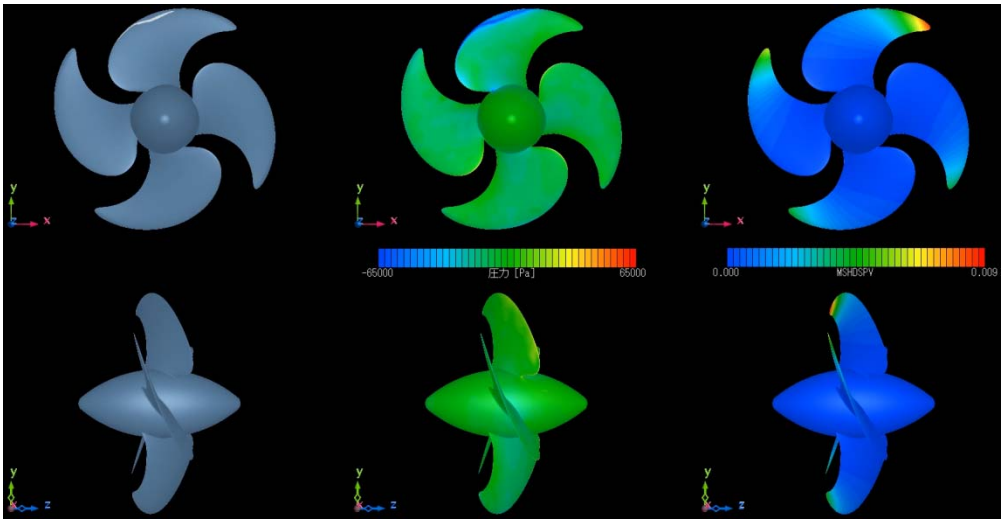

Figure 9: Simulation result at 30deg.(right; deformation, mid: pressure distribution, left: cavitation pattern)

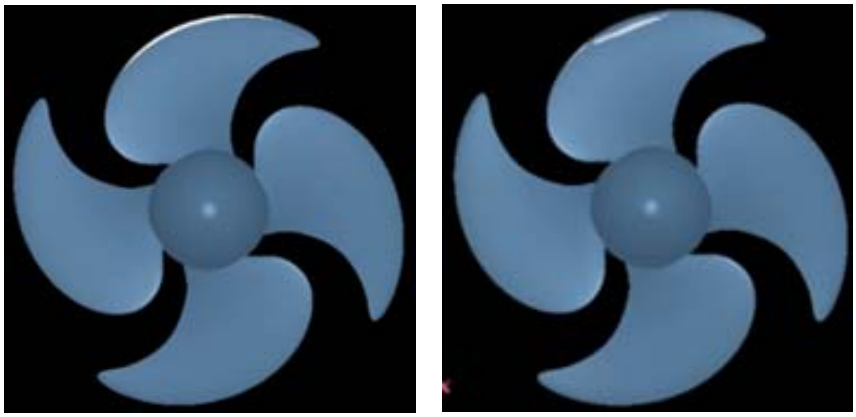

Figure 10: Comparison of cavitation pattern of with and w/o deformation at 30deg.

5 Conclusions

- Simple simulation concept of cavitation on composite propellers was suggested.
- Quick and stable convergence was achieved.
- Simulation well captured the tip unloading deformation and reduction of cavitation at high wake region.

These results are attractive for daily composite propellers design. More detail check with detail measurement result of deformation and blade loading are future works to prove accuracy of this concept.

Acknowledgement

These valuable cavitation tests were conducted by Akishima Laboratories (Mitsui E&S).

References

[1] Hasuike, N., Kajihama, T. and Fukuda, K., “Numerical simulation of pressure fluctuation induced by cavitating propellers in wake flow”, NUTTS2015, 2015

[2] Fujiyama K., “Numerical Simulation of Ship Hull Pressure Fluctuation Induced by Cavitation on Propeller with Capturing the Tip Vortex”, Fourth International Symposium on Marine Propulsors SMP’15, June 2015

[3] Gindroz, B.,Hoshino, T. & Pylkkanen, V., “Propeller RANS/Panel Method Workshop, 22nd ITTC Propulsion Committee Propeller RANS/Panel Method Workshop”, Grenoble, Apr.1998.

[4] Hoshino,T. , “Experimental Data For Unsteady Panel Calculations And Comparison (Seiun-Maru HSP)”, Proceedings of Propeller RANS/Panel Method Workshop, 22nd ITTC Propulsion Committee, Grenoble, Apr.1998.

Improvements in the Methodology for Identifying Noise Sources in Ducted Marine Propellers

Adam Higgens*, Philip Joseph†, and Stephen Turnock*
*FSI, University of Southampton, UK, †ISVR, University of Southampton, UK
a.d.higgens@soton.ac.uk

1 Introduction

Ducted propeller noise can be classified into several components including: turbulence ingestion, trailing edge noise, cavitation and tip gap interaction noise. While there has been extensive research into the first three mechanisms, the mechanism which generates noise from the tip vortex is less well understood. The noise generated by an aerodynamic fan in a duct has been the focus of a significant amount of research for aircraft engines, due in part to requirements near airports for limiting the maximum sound levels for the comfort of nearby residents. However, research into this noise component in the context of marine propellers has been far less extensive. As ducts are common on naval vessels and increasingly more so on merchant ships, understanding the noise mechanisms involved is important from an environmental and signature reduction point of view.

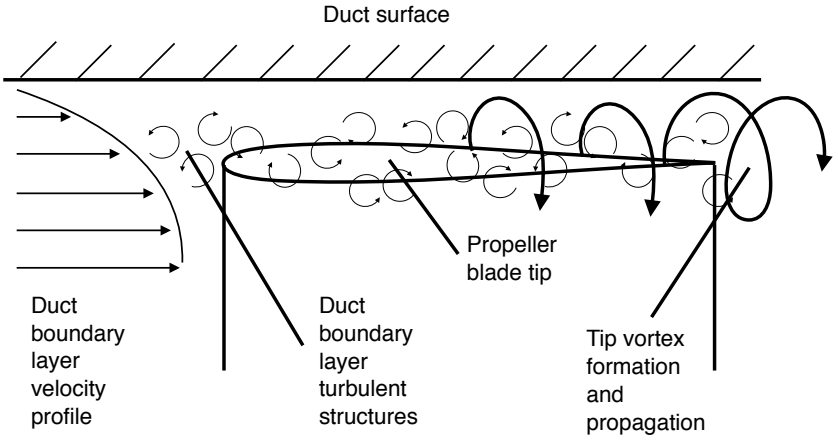

Fig. 1: Schematic representation of the tip vortex interaction with the duct boundary layer

Open-tipped foils have been found to have an increased drag coefficient when compared to 2D foils due to the drag induced by the tip vortex. This vortex is generated due to the difference in pressure on the opposing sides of the foil causing a leaking of flow from the pressure side to suction side across the tip. Therefore, any reduction in the drag coefficient implies a reduction in the strength of the tip vortex, and therefore will impact the noise generated within the tip gap. While a high proportion of the aerodynamic research has involved experimental procedures, this research aims to analyse the flow regime between the tip of the blade and the duct, and understand the flow characteristics in this region, allowing the design of effective noise mitigating arrangements. In order to understand the complex tip gap flow, simulations have been performed using a simplified arrangement of a single foil of constant cross section with a square tip, using a range of tip gap heights, h. A schematic representation of the investigation is given in Figure 1.

2 Test case methodology

This case was chosen as a premilinary study into the far-field noise prediction for comparison against the experimental work conducted by Jacob, et al. (2010). This study investigates the use of the Ffowcs-Williams Hawkins (FW-H) analogy in predicting the far-field noise, specifically with a view to identifying the location of the noise sources.

The simulations presented in this section are setup with the origin, $(0, 0, 0)$ in the computational domain at the centre of the chordline of the foil, on the lower table surface. There is a unit span between

Table 1: LES numerical model settings

Parameter	Unit	Setting
Opening span	m	1
Foil chord	m	1
Mesh Type	-	Unstructured (Hex)
No. of Elements	-	$\approx$ 10M
y^+	-	≈ 1
Inlet	-	BL Profile ($U_\infty = 10m/s$)
Outlet	-	Zero gradient
Domain roof/floor/side walls	-	Slip
Table	-	No slip
Foil	-	No slip
Reynolds' Number	-	6.5×10^5
SGS Model	-	WALE
Solver algorithm	-	PIMPLE

the table surfaces which is held constant, the foil is of a unit chord and the span is adjusted to produce the desired gap, h between the tip of the foil and the lower surface. The table extends 2 chord lengths, C, downstream of the foil, $2.5\,C$ to either side, and $5\,C$ lengths up stream to the inlet. The domain is C-shaped and extends for $20\,C$ laterally and downstream, beyond the constant span of the table section of the domain, as shown in Figure 2.

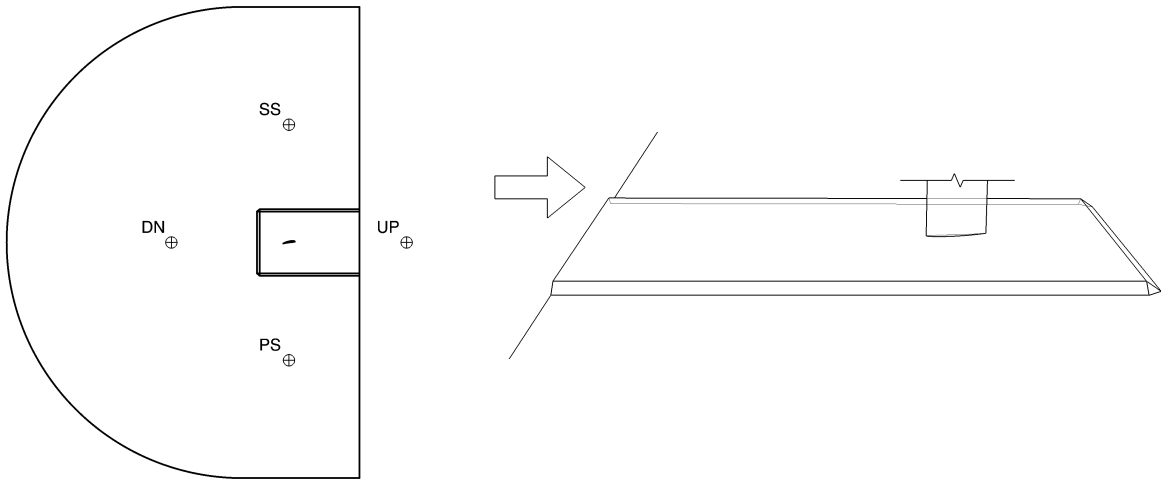

(a) C-Shaped domain topology used in NACA5510 investigation, with the inlet on the right and semi-circular outlet on the left.

(b) A zoomed in schematic showing the arrangement of the foil above the table as well as the chamfered edges of the table. The inlet flow is shown on the left.

Fig. 2: Scehmatic representations of overall domain layout, far-field locations, and local details.

It has been shown that in order to predict broadband noise, high resolution, unsteady simulations must be performed. This study uses Large Eddy Simulations (LES) to capture the large, unsteady flow feautres which are expected to be responsible for generating the majority of the noise in this case. Table 1 shows the simulation settings used in this study. The sub-grid scale (SGS) model used was the Wall Adapting Local Eddy (WALE) viscosity model, chosen as it has been shown to perform well in wall bounded and channel flows. The tip gap region of this study is very similar to a channel flow as the thickness of the foil is much larger than the tip gap height.

The simulations carried out in this work use the NACA 4-digit aerofoil series. The foils were first created using a mathematical description of a spline based on thickness, camber and chord. They were later extruded to form a finite aspect-ratio foil.

In order to allow the discretised equations of motion of the fluid to be solved, volume surrounding the geometries was dividied to form a volumetric mesh using proprietary Pointwise software. First, solid surfaces of the foil and duct were triangulated and the surface triangles were extruded to yield a prismatic boundary layer mesh. Particular care was devoted to the region between the tip and the surface of the duct where bad quality cells had to be avoided to yield a high-quality solution. Remaining volume was then further triangulated to form a tetrahedral mesh with additional refinement around the wake of the foils. The combination of these techniques can be seen in Figure 3 for the NACA5510 case.

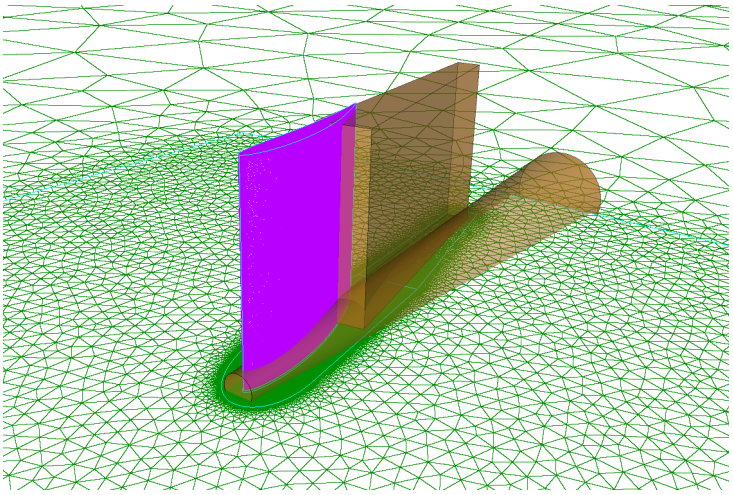

Fig. 3: Schematic representation of the meshing methodology. The foil surface mesh is shown in pink, with the table and outer domain surface meshes shown in green and the volumetric refinement zones are shown in orange. The tip of the foil is at the bottom in this figure, hence the high refinement shown on the table mesh in that region.

The FW-H analogy was used to predict the propagated noise into the far-field for a number of receiver locations to assess the suitability of the anaolgy for predicting the dependence of the farfield noise on the tip gap height. This analogy requires the specification of a solid surface or volume which can be integrated over to imply the far-field pressure fluctuations.

In this work, the stationary control surface has been chosen to be fixed on the solid boundaries of the foil in the arrangement. This allows the surfaces (patches in OpenFOAM) to be sampled at a chosen, fixed time step, recording the instantaneous pressure, p and time derivative of pressure, $\dot{p}$, for every face of the respective patches. The analogy is then implemented with the use of a post-processing script which calculates the contribution to the acoustic pressure at each receiver location of each face of each patch, accounting for retarded time, τ. This methodology is computationally expensive regarding memory usage, by saving the data from every face for every time step and has been verified in its previous implementation Lidtke et al. (2016).

It is also possible to implement a run-time implementation of this analogy, which greatly reduces the memory requirements. The disadvantage of this method however, is that the receiver locations need to be selected in advance, and any new receivers require a new simulation. This is the reason the current implementation has been chosen here, to allow flexibility in the post-processing analysis to change receiver locations if required, as well as allowing surface pressure samplings.

This analysis will focus on the transverse receiver on the suction side of the foil and the FW-H integration will be carried out over the foil surface and not the table, which has previously been demonstrated to be the dominant location Higgens, et al. (2018). The foil was divided during post-processing to split the foil into ten equal strips in the span-wise direction (from root to tip) and 5 equal regions in the chord-wise direction (from LE to TE). This allows the comparison of different areas of the foil with regard to

far-field radiated noise and will be the primary focus of this study. The analysis has been carried out at the characteristic tip gap height of 1% following on from the author's previous study.

3 Far-field noise predictions

Figure 4 shows the far-field noise prediction to the suction side receiver, with contributions broken down in the span-wise and chord-wise directions.

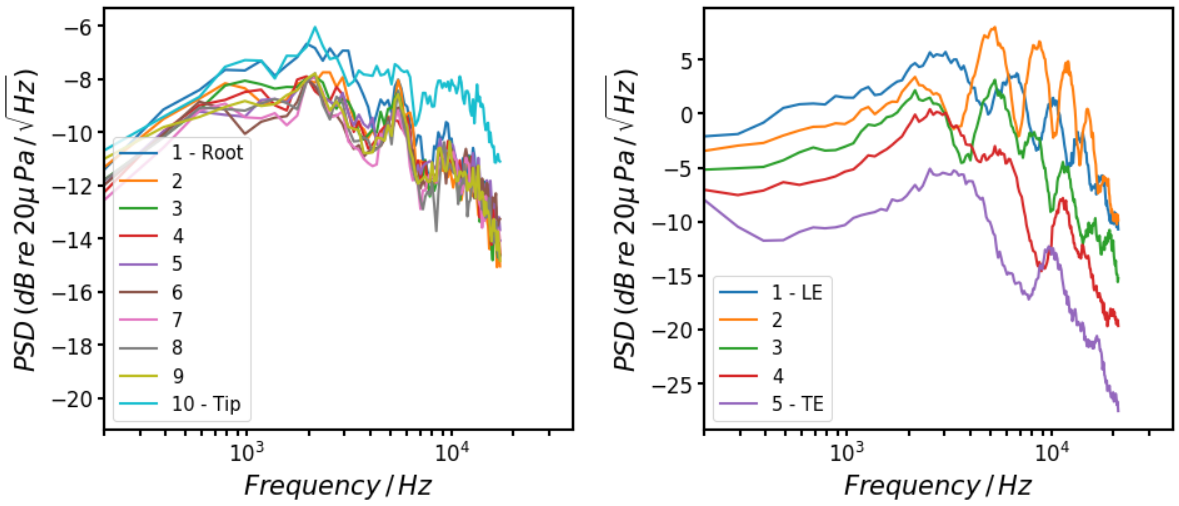

(a) Spanwise sections

(b) Chordwise sections

Fig. 4: Contributions to far-field noise of different regions of the foil.

It can be seen from Figure 4a that the tip section is producing higher power levels over most of the spectra, with the root section producing higher power levels in the $0.5 - 5kHz$ frequency range. Due to the tip leakage flow and the shedding of strong vortices in the tip region it is expected that the foil tip would be producing more far-field noise than the other span-wise regions. The small difference between the tip and the other regions however was believed to be due to the dominance of the trailing edge in the far-field propagation.

Figure 4b shows the contributions of the different chord-wise regions of the foil. It can be seen here that contrary to expectations, the trailing edge is shown to be the weakest source region with regard to the far-field propagations.

4 Discussion

The highly turbulent structures produced by the tip gap region have been discussed previously by the authors Higgens, et al. (2017) Higgens, et al. (2018). It is well understood that when strong, turbulent structures encounter a sharp edged surface, such as a trailing edge, that the scattering of these structures across the solid surface causes strong dipole acoustic sources near the sharp edge. This effect is well documented and has been the subject of study by many aeroacoustic investigations, so this has cast doubt on the suitability of the current methodology for predicting this noise source. It is suggested that there could be two possible explanations for this effect not being captured: the incompressibility assumption, or the importance of quadrupole sources.

Due to the very low Mach numbers involved in this study, the assumption of incompressibility should be valid. With regard to the flow features and overall forces observed this seems to have been a legitimate assumption. However, the mechanism of producing noise at the trailing edge involves this scattering of waves within the boundary layer, which on the small scales may need the compressibility to be taken into account. This would suggest that the simulations need to be run using a compressible solver in order to capture these scattered waves, which in turn would create the pressure fluctuations on the solid surface, allowing the current implementation of the FW-H analogy to correctly predict the far-field noise prediction.

Another assumption made in this work is that the quadrupole sources within the fluid would be insignificant compared to the dipole sources due to the Mach number scaling effect for multipole sources. It is suggested that the strength of these sources may be sufficient, combined with low mach numbers, that the quadrupole sources can not be neglected in this case. This would imply that a different implementation of the FW-H analogy may be required, either using a porous integration surface within the fluid, or by computing a volume integral within a volume of the fluid surrounding the aerofoil.

A third possible explanation is that the mesh resolution is not sufficient to capture the scattering effect, however, it is believed that the resolution is indeed sufficient as the power levels can be seen to be comparable through the frequency range to the limit of the time resolution and Nyquist criterion.

5 Conclusion

It is suggested that the mechanism by which tip leakage noise is generated is very similar to that of trailing edge noise. Previous studies by the authors have identified to presence of strongly turbulent flow passing over sharp edges, which would be expected to be a significant source of noise. The far-field noise predictions have not agreed with this hypothesis. This has called in to question the efficacy of the current implementation of the acoustic analogy for predicting this noise mechanism. It is proposed that further study is required to identify the missing link between the hydrodynamic flow features observed and the far-field noise predicted.

Acknowledgements

The authors thank DSTL and EPSRC for providing the funding for this work, and the University of Southampton for use of the Iridis 4 High Performance Computing cluster.

References

A.D. Higgens, P.F. Joseph, and S.R. Turnock (2017). Investigation into the Tip Gap Flow and its Influence on Ducted Propeller Tip Gap Noise Using CFD. Proceedings of NuTTS 2017, Wageningen, The Netherlands.

A.D. Higgens, P.F. Joseph, A.K. Lidtke, and S.R. Turnock (2018). Investigation into the Tip Gap Flow and its Influence on Ducted Propeller Tip Gap Noise Using Acoustic Analogies. Proceedings of Symposium of Naval Hydrodynamics 2018, Hamburg, Germany.

M.C. Jacob, J. Grilliat, R. Camussi, and G. C. Gennaro (2010). Aeroacoustic investigation of a single airfoil tip leakage flow. *International Journal of Aeroacoustics, Multi-Science Publishing*, **9**(3),253–272.

A. K. Lidtke, S. R. Turnock, and V. F. Humphrey (2016). Characterisation of sheet cavity noise of a hydrofoil using the Ffowcs Williams-Hawkings acoustic analogy. *Journal of Computers and Fluids*, 130:8–23.

Simulation of Non-breaking and Breaking Waves with OpenFOAM

Qiu Jin, Dominic Hudson, Pandeli Temarel
Fluid Structure Interactions group, Faculty of Engineering and Environment,
University of Southampton, Southampton SO16 7QF, qj1n17@soton.ac.uk

1. Introduction

Wave breaking is one of the most violent phenomena of air-water interface interactions, producing strong turbulence with air bubbles, water droplets, jets and sprays. These phenomena commonly occur in ship flows and are one of the main sources of underwater noise and white-water wakes. The investigation of these phenomena is important in ship and ocean engineering. OpenFOAM is a valuable open source and continuum mechanics library for building multi-physics simulations and its use growing rapidly in both research and industry. This paper investigates the ability of OpenFOAM to simulate non-linear waves, wave transformation and breaking with k-ω SST-RANS model through the study of wave generation and propagation over a submerged bar.

In the first instance an empty numerical wave flume is constructed. In earlier versions of OpenFoam, water wave modelling was developed by various software packages, such as olaFoam, waves2Foam and IHFoam. Among them, waves2Foam, developed by Jacobsen et al. (2012), is probably the most common toolkit used in ship-wave interaction simulations. However, these packages are no longer supported in the newest standard release of OpenFOAM 5.0.0 (OF500), due to installation, maintenance and coding standard problems. A new framework of waveModel is instead supported for wave generation. In this study, the waves2Foam implemented in OpenFOAM 3.0.1 (OF301) and waveModel in OF500 are employed and compared to examine their abilities and stability in modelling of regular wave propagation.

Based on the numerical wave flume, the waves2Foam model is used to simulate both non-breaking and breaking waves. The numerical results are compared with the experimental measurements by Beji and Battjes (1993). Several previous studies of breaking waves using waves2Foam have only performed numerical calculations for breaking waves on a beach profile (Jacobsen et al., 2012; Jacobsen et al., 2014; Zhou et al., 2017). The effect of obstacles on wave propagation was modelled by Gadelho et al. (2014), but they only reported non-breaking wave transformations. In the current study, non-breaking and spilling breaking waves generated by Stokes waves of different incident wave heights are investigated with waves2Foam.

Finally, the study is extended to investigate the effects of convection schemes on the multiphase simulations. Four different schemes are tested for their ability to predict regular wave propagation as well as wave transformation and breaking over the bar.

2. Numerical methods

2.1. Governing equation and VOF method

In the conventional volume-of-fluid (VOF) method, the transport equation for an indicator function, representing the volume fraction of one phase, is solved simultaneously with the continuity and momentum equations:

$$\nabla \cdot \mathbf{U} = 0 \tag{1}$$

$$\frac{\partial \gamma}{\partial t} + \nabla \cdot (\mathbf{U}\gamma) = 0 \tag{2}$$

$$\frac{\partial(\rho\mathbf{U})}{\partial t} + \nabla \cdot (\rho\mathbf{U}\mathbf{U}) = \quad -\nabla p + \nabla \cdot \mathbf{T} + \rho\mathbf{f}_b \tag{3}$$

where **U** is the velocity field shared by the two fluids throughout the flow domain, γ is the phase fraction, **T** is the deviatoric viscous stress tensor, ρ is density, p is pressure, $\mathbf{f}_b$ are body forces per unit mass. In VOF simulations, the latter forces include surface tension effects at the interface. The phase fraction γ can take values within the range $0 \leq \gamma \leq 1$, with the values of zero and one corresponding to regions accommodating only one phase. Two immiscible fluids are considered as one effective fluid throughout the domain, the physical properties of which are calculated as weighted averages based on the distribution of the liquid volume fraction, $\rho = \rho_l\gamma + \rho_g(1-\gamma)$ and $\mu = \mu_l\gamma + \mu_g(1-\gamma)$ Where ρ_l and ρ_g are densities of liquid and gas, respectively.

2.2. Convection schemes

In the finite volume approach used in OpenFOAM, the role of the convection differencing schemes is to determine the value on the face from the values in the cell centres. Besides central and upwind schemes, two limited TVD schemes are tested in this paper.

Limited TVD schemes are constructed by blending a higher and lower order scheme based on the local flux gradients as:

$$\phi_f = \phi_f^{UD} + \Psi(\phi_f^{CD} - \phi_f^{UD}) \tag{4}$$

Where ϕ_f^{CD} and ϕ_f^{UD} are the calculated using a higher (central differencing) and lower (upwind differencing) order scheme, and Ψ is the blending function.

The **limitedLinear schemes** in OpenFOAM uses a limiter that satisfies the TVD conditions:

$$\Psi = \frac{2(\phi_C - \phi_U)}{c(\phi_D - \phi_C)} \tag{5}$$

Where $\phi_{C,U,D}$ is the flux from the owner cell, the upwind cell and the downwind cell for a face respectively, c is a constant multiplicator weighting the limiter between central and upwind differencing schemes.

The **filteredLinear scheme** uses an alternative control on the limiter Ψ as:

$$\Psi = 2 - 0.5\frac{min(|\Delta\phi - \phi_P^G|, |\Delta\phi - \phi_N^G|)}{max(|\phi_P^G|, |\phi_N^G|)} \tag{6}$$

Where $\Delta\phi$ is the difference in flux between the current cell P and its neighbour N, and ϕ_P^G and ϕ_N^G are the gradients of ϕ_P and ϕ_N along the direction vector between the two cell centres respectively.

These two TVD schemes together with central and upwind differencing schemes are applied to the interpolation of the divergence of the variables *u, k* and ω in all cases and to test their effect on wave elevation.

2.3. Numerical wave tank

The waves2foam toolkit in OF301 is used to model a numerical wave tank. It uses a technique known as 'relaxation zone' to facilitate the modelling of a numerical wave tank. Two relation zones are set at the inlet and outlet of the domain to help generate and absorb surface waves respectively. The relaxation zones can be employed to prevent wave reflection from the outlet boundary and to prevent internally reflected waves, e.g. the waves reflected by an internal structure to influence the wave generation at the inlet boundary.

In the new version OF500, wave initialisation was provided by a Level Set method that calculates the integrals of discontinuous functions such as the wave elevation. Wave models are directly introduced through two boundary conditions, waveVelocity and waveAlpha that provide an inlet condition for the velocity and phase-fraction fields.

3. Results

Simulations are carried out based on the experimental studies of Beji and Battjes(1993). The submerged trapezoidal bar with a seaward slope of 1:20 and a leeward slope of 1:10 is placed at 6.0m from the wave generation zone in a water depth d=0.4m. Wave probes are placed in the numerical wave tank at 6.0m, 11.0m, 12.0m, 13.0m, 14.0m, 15.0m, 16.0m and 17.0m from the end of the wave generation zone as shown in Figure 1.

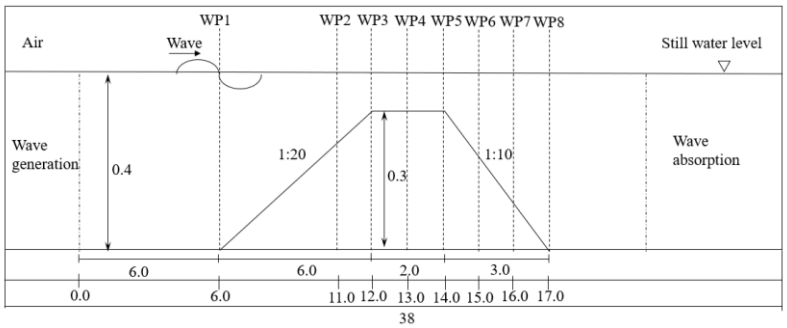

Fig.1. Schematic diagram of the wave tank

Wave generation and propagation in an empty wave flume is simulated first to examine and compare the two wave makers in OF301 and OF500. Then, the wave transformation and breaking over a submerged bar is studied using the data obtained from wave gauges at different locations along the bar. Finally, the effect of the convection scheme on wave propagation is examined through the variation of the relative wave elevations.

3.1. Basic numerical wave tank

A basic numerical wave tank with a flat bottom is used to generation second order Stokes wave with wave period T=2.5s, wavelength L=4.74m and wave height H1=0.022m in a water depth of d=0.4m. The results presented in figure 2 show that the wave elevation at x=6m with wave2Foam in OF301 and waveModel in OF500. In waves2Foam, waves are generated from a zero-water level while in waveModel the initial wave profile is set to the shape of the desired Stokes wave. The relative errors shown in figure 3 are based on averaging steady amplitudes between t=10T and t=14T at different locations.

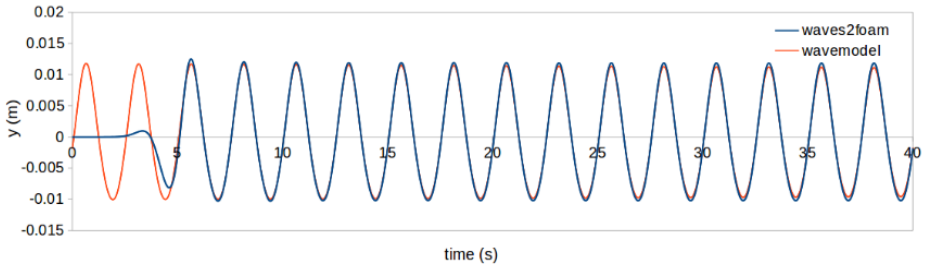

Fig. 2. Wave elevation for Stokes wave at WP1 (x=6m) with OF301 and OF500.

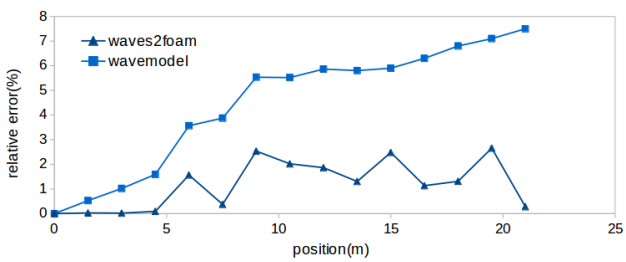

Fig. 3. Relative errors of wave amplitude with OF301 and OF500.

From the comparison results, it can see that the new waveModel is not as accurate as waves2Foam. In waves2Foam, the relaxation zones can be employed to prevent wave reflection from the outlet boundary and to prevent internally reflected waves. However, in the waveModel, the wave conditions are only added in the incident boundary conditions and there is no wave absorption process in the outlet boundary conditions. This process can cause wave instability, and this instability can become more and more severe with time. Furthermore, the introduction of the Level Set algorithm in the waveModel increased the complexity of the solvers. The degree of complexity results in a decrease in computational efficiency.

3.2. Non-breaking wave propagation over a bar

Waves2Foam based on OF301 is continually used to simulate wave propagation over a bar. A simulation is carried out with the same wave parameters as section 3.1. The transformation of the wave as it propagates over the bar is recorded using the wave probes and the results are compared with the experimental measurements in figure 4.

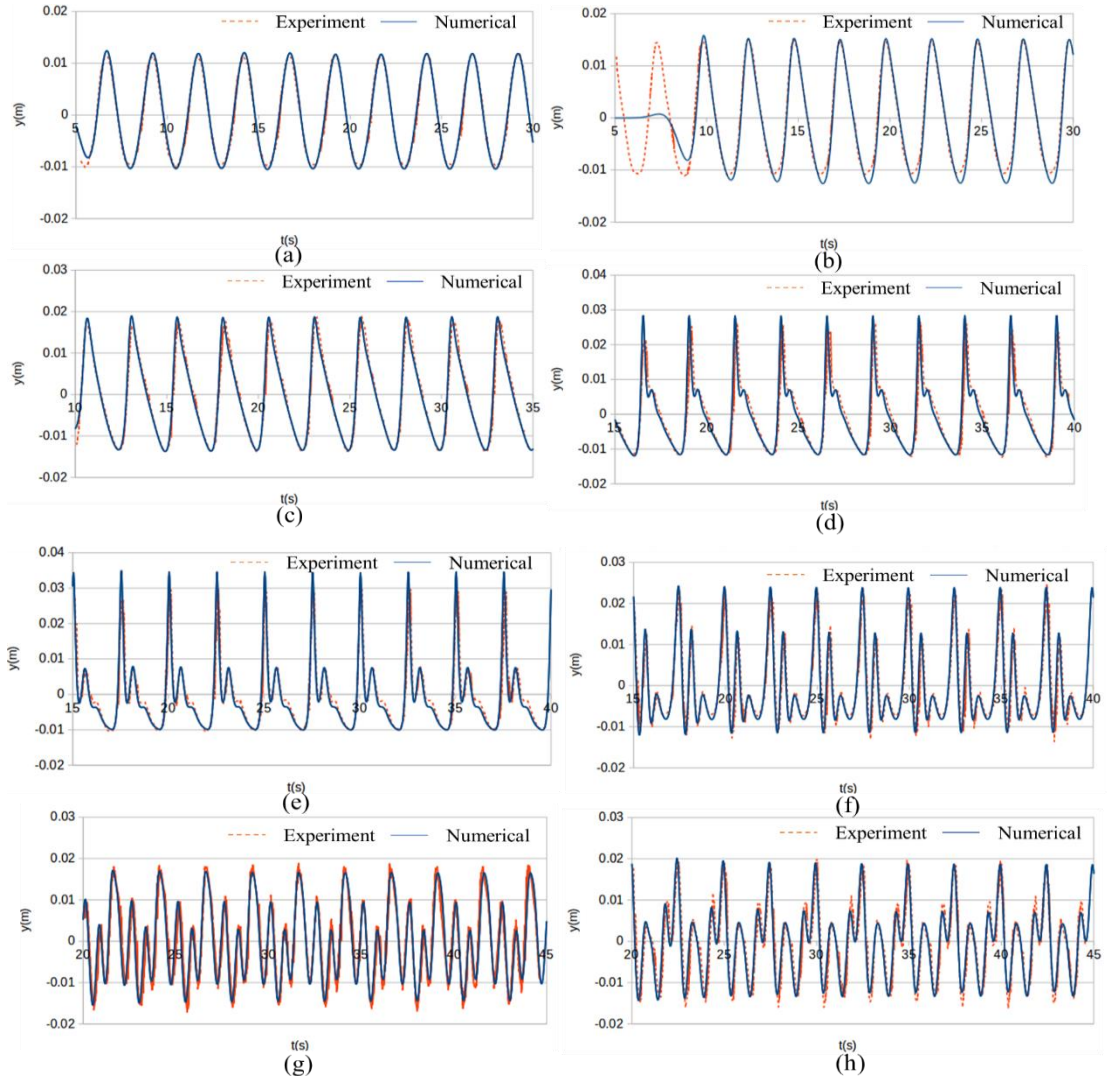

Fig. 4. Wave elevations at various locations for H=0.022m. (a) WP1:6m; (b)WP2:11m;(c)WP3:12m;(d)WP4:13m(e)WP5:14m(f)WP6:15m(g)WP7:16m(h)WP8:17m

The calculated phase and amplitude of the transformed waves agree well with the experimental data. Also, slight deformation on the saw-toothed wave profile is observed at x = 11.0 m in Figure 4, and sharp wave crests are observed at x = 13.0m in Figure 4(d). In addition, as higher harmonic

wave components evolve, wave decomposition phenomenon occur at x = 14.0m onwards (Figure 4(e)). The wave elevation increases and a process opposite to wave shoaling occurs, consistent with Beji and Battjes (1993). Afterwards, the wave decomposition forms behind the bar crest, as observed in Figures 4(f), 4(g) and 4(h).

3.3. Spilling wave propagation over a bar

In this section, spilling breakers are simulated by increasing the incident wave height to H3 = 0.042 m. Figure 5 compares the calculated free surface elevation with the experimental data. In general, good agreement is achieved between the present results and the experimental data, although some differences are observed at x=13.0, 14.0 and 15.0 m (figure 5 (d), (e), (f)). This is due to the fact that wave breaking occurs over the crest of the bar, between x = 13.0m and x = 14.0m. Small-scale wave breaking causes complex flow regimes, leading to instantaneous changes in free surface elevation. It is challenging to capture these free surface effects with violent mixing of air and water in the near post-breaking region, both experimentally and numerically. The difference is observed in the free surface elevations at x = 13.0m and x = 14.0m in Figures 5(d) and 5(e), and it decreases to 0.0036 m at WP7 at x = 16.0m. In addition, the numerical results for WP8 at x = 17.0 m agree with the experimental results, further validating the present numerical results.

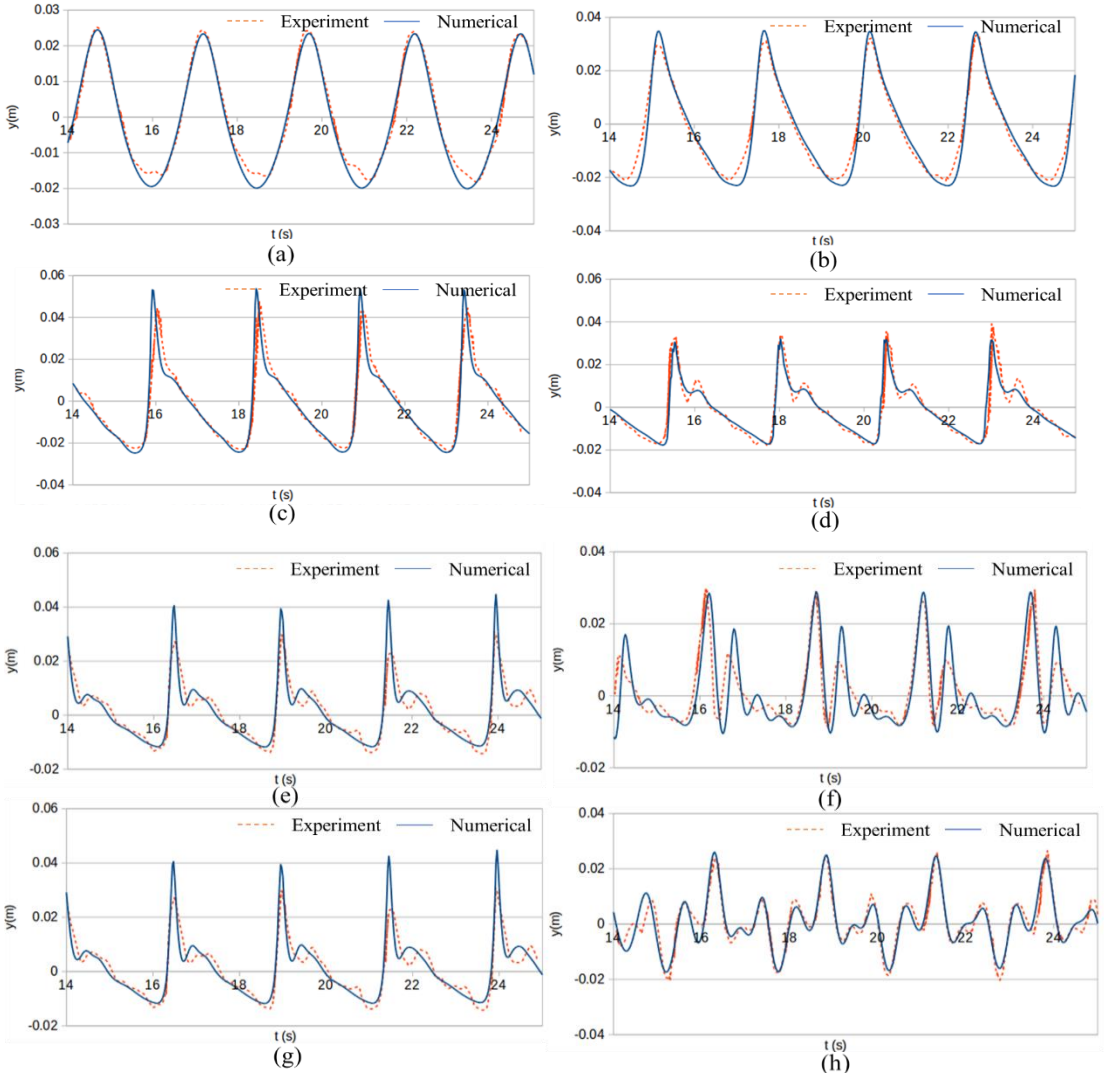

Fig. 5. Wave elevations at various locations for H=0.042m. (a) WP1:6m; (b)WP2:11m;(c)WP3:12m;(d)WP4:13m(e)WP5:14m(f)WP6:15m(g)WP7:16m(h)WP8:17m

3.4. Effect of convection schemes on wave propagation

The numerical representation of the convective terms of the RANS equations often requires corrections to handle stability problems due to the inability of a central differencing scheme to identify the flow direction. Various upwind schemes have been proposed to cope with this. To study the effects of the convection scheme on multiphase simulations, four schemes are tested for their ability to predict non-breaking and breaking waves, as shown in Figure 6. It can be seen that the two TVD schemes perform much better than a pure upwind scheme but also significantly worse than the central differencing scheme in the early stages of the simulation. However, the differences between them decrease with increased simulation time. This may be due to the steadiness of the wave pattern and the fact that each wave introduced at the inlet contributes to more energy in the pattern. The dissipation will thus be less and less significant as time advances.

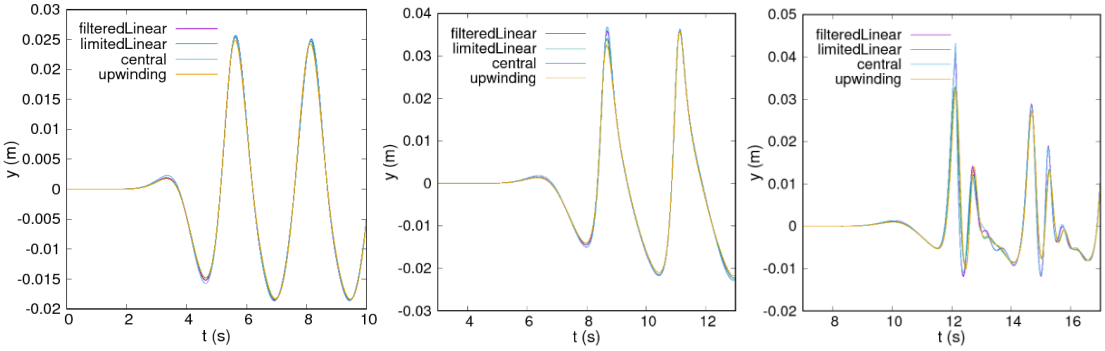

Fig. 6. Wave elevations at WP 1, WP 2 and WP6 with four schemes.

4. Conclusion

The Open Source platform OpenFOAM is applied to construct a numerical wave tank and to simulate the wave transformation and breaking over a submerged bar. The numerical results are compared to experimental measurements and good agreement is seen. It is observed that waves2Foam in OF301 performs better than the new waveModel in OF500 with regard to both accuracy and efficiency. The effect of convection scheme on wave elevation is also investigated in this study. When considering a quasi-steady situation with regular waves, even breaking waves, it is worth using a TVD scheme and a longer simulation time. Further studies can be extended to irregular wave propagation over a submerged bar along with the effect of convection schemes on unsteady free surface simulation.

References

Jacobsen, N. G., Fuhrman, D. R., & Fredsøe, J. (2012). A wave generation toolbox for the open-source cfd library: openfoam®;. International Journal for Numerical Methods in Fluids, 70(9), 1073–1088.

Beji, S., & Battjes, J. A. (1993). Experimental investigation of wave propagation over a bar. Coastal Engineering, 19(1–2), 151-162.

Gadelho, J. F. M., Lavrov, A., & Soares, C. G. (2014). Modelling the effect of obstacles on the 2D wave propagation with OpenFOAM. Developments in Maritime Transportation and Exploitation of Sea Resources.

Jacobsen, N. G., Fredsoe, J., & Jensen, J. H. (2014). Formation and development of a breaker bar under regular waves. part 1: model description and hydrodynamics. Coastal Engineering, 88(3), 182-193.

Zhou, Z., Hsu, T., Cox, D., & Liu, X. (2017). Large-eddy simulation of wave-breaking induced turbulent coherent structures and suspended sediment transport on a barred beach. Journal of Geophysical Research Oceans, 122(1).

Channel Flow at $Re_\tau = 395$: LES is more (turbulent than PANS)

Maarten Klapwijk[*†], **Thomas Lloyd**[‡], **Guilherme Vaz**[‡] **and Tom van Terwisga**[*‡]
[*]Delft University of Technology, [†]MARIN Academy and [‡]MARIN
m.d.klapwijk@tudelft.nl

1 Introduction

An increase in available computing power has led to a shift in focus in Computational Fluid Dynamics (CFD) research towards Scale Resolving Simulation (SRS) approaches for high Reynolds number flows. It has been repeatedly shown that the results of Large Eddy Simulation (LES), Partially Averaged Navier-Stokes (PANS) or Direct Numerical Simulation (DNS) can be dependent on inflow conditions, e.g. [1]. In order to properly simulate turbulent flows with SRS approaches the inflow must contain time-varying components, otherwise laminar solutions can be obtained [2]. It is likely that these problems persist or worsen for multiphase flows, consequently it is a focus point of the current research to predict cavitation induced noise. This paper aims to obtain a set of reference data to verify an inflow turbulence generation technique to be used with SRS. Next to that a comparison between a PANS approach and LES models is presented. Such comparisons are rare, and are often based on different codes, grids and numerical settings. In this paper we compare these methods using the same grid and settings, while quantifying the numerical errors. The chosen test case is a turbulent channel flow, due to the simple geometry and abundance of reference data. Since the 1980s numerical studies have been performed using LES and DNS [3, 4, 5]. The paper consists of a description of the setup, estimation of the iterative and statistical errors, and a comparison between different modelling approaches and DNS results from Moser et al. [5].

2 Numerical setup and solver

Computations are made using a rectangular domain, with two no-slip walls oriented normal to the y-axis (see Figure 1). The remaining boundaries are connected using periodic boundary conditions in order to approximate an infinite channel. The Cartesian grid density is $N_x = 127$, $N_y = 95$ and $N_z = 95$ with clustering towards the walls, resulting in $x^+ \approx 12$, $y^+ \approx 0.1$ and $z^+ \approx 10$. The non-dimensional time step $\Delta t^* = \frac{u_\tau \Delta t}{2\delta} \approx 1 \times 10^{-3}$ leads to $\Delta t^+ = \frac{u_\tau^2 \Delta t}{\nu} \approx 0.08$ (i.e. 2000 time steps per flow-through time). The grid density and time step are below LES guidelines and approach DNS resolution [6]. To maintain the proper bulk and friction Reynolds numbers, $Re_b = \frac{U_b 2\delta}{\nu}$ and $Re_\tau = \frac{u_\tau \delta}{\nu}$ respectively, a body force is applied which is proportional to the pressure gradient $\frac{\mathrm{d}p}{\mathrm{d}x} = -\frac{\tau_w}{\delta}$, with $\tau_w = \rho u_\tau^2$ [7].

The numerical solver used for all simulations in this work is ReFRESCO, a multiphase unsteady incompressible viscous flow solver using RANS and Scale-Resolving Simulation models such as SAS, DDES/IDDES, XLES, PANS and LES approaches, complemented with cavitation models and volume-fraction transport equations for different phases [8]. Time integration is done using a second-order scheme, the convection terms are discretised using a second-order accurate central differencing scheme. The Péclet number has a magnitude of $O(10)$.

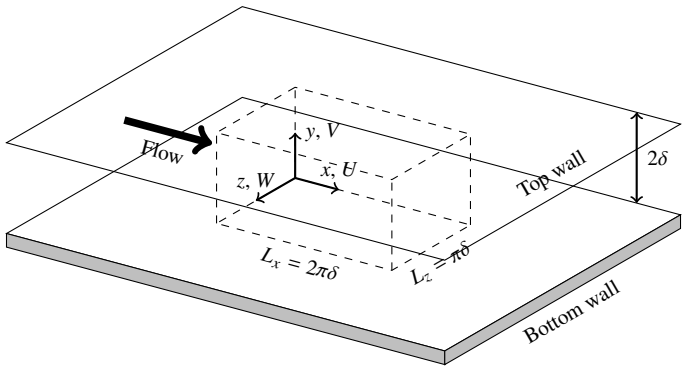

Symbol	Value
δ [m]	0.1
U_b [m/s]	6.928×10^{-2}
u_τ [m/s]	3.966×10^{-3}
τ_w [N/m^2]	1.570×10^{-1}
ν [m^2/s]	1.004×10^{-6}
Re_τ	395
Re_b	13800

Fig. 1: Schematic overview of the domain and physical parameters. The dashed lines indicate the computational domain. The figure is based on the drawing of de Villiers [9].

As shown in the literature, as well as in this paper, the use of scale-resolving turbulence models for a turbulent channel yields a so-called supercritical laminar solution for which many flow-through times are needed to trigger transition to the turbulent regime [9]. In order to speed up the transition, the method suggested by Schoppa and Hussain [10] is used here. This method is only applicable to cases where periodic boundary conditions can be used, and is tuned for a turbulent channel flow; it is therefore not a general approach. The flow is initialised as a laminar parabolic flow profile, u_0^+, on which near-wall parallel streaks of slower and faster moving fluid are superimposed according to the equation

$$u^+\left(y^+, z^+\right) = u_o^+\left(y^+\right) + \frac{\Delta u_0^+}{2}\cos\left(\beta^+ z^+\right)\frac{y^+}{30}\exp\left(-\sigma y^{+2} + 0.5\right)\cdot\left(1 + 0.2X\right). \tag{1}$$

Here Δu_0^+ is the streak's normal (y) circulation per unit length, taken as $\frac{1}{4}U_b$, $\beta^+ = \frac{2\pi}{z^+}$ is the spanwise wave number, chosen to produce a sparse streak spacing ($z^+ \approx 200$), $\sigma = 0.00055$ and X is an added random signal, $X \in [0, 1]$, to enhance symmetry breaking. To generate instabilities, based on linear stability analysis the streaks are perturbed according to the relation

$$w^+\left(y^+, z^+\right) = \epsilon\sin\left(\alpha^+ x^+\right)y^+\exp\left(-\sigma y^{+2}\right)\cdot\left(1 + 0.2X\right), \tag{2}$$

with a linear perturbation amplitude $\epsilon = \frac{U_b}{200}$ and an axial wave number $\alpha^+ = \frac{2\pi}{500}$.

3 Numerical errors

A distinction can be made between input, iterative, discretisation, and, in the case of unsteady computations, statistical errors. In this work the discretisation error is not assessed; the grid is equal to the one used for the DNS reference data [5], and is assumed to be sufficient. Instead here, the focus is on the iterative and statistical error, both of which are often assumed to be small in literature.

The iterative convergence was estimated based on the normalised residuals, which reached at least 10^{-5} for the L_∞ and 10^{-6} for the L_2 norm in each time step for momentum. The residuals for pressure and turbulence equations are at least one order of magnitude smaller. In order to assess whether this level of convergence is satisfactory to obtain the Reynolds stresses a second estimator is used, based on the changes in velocity between outer iterations. These changes drop during a time step from 10% to below 0.05% of the velocity fluctuations (both L_∞ and L_2), and in most cases even an order of magnitude lower. Therefore performing more outer iterations will not affect the computed velocities. This was verified by performing the same computation with double the number of outer iteration (and thereby reducing the residuals one order of magnitude further), which yielded a negligible difference in the results. Consequently it is concluded that the convergence achieved is satisfactory.

To remove the start-up effects and estimate the statistical uncertainty of the results, the Transient Scanning Technique (TST) is employed [11]. This technique allows an estimation of the statistical uncertainty u_1 based on a signal of a finite length; the uncertainty is expanded to obtain a 95% confidence interval. The TST is applied to the axial velocity at measurement points along the height of the channel. Figure 2 shows as example the case with the LES Smagorinsky model at wall-normal location $y/\delta = 1$. The graphs show the decrease in statistical uncertainty based on an increasing number of timesteps; the graphs are similar for other measurement points and turbulence models. Based on the TST it is found that the first 11 flow-through times must be removed to eliminate the start-up effects. This conclusion is independent of the wall-normal distance of the measurement point, and is in contradiction with literature in which fully turbulent flow was assumed after approximately six flow-through times [9]. The mean values are then computed based on approximately 45 flow-through times, resulting in a statistical uncertainty for the mean axial velocity between 0.5 and 2.5%, and for the Reynolds stress components between 5 and 10%. This is non-negligible, indicating that more flow-through times should be computed.

4 Results

In the current computations different turbulence models were applied, ranging from XLES, explicit LES (using Smagorinsky, Dynamic Smagorinsky and $k-$ SGS subgrid models), implicit LES (ILES) to PANS (based on $k-\omega$ SST) with different settings for the physical parameter ($f_k = \frac{k_{modelled}}{k_{total}}$) and $f_\epsilon = 1$

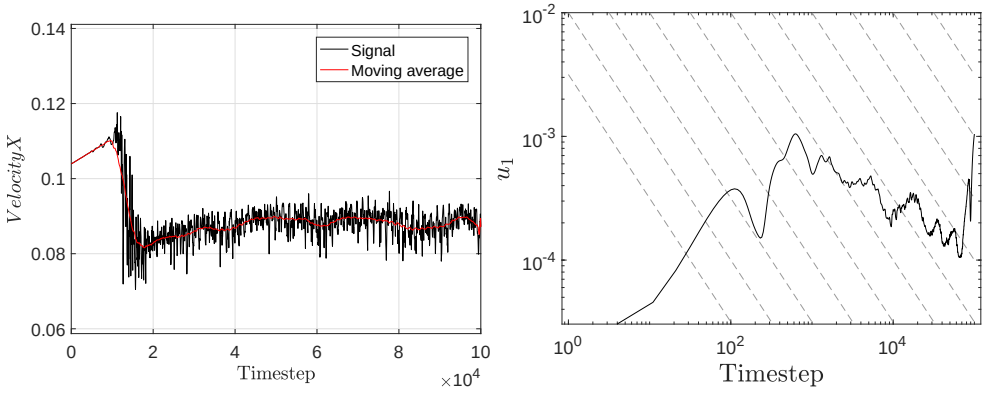

Fig. 2: Time signal (left) and TST plot (right) of the axial velocity for LES using the Smagorinsky model, probed at $y/\delta = 1$ on the domain centreline. In the stationary range the TST follows a slope equal to -1 (the dashed lines), the increase in uncertainty at the right of the graph indicates the start-up effects. The vertical axis shows the absolute uncertainty u_1.

[12, 13, 14, 15]. Figure 3 shows the mean velocity profiles with respect to the wall distance and the wall-normal coordinates. In the graphs only half the channel height is shown. The LES results all capture the trend of the DNS data; the poorest match is for the Dynamic Smagorinsky model which has an undershoot in the buffer-layer ($5 < y^+ < 30$), an overshoot in the log-law region ($y^+ > 30$, $y/\delta < 0.3$) and again an under-prediction in the outer layer ($y^+ > 50$). The regions are defined according to Pope [7]. The XLES also underpredicts the velocity in the buffer-layer. In the PANS results, the effect of reducing the f_k parameter is clearly visible: $f_k = 1.00$ yields a RANS result as expected, while changing from $f_k = 0.75$ to 0.20 the modelled turbulence kinetic energy is reduced and more turbulence kinetic energy should be resolved. However, by reducing f_k the flow profile becomes more parabolic; rather than resolving turbulence the velocity perturbations are damped and the flow remains laminar. The highest f_k values still have a reasonable match with the DNS, since these are mostly turbulent RANS solutions. Below $f_k = 0.20$ the fluctuations are not damped and a fully turbulent flow develops. $f_k = 0.15$ follows the same trend as the DNS data but underpredicts the velocity, $f_k = 0.10$ and 0.05 match the DNS data almost perfectly. The same behaviour occurs in cases where the PANS model is applied to an already developed turbulent flow, for which the fluctuations are damped after between five to seven flow-through times. In a wall-turbulence flow, such as a turbulent channel, the small scales near the wall built up to large scales in the centre of the flow. The large scales in the centre then break up into small scales and are dissipated. This process is known as energy backscatter, or the inverse energy cascade [16]. For the PANS computations only a turbulent flow develops if the filter length (defined by the physical resolution f_k) is smaller than the length scales of the small scales, otherwise the driving mechanism is filtered out. This is confirmed by the guideline for SRS that the effective computational Reynolds number, $Re_e = \frac{U\delta}{\nu+\nu_{modelled}}$, must exceed the critical Reynolds number needed for the onset of instability, $Re_c = 519$ [15, 17]. This guideline is satisfied for the cases with $f_k < 0.20$.

The normalised Reynolds stress profiles ($Re_{ij} = \overline{u_i' u_j'}/u_\tau^2$), vorticity fluctuations ($\omega'^+ = \omega' \nu/u_\tau^2$) and turbulence kinetic energy spectrum for the different LES and PANS computations are shown in Figures 4 and 5 respectively. The highest Reynolds stress terms are generally obtained for the ILES, followed by the Smagorinsky and $k-$ SGS and then the Dynamic Smagorinsky and XLES model. Except for Re_{ww} the magnitude of the Reynolds stress terms is generally underpredicted. For Re_{vv} for all models the peak is shifted towards the right indicating that the main turbulence fluctuations occur further from the wall; for the Dynamic Smagorinsky model the magnitude is significantly lower. The trend in the vorticity profiles is captured by all models; ILES captures the magnitude best, (Dynamic) Smagorinsky and $k-$ SGS yield similar results but underpredict the amplitudes. The turbulence kinetic energy spectra for the LES models are comparable, ILES shows the highest cut-off frequency. This is to be expected, since for the ILES all turbulence is resolved as fluctuations, whereas in the explicit LES models it is partly modelled, thereby reducing the energy visible in the spectrum. Remarkably, the spectra contains more

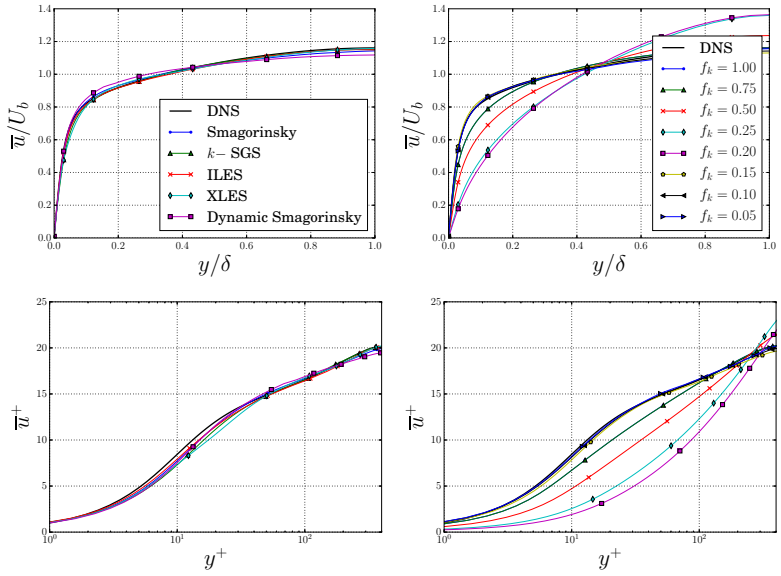

Fig. 3: Normalised mean velocity profiles using LES (left) and PANS models (right) with DNS [5].

energy for the entire frequency range than DNS. This could be an effect of the transformation of the DNS wavenumber spectrum to a frequency spectrum, or an effect of the computation method on the spectrum. The shapes of the spectra are comparable.

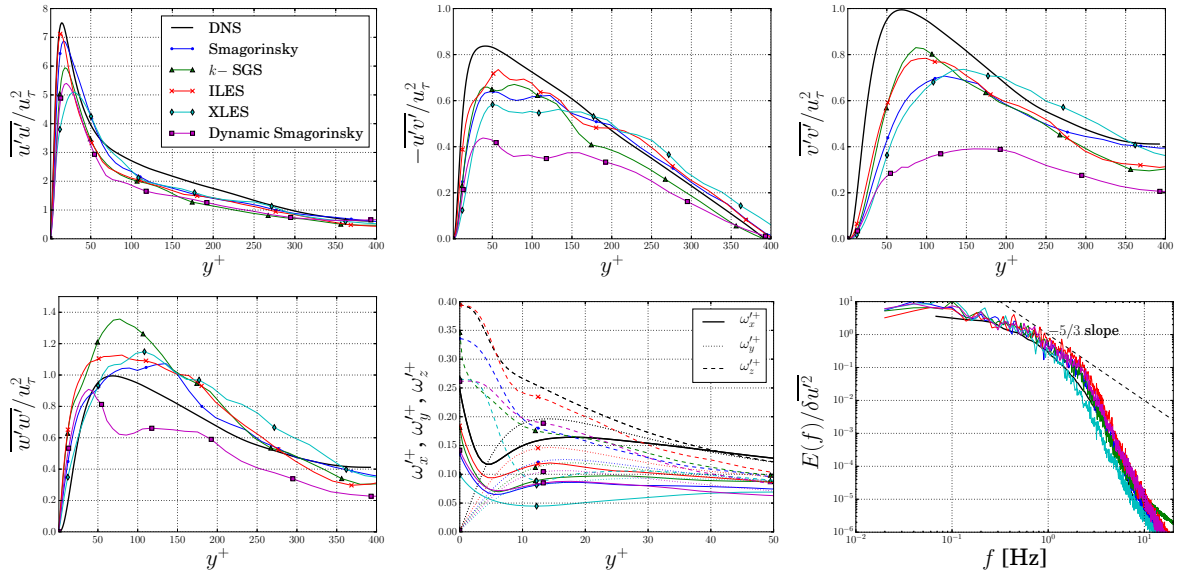

Fig. 4: Normalised Reynolds stress profiles, vorticity fluctuations and turbulence kinetic energy spectra using LES and DNS [5]. From left to right, and top to bottom Re_{uu}, Re_{uv}, Re_{vv}, Re_{ww}, ω'^+ and $E(f)$.

For PANS, it is clear that for computations with f_k in the range $0.75 - 0.20$ a laminar solution is obtained; the Reynolds stress tensor components equal zero. The results for $f_k = 0.15$, 0.10 and 0.05 are comparable and obtain the proper trends and order of magnitude. Interestingly the peaks for $f_k = 0.10$ are higher than for $f_k = 0.15$ and 0.05. This might indicate that a lower f_k requires finer grids and iterative convergence. The vorticity profiles show a similar image, again only the turbulent solutions have a non-zero profile. For both $f_k = 0.10$ and 0.05 the match is considerably better than for explicit LES, which is related to the increased turbulence resolution. For $\omega_x'^+$ and $\omega_z'^+$ both the trend and amplitude are captured, for $\omega_y'^+$ the shape is correct but the amplitude is lower. The turbulence kinetic energy spectra for $f_k = 0.15$, 0.10 and 0.05 are similar, and also show a larger energy than DNS (similar to ILES). It appears that the

cases with low f_k are equal to ILES, however this is not true when looked at the eddy-viscosity. The maximum eddy-viscosity ratio, ν_t/ν, in the field for $f_k = 0.15$ has a magnitude of $O(10^2)$, whereas for $f_k = 0.05$ this is $O(10)$, and for ILES it is zero by definition. For comparison, for a turbulent RANS solution $\nu_t/\nu = O(10^5)$.

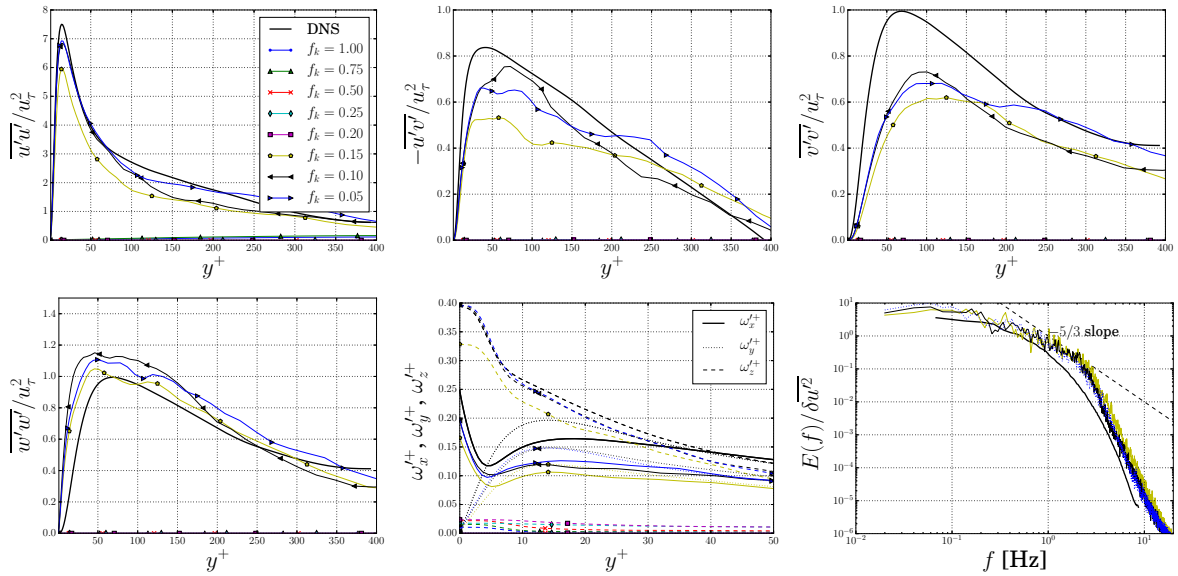

Fig. 5: Normalised Reynolds stress profiles, vorticity fluctuations and turbulence kinetic energy spectra using PANS and DNS [5]. From left to right, and top to bottom Re_{uu}, Re_{uv}, Re_{vv}, Re_{ww}, ω'^+ and $E(f)$.

Finally the turbulent structures in the flow for a number of representative models are shown based on the instantaneous contour plots of $Q = 0.3$ in Figure 6. The contour plots and the sides of the domain are coloured by the normalised axial velocity ($\overline{u}^* = \frac{\overline{u}}{U_b}$). Only turbulent results are compared. There is little difference between the structures of different LES models and of the PANS with low f_k. Occasionally horseshoe shapes can be distinguished.

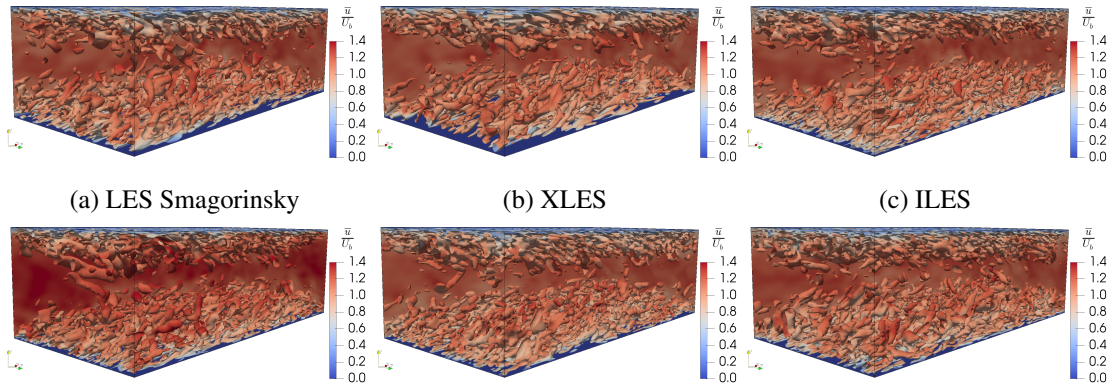

(a) LES Smagorinsky (b) XLES (c) ILES

(d) PANS, $f_k = 0.15$ (e) PANS $f_k = 0.10$ (f) PANS $f_k = 0.05$

Fig. 6: Instantaneous turbulent flow fields, visualised by $Q = 0.3$. The structures and the sides of the domain are coloured by the normalised axial velocity ($\overline{u}^* = \frac{\overline{u}}{U_b}$).

5 Conclusions

Turbulent channel flow at $Re_\tau = 395$ was simulated using different LES models and PANS at different physical resolutions (f_k) and compared to DNS reference data. The iterative convergence was assumed to be negligible. The statistical uncertainty based on 45 flow-through times was below 2.5% for the

mean values, and below 10% for the Reynolds stresses. LES, both explicit and implicit, can capture both the mean behaviour and turbulent fluctuations. The magnitude of the fluctuations differs and depends on the subgrid modelling; in terms of the turbulence kinetic energy spectrum, there appears to be little difference. ILES performs satisfactorily; however due to the high grid density the effect of the subgrid model is small anyway. For ILES most of the dissipation which should act as a subgrid model is added by the use of second-order schemes; it can be questioned whether this is sufficient.

With respect to the PANS results, in line with earlier observations by Pereira [1] the use of PANS is not straightforward. There is no smooth bridging in the results between RANS and DNS, instead there is a case-dependent threshold which separates two solution regimes: $0.20 \leq f_k < 1.0$ yields a laminar solution; $f_k < 0.20$ results in a turbulent solution. The hypothesis for this behaviour is that for PANS, the small scale turbulent fluctuations near the wall (resolved turbulence) are transferred to turbulence kinetic energy (modelled turbulence) due to diffusion in the turbulence model. The small scale fluctuations are filtered out, therefore removing the driving mechanism in the inverse energy cascade. Also the kinetic energy in the RANS formulation decays, leading to a reduction in k and in the end to the total destruction of the turbulence. This behaviour is reminiscent of the turbulence decay issues observed in transition modelling [18]. The laminar solution occurs regardless of the initialisation of the flow. It is often remarked that PANS with $f_k = 0.20$ should be similar to a well-resolved LES, but it is clear that this comparison must be made with care. The observed structures for the lowest f_k values are similar to the ones for LES. The eddy-viscosity levels between $f_k = 0.15$ and 0.05 differ an order of magnitude, yet this appears to have little effect.

For further work the discretisation error remains to be assessed. Also it is clear that a turbulence generator is necessary not only for complicated flow cases, but also for relatively simple geometries such as a turbulent channel, if SRS is to be used. Such a turbulence generator can counteract the turbulence decay, yielding a fully turbulent flow.

Acknowledgements

This research was financially supported by the Netherlands Organisation for Scientific Research, NWO, as part of the NOISOURCE project. The work was carried out on the Dutch national e-infrastructure, with the support of SURF Cooperative, on the *Reynolds* (TU Delft) and *Marclus3* (MARIN) clusters.

References

[1] F.M.S. Pereira. *Towards Predictive Scale-Resolving Simulations of Turbulent External Flows*. PhD thesis, Universidade de Lisboa, Instituto Superior Técnico, 2018.

[2] T.S. Lund, X. Wu, and K.D. Squires. Generation of Turbulent Inflow Data for Spatially-Developing Boundary Layer Simulations. *Journal of computational physics*, 140(2):233–258, 1998.

[3] P. Moin and J. Kim. Numerical investigation of turbulent channel flow. *Journal of fluid mechanics*, 118:341–377, 1982.

[4] J. Kim, P. Moin, and R. Moser. Turbulence statistics in fully developed channel flow at low Reynolds number. *Journal of fluid mechanics*, 177:133–166, 1987.

[5] R.D. Moser, J. Kim, and N.N. Mansour. Direct numerical simulation of turbulent channel flow up to $Re_\tau = 590$. *Physics of fluids*, 11(4): 943–945, 1999.

[6] N.J. Georgiadis, D.P. Rizzetta, and C. Fureby. Large-Eddy Simulation: Current Capabilities, Recommended Practices, and Future Research. *AIAA journal*, 48(8):1772–1784, 2010.

[7] S.B. Pope. *Turbulent Flows*. Cambridge University Press, 2000. ISBN 9780521598866.

[8] MARIN. ReFRESCO description, May 2018. URL `http://www.refresco.org/`.

[9] E. de Villiers. *The Potential of Large Eddy Simulation for the Modelling of Wall Bounded Flows*. PhD thesis, University of London, 2007.

[10] W. Schoppa and F. Hussain. Coherent structure dynamics in near-wall turbulence. *Fluid Dynamics Research*, 26(2):119–139, 2000.

[11] J. Brouwer, J. Tukker, and M. Van Rijsbergen. Uncertainty analysis and stationarity test of finite length time series signals. In *The 4th International Conference on Advanced Model Measurement Technology for the Maritime Industry (AMT15), Istanbul, Turkey*, 2015.

[12] J.C. Kok, H.S. Dol, B. Oskam, and H. van der Ven. Extra-Large Eddy Simulation of Massively Separated Flows. *AIAA paper*, 264, 2004.

[13] J. Smagorinsky. General circulation experiments with the primitive equations, I. The basic experiment. *Monthly weather review*, 91(3): 99–164, 1963.

[14] A. Yoshizawa and K. Horiuti. A Statistically-Derived Subgrid-Scale Kinetic Energy Model for the Large-Eddy Simulation of Turbulent Flows. *Journal of the Physical Society of Japan*, 54(8):2834–2839, 1985.

[15] F.S. Pereira, L. Eça, G. Vaz, and S.S. Girimaji. Challenges in Scale-Resolving Simulations of turbulent wake flows with coherent structures. *Journal of Computational Physics*, 363:98–115, 2018.

[16] A. Cimarelli and E. De Angelis. The physics of energy transfer toward improved subgrid-scale models. *Physics of Fluids*, 26(5):055103, 2014.

[17] Y. Zhang. Critical transition Reynolds number for plane channel flow. *Applied Mathematics and Mechanics*, 38(10):1415–1424, 2017.

[18] L. Eça, R. Lopes, G. Vaz, J. Baltazar, and D. Rijpkema. Validation Exercises of Mathematical Models for the Prediction of Transitional Flows. In *Proceedings of 31st Symposium on Naval Hydrodynamics, 11th-16th September, Berkeley*, 2016.

Hydrofoil simulations – non-linear lifting line vs CFD

Jarle V. Kramer, John Martin K. Godø, Sverre Steen
Norwegian University of Science and Technology, Trondheim/Norway
jarle.a.kramer@ntnu.no

1 Introduction

In this article we present results from two different simulation methods. One is a relatively simple and computational fast lifting line method, with significant extensions from the classical lifting line theory in order to handle non-linear lift, non-planar geometry, interaction effects between several wings in close proximity, and model free surface effects at high speed. The other is three-dimensional RANS CFD using OpenFOAM. We present comparisons of the integrated forces as well as the lift distribution over the span of the wing from the two methods for some test cases. The validity of the lifting line method is discussed relative to the free surface modelling and the capability of modelling non-planar geometry

Our motivation for developing the lifting line method is to create a computational tool for design of hydrofoils. In order to optimize a hydrofoil design, one needs to perform many simulations of different wing geometries. The problem with three-dimensional CFD simulations for this task is the computational time. The required mesh size for a hydrofoil CFD simulation will typically be 10-20 million cells – even with a relatively coarse resolution – and this can take days to complete on a relatively fast desktop workstation. A solution is to first use a simpler and faster simulation method in an optimization loop with all necessary design variables in order to create an initial design. The practical limitation on the range and number of design variables are dependent on the computational speed of the simulation method. Based on the initial design one can further *fine tune* the geometry based on CFD simulations– or other advanced simulation methods – by for instance using fewer design variables in the final optimization process.

The lifting line method is an interesting candidate for a simplified simulation tool due to its ability to handle viscous effects. This can be important to take into account, as the lift can easily vary with 5-10% for a given wing geometry as a function of Reynolds number. Neglecting viscous effect on the lift can therefore introduce relatively large errors in the results. The lifting line method finds the circulation along the span of the wing by matching Kutta-Juokowski's law with the lift calculated from sectional lift coefficients that is dependent on the local two-dimensional foil geometry. Viscous effects on both drag and lift can be included in the model, for instance by using two-dimensional CFD simulations to calculate the force coefficients. This is an advantage relative to other potential theory methods such as panel methods and vortex lattice methods. Although it is possible to include viscous effects in panel methods as well, it is significantly more complex, and it relies on simplified models of boundary layer theory.

That being said, the lifting line method introduces large simplifications as well and will only be valid for a limited set of hydrofoil designs. The purpose of this work is to investigate when the lifting line method is accurate, and when the fundamental simplifications are too large.

2 Non-linear lifting line method

Our non-linear lifting line method builds on the same basic principle as Prandtl's classical lifting line theory but is extended to include more physics and to be more flexible in terms of geometry. Specifically, the following features are included in our method:

- Non-linear lift model which can take into account viscous effects, including stall
- Free surface effects based on the simplified *high-speed* version of the linear free surface condition

- Arbitrary span shape, which for instance can include features such as winglets, wing-sweep and dihedral.
- Interaction effects between several wings in close proximity – e.g. a main wing and a tail wing
- Unsteady simulations, which is explained more in detail in reference [1]. In this paper, only the steady state version of the lifting line method is used

Similar modern extensions of Prandtl's lifting line theory have been made before. Examples can be found in reference [2], [3] and [4]. However, we have not found any examples that include a model of free surface effects. The free surface can have a large effect on the lift distribution and is therefore important to consider when analyzing and designing hydrofoils.

The lifting line algorithm works as follows:
The lifting line model collapses the three-dimensional wing geometry into a several horseshoe vortices with constant vortex strength. There are *bound vortices* that makes up the span geometry of the wing, and *free vortices* that extends from the wing in the direction of the incoming velocity. The bound vortex represents the circulation created by the wing, while the free vortices represents the circulation that is shed into the wake while the wing is moving.

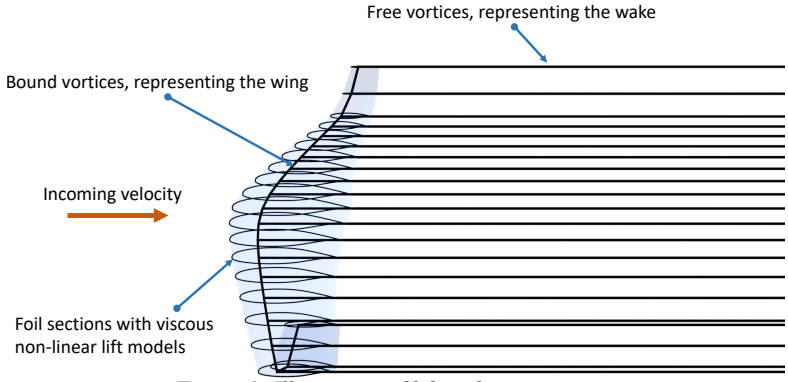

Figure 1: Illustration of lifting line geometry

Each line segment making up the horseshoe vortices induces velocity at every point in space. This velocity is calculated based on the line geometry and the strength of the horseshoe vortex. The induced velocity at any point in space will be linearly dependent on the strength of each horseshoe vortex. In order model a wing we need to calculate the induced velocity at several control points which is defined to be in the middle of each bound vortex. The induced velocity at every control point can be expressed as a matrix, $\boldsymbol{A}$, that is only dependent on the geometry of the lifting line multiplied with a vector representing the strength of each vortex, $\boldsymbol{\Gamma}$, so that the induced velocity, $\boldsymbol{u}_i = \boldsymbol{A\Gamma}$. The strength of each horseshoe vortex is the unknown quantity in the simulation. The basic principle behind the equation system to be solved is to require that lift calculated from Kutta-Juokowski's law matches the lift calculated from the sectional lift coefficient at each control point along the wing. The sectional lift from Kutta-Juokowski's law can be calculated from the following equation, where U is the incoming velocity and ρ is the density:

$$L = \rho \Gamma U$$

The lift from the sectional lift coefficient is dependent on the foil geometry and the angle of attack. In order to calculate the lift coefficients for a section of the wing, one can use two-dimensional CFD, panel methods such as XFoil or use experimental data if available. The lift function can be linear for small angles of attack but will have non-linear behavior for angles of attacks close to stall. The angle of attack on each control point along the wing is dependent on the geometric angle of attack and the induced angle of attack – and therefore the strength of each horseshoe vortex. The following equation ca be used to calculate the lift, where c is the chord length, C_L is the sectional lift coefficient, which is dependent on the effective angle of attack α_{eff}:

$$L = \frac{1}{2}\rho C_L(\alpha_{eff}) c U^2$$

These two equations can be combined to solve for the strength of each horseshoe vortex which gives the following relation at every control point.

$$\frac{2\Gamma}{cU} = C_L(\alpha_{eff})$$

This gives a non-linear equation system, where α_{eff} is dependent on both the geometrical and the induced angle of attack. Using the expression for the induced velocity, we get the following equation for the effective angle of attack, where $\boldsymbol{n}$ is a vector on each horseshoe vortex that is normal to both the incoming velocity and the bound vortex line, while $\boldsymbol{t}$ is a vector that is parallel to the incoming velocity:

$$\alpha_{eff} = \alpha + \alpha_i = \alpha + \tan^{-1}\left(\frac{\boldsymbol{u_i}\cdot\boldsymbol{n}}{\boldsymbol{U}+\boldsymbol{u_i}\cdot\boldsymbol{t}}\right) = \alpha + \tan^{-1}\left(\frac{\boldsymbol{A_i}\,\boldsymbol{\Gamma}\cdot\boldsymbol{n}}{\boldsymbol{U}+\boldsymbol{A_i}\,\boldsymbol{\Gamma}\cdot\boldsymbol{t}}\right)$$

In order to linearize this equations system, we can assume the lift is linearly dependent on the effective angle of attack such that $C_L = C_{L0} + \frac{\partial C_L}{\partial \alpha}\alpha_{eff}$, that $\tan^{-1} x \approx x$, and that $u_i \cdot t \approx 0$. In order to solve the complete non-linear system, we perform several iterations, where we construct a new local linear version of the system that is always based on the last estimate of the effective angle of attack. That is, the linear lift model is updated to match the complete non-linear model in the vicinity of the last effective angle of attack and the tangential velocity is updated to include the induced velocity from the last iteration. The iteration loop stops when the estimated circulation distribution converges.

In order to capture the effect of the free surface, we use a simplified model. Under the assumption of high speed, linear free surface condition and potential theory, the velocity potential due to the wing at the free surface should be constant. See for instance reference [5] for an in-depth explanation. This can be achieved by mirroring the lifting line geometry about the free surface and reversing the vortex strength. That is, the line geometry is mirrored, but the direction of the lift is the kept the same for the mirrored geometry. This is different from a *normal* mirroring that could be used to model a ground plane, as in that case, the direction of the lift would also be reversed. The induced velocity from the mirrored vortex lines is evaluated at the three-quarter chord, or half a chord length behind the bound vortex. This was deemed necessary in order to model the vertical induced velocity from the mirrored line, and greatly improves the results relative to evaluating the induced velocity at the bound vortex. This was inspired by the Weissinger approximation [6], which suggest that the three-quarter chord is good location to evaluate the induced velocity.

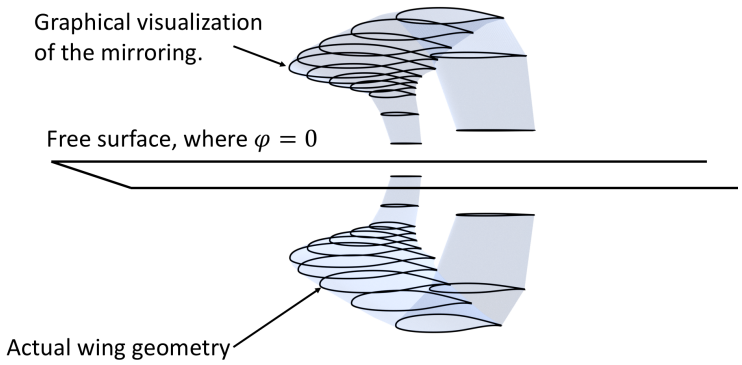

Figure 2: Illustration of the free surface. Notice the direction of the foils in the mirrored wing geometry

3 CFD setup

OpenFOAM version 1712+ is used to do the CFD simulations. Simulations with free surface modelling is done with the *interFoam* solver which is based on the unsteady PISO algorithm and the *Volume of* Fluid (VoF) model to capture the free surface. Simulations without free surface effects are done with *simpleFoam* which is a steady state solver based on the SIMPLE algorithm. The turbulence model is k-omega SST. We use a custom Python library that we develop to set up the CFD simulations in a consistent and automated manner. The library uses the dimensions of the geometry, the Reynolds

number and best practices based on our own past experience to create the case folders and setup files for OpenFOAM. The mesh is created using SnappyHexMesh. Right outside the wing geometry there are inflation layers. The friction on the wing surface is first estimated using a friction line, and the thickness of the first layer is then calculated based on the estimated friction coefficient and a target y+ value. The cell length right outside the inflation layers is set according to a maximum cell length value that ensures the geometry is captured. An illustration of the mesh can be seen in the figure below, also showing refinement regions in the wake and around the free surface. Table 1 shows the most important settings in the CFD simulation as created by the Python library for this specific case. There are two columns; one for the three-dimensional simulations and one for the two-dimensional simulations that are used to generate data to be used together with the lifting line model. The three-dimensional simulations are performed with lower resolution than the two-dimensional simulations in order to keep the simulation time down to a practical level.

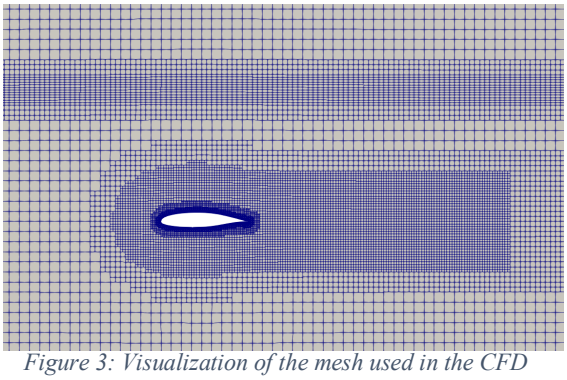

Figure 3: Visualization of the mesh used in the CFD simulations. The plane shown is the mid-plane of the wing. There are refinement zones in the wake of the wing and in the area close to the free surface.

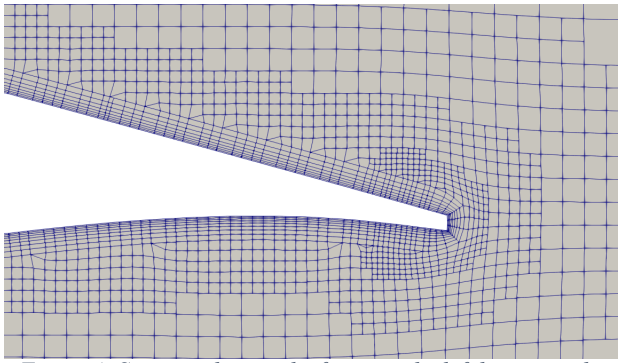

Figure 4: Same mesh as in the figure to the left but zoomed into the trailing edge of wing.

Table 1: Simulation parameters

Parameter name	3D wing simulations	2D foil simulations
Max feature cell size / chord length	0.0021	0.001
Max background cell size / chord length	0.14	0.1
Wake refinement cell size / chord length	0.35	0.01
Number cells between layers	5	5
Number of wall layers	7-9	5-10
Target y+	60	60
Approximate number of cells	15 Million	100 000
Max Courant number	20	10

4 Results

The results of our validation study are shown below. The goal is to answer two fundamental questions: can the lifting line method model free surface effects at speeds that are realistic for hydrofoil vessels, and can it model non-linear wing geometries? First, we tested non-linear wing geometries using steady state CFD simulations, without free surface modelling. Then we tested a planar wing geometry at different speeds and different Froude submergence numbers, with free surface modelling. All wing geometries tested used the foil profile NASA LS417, which is a common foil geometry for low-speed airplanes. The sectional lift and drag for the foil profile as a function of Reynolds number and angle of attack was computed using two-dimensional CFD simulations. The results are presented as the lift distribution over the non-dimensional span of the wing, and as integrated forces in terms of coefficients. The difference in the lift distribution between the CFD and lifting line is also plotted. The non-dimensional span distance goes from 0.0 at the mid-section of the wing, to 1.0 at the wing tip.

Non-linear wing geometry – sweep and winglet

The non-linear wing geometries we tested consisted of a non-swept wing with a simple winglet design with varying *winglet radius* and a wing without any winglet, but with different sweep angles. The wings had an aspect ratio of 8 and a mean chord length of 0.5. The wings with the winglet had a taper ratio of 0.3, while the swept wings had a taper ratio of 0.5. The geometry and results from the simulations can be seen in the figures below

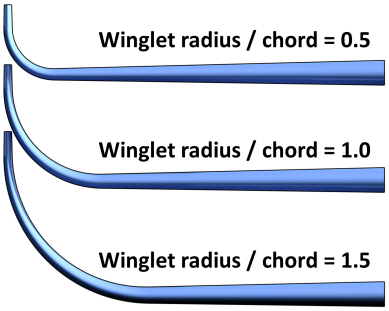

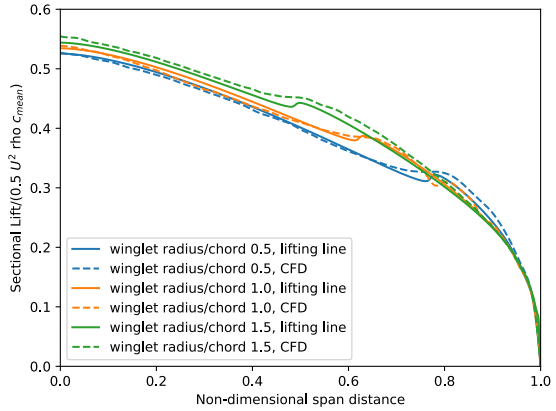

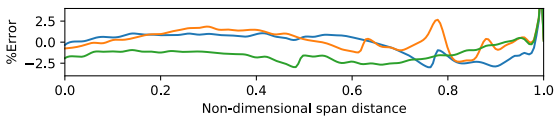

Case	C_L LL	C_L CFD	E[%]	C_D LL	C_D CFD	E[%]
	0.415	0.411	0.8	0.01732	0.01710	1.3
	0.434	0.423	2.6	0.01825	0.01945	-6.2
	0.450	0.455	-1.1	0.01915	0.01895	1.1

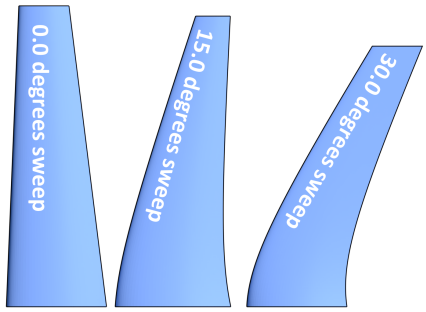

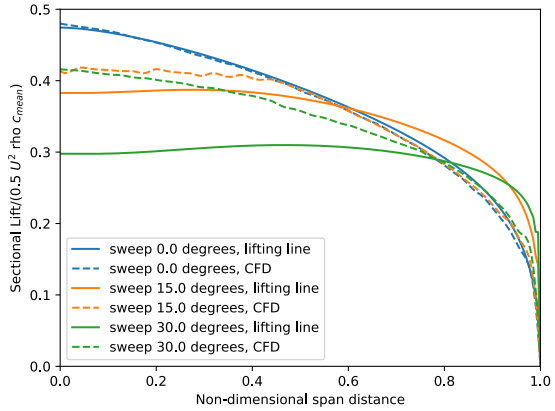

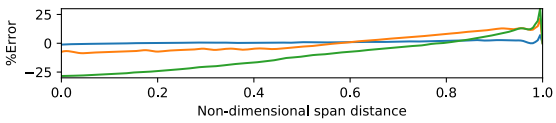

Case	C_L LL	C_L CFD	E[%]	C_D LL	C_D CFD	E[%]
	0.368	0.365	0.8	0.01523	0.01542	-1.2
	0.346	0.353	-2.1	0.01522	0.01468	3.6
	0.280	0.297	-6.0	0.01483	0.01318	12.6

Free surface effects

In order to test the free surface model in the lifting line method we simulated a planar wing with aspect ratio of 8, taper ratio of 0.5 and a mean chord length equal to 0.5 m. The importance of the free surface is dependent on both the actual submergence – the less the foil is submerged, the more important is the free surface – and on the Froude submergence number defined as $Fr_h = U/\sqrt{gh}$, where h is the submergence – the higher the Froude submergence number, the more valid should the high-speed version of the free surface condition be. There are many types of hydrofoils with different speeds and submergence, but a case we are currently working on is hydrofoils for high-speed passenger ferries. These hydrofoils will have a submergence between 1 – 2 chord lengths, and Froude submergence numbers between 4 and 6. These numbers are based on a design speed of 30-35 knots and mean chord length of roughly 1 m. We have chosen to use these numbers in our test case. The results are shown below

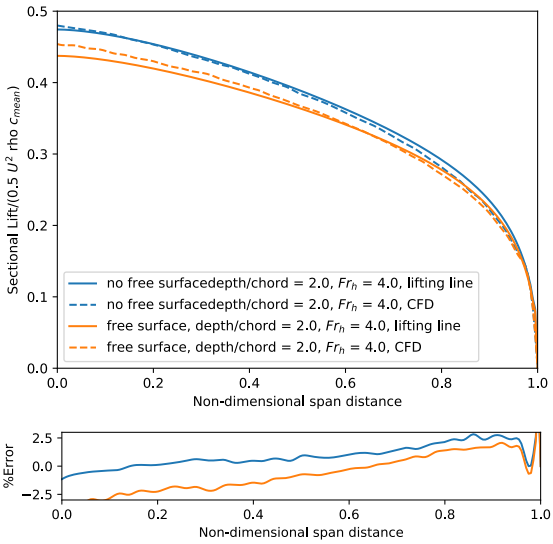

Case	C_L LL	C_L CFD	E[%]	C_D LL	C_D CFD	E[%]
	0.368	0.365	0.8	0.01523	0.01542	-1.2
	0.344	0.349	-1.3	0.01586	0.01574	-0.7

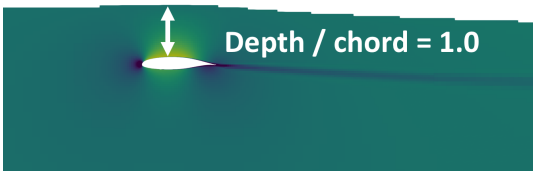

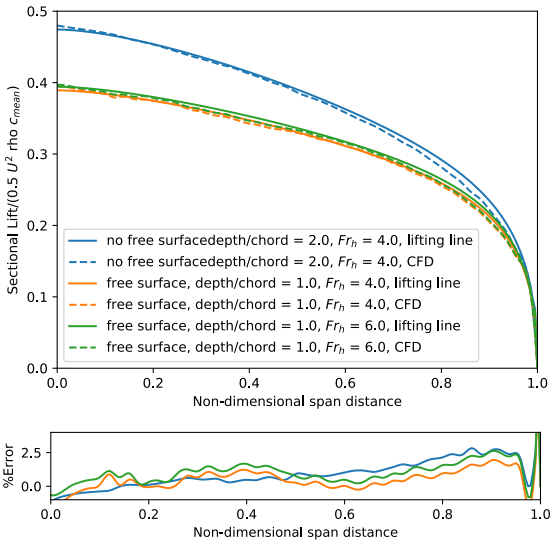

Case	C_L LL	C_L CFD	E[%]	C_D LL	C_D CFD	E[%]
	0.368	0.365	0.8	0.01523	0.01542	-1.2
	0.312	0.311	0.3	0.01681	0.0157	7.0
	0.317	0.315	0.9	0.01634	0.01503	8.7

5 Conclusion

The lifting line method – including the high-speed version of the linear free surface condition - is both simple to implement and fast to execute on a computer. While a CFD simulation can take days, the lifting line method takes seconds. The test cases presented in this paper show a relatively good match between the lift distribution calculated with lifting line and CFD both with winglet and with free surface. However, the lifting line method shows relatively large differences in the lift distribution when sweep is introduced. This suggest that the lifting line method is limited to wing geometries that lies in the plane that is normal to the incoming velocity. Considering the simplicity of the method, we are particularly happy about the match between the CFD simulations with a non-linear free surface model (VoF) and the lifting line method with a high-speed version of the linear free surface condition.

Bibliography

[1] J. M. K. Godø, J. V. Kramer, S. Steen and L. Savio, "Unsteady forces on hydrofoil vessels in waves - validation of a dynamic lifting line using CFD," in *Numerical Towing Tank Symposium*, Cortona, 2018.

[2] D. F. Hunsaker, "A Numerical Lifting-Line Method Using Horseshoe Vortex Sheets," Utah State Univeristy, 2011.

[3] W. F. Phillips and D. O. Snyder, "Modern Adaptation of Prandtl's Classic Lifting-Line Theory," *Journal of Aircraft,* vol. 37, no. 4, pp. 662-670, 2000.

[4] C. Duport, M. Deberque, J.-B. Leroux, K. Roncin and C. Jochum, "Local Results Verification of a 3D Non-Linear Lifting Line Method for Fluid-Structure Interactions Simulation on a Towing Kite for Vessels," in *High-Performance Marine Vehicles*, Zevenwacht, 2017.

[5] O. M. Faltinsen, Hydrodynamics of High-Speed Marine Vehicles, Cambridge University Press, 2005.

[6] J. Weissinger, "The Lift Distribution of Swept-Back Wings," NASA, 1947.

[7] J. D. Anderson, Fundamentals of aerodynamics, Tata McGraw-Hill, 2010.

[8] B. Maskew, "VSAERO Theory Document," NASA, 1987.

Evaluation of a Coupled Level Set and Volume of Fluid Method for Unstructured Meshes

Benoît LeBlanc*⋆, Hamn-Ching Chen†, and Christiaan M. Klaij‡
*University of New Brunswick, Fredericton/Canada, ⋆MARIN Academy, Wageningen/Netherlands
†Texas A&M University, College Station/USA, ‡ MARIN, Wageningen/Netherlands
bleblan9@unb.ca

1 Introduction

A model for free surface flows has been developped for fully unstructured CFD solvers, coupling a Volume of Fluid (VOF) method (Hirt et al. 1981) with a Level Set (LS) method (Sussman et al. 1994) for the interface capturing, in the context of an unsteady formulation of the mass-momentum equations. The present study seeks to overcome some of the challenges brought by coupling both methods for an unstructured solver using basic test cases.

The goal of coupling both VOF and LS methods is to leverage the advantages. Ideally, an interface capturing method would be able to describe the interface as sharply as possible without leading to instability of the mass-momentum equations, while also achieving global conservation of quantities. Traditionally, either method can only achieve one of these two goals. The VOF method succeeds in conserving mass but has difficulty in controlling the interface thickness without complicated reconstruction; the LS method succeeds in defining an interface thickness, but fails at globally conserving mass (Wang et al. 2009). The blending method often employed uses a VOF method with Piecewise Linear Interface Calculation (PLIC) as a base for transport of the phases, from which the interface location is calculated. This is followed by a redistancing function based on the LS method around the VOF interface, which then allows to prescribe an interface thickness (Figure 1). This new interface is then used to update densities and viscosities of the fluids in the mixed cells (Zhao & Chen 2015).

One of the challenges lies in the redistancing algorithm. In structured solvers, the redistancing equation, which takes the form of an Eikonal equation (Sethian 1999), can be solved using higher-order Essentially Non-Oscillatory (ENO) or Weighted Essential Non-Oscillatory (WENO) discretization schemes for the spatial derivatives (Chen 2011). In unstructured solvers, however, the use of such higher order schemes is complicated by the access to only direct neighbouring cell information.

This study examines the implementation of a Coupled Level Set and Volume of Fluid (CLSVOF) method, using a Flux-Positive (FP) scheme for calculating the spatial derivative in the redistancing algorithm, with an extremum correction for the level set field. The algorithm has been implemented in ReFRESCO, and numerical tests were done using the slotted disk case geometry (Zalesak 1979) and the breaking dam case (Martin et al. 1952). ReFRESCO is a fully unstructured CFD code developped by MARIN and collaborating universities, with a VOF formulation for free surface capturing (Klaij et al. 2018). For the momentum-pressure coupling, the SIMPLE algorithm (Patankar 1983) is used.

2 Coupled Level Set and Volume of Fluid method

The Navier-Stokes equations for momentum and mass transport, given below (bold font denotes vector, double overbar denotes tensor)

$$\frac{\partial \mathbf{u}}{\partial t} + \nabla \cdot (\mathbf{u} \otimes \mathbf{u}) = \nabla \cdot (2\nu \bar{\bar{\mathbf{s}}}) - \frac{\nabla p}{\rho} + \mathbf{g} \qquad \text{and} \qquad \nabla \cdot \mathbf{u} = 0 \quad , \tag{1}$$

are accompanied by a transported scalar field to implicitly describe the free surface. For VOF, it is the volume fraction field c, and for LS it is a set of equidistant surfaces called levels and described by the field ϕ:

$$\frac{\partial c}{\partial t} + \mathbf{u} \cdot \nabla c = 0 \quad \text{(VOF)} \qquad \text{or} \qquad \frac{\partial \phi}{\partial t} + \mathbf{u} \cdot \nabla \phi = 0 \quad \text{(LS)} \quad . \tag{2}$$

For VOF, the c scalar field takes the value of 0 or 1 and has a sharp variation at the interface $c = 0.5$. The density and viscosity, ρ and ν, are defined with a linear relation to c:

$$\rho = c\,\rho_1 + (1-c)\rho_2 \quad , \qquad \nu = c\,\nu_1 + (1-c)\nu_2 \quad ,$$

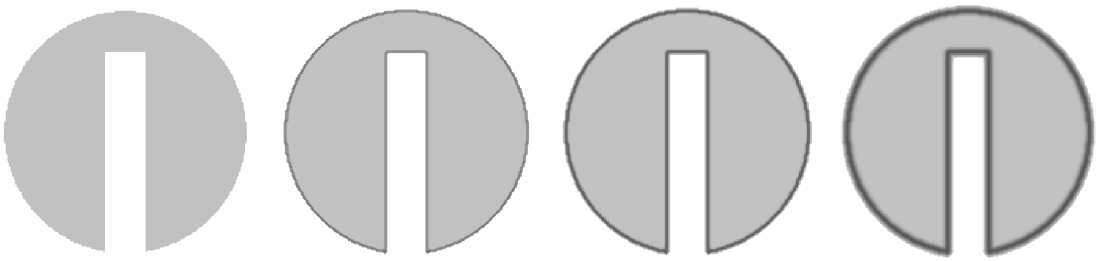

Fig. 1: Values of ϕ from redistancing on four separate cases of a stationary 2D slotted disk, using 512^2 cells, at timestep zero. From left to right, density change is prescribed over zero cells, two cells, four cells and eight cells, respectively. The dark grey line indicates the controllable transition layer.

where $\{\rho_1, \nu_1\}$ are the properties of fluid 1, and $\{\rho_2, \nu_2\}$, the properties of fluid 2.

For LS, a scalar field ϕ is defined as a signed distance from the interface $d = |\phi|$. The interface is implicitly defined as the location where $\phi = d = 0$, and it follows that $(|\nabla\phi| = 1)$ everywhere in the field. LS has the advantage to define the interface thickness as a function of ϕ, over a prescribed distance 2ϵ. The properties are a function of ϕ via a mollified Heaviside function from $-\epsilon$ to ϵ :

$$\{\rho, \nu\} \;=\; H(\phi)\,\{\rho_1, \nu_1\} + H(-\phi)\{\rho_2, \nu_2\} \quad , \qquad H(\phi) = \begin{cases} 0 & \textbf{if} \quad \phi < -\epsilon \\ \frac{1}{2}\frac{(1+\phi)}{\epsilon} + \frac{1}{2\pi}\sin(\frac{\pi\phi}{\epsilon}) & \textbf{if} \quad -\epsilon \le \phi < \epsilon \\ 1 & \textbf{if} \quad \epsilon \le \phi \end{cases} . \tag{3}$$

For the case of the LS method, due to the deformation to ϕ entrained by advection, it is accompanied by a redistancing step following the advection step. The property $|\nabla\phi| = 1$ is rearranged into an explicit pseudo time-stepping formulation (Sussman et al. 1994), given by

$$\frac{\partial\phi}{\partial\tau} \;=\; \mathrm{sgn}(\phi_0)\,(1 - |\nabla\phi|) \quad , \tag{4}$$

which must converge to steady state, with ϕ_0 the initial value at $\tau = 0$. In practice, only a few pseudo-timesteps are needed per timestep (less than 10) in order to converge to a steady state.

In the case of the Coupled Level Set and Volume of Fluid method (CLSVOF), however, both variables undergo an advection step within the algorithm, and the redistancing function uses the interface at $c = 0.5$ for determining the sign value, using instead

$$\frac{\partial\phi}{\partial\tau} \;=\; \mathrm{sgn}(0.5 \;-\; c)\,(1 - |\nabla\phi|) \quad . \tag{5}$$

This ensures the calculation of the new ϕ value based on the interface computed by c, which is mass conserving (Chen 2011). Once ϕ is determined, the value of ρ and ν is computed. It is to be noted that this coupling does not retroactively change the value of c, since this would introduce some mass loss (Wang et al. 2009). A flow chart of the coupled algorithm can be seen in the left image of Figure 4, with red dotted lines indicating changes for coupling.

3 Unstructured Formulation

Problems arise in the coupling when solving Equation (5). For structured solvers, it is possible to calculate the gradient $\nabla\phi$ to a high degree of accuracy using a higher order scheme which can handle discontinuities encountered at extremum lines (like between two interfaces) or at the interface of the free surface. The most commonly used schemes for this purpose are the higher order ENO and WENO schemes (Chen 2011).

Using an unstructured code renders the use of a wide-stencil gradient calculation difficult. Unfortunately, defaulting to using a smaller stencil for the calculation of the gradient on the cells containing the extrema leads to flux superposition or flux cancellation if neighbouring values are summed. This causes the ϕ field to converge to a false value in valleys or peaks, as visible from Figure 5 (b).

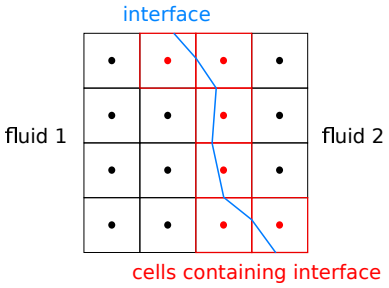

(a) global view

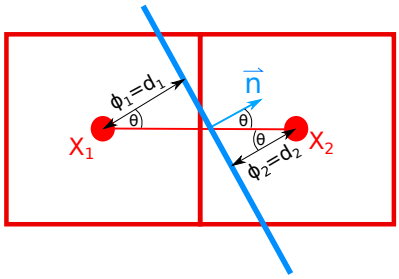

(b) local view, distance calculation

Fig. 2: Extrapolation of interface values for ϕ.

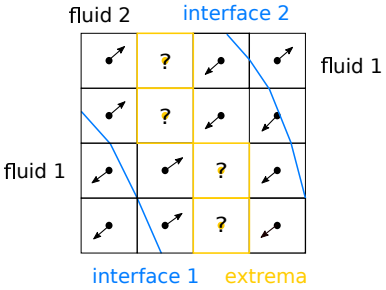

(a) global view, arrows represent $\nabla\phi$

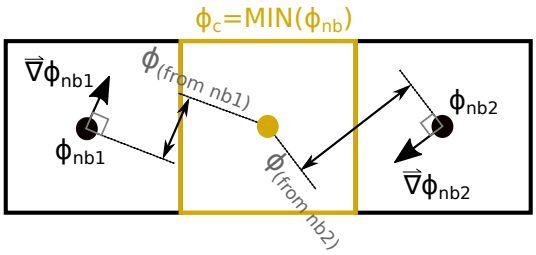

(b) local view showing extrapolation

Fig. 3: Extrapolation of extrema values for ϕ.

In this study, various methods were attempted for approximating the gradient $\nabla\phi$, and a two-pass method was finally chosen for the gradient calculation, which will be denoted the Flux-Positive (FP) gradient calculation ($\nabla^+\phi$). It consists of a first pass to calculate a Gaussian approximation of the gradient from all neighbours, $\nabla\phi_c$, followed by a second pass to calculate a new gradient based uniquely on the contributions from adjacent surfaces with positive flux (i.e. the neighbouring nodes which have a lower $|\phi|$ value),

$$\nabla\phi_c = \sum_{nb} \frac{\phi S \mathbf{n}}{V_c} \quad , \quad \nabla^+\phi_c = \sum_{nb} \mathrm{MIN}(0, \nabla\phi_f \cdot \mathbf{n}) \frac{\phi S \mathbf{n}}{V_c} \quad . \tag{6}$$

Using only flux-positive neighbour nodes for the gradient calculation ensures that the solution spreads from the zero level of the LS outward. Unfortunately the FP gradient alone tends to approximate values as too high at peak values of ϕ between two interfaces, due to the aforementioned flux cancellation. To avoid this, a correction is employed. The value of ϕ on the interface containing cells is approximated based on the captured interface from the c function, and ϕ at the valley/peak extrema are extrapolated from each neighbouring cell with a projected distance using the unit vector of the gradient and cell distance.

The ϕ value on the cells at the interface is approximated by calculating the distance between the interface and the cell centre using the gradient unit vector $\mathbf{n} = \frac{\nabla c}{|\nabla c|}$ and the cell-centre to cell-centre vector $\overline{\mathbf{X}_1\mathbf{X}_2}$. This is illustrated in the Figure 2. The cosine of θ between both vectors $\mathbf{n}$ and $\overline{\mathbf{X}_1\mathbf{X}_2}$, and the intersection $\overline{\mathbf{X}_1\mathbf{X}_{intf}}$ between the interface and $\overline{\mathbf{X}_1\mathbf{X}_2}$, is then used to directly compute the ϕ value at the cell neighbouring the interface using geometry:

$$\phi_{intf} = \mathrm{sgn}(0.5 - c)\, \overline{\mathbf{X}_c\mathbf{X}_{intf}} \cos(\theta) \quad , \quad \text{where} \quad \begin{cases} \overline{\mathbf{X}_1\mathbf{X}_{intf}} = \mathbf{X}_1 + \overline{\mathbf{X}_1\mathbf{X}_2} \frac{c_1 - 0.5}{c_1 - c_2} \\ \cos(\theta) = \frac{\mathbf{n} \cdot \overline{\mathbf{X}_1\mathbf{X}_2}}{|\mathbf{n}|\, |\overline{\mathbf{X}_1\mathbf{X}_2}|} \end{cases} \quad . \tag{7}$$

As for the extremum calculation, first the location of the cells containing local extrema must be determined. Since the problem is related to the fact that the summed FP gradient converges to a value greater than one, these erroneously converged cells are identified as the ones to be corrected.

It is possible to generalize this expression to project a distance value ϕ from any point, knowing the gradient and the value at the point. Then, using the lowest value obtained by doing this process over all neighbours, one obtains the lowest distance guess from the given neighbours, as shown in Figure 3.

$$\phi_{c\ corr.} = \mathrm{MIN}\left(\phi_{nb} + \overline{\mathbf{X}_c\mathbf{X}_{nb}} \cdot \frac{\nabla\phi_{nb}}{|\nabla\phi_{nb}|}\right) \quad . \tag{8}$$

Incorporation of the extrapolation corrections into the redistancing algorithm is shown by the pseudocode in Figure 4.

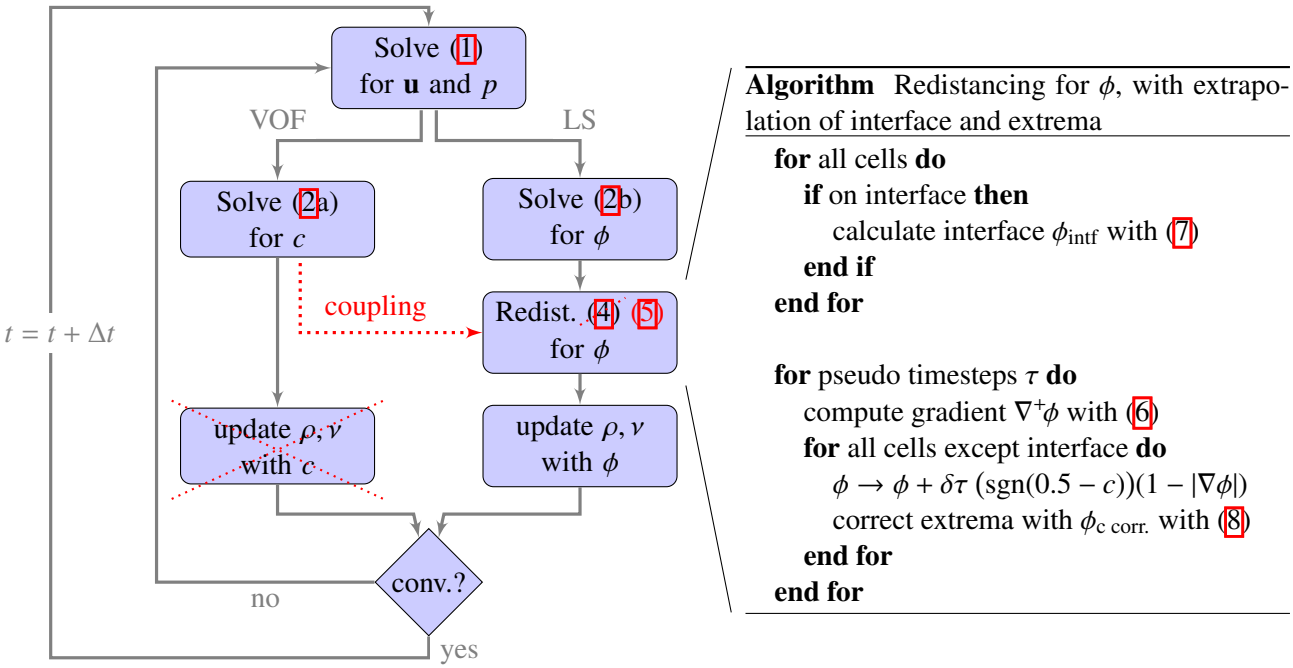

Fig. 4: Global view of algorithm for the Coupled Level Set and Volume of Fluid method, showing both previous uncoupled branches (following a grey arrow for VOF or LS) and showing the modification for a coupled method (modifications in dotted red lines). The redistancing algorithm is shown in more detail on the right, to include the corrections.

4 Numerical results

The first case studied uses the geometry from the slotted disk case (Zalesak 1979). This case is intended to verify the results from the redistancing algorithm from the CLSVOF solver without mass and momentum. The velocity and pressure fields are set to zero, and the results from the CLSVOF serve to determine if the redistancing converges to the analytical solution. The geometry has adjacent interfaces, which serves to verify the redistancing correction in peaks and valleys.

The results for the slotted disk in Figure 5 show that the extremum correction eliminates the sharp error peaks upon convergence of the redistancing algorithm. This means that the interface should exhibit less instability upon breakup and merging of interfaces for unstructured solvers.

The CLSVOF solver was then tested on a 2D breaking dam test case, based on an experiment (Lobovský et al. 2014, Martin et al. 1952). An initial column of water at rest is released and gravity causes the column to collapse and accelerate to the opposite side of a tank. Pressure and time of impact are measured. The breaking dam case proves more challenging due to the coupled nature of momentum, pressure, and the free surface. To stabilize the pressure/momentum coupling, density-weighted interpolation was used (Klaij et al. 2018). In the case of a CLSVOF simulation which is coupled to mass and momentum, the c field is advected and then the ϕ field is reconstructed. Then, ϕ is used to determine the values of ρ and ν over the prescribed thickness, which are then used in the momentum equations, completing the coupling.

Figure 6 shows a summary of the breaking dam test case results for pressure and the free surface location. The mass loss, which can reach values of up to 30% with pure level set (Wang 2009), was reduced to the order of the convergence tolerance by using CLSVOF, set to 10^{-6} in this case. The thickness of the interface was controllable; however, the model stability was sensitive to the choice of thickness

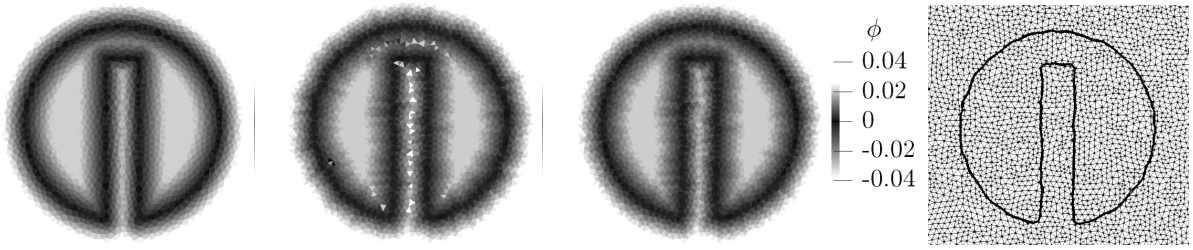

(a) analytical solution of ϕ (b) converged ϕ before correction (c) converged ϕ from redistance with extremum correction (d) 30k element mesh used

Fig. 5: Corrections applied on level set algorithm for ϕ on the 2D slotted disk problem with a 30k cell prism mesh, on the left image showing the analytical solution of the redistancing algorithm for ϕ. The middle image shows the converged values from the redistancing algorithm using $\nabla^{+}\phi$, and the right shows the converged value of ϕ with correction (8) applied.

when the interface is too thin (less than two cells).

A uniform Cartesian mesh was used, and the conditions for the test case were: a peak Courant number at the advancing front of around 1, momentum equations were discretized with van Leer's second order upwind Harmonic scheme, and the VOF equation was discretized using the REFRICS scheme (Klaij et al. 2018). The water reaches the opposite wall at $T = 3.16$, compared to between $T = 3.2$ and 3.4 in experiment (Lobovský et al. 2014, Martin et al. 1952). The second peak around $T = 9$ is due to the column falling back down. Impact pressure and convergence are shown in Figure 7.

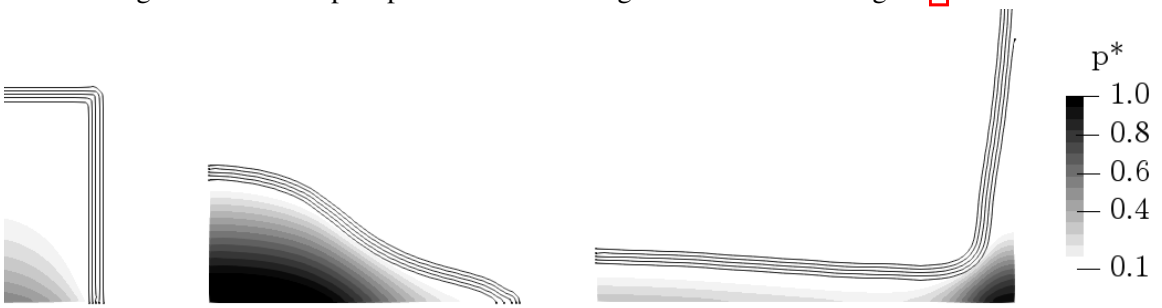

(a) T = 0.01 (b) T = 1.54 (c) T = 3.48

Fig. 6: Results with the 2D breaking dam case, with pressure in greyscale (nondimensionalized by hydrostatic pressure at bottom of initial water column). The ϵ used was of 0.02m, or about 4-5 cells.The interface is shown by lines of $\phi = -0.02, 0.01, 0, 0.01$ and 0.02m.

Both a conservative form and a non-conservative form of the momentum question were used for the VOF, while only a non-conservative form was used for CLSVOF, with different interface sizes. According to Tryggvason (2011) this is to be expected when employing two different schemes for momentum and volume fraction advection.

During the impact, an expected slowing down of convergence can be observed in Figure 7, due to high accelerations and steep pressure gradients in the bottom right corner of the tank. The solution has some timesteps around the impact in which the convergence tolerance is not reached by the pressure and c equations (seen by flatline regions).

The use of different ϵ values lead to different peak impact pressures, ranging from $p^* \approx 1$ for $\epsilon = 2cm$ to $p^* \approx 3$ for $\epsilon = 2mm$. Experiments show values of peak p^* between 3 and 4.5 (Lobovský et al. 2014), albeit for a larger dam and domain. A grid refinement study has not yet been performed, so for the time being, the possibility of insufficient resolution has not yet been excluded.

5 Conclusion

Results from the slotted disk case show solvability of the redistancing function in unstructured formulation, using local corrections to eliminate the error spikes in redistancing, and thus avoiding interface

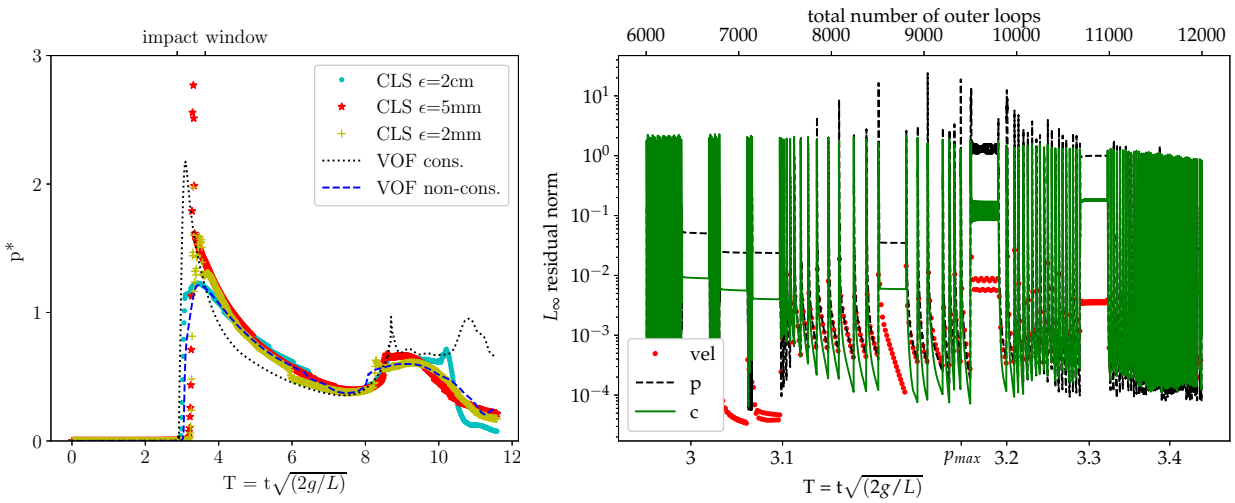

Fig. 7: Pressure in the bottom right impact corner, for VOF and CLSVOF (left), using three different ϵ values for CLSVOF. L_∞ convergence is given between $T = 3$ to $T = 3.4$ for CLSVOF with $\epsilon = 2$cm (right).

splitting/reconstruction and higher order discretization schemes, which are used in current CLSVOF solvers (Wang et al 2018, Zhang et al 2015).

Tests with the breaking dam also showed the ability to solve the CLSVOF equations coupled with mass and momentum. Convergence was much improved with the use of a non-conservative formulation of the momentum equations, as suggested in literature when using different advection schemes for momentum and the volume fraction equations (Tryggvason 2011). Differing impact pressures indicate a necessary grid convergence study in further work.

Further tests with the breaking dam on a Delaunay mesh, not present here, have also shown the need for robustness improvements in the CLSVOF. Further tests underway are exploring improvements to the robustness of the CLSVOF solver on Delaunay prism meshes.

Acknowledgements

This research is partly funded by the Dutch Ministry of Economic Affairs.

References

Chen, H.-C. (2011). CFD simulation of compressible two-phase sloshing flow in a LNG tank. *Ocean Sys. Eng.*, **1**(1), 31-57.

Hirt, C. W.; Nichols, B. (1981). Volume of fluid method for the dynamics of free boundaries. *J. Comput. Phys.*, **39**(1), 201–225.

Klaij, C. M.; Hoekstra, M.; Vaz, G. (2018). Design, analysis and verification of a volume-of-fluid model with interface-capturing scheme. *Comput. Fluids*, **170**, 324–340.

Lobovský, L.; Botia-Vera, E.; Castellana, F.; Mas-Soler, J; Souto-Iglesias, A. (2014). Experimental investigation of dynamic pressure loads during dam break. *J. Fluids Struct.*, **48**, 407–434.

Martin, J. C.; Moyce, W. J. (1952). An experimental study of the collapse of liquid columns on a rigid horizontal plane. *Phil. Trans. R. Soc. Lond. A*, **244**(882), 312–324.

Patankar, S. V.; Spalding, D. B. (1983). A calculation procedure for heat, mass and momentum transfer in three-dimensional parabolic flows. *Int. J. Heat Mass Transf.* **15**, 1787–1806.

Sethian, J. A. (1999). *Level Set methods and fast marching methods: evolving interfaces in computational geometry, fluid mechanics, computer vision, and materials science* **(Vol. 3)**. Cambridge University Press.

Tryggvason, G. (2011). *Direct Numerical Simulations of Gas-Liquid Multiphase Flows*, Camb. U. Press.

Sussman, M.; Smereka, P.; Osher, S. (1994). A level set approach for computing solutions to incompressible two-phase flow. *J. Comput. Phys.*, **114**(1), 146–159.

Wang, Z.; Yang, J.; Koo, B.; Stern, F. (2009). A coupled level set and volume-of-fluid method for sharp interface simulation of plunging breaking waves. *International Journal of Multiphase Flow*, **35**(3), 227–246.

Wang, Z.; Stern, F. (2018). VOF Based Fully-Coupled Two-Phase Method for General Curvilinear and Dynamic Overset Grids. *32nd Symposium on Naval Hydrodynamics, Hamburg*.

Zalesak, S. T. (1979). Fully multidimensional flux-corrected transport algorithms for fluids. *J. Comput. Phys.*, **31**(3), 335–362.

Zhao, Y.,; Chen, H.-C. (2015). Numerical simulation of 3D sloshing flow in partially filled LNG tank using a coupled level-set and volume-of-fluid method. *Ocean Engineering*, 104, 10–30.

Implementation and Verification of an Explicit Overset Grid Method

Sébastien Lemaire[*†], **Guilherme Vaz**[*], **and Stephen Turnock**[†]
[*]MARIN, Wageningen/Netherlands, [†]FSI Group, University of Southampton, Southampton/UK
sebastien.lemaire@soton.ac.uk

1 Introduction

The design of modern ships capable of achieving complex manoeuvres and handle dynamic ocean environment requires a precise understanding of the flow around hulls, propellers and control surfaces. Computational fluid dynamics already allows complex simulations to be performed thanks to conventional mesh techniques. Moving, sliding and deforming grids allow for some dynamic simulation of moving bodies (Toxopeus and Bhawsinka, 2016). However, when considering more complex motions, e.g. 6 degrees of freedom of several bodies, the combination of previously mentioned conventional techniques is at its limit. The overset grid method (or overlapping grid method), allows large and arbitrary relative motion of bodies by overlapping several meshes. The overset method was first designed for the aerospace industry (Benek et al., 1985) but is now also used for maritime applications like ship motions (Carrica et al., 2013), submarine maneuvers (Martin et al., 2015), etc.

This paper presents an initial implementation of overset using the two libraries Suggar++ and DiRTlib to compute the domain connectivity information (DCI). Manufactured solutions and analytical solutions are used in order to quantitatively assess the discretisation errors.

The paper is organised as follows: section 2 presents the overset approach and its nomenclature. Details of the implementation are introduced in section 3. Section 4 describes the test cases used for the study. Results are presented in section 5 and conclusions are given in section 6.

2 The overset approach

The overset method, sometimes called *chimera technique* or *overlapping grid method*, works by transferring field data between meshes and by ignoring certain cells which are outside the domain or overlapped by another mesh. Each cell has a given geometrical status and solver status which can change during the calculation:

- *Hole cell*: a field cell that is outside the boundary of the domain or not used because it is overlapped by another mesh. It is ignored when solving the transport equations (ignore status).
- *Fringe cell*: a fringe cell is a cell adjacent to a *hole* or at the boundary of an embedded grid. It will act as boundary cell for its grid and get its field value from the interpolation of donor cells of another mesh (interpolated status).
- *Orphan cell*: an orphan cell is a *fringe* cell that does not have an acceptable donor to compute its interpolated value. Its field value is usually then computed as the average of its neighbouring cells.
- *In cell*: every cell that is an active solution cell and not a *hole*, a *fringe* nor an *orphan* cell is called *in* cell. The equations are solved only for these cells. No particular treatment related with the grid assembly is needed (solved status).

The *domain connectivity information* (DCI) contains the cell status information sometimes associated with the interpolation weights needed to compute fringe values from donor cells. When grids are moving or being modified, the DCI needs to be recomputed. From the DCI, the flow solver will modify its equations and matrix system to ignore *hole* cells, get interpolation data on *fringe* and *orphan* cells and solve normally *in* cells.

3 Overset implementation

ReFRESCO (`refresco.org`) is a community-based open-usage CFD code for the maritime world. It solves multiphase incompressible flows using the Navier-Stokes equations, complemented with turbulence models, cavitation models and volume-fraction transport equations for different phases. The equations are discretised using a finite-volume approach with cell-centered collocated variables.

The implementation of the overset conducted here is using two external libraries called Suggar++ (Noack and Boger, 2009) and DiRTlib (Noack, 2005). Suggar++ computes the DCI and interpolation weights from the grid geometry and DiRTlib ease the treatment and use of the output from Suggar++. In this first implementation, Suggar++ provides cell status information (*fringe/hole/orphan/in* cells), donor associated to each *fringe* cell as as well as the interpolation weights via a `.dci` file. DiRTlib then provides to the flow solver an IBLANK array, an integer field data where the status of each cell is defined. Each outer loop, *fringe* cells get interpolated data from their donor cells currently using a first order inverse distance scheme provided by Suggar++. The coupling with the flow solver is done explicitly. Interpolated values are set at the right hand side of the system, and a unitary diagonal is applied on the lines corresponding to the *fringe* cells. Brunswig et al., 2010 compared several coupling approaches for overset method, and concluded that an explicit coupling needs more outer loops to converge to the same level as an implicit one and is more challenging to make mass conservative. However an implicit coupling demands more modifications on the flow solver code, hence an explicit method has been implemented as a first approach. When the continuity equation is used, the SIMPLE algorithm is employed to correct the pressure field. In this method, an estimated pressure is used to solve the momentum equation, then a pressure correction is solved to compensate for mass imbalance. In the overset explicit coupling implemented here, the pressure on the *fringe* cells is known (from interpolated data from the donor cells), and no pressure correction is performed on these cells. To implement this, a unitary diagonal is set for each *fringe* cells in the pressure correction matrix, together with a value of zero in the right hand side, and therefore the pressure field on the *fringe* cells is directly interpolated from its donor cells. Several methods have been described in Völkner et al., 2017 and Hadžić, 2005 to enforce mass conservation on the fringe of the overlapping grids, but none of them are used here.

4 Test cases definition

The overset implementation have been tested on three different analytical/manufactured 2D cases: *Advection* only case, *Advection-diffusion* case and *Poiseuille* flow case. Only the latter two will be presented here. The same five grid assemblies were used on the two test cases. It consists of a background grid and a foreground one, both being 2D Cartesian meshes with a 2:1 ratio. The foreground grid is twice smaller in both direction compared to the background grid and is positioned in the middle of the background grid. The cell size in between the two grids is the same, hence in the overlapping region the two grids are perfectly aligned, leading to a one-to-one match between cells in this area. Table 1 shows the different cell counts.

	Background	N_i	Foreground	N_i^f
G1	32x16	512	8x4	32
G2	64x32	2048	16x8	128
G3	128x64	8192	32x16	512
G4	256x128	32768	64x32	2048
G5	512x256	131072	128x64	8192

Table 1: Details of the Cartesian grids used for the two test cases and cell count (N_i)

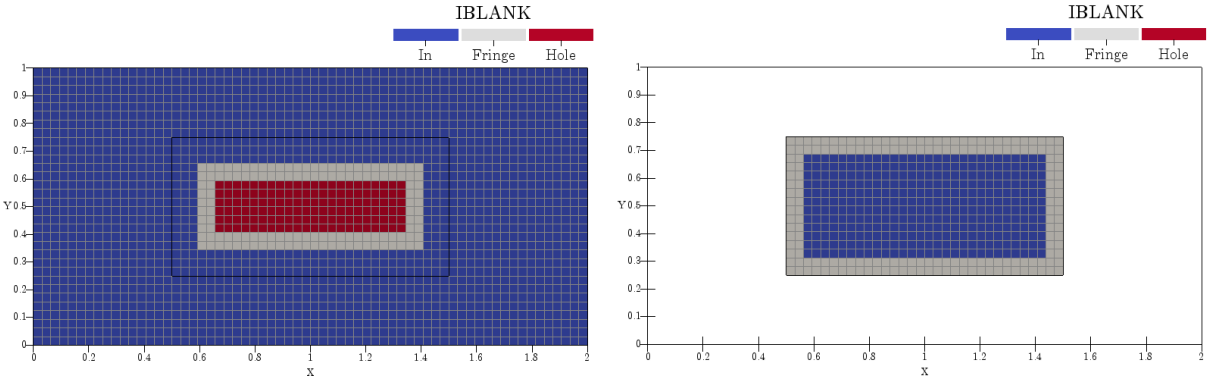

(a) Background grid

(b) Foreground grid

Fig. 1: G2 grids and DCI colored thanks to the IBLANK array. The overlap region is composed of five "layers" of cells.

Figure 1 shows the grid assembly, which has been precomputed by Suggar++. Two layers of *fringe* cells are used and one layer of *in* cells is defined between the *fringe* cells of the background and foreground grids. This leads to an overlap of five cells between the two grids of the assembly. Cells in the middle part of the background mesh, which overlap the foreground one, are *hole* cells. Each *fringe* cell has one donor from the other grid. Such grid assembly was designed as a first step to remove the influence an interpolation scheme can have on results.

4.1 Advection-diffusion case

The *Advection-diffusion* case was generated using a manufactured solution. To construct a manufactured solution case, a field solution is defined. Here, the advection of a Gaussian profile in a circular velocity field was chosen (Eq. 3).

$$\nabla \cdot (\rho U \phi) - \nabla \cdot (\mu \nabla \phi) = q \quad . \tag{1}$$

$$U_x = y \quad , \quad U_y = 1 - x \quad . \tag{2}$$

$$\phi(r) = e^{-2r} sin^2(\pi r) \quad , \quad r = \sqrt{(1-x)^2 + y^2} \quad . \tag{3}$$

Eq. 1 is being solved with the velocity field enforced with Eq. 2. The source term q is chosen in order to have ϕ (Eq. 3) as the analytical solution of the advection-diffusion equation (Eq. 1). This method allows to construct test cases where the exact analytical solution is known. The exact solution is enforced at the boundary thanks to Dirichlet boundary conditions. The steady computation is stopped when the infinity norm of the residuals is below 10^{-12}. A QUICK scheme is used for the discretisation of the convective fluxes.

4.2 Poiseuille flow test case

In the *Poiseuille* flow case an analytical solution is known. The flow is bounded between two walls (top and bottom) and driven by an axial pressure gradient. The analytical solution is presented in Eq. 4 with L the length of the channel (X direction), and h the distance between the walls.

$$U_x(y) = \frac{Ph^2}{2\mu}\left(1 - \frac{y^2}{h^2}\right) \quad , \quad U_y = 0 \quad , \quad \frac{\partial p}{\partial x} = -P \quad , \quad p(x) = -P(x - L) \quad . \tag{4}$$

In this test case the momentum equation and the pressure correction via the SIMPLE method are solved. The Reynolds number, based on the height of the channel, is $Re_h = 10$.

At the inlet, the analytical velocity profile is set and the outlet the pressure is enforced. The top and bottom of the domain uses non slip wall boundary conditions. Convergence is ensured by an iterative criterion of 10^{-12} for the infinity norm of the residuals. A second order central difference scheme is used for the discretisation of convective fluxes.

5 Results and discussion

For both test cases, simulations with overset as well as simulations done using only the background grid were performed (without overset). Comparison with the exact analytical solution is also available.

Grid	$\|\phi^{os} - \phi^{exact}\|_\infty$	order	$\|\phi - \phi^{exact}\|_\infty$	order
G1	$0.787738275518 \cdot 10^{-02}$		$0.787738275519 \cdot 10^{-02}$	
G2	$0.225550008727 \cdot 10^{-02}$	1.80	$0.225550008725 \cdot 10^{-02}$	1.80
G3	$0.590247617471 \cdot 10^{-03}$	1.93	$0.590247617400 \cdot 10^{-03}$	1.93
G4	$0.149722446897 \cdot 10^{-03}$	1.98	$0.149722446791 \cdot 10^{-03}$	1.98
G5	$0.375999643849 \cdot 10^{-04}$	1.99	$0.375999643008 \cdot 10^{-04}$	1.99

Table 2: *Advection-diffusion* convergence with (left) and without (right) overset. Similar orders of convergence and errors are observed.

From Table 2 one can conclude that the *Advection-diffusion* case is converging when refining the grid toward the exact analytical solution with an order 2. The level of the error is also similar to the simulation without overset (right column of the table). The error distribution at the end of the computation can be visualized on Figure 2, no particular artefact due to the overset assembly is visible: the error does not increase around the edges of the foreground grid. Figure 3 presents the differences between the simulations with and without overset, showing that the difference is below 10^{-10}

and are slightly impacted by the overset assembly. An *Advection* only case was also run and yielded very similar results to this *Advection-diffusion* case.

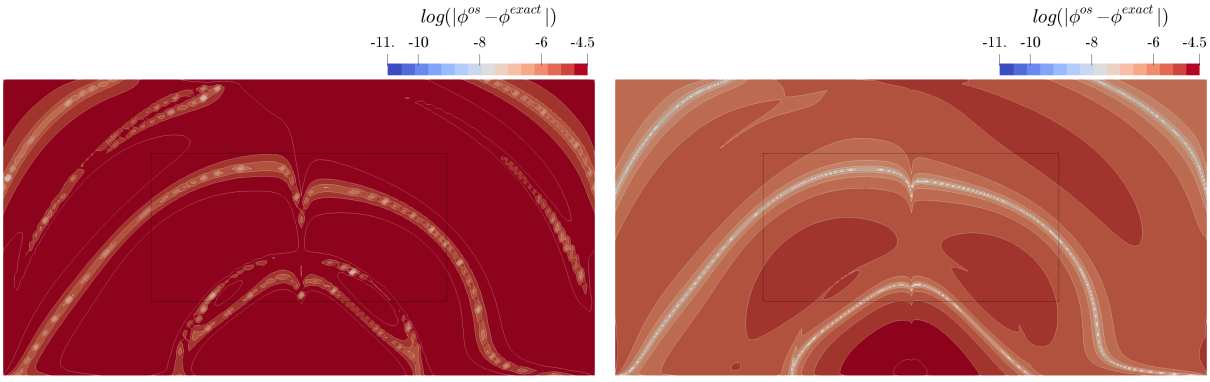

(a) G3 (b) G5

Fig. 2: Difference between exact solution and overset simulation for the *Advection-diffusion* case. The error reduces when refining the grid and no effect of the overset assembly is visible.

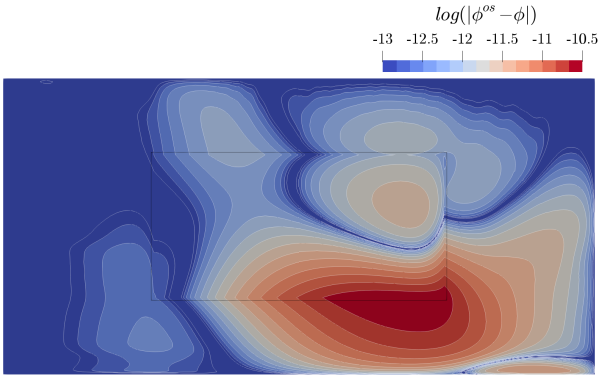

Fig. 3: Difference between with and without overset for the finest grid (G5) for the *Advection-diffusion* case. The difference is slightly impacted by the overset assembly.

	$\|P^{os} - P^{exact}\|_\infty$	order	$\|U^{os} - U^{exact}\|_\infty$	order	$\|P - P^{exact}\|_\infty$	order	$\|U - U^{exact}\|_\infty$	order
G1	$0.570951568 \cdot 10^{-01}$		$0.106355136 \cdot 10^{-01}$		$0.570951568 \cdot 10^{-01}$		$0.106355136 \cdot 10^{-01}$	
G2	$0.221288355 \cdot 10^{-01}$	1.37	$0.338702389 \cdot 10^{-02}$	1.65	$0.221290412 \cdot 10^{-01}$	1.37	$0.338700864 \cdot 10^{-02}$	1.65
G3	$0.934912126 \cdot 10^{-02}$	1.24	$0.944148824 \cdot 10^{-03}$	1.84	$0.934912218 \cdot 10^{-02}$	1.24	$0.944148756 \cdot 10^{-03}$	1.84
G4	$0.424055832 \cdot 10^{-02}$	1.14	$0.248345462 \cdot 10^{-03}$	1.93	$0.424054967 \cdot 10^{-02}$	1.14	$0.248345483 \cdot 10^{-03}$	1.93
G5	$0.201178414 \cdot 10^{-02}$	1.08	$0.637460767 \cdot 10^{-04}$	1.96	$0.201182292 \cdot 10^{-02}$	1.08	$0.637460542 \cdot 10^{-04}$	1.96

Table 3: *Poiseuille* case convergence with (left) and without (right) overset. Similar orders of convergence and errors are observed for the two sets of simulations.

For the *Poiseuille* flow case, Table 3 shows that the order of convergence is second order for the velocity and first order for the pressure. Similarly to the *Advection-diffusion* case, comparable errors and thus convergence orders are observed when running a simulation without overset. Figure 4 displays the pressure difference between the exact solution and the overset simulation. The pressure being enforced at the outflow the error is null at that location. No variation of the error is visible around the boundary of the foreground grid. However, when comparing simulations with and without overset, some effects of the overlapping method are visible. Figure 5a shows the difference in pressure between simulations with and without overset, and a pressure variation is observed close to the inlet of the foreground mesh. The differences between the two simulations are higher in the foreground mesh when compared to the rest of the domain. Since pressure and momentum are coupled (via the SIMPLE method), a similar effect is visible on Figure 5b presenting the velocity difference between overset and non overset simulation. As presented in section 3, no particular treatment is being done at the fringe of overlapping grids to

account for pressure correction. Another way of quantifying the error introduced by the overset mesh method is by assessing the mass fluxes difference between the inflow and outflow. Figure 6 presents the mass imbalance with and without overset for all grids. For both set of simulations, the mass imbalance decreases when refining the grids, going down to machine accuracy for the non overset simulations. Three to four orders of magnitude are however noticeable between the two sets of simulations. Figure 7 shows residuals convergence with and without overset simulations. Some oscillations are observed for the overset simulation, this is related to the under relaxation and the explicit coupling used. One can also note that the overset simulation does not converge slower than the simulation without overset.

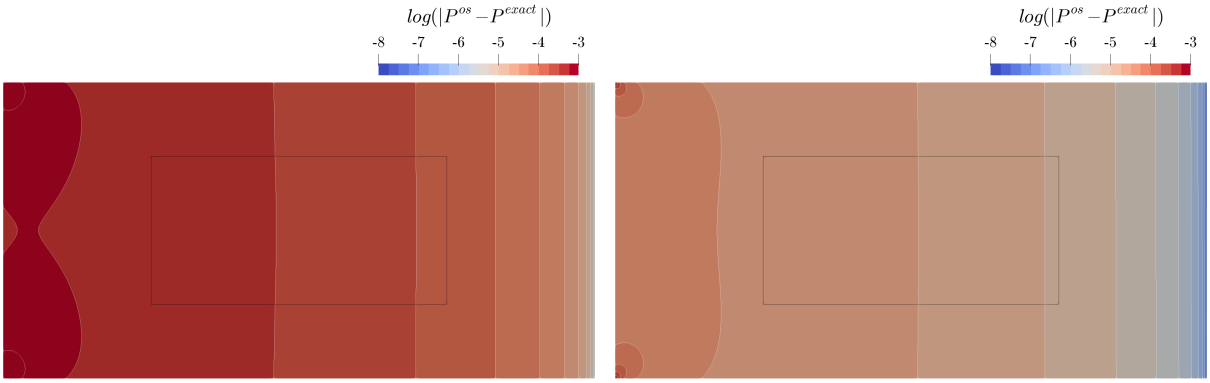

(a) G3 (b) G5

Fig. 4: Pressure error for the overset simulation of the *Poiseuille* flow. The error is minimal at the outflow where it is enforced, and no effect of the overset method is visible.

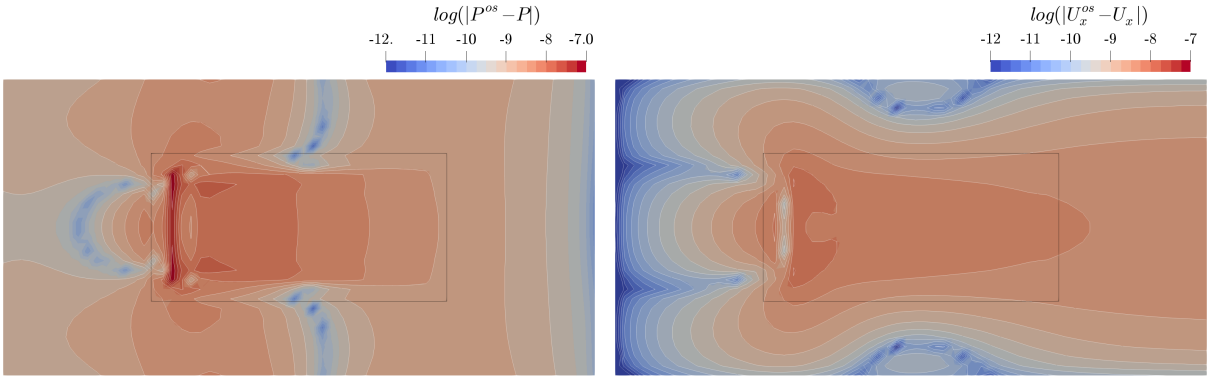

(a) Pressure difference (b) Velocity difference

Fig. 5: Pressure (left) and velocity (right) differences between simulations with and without overset for grid G2 (*Poiseuille* case). A pressure variation at the boundary of the foreground mesh leading to a velocity variation is visible.

6 Concluding remarks

An initial explicit overset implementation has been tested and results from two different cases presented here. The use of manufactured and analytical solutions permitted the quantitative assessment of the errors involved, and check the implementation for bugs. Convergence towards the exact solution is not affected by the use of the overset method. The difference between simulations with and without overset is below 10^{-10} for the *Advection-diffusion* case and below 10^{-7} for the *Poiseuille* case. When solving the continuity equation, however, pressure variations at the boundary of the overlapping area are introduced. This leads to a mass imbalance between the inflow and outflow. Quantitatively, for the *Poiseuille* test case, the mass imbalance introduced is of about four orders of magnitude higher when using overset compared to simulations without overset. To overcome this, other CFD codes usually use methods to compensate for the loss or gain of mass at the grid interfaces (Völkner et al., 2017). Future developments will focus on

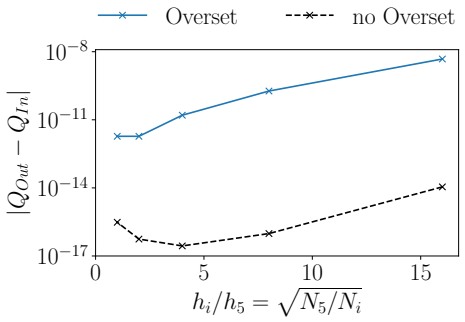

Fig. 6: Mass flux differences between the inflow and outflow of the domain for the *Poiseuille* case.

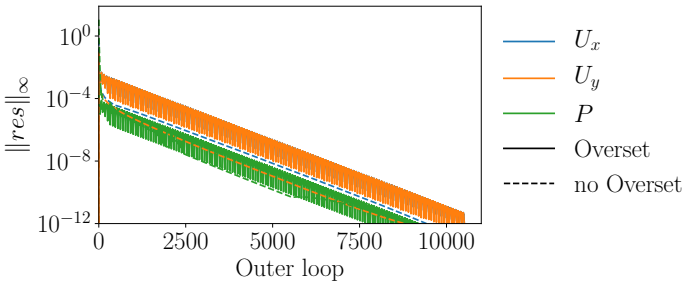

Fig. 7: Residual convergence for the finest grid (G5) for the Poiseuille test case. Oscillations related to the under relaxation are visible for the overset simulation.

various aspects. Different methods available in the literature to correct mass imbalance will be assessed. The impact of the interpolation scheme used for fringe field data will be examined. Finally, the influence of an implicit coupling toward mass conservation will also be investigated.

Acknowledgements

The authors would like to thank Dr. Ralph Noack for his help on the coupling with DiRTlib and for the computation of the DCI used in the presented test cases.

References

Benek, J., Buning, P. G., and Steger, J. (1985). A 3-D chimera grid embedding technique. In *7th Computational Physics Conference*, page 10, Reston, Virigina. American Institute of Aeronautics and Astronautics.

Brunswig, J., Manzke, M., and Rung, T. (2010). Explicit and implicit coupling strategies for overset grids. In *Proceedings of the 10th Symposium on Overset Composite Grids and Solution Strategies*, page 56. NASA AMES Research Center.

Carrica, P. M., Ismail, F., Hyman, M., Bhushan, S., and Stern, F. (2013). Turn and zigzag maneuvers of a surface combatant using a URANS approach with dynamic overset grids. *Journal of Marine Science and Technology (Japan)*, 18(2):166–181.

Hadžić, H. (2005). *Development and Application of a Finite Volume Method for the Computation of Flows Around Moving Bodies on Unstructured , Overlapping Grids*. PhD thesis.

Martin, J. E., Michael, T., and Carrica, P. M. (2015). Submarine Maneuvers Using Direct Overset Simulation of Appendages and Propeller and Coupled CFD/Potential Flow Propeller Solver. *Journal of Ship Research*, 59(1):31–48.

Noack, R. W. (2005). DiRTlib: A library to add an overset capability to your flow solver. In *17th AIAA Computational Fluid Dynamics Conference*, number June 2005, pages 1–20, Reston, Virigina. American Institute of Aeronautics and Astronautics.

Noack, R. W. and Boger, D. A. (2009). Improvements to SUGGAR and DiRTlib for Overset Store Separation Simulations. *47th AIAA Aerospace Sciences Meeting*, (January):5–9.

Toxopeus, S. and Bhawsinka, K. (2016). Calculation of Hydrodynamic Interaction Forces on a Ship Entering a Lock Using CFD. In *4th MASHCON-International Conference on Ship Manoeuvring in Shallow and Confined Water with Special Focus on Ship Bottom Interaction*, pages 305–314.

Völkner, S., Brunswig, J., and Rung, T. (2017). Analysis of non-conservative interpolation techniques in overset grid finite-volume methods. *Computers and Fluids*, 148:39–55.

Assessment of RANS Transition Models

Rui Lopes[1], **Luís Eça**[1], **and Guilherme Vaz**[2]
[1] Instituto Superior Técnico - University of Lisbon,
[2] Maritime Research Institute Netherlands
rui.a.lopes@tecnico.ulisboa.pt

1 Introduction

Many naval and aeronautical applications deal with flows which occur at Reynolds numbers that are typically larger than 10^7. Under these conditions the laminar regime is confined to a very small region near the leading edge of the body and consequently the correct prediction of transition is not relevant. Therefore, the premature transition predicted by most turbulence models (Wilcox (1998)) is not an issue.

On the other hand, there are several applications that operate in the Reynolds number range of 10^5 to 10^6, such as underwater gliders, unmanned aerial vehicles (UAVs) and wind turbines. In these cases, the correct prediction of transition from laminar to turbulent flow becomes essential for the determination of the forces acting on the body and correct flow analysis. Therefore, standard turbulence models are not adequate for these low Reynolds number flows, which led to the development of transition models, such as the intermittency based γ-$\tilde{Re}_{\theta_t}$ (Langtry and Menter (2009)) and γ (Menter et al. (2015)) models, the $k_T - k_L - \omega$ model (Walters and Cokljat (2008)), built on the concept of laminar kinetic energy, and the amplification factor transport (AFT) transition model (Coder and Maughmer (2015)).

This paper presents a study of several features of the application of these transition models, namely: numerical robustness, i.e. the ability to reduce the iterative error to negligible levels; discretization errors and sensitivity to inlet conditions. To this end we have selected two test cases: the flow over a flat plate and the flow around the Eppler 387 airfoil. The availability of experimental data for both cases allows the determination of the modelling error of the skin friction coefficient for the flat plate and of the pressure coefficient on the surface of the airfoil. The different turbulence and transition models used here are described in section 2. Definition of the test cases including domain size and selected boundary conditions are presented in section 3, whereas section 4 describes the numerical settings and grid sets. The results obtained for each model are presented and discussed in section 5. Finally, section 6 presents the conclusions of this study.

2 Mathematical Models

The two test cases addressed in this study are statistically steady flows of a single-phase Newtonian fluid that is assumed to be incompressible. Therefore, time-averaging is applied to the flow properties and to the continuity and momentum equations leading to the Reynolds-Averaged Navier-Stokes (RANS) equations, which require the determination of the Reynolds-stress tensor, i.e. a turbulence closure. All of the turbulence models used in this study use the concept of eddy-viscosity, ν_t, which is determined from the solution of the transport equations that comprise the turbulence model. The turbulence and transition models used in this study are now addressed.

γ-$\tilde{Re}_{\theta_t}$ model

The γ-$\tilde{Re}_{\theta_t}$ transition model (Langtry and Menter (2009)) solves two transport equations: one for the intermittency γ and one for the transition momentum thickness Reynolds number $\tilde{Re}_{\theta_t}$. The transition model produces an effective intermittency γ_{eff} calculated from $\gamma_{eff} = \max(\gamma, \gamma_{sep})$, where γ_{sep} is related to separation-induced transition. It is coupled to the SST $k - \omega$ model, where the production and dissipation terms of the k transport equation are affected by γ_{eff}, while the ω transport equation remains unchanged. On the other hand, the F_1 blending function must also be changed to remain equal to one close to solid walls and equal to zero in the outer flow region.

γ model

The γ transition model (Menter et al. (2015)) is an alternative to the γ-$\tilde{Re}_{\theta_t}$ model that solves only one extra transport equation for γ. Instead of using $\tilde{Re}_{\theta_t}$, the onset of transition requires the determination of a pressure gradient parameter that is a function of the derivative of the wall-normal velocity component

along the wall-normal direction, $\frac{\partial V_n}{\partial y_n} = \nabla\left(\vec{n}\cdot\vec{V}\right)\cdot\vec{n}$. The unit vector along the wall-normal direction $\vec{n}$ is calculated from the gradient of the wall distance d, $\vec{n} = \nabla d$. The coupling to the $k-\omega$ SST turbulence model is performed in a similar way to that of the γ-$\tilde{Re}_{\theta_t}$ model. However, there is no γ_{sep} because separation-induced transition is handled by an additional production term in the k equation.

AFT model

The AFT model (Coder and Maughmer (2015)) is inspired on linear-stability theory (e^N methods) and it solves a transport equation for the amplification factor $\tilde{n}$. The onset of transition is controlled by the specification of N_{crit}, which can be determined from the turbulence intensity of the incoming flow. This model does not include any special features for bypass or separation-induced transition. This model is coupled to the $k-\omega$ SST model by including a new term in the k equation, responsible for suppressing the production of turbulence kinetic energy in the laminar boundary layer. As for the two previous methods, the F_1 blending function is also modified.

$k_T - k_L - \omega$ model

Unlike the three previous transition models, this model is not coupled to a standard two-equation eddy-viscosity model. It solves three transport equations (Walters and Cokljat (2008)), one for the turbulent kinetic energy k_T, one for the laminar kinetic energy k_L and one for the turbulence specific dissipation rate ω. The k and ω equations are not identical to those of the standard $k-\omega$ turbulence models including several changes in the production and dissipation terms. The eddy-viscosity is calculated as the sum of two different components, unlike other turbulence models.

3 Test Cases

The two test cases selected for this study are the two-dimensional, statistically steady flows of a single-phase, incompressible, Newtonian fluid over a flat plate and around the Eppler 387 airfoil. Both cases have been used in previous studies (Eça et al. (2016)) and so we just indicate the domain sizes, Reynolds numbers and selected boundary conditions.

The flow over the flat plate has a Reynolds number based on the plate length L and incoming flow velocity V_∞ of $Re_L = 10^7$. The domain is a rectangle of length of $1.5L$ and $0.25L$ width. The inlet is located $0.25L$ upstream of the leading edge of the plate, the outlet is placed $0.25L$ downstream of the trailing edge of the plate.

The Reynolds number of the flow around the Eppler 387 airfoil is $Re_c = 3\times10^5$ with the reference length equal to the chord of the airfoil c. The domain is a rectangle of length $36c$ and width $24c$ with the horizontal axis aligned with the incoming flow and the airfoil chord rotated to obtain the desired angle of attack, which in our study is 1°. The inlet, top and bottom boundaries are approximately $12c$ away from the airfoil whereas the outlet boundary is $23c$ downstream of the trailing edge.

Velocity components and turbulence quantities are specified at the inlet of the two test cases and the pressure is extrapolated from the interior. At the outlet boundary, zero streamwise derivatives (Neumann conditions) are applied to all flow quantities for the flat plate flow, whereas pressure is fixed for the flow around the airfoil (Neumann conditions apply to all remaining flow variables). Free slip is applied at the top and bottom boundaries (normal velocity component equal to zero and Neumann conditions for remaining variables) of the airfoil domain and pressure is imposed at the top of the flat plate domain. Symmetry conditions are applied upstream and downstream of the plate on the bottom boundary. At the surface of the plate and airfoil the two velocity components and the pressure normal derivative are set equal to zero. At the wall k, k_T and k_L are equal to zero, whereas Neumann conditions apply to γ, $\tilde{Re}_{\theta_t}$, $\tilde{n}$ and ω in the $k_T - k_L - \omega$ model. On the other hand, for the $k-\omega$ SST model, ω is specified at the near-wall cell centre according to the near-wall solution (Wilcox (1998)).

4 Numerical Settings

All calculations were performed with the flow solver ReFRESCO (www.refresco.org) that uses a finite-volume discretization with cell-centered collocated variables and a pressure-correction equation based on the SIMPLE algorithm to ensure mass conservation. Second-order schemes are applied to

convective and diffusive terms of all transport equations. Iterative convergence criteria requires that the L_∞ norm of the normalized residuals of all transport equations must be below 10^{-6} for the flat plate flow and below 10^{-8} for continuity, momentum and turbulence equations in the flow around the Eppler 387 airfoil. The normalized residuals are equivalent to dimensionless variable changes in a simple Jacobi iteration.

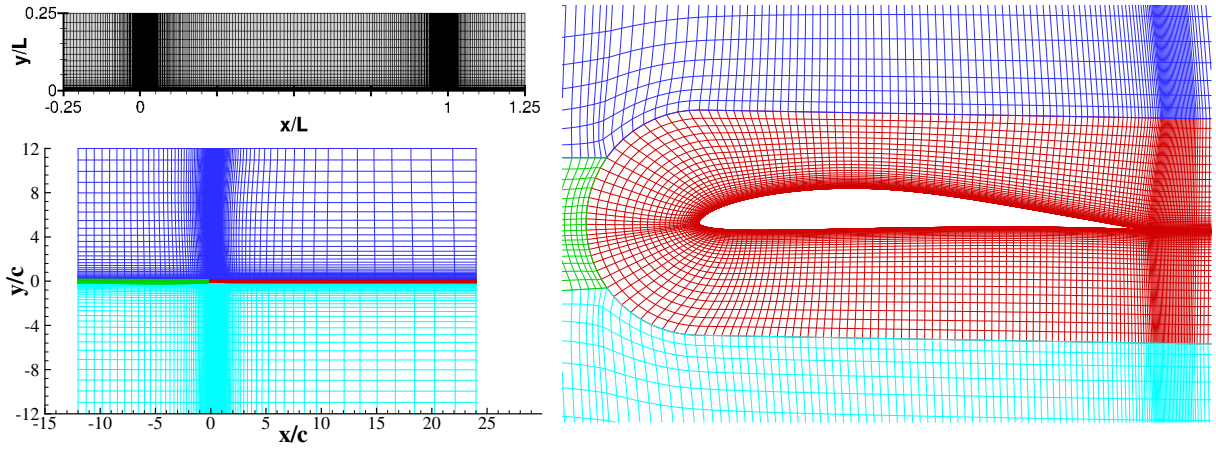

Fig. 1: Illustration of the domain and grids of the two test cases.

For each test case, sets of 5 geometrically similar grids covering a grid refinement ratio of 2 are generated to estimate the numerical uncertainty of the quantities of interest. The finest grid of the flat plate flow includes 294, 962 cells with 1024 cells on the plate surface, whereas the finest grid around the airfoil contains 363, 000 cells with 600 on the airfoil surface. The maximum dimensionless near-wall cell size is always below $y^+_{max} < 0.6$. Figure 1 presents an illustration of the grids used in this study.

4.1 Results

Sensitivity to inlet boundary conditions

We have selected the experiment with the lowest turbulence intensity at the inlet from the ERCOFTAC database (Coupland (1993)), designated by T3AM, to avoid bypass transition. Three different sets of boundary conditions are considered: BC1, BC2 and BC3. The values for the inlet turbulence intensity and the eddy-viscosity for BC1 are selected in order to match the experimental decay of turbulence for the $k-\omega$ SST model, while the other sets are built from the first. The combinations are shown in table 1.

In order to deal with the decay of turbulence in the freestream, we introduce the variable x_{tin}: for x locations between the inlet and the plane $x = x_{tin}$ the transport equations of the turbulence model are solved without dissipation terms, which transports the values of the turbulence variables from the inlet to the plane $x = x_{tin}$ without any decrease (Eça et al. (2016)). This implies that the incoming flow is aligned with the x axis.

Table 1: Inlet boundary conditions for the turbulence quantities of the two test cases.

	Flat Plate			Eppler 387
Conditions	BC1	BC2	BC3	-
$\frac{(\nu_t)_{in}}{\nu}$	7.6	7.6	0.1	0.003
x_{tin}/L	-0.005	-	-	-
Tu_{in}	1.0%	1.0%	1.0%	1.0%

Figure 2 presents the local skin friction coefficient for the T3AM case, showing that the change of the inlet boundary conditions greatly influences the location of the transition region for all models with the exception of the AFT transition model. Decreasing the eddy-viscosity at the inlet or removing x_{tin} results in later transition, due to the increased decay of turbulence (Eça et al. (2016)). The $k_T - k_L - \omega$ model appears to be the most sensitive, as it displays the greatest change from the BC1 to the BC3 set.

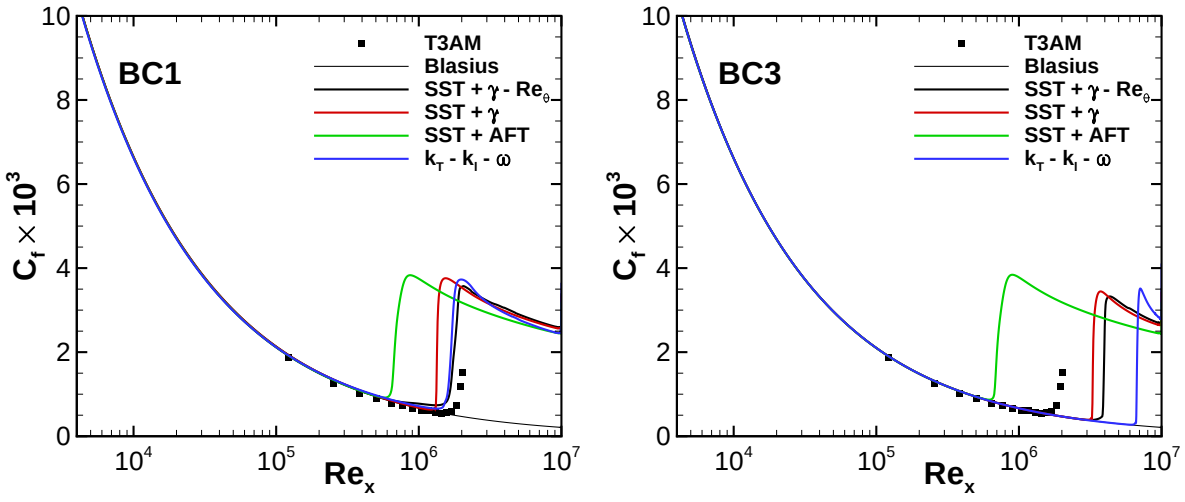

Fig. 2: Local skin friction coefficient C_f along the plate for the BC1 (left) and BC3 (right) sets.

Numerical Robustness

The behavior of the highest residual in the two test cases is shown in figure 3. For the flat plate flow, with the exception of the $k_T - k_L - \omega$, the highest residual is tied to a variable of the transition model. The convergence of these variables can be quite noisy as evidenced mostly by the AFT model and the surges in the $\gamma - Re_\theta$ model. In the Eppler 387 case the noise is not as noticeable and the highest residual always comes from the momentum equations since we do not consider the transition equations for the convergence criteria. Despite exhibiting the fastest convergence in the flat plate case, the $k_T - k_L - \omega$ fails to converge in the airfoil flow, reaching the limiting value of 500,000 iterations. In both cases the γ model improves on the $\gamma - Re_\theta$ formulation, converging in fewer iterations. Inclusion of a transition model leads to a higher number of iterations required to achieve the set iterative convergence criteria.

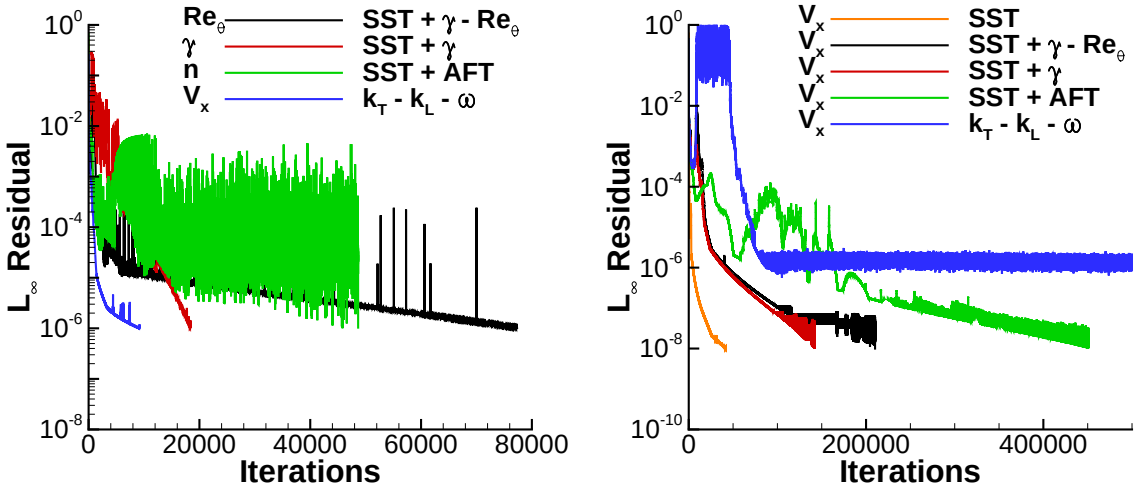

Fig. 3: Evolution of the highest residual in each model for the flat plate flow (left) and for the E387 airfoil (right).

Discretization errors

Figure 4 shows the friction resistance coefficient of the flat plate, C_F, and the lift and drag coefficients obtained for the Eppler 387 airfoil, along with an estimate of the numerical uncertainty arising from the discretization error. In the latter case, force coefficients obtained with the $k - \omega$ SST model without any transition model are presented as well.

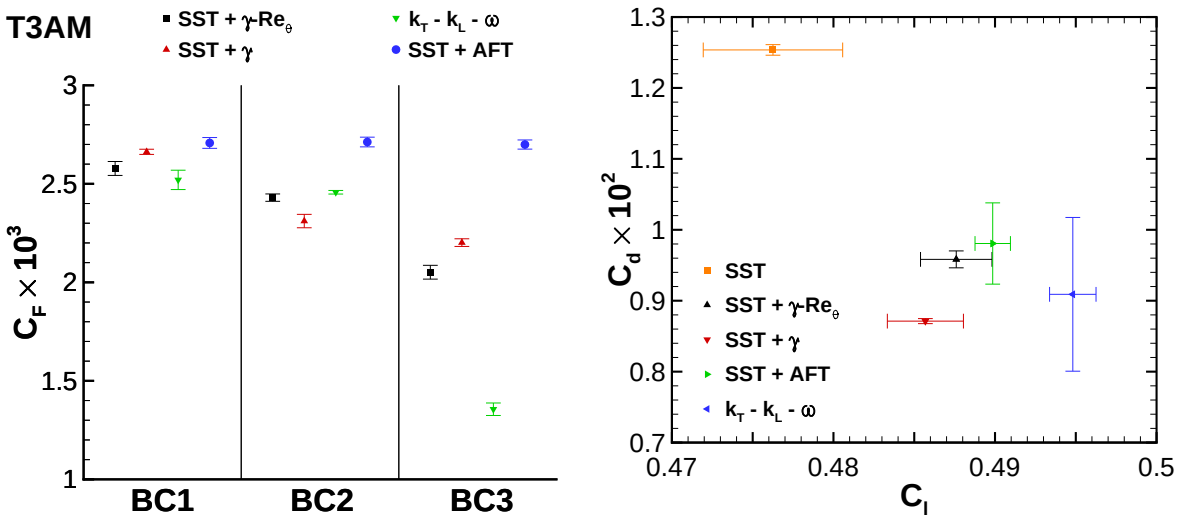

Fig. 4: Friction resistance coefficient C_F for the flat plate (left) and force coefficients for the airfoil (right).

While in the flat plate flow the numerical uncertainty appears to be small for most cases, the discretization error appears to be considerable in the drag coefficient of the Eppler 387 airfoil, namely for the $k_T - k_L - \omega$ and AFT models, reaching up to 10%. This is a consequence of non-monotonic behaviour in both the pressure and friction contributions of the drag coefficient. For the lift coefficient the discretization error leads to much smaller numerical uncertainty.

Modelling errors

The modelling errors obtained by each model can be discussed by first addressing figure 2, presented previously. The agreement with experimental data is good in the laminar region, although all models present transition earlier than the experimental data on the BC1 set. It is possible to match the experimental location for transition by choosing appropriate values for the turbulence intensity and the eddy-viscosity.

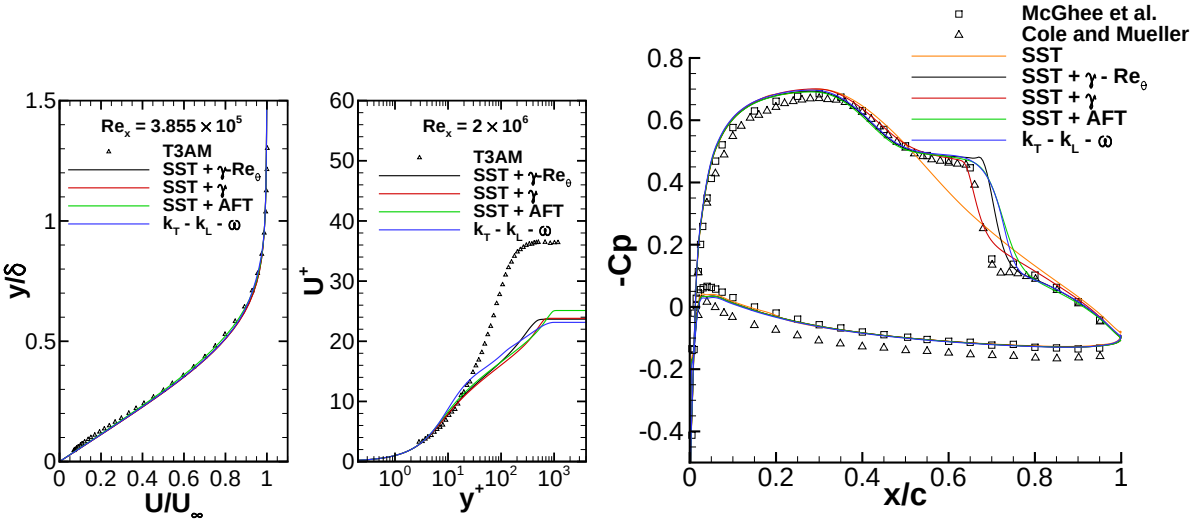

Fig. 5: Non-dimensional mean streamwise velocity profiles for the flat plate flow (left) and pressure coefficient along the surface on the E387 airfoil (right).

We now turn to figure 5 showing the non-dimensional mean streamwise velocity profiles for the BC1 set. At the laminar location there is good agreement between all cases and the experimental data. At $Re_x = 2 \times 10^6$ the flow is undergoing transition, while the numerical predictions correspond to turbulent flow. It would be necessary to change the inlet conditions in order to improve the numerical prediction.

For the Eppler 387 airfoil we consider the pressure coefficient distribution along the surface of the airfoil, also shown in figure 5, and compare to two sets of experimental data by Mcghee et al. (1988) and Cole and Mueller (1990). There are some differences between the experimental measurements, hinting at a significant experimental uncertainty. In the upper surface, the pressure coefficient presents a plateau near mid-chord due to the presence of a laminar separation bubble. This effect is not captured by the $k-\omega$ SST model if a transition model is not used. After separating, the flow undergoes transition to turbulence and reattaches, causing the pressure coefficient to increase. Although these features are common to all transition models, their location as well as details of the pressure recovery vary between the models.

5 Conclusions

This paper presents a study on several popular transition models: the intermittency based γ-$\tilde{Re}_{\theta_t}$ and γ models, the AFT model and the $k_T - k_L - \omega$ model. Several features of these models were studied: sensitivity to inlet conditions, numerical robustness, discretization error and modelling error. Two test cases were considered - the flow over a flat plate and the flow around the Eppler 387 airfoil.

With the exception of the AFT formulation, all models exhibit a strong dependence on the value of the eddy-viscosity at the inlet. This has a significant impact on the prediction of the location where the flow undergoes transition. Despite having no specific features to handle separation-induced transition, the AFT and $k_T - k_L - \omega$ models perform adequately when it took place.

The inclusion of a transition model allows for flow features such as the laminar boundary layer and laminar separation bubbles to be correctly captured, at the cost of lower numerical robustness. Achieving good agreement with experimental data and obtaining an entirely accurate prediction for the location of transition requires a correct specification of the turbulence quantities at the inlet.

Acknowledgements

The first author acknowledges the financial support provided by Fundação para a Ciência e Tecnologia through a research grant under the Bolsas de Doutoramento and Pós-Doutoramento 2016 program. We also acknowledge the funding of the Dutch Ministry of Economic Affairs.

References

Coder, J. G. and Maughmer, M. D. (2015). Application of the Amplification Factor Transport Transition Model to the Shear Stress Transport Model. In *53rd AIAA Aerospace Sciences Meeting*.

Cole, G. M. and Mueller, T. J. (1990). Experimental measurements of the laminar separation bubble on an Eppler 387 airfoil at low Reynolds numbers. *NASA STI/Recon Technical Report N*, 90:15380.

Coupland, J. (1993). ERCOFTAC Classic Database.

Eça, L., Lopes, R., Vaz, G., Baltazar, J., and Rijpkema, D. (2016). Validation Exercises of Mathematical Models for the Prediction of Transitional Flows. In *Proceedings of 31st Symposium on Naval Hydrodynamics, 11th-16th September, Berkeley*.

Langtry, R. B. and Menter, F. R. (2009). Correlation-based Transition Modeling for Unstructured Parallelized Computational Fluid Dynamics Codes. *AIAA journal*, 47(12):2894–2906.

Mcghee, R. J., Walker, B. S., and Millard, B. F. (1988). Experimental results for the Eppler 387 airfoil at low Reynolds numbers in the Langley low-turbulence pressure tunnel.

Menter, F. R., Smirnov, P. E., Liu, T., and Avancha, R. (2015). A One-equation Local Correlation-based Transition Model. *Flow, Turbulence and Combustion*, 95(4):583–619.

Walters, D. K. and Cokljat, D. (2008). A Three-equation Eddy-viscosity Model for Reynolds-averaged Navier–Stokes Simulations of Transitional Flow. *Journal of Fluids Engineering*, 130(12):121401.

Wilcox, D. C. (1998). *Turbulence Modeling for CFD, 2nd ed.* DCW Industries.

Code Verification exercise for 2D Poiseuille flow with non-Newtonian fluid

Stefano Lovato[*], **Guilherme Vaz**[†], **Serge Toxopeus**[†], **Geert Keetels**[*], **Just Settels**[†]
[*]Delft University of Technology, Delft/Netherlands. [†] MARIN, Wageningen/Netherlands.
s.l.lovato@tudelft.nl

1 Introduction

Safe navigation in port and waterways is ensured by setting a minimum distance between the ship's keel and the bottom, known as the under keel clearance (UKC). However, in ports situated at the estuary, the bottom is often covered by a layer of mud. Under these circumstances, the UKC is no longer unequivocally determined and the prediction of ship's manoeuvring behaviour becomes more challenging. Understanding the ships' behaviour in presence of mud layers is necessary both to improve safety during navigation and to optimize dredging operations in the interest of reducing the associated costs.

Model-scale experiments were done to link mud properties and ship's manoeuvrability (Delefortrie et al. (2005)). The large number of parameters to be addressed and the complex time dependent non-Newtonian behaviour of mud made very difficult to apply model-scale results to full-scale. CFD approach seems to be a good choice to overcome these obstacles (Toorman et al. (2015)).

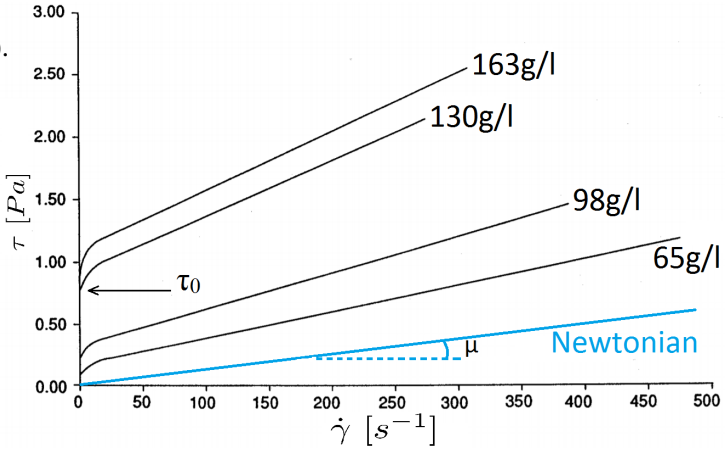

Fig. 1: Shear stress/Shear rate flow curves for different mud concentrations. In blue is shown the Newtonian model. Picture adapted from Whitehouse (2000).

The Newtonian model is widely used as constitutive equation for many fluids, such as water and air. However, it is not suitable to represent the flow behaviour of fluid mud[1], which acts like a solid at low stress levels, but starts to flow when the stress exceeds a critical value, the yield stress, τ_0 (see Figure 1). Rheological measurements (e.g. Wurpts (2005)) have revealed that the Herschel-Bulkley model (Herschel and Bulkley (1926)) is appropriate to represent the flow behaviour of fluid mud. Thus, this non-Newtonian model has been implemented in a viscous-flow multiphase open-source code ReFRESCO (www.refresco.org).

The procedure and results of a Code Verification exercise are presented in this paper for the case of steady, laminar, two-dimensional Poiseuille flow with Herschel-Bulkley fluid.

2 A non-Newtonian constitutive equation for fluid mud: the Herschel-Bulkley model

The deviatoric stress tensor $\boldsymbol{\tau}$ obeys the following constitutive equation for Herschel-Bulkley fluids:

$$\begin{cases} \boldsymbol{\tau} = 2\left(\frac{\tau_0}{|\dot{\gamma}|} + K\,|\dot{\gamma}|^{n-1}\right)\mathbf{D}\,, & \tau_0 \le |\boldsymbol{\tau}|\,, \\ \mathbf{D} = 0\,, & |\boldsymbol{\tau}| < \tau_0\,, \end{cases} \tag{1}$$

where $\mathbf{D} = \frac{1}{2}(\nabla\mathbf{u} + \nabla\mathbf{u}^T)$ is the rate of strain tensor, $\tau_0\,[Pa]$ is the yield stress which represents the initial stress below which the fluid behaves as solid, $K\,[Pa \cdot s^n]$ is the consistency parameter, $|\boldsymbol{\tau}| = \sqrt{2\tau_{ij}\tau_{ij}}$ and $|\dot{\gamma}| = \sqrt{2D_{ij}D_{ij}}$ are the second invariant of the shear stress and rate of strain tensor respectively, which in some way are representative of the magnitude of the respective tensor. The parameter n is called flow index because it characterizes the flow behaviour of the fluid.

[1]The definition of fluid mud in not univocal. Here fluid mud is referred to as intermediate state between "black water", which has Newtonian flow characteristics, and consolidated mud, which behaves more like as an visco-elastic material.

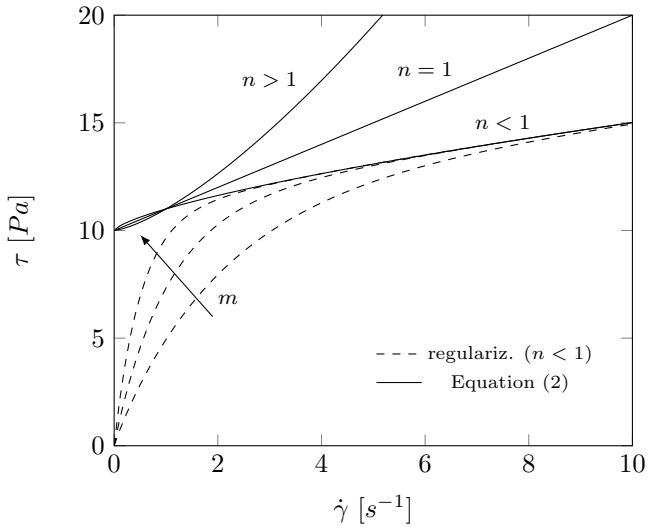

Fig. 2: Shear stress versus shear rate for $\tau_0 = 10\,[Pa]$, $K = 1[Pa \cdot s^n]$ and different values of the flow index n. The Papanastasiou regularization is plotted varying the parameter m.

Depending on whether $n < 1$ (shear-thinning behaviour) or $n > 1$ (shear-thickening behaviour) the fluid displays different flow curves (Figure 2). Note that when $n = 1$ and $\tau_0 = 0$ the model reduces to the Newtonian model. In addition, when $n = 1$, the consistency parameter K has dimensions of dynamic viscosity.

2.1 Regularization approach

From the constitutive equation (1) two regions can be distinguished: one, called *unyielded* region, where $|\boldsymbol{\tau}| < \tau_0$ and the fluid does not experience any shear deformation; the other, called *yielded* region, where $\tau_0 \leq |\boldsymbol{\tau}|$ and the fluid deforms. These two regions are not known a priori, so the solver does not know whether apply the first or the second relation in the equation (1).

To circumnvent this issue there are mainly two solution methods (Saramito et al. (2017)): the augmented Lagrangian algorithm and the regularization approach. The second method has been adopted because of its relatively simple implementation. It consists in approximating the curve described by Eq.(1) by a single smooth curve (Figure 2). Among the several regularizations that have been proposed by different authors, the most widely used is the one proposed by Papanastasiou (1987), which yields

$$\boldsymbol{\tau} = 2\left[\frac{\tau_0}{|\dot{\gamma}|}\left(1 - e^{-m|\dot{\gamma}|}\right) + K\,|\dot{\gamma}|^{n-1}\right]\mathbf{D}\,. \tag{2}$$

The term in the square brackets can be seen as one non-constant viscosity, generally called *apparent viscosity*:

$$\mu_{app} = \frac{\tau_0}{|\dot{\gamma}|}\left(1 - e^{-m|\dot{\gamma}|}\right) + K\,|\dot{\gamma}|^{n-1}\,. \tag{3}$$

The main advantage of the regularization approach is that ReFRESCO was already developed to solve flows with non-constant viscosity [2], therefore the solver algorithm does not require major modifications. The implementation of the apparent viscosity then becomes quite straightforward.

It can be demonstrated that as $m \to \infty$ the Eq.(2) tends to Eq.(1) and the solution with the regularized model tends to the exact solution of the Herschel-Bulkley model. However, with large values of m the iterative solver might not converge. Hence, a good compromise between accurate representation of the Herschel-Bulkley model and convergence must be found, depending on the objective of the computation.

3 Two-dimensional Poiseuille laminar flow

Poiseuille flow is the pressure driven, incompressible, steady, unidirectional and laminar flow that takes place in a duct when the Reynolds number is in the laminar range. Let consider x-y Cartesian reference system with the origin a the bottom of the duct and x axis pointing in the flow direction. Then the velocity field is like $\mathbf{u} = (u(y), 0, 0)$ and the momentum equations written in a Cartesian coordinate system reduce to only one equation in the x direction:

$$\frac{dp}{dx} = \frac{d\tau_{xy}}{dy} \tag{4}$$

where p is the pressure which incorporates also the gravity term. Imposing the no-slip condition at the walls, i.e. $u(y) = 0$ at $y = 0$ and $y = H$, where H is the height of the duct, the analytical solution of Eq.(4)

[2] Non-constant viscosity with Newtonian fluid occurs when using, for instance, the Volume of Fluid method for multiphase problems, or eddy turbulent viscosity in the RANS equations.

combined with Eq.(1) yields (Ferrás et al. (2012)):

$$u(y) = \begin{cases} \frac{n}{n+1}(-\frac{dp}{dx}/2K)^{1/n}\left[(H/2-H_0)^{(n+1)/n} - (|y-H/2|-H_0)^{(n+1)/n}\right], & H_0 \leq |y-H/2| \\ \\ \frac{n}{n+1}(-\frac{dp}{dx}/2K)^{1/n}\,(H/2-H_0)^{(n+1)/n}, & |y-H/2| \leq H_0 \end{cases} \tag{5}$$

where $\frac{dp}{dx} < 0$ is given as the flow is pressure driven, $H_0 = \tau_0/|\frac{dp}{dx}|$ is the height of half portion of the unyielded region (i.e., the region where $|\boldsymbol{\tau}| < \tau_0$).

In contrast with Newtonian fluids, Poiseuille flows of Herschel-Bulkley fluids are characterized by two non-dimensional numbers, the generalized Reynolds and Bingham numbers, defined respectively as

$$Re^* = \rho\frac{\bar{U}^{2-n}L^n}{K}, \qquad Bi^* = \frac{\tau_0}{K(\bar{U}/L)^n} \tag{6}$$

where $\bar{U}$ is the reference velocity, ρ is the fluid density and L is the reference length of the flow. In case of Poiseuille flow L is defined as the duct height and $\bar{U}$ is the average velocity along the cross section. The Bingham number represents the non-dimensional yield stress. When $n = 1$ and $Bi^* = 0$, the Newtonian case is retrieved. Note that when Poiseuille flow is in laminar regime the Reynolds number is irrelevant.

4 Discretization error estimation

Performing a Code Verification exercise (which must be distinguished from Solution Verification and Validation) aims to check that (Eça et al. (2016)):

- the discretization error tends to zero as the grid reference spacing h tends to zero[3].
- the rate of convergence p of the discretization error with the grid refinement tends to the order of the scheme adopted for the computations.

The *discretization error* is the difference between the exact solution of the original differential equation, ϕ_{exact}, and the solution of the discretized equation, ϕ_h, on a grid h. The other two components of numerical errors, the iterative and round-off error, must be kept as low as possible is order to have the best possible estimation of the discretization error. The iterative error can be neglected by dropping the solution residuals by at least three or four order of magnitude, whereas the round-off error is negligible as nowadays almost every computer uses double precision number format.

Although Eq.(5) is theoretically the exact solution, the use of the regularized approach in place of the original Herschel-Bulkley model makes it no longer appropriate for the estimation of discretization error. Thus, the exact solution has been computed numerically by solving Eq.(4), combined with the regularized Herschel-Bulkley model, Eq.(2). The equations have been discretized with the Finite Difference Method, dividing the height of the duct by approximately 10^5 points, a very large number of points compared to the finest grid used for the grid refinement study. For this reason, this solution is still referred to as "exact" even though it was computed numerically.

5 Computational setup

The computation was set up to solve (steady) 2D computations. The duct considered for the grid refinement study has a length that is twice the height and has been discretized with Cartesian uniform grids having $\frac{h_x}{h_y} = 1.5$, where h_x and h_y are the cell size in the x and y direction respectively (see Figure 3). The coarsest grid, consisting of 24 cells, is systematically refined six times, halving both h_x and h_y, for a total of seven grids. Dividing h_x and h_y by the same factor is of utmost importance to preserve geometrical similarity between the grids.

The exact velocity profile is imposed at the inlet boundary. Fixed pressure and the no-slip condition are imposed at the outlet and wall boundaries respectively. The boundary conditions for both velocity and pressure are summarized in Table 1. The calculations on the seven grids were conducted for several combinations of Bingham number, Bi^*, and flow index, n. The regularization parameter, m, was to set equal to 10 [s] for all the cases to facilitate iterative convergence.

[3] for unsteady problems also time refinement should be performed

Boundary conditions			
Inlet	Outlet	Wall	Side
$\mathbf{u} = \mathbf{u}_{exact}(y)$	$\nabla \mathbf{u} \cdot \mathbf{n} = \mathbf{0}$	$\mathbf{u} = \mathbf{0}$	$\nabla \mathbf{u} \cdot \mathbf{n} = \mathbf{0}$
$\frac{\partial p}{\partial n} = 0$	$p = const.$	$\frac{\partial p}{\partial n} = 0$	$\frac{\partial p}{\partial n} = 0$

Table 1: Boundary conditions for velocity and pressure on the computational domain

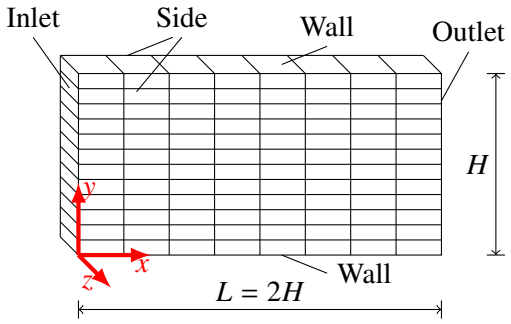

Fig. 3: Example of computational domain with 96 cells.

6 Results and discussion

Figure 4 shows how the iterative convergence of velocity along the x direction is influenced by Bi^* and n on the grid 64x96, which has an intermediate resolution. As a convergence criteria, the iterative solution was considered to be converged when the infinity norm of all the residuals was less than 10^{-11}. Note that the least amount of iterations to find the converged solution are required for $Bi^* = 0$.

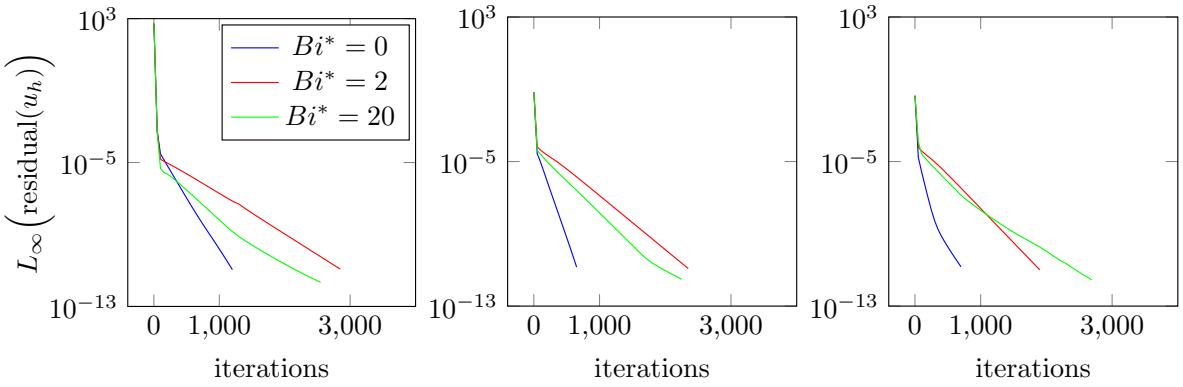

(a) n = 0.8 **(b)** n = 1.0 **(c)** n = 1.25

Fig. 4: Infinity norm of the velocity residuals in the x direction for the nine test cases.

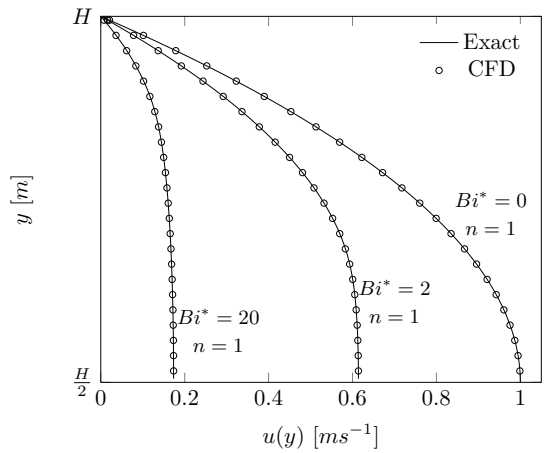

Fig. 5: Velocity profiles obtained with ReFRESCO and exact solution for different Bn^*. The duct has $L = 20H$ and was discretized with a grid 640x96.

As additional verification, the velocity profile on a duct having length $L = 20H$ was also computed, imposing this time an uniform velocity profile at the inlet boundary, providing no hints to the solver about the exact solution. The comparison between CFD solution and the exact solution reveals a very good agreement (Figure 5), with a maximum percentage error[4] below 0.2%.

The results of the grid refinement study are presented in Figure 6, showing the discretization errors of the velocity. As expected, the curves of discretization error converge to second order (i.e., converge to the line having slope $p = 2$) as the grid spacing h_i/h_1 tends to 1, with h_1 the grid spacing of the finest grid. It can also be seen that, for higher Bi^*, finer grids are required to obtain the same accuracy as for $Bi^* = 0$. Similar results were found also for pressure and veloc-

[4] normalized with the velocity at $y = H/2$

ity gradient. Other combinations of Bi^* and n, which are not reported here, were also tested, providing analogous results. The agreement of the observed order of convergence and the theoretical order of convergence demonstrates the correct implementation of the Herschel-Bulkley model.

Ultimately, it was found that when $n \lesssim 0.7$, or $m \gtrsim 10^2$, the solution did not converge anymore. If values beyond these thresholds need to be used in more realistic scenarios, (under-)relaxation methods should be considered to facilitate convergence.

7 Conclusions

In this study, a code verification exercise was performed on the implementation of the Herschel-Bulkley model, which was adopted as non-Newtonian model to simulate the dynamics of fluid mud.

Results showed that the code is able to find an accurate solution (Figure 5), at least for a steady two-dimensional test case. In addition, this work highlighed that not only the discretiziation errors tends to zero as the grid is refined, but also that decreases with the expected second order (Figure 6). This seems to be a valid proof that the Herschel-Bulkley model is correctly implemented in ReFRESCO and thus that the code can be considered ready to solve problems with higher level of complexity (e.g., 3D domain, unsteady and multi-phase flows.).

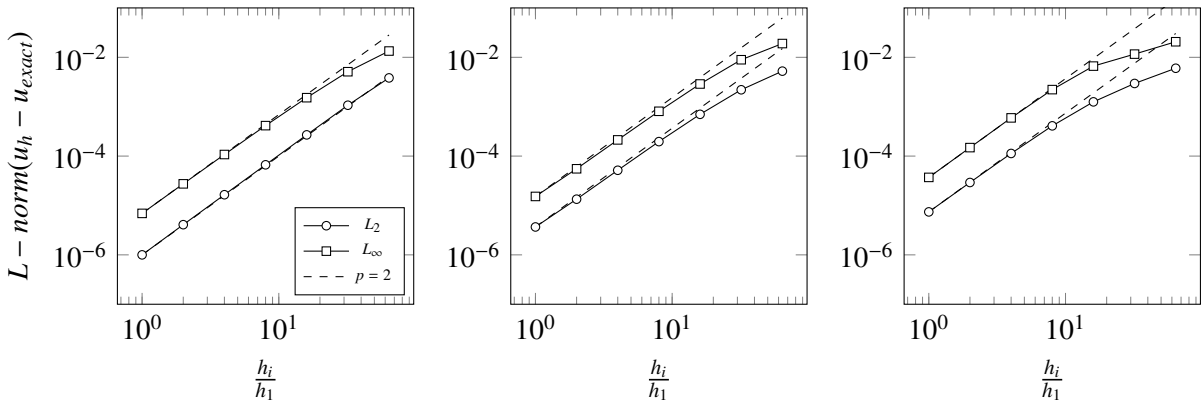

(a) $n = 0.8$, $Bi^* = 0$ **(b)** $n = 0.8$, $Bi^* = 2$ **(c)** $n = 0.8$, $Bi^* = 20$

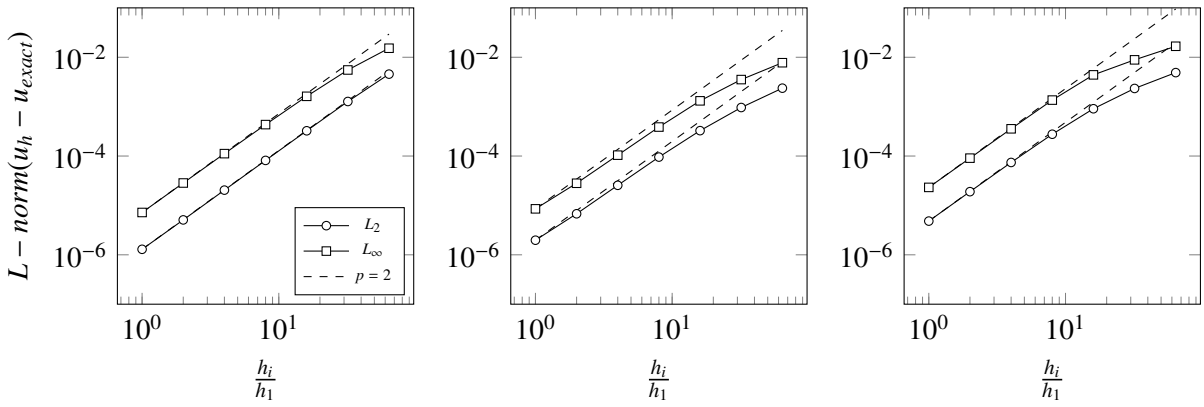

(d) $n = 1.0$, $Bi^* = 0$ (Newtonian case) **(e)** $n = 1.0$, $Bi^* = 2$ **(f)** $n = 1.0$, $Bi^* = 20$

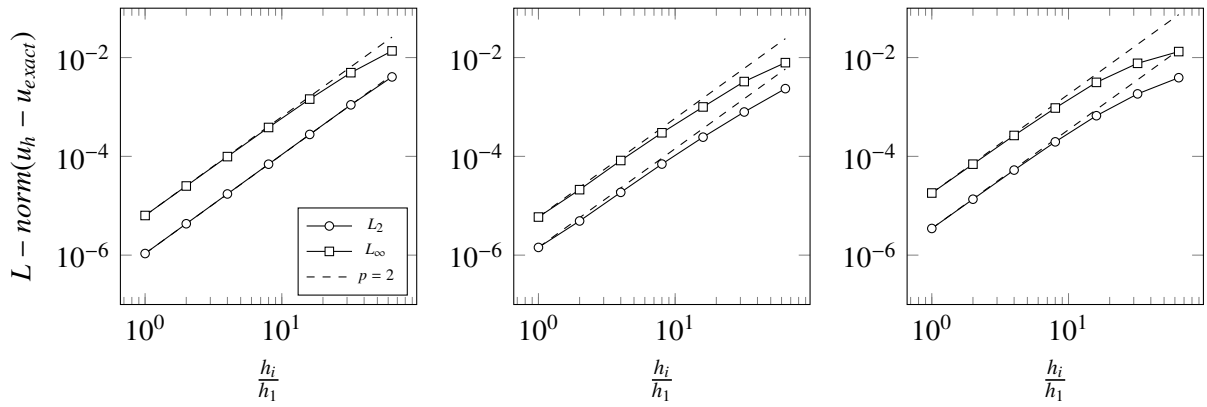

(g) $n = 1.25$, $Bi^* = 0$ **(h)** $n = 1.25$, $Bi^* = 2$ **(i)** $n = 1.25$, $Bi^* = 20$

Fig. 6: L_2 and L_∞ norm of the discretization error of the velocity for different combinations of Bi^* and n. u_h is the solution computed on the grid h.

References

G. Delefortrie, M. Vantorre, K. Eloot (2005). Modelling navigation in muddy areas through captive model tests. Journal of marine science and technology, 10(4), pp. 188-202.

L. Eça, C.M. Klaij, G. Vaz, Hoekstra, F.S. Pereira (2016). On code verification of RANS solvers. Journal of Computational Physics, vol. 310, pp. 418 - 439.

L.L. Ferrás, J.M. Nóbrega and F.T. Pinho (2012). Analytical solutions for Newtonian and inelastic non-Newtonian flows with wall slip. Journal of Non-Newtonian Fluid Mechanics, 175-176, 76-88.

W.H.Herschel, R. Bulkley (1926). Konsistenzmessungen von Gummi-Benzllösungen, Kolloid Zeitschrift, 39:291-300.

T.C. Papanastasiou (1987). Flows of materials with yield. Journal of Rheology, vol. 31, pp. 385.

P. Saramito, A. Wachs (2017). Progress in numerical simulation of yield stress fluid flows. Rheol Acta (2017) 56 : 211 – 230.

F. Stern, R. Wilson, V., H. W. Coleman, and E. G. Paterson. Comprehensive Approach to Verification and Validation of CFD Simulations - Part 1: Methodology and Procedures, Journal of Fluids Engineering, 2001, 123: pp. 793-802.

E. A. Toorman, I. Vandebeek, M. Liste-Munoz, M. Heredia, I. Rocabado, J. Vanlede, G. Delefortrie, M. Vantorre, Y. Meersschaut(2015). Drag on an object towed through a fluid mud layer: CFD versus experiment. International conference on cohesive sediment transport processes, Abstracts, pp. 114-115.

R. Whitehouse (2000). Dynamics of Estuarine Muds: A Manual for Practical Applications, p. 31

R. Wurpts (2005). 15 Years Experience with Fluid Mud: Definition of the Nautical Bottom with Rheological Parameters. Terra et Aqua number 99, pp. 22-32.

An Investigation of the Vortex Shedding Frequency and Natural Frequency of a Ship Propeller

Nicholas McCaw[1] ,Stephen Turnock[2], William Batten[3]
[1] University of Southampton, n.mccaw@soton.ac.uk
[2] University of Southampton, S.R.Turnock@soton.ac.uk
[3]QinetiQ, WMBatten@QinetiQ.com

September 21, 2018

1 Introduction

Propellers are used extensively in marine environments, renewable energy systems and for aircraft propulsion. A propeller blade is effectively a series of foils working at an angle of attack to produce lift and drag. The lift and drag are components of thrust and torque. An issue of propeller is noise which produces acoustic signatures which are of interest in military applications and environmental noise, it is desirable to reduce noise from the propeller. A cause of the noise is propeller vibration, this is caused by: unsteadiness in the inflow, cavitation, turbulent perturbation and trailing edge vortices.

It is therefore desirable to understand the causes of this vibration and design against it. Although tools and processes have been established to compute the vibration of the propeller blades, these are often have large computational cost and are impractical for a design process. The aim of the paper is to study the trailing edge vortex of the PPTC propeller and to match the shedding frequency to modal frequency in an attempt to predict singing. This will be complete by fulfilling the following objectives:

- Perform a modal analysis of the PPTC submerged in water.
- Perform a 2D CFD simulation in OpenFoam of the PPTC at blade section $\frac{r}{R} = 0.8$
- Compare vortex shedding to modal frequencies and shapes to predict lock-in and singing.
- Compare the shedding frequency from the 2D simulation with the empirical approximation from Carlton [Saunders, 1961]

This investigation is part of the EngD currently being undertaken. The aim of the EngD is to develop tools for obtaining propeller vibration characteristics under loading to be used in a design environment, therefore reducing computational cost. Hence the use of empirical formula is desirable for use due to low computational cost when compared to CFD simulations.

The PPTC propeller is used as it has been studied in depth with extensive experimental data available for validation. OpenFOAM is an open source simulation software. It stands for open source field operation and manipulation so can be used as a general numeric solver. The software is C++ orientated and has the benefit of being open source meaning the source code can be added to and changed to suit the user. OpenFOAM has been used in many engineering studies in both academia and industry, with good documentation and online support making it a good open source option.

Propeller vibration has been studied previously with [Kim et al., 2018] conducting a numerical and experimental investigation on the singing properties of a blunt trailing edge propeller. [Nu Rhahida Arini, 2018] conducted extensive numerical investigations on a 2D foil with an equation based structural model. The theses also simulated trailing edge vortex generation. Moreover there has been significant investigation into fully coupled fluid structure interaction using computationally expensive finite element and CFD coupled methods [Young, 2008],[Young and Savander, 2011], [Andersson and Ahl, 2011] ,[Balaras et al., 2015]. These papers predominantly investigate the structural deformation of the propeller blades or hydrofoils whereas [Viitanen et al., 2017], [Akcabay et al., 2014],[Akcabay and Young, 2015] focus more on the vibration of the propeller, however these are still large, computationally expensive methods of fluid-structure. There seems to be a lack of computationally cheap methods of predicting propeller vibration properties under loading, the aim of the EngD is to fill this gap.

2 Numerical Simulations

To simulate the fluid over the hydrofoil a detached eddy simulation (DES) was used using the open source software OpenFoam. DES was chosen as the unsteady Von Karman sheet is being studied, so traditional Reynolds Averaged Navier Stokes Equations (RANS) or Unsteady Reynolds Averaged Navier Stokes (URANS) are not capable to capture this phenomena as they are better suited for more statistically standard flows not separated flow [Squires,]. Moreover DES uses RANS for attached flow and large eddy simulation (LES) for separated flow, this allows for a great saving in computational expense. An issue with DES is that it requires a turbulence model, the turbulence model is applied in the attached flow region where RANS is used. Depending on the turbulence model selected this can be cause inaccuracies. The turbulence model used in this case is the $k-\omega SST$ model. This is used as it gives good results for separating flow, it can give oversensitive to adverse pressure gradients [Greenshields, 2016]. Finally the DES requires 3D meshes to fully model the physics otherwise as it resolves the 3D eddies in the turbulent fluid. Therefore, the simulations will not give fully physical results however for the purposes of capturing the trailing edge vortices it is sufficient.

This study uses the PPTC propeller as the geometry being studied, this is due to the abundance of data available for comparisons due to the smp 11 and smp 15 propeller workshops [Viitanen et al., 2017] [Charalambous and Eames, 2017]. The PPTC has a diameter of 0.25m and 5 blades. The operating conditions have been tested giving the open water efficiency curve . An advance ratio of 0.62 is chosen as it is the position of maximum efficiency as shown in [Klasson, 2012]. The blade section used in the propeller is the NACA66MOD with chord 107m and at position $\frac{r}{R} = 0.8m$. This foil shape has been used in the 2D simulation. The grid for the simulations was built in the meshing software Pointwise. In each configuration a C-grid has been created consisting of approximately 80,000 cells. The mesh is shown in figure 1. The mesh was set such that the leading edge was 10 chord lengths from the inlet, the trailing edge is 10 chord lengths from the outlet and the width of the domain is 20 chord lengths.

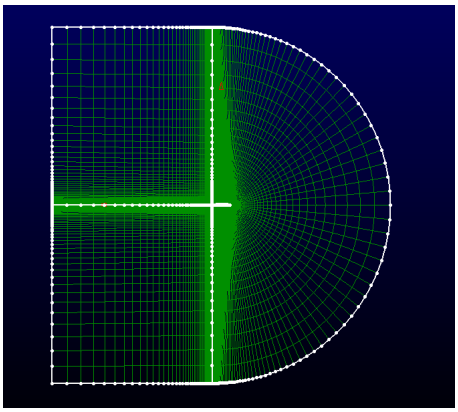

Figure 1: C Grid mesh for NACA66MOD foil consisting of 80,000 cells

Four configurations are used to determine the effect of leading edge and trailing edge shape. The four configurations are:

- Blunt leading edge, blunt trailing edge
- Blunt leading edge, rounded trailing edge
- Sharp leading edge, blunt trailing edge
- Sharp leading edge, rounded trailing edge

The velocity and angle of attack of the foil was computed by using a blade element momentum theory code. This also gives the section lift and drag coefficient and propeller thrust and torque coefficients. For this advance ratio a section velocity of 30 m/s was computed at an angle of attack of 0.13^o. Due to OpenFoam using finite volume method for computations the mesh requires a dimension in the z-direction. This was chosen to be 20x the trailing edge thickness then 200x the trailing edge thickness . The Courant number is defined as $C = \frac{u\Delta t}{\Delta x}$ where u is the fluid speed, Δt is the time step and Δx is the cell size. To run an effective simulation the Courant number is required to be ¡1 meaning a fluid particle does not

cross more than 1 cell in 1 time step, care was taken to ensure this was the case hence a timestep value of 1e-5s was chosen. A summary of simulation set up is shown in table 1.

Table 1: Summary of simulation conditions

Simulation type	DES
Turbulence Model	$k-\omega SST$
Inlet Velocity	30 m/s
Angle of attack	0.13^o
Cell size	80,000
Chord	107m
Time step	1e-5 s
Trailing edge thickness	0.0625 m

The vortex shedding has been captured for all configurations and is shown in figures 2a, 2b, 2c and 2d. From the images it is indicated that the changing of the leading edge does not change the vortex shedding frequency. Moreover, the blunt or rounded trailing edge does not effect the vortex shedding frequency but does effect the vortex strength. This can be looked at in more detail by placing a probe at the vortex core of the 1st trailing edge vortex. The y component of velocity is plotted against time as it clearly indicates the presence of vorticity. The resultant figures are shown in figures 2a, 2b, 2c and 2d

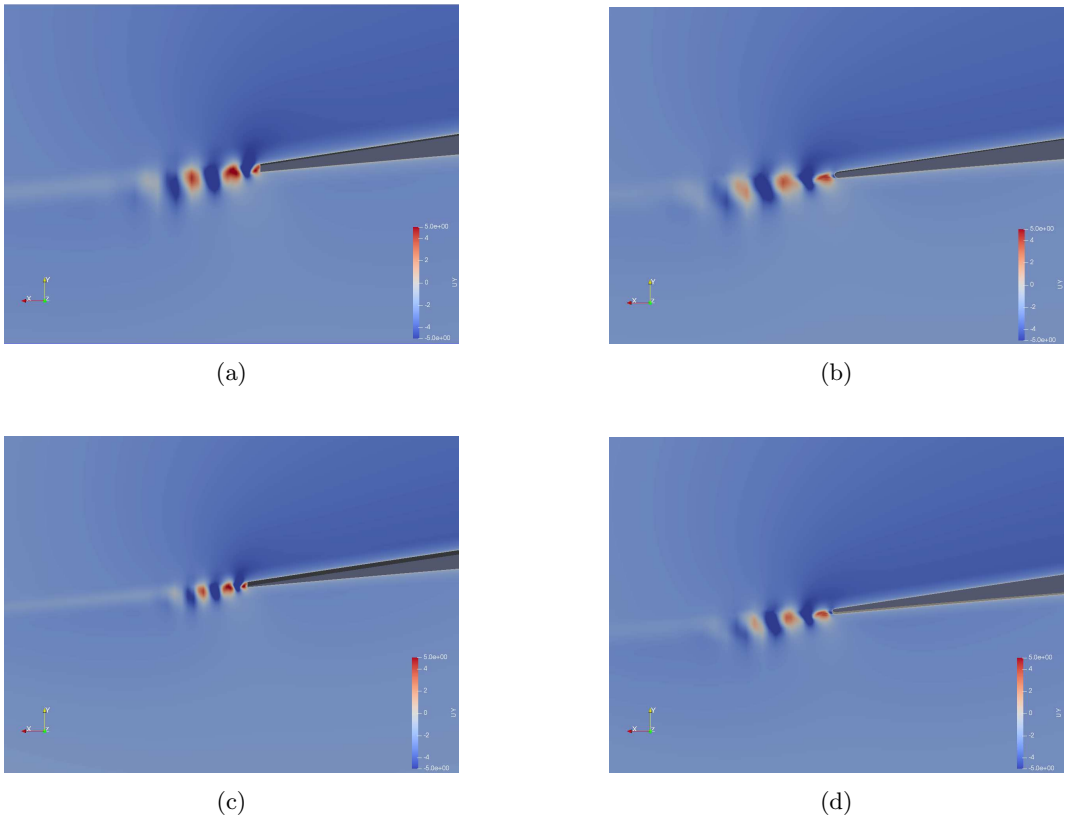

(a) (b)

(c) (d)

Figure 2: Trailing Edge vortex shedding of the NACA66 MOD hydrofoil with a) blunt leading and trailing edge b) blunt leading and rounded trailing edge c) sharp leading and blunt trailing edge d) sharp leading and round trailing edge

To compute frequency the difference in time from each peak was found. The shedding frequencies for each configuration are shown in table 2. It is noted that the frequency increases for the rounded trailing edge. This is because, even though the trailing edge thickness is the same for both configurations, the separation point is located further downstream of the foil in the rounded trailing edge configuration thus reducing the effective trailing edge thickness which will increase the shedding frequency.

It is important to note the difference between plots 3a, 3d, 3d and 3b. It is noted that the plot shape differs at the higher velocity section when compared to the other configurations, this is as yet unknown. Moreover, the velocities differ greatly with the maximum occurring at 4.5 m/s for plot 3b whereas it is -4.3 m/s for the rest. This is again unknown.

A slight drift is seen in in velocity figure 3d. This indicates that a steady state condition has not yet been reached. However, as an indicator that the simulation gives correct results the lift coefficient of the foil was monitored. The value of lift coefficient was 0.39 which corresponds well to the work conducted by [Darottkno, 1966]. When plotted the lift coefficient oscillates around 0.39 which indicates the presence of the trailing edge vortices. The vortex shedding frequency was also checked by increasing the z-direction dimension to 200x the trailing edge thickness to check this dependence. It was found that the vortex shedding frequency did not change.

Table 2: Shedding frequencies for the 4 configurations

Simulation Configuration	Computed Shedding frequency (Hz)
a)	62.5
b)	50
c)	62.5
d)	50

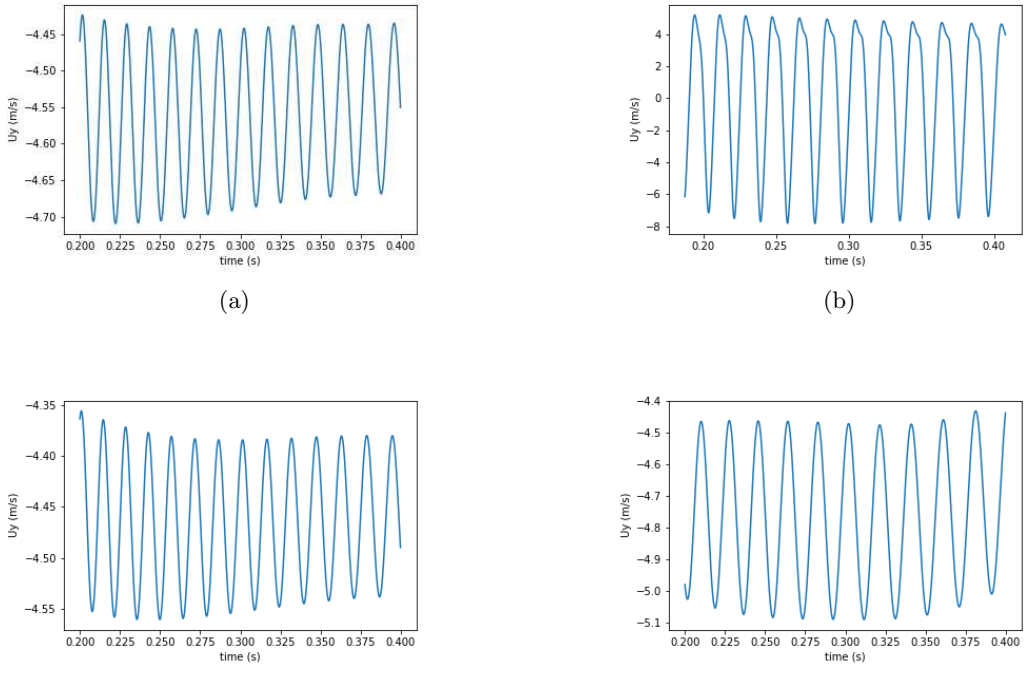

Figure 3: y-component of velocity at the trailing edge of the NACA66 MOD hydrofoil with *a*) blunt leading and trailing edge *b*) blunt leading and rounded trailing edge *c*) sharp leading and blunt trailing edge *d*) sharp leading and round trailing edge

It is noted that the scaling issues arise here. The model scale chord was 0.107m however this was increased to 107m due to a mistake in the OpenFoam file structure. This will need to be corrected in future simulations, although it can be argued that both the model scale and large scale models lie within the turbulent regime therefore changes in Strouhal number are not severe. Moreover, like for like comparisons are made between the simulation and empirical formula. The simulated shedding frequency is then compared to an empirical prediction. This is done by calculating the velocity of the fluid at the blade by using equation 1

$$U_{Blade} = [U_{ship}^2 + (0.8\pi Dn)^2]^{0.5} \tag{1}$$

Where U_{ship} is the velocity of the inlet to the propeller, D is the diameter of the propeller and n is the number of revolutions per second.

The Reynolds number of the foil is then calculated by $Re = \frac{U_{blade}C\rho}{\mu}$ where C is the chord of the foil. The Strouhal number is estimated using the empirical formula from [Sunden,]:

$$Sn = 0.198(1 - \frac{19.7}{Re}) \tag{2}$$

The shedding frequency is then computed by $f = \frac{U_{blade}Sn}{d}$ where d is the trailing edge thickness. This process was applied to this configuration resulting in a Reynolds number of 2 million which is in the turbulent regime a Strouhal number of 0.198 which is reasonable according to the literature and the resulting shedding frequency was given as 94Hz.

This is nearly double the shedding frequency of the simulated flow. This indicates either the simulation is poor or the empirical formula cannot be used for predicting the vortex shedding frequency. There is little confidence in the simulated results given the 2D nature and issues with scaling. Moreover a more sophisticated method of empirically predicting the trailing edge vortex shedding is desirable.

Finally a modal analysis simulation of the PPTC propeller submerged in a spherical domain was conducted. The model was of the PPTC with all but one of the blades removed, this was done to reduce computational time, the domain was a sphere of diameter 270m. The sphere diameter was chosen to be 0.27m in the model scale case where the propeller diameter was 0.25m, as it has been shown that a smaller domain leads to a more stable simulation with less errant modes [Javdani et al., 2016]. The hub of the propeller was constraint such that only the blade was free to vibrate. A fluid structure interaction face was then created between the propeller and the domain. The mesh is of size 200,000 elements with SOLID187 elements used for the propeller and FLUID221 elements used for the fluid domain. The outer boundary of the domain was set to an absorption boundary condition. This condition reduces the sound waves propagated back to the propeller, therefore reducing the number of errant modes. This was chosen over a radiation boundary condition as, for this case, it produces less erroneous modes.

The modal analysis of the submerged propeller gave frequencies of 0.5 Hz to 4 Hz for the first ten modes with the first mode giving a bending shape and the second mode a clear torsion mode as expected,shown in figure 4. The process used has been verified by using the same process for a geometry with experimentally found modal results. When the frequency range is increased to incorporate the frequency range predicted by the DES simulation and empirical formula the simulation resulted in no modes found.

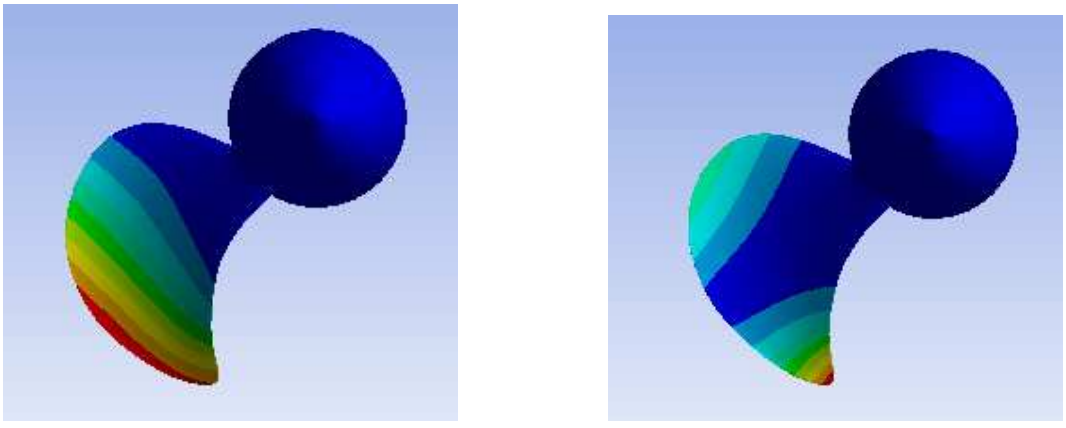

(a) Bending mode

(b) Torsion mode

Figure 4: 1st 2 vibration mode shapes for the single bladed PPTC with hub constraint. *a*) shows the clear bending mode and *b*) shows the clear torsion mode. These two mode shapes are expected for the blade giving some confidence in the results

3 Conclusions and Future work

An attempt was made to use empirical formula to predict the shedding frequency and therefore the singing conditions of the Potsdam propeller test case. It was found that, for the conditions tested, the empirical formula gave poor results when compared to the detached eddy simulation. Moreover, a modal analysis of the PPTC was done using Ansys and resulted in good bending and torsion mode shapes. However, when set to the expected shedding frequency range no modes where found. This could indicate that the PPTC does not sing under these operating conditions or further work is required to attempt to capture the modes in this frequency range by using various the mode extraction methods available in Ansys. Finally when conducting the DES issues were encountered with scaling between mm and m. This will need to be corrected to ensure the results achieved so far scale with Reynolds number correctly. Moreover, to correctly utilize the detached eddy simulation a 3D model will be required.

References

[Akcabay et al., 2014] Akcabay, D. T., Chae, E. J., Young, Y. L., Ducoin, A., and Astolfi, J. A. (2014). Cavity induced vibration of flexible hydrofoils. *Journal of Fluids and Structures*, 49:463–484.

[Akcabay and Young, 2015] Akcabay, D. T. and Young, Y. L. (2015). Parametric excitations and lock-in of flexible hydrofoils in two-phase flows. *Journal of Fluids and Structures*, 57:344–356.

[Andersson and Ahl, 2011] Andersson, C. and Ahl, D. (2011). Fluid Structure Interaction: Evaluation of two coupling techniques. (June):55.

[Balaras et al., 2015] Balaras, E., Schroeder, S., and Posa, A. (2015). Large-Eddy Simulations of Submarine Propellers. *Journal of Ship Research*, 59(4):227–237.

[Charalambous and Eames, 2017] Charalambous, N. and Eames, I. (2017). A detail computational hydro - acoustics analysis for hydrofoils with straight and wavy leading edges. *Proceedings of the Fifth International Symposium on Marine Propulsors*, 3(June).

[Darottkno, 1966] Darottkno, T. (1966). Mimimum Pressure Envelopes for Modified NACA66 sections with NACA a = 0.8 camber.

[Greenshields, 2016] Greenshields, C. J. (2016). OpenFOAM. *OpenFOAM Foundation Ltd*, (June).

[Javdani et al., 2016] Javdani, S., Fabian, M., Carlton, J. S., Sun, T., and Grattan, K. T. (2016). Underwater Free-Vibration Analysis of Full-Scale Marine Propeller Using a Fiber Bragg Grating-Based Sensor System. *IEEE Sensors Journal*, 16(4):946–953.

[Kim et al., 2018] Kim, T., Hur, J., and Hyundai, H. L. (2018). Cavitation Influence on Singing Propellers. (August):5–10.

[Klasson, 2012] Klasson, O. (2012). Open Source Calculations for the Potdam Propeller Test Case using Open Source and Commercial Meshers. *CRS*.

[Nu Rhahida Arini, 2018] Nu Rhahida Arini (2018). *The Influence of Trailing Edge Shape on Fluid Structure Interaction of a Vertical Axis Tidal Turbine Blade*. PhD thesis.

[Saunders, 1961] Saunders, H. (1961). *Hydrodynamics in Ship Design*.

[Squires,] Squires, K. D. Detached Eddy Simulation : Current Status And Perspectives.

[Sunden,] Sunden, B. Vortex Shedding, DOI: 10.1615/AtoZ.v.vortex_shedding.

[Viitanen et al., 2017] Viitanen, V. M., Hynninen, A., Lars, L., Klose, R., Siikonen, T., and Tanttari, J. (2017). CFD and CHA simulation of underwater noise induced by a marine propeller in two-phase flows. *Proceedings of the Fifth International Symposium on Marine Propulsors*, 1(June).

[Young, 2008] Young, Y. L. (2008). Fluid-structure interaction analysis of flexible composite marine propellers. *Journal of Fluids and Structures*, 24(6):799–818.

[Young and Savander, 2011] Young, Y. L. and Savander, B. R. (2011). Numerical analysis of large-scale surface-piercing propellers. *Ocean Engineering*, 38(13):1368–1381.

Application of the SIMPLE Algorithm to a Manufactured Subsonic Flow

João Muralha*, Luís Eça*, and Christiaan Klaij†
*IST Técnico Lisboa, Lisbon/Portugal, †MARIN Maritime Research Institute Netherlands,
Wageningen/The Netherlands
joao.muralha@tecnico.ulisboa.pt

1 Introduction

In general, numerical flow simulations in naval and offshore industries consider the fluids to be incompressible, i.e., with constant density. Although this approximation is valid for most flow cases, there are several phenomena, e.g., slamming, sloshing and cavitation, that involve compressible fluids. The goal of the present development of ReFRESCO is to modify the current flow solver to accurately solve compressible two-phase flows.

The first step of this development is to extend the current ReFRESCO pressure-based SIMPLE solver to laminar subsonic flows of perfect gases. The new solver will be based on the pressure-velocity-density coupling described in Ferziger and Perić, 2001. Besides the introduction of a new pressure correction equation the momentum and energy equations must be updated. It is also necessary to introduce an equation of state that relates pressure, density and temperature.

In the present work a code verification exercise for the modifications done in the momentum and pressure correction equations is presented. In this exercise the Method of Manufactured Solution is used to obtain an analytical solution for the compressible Navier-Stokes equations.

2 Governing Equations

The continuity, momentum, energy equations for a compressible steady state flow are:

$$\nabla \cdot \left(\rho \overrightarrow{V}\right) = 0 \tag{1a}$$

$$\nabla \cdot \left(\rho \overrightarrow{V} \otimes \overrightarrow{V}\right) = -\nabla \cdot (p\mathbf{I}) + \nabla \cdot \tau + S \tag{1b}$$

$$\nabla \cdot \left(\rho \overrightarrow{V} c_p T\right) = \overrightarrow{V} \cdot \nabla p + \tau : \nabla \overrightarrow{V} - \nabla \cdot q \tag{1c}$$

where $\overrightarrow{V} = (u, v, w)$, ρ, p, T and c_p represent the velocity vector, density, pressure, temperature and specific heat at constant pressure, $\mathbf{I}$ is the identity matrix, S represents a source term and τ and q are given by:

$$\tau = \mu\left(\nabla \overrightarrow{V} + \left(\nabla \overrightarrow{V}\right)^T\right) - \frac{2}{3}\mu\left(\nabla \cdot \overrightarrow{V}\right)\mathbf{I},\ q = -k_T \nabla T \tag{2}$$

with μ and k_T being the dynamic viscosity and thermal conductivity coefficient.

Pressure, temperature and density are related by the perfect gas equation of state:

$$p = \rho R T \tag{3}$$

The momentum and continuity equations[1] are going to be solved in a squared domain with side L, so in dimensionless variables, $(x/L, y/L)$, the domain is the unit square. The energy equation is not solved and the exact temperature is used when needed. The boundary conditions are presented in Table 1. In the present work Neumann boundary conditions refer to zero normal derivative. The selection of a consistent set of boundary conditions is crucial to obtain a well-posed problem. The use of over-constrained boundary conditions in a subsonic flow may lead to spurious oscillations in the numerical solution[2].

[1] The selected problem is two-dimensional.

[2] As for example using Dirichlet conditions for the density on the four boundaries.

Table 1: Boundary conditions

Variable	Domain side			
	Left (Inflow)	Right (Outflow)	Top (Outflow)	Bottom (Inflow)
u	Dirichlet	Neumann	Neumann	Dirichlet
v	Dirichlet	Neumann	Neumann	Dirichlet
ρ	Dirichlet	Neumann	Neumann	Dirichlet
p	Neumann	Dirichlet	Dirichlet	Neumann

3 ReFRESCO Flow Solver

ReFRESCO (www.refresco.org) uses a finite-volume approach with cell-centered collocated variables to discretize the governing equations. A pressure-correction equation based on the SIMPLE algorithm is used to ensure mass conservation. To avoid checkerboard oscillations ReFRESCO uses the pressure-weighted interpolation method described in Miller and Schmidt, 1988. The non-linear system is linearized with Picard's method. In the present work the system of equations is solved in a segregated manner.

3.1 Momentum Equations

The necessary changes in the momentum equation are related to the viscous stress tensor. ReFRESCO uses the finite volume method to discretize the equations so the integral over a control volume of the viscous stress tensor divergence can be divided in an incompressible part and an extra term:

$$\int_{\mathrm{V}} \nabla \cdot \tau d\mathrm{V} = \int_{\mathrm{V}} \underbrace{\nabla \cdot \left(\mu \left(\nabla \overrightarrow{V} + \left(\nabla \overrightarrow{V} \right)^T \right) \right)}_{\text{incompressible part}} d\mathrm{V} + \int_{\mathrm{V}} \underbrace{\nabla \cdot \left(-\frac{2}{3} \mu \left(\nabla \cdot \overrightarrow{V} \right) \mathbf{I} \right)}_{\text{extra term}} d\mathrm{V} \tag{4}$$

ReFRESCO's incompressible solver only takes in consideration the incompressible part, dividing it into two terms. The first term $\int_{\mathrm{V}} \nabla \cdot \left(\mu \nabla \overrightarrow{V} \right) d\mathrm{V}$ is considered in a conservative way (Eq. (5)). The second term is taken care in a non-conservative form and after mathematical manipulation takes the form presented in Eq. (6).

$$\int_{\mathrm{V}} \nabla \cdot \left(\mu \nabla \overrightarrow{V} \right) d\mathrm{V} = \int_{\mathrm{S}} \mu \nabla \overrightarrow{V} \cdot \overrightarrow{n} d\mathrm{S} \tag{5}$$

$$\int_{\mathrm{V}} \nabla \cdot \left(\mu \nabla \overrightarrow{V} \right)^T d\mathrm{V} = \int_{\mathrm{V}} \nabla \mu \cdot (\nabla \overrightarrow{V})^T d\mathrm{V} + \int_{\mathrm{V}} \mu \nabla (\nabla \cdot \overrightarrow{V}) d\mathrm{V} \tag{6}$$

were $\overrightarrow{n}$ is the outer normal to the cell surface.

After mathematical manipulation the extra term in Eq. (4) can be written as:

$$\int_{\mathrm{V}} -\frac{2}{3} \nabla \left(\mu \nabla \cdot \overrightarrow{V} \right) d\mathrm{V} = \int_{\mathrm{V}} -\frac{2}{3} \left\{ \nabla \mu \left(\nabla \cdot \overrightarrow{V} \right) + \mu \nabla \left(\nabla \cdot \overrightarrow{V} \right) \right\} d\mathrm{V} \tag{7}$$

Combining the second term in Eq. (6) with Eq. (7) the terms that have to be introduced are:

$$\int_{\mathrm{V}} -\frac{2}{3} \nabla \mu \left(\nabla \cdot \overrightarrow{V} \right) d\mathrm{V} + \int_{\mathrm{V}} \frac{1}{3} \mu \nabla \left(\nabla \cdot \overrightarrow{V} \right) d\mathrm{V} \tag{8}$$

From the equation above it is possible to see that the terms to be modified require the calculation of the divergence of the velocity and its gradient. The divergence of the velocity is calculated based on the trace of the velocity gradient and the gradient of the divergence of the velocity is calculated using Gauss theorem.

3.2 Pressure Correction Equation for Compressible Flows

The linearized steady, compressible Navier–Stokes equations are solved in a segregated way, i.e., the equations for velocity, pressure correction and energy are solved in turn and when solving for one of the variables the others are considered known.

For the compressible pressure correction method it is assumed that for a given iteration k velocity, density and pressure are known and define a velocity and density prediction, identified with the superscript *, and a velocity, density and pressure correction, identified with the superscript $'$, so that velocity, density and pressure at iteration $k+1$ are:

$$\overrightarrow{V}^{k+1} = \overrightarrow{V}^* + \overrightarrow{V}' \tag{9}$$

$$\rho^{k+1} = \rho^* + \rho' \tag{10}$$

$$p^{k+1} = p^k + p' \tag{11}$$

The velocity prediction at cell P is obtained by solving the discretized momentum equations using the density and pressure from the previous iteration (Eq. 12).

$$\overrightarrow{V}^*_P = \frac{S - \sum_{nb} A^u_{nb} \overrightarrow{V}^*_{nb}}{A^u_P} - \frac{\Delta \mathrm{V}}{A^u_P} \nabla p^k \tag{12}$$

where A^u_p and A^u_{nb} are the coefficients obtained from the discretization of momentum equations for cell P and neighbour cells nb and $\Delta \mathrm{V}$ is the cell volume.

The density prediction is calculated using the equation of state considering pressure and temperature from the previous iteration (Eq. 13).

$$\rho^* = \frac{p^k}{RT^k} \tag{13}$$

The linearized momentum equations are satisfied by the values of velocity and pressure at iteration $k+1$ (Eq. (14)) so:

$$\overrightarrow{V}^{k+1}_P = \frac{S - \sum_{nb} A^u_{nb} \overrightarrow{V}^{k+1}_{nb}}{A^u_P} - \frac{\Delta \mathrm{V}}{A^u_P} \nabla p^{k+1} \tag{14}$$

Subtracting Eq. (14) and Eq. (12) and applying the SIMPLE approximation the velocity correction is obtained:

$$\overrightarrow{V}'_P = -\frac{\Delta \mathrm{V}}{A^u_P} \nabla p' \tag{15}$$

Density correction must also be expressed in terms of the pressure correction. Considering that in each outer iteration temperature is constant, density and pressure correction can be related by:

$$\rho' = \left(\frac{\rho}{p}\right)_T p' = \frac{1}{RT} p' = C_\rho p' \tag{16}$$

Mass conservation at iteration $k+1$ is enforced by calculating the pressure correction from the continuity equation. For a control volume the continuity equation takes the form:

$$\int_{\mathrm{V}} \nabla \cdot \left(\rho \overrightarrow{V}\right) d\mathrm{V} = \int_{\mathrm{S}} \left(\rho \overrightarrow{V}\right) \cdot \overrightarrow{n} \, d\mathrm{S} = \sum_{nf} \left(\rho \overrightarrow{V}\right)_f \cdot \overrightarrow{n}_f S_f = 0 \tag{17}$$

the subscript f represents the value at a cell face and the number of faces in a cell is given by nf.

To avoid checkerboard oscillations related to the use of a collocated grid arrangement the pressure-weighted interpolation method presented in Miller and Schmidt, 1988 is used to interpolate velocity to the cell faces:

$$\overrightarrow{V}_f = \underbrace{\gamma \overrightarrow{V}_1 + (1-\gamma)\overrightarrow{V}_2}_{\overrightarrow{V_f}} + \underbrace{\left\{\gamma \frac{\Delta \mathrm{V}_1}{A^u_1} \nabla p_1 + (1-\gamma) \frac{\Delta \mathrm{V}_2}{A^u_2} \nabla p_2\right\}}_{\overrightarrow{\nabla p_f}} - \underbrace{\left[\gamma \frac{\Delta \mathrm{V}_1}{A^u_1} + (1-\gamma) \frac{\Delta \mathrm{V}_2}{A^u_2}\right]}_{\overline{\Delta \mathrm{V}/A^u}} \nabla p_f \tag{18}$$

where index 1 and 2 represent the cells adjacent to face f and γ is an interpolation factor.

Substituting Eq. (18) in Eq. (17):

$$\sum_{nf} \rho_f \left(\overline{\overrightarrow{V_f}} + \overline{\nabla p}_f - \overline{\frac{\Delta \mathrm{V}}{A^u}} \nabla p_f \right) \cdot \overrightarrow{n}_f S_f = \sum_{nf} \rho_f \overline{\overrightarrow{V_f}} \cdot \overrightarrow{n}_f S_f + \sum_{nf} \rho_f \left(\overline{\nabla p}_f - \overline{\frac{\Delta \mathrm{V}}{A^u}} \nabla p_f \right) \cdot \overrightarrow{n}_f S_f = 0 \quad (19)$$

Replacing Eqs. (9), (10) and (11):

$$\sum_{nf} \left(\rho_f^* + \rho_f' \right) \left(\overline{\overrightarrow{V_f}^*} + \overline{\overrightarrow{V_f}'} \right) \cdot \overrightarrow{n}_f S_f + \sum_{nf} \left(\rho_f^* + \rho_f' \right) \left[\left(\overline{\nabla p^k}_f + \overline{\nabla p'}_f \right) - \overline{\frac{\Delta \mathrm{V}}{A^u}} \left(\nabla p_f^k + \nabla p_f' \right) \right] \cdot \overrightarrow{n}_f S_f = 0 \quad (20)$$

Rearranging the terms in the above equation and neglecting second order terms, i.e. product of corrections:

$$\sum_{nf} \dot{m}_f^* + \sum_{nf} \dot{v}_f^* \rho_f' + \sum_{nf} \rho^* \left[\underline{\overline{\overrightarrow{V_f}'} + \overline{\nabla p'}_f} - \overline{\frac{\Delta \mathrm{V}}{A^u}} \nabla p_f' \right] \cdot \overrightarrow{n}_f S_f = 0 \quad (21)$$

where:

$$\dot{m}_f^* = \rho_f^* \dot{v}_f^* = \rho_f^* \left(\overline{\overrightarrow{V_f}^*} + \overline{\nabla p^k}_f - \overline{\frac{\Delta \mathrm{V}}{A^u}} \nabla p_f^k \right) \cdot \overrightarrow{n}_f S_f \quad (22)$$

The underline term represents the effect of the neighbour cells. When considering the SIMPLE approximation for the relation between pressure and velocity corrections (Eq. (15)) this term cancels out.

Substituting the density correction (Eq. (23)) an equation for pressure correction is obtained:

$$\sum_{nf} \dot{v}_f^* C_\rho p_f' - \sum_{nf} \rho^* \overline{\frac{\Delta \mathrm{V}}{A^u}} \nabla p_f' \cdot \overrightarrow{n}_f S_f = - \sum_{nf} \dot{m}_f^* \quad (23)$$

For the case of compressible flow the pressure correction equation is no longer a Poisson equation, but a convection-diffusion equation. The first term in the left hand side corresponds to the convective part and the second to the diffusion term. The boundary conditions in the pressure correction equation are applied in the same way they would be in a general convection diffusion equation, but considering that the field is zero at the beginning of every iteration, i.e., boundary terms that for a general variable would appear in the right hand side vanish.

3.3 SIMPLE algorithm

Having determined the new momentum and pressure correction equations the prediction and correction steps in the SIMPLE algorithm are as follows:

1. Assemble and solve Eq. (12) to obtain a velocity prediction, $\overrightarrow{V}^*$;
2. Assemble and solve the pressure correction equation (Eq. (23));
3. Update[3] velocity, pressure and density using the corrections obtained from Eqs. (15), (23) and (16), respectively;
4. Update mass flux using $\dot{v}_f^* \rho_f' - \rho^* \left(\overline{\Delta \mathrm{V}/A^u} \right) \nabla p_f' \cdot \overrightarrow{n}_f S_f$;
5. Calculate volume fluxes;
6. Solve energy equation (in the present work this equation is not solved and it is replaced by the use of the exact temperature)
7. Calculate density at cell centres and interpolate for cell faces, to obtain ρ^* and ρ_f^*.

These steps are repeated until convergence is obtained.

[3] Under-relaxation may be applied.

4 Code Verification

Several authors, Roache, 2002, Roy et al., 2002, Veluri et al., 2010, Eça et al., 2012, define code verification as a mathematical exercise that aims at ensuring that a certain computer code is free of coding mistakes. In the present code verification exercise code correctness is evaluated using the order-of-accuracy test. In this test the discretization error must tend to zero with an observed order of convergence similar to the formal order of the numerical scheme applied, which in the present flow solver is equal to 2.

This test requires the calculation of the discretization error, so the exact solution of the governing equations must be known, which is guaranteed by the use of a manufactured solution, Roache and Steinberg, 1984. The manufactured solution used in the present work is based on the work of Roy et al., 2002 and Eça et al., 2012. The analytical solution for a variable ϕ takes the form presented in Eq. (24),

$$\phi(x,y) = \phi_0 + \phi_x f_{s,x}\left(\frac{a_{\phi x}\pi x}{L}\right) + \phi_y f_{s,y}\left(\frac{a_{\phi y}\pi y}{L}\right) + \phi_{xy} f_{s,xy}\left(\frac{a_{\phi xy}\pi xy(x-1)(y-1)}{L^4}\right), \tag{24}$$

where f represents a sine or cosine function, ϕ_0, ϕ_x, ϕ_y, ϕ_{xy}, $a_{\phi x}$, $a_{\phi y}$ and $a_{\phi xy}$ are constants.

The constants and functions that define ρ, u, v and p are given in Table 2, which also presents the fluid properties γ, R, μ and Pr. Temperature is calculated from the equation of state (Eq. (3)). These constants were chosen so different terms in the transport equation are of the same order of magnitude. The functions, f_s, were selected so that the normal derivative to boundaries where Neumann boundary condition is applied is zero. This choice of flow variables leads to a Mach number between 0.32 and 0.52.

Table 2: Constants and function for manufactured solutions and fluid properties

Variable	ϕ_0	ϕ_x	ϕ_y	ϕ_{xy}	$f_{s,x}$	$f_{s,y}$	$f_{s,xy}$	$a_{\phi x}$	$a_{\phi y}$	$a_{\phi xy}$
ρ [kg/m^3]	1	0.1	0.15	-0.08	sin	sin	cos	0.5	0.5	0.5
u [m/s]	30	4	-12	7	sin	sin	cos	0.5	0.5	0.5
v [m/s]	38	-20	4	-11	sin	sin	cos	0.5	0.5	0.5
p [Pa]	1×10^4	-0.3×10^4	0.2×10^4	-0.25×10^4	cos	cos	cos	0.5	0.5	0.5
Fluid Properties:	$\gamma = 1.4$, $R = 287m^2/(s^2K)$, $\mu = 100kg/(ms)$ and $Pr = 10$									

5 Results

The determination of the observed order of grid convergence, p_o, was performed for a set of six equally spaced Cartesian grids, with the finest grid including 256^2 cells and the coarsest 8^2 cells. The correct determination of the observed order of grid convergence requires the iterative error to be negligible when compared to the discretization error. Therefore, the maximum values of the residuals of all the equations solved was reduced to values close to machine accuracy. Figure 1a (left plot) illustrates the iterative convergence of u, v and p in the finest grid tested (256^2 cells).

Table 3 presents the observed order of grid convergence and Figure 1b (right plot) presents the L_∞ norm of the discretization error of u, v and p as a function of the cell size h_i/h_1. The results exhibit the expected second-order of grid convergence.

Table 3: Observed order of grid convergence, p_o

Number of Cells	L_2			L_∞		
	u	v	p	u	v	p
16^2	2.00	2.00	2.00	1.94	1.96	1.91
32^2	2.00	2.00	2.00	1.97	1.98	2.32
64^2	2.00	2.01	2.00	1.99	1.99	2.01
128^2	2.00	2.01	2.00	1.99	2.00	2.01
256^2	2.02	2.06	2.00	2.02	2.08	2.01

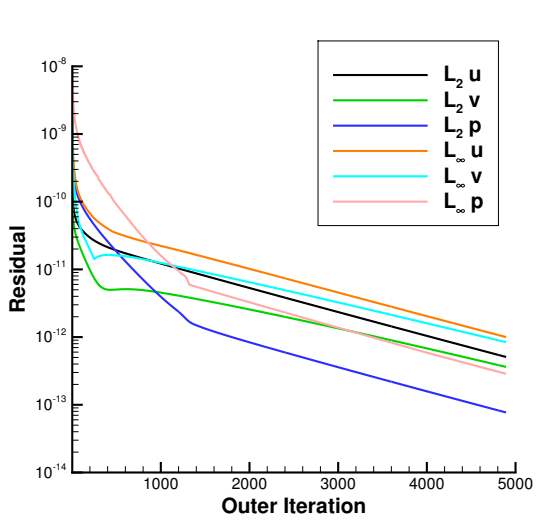

(a) L_2 and L_∞ norms of the residuals.

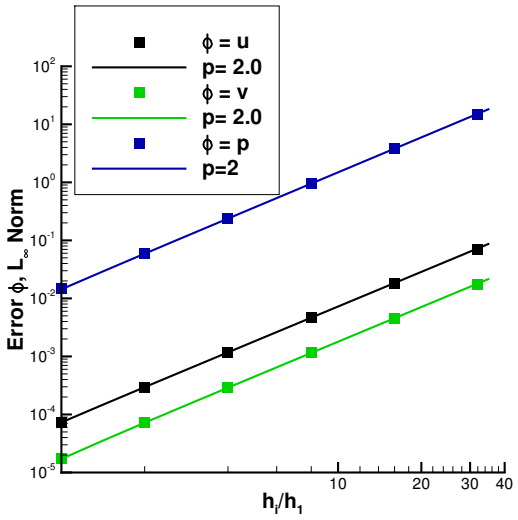

(b) L_∞ norm of the discretization error as function of h_i/h_1.

Fig. 1: Iterative convergence for the grid with 256^2 cells and grid convergence of the L_∞ error norm.

6 Conclusion

The present paper describes the modification of ReFRESCO to solve compressible flows of perfect gases. It contains a code verification exercise for a manufactured solution of a two-dimensional subsonic flow.

The present work demonstrated second-order grid convergence for all flow variables. However, such results depend on the selection of a consistent set of boundary conditions to avoid spurious oscillations in the numerical solutions that deteriorate the order of grid convergence.

Acknowledgements

This research is partly funded by the Dutch Ministry of Economic Affairs.

References

Eça, L., Hoekstra, M., and Vaz, G. (2012). Manufactured solutions for steady-flow Reynolds-averaged Navier-Stokes solvers. *International Journal of Computational Fluid Dynamics*, 26(5):313–332.

Ferziger, J. H. and Perić, M. (2001). *Computational Methods for Fluid Dynamics*. Springer-Verlag GmbH, 3rd edition.

Miller, T. F. and Schmidt, F. W. (1988). Use of a Pressure-Weighted Interpolation Method for the Solution of the Incompressible Navier-Stokes Equations on a Nonstaggered Grid Systam. *Numerical Heat Transfer: An International Journal of Computation and Methodology*, 14(2):213–233.

Roache, P. J. (2002). Code Verification by the Method of Manufactured Solutions. *Journal of Fluids Engineering*, 124(1):4.

Roache, P. J. and Steinberg, S. (1984). Symbolic manipulation and computational fluid dynamics. *AIAA journal*, 22(10):1390–1394.

Roy, C. J., Smith, T. M., and Ober, C. C. (2002). Verification of a Compressible CFD Code Using the Method of Manufactured Solutions. In *32nd AIAA Fluid Dynamics Conference and Exhibit*, pages 1–14.

Veluri, S., Roy, C., and Luke, E. (2010). Comprehensive Code Verification for an Unstructured Finite Volume CFD Code. *48th AIAA Aerospace Sciences Meeting Including the New Horizons Forum and Aerospace Exposition*.

Numerical study of hull pressures induced by a cavitating propeller

Carlo Negrato[*†], **Tom van Terwisga**[ш], **Rickard Bensow**[*]
[*]Chalmers University of Technology, Gothenburg/Sweden;
[†]MARIN Academy, [ш]MARIN, Wageningen/Netherlands.
negrato@chalmers.se

1 Introduction

Following the disinction made by Carlton (2007), the interaction between the ship and the propeller can be split into the mechanical loads transmitted through the shaft and the hydrodynamic loads transmitted through the surrounding water. While the mechanical loads correspond to the bearing forces, the hydrodynamics loads result from the integration of the pressures on the hull surface. Additionally, the fluctuating components are the primary concern; the reason is that periodic propeller-induced forces can excite structural vibrations, which affect comfort on-board and structural integrity.

When considering the hydrodynamic interaction, the pressure fluctuations are induced by the propeller, which is rotating in the vicinity of the hull. For the cavitating condition, the pulsating sheet cavity and the tip vortex dynamics are known to provide large contributions to the induced pressures (Van Wijngaarden (2011) , Bosschers (2009)). Since modern propellers are designed to work under cavitating condition to achieve high efficiency, there is the need to address the problem at the design stage. To do so, model-scale testing is possible in cavitation tunnel or depressurized water basins; one example is given by Pereira et al. (2016). On the other hand, computational fluid dynamics allows for model scale and full scale predictions, Berger et al. (2016).

The scope of this study is to validate the prediction of propeller-induced hull-pressure fluctuations for a model scale container vessel, using a multi-phase viscous flow solver to simulate the flow dynamics. The investigation is limited to model scale and emphasis is given to the accuracy in the prediction of pressure fluctuations at higher harmonics.

2 Test case

The vessel used for this study was tested in the HYKAT cavitation tunnel of HSVA as part of the European project SONIC. The ship geometry is a variant of the container vessel originally used in the VIRTUE project; the full scale characteristics and operating condition are listed in Table 1. The free surface was substituted by wooden plates, which required an adjustment of the draft to compensate for the boundary layer growth at the tunnel ceiling. The operating condition is set to fullfill identity of thrust coefficient and cavitation number (evaluated at 80% of the propeller radius). Thirteen pressure probes are located on the hull, in the vicinity of the propeller plane, as shown in Figure 1. On the basis of the model test and the earlier numerical study of Ge et al. (2018), unsteady tip vortex cavitation is expected, with large amplitudes of pressure fluctuations corresponding to the first, second and third harmonics of the blade passage frequency.

3 Numerical framework

3.1 Flow solver

The flow solver used in this study is ReFRESCO (`http://www.refresco.org/`), developed at the Maritime Research Institute of the Netherlands (MARIN). The flow modeling relies on the unsteady, incompressible Reynolds Averaged Navier-Stokes equations. For the multi-phase flow, a homogeneous-mixture approach is employed, where the mass transfer term in the volume fraction equation is given by the Sauer(2000) model. For turbulence closure, a standard $k-\omega SST$ model and a scale-adaptive $k-\sqrt{kL}$ model are tested. Finally, a moving-grid approach with sliding interface is adopted to deal with the propeller rotation.

Ship data		
Length	L_{pp} [m]	232
Draft	T [m]	11.3
Scale ratio	λ[-]	29.1
Propeller data		
Diameter	D_P [m]	7.9
Number of blades	Z [-]	5
Tip clearance	[m]	2.19
Operating conditions		
Thrust coefficient	K_T [-]	0.2234
Rotational speed	n [rpm]	95.3
Cavitation number	σ_n	0.2354

Table 1: Main characteristics of the test case.

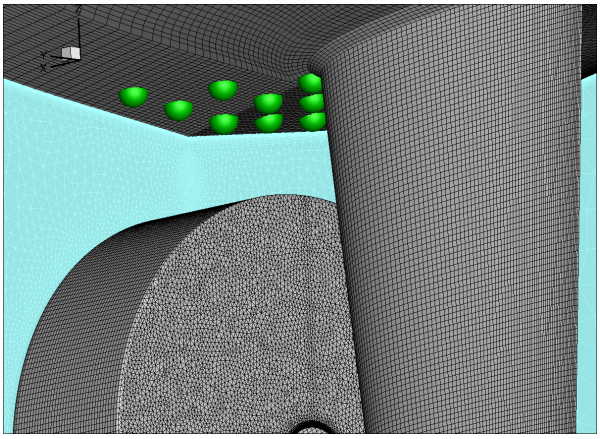

Fig. 1: Location of the pressure probes.

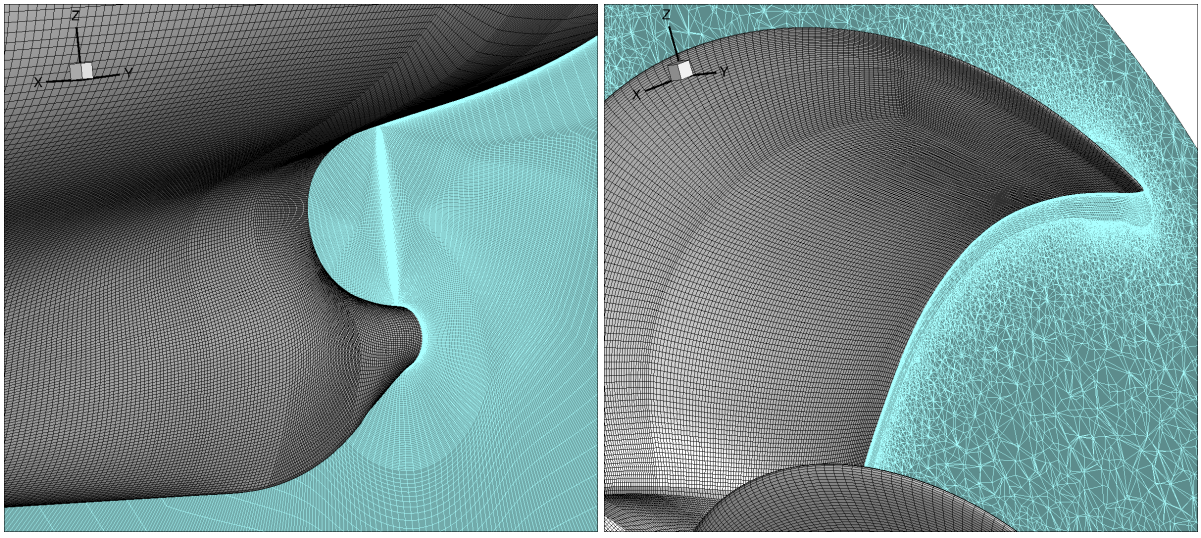

(a) Block with structured grid upstream of the propeller. (b) Hybrid grid topology at the propeller region.

Fig. 2: Overview of the mesh for the aft-ship and the propeller blocks. The surface mesh is shown in black, while in cyan cross-plane cuts are plotted.

3.2 Grid design

The geometry of the cavitation tunnel is discretized using a multi-block topology generated in Pointwise. Along the hull, in longitudinal direction, four blocks are present: one block encloses the bulbous bow and the immediate bow sections; two blocks are used for the mid ship, and one more block is used for the stern. The two blocks at mid-ship have structured grids (Figure 2a) while close the bow and close to the propeller a hybrid topology is introduced. The hybrid topology is a combination of structured cells in the boundary layer region and unstructured - tetrahedral - cells in the remaining volume. In addition to the four hull blocks, a fifth block is defined around the propeller; the boundary of the propeller block is a sliding-interface and the topology is hybrid, as shown in the close-up of Figure 2b.

The total number of cells is approximately 25M, of which about 9.4M for the propeller. Regarding the near-wall resolution, the boundary layer on the ship, the propeller and the rudder is fully resolved, with a target $y^+ = 1$. Contrarily, at the upper, lower and side walls of the cavitation tunnel, slip velocity is allowed, in order to decrease the computational cost. While a slip-wall condition is reasonable for the side and bottom walls, the effect of lacking the boundary layer at the upper wall should be looked into.

4 Present work

At the present time, the setup of the simulations is ongoing, hence there are no sensible results to show in this abstract to-date. As stated in the introduction, the aim of this work is validation of pressure pulse levels within the limitations of our computational approach. And much of the interest is directed towards the capability to predict higher harmonic components.
For completeness, the authors also plan to analyze the unsteady propeller cavitation with the modal decomposition technique employed in our previous work (Negrato(2017)). An anticipation of such study might also be given in the context of this paper.

Acknowledgements
Special thanks goes to Muye Ge (Chalmers University of Technology) for sharing the computational mesh and Bram Starke (MARIN) for his support on simulating unsteady propeller cavitation with Re-FRESCO.

References

J.S. Carlton. *Marine Propellers and Propulsion.* Second Edition, Elsevier Ltd (2007).

H. C. J. Van Wijngaarden. *Prediction of Propeller-Induced Hull-Pressure Fluctuations.* PhD thesis, Technical University of Twente (2011).

J. Bosschers. *Investigation of hull pressure fluctuations generated by cavitating vortices.* First International Symposium on Marine Propulsors, Trondheim, Norway (2009).

F. A. Pereira, F. Di Felice and F. Salvatore. *Propeller Cavitation in Non-Uniform Flow and Correlation with the Near Pressure Field.* J. Mar. Sci. Eng. 4, 70 (2016).

S. Berger, M. Bauer, M. Druckenbrod and M. Abdel-Maksoud. *Investigation of Scale Effects on Propeller-Induced Pressure Fluctuations by a Viscous/Inviscid Coupling Approach.* Third International Symposium on Marine Propulsors, Launceston, Australia (2013).

M. Ge, R. Bensow and U. Svennberg. *Investigation on Numerical Prediction of Propeller Induced Hull Pressure Pulses.* Tenth International Symposium on Cavitation, Baltimore, Maryland, USA (2018).

J. Sauer. *Instationär Kavitierende Strömungen - Ein neues Modell, basierend auf Front-Capturing(VoF) und Blasendynamik.* PhD Thesis, University of Karlsruhe, Germany (2000).

C. Negrato, T.van Terwisga and R. Bensow. *Analysis of hydrofoil cavitation using Proper Orthogonal Decomposition.* Numerical Towing Tank Symposium , NuTTS (2017).

On the estimation of discretization and modeling errors and their interaction

Milovan Perić, CoMeT Continuum Mechanics Technologies GmbH, Erlangen/Germany, milovan@comet-cfd.de

Numerical solutions of fluid flow and related phenomena are affected by three systematic error kinds, due to (i) iterations, which have to be stopped at some stage, (ii) discretization, because we are solving discrete approximations of governing equations, and (iii) modeling, because the original equations are not exact (e.g. due to turbulence and cavitation models). When solving engineering problems, it is important to estimate the contribution of each individual error component and thus be able to give a reliable estimate of the accuracy of solution. This is not a simple task, because the equations being solved are highly non-linear and errors from different sources influence each other: they may augment, but also partially cancel each other. It will be assumed here that iteration errors are kept under control, so the discussion will be limited to discretization and modeling errors.

Discretization errors are usually estimated by analyzing grid-dependence of solutions and using Richardson-extrapolation:

$$\varepsilon_h = (\phi_h - \phi_{rh})/(r^p - 1) \quad ,$$

where ε_h is the discretization error estimate for the grid with spacing h, ϕ_h is the solution obtained using grid with spacing h, ϕ_{rh} is the solution obtained using the next coarser grid with spacing rh (r being the refinement factor; it is usually chosen to be 1.5 or 2) and p is the representative order of approximation.

For steady-state laminar flows, for which modeling errors can be considered negligible, one usually obtains solutions which converge towards the so-called "grid-independent solution" with expected order (typically second, when the usual approximations are used: midpoint-rule integral approximation, central-difference approximation of gradients, and linear interpolation). This is demonstrated in Figs. 1 – 3 for the laminar flow around a circular cylinder at the Reynolds number Re = 20. The errors were estimated separately for the pressure and shear component of the drag force; both show convergence with second order, i.e. when the grid spacing is reduced one order of magnitude, the discretization error is reduced two orders of magnitude. In this case structured grids were used, but similar results are obtained with unstructured grids as well – as long as they are systematically refined (i.e. grid design and local refinements are kept unchanged, only the cell size is reduced everywhere by the same factor).

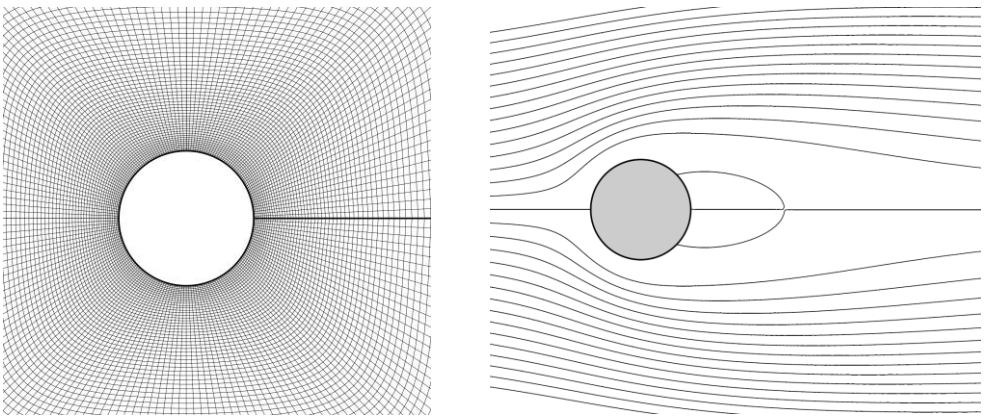

Fig. 1: Computational grid at level 4 (left) and computed streamlines (right) for the flow around circular cylinder at Re = 20.

In order to be able to reliably estimate modeling errors, one needs to have accurate information about the real flow. Such information is usually not available (especially not at full scale), which is why modeling errors are difficult to estimate. Accurate data from experiments at model scale is essential for the analysis of modeling errors in CFD-simulations; one hopes that modeling errors remain of the same order relative to discretization errors when simulations are performed at full scale. This is often the case

– but not always; since most experiments in shipbuilding are conducted at the same Froude number in model and full scale, the Reynolds numbers are different – significantly lower at model than at full scale. It is not unusual that some phenomena occur in model scale that are not present at full scale, or vice-versa (usually associated with flow separation and unsteadiness).

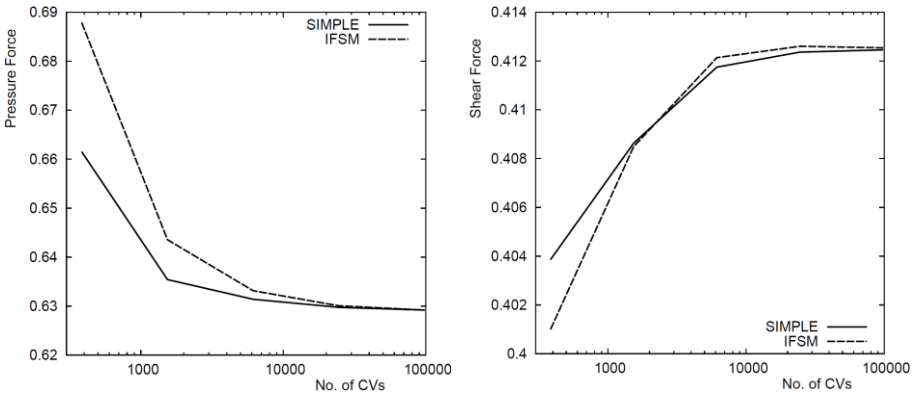

Fig. 2: Convergence of pressure (left) and shear (right) drag force on circular cylinder at Re = 20 when the grid is systematically refined by halving the grid spacing in both directions; results are shown for two solution methods. Note that coarser grids *overestimate* the pressure and *underestimate* the shear stress contribution.

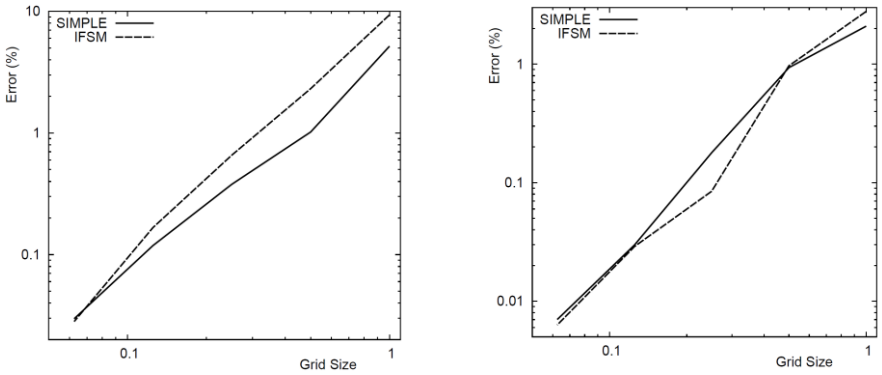

Fig. 3: Reduction of discretization errors with grid refinement (estimated using Richardson extrapolation) for pressure (left) and shear (right) drag force on circular cylinder at Re = 20.

When turbulent flows at high Reynolds numbers are computed, the situation is much more complicated. Turbulence models are employed to enable computation of mean values of variables using Reynolds-averaged Navier-Stokes Equations (RANSE), without resolving the turbulent fluctuations in space and time. This is necessary because neither direct (DNS) nor large-eddy simulation (LES) is possible at full scale using the present-day computing resources. Even at model scale one needs around 100 billion grid points to be able to perform a decent LES. RANSE-models introduce turbulent viscosity which varies by up to 5 orders of magnitude within the solution domain, thus increasing the non-linearity of equations. Especially the turbulent kinetic energy and its dissipation rate (which are the typical variables in turbulence models) show pronounced peaks in their profiles across boundary and shear layers, which requires a careful design of computational grid using local refinement where high rates of variation in variables and their gradients are expected. Failure to adapt the grid to solution may result in wrong conclusions from a grid-dependence study, as will be demonstrated below.

Estimation of discretization and modeling errors when solving RANSE is difficult for another reason: the two kinds of errors interact and influence each other. When the grid is not fine enough, some of the modeled physics may not be represented well enough (e.g., cavitation in a tip vortex of a propeller). By comparing solutions on a series of grids it may appear that discretization errors are small, and by comparing the results from the finest grid with experimental data one may conclude that modeling errors are large. However, when the grid is adequately locally refined so that tip vortex is significantly better

resolved, the modeling error (in this case the combined turbulence and cavitation model effects) may turn out to be much smaller, while the discretization errors from previous grids may turn out to be larger than initially concluded. This is demonstrated below for a cavitating flow around propeller.

Another source of difficulty with RANSE are wall boundary conditions. At high Reynolds numbers, wall functions are usually used since resolving the near-wall laminar sublayer may be prohibitively expensive in terms of the required number of cells and computing time. However, when wall functions are used and the grid is refined, the boundary conditions effectively change: we do not use a fixed condition at boundary, but rather a floating condition which relates wall shear stress with the velocity at the next-to-wall grid point, assuming that it is within the logarithmic boundary layer range and that the so-called "log-law" is valid. While the log-law is reasonably well valid in case of flow over a flat plate, in a plane channel or a straight pipe, it is not as well valid on curved surfaces, exhibiting pressure gradients both along and normal to wall. Thus, as the first grid point next to wall moves, the boundary condition also changes and the results obtained from grid-dependence studies may not show the expected convergence rate, making the use of Richardson extrapolation less reliable or even impossible.

These aspects will be demonstrated by studying the flow around a propeller in open-water test condition, i.e., the propeller is operating in a uniform flow, rotating at a fixed, prescribed rate. Under these conditions one can study the flow around a single propeller blade, using periodic boundary conditions in circumferential direction and the rotating frame of reference. This reduces computational cost and allows the use of much finer grids than would be possible if the ship and rudder were included, in which case the whole propeller has to be included in the simulation and the grid attached to propeller has to move, requiring the use of either a sliding interface or overlapping grids. The propeller is the one used at the **smp'11** workshop; the operating conditions are from the cavitating test case (Propeller VP1304 from SVA Potsdam, test case 2.3.1; see workshop proceedings for a detailed description of the test case). Since the propeller is at model scale (the diameter is 250 mm), both wall functions and the so-called "low-Re" approach (with the first computational point being within the laminar sublayer, around y^+ = 1) are tested. Unstructured grids with local refinements are used; for each test case, three systematically refined grids with a refinement factor 1.5 are used. Both non-cavitating and cavitating conditions are considered. No attempt is made to determine the so-called "grid-independent solution"; the results of test calculations are used to demonstrate the difficulties in performing grid-dependence studies due to grid quality and wall boundary conditions.

The commercial software STAR-CCM+ from Siemens was used, but similar results would most probably be obtained with other codes using the same grids and boundary conditions. The grids were automatically created using locally refined Cartesian control volumes which are trimmed by an offset boundary surface; between this surface and the wall boundary, prismatic cells are created (so-called "prism layers"). The total thickness of these layers can be either a function of the reference mesh unit ("base size") or prescribed independently. The number of prism layers is prescribed by the user; in addition, either the stretching factor (thickness of one layer divided by the thickness of the preceding layer) or the thickness of the first layer next to wall is specified. Outside prism layers, the grid spacing is defined as a function of the base size, so that a systematic grid refinement is easily achieved by just reducing the base size by a factor of 1.5.

For the non-cavitating condition, six sets of three grids were created. In all sets, the base size was 22.5 mm for the coarsest grid, 15 mm for the medium grid and 10 mm for the finest grid. Figure 4 shows the medium grid in one longitudinal section and one cross-section.

In the first set, 6 prism layers were created and the thickness of all prism layers was set to 5% of base size; the stretching factor was set to 1.25. In the second set, the thickness of prism layers was set to 10% of base size (twice the value from the first set – everything else being the same). In the third set, the thickness of all 6 prism layers was also 10% of base size, but the thickness of the first prism layer next to wall was fixed to 0.13 mm and is kept the same for all three grids; the stretching factor thus varies from one grid to another. In the fourth set, the thickness of all 6 prism layers was fixed to 1.5 mm, and

the thickness of the first prism layer next to wall was fixed to 0.13 mm. Thus, prism layers remain of the same thickness in all grids; the refinement inside prism layers is only performed in wall-tangential direction, while outside prism layers, the grid is refined in all three directions. The fifth set contains only the medium grid; it is the same as the one from the fourth set, except that the minimum surface element size on propeller blade was reduced from 0.2% of base size to 0.1%, and the resolution of boundary curvature was also doubled – from 16 points on a circle to 32 points. Finally, in the sixth set, 15 prism layers were created in all three grids; the thickness of all prism layers was set to 10% of base size, but the first layer next to wall was fixed to 3 μm on the blade and 10 μm on the hub. The predicted thrust and torque for all grids in all sets are summarized in Tables 1 to 6.

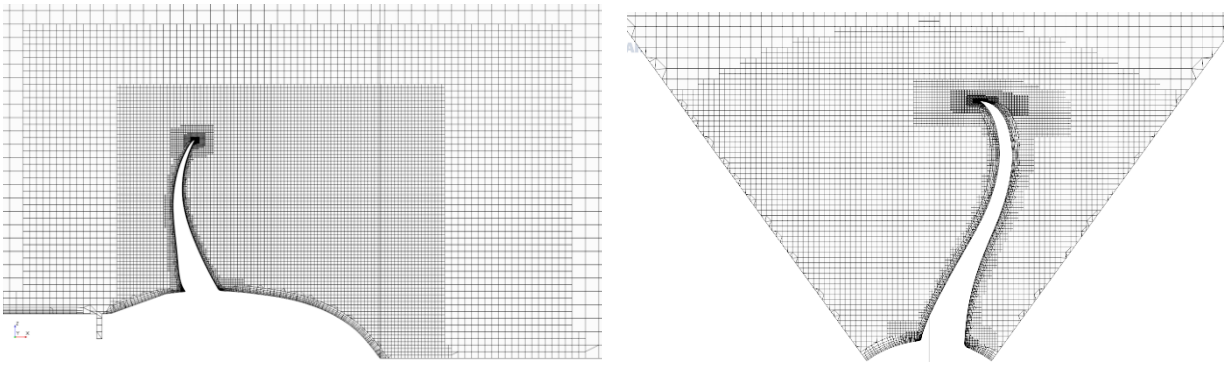

Fig. 4: Medium grid around propeller blade: longitudinal section at $y = 0$ (left) and cross-section at $x = 0$ (right), showing grid design and local refinements. The solution domain is substantially larger in axial and radial direction.

Table 1: Number of control volumes, predicted thrust and torque and the average y^+ for three systematically refined grids from the first set (thickness of all 6 prism layers 5% of base size, stretching factor 1.25).

	Coarse (C)	Medium (M)	Fine (F)	Difference M-C	Difference F-M
No. of cells	864,209	1,570,014	3,418,747		
Thrust (N)	177.70	179.04	177.50	1.34 (0.75%)	-1.54 (-0.87%)
Torque (Nm)	11.728	11.801	11.695	0.073 (0.62%)	-0.106 (-0.91%)
Average y^+	36	24	16		

Table 2: Number of control volumes, predicted thrust and torque and the average y^+ for three systematically refined grids from the second set (thickness of all 6 prism layers 10% of base size, stretching factor 1.25).

	Coarse (C)	Medium (M)	Fine (F)	Difference M-C	Difference F-M
No. of cells	802,772	1,481,282	3,307,767		
Thrust (N)	177.35	177.25	179.20	-0.1 (-0.06%)	1.95 (1.2 %)
Torque (Nm)	11.704	11.670	11.760	-0.034 (-0.30%)	0.09 (0.77%)
Average y^+	74	50	34		

Table 3: Number of control volumes, predicted thrust and torque and the average y^+ for three systematically refined grids from the third set (thickness of all 6 prism layers 10% of base size, first layer 0.13 mm).

	Coarse (C)	Medium (M)	Fine (F)	Difference M-C	Difference F-M
No. of cells	794,563	1,456,147	3,276,576		
Thrust (N)	177.65	177.60	177.25	-0.05 (-0.03%)	-0.35 (-0.2 %)
Torque (Nm)	11.695	11.680	11.644	-0.015 (-0.13%)	-0.036 (-0.31%)
Average y^+	45	45	45		

In all cases from Tables 1 to 5, the *k-ω* SST turbulence model with wall functions (the so-called "all-y^+"-version) was used. One would expect that the difference between solutions obtained on fine and

medium grid is smaller than the difference between medium and coarse grid; this would indicate convergence towards grid-independent solution and, for the refinement factor of 1.5, the ideal ratio between the two differences (fine – medium vs. medium – coarse) would be 2.25 for a second-order method. As one can see from Table 1, this is not the case for the chosen variation of the prism layer: the thrust and torque computed on the medium grid are larger than the values from coarse grid, but the values from the fine grid are smaller than those obtained on the coarse grid! The reason lies in the fact that the prism layers are relatively thin and the first computational point next to blade wall falls into the buffer layer when the grid is refined, as indicated by the average y^+-values on the fine grid around 16. Using the "all-y^+"-version of wall functions is better than using the high-Re-version when y^+-values are in this intermediate range, but it is still better to ensure that, when wall functions are used, the y^+ lies above 30 over most of the wall surface in any grid.

Table 4: Number of control volumes, predicted thrust and torque and the average y^+ for three systematically refined grids from the fourth set (thickness of all 6 prism layers 1.5 mm, first layer 0.13 mm).

	Coarse (C)	Medium (M)	Fine (F)	Difference M-C	Difference F-M
No. of cells	829,752	1,456,142	3,223,357		
Thrust (N)	177.70	177.65	177.50	-0.05 (-0.03%)	-0.15 (-0.09 %)
Torque (Nm)	11.690	11.686	11.656	-0.004 (-0.03%)	-0.03 (-0.26%)
Average y^+	45	45	45		

Table 5: Number of control volumes, predicted thrust and torque and the average y^+ for the medium grid from the fifth set (minimum surface element size reduced from 0.2% to 0.1% of base size; curvature resolution increased from 16 points on circle to 32 points).

	Coarse (C)	Medium (M)	Fine (F)	Difference to M from Table 4
No. of cells	-	2,164,413	-	
Thrust (N)	-	176.10	-	-1.55 (-0.88%)
Torque (Nm)	-	11.548	-	-0.138 (-1.2%)
Average y^+	-	45	-	

In the case presented in Table 2, prism layers are twice as thick as in the first case. Now the computational points near wall are always at y^+-values greater than 30, but the variation in computed thrust and torque is still not monotone and one cannot use Richardson extrapolation to estimate grid-independent solution. One of the reasons is that, when wall functions are used and the computational points next to wall are moved as the grid is refined, the boundary conditions are effectively changing (especially because the standard log-law is strictly speaking not valid over large part of propeller blade surface due to strong pressure and velocity variation in all directions).

Table 3 presents results obtained when the first prism layer has the same thickness in all three grids. This makes things a little bit better: now the variation in predicted thrust and torque is monotone, but still not perfect: the difference between solutions obtained on fine and medium grid is larger than between solutions from medium and coarse grid. When the thickness of all prism layers is kept fixed during grid refinement (see Table 4), the variation is monotone but still not as expected. The cause might lie in the change of boundary conditions with grid refinement for another reason: better resolution of leading-edge curvature by finer grids and thus effectively changing the geometry of the solution domain. As can be seen from Table 5, the change in grid generation parameters affecting curvature resolution leads to a substantial increase in cell count and also to significantly lower values of predicted thrust and torque. Thus, when the geometry is complex, finer grids represent not only smaller cell sizes but also a different (more accurate) representation of the solution domain geometry. Only when the unique boundary conditions (no-slip) at walls are used, i.e. y^+-values are around 1, the expected monotone convergence is obtained (see Table 6). This approach, however, is not practical for full-scale analysis, since it requires excessively large number of cells.

Table 6: Number of control volumes, predicted thrust and torque and the average y^+ for three systematically refined grids from the sixth set (thickness of all 15 prism layers 10% of base size, first layer 3 µm).

	Coarse (C)	Medium (M)	Fine (F)	Difference M-C	Difference F-M
No. of cells	1,310,622	2,207,078	4,358,444		
Thrust (N)	180.45	181.04	181.08	0.59 (0.33%)	0.04 (0.02 %)
Torque (Nm)	11.745	11.754	11.760	0.009 (0.08%)	0.006 (0.05%)
Average y^+	1	1	1		

Table 7: Number of control volumes, predicted thrust and torque and the average y^+ for the medium grid from Table 5 and for the same grid with additional local refinement within tip vortex zone; cavitating flow.

	Medium (M)	M with local refinement (R)	Difference R-M
No. of cells	2,164,413	3,810,773	
Thrust (N)	176.5	176.1	-0.4 (-0.23%)
Torque (Nm)	11.600	11.564	-0.036 (-0.31%)
Average y^+	45	-	

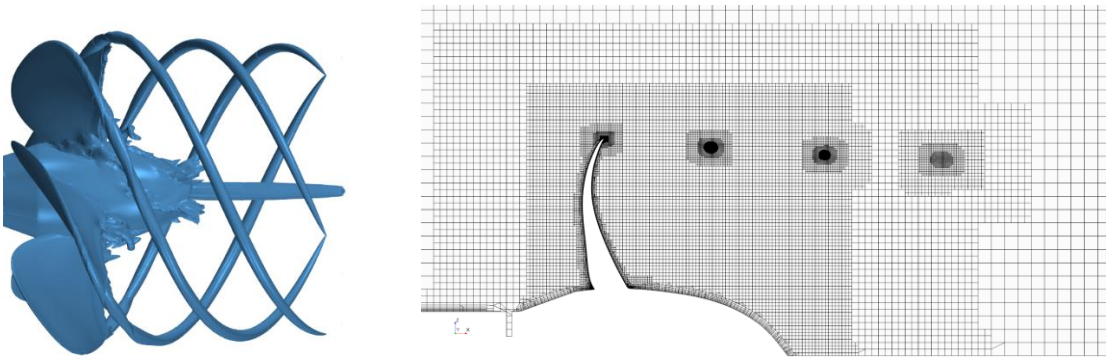

Fig. 5: Iso-surface of vorticity magnitude (left), used to determine the local refinement zones for tip vortex shown in the longitudinal section through the grid (right).

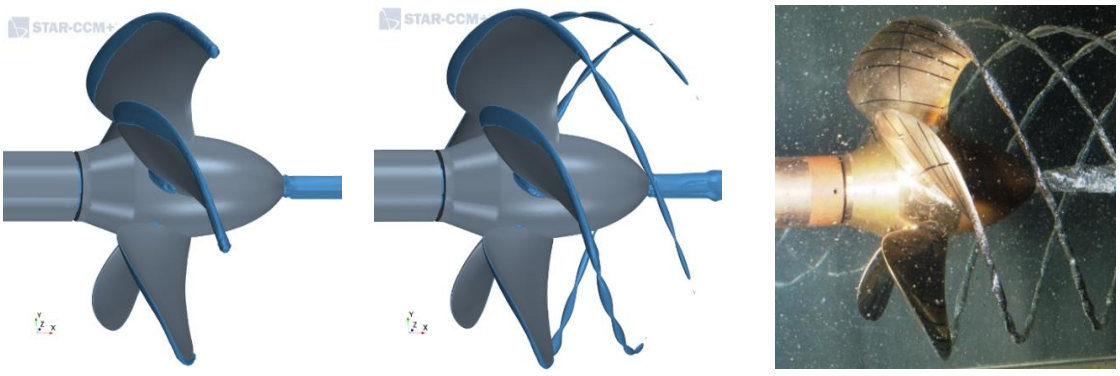

Fig. 6: Iso-surface of vapor volume fraction of 0.05 computed on medium grid from Table 5 without (left) and with (middle) local refinement to capture tip vortex cavitation, compared to visualization of tip vortex cavitation in experiment at SVA Potsdam (right).

When the cavitating flow is computed using the grid from Table 5, no cavitation in tip vortex is obtained (see Fig. 6, left picture). This might lead to the conclusion that the deficiency of cavitation model is the cause, since discretization errors appear small (results from all grids differ by max. 1%). However, using the computed distribution of vorticity magnitude to guide local grid refinement (see Fig. 5), a good portion of tip-vortex cavitation becomes visible in simulation (Fig. 6, middle picture), which compares well with visualization from experiment (Fig. 6, right picture).

Influence of Choice of Boundary Treatment for 3D Flow Simulations with Free-Surface Waves

Robinson Perić and Moustafa Abdel-Maksoud
Institute for Fluid Dynamics and Ship Theory, Hamburg University of Technology (TUHH), Am Schwarzenberg-Campus 4, 21073 Hamburg, Germany
robinson.peric@tuhh.de

1 Introduction

Undesired wave reflections in flow simulations can be reduced by attaching forcing zones to the domain boundaries. Within the forcing zones, the flow is gradually forced towards a reference solution. Forcing zones have three case-dependent parameters: the source term strength γ, which regulates the magnitude of the source term, the blending function $b(\tilde{x})$, which regulates how the source term strength varies within the zone, and the zone thickness x_d. The optimum parameters can be tuned using analytical predictions (Perić and Abdel-Maksoud, 2018a); a code for evaluating the theory was published as free software under the link `https://github.com/wave-absorbing-layers/absorbing-layer-for-free-surface-waves`. In practice, different reference solutions may be used, and forcing may be applied to different governing equations. Both choices influence the behavior of the forcing zone.

If the reference solution is the calm free-surface, then the forcing acts like damping and damps out the waves; such approaches have been called e.g. wave damping zone (e.g. Park et al., 1999), sponge layer (e.g. Choi and Yoon, 2009), absorbing layer (e.g. Wei et al., 1999), or dissipation zone (Park et al., 1993). Applying the source terms to only one governing equation will already suffice to damp the whole wave, i.e. the source term in one governing equation acts also on the other governing equations. However, the choice of governing equation can – especially for greater source term magnitudes – influence the damping behavior (Perić and Abdel-Maksoud, 2018a).

While damping the whole wave works fine for the outlet boundary, it is not a suitable choice for the inlet boundary where the waves are generated. Therefore, recently an increasing number of researchers apply forcing zones at all vertical domain boundaries, and force all governing equations to the reference solution for the far-field wave. Thus all boundaries may act as 'wave-makers' while at the same time reducing undesired wave reflections; such approaches have also been called relaxation zones and have been shown to give satisfactory results for several flow problems, see e.g. Chen et al. (2006), Jacobsen et al. (2012), Meyer et al. (2017), or Vukčević et al. (2016). However, so far it is an open question whether and to which extent this approach introduces flow disturbances and thus errors, when the forcing is applied to the domain sides. Discretization errors and iteration errors usually produce a certain amount of numerical diffusion and dispersion; thus the wave height and phase change the further the wave travels through the domain (Larsen et al., 2018). Especially when forcing zones are attached to a boundary with normal vector orthogonal to the wave propagation direction, then there will be a certain discrepancy between the flow solution within the domain and the reference solution in the forcing/relaxation zone.

The aim of this paper is to investigate and discuss the aforementioned concern by running 3D flow simulations with forcing towards the far-field wave, without flow-disturbing bodies within the domain, and investigate the influence of disturbances caused by the boundary conditions. In this manner, practical conclusion are reached under which conditions such forcing/relaxation zones may be applied, and what to do for problems when they cannot be applied.

2 Forcing Zones

Undesired wave reflections can be minimized by applying forcing source terms in the conservation equations for momentum and volume fraction

$$\frac{\mathrm{d}}{\mathrm{d}t}\int_V \rho u_i \,\mathrm{d}V + \int_S \rho u_i \mathbf{v}\cdot\mathbf{n}\,\mathrm{d}S = \int_S (\tau_{ij}\mathbf{i}_j - p\mathbf{i}_i)\cdot\mathbf{n}\,\mathrm{d}S + \int_V \rho\mathbf{g}\cdot\mathbf{i}_i\,\mathrm{d}V + \int_V \rho q_i\,\mathrm{d}V \quad , \tag{1}$$

$$\frac{\mathrm{d}}{\mathrm{d}t}\int_V \alpha \,\mathrm{d}V + \int_S \alpha \mathbf{v}\cdot\mathbf{n}\,\mathrm{d}S = \int_V q_\alpha \,\mathrm{d}V \quad , \tag{2}$$

with volume V of control volume (CV) bounded by the closed surface S, fluid velocity vector $\mathbf{v}$ with the Cartesian components u_i, unit vector $\mathbf{n}$ normal to S and pointing outwards, time t, pressure p, fluid density ρ, components τ_{ij} of the viscous stress tensor, unit vector $\mathbf{i}_j$ in direction x_j, and volume fraction α of water. The forcing source terms are

$$q_\alpha = \gamma b(\tilde{\mathrm{x}})\,(\alpha_{\mathrm{ref}} - \alpha) \quad , \quad q_{\mathrm{i}} = \gamma b(\tilde{\mathrm{x}})(u_{i,\mathrm{ref}} - u_i) \quad , \tag{3}$$

with reference volume fraction α_{ref}, reference velocity component $u_{i,\mathrm{ref}}$, forcing strength γ and blending function $b(\tilde{\mathrm{x}})$. Forcing strength γ regulates the magnitude with which the solution at a given cell is forced against the reference solution. The blending term $b(\tilde{\mathrm{x}})$ regulates how the source term varies within the zone. In this work, exponential blending is used

$$b(\tilde{\mathrm{x}}) = \left(\frac{e^{b(\tilde{\mathrm{x}})^2} - 1}{e^1 - 1}\right) \quad . \tag{4}$$

where $\tilde{\mathrm{x}}$ is the shortest distance to the closest domain boundary and the zone thickness is x_{d}. Optimum zone thickness x_{d} and forcing strength γ are case-dependent and must be adjusted for each simulation.

3 Simulation Setup

The simulation domain has dimensions $-80\,\mathrm{m} < x < 140\,\mathrm{m}$, $0 < y < 156\,\mathrm{m}$, $-13.104\,\mathrm{m} < z < 14.976\,\mathrm{m}$. The coordinate system lies at the calm free surface level $(0, 0, 0)^{\mathrm{T}}$, with x pointing in wave propagation direction and z pointing upwards as shown in Fig. 1.

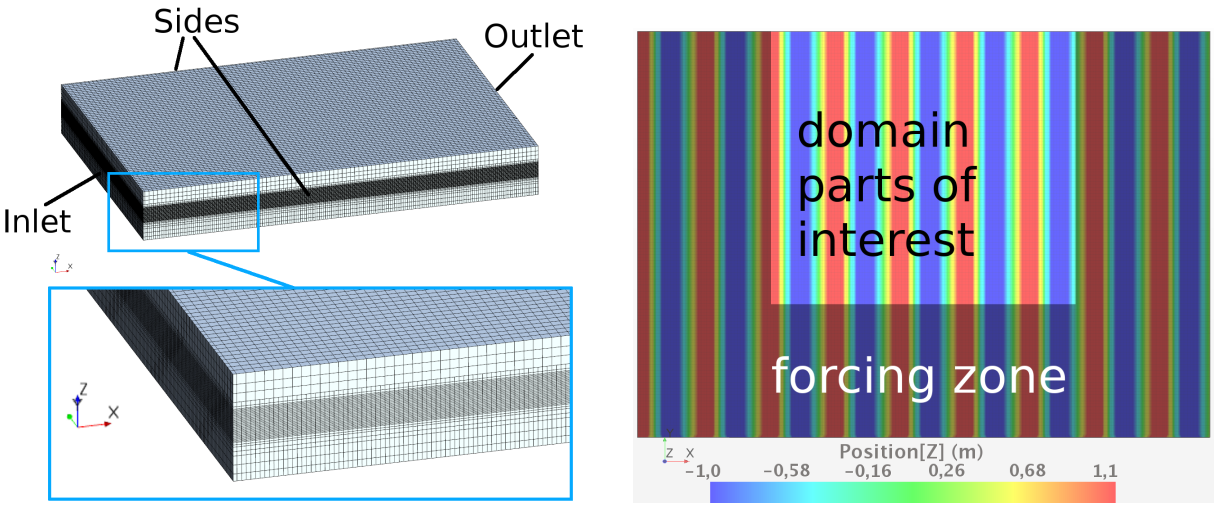

Fig. 1: Computational grid with local mesh refinement near the free surface (left), and top view on solution domain (right) with forcing zones (shaded gray) attached to inlet, outlet, and one side boundary

The wave is generated by applying forcing zones as given in Sect. 2 in combination with prescribing volume fraction and velocities at all vertical domain boundaries, except for $y = 156\,\mathrm{m}$ which is set to a symmetry boundary condition to reduce the total number of cells. At the top boundary $z = 14.976\,\mathrm{m}$ atmospheric pressure is prescribed and the bottom boundary $z = -13.104\,\mathrm{m}$ is set to a slip wall. The forcing zones' thickness is $x_{\mathrm{d}} = 50\,\mathrm{m} \approx 2\lambda$, so that no significant wave reflections will occur as expected from the theory predictions shown in Fig. 2. Unless mentioned otherwise, the solution is forced against the far-field wave. As intial condition, volume fraction and velocities in the whole domain are initialized according to the far field wave. The wave parameters are (peak) wave period $T = 4\,\mathrm{s}$, wave height $H = 3\,\mathrm{m}$, (peak) wavelength $\lambda \approx 25\,\mathrm{m}$ according to linear wave theory, and thus steepness $H/\lambda \approx 85\%$ of the maximum steepness. Deep water conditions apply.

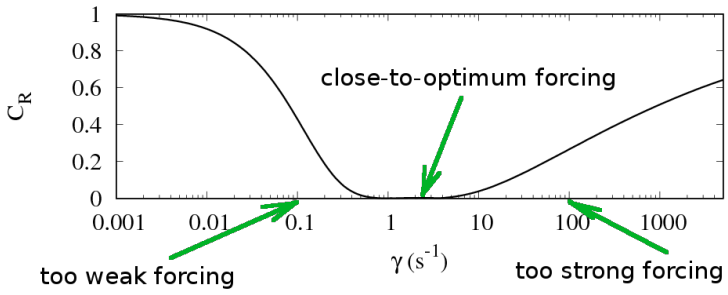

Fig. 2: Reflection coefficient $C_R = H_{refl}/H$ over forcing strength γ for the (peak) wave used in this study according to the theory by Perić and Abdel-Maksoud (2018a); H_{refl} is the wave height of the waves reflected at the forcing zone; at close-to-optimum forcing ($\gamma = 2.5$), wave reflections from the forcing zone should be negligible, though the forcing zone at the side boundaries may still produce disturbances if there are discrepancies between the reference and the flow solution in the domain

The finite-volume-based commercial flow solver STAR-CCM+ version 11.06.010-R8 from Siemens (formerly CD-adapco) is used. The volume of fluid (VOF) method accounts for the two phases, liquid water and gaseous air, using the High Resolution Interface Capturing scheme (HRIC) as given in Muzaferija and Perić (1999). All discretization approximations are of second order. The linearized equation system is solved by the iterative STAR-CCM+ implicit unsteady segregated solver, using an algebraic multigrid method with Gauss-Seidel relaxation scheme, V-cycles for pressure and volume fraction of water, and flexible cycles for velocity calculation. The under-relaxation factor is 0.9 for velocities and volume fraction and 0.4 for pressure. Six iterations are performed per time-step; one iteration consists of solving the governing equations for the velocity components, the pressure-correction equation (using the SIMPLE method for collocated grids to obtain the pressure values and to correct the velocities) and the transport equation for the volume fraction of water. Further information on the discretization of and solvers for the governing equations can be found in Ferziger and Perić (2002) or the STAR-CCM+ software manual.

The domain is discretized using a rectilinear grid with local mesh refinement around the free surface as shown in Fig. 1. The free surface stays at all times within the region of the finest mesh with $\approx$ 23 (coarser grid) or 47 (finer grid) cells per (peak) wavelength and $\approx$ 10 cells per (significant) wave height. The computational grid, which consists of $\approx 1 \cdot 10^6$ (coarser grid) or $\approx 4 \cdot 10^6$ (finer grid) cells, is shown in Fig. 1. The total simulated time is 60 s $\approx 15T$ with a time step of $\Delta t = T/500$.

4 Results and Discussion

First, the reference solution for the forcing will be the linear wave theory solution for the steep wave as described in Sect. 3. Since no flow-disturbing body is present within the domain, the correct solution would be a long-crested wave traveling through the domain undisturbed. The linear wave theory was deliberately chosen as an example for a reference solution that does not fit the flow solution within the domain, since the flow within the domain will take on a realistic wave shape, which for the given steepness would have a slightly different shape and an 11.8% larger wavelength and phase velocity than the linear reference solution. Figure 3 shows that even for $\approx$ optimum tuning of the forcing zone parameters, the mismatch of reference to computed flow solution produces disturbances within the whole domain. Further, an additional loss in wave height is observed; when using a finer discretization, this loss is partly reduced in the domain parts several wavelengths away from the forcing zones at the domain sides, but remains for the closer domain parts due to the cancellation between reference and computed flow solution. The disturbances within the whole domain generated from the forcing zone at the domain sides seemed unaffected by the discretization, if not being even more pronounced on the finer grid. This highlights that if there is a discrepancy between the reference solution for the forcing and the actually computed flow within the domain (including effects of discretization and iteration errors), then the forcing zone at the domain sides can produce significant disturbances to occur in the whole solution domain.

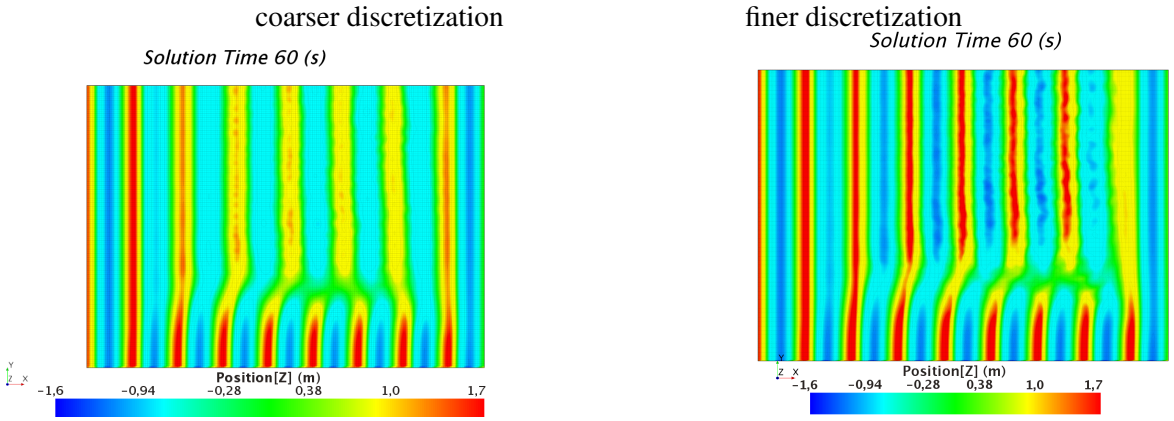

Fig. 3: Free-surface elevation in solution domain for forcing towards *linear wave theory* for ≈ optimum forcing strength γ; for coarser ($\approx 1 \cdot 10^6$ cells) and finer discretization ($\approx 4 \cdot 10^6$ cells)

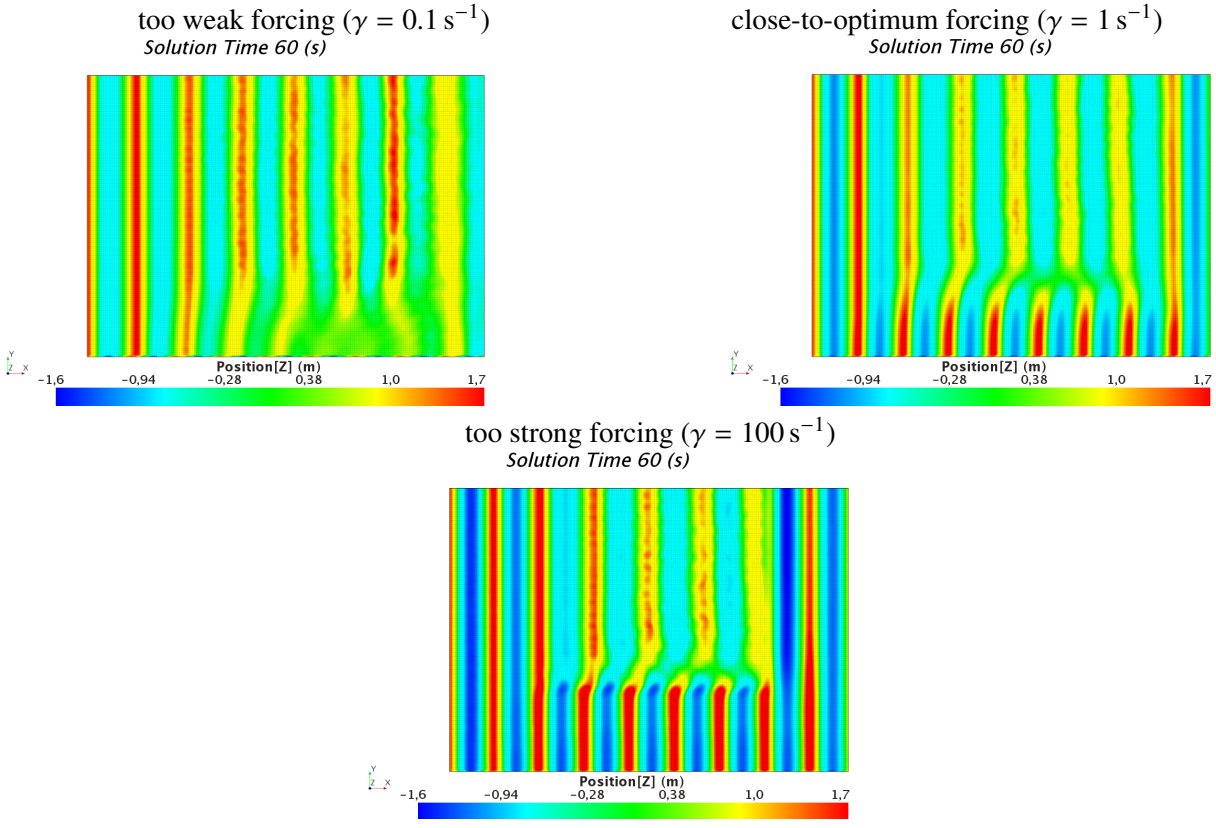

Fig. 4: Free-surface elevation in solution domain for forcing towards *linear wave theory* solution at all domain boundaries for different values of forcing strength γ

Figure 4 shows that if the forcing zone parameters are set to theoretically ineffective values, these also produce unsatisfactory forcing in the flow simulations. If the source terms are too weak, then even close to the domain boundaries the reference solution is not maintained (Fig. 4 top left), and reflections at the outlet boundary produce a partial standing wave, which can be seen by the larger wave height next to the outlet or on the videos from that simulation. For too large source terms, the reference solution is enforced nearly up to the entrance to the forcing zone, so reflections occur at the entrance to the forcing zone and disturbances reach even further into the solution domain (Fig. 4 bottom).

The question is now to which extent these disturbances will be present if a more accurate reference solution is used. Thus the simulations were repeated using Fenton's (1985) Stokes 5th-order theory to obtain a highly accurate prediction of the wave propagation for the case that no discretization or iteration errors are present. Figure 5 shows that with this setup, the discrepancy between reference and computed flow solution are smaller; yet even for the fine discretization, disturbances are clearly visible, although especially on the finer grid the discrepancy between theoretical and computed wave phases is rather small. While this error is expected to reduce with increasing mesh resolution, the results suggest that much finer than conventionally used grids would be required so that the disturbances vanish.

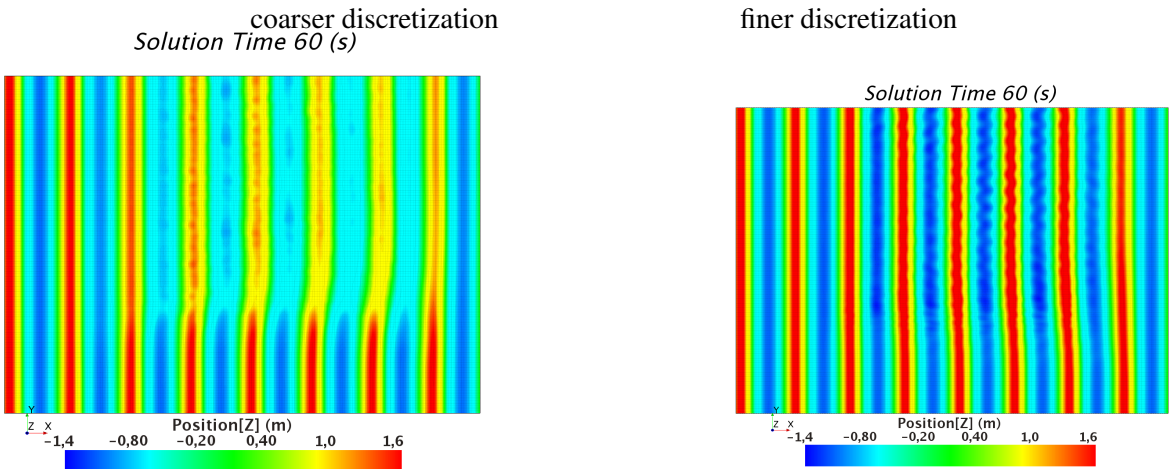

Fig. 5: Free-surface elevation in solution domain for forcing towards *Stokes 5th-order wave theory* for ≈ optimum forcing strength γ; for coarser ($1 \cdot 10^6$ cells) and finer discretization ($4 \cdot 10^6$ cells)

Another case when theoretical and computed solutions will usually show considerable discrepancies is when simulating irregular waves as shown in Fig. 6 left.

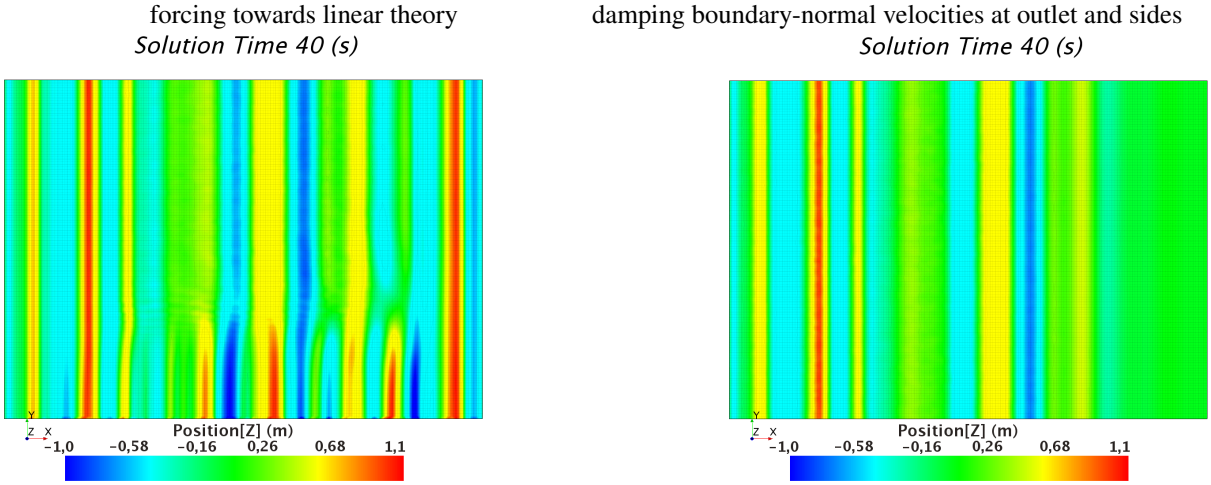

Fig. 6: Free-surface elevation in solution domain for forcing towards linear wave theory solution for an irregular wave as a *superposition of linear wave components* (left) and for forcing only boundary-normal velocities towards zero at the outlet and domain sides (right)

Perić and Abdel-Maksoud (2018b) suggested a way such errors can be avoided. At the side and outlet boundaries, they applied forcing only to the boundary-normal velocities, and forced them to zero as shown in Fig. 6 right. Thus waves reflections from these boundaries are minimized, but the waves pass

undisturbed through the forcing zones attached to the side boundaries, since the long-crested far-field waves have no velocity components in the direction normal to the side boundaries and thus the source terms do not affect them.

5 Conclusion

Forcing the flow towards the far-field wave solution near all vertical domain boundaries can produce flow disturbances. These disturbances originate from the difference between the reference solution and the actual flow solution subjected to iteration and discretization errors. Although the differences and thus also the disturbances should vanish with increasing grid resolution, the present results indicate that much finer than commonly used grids would be necessary before these errors become insignificant. Thus further research is necessary to better understand and quantify the disturbances generated by forcing towards the far-field waves at all boundaries. An approach to avoid these disturbances for flow simulations with long-crested waves was presented briefly.

Acknowledgements

The authors gratefully acknowledge the financial support by the Deutsche Forschungsgemeinschaft (DFG) for this study.

References

Chen, H. C., Yu, K., & Chen, S. Y. (2006). Simulation of Wave Runup Around Offshore Structures by a Chimera Domain Decomposition Approach. In Civil Engineering in the Oceans VI (pp. 267-280).

Choi, J., Yoon, S. B., 2009. Numerical simulations using momentum source wave-maker applied to RANS equation model. Coast. Eng., 56(10), 1043-1060.

Fenton, J.D., 1985. A fifth-order Stokes theory for steady waves. J. Waterway, Port, Coastal, Ocean Eng. 111 (2), 216-234.

Ferziger, J., Perić, M., 2002. Computational Methods for Fluid Dynamics, Springer, Berlin.

Jacobsen, N. G., Fuhrman, D. R., Fredsøe, J., 2012. A wave generation toolbox for the open-source CFD library: OpenFoam®. Int. J. Numerical Methods in Fluids, 70(9), 1073-1088.

Larsen, B.E., Fuhrman, D.R. and Roenby, J., 2018. Performance of interFoam on the simulation of progressive waves. arXiv preprint arXiv:1804.01158.

Meyer, J., Graf, K., & Slawig, T. A new adjustment-free damping method for free-surface waves in numerical simulations, VII International Conference on Computational Methods in Marine Engineering, MARINE 2017.

Muzaferija, S., Perić, M., 1999. Computation of free surface flows using interface-tracking and interface-capturing methods, in: Mahrenholtz, O., Markiewicz, M. (Eds.), Nonlinear Water Wave Interaction, WIT Press, Southampton, pp. 59-100.

Park, J. C., Kim, M. H., Miyata, H., 1999. Fully non-linear free-surface simulations by a 3D viscous numerical wave tank. Int. J. Numerical Methods in Fluids, 29(6), 685-703.

Park, J. C., Zhu, M., Miyata, H., 1993. On the accuracy of numerical wave making techniques. J. Society of Naval Architects of Japan, 1993(173), 35-44.

Perić, R., Abdel-Maksoud, M. 2018a. Analytical prediction of reflection coefficients for wave absorbing layers in flow simulations of regular free-surface waves. Ocean Engineering, 147, 132-147.

Perić, R., Abdel-Maksoud, M. 2018b. Reducing undesired wave reflection at domain boundaries in 3D finite-volume-based flow simulations via forcing zones. Proceedings of 32nd Symposium on Naval Hydrodynamics, Hamburg, Germany.

Vukčević, V., Jasak, H., Malenica, Š., 2016. Decomposition model for naval hydrodynamic applications, Part I: Computational method. Ocean Eng., 121, 37-46.

Wei, G., Kirby, J. T., Sinha, A., 1999. Generation of waves in Boussinesq models using a source function method. Coast. Eng., 36(4), 271-299.

An Investigation of Air Cavity Closure Mechanisms using Scale Resolving Simulations

Gem Rotte[*], Maarten Kerkvliet[†], and Tom van Terwisga[*†]
[*]TU Delft, Delft/The Netherlands [†]MARIN, Wageningen/The Netherlands
G.M.Rotte@tudelft.nl

1 Introduction

Air lubrication techniques have the potential to significantly reduce a ship's fuel consumption by reducing the frictional drag, benefiting sustainable employability and cost reduction. Several techniques are available, of which an overview is provided in Rotte et al. (2016). One of the most promising techniques applicable to ships is the external air cavity technique, these applications are claimed to lead to propulsive power reduction of 10-20% (Gorbachev and Amromin (2012), Zverkhovskyi (2014)). An external cavity is created beneath the ship's hull with the help of a cavitator, which is located directly upstream of an air injection point (at the left of figure 1). It is used to separate the mean water flow from the hull, thereby providing a stable air layer a length prescribed by half the wavelength of the gravity-dominated surface wave (Gorbachev and Amromin (2012)). However, a complete understanding of the influence of the ship's hull form on the relevant two-phase flow physics and thereby also on the length and stability of the air cavities is still lacking. This inability to predict the air cavity characteristics hampers the application of air cavity techniques in the shipping industry. Multiphase CFD methods can help us to gain a better understanding of the relevant physics.

Fig. 1: The external air cavity

The largest challenge in predicting the air cavity characteristics lies in correctly modelling the closure region (Shiri et al. (2012), Zverkhovskyi et al. (2015)). Both the re-entrant jet mechanism and the wave pinch-off mechanism are cited as possible mechanisms for air discharge from the cavity (e.g. Mäkiharju (2012), Shiri et al. (2012), Zverkhovskyi (2014)). The re-entrant jet mechanism for an air filled cavity is here assumed to be similar to the re-entrant jet mechanism responsible for the break-up of vapour sheet cavities as described by Callenaere et al. (2001). The wave pinch-off mechanism is governed by waves on the air-water interface. These waves are hypothesised to be formed by turbulence structures interfering with the interface. If the resulting wave amplitudes are of the same magnitude as the cavity thickness, the free surface interface hits the ship's bottom and a pocket of air will be shed from the cavity.

In Rotte et al. (2017) and Rotte et al. (2018) RaNS simulations of the cavity were performed and it was concluded that the simulated mean velocity profiles at different streamwise locations in the boundary layer around the cavity compare reasonably well with the experimental profiles. However, it was also concluded that RaNS two-equation turbulence models like the $k - \sqrt{k}L$ model show serious deficiencies for the modelling of the re-entrant jet mechanism for air cavities. Also after including an ad-hoc eddy-viscosity correction model as proposed by Reboud et al. (1998) and in Rotte et al. (2017). Next to the modelling of the re-entrant jet, the simulation of the wave pinch-off mechanism also needs to be included to be able to capture the cavity closure dynamics. Since this mechanism is hypothesised to be governed by waves formed by turbulence structures disturbing the interface, scale resolving simulations (SRS) are required. This article aims to identify the physical conditions at the cavity interface and the shedding mechanisms in the closure region using eXtra Large Eddy Simulation (XLES), a hybrid RaNS-LES method as described by Kok et al. (2004).

The numerical solver used for all simulations is ReFRESCO (MARIN (2018)). It is a multiphase unsteady incompressible viscous flow solver using RANS and multiple SRS models such as DDES/IDDES, XLES, PANS and LES approaches. ReFRESCO is complemented with cavitation models and volume-fraction transport equations for different phases. Time integration is performed implicitly with first or second-order backward schemes.

2 Boundary layer characterisation

In Rotte et al. (2017) and Rotte et al. (2018) it was shown that the cavity profile is very sensitive to the boundary layer thickness upstream of the cavity as well as the pressure distribution around the cavity. For the current scale-resolving simulations an unsteady turbulent boundary layer needs to be generated upstream of the cavity in order to investigate the influence of the turbulence structures on the cavity interface and overall cavity profile. Next to the

need for a mean velocity profile, the boundary layer needs to be provided with time-varying velocity components to prevent the solution becoming laminar (Lund et al. (1998)).

To characterize the boundary layer, preliminary single-phase unsteady simulations were carried out with a water tunnel inlet velocity of 1 m/s. The simulations were carried out using the XLES turbulence model as described by Kok et al. (2004). A second order backward scheme is used for the time discretisation and the discritisation of the momentum equations is treated by Van Leer's harmonic TVD scheme van Leer (1974). The turbulence equations are treated by a blend between a first-order upwind and central differencing scheme. Regarding the iterative convergence of the simulation presented; the L_∞ norm is in the order of 10^{-6} for all residuals.

The computational domain dimensions (L*B*H) are 0.7*0.045*0.3 m. Next to the wall-normal contraction of cells to achieve a z^+ value below 1 near the wall, the computational cells in the upper part of the domain $(0,06m\ 2 * \delta_{99})$ are refined using hanging-node refinement to achieve x^+ and y^+ values in the order of 35. The time step used in the calculations was 0.55ms to ensure Courant numbers smaller than 1, for this case the viscous timescale $\Delta t^+ = \frac{u_\tau^2 \Delta t}{\nu} = 0.97$. For these preliminary computations it was decided to use a small turbulence trip upstream of the location where the cavity is generated. The idea for the use of such a trip is comes from the experimental use of transition tripping wires or strips. The height $h = 0.1\delta_{99}$ and width $w = 0.25\delta_{99}$ of the trip are based on the initial boundary layer thickness $\delta_{99} = 0.032m$ as reported by Zverkhovskyi (2014). The cross section of the trip remains constant. An overview if the computational domain used for these simulations is given in Figure 2.

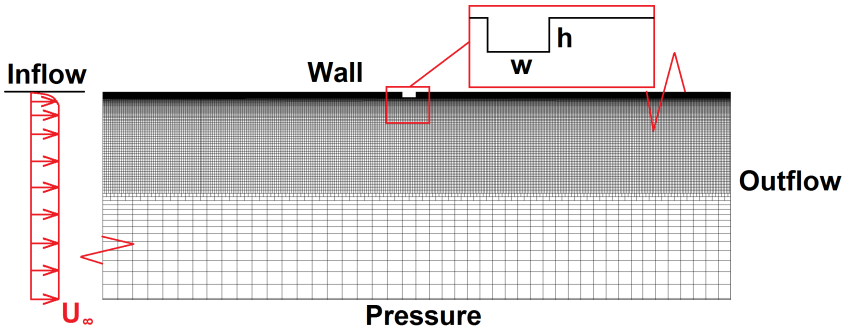

Fig. 2: Computational domain including boundary layer trip for initial boundary layer characteristics

The domain is initialised with a prescribed boundary layer velocity profile, which is also precribed as an inlet velocity condition at each timestep. Ideally, the boundary layer characteristics are based on experimental data. Unfortunately the results of the experimental measurements from Zverkhovskyi (2014) close to the wall are not of sufficient resolution to quantitatively compare the viscous sub-layer of the boundary layer, which determines the wall shear stress. *High resolution stereographic PIV experiments to measure the boundary layer characteristics are planned for the beginning of July, these results can hopefully be used for the final version of this article.* For now, we rely on the experiments with a low resolution as well as theoretical descriptions of the turbulent boundary layer. The work by Zverkhovskyi (2014) provided four different time-averaged velocity profiles along the test plate. One at the beginning of the test plate without a cavity present, and three profiles as observed with a cavity present. One just upstream of the cavitator, one at the middle of the cavity and one just downstream of the cavity.

Figure 3(a) shows the time-averaged experimental data for the velocity profile in the boundary layer just in front of the cavity from Zverkhovskyi (2014). It is here compared with the $1/7^{th}$ power law, the time-averaged velocity profile from ReFRESCO and the initially prescribed velocity profile in the boundary layer and at the inflow. For the region $z < 15mm$ the produced velocity profiles show significantly higher velocities than found in the experimental data. It is not completely clear what the field of view was for the experimental data, and how close it was to the cavity in x-direction. It is preliminary hypothesised that the experimentally found profile already shows a decelerated flow due to the blockage effect of the cavity just downstream of the measurement location. In Zverkhovskyi (2014) it was also reported that the incoming flow compared reasonably well to Prandtl's $1/7^{th}$ power law as reported in e.g. White (2008). Zverkhovskyi (2014) reported a shape factor $H = 1.38$ in the boundary layer and in the current simulation a shape factor $H = 1.4$ is found. The shape factor is the ratio between displacement and momentum thickness and indicates if the boundary layer is laminar or fully turbulent. A shape factor $H = 2.59$ is typical of laminar flows, while $H = 1.3 - 1.4$ is typical of turbulent flows.

The major part of the prescribed profile is based on a combination of the $1/7^{th}$ power law as well as the theory for turbulent boundary layers as described in e.g. Pope (2000). Here, the mean velocity in the viscous sub-layer ($y^+ < 5$) is prescribed by $u^+ = y^+$ and by $u^+ = ln(y^+)/0.41 + 5.0$ in the log-layer ($30 < y^+ < 300$). For the regions in between, a smooth mathematical function is used to ensure a smooth transition from one region to the following.

The velocity profile as prescribed and the profile resulting from ReFRESCO are compared with the experimental data as well as the theoretical description in figure 3(b). The profile following from ReFRESCO shows a reasonable agreement with the theory. However, the profile following from the experimental data does not fit the theoretical data. The behaviour in the region around the viscous sub-layer is not resolved. This makes it impossible to directly derive the local wall shear stress and thus friction velocity u_τ which is needed to compute u^+. For now, u_τ for the experiments is estimated based on more recent experiments in the Delft water tunnel (by A. Greidanus). *These results are not made public yet, so for the final article we hope to be able to use the data to be following from the experiments upcoming in July.* The shift of the experimental profile to the right with respect to the theoretical lines can be partly explained by the (unknown) uncertainty of the experimental data, there is no data available on the uncertainty of the exact distance of the first datapoint to the wall. Lastly, the slope of the experimental data in the so-called log-layer does not approximate the theoretical slope at all. For the more recent boundary layer profiles by Greidanus however, this fits significantly better.

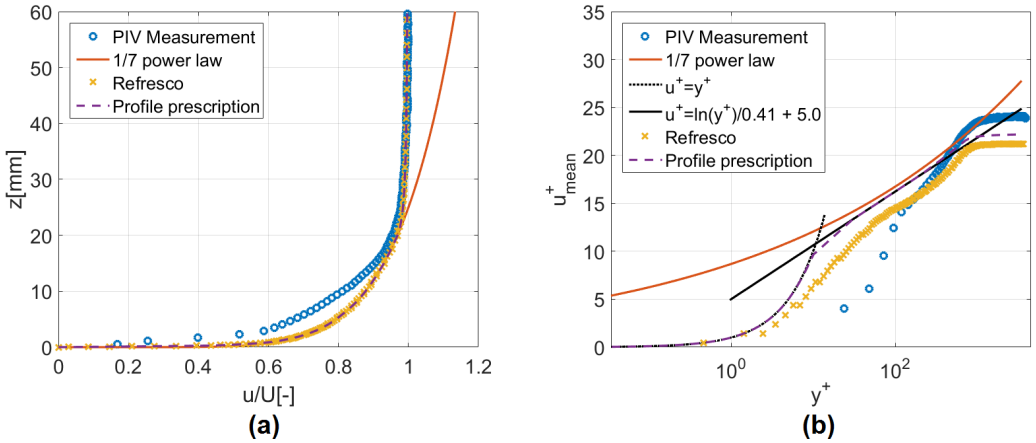

Fig. 3: **(a)**The time-averaged experimental data from Zverkhovskyi (2014) compared with the $1/7^t h$ power law, the time-averaged velocity profile from ReFRESCO and the prescribed velocity profile in the boundary layer. **(b)** The time-averaged experimental data compared with the $1/7^t h$ power law, the theory for viscous sublayer and log-layer, the time-averaged velocity profile from ReFRESCO and the prescribed velocity profile in the boundary layer in viscous wall units

Next to the mean velocity profiles, the Reynolds stress profiles as well as the turbulence kinetic energy profiles are given in figure 4. At this stage, it can be said that the order of magnitude for the Reynolds stresses as well as the shape of the profiles compare reasonably well with the profiles reported for similar momentum thickness Reynolds numbers Re_θ (e.g. Schlatter et al. (2009)). The profile is given here at the location right in front of where the cavitator position the computations including the cavity, which results in $Re_\theta = 2240$. *A more extensive comparison as planned to be made with the upcoming experiments in the final article.*

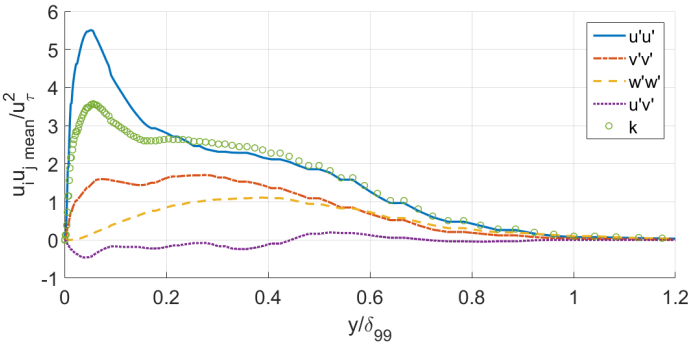

Fig. 4: Reynolds stress and turbulence kinetic energy profiles in the turbulent boundary layer

3 Air cavity simulation

The XLES simulations of the air cavity case are based on the measurements performed in the Delft Cavitation Tunnel by Zverkhovskyi (2014). The cavitation tunnel has a test section length of 2m and a 0.3·0.3m cross-sectional area. The computational domain up until the cavitator is equal to the domain as described in the previous section and also includes the boundary layer trip. A schematic of the domain including the applied boundary conditions is shown in figure 5. The computational domain dimensions (L*B*H) are 1.7*0.045*0.3 m for the tunnel, and contains a diffuser at the air inlet where a constant pressure of 75Pa is prescribed. Next to the wall-normal contraction of cells to achieve a z^+ value below 1 near the wall, the computational cells in the upper part of the domain $(0,06m\ 2 * \delta_{99})$ are refined using hanging-node refinement to achieve x^+ and y^+ values in the order of 35. The time step used in the calculations was 0.5ms to ensure Courant numbers smaller than 1, for this case the viscous timescale $\Delta t^+ = \frac{u_\tau^2 \Delta t}{\nu} = 0.9$. The close-up shows the grid topology in the region including the cavity, with refinement zones in the region around the cavitator and the expected cavity interface. The total number of grid cells is around 8M. Unsteady simulations were carried out with a water tunnel inlet velocity of 1 m/s. The simulation is carried out using the XLES turbulence model as described by Kok et al. (2004). As for the boundary layer computations, a second order backward scheme is used for the time discretisation and the discritisation of the momentum equations is treated by Van Leer's harmonic TVD scheme van Leer (1974). The turbulence equations are treated by a blend between a first-order upwind and central differencing scheme. For the volume fraction transport equation Roe's compressive SUPERBEE scheme is used, which is also TVD Roe (1986). Due to time considerations, the simulation is first started on a computational grid which was coarsened by a factor of 2 in both the streamwise and spanwise direction, and the timestep used was also 2 times larger. Due to the lack in resulution and the nature of the XLES formulation, this was practically still a RaNS computation. When the cavity was developed the solution was transferred to the original grid and restarted with the above described settings.

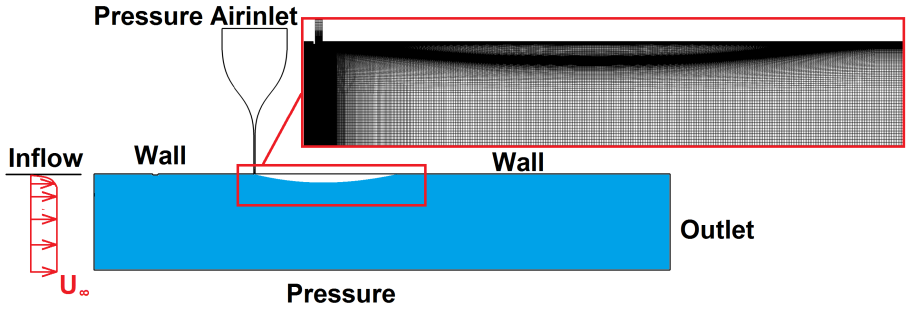

Fig. 5: Computational domain and boundary conditions

It is not yet possible to make firm conclusions yet, since the simulation is still running. As a preliminary result it can already be said that the mean cavity profile (length and thickness) seems to compare reasonably well to the experimental profile. Figure 6 shows the time-averaged velocity profiles in the boundary layer upstream, in the middle and downstream of the air cavity. The simulation is still running at this moment, and the time-averaged velocity profiles are not yet converged. We are currently waiting for the simulation to finish to be able to conclude something from these profiles.

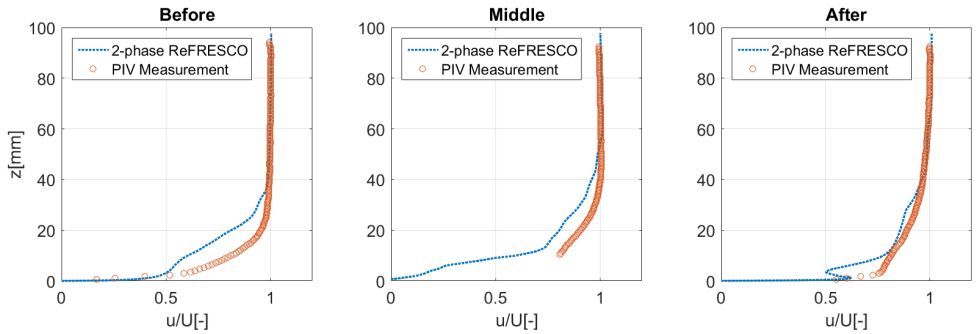

Fig. 6: time-averaged boundary layer profiles at three different streamwise locations: upstream, in the middle and downstream of the cavity. Compared are the 2-phase base case simulations from the current project and the time-averaged experimental data from Zverkhovskyi (2014)

Figure 7 shows a time series for the developing cavity. The time $t = 0.0s$ is here defined as the time from the restart from the coarse grid computation. The top figure of figure 7, at time $t = 0.5s$, shows a very stable cavity interface. As expected, this is very similar to what was earlier found in the RaNS simulations (e.g. Rotte et al. (2017)). A constant air flow is found in the closure area and no periodic shedding is observed. Just upstream of the cavity, the developing boundary layer with velocity fluctuations can already be observed. In the second figure of 7, at time $t = 0.6s$, the fluctuating flow is advected along the first part of the cavity, causing the first disturbances on the cavity interface. This is a significant disturbance clearly marking the developing turbulence front, travelling along the cavity interface. The further development of the flow can be observed in the developing time, from $t = 0.7s$ to $t = 1.3s$. It also seems that the initial disturbance is more significant than the following velocity fluctuations, the cavity interface at the beginning of the cavity stabilises again. *Unfortunately, no conclusions can be drawn yet regarding the closure mechanism since the cavity is not yet completely developed. The simulation is still running and we expect to be able to conclude more on these mechanisms in the final article.*

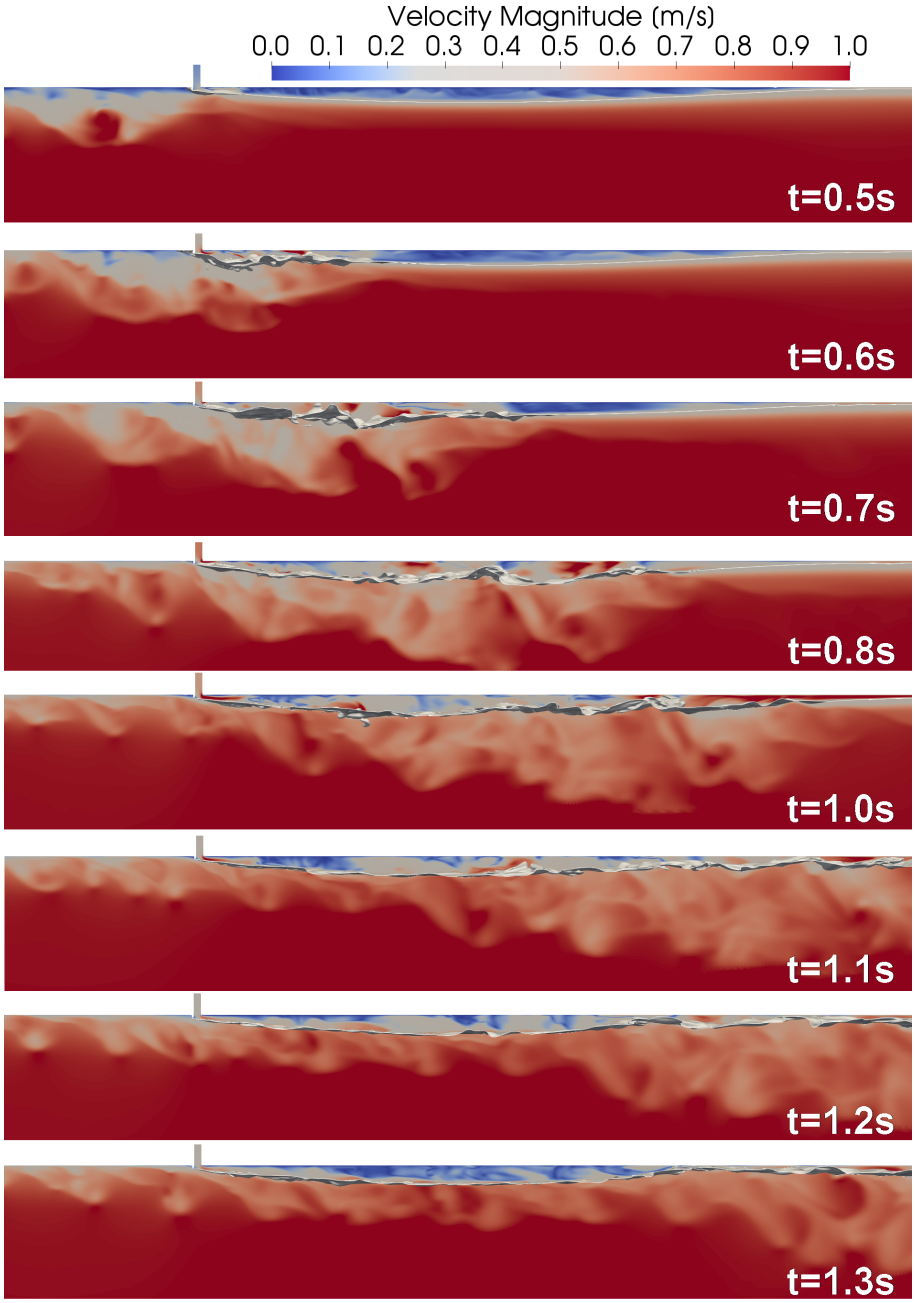

Fig. 7: Time series of the developing cavity. The cavity interface is visualised using the iso surface for the air volume fraction $\alpha = 0.5$. The velocity contour is shown at the back symmetry plane of the domain. Flow from left to right.

4 Conclusions and further work

The computational domain is initialised with a prescribed boundary layer velocity profile, which is also prescribed as an inlet velocity condition at each timestep. Unfortunately these characteristics could not yet be based on experimental data, since the data provided by Zverkhovskyi (2014) close to the wall are not of sufficient resolution to quantitatively compare the viscous sub-layer of the boundary layer. *High resolution stereographic PIV experiments to measure the boundary layer characteristics are planned for the beginning of July, these results can hopefully be used for the final version of this article.* For now, we relied on the experiments with a low resolution as well as theoretical descriptions of the turbulent boundary layer. From these, we can conclude that we find a reasonable agreement with theory and what was earlier found in literature, but not with what was found in the experiments by Zverkhovskyi (2014). The reason for this is not completely clear, but it is hypothesised that it is partly due to the (unknown) uncertainty of the experimental data, especially in the exact distance of the first datapoint to the wall. Lastly, the slope of the experimental data in the so-called log-layer does not approximate the theoretical slope at all. For the more recent boundary layer profiles by Greidanus however, this fits significantly better. The upcoming experiments in July will hopefully give us more insight in both the time-averaged velocity profiles as the Reynolds stresses in the boundary layer upstream of the cavity.

For the cavity simulations, no firm conclusions can be drawn yet regarding the closure mechanisms. On a preliminary basis however, it can be stated that the turbulence structures in the flow upstream of the cavity indeed disturb the cavity interface, this could well be related to the wave pinch-off mechanism later on. For the final article, we aim to relate the free surface deformations to the turbulence energy spectrum and Reynolds stresses.

Acknowledgements

We thank the Netherlands Organisation for Scientific Research NWO, by whom this research is financially supported.

References

Callenaere, M., Franc, J.-P., Michel, J.-M. and Riondet, M. (2001). The cavitation instability induced by the development of a re-entrant jet. *J. Fluid Mech* 444, 223-256

Gorbachev, Y. and Amromin, E. (2012). Ship Drag Reduction by Hull Ventilation from Laval to Near Future: Challenges and Successes. *ATMA 2012*

Kok, J.C., Dol, H.S., Oskam, B., van der Van, H. (2004). Extra-Large Eddy Simulation of Massively Separated Flows. *Proceedings of the 42th American Institute of Aeronautics and Astronautics Aerospace Sciences Meeting and Exhibit*, January 5-8, Reno, United States of America

Lund, T.S., Wu, X., Squires, K.D., (1998). Generation of Turbulent Inflow Data for Spatially-Developing Boundary Layer Simulations. *J.of Comp. Phys. 140*, p 233-258, 1998

Mäkiharju, S.A. (2012). The Dynamics of Ventilated Partial Cavities over a Wide Range of Reynolds Numbers ans Quantitative 2D X-Ray Densitometry for Multiphase Flow. *Ph.D. Thesis* The University of Michigan

van Leer, B. (1974). Towards the ultimate conservative difference scheme. Part II. Monotonicity and conservation combined in a second-order scheme. *Journal of Computational Physics*, **14**(4):361-370

Pope, S. B. (2000). *Turbulent Flows*, Cambridge University Press

Reboud, J., Stutz, B. and Coutier, O. (1998). Two-phase Flow Structure of Cavitation: Experiment and modelling of Unsteady Effects. *Third International Symposium on Cavitation*, Grenoble, France

ReFRESCO (2018) http://www.refresco.org, Online; accessed 25 June 2018

Roe, P.L. (1986), Characteristic-Based Schemes for the Euler Equations, *Annual Review of Fluid Mechanics*,**18**, 337

Rotte, G., Zverkhovskyi, O., Kerkvliet, M., van Terwisga, T. (2016). On the physical mechanisms for the numerical modelling of flows around air lubricated ships. *Proceedings of the International Conference on Hydrodynamics (ICHD)*, Wijk aan Zee, The Netherlands

Rotte, G., Kerkvliet, M., van Terwisga, T. (2017). On the Turbulence modelling for an Air Cavity Interface. *Proceedings of NuTTS 2017*, Wageningen, The Netherlands

Rotte, G., Kerkvliet, M., van Terwisga, T. (2018). On the Influence of Eddy Viscosity in the Numerical Modelling of Air Cavities. *Proceedings of The 10th International Symposium on Cavitation (CAV2018)*, Baltimore, Maryland, USA

Schlatter, P., Örlü, R., Li, Q., Brethouwer, G., Fransson, J.H.M., Johansson, A.V., Alfredsson, P.H., Henningson, D.S. (2009). Turbulent boundary layers up to $Re_\theta = 2500$ studied through simulation and experiment. *Physics of Fluids*, **21**

Shiri, A., Leer-Andersen, M.,Bensow, R.E. and Norrby, J. (2012). Hydrodynamics of a Displacement Air Cavity Ship. *29th Symposium on Naval Hydrodynamics*, Gothenburg, Sweden

White, F. (2008). *Fluid Mechanics Sixth Edition*, McGraw-Hill

Zverkhovskyi, O. (2014). Ship Drag Reduction by Air Cavities. *Ph.D. Thesis*, TU Delft

Zverkhovskyi, O., Kerkvliet, M., Vaz, G. and van Terwisga, T. (2015). Numerical Study on Air Cavity Flows. *Proceedings of NuTTS 2015*, Cortona, Italy

Unsteady propeller forces and hull pressure pulses in waves

Simone Saettone[*,†], **Bhushan Taskar**[*], **Pelle Bo Regener**[*], **and Poul Andersen**[*]
[*]Technical University of Denmark, Kgs. Lyngby, Denmark
[†]Norwegian University of Science and Technology, Trondheim, Norway

1 Introduction

Ship propellers are traditionally designed for calm water conditions. Propulsion factors and wake distribution are considered time-invariant and speed loss, ship motions and propeller rpm fluctuations are simply neglected. This can be explained by insufficient tools to optimize propellers in waves and by the general lack of knowledge regarding operating conditions in waves.

Nevertheless, results of experiments carried out by Moor and Murdey (1970) showed that propulsion factors change significantly in the presence of waves. Unsteady RANS simulations performed by Guo et al. (2012) indicated that axial velocities at the propeller disk can increase up to 35% of the ship forward speed. Speed loss (caused by added resistance, thrust loss and change of propulsion point), propeller rpm fluctuations (due to the time-varying wake in waves) and motions of the ship (due to the interaction between ship and surface waves) influence the propeller performance and ultimately cause an increase in propeller-induced hull pressure pulses (Taskar, 2017).

Taskar et al. (2016) carried out an investigation regarding the effect of waves on the propeller performance of the KVLCC2 tanker. It was found that the time-variation of wake distribution has the largest impact on the propeller performance. The entire analysis was carried out by treating wake fields in a quasi-steady manner. This means that for each time instant, the flow field entering the propeller disk was treated as time-invariant. The underlying assumption is that the ratio of propeller blade frequency and wave encounter frequency is sufficiently large. Ideally, however, the propeller performance and resulting hull pressure pulses should be analyzed with fully unsteady calculations.

The purpose of this paper is to investigate if the quasi-steady approach predicts the propeller performance in waves with sufficient accuracy. Therefore, the KVLCC2 propeller is simulated both using a quasi-steady and an unsteady approach in full scale in waves behind the ship. The unsteady approach takes into account the time-variation of the wake field. The two approaches are compared by observing the differences in unsteady propeller forces and hull pressure pulses.

2 Methods

2.1 Propeller Analysis – ESPPRO

For the actual propeller analysis, i.e. the computation of propeller forces and hull pressure pulses, the DTU-developed panel code ESPPRO (see Regener 2016) is used. It is based on a potential-based formulation of the boundary element method and uses low-order panels.

To establish the blade wake geometry, or align the trailing vortices, multiple wake models are available in ESPPRO. For the present work a very simple but robust blade wake model was chosen that places the trailing wake sheets on helicoidal surfaces. In this model, the blade wake pitch is dependent on the blade pitch at $r/R = 0.9$ and the advance ratio (Streckwall, 1998). The blade wake geometry is "frozen" during the simulation, i.e. it is considered time-invariant.

The ship's wake field, on the other hand, may vary in time. The propeller immersion, relevant for the hydrostatic pressure and therefore cavitation estimation, may also change in time. These two features were added to ESPPRO as part of the present work.

For a propeller diameter D, constant shaft speed n, constant ship speed V_s and varying inflow velocity (expressed using the wake fraction w), the apparent advance ratio $J_A = V_s\,(1 - w)\,(nD)^{-1}$ will change over time. When performing calculations with time-varying inflow, currently the time-average of w (and corresponding J_A) is used in the blade wake model.

Hull pressure pulses are estimated by computing the time-varying pressure in an offbody point using the Bernoulli equation. The hull geometry is not modeled, but rather represented by a user-supplied solid boundary factor (defaulting to 2).

Table 1: KVLCC2 main particulars

Length between perpendiculars	320.0 m
Breadth	58.0 m
Design Draft	20.8 m
Service Speed	15.5 kts

Table 2: KP458 propeller characteristics

Diameter	9.86 m
Number of blades	4
A_E/A_O	0.431
$(P/D)_{\text{Mean}}$	0.47

2.2 Ship Motions in Waves and Potential Wake Fields – Shipflow Motions

Taskar et al. (2016) used the commercial software Shipflow Motions to compute ship motions (heave and pitch) as well as potential wake fields in regular waves. Shipflow Motions implements a fully nonlinear, unsteady boundary element method described by Kjellberg (2013).

The results by Taskar et al. (2016) are also used in the present work. Potential wake fields were extracted at all timesteps, and the propeller shaft submergence (for hydrostatic pressure) was calculated based on the ship motions. In addition, the potential wake field in calm water was computed using the same method.

2.3 Effective Wake Field in Calm Water – Shipflow-XCHAP and ESPPRO

The present work uses a RANS-BEM coupling approach to compute the ship's full scale effective wake field in calm water. This hybrid approach uses a viscous flow solver (RANS) to compute the flow around the ship hull and a panel code (BEM) to compute the propeller flow. An iterative two-way coupling is established by transferring the total flow field from RANS to the BEM code and adding the BEM-computed propeller forces as body forces (momentum source terms) to the RANS computation. As the propeller-induced velocities are known from the previous coupling iteration, the effective wake field can be computed by subtracting the induced velocities from the total velocity field provided by the RANS solver. The propeller code is then run in this effective wake field.

In the present work, the commercial Shipflow-XCHAP is used on the RANS side. On the BEM side of the RANS-BEM coupling, the panel code ESPPRO is used.

The coupling plane (and therefore the plane where the effective wake field is evaluated) is located upstream of the propeller, following the contour of the blade's leading edge at an upstream distance of 5% of the propeller radius. This results in a curved upstream coupling plane as initially described by Rijpkema et al. (2013).

3 Calculation Case

The time-varying potential wake fields and propeller immersion values in regular waves obtained by Taskar et al. (2016) are also used in the present work (also see Sec. 2.2). Therefore, the same ship and propeller (the KVLCC2 tanker with MOERI's corresponding model propeller, see Tab. 1 and 2 or Kim et al. 2001) in the same wave conditions are analyzed. Head sea conditions at design speed were considered for three different regular waves ($\lambda/L = 0.6, 1.1, 1.6$), all with a wave amplitude of 3 m.

4 Estimating the Effective Wake Field in Waves

The idea is to express the wake field in waves at any point in time by decomposing it into a time invariant and a time-varying wake field. Specifically, the potential part of the wake distribution in calm water (w_{PC}) is subtracted from the wake distribution in calm water (w_0), and then the potential part in waves (w_{PW}) is added:

$$w = w_0 - w_{PC} + w_{PW}$$

Taskar et al. (2016) used this approach to investigate the change of nominal wake distribution in waves. In that case, the base wake field was the nominal wake field in model scale, as computed using CFD. The potential wake fields were obtained using potential flow calculations (also see Sec. 2.2). Comparing the resulting wake fields in waves with nominal wake fields in waves obtained from CFD showed that for the case investigated, viscous effects not only dominate the overall instantaneous wake distibution, but also appear to strongly affect the time-varying part of the wake field in waves. Based

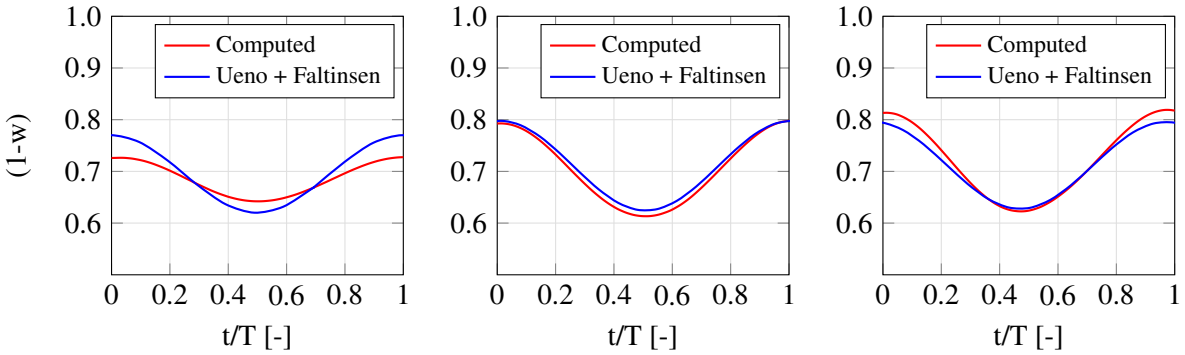

(a) $\lambda/L = 0.6$ (b) $\lambda/L = 1.1$ (c) $\lambda/L = 1.6$

Fig. 1: Comparison effective wake fraction and wake variation procedure

on this, it was concluded that potential flow calculation methods might not be suitable to estimate the time-variation of the wake field in waves.

However, viscous effects and their impact on the wake field change substantially between model scale and full scale. Thus, the same approach initially carried out by Taskar et al. (2016) is employed, but using the effective calm water wake distribution in full scale as the basis (obtained using the method described in Sec. 2.3). In addition, the effective wake field in calm water is scaled to match the full scale effective wake fraction obtained by Kim et al. (2001).

The wake fractions of the resulting wake fields are compared with wake fractions estimated by a method discussed by Taskar (2017), which combines the mean change in propeller inflow as outlined by Faltinsen et al. (1980), and the fluctuation of wake velocities, as described by Ueno et al. (2013).

The comparison for three wavelengths is shown in Fig. 1. Differences in the fluctuation amplitude can be noticed for short wavelengths. This overestimation by the method of Ueno et al. (2013) was also reported by Taskar (2017).

5 Calculation of propeller speed and ship speed loss in waves

Realistic ship operating conditions have to be considered for the current investigation. Therefore, the added resistance is calculated in irregular waves and the propeller rate of revolution is kept constant and equal to the value computed for calm water. In this way, speed reduction in waves is estimated for the three wave conditions: 11.5, 11.2 and 12.1 knots ($\lambda/L = 0.6$, 1.1, 1.6).

For calculating the added resistance in irregular waves, the method described in ITTC (2014) is used along with the modified Pierson-Moskowitz wave spectrum. The significant wave height is considered equal to the wave height of the regular wave simulated in Shipflow Motions (6 m) (see Sec. 2.2 and Sec. 3) and the peak frequency for irregular waves is set equal to the wave frequency of the regular waves simulated ($\lambda/L = 0.6$, 1.1, 1.6).

The wind resistance is calculated following the method described in ITTC (2014). The KVLCC2 superstructure is assumed to be located at the aft with dimensions typical for a tanker of that size.

The calm water ship resistance curve is estimated using the empirical method by Guldhammer and Harvald (1974). This is done because the resistance over a range of velocities is needed and not for one velocity only. Propulsion factors were determined experimentally in model scale and extrapolated to full scale by Kim et al. (2001). Experimental propeller open water data are available from MOERI for the KP458 model propeller (also see Tab. 2). Additionally, open water characteristics were also computed by the panel code ESPPRO. Both experimental and calculated open water data can be seen in Fig. 2.

The propeller rate of revolutions is estimated by considering the intersection between the required thrust relation K_T/J^2 and the open water thrust coefficient curve K_T. This yields a value for the propeller rate of revolutions of 76.25 rpm at design speed in calm water.

The classical power prediction approach is applied to compute the speed loss. Generally, in this

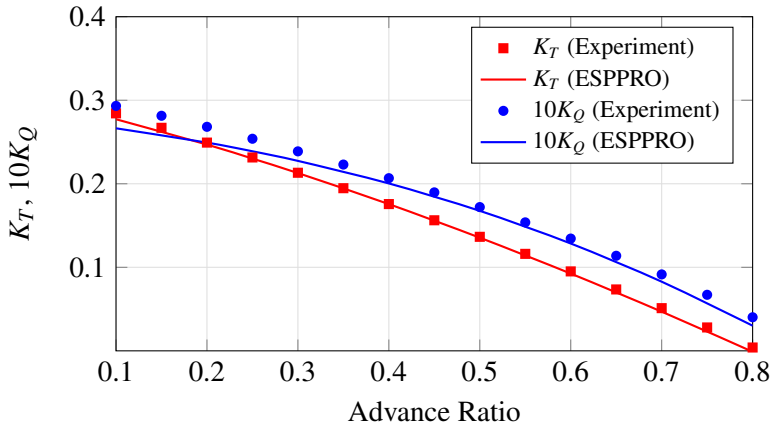

Fig. 2: Open Water Diagram for MOERI KP458

method, the resistance curve is modified by adding the resistance due to waves, wind, yawing, steering and other effects to the calm water resistance (Steen and Chuang, 2013). In the present work, only wind resistance and added resistance in waves are considered.

6 Results

The largest differences in unsteady forces and hull pressure pulses due to waves were observed for $\lambda/L = 1.1$. Therefore, although calculations were carried out for three different waves lengths, for brevity, results are only presented for this case.

Figures 3–5 show the variation of K_T, K_Q, and propeller-induced pressure in a point on the hull above the propeller. All results are shown over one wave encounter period. Results from both the quasi-steady (red curve) and the fully-unsteady calculations (blue curve) are shown.

In addition, Fig. 3 and 4 show the instantaneous wake fraction (solid black curve) and the time-averaged wake fraction (dashed black curve). The discrete time instances for the quasi-steady calculations are displayed as violet vertical lines.

Comparing the mean values of K_T and K_Q over one wave encounter period, negligible differences between the quasi-steady and the unsteady results were found (see Tab. 3).

As can also be seen from both Fig. 3 and Tab. 3, there are larger differences in minimum and maximum values. The magnitude of the fluctuations (i.e. the difference between overall maximum and minimum value) relative to the mean K_T, are 20% for the quasi-steady calculations and 24% for the unsteady calculations. For K_Q, the fluctuations have smaller magnitudes of 14% and 17%, respectively. This is believed to be mainly due to smaller magnitudes of $\frac{\partial K_Q}{\partial J}$ compared to $\frac{\partial K_T}{\partial J}$ (see Fig. 2).

7 Conclusions

The results from the quasi-steady approach and the current unsteady approach agree well for the case investigated. This indicates that the unsteady effects of wake distribution on blade forces are small.

The current results are in line with the assumption that the quasi-steady approach is sufficient when the ratio of propeller blade frequency and wave encounter frequency is sufficiently large. However, the unsteady results might be affected by the time-accurate evolution of the blade wake, which currently is not included in the model.

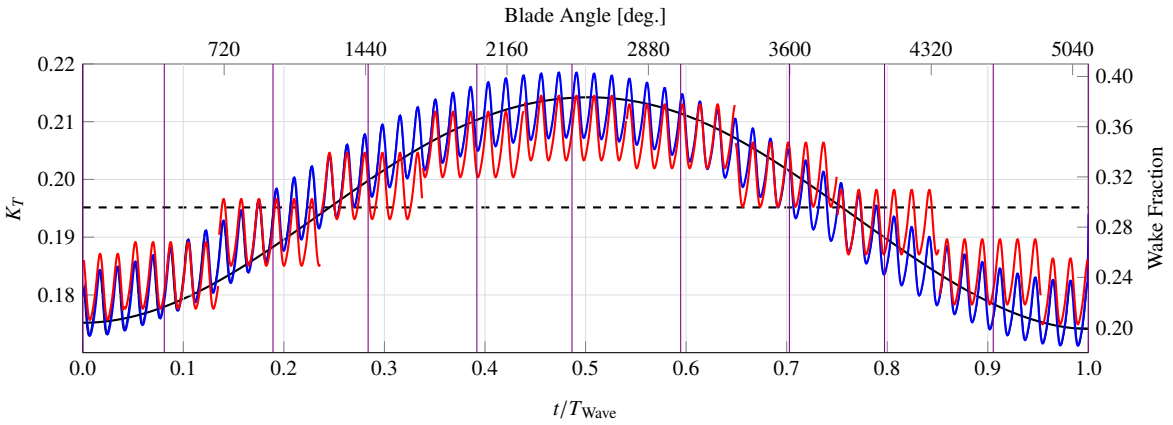

Fig. 3: K_T Variation (red: quasi-steady, blue: unsteady)

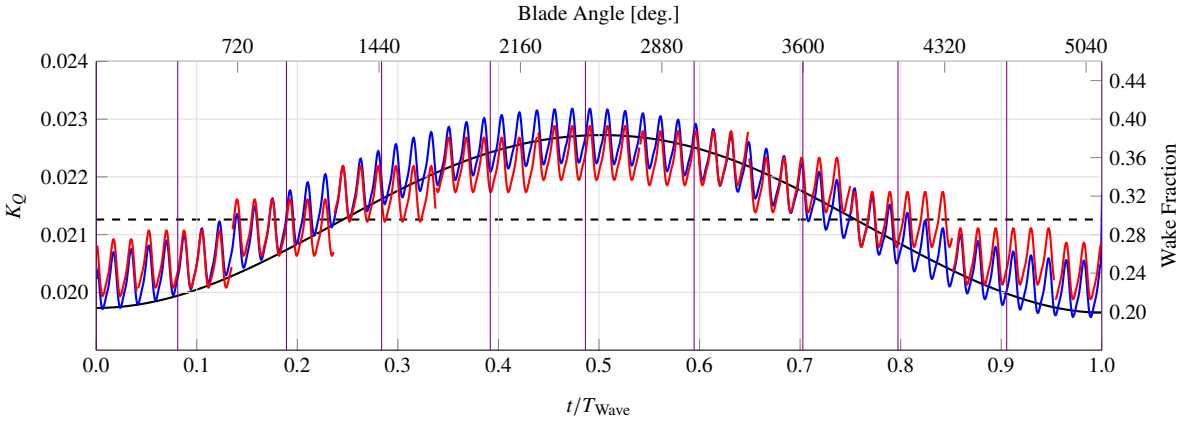

Fig. 4: K_Q Variation (red: quasi-steady, blue: unsteady)

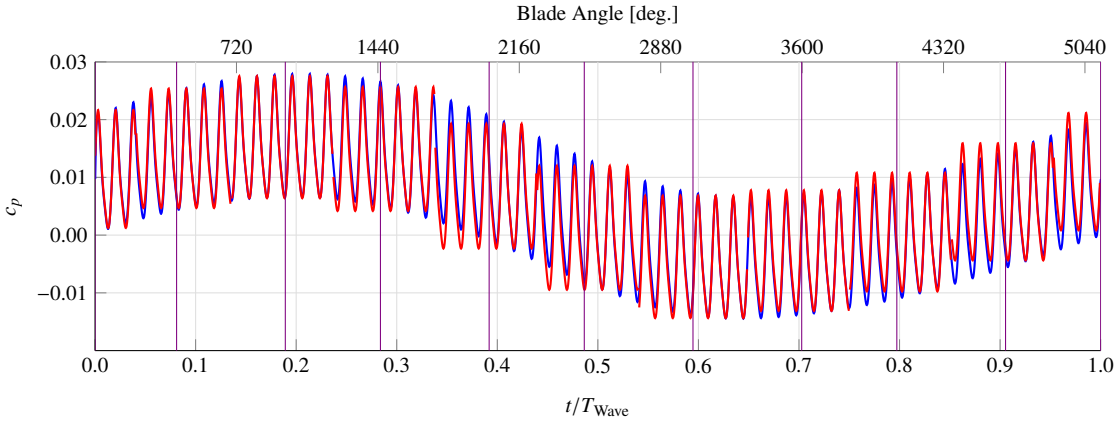

Fig. 5: Pressure at a point on the hull surface, located in the propeller plane, 1.6R above the shaft center

Table 3: Mean, minimum, maximum values of K_T, K_Q

	Mean	Min	Max
KT, Quasi-Steady	0.1953	0.1749	0.2144
KT, Unsteady	0.1954	0.1712	0.2184
KQ, Quasi-Steady	0.02143	0.01989	0.02287
KQ, Unsteady	0.02144	0.01958	0.02317

References

OM Faltinsen, KJ Minsaas, N Liapis, and SO Skjordal. Prediction of Resistance and Propulsion of a Ship in a Seaway. *13th Symposium on Naval Hydrodynamics*, pages 505–529, 1980.

NE Fine. *Nonlinear Analysis of Cavitating Propellers in Nonuniform Flow*. PhD thesis, Massachusetts Institute of Technology, 1992.

HE Guldhammer and SA Harvald. *Ship Resistance – Effect of Form and Principal Dimensions*. Akademisk Forlag, Copenhagen, 1974.

BJ Guo, S Steen, and GB Deng. Seakeeping prediction of KVLCC2 in head waves with RANS. *Applied Ocean Research*, 35:56–67, 2012. doi:10.1016/j.apor.2011.12.003.

ITTC. Recommended Procedures and Guidelines: Speed and Power Trials, Part 2 Analysis of Speed/Power Trial Data, 2014.

WJ Kim, SH Van, and DH Kim. Measurement of flows around modern commercial ship models. *Experiments in fluids*, 31(5):567–578, 2001.

M Kjellberg. *Fully Nonlinear Unsteady Three-Dimensional Boundary Element Method for Ship Motions in Waves*. PhD thesis, Chalmers University of Technology, 2013.

DI Moor and DC Murdey. Motions and Propulsion of Single Screw Models in Head Seas, Part II. *Quarterly Transactions of the Royal Institution of Naval Architects*, 112(2):121–127, 1970.

PB Regener. *Hull-Propeller Interaction and Its Effect on Propeller Cavitation*. PhD thesis, Technical University of Denmark, 2016.

D Rijpkema, B Starke, and J Bosschers. Numerical simulation of propeller-hull interaction and determination of the effective wake field using a hybrid RANS-BEM approach. In *3rd International Symposium on Marine Propulsors (smp'13)*, pages 421–429, Launceston, Australia, 2013.

S Steen and Z Chuang. Measurement of speed loss due to waves. In *3rd International Symposium on Marine Propulsors (smp'13)*, pages 439–446, Launceston, Australia, 2013.

H Streckwall. Hydrodynamic analysis of three propellers using a surface panel method for steady and unsteady inflow conditions. In *22nd ITTC Propulsion Committee Propeller RANS/Panel Method Workshop*, Grenoble, France, 1998.

B Taskar. *The Effect of Waves on Marine Propellers and Propulsion*. PhD thesis, Norwegian University of Science and Technology, 2017.

B Taskar, S Steen, RE Bensow, and B Schröder. Effect of waves on cavitation and pressure pulses. *Applied Ocean Research*, 60:61–74, 2016. doi:10.1016/j.apor.2017.04.005.

M Ueno, Y Tsukada, and K Tanizawa. Estimation and prediction of effective inflow velocity to propeller in waves. *Journal of Marine Science and Technology*, 18(3):339–348, 2013. doi:10.1007/s00773-013-0211-8.

Development of Propeller Shape Optimization System Using CFD Analysis

Yuki Saito[*] and Takanori Hino[†]
[*]Japan Marine United Corporation, Mie/Japan, [†]Yokohama National University, Kanagawa/Japan
saitoh-yuhki@jmuc.co.jp

1 Introduction

Wake adapted propellers have been studied to improve propeller performance operating behind a ship for a long time. In the early days, propellers were designed by adjusting pitch distribution based on the optimum circulation distribution[1)]. In recent years, propeller shape optimization considering wake distribution at a propeller position or interaction between a hull and a propeller is also studied. Most of these studies adopt a panel method based on potential flow for estimating propeller performance in order to save time[2)3)]. There have been few optimization cases using CFD because CFD needs longer computational time than a panel method for obtaining performance. As CPU time becomes shorter than before due to the improved computer performance, CFD-based propeller shape optimization applications are increasing[4)5)]. However, these approaches generally do not consider design conditions such as rotational speed or horse power which are determined from the engine specifications. The ultimate goal of the present study is to establish a propeller shape optimization method with the practical design conditions. For the first step, a propeller shape optimization system using CFD is presented and the system is applied to the optimization for the simplified design condition with uniform and non-uniform inflows.

2 Optimization system

2.1 Overview

Flowchart of the present propeller shape optimization system is shown in Fig.2.1. The system consists of an optimization tool, CFD with a grid generator for performance prediction and a shape modification tool. The system is organized to be flexible enough to cope with the various design conditions. When the inflow condition of CFD part is a uniform flow, the optimized design for a uniform flow is obtained. If the wake adapted propeller is desired, the inflow condition is replaced by a non-uniform wake field.

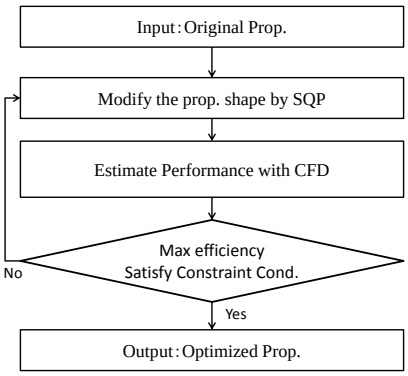

Fig. 2.1: Flowchart of the optimization system.

2.2 Shape modification method

A propeller radius and the number of blades are fixed and the following parameters are used to define a propeller shape.

A) Pitch distribution in the radial direction.

B) Maximum camber distribution in the radial direction.

C) Chordwise thickness distribution from mid. chord to trailing edge.

A modified propeller shape is obtained by multiplying the original shape parameter by the modification rate. The modified shape parameter is obtained from the original shape parameter as shown in eq. (2.1).

$$F_{(r)} = f_{(r)} \times dp_{(r)} \tag{2.1}$$

where

$F_{(r)}$: Modified shape parameter

$f_{(r)}$: Original shape parameter

$dp_{(r)}$: Modification rate

r : Radial coordinate

The shape parameter is pitch distribution, maximum camber distribution or chord length distribution and the modification rate is defined for each shape parameter.

Each modification parameter is defined by the values at five radial position (r/R=0.1800, 0.4000, 0.6000, 0.8000 and 1.0000, where R is a propeller radius) and $dp_{(r)}$ is obtained as a spline function using five points above. Actual propeller geometry is made using above shape parameters by the multipurpose 3D CAD software, Rhinoceros.

2.3 Propeller performance estimation

Propeller performance estimation is performed using CFD. Computational grid is generated using the commercial code, Hexpress and propeller performance is estimated using another commercial code, Fluent. Calculation model is shown in Fig.2.2 and grid distribution in a center plane is shown in Fig.2.3. The fore boundary of calculation region is 4 propeller diameters away, the side boundary is 6 propeller diameters away and the aft boundary is 10 propeller diameters away from a propeller. This calculation model includes about 1.5 million cells. The calculation condition is listed in Table 2.1.

Table 2.1 Calculation condition.

Turbulence model	Transition k-ω SST
Reynolds number (based on prop. dia.)	$R_{nD}=1.10\times10^{6}$
Propeller diameter [m]	0.2400
Rotational speed [r.p.s]	19.189

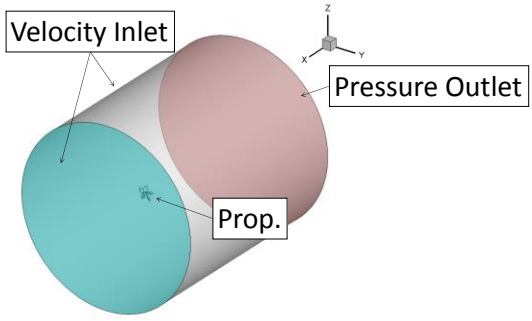

Fig. 2.2: Calculation model

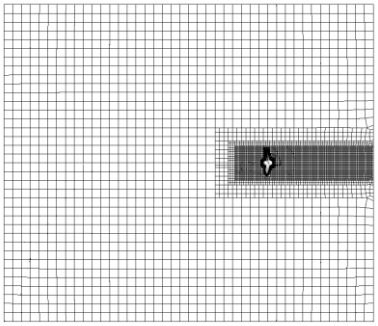

Fig. 2.3: Grid distribution in a center plane.

2.4 Optimization algorithm

The Sequential Quadratic Programming method (SQP) is used as an optimization algorithm. Many recent optimization studies use Genetic Algorithm and it is able to find globally optimized result easier than SQP.

However, it needs large number of calculations in an optimization sequence and hence large amount of calculation time when CFD method is utilized. For the calculation time saving, SQP is selected in this system. The objective function is propeller open efficiency η_o as shown in eq. (2.2) where J, K_T and K_Q are the advance coefficient, thrust coefficient and torque coefficient, respectively. The constraint condition is applied for the torque variation as shown in (2.3) where K_{Q0} is the initial torque coefficient.

$$\eta_O = \frac{J}{2\pi}\frac{K_T}{K_Q} \tag{2.2}$$

$$99.5\%K_{Q0} \le K_Q \le 100.5\%K_{Q0} \tag{2.3}$$

3 Optimization application

3.1 Design conditions

To confirm effectiveness of this system, the MAU propeller is optimized in a uniform flow and a VLCC's wake. In this optimization, the wake distribution is circumferentially averaged distribution for estimating propeller performance by steady calculation of CFD. Original and averaged wake distributions are shown in Fig.3.1. The particulars of the original propeller are shown in Table 3.1. The design condition is shown in Table 3.2. In this study, initial shape of the optimization in the wake flow is set to the optimized shape in a uniform flow.

Table 3.1 Particulars of original propeller.

Propeller name	Case0
Blade section	MAU
Num. of blade	5
Propeller diameter	0.2400 (m)
Pitch ratio	0.6689(Const.)
Exp. Area ratio	0.5350
Boss ratio	0.1939

Table 3.2 Design condition.

Optimization point	J=0.250
Shape parameters	• Pitch dist. • Max. Camber dist. • Chordwise thickness dist.

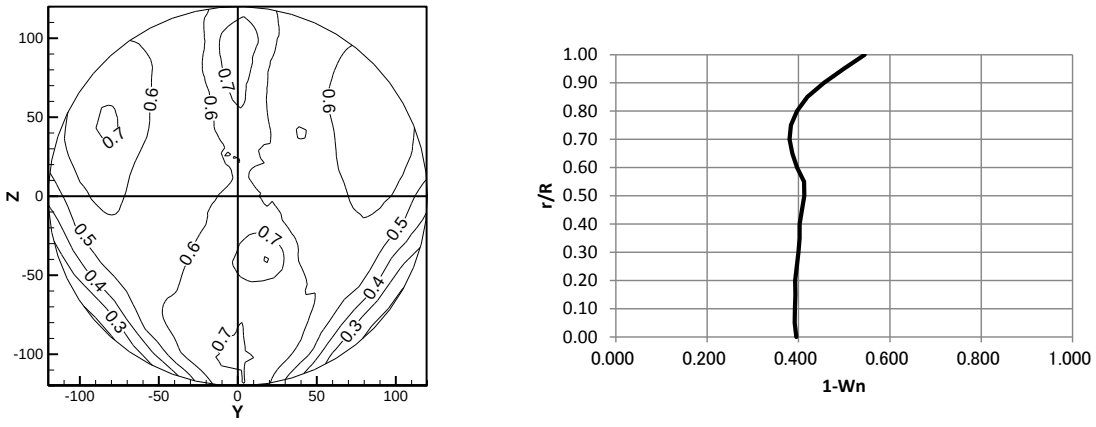

Fig. 3.1 Wake distributions. (Left: Original wake. Right: Circumferentially averaged wake.)

3.2 Optimization result

Each shape parameter distributions of case0, case1 and case2 (where case0 is the original, case1 is the optimized shape in the uniform flow and case2 is the optimized shape in the wake) are shown from Fig. 3.2 to Fig.3.4. The blade section of r/R=0.700 are shown in Fig. 3.5. Shape characteristics of optimization results are as follows:

- Pitch distribution is smaller than the original and this trend becomes stronger at the tip. (Case1 and case2 have same trend.)

- Pitch of the optimized shape has more complex distribution than original shape which is constant. (Case1 and case2 have same trend.)
- Maximum camber distribution of the optimized shape is almost the same from root to r/R=0.500 and become larger than the original from there to the tip. (Case1 and case2 have same trend.)
- Chordwise thickness is decreases from the Case0 at r/R=0.400 and r/R=0.800. (Case1 and case2 have same trend.)
- There are small differences of shape characteristics between case1 and case2.

Table 3.3 shows comparison result of propeller open characteristics between case0 and case1 estimated by CFD. It shows the thrust of case1 is higher than that of case0 whereas the torque is almost the same between the two at the design point J=0.250. Table3.4 shows these propellers' performance in wake which are also estimated by CFD. Where η_R, W_Q, $\eta_H{}^*$ and η are the relative rotative efficiency, wake fraction which is obtained by K_Q identity method, pseudo hull efficiency and propulsive efficiency, respectively.

As the result, case1 and case2 improve propeller efficiency about 2% compared with case0, and the torques of these cases are almost same as case0. This performance change is consistent with the constraint condition applied and the efficiency improvement has been achieved. On the other hand, superiority of performance of case2 in the wake is marginal compared to case1. In general, η_R of wake adapted propeller must be better than η_R of a propeller which is not wake-adapted. However, the presented result shows η_R of case2 is almost same as case1. The following reasons are conceivable for this result.

- The effect of wake adapting is smaller than the effect of optimization in a uniform inflow. Therefore, improvement from the optimization result in a uniform flow to that in a wake is too small to appear.
- By averaging wake distribution, the non-uniformity of velocity field is weakened. Therefore, difference between the wake and the uniform flow is become small.
- Non-uniformity of the wake used in this study is weak compared to the past studies.

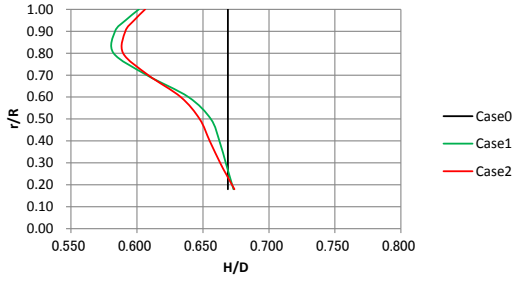

Fig. 3.2 Comparison of pitch distributions between Case0, Case1 and Case2.

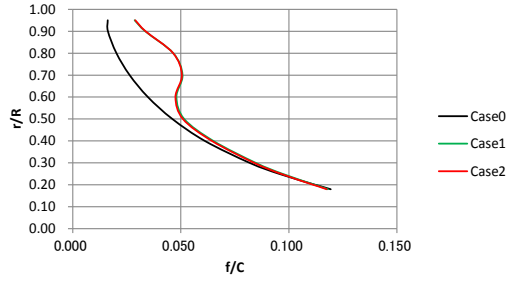

Fig. 3.3 Comparison of camber distributions between Case0, Case1 and Case2.

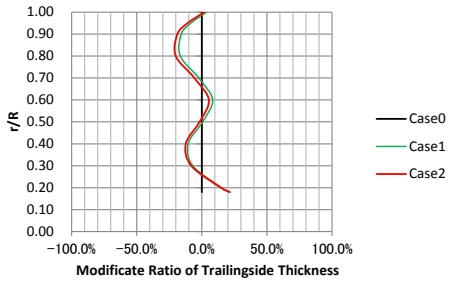

Fig.3.4 Comparison of thickness reduction ratio distribution between Case0, Case1 and Case2.

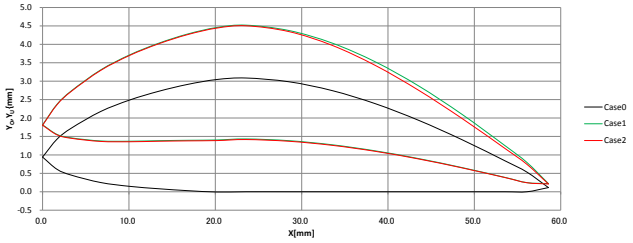

Fig. 3.5 Comparison of blade section of r/R=0.7 between Case0, Case1 and Case2.

Table 3.3 Estimated result of propeller performance at J=0.250

	KT	diff.	10KQ	diff.	η_O	diff.
Case0	0.2246	Base	0.2434	Base	0.3672	Base
Case1	0.2283	+1.6%	0.2424	-0.4%	0.3748	+2.0%

Table 3.4 Estimated results of propeller performance in wake.

	K_T	diff.	$10K_Q$	diff.	η_O	diff.
Case0	0.2254	Base	0.2434	Base	0.3683	Base
Case1	0.2297	+1.9%	0.2433	0.0%	0.3706	+0.6%
Case2	0.2294	+1.8%	0.2424	-0.4%	0.3686	+0.1%
	η_R	$1\text{-}W_Q$	η_H^*	diff	η	Diff
Case0	0.3%	0.5002	1.999	Base	0.7362	Base
Case1	0.1%	0.4940	2.024	+1.3%	0.7503	+1.9%
Case2	0.0%	0.4902	2.040	+2.1%	0.7520	+2.1%

3.3 Cavitation risk

The pressure distribution on back side of case2 is shown in Fig.3.6. It's estimated by CFD. There is a high negative pressure region around mid-chord at r/R=0.800. It may generate bubble-cavitation and ultimately causes erosion. In order to avoid this risk, an additional constraint condition is examined. The constraint condition is shown in eq.(3.1) where P_{ref} and σ_n is pressure at mid-chord and cavitation number respectively. This constraint condition is applied at r/R=0.700,0.800 and 0.900 and propeller performance is estimated by unsteady CFD calculation.

$$Min(P_{ref}) < -\sigma_n \tag{3.1}$$

Optimization with this constraint condition applies to case1. Its history is shown in Fig.3.7 and pressure distributions of case3 and case4 are shown in Fig.3.8 and Fig.3.9 respectively. As a result, pressure around mid-cord at r/R=0.800 of case3 and case4 are higher than case2. (High negative pressure region becomes small.) It shows that the erosion risk caused by cavitation can be reduced by constraint condition about pressure on the back side. Table3.5 shows propeller performance that is estimated by CFD. The performance of case4 is slightly lower than other propellers, but it still has higher performance than case1. From these results, it is considered that optimization to improve performance with suppressing cavitation risk is possible.

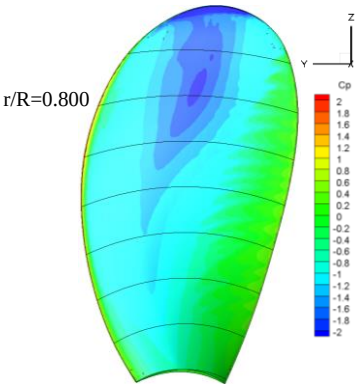

Fig.3.6 Pressure distribution on back side of Case2.

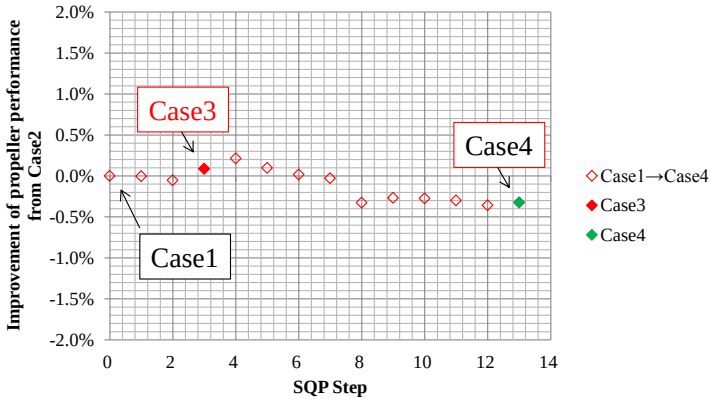

Fig. 3.7 History of optimization with applying pressure constraint condition.

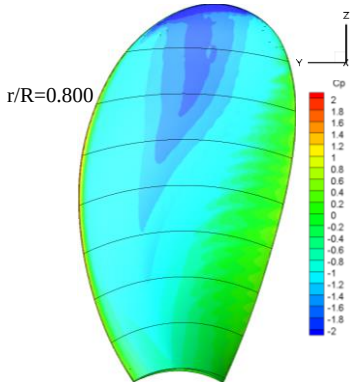

Fig.3.8 Pressure distribution on back side of Case3.

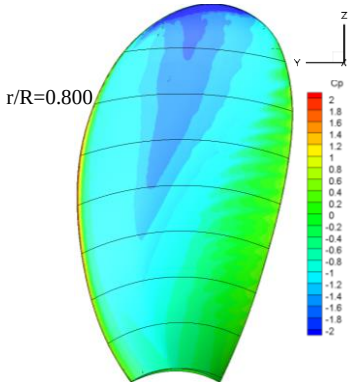

Fig. 3.9 Pressure distribution on back side of Case4.

Table 3.5 Estimated results of propeller performance in wake.(Unsteady)

	Case0	Case2	Case3	Case4
η_O	0.3659 (Base)	0.3697 (+1.0%)	0.3713 (+1.5%)	0.3694 (+1.0%)
η_R	1.003 (Base)	1.000 (-0.3%)	1.001 (-0.2%)	1.001 (-0.2%)
η_H	1.771 (Base)	1.791 (+1.1%)	1.781 (+0.6%)	1.7824 (+0.6%)
η	0.6499 (Base)	0.6623 (+1.9%)	0.6620 (+1.9%)	0.6592 (+1.4%)

4 Conclusions

The following conclusions are obtained in the present study.

- The propeller shape optimization system using CFD and SQP is developed with the shape parameters for pitch, maximum camber and chordwise thickness distributions.
- Under the constraint condition for the limited torque variations, the optimized shape is obtained which achieves about 2% improvement of efficiency.
- There is no big difference of shape between optimization results in a uniform flow and in a wake, and performances of both of them are almost same. Several reasons are conceivable for this aspect, and it is necessary to study further.
- The cavitation risk can be suppressed by incorporating constraint condition about the pressure value on the back side of propeller.

References

1) Lerbs, H.W. (1952), Moderately Loaded Propellers with a Finite Number of Blades and an Arbitrary Distribution of Circulation, Trans. SNAME, Vol.60, 73-117.
2) Vesting, F. and Bensow, R. (2011), Propeller Optimization Considering Sheet Cavitation and Hull Interaction, Proc. Second International Symposium on Marine Propulsors, 2011.
3) Gaggero, S., Viviani, M. et al. (2015), A Design by Optimization of Tip Loaded Propellers, Proc. Fourth International Symposium on Marine Propulsors, 2015.
4) Ikeda, T., Kimura, K et al. (2016), Advanced propeller design optimization system based on open source codes and its application, Proc. PRADS2016, 2016.
5) Park, J., Choi, G. and Park, D. (2016), Systematic propeller optimization considering hull interaction based on CFD, Proc. PRADS2016, 2016.

Implementation of THINC-type VoF Advection Scheme on Structured FVM Solver

Nobuaki SAKAMOTO and Kunihide OHASHI
National Maritime Research Institute (NMRI), Mitaka, Tokyo JAPAN
sakamoto@nmri.go.jp k-ohashi@nmri.go.jp

1. INTRODUCTION

As the Eulerian approach to resolve interface of two phase flow, there are several numerical methods summarized in Fig. 1 by Mirjalili et al. (2017)[1]. In the field of ship hydrodynamics, there are two major interfacial problems around a hull and a propeller, e.g. free surface wave and cavitation. To solve these physics, it is quite popular to formulate momentum equation under the assumption of single fluid. Focusing on the propeller cavitation, the phase change of the fluid is taken into consideration as the source term of continuity equation with appropriate cavitation model. Among two well-known models, e.g. Volume of Fluid (VoF) and Level Set methods, to capture the interface of propeller cavitation, VoF is still the main stream to be adopted. Since the volume fraction is the conservative property, it is physically straightforward to be coupled with the continuity equation.

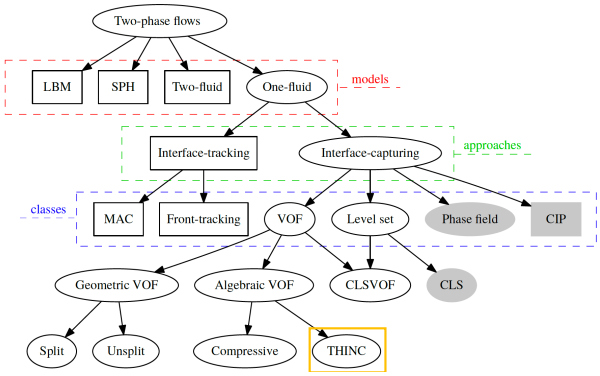

Fig. 1 Classification of numerical methods for two phase flow according to Mirjalili et al. (2017) [1]

According to Fig. 1[1], VoF advection schemes can be categorized as "geometric" and "algebraic". The major difference of the two exists on the evaluation of face flux. Piecewise Linear Interface Calculation (PLIC)[2] is considered as one of the most accurate geometric VoF schemes yet its coding is quite complicated because geometrical manipulations, e.g. computing cross points between interface and cell edges etc., are required to reconstruct face flux. Algebraic VoF utilizes a certain functional form to reconstruct face flux, therefore, it is free from complexity seen in geometric VoF. Different to the existing compressive schemes[3], Tangent of Hyperbola for INterface Capturing (THINC) scheme[4] utilizes hyperbolic tangent profile to assume distribution of VoF within a cell containing the interface. Since the THINC scheme is considered to have better capability in preserving interfacial profile and volumetric amount of volume fraction without artificial compression[1][9], it could definitely be one of the schemes to be adopted to capture the interface due to propeller cavitation. Among several THINC schemes[5][6][7][8][9], some of the formulations proposed by Ii et al. (2012, 2014)[6][7] and Xie et al. (2014)[8] will be utilized herein to develop unsplit THINC-type VoF advection scheme with structured grid.

2. MULTI-DIMENSIONAL THINC SCHEME

2.1 Overview of THINC scheme

To describe gas-liquid interface, the volume fraction ϕ_i is defined at a cell center. The ϕ_i varies $0.0 \leq \phi_i \leq 1.0$ where $\phi_i = 0.0$ and $\phi_i = 1.0$ represent gas and liquid phase, respectively, which means that $\phi_i = 0.5$ describes the interface. The advection equation of ϕ_i is written in the conservation form as

$$\frac{\partial \phi_i}{\partial t} + \nabla \cdot (\phi_i \vec{u}) - \phi_i (\nabla \cdot \vec{u}) = 0 \quad (1)$$

where $\vec{u} = (u, v, w)$ is the velocity vector also defined at a cell center. Since the flow field in the present study satisfies divergence free condition, the 3rd term of left hand side (LHS) of Eq. (1) is zero and thus will not be appeared in the further description. When Eq. (1) is integrated over a cell using Gauss divergence theorem, resultant advection equation is written in the semi-discrete form as

$$\frac{\partial \phi_i}{\partial t} + \frac{1}{V_i} \sum_{faces} (\overrightarrow{u_f} \cdot \vec{n}) H_i \Delta s = 0 \quad (2)$$

where V_i is the cell volume, $\overrightarrow{u_f}$ is the velocity vector redefined on the cell face, $\vec{n}$ is the unit normal vector of the cell face pointing toward outside, H_i is the reconstructed value of ϕ_i defined on a cell face, and Δs is the area of the cell face. THINC scheme approximates the H_i as

$$H_i(\vec{x}) = \frac{1}{2}\{1 + tanh(\beta(P_i(\vec{x}) + d_i))\} \quad (3)$$

where $\vec{x}$ is the position vector of a cell in a physical domain, β is the parameter to define the steepness of interface jump inside a cell, and d_i is the parameter which defines the location of interface jump inside a cell. According to the functional form of Eq. (3), the H_i theoretically varies $0.0 \leq H_i \leq 1.0$. As explained in the later section 2.3, numerical integration of H_i over cell faces is required and such manipulation can easily be done in a computational domain(ξ, η, ζ) rather than a physical domain (x, y, z). The Eq. (3) is therefore redefined in the computational domain as

$$H_i(\vec{\xi}) = \frac{1}{2}\left\{1 + tanh\left(\beta\left(P_i(\vec{\xi}) + d_i\right)\right)\right\} \quad (4)$$

where $0.0 \leq \vec{\xi} = (\xi, \eta, \zeta) \leq 1.0$. In the right hand side (RHS) of Eq. (4), $P_i(\vec{\xi}) + d_i = 0$ defines the shape of interface inside a cell. According to the references[6][8], $P_i(\vec{\xi})$ is expressed as a quadratic polynomial as

$$P_i(\vec{\xi}) = c^{(\xi)} a_{200} \xi^2 + c^{(\eta)} a_{020} \eta^2 + c^{(\zeta)} a_{002} \zeta^2 + c^{(\xi)} c^{(\eta)} a_{110} \xi\eta + c^{(\eta)} c^{(\zeta)} a_{011} \eta\zeta + c^{(\zeta)} c^{(\xi)} a_{101} \zeta\xi + a_{100} \xi + a_{010} \eta + a_{001} \zeta \quad (5)$$

where a_{str} (s,t,r=0,1,2 and s+t+r$\leqq$2) are computed from the gradient of fluid interface which will be explained in section 2.2. $c^{(\xi,\eta,\zeta)}$ is set 0 or 1 according to the criteria described in section 2.3. When all the 2nd order and cross-coupling terms are ignored

in Eq. (5), the $P_i(\vec{\xi}) + d_i = 0$ becomes the plane surface[7].

2.2 Evaluation of interface normal vector

To define a_{str} in Eq. (5), two methods are adopted in the present study. First method is to utilize Gauss divergence theorem over the control volume (CV) described in the green dotted line in Fig. 2 (termed "shifted CV"). This method determines $\nabla\phi$ on six surfaces of a cell, therefore, simple arithmetic mean of $\nabla\phi$ over cell surfaces (i.e. i$\pm$1/2, j$\pm$1/2, k $\pm$1/2) gives $\nabla\phi_i$ at a cell center. Since this method directly estimates $\nabla\phi$ at cell center, the 2nd order and cross-coupling terms are not evaluated and thus set to zero.

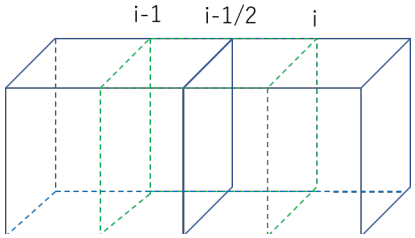

Fig. 2 Control volume (green dotted line) to evaluate $\nabla\phi$ on a cell surface, the CV in this figure is for the cell face i-1/2

Second method is based on node-based least square (termed "node LSQ") proposed by Xie et al. (2014)[8]. To avoid confusion, the subscript "ij" is given to the nodal value of ϕ and $\nabla\phi$. The linear function $\Phi(x,y,z)$ which interpolates nodal variables to a cell center is defined as

$$\Phi(\mathrm{x},\mathrm{y},\mathrm{z}) = \phi_{ij} + \frac{\partial\phi}{\partial x}|_{ij}x_k + \frac{\partial\phi}{\partial y}|_{ij}y_k + \frac{\partial\phi}{\partial z}|_{ij}z_k \quad (6)$$

where $\overrightarrow{x_k}$ is the position vector of a cell center of k[th] surrounding cell. Taking eight surrounding cells of a node, minimizing the following equation by LSQ gives ϕ_{ij} and $\nabla\phi_{ij}$.

$$I_{ij} = \sum_{k=1}^{8}(\Phi(x,y,z) - \phi_k)^2 \quad (7)$$

where ϕ_k is the volume fraction defined at k[th] cell center. Simple arithmetic mean of $\nabla\phi_{ij}$ gives $\nabla\phi_i$ at a cell center as

$$\nabla\phi_i(x,y,z) = \frac{1}{8}\left(\sum_{j=1}^{8}\frac{\partial\phi}{\partial x}|_{ij}, \sum_{j=1}^{8}\frac{\partial\phi}{\partial y}|_{ij}, \sum_{j=1}^{8}\frac{\partial\phi}{\partial z}|_{ij}\right)^T \quad (8)$$

Transformation of $\nabla\phi_{ij}$ and/or $\nabla\phi_i$ from physical domain to computational domain is carried out utilizing the 3x3 metric tensor as

$$\nabla\phi_{ij/i}(\xi,\eta,\zeta) = \begin{bmatrix} \frac{\partial x}{\partial\xi} & \frac{\partial y}{\partial\xi} & \frac{\partial z}{\partial\xi} \\ \frac{\partial x}{\partial\eta} & \frac{\partial y}{\partial\eta} & \frac{\partial z}{\partial\eta} \\ \frac{\partial x}{\partial\zeta} & \frac{\partial y}{\partial\zeta} & \frac{\partial z}{\partial\zeta} \end{bmatrix} \nabla\phi_{ij/i}(x,y,z) \quad (9)$$

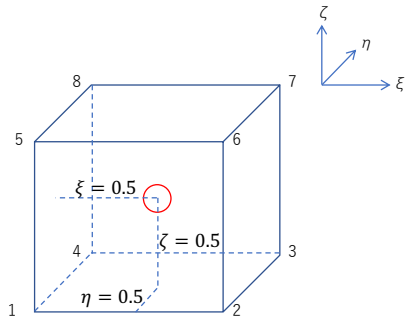

Fig. 3 Numbering criterion of $\vec{f_j}, (j = 1\sim8)$. Set $\xi = \eta = \zeta = 0.5$ to map cell center variables (○) from physical to computational domain using Eq. (10).

To define the metric tensor in the RHS of Eq. (9), position vector $\vec{x}$ in the physical domain is parametrized by tri-linear interpolation function (or sometimes termed mapping/shape function) defined as

$$\vec{x} = \vec{A} + \vec{B}\xi + \vec{C}\eta + \vec{D}\zeta + \vec{E}\xi\eta + \vec{F}\eta\zeta + \vec{G}\zeta\xi + \vec{H}\xi\eta\zeta \quad (10)$$

where $\vec{A}\sim\vec{H}$ are the weight vectors calculated utilizing the nodal position vector $\vec{f_j}, (j = 1\sim8)$ in the physical domain defined in Eq. (11) as

$$\begin{aligned} &\vec{A} = \vec{f_1}, \vec{B} = \vec{f_2} - \vec{f_1}, \vec{C} = \vec{f_4} - \vec{f_1}, \vec{D} = \vec{f_5} - \vec{f_1}, \\ &\vec{E} = \vec{f_1} - \vec{f_2} - \vec{f_4} + \vec{f_3}, \vec{F} = \vec{f_1} - \vec{f_2} - \vec{f_5} + \vec{f_6} \\ &\vec{G} = \vec{f_1} - \vec{f_4} - \vec{f_5} + \vec{f_8} \\ &\vec{H} = \vec{f_2} - \vec{f_1} + \vec{f_4} - \vec{f_3} + \vec{f_5} - \vec{f_6} + \vec{f_7} - \vec{f_8} \end{aligned} \quad (11)$$

with the numbering criterion depicted in Fig. 3. Notice that the mapping function Eq. (10) is different to the one utilized in the references[7][8][9].

The six components of second order derivatives of the volume fraction, $\frac{\partial^2\phi_i}{\partial\xi^2}, \frac{\partial^2\phi_i}{\partial\eta^2}, \frac{\partial^2\phi_i}{\partial\zeta^2}, \frac{\partial^2\phi_i}{\partial\xi\partial\eta}, \frac{\partial^2\phi_i}{\partial\eta\partial\zeta}, \frac{\partial^2\phi_i}{\partial\zeta\partial\xi}$ are computed at a cell center using central differencing of pre-determined $\nabla\phi_{ij}$. Readers can find their complete formulations in Xie et al. (2014)[8]. Utilizing these second order derivatives, a_{str} in Eq. (5) are determined as

$$\begin{cases} a_{100} = n_\xi - \frac{1}{2}\left(c^{(\xi)}l_{\xi\xi} + c^{(\xi)}c^{(\eta)}l_{\xi\eta} + c^{(\xi)}c^{(\zeta)}l_{\xi\zeta}\right) \\ a_{010} = n_\eta - \frac{1}{2}\left(c^{(\eta)}l_{\eta\eta} + c^{(\xi)}c^{(\eta)}l_{\xi\eta} + c^{(\zeta)}c^{(\eta)}l_{\eta\zeta}\right) \\ a_{001} = n_\zeta - \frac{1}{2}\left(c^{(\zeta)}l_{\zeta\zeta} + c^{(\xi)}c^{(\zeta)}l_{\xi\zeta} + c^{(\eta)}c^{(\zeta)}l_{\eta\zeta}\right) \\ a_{110} = c^{(\xi)}c^{(\eta)}l_{\xi\eta}, a_{011} = c^{(\zeta)}c^{(\eta)}l_{\eta\zeta}, a_{101} = c^{(\xi)}c^{(\zeta)}l_{\xi\zeta} \\ a_{200} = \frac{1}{2}c^{(\xi)}l_{\xi\xi}, a_{020} = \frac{1}{2}c^{(\eta)}l_{\eta\eta}, a_{002} = c^{(\zeta)}l_{\zeta\zeta} \end{cases} \quad (12)$$

where

$$\begin{cases} \frac{\partial^2\phi_i}{\partial\xi^2} = l_{\xi\xi}, \frac{\partial^2\phi_i}{\partial\eta^2} = l_{\eta\eta}\ \frac{\partial^2\phi_i}{\partial\zeta^2} = l_{\zeta\zeta} \\ \frac{\partial^2\phi_i}{\partial\xi\partial\eta} = l_{\xi\eta}, \frac{\partial^2\phi_i}{\partial\eta\partial\zeta} = l_{\eta\zeta}, \frac{\partial^2\phi_i}{\partial\zeta\partial\xi} = l_{\zeta\xi} \\ \frac{\partial\phi_i}{\partial\xi} = n_\xi, \frac{\partial\phi_i}{\partial\eta} = n_\eta, \frac{\partial\phi_i}{\partial\zeta} = n_\zeta \end{cases} \quad (13)$$

The "l_{pq}" is termed curvature tensor.

2.3 Treatment of "d_i" variable

Integrating Eq. (4) over cell faces in the computational domain, the d_i is determined in such a way that the integrated result must satisfy the following relationship.

$$\int_0^1\int_0^1\int_0^1 H_i(\vec{\xi})\,d\xi d\eta d\zeta = \phi_i \quad (14)$$

Since it is not possible to integrate tangent hyperbolic function in multi-dimension analytically, several numerical approaches have been suggested by the references[6][7][8][9]. Prior to the integration, the dominant interface direction is determined utilizing the maximum absolute value of n_ξ, n_η and n_ζ for which this procedure is common among all the approaches. Ii et al. (2012, 2014)[6][7] and Xie et al. (2014)[8] utilizes hybrid integration. Towards the dominant direction, Eq. (14) is analytically integrated, and then, Gauss-Legendre integrations (GLI) are utilized toward the rest of directions. Ii et al. (2012) utilizes 2-points rule in GLI with quadratic surface representation in Eq. (5) which yields quartic equation to be solved to determine d_i. Ii et al. (2014)[7] utilizes midpoint rule in GLI with linear surface representation in Eq. (5) which yields much simpler form to obtain d_i. Notice that this approach is likely to have less numerical accuracy compared to the other methods[6][8][9] due to degrading the order of interface polynomial and the number of Gaussian points for GLI. Xie and Xiao (2017)[9] integrates LHS of Eq. (14) over all directions by

GLI with up to 4-points rule in the dominant direction and 2-points rule in the rest of directions for hexahedral cell. Taking computational costs and numerical robustness into considerations, the present study adopts the approach by Ii et al. (2014)[7] but reformulated for square element with quadratic surface representation. The resultant formula to compute d_i is

$$d_i = \frac{1}{2\beta}\ln\left(\frac{1-AQ}{AB(Q-A)}\right) \quad (15)$$

where A, B and Q are determined as

Case 1: $|n_\xi| = max(|n_\xi|, |n_\eta|, |n_\zeta|)$

$$A = \exp.(\beta a_{100})$$
$$B = \exp.\left(\beta(0.5(a_{020}+a_{002}+a_{011})+a_{010}+a_{001})\right)$$
$$Q = \exp.\left(\beta a_{100}(2\phi_i-1)\right), c^{(\xi)} = 0 \quad (16)$$

Case 2: $|n_\eta| = max(|n_\xi|, |n_\eta|, |n_\zeta|)$

$$A = \exp.(\beta a_{010})$$
$$B = \exp.\left(\beta(0.5(a_{200}+a_{002}+a_{101})+a_{100}+a_{001})\right)$$
$$Q = \exp.\left(\beta a_{010}(2\phi_i-1)\right), c^{(\eta)} = 0 \quad (17)$$

Case 3: $|n_\zeta| = max(|n_\xi|, |n_\eta|, |n_\zeta|)$

$$A = \exp.(\beta a_{001})$$
$$B = \exp.\left(\beta(0.5(a_{200}+a_{020}+a_{110})+a_{100}+a_{010})\right)$$
$$Q = \exp.\left(\beta a_{001}(2\phi_i-1)\right), c^{(\zeta)} = 0 \quad (18)$$

2.5 Flux computation and time integration

Once the d_i is determined, Eq. (4) is utilized to compute numerical flux across cell faces. Following Xie et al. (2014)[8]'s description, Eq. (2) is re-written as

$$\frac{\partial \phi_i}{\partial t} = -\frac{1}{V_i}\sum_{faces} v_{n_{ij}} H_{iup} \Delta s \quad (19)$$

where $v_{n_{ij}} = \overrightarrow{u_f}\cdot\vec{n}$. In the present study, $\overrightarrow{u_f}$ is the simple average of cell center values at left and right sides of a cell face. H_{iup} is the reconstruction function of ϕ_i at the upwind (or donor) cell of a cell face where the flux is to be evaluated. The upwind cell is determined by the sign of $v_{n_{ij}}$. Figure 4 explains the example of computation in the RHS of Eq. (19) when the flux at i+1/2 face of cell i is to be evaluated.

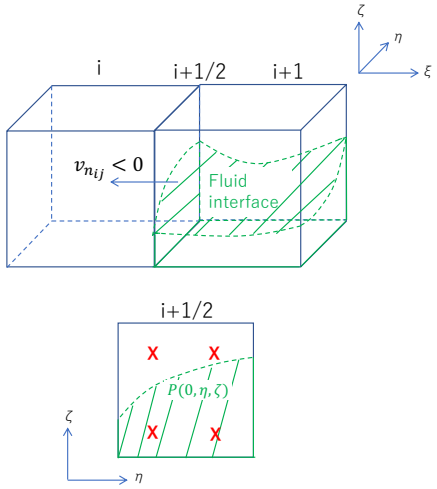

Fig. 4 Schematic figure of flux evaluation in ξ-direction, "X" describes the Gaussian points on the computational domain

Given velocity field determines the sign of $v_{n_{ij}}$ at i+1/2 for which it is negative for this case. This determines the upwind cell as cell i+1. On the computational domain, i+1/2 face of cell i+1 is ξ=0 plane, therefore, Eq. (5) which determines the distribution of ϕ_{i+1} is the function of η and ζ. The 2-points GLI over ξ=0 plane using Gaussian points $g_p = \frac{1}{2}\left(1 \pm \frac{1}{\sqrt{3}}\right)$ with Gaussian weight w_p=0.5 gives the flux at i+1/2 as

$$f_{i+\frac{1}{2}} = \sum_{n=1}^{4} w_p H_{iup}\left(0, \eta_{g_p}, \zeta_{g_p}\right) \quad (20)$$

For the time integration of Eq. (19), three schemes are implemented, e.g. 2nd order Adams-Bashforth (AB2) and three/four stage TVD Runge-Kutta (RK3 and RK4, respectively). Stability region of these scheme are well known as depicted in Fig. 5[10]. Followed by the references[6][7][8][9], the ϕ_i subjected to the advection is $\varepsilon \le \phi_i \le 1.0-\varepsilon, \varepsilon = 1.0e-8$.

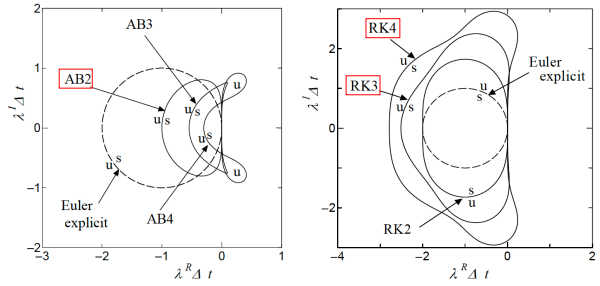

Fig. 5 Stability region of AB(left) and RK(right) schemes[10], "s" and "u" represent stable and unstable, respectively.

As described in chapter 2, the THINC scheme of the present study has been inspired by the references[6][7][8] yet some formulations have been changed. For convenience, the implemented THINC scheme is termed SMTHINC-v0 (Structured Multidimensional THINC version 0) hereafter.

3. VALIDATION CASES

3. 1 2D benchmark cases

Four of two dimensional benchmark cases presented in Fig. 6 are considered to validate the present implementation.

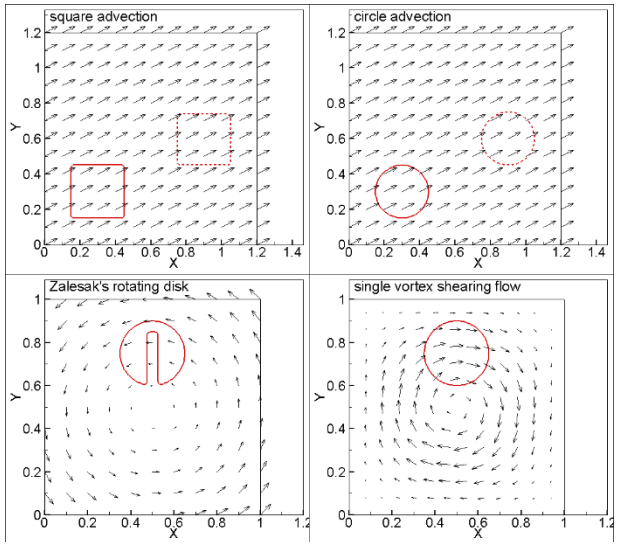

Fig. 6 Initial distribution of volume fraction (solid red line) and prescribed velocity vector for 2D benchmark cases

First problem is the square advection for which 0.3x0.3 square profile of volume fraction is advected diagonally with the velocity (u,v)=(2.0, 1.0) in time[3]. Second problem is the circle advection for which the computational configuration is the same as the first problem with the exception in the circular distribution of volume fraction with its radius of 0.15[3]. For these two cases, geometrical center of the initial profile and advected profile of ϕ_i is set at (x_c, y_c)=(0.3, 0.3) and (0.9, 0.6), respectively, where x_c and y_c is the physical coordinate values of cell center. Third problem is the Zalesak's rotating disk. The

disk profile initially given by Eq. (21) is rotated by the velocity (u,v)=(0.5-y_c, x_c-0.5).

$$\phi_i = \begin{cases} 1: if\ \sqrt{(x_c-0.5)^2+(x_c-0.75)^2} \le 0.15, |x-0.5| \le 0.025\ and\ y \le 0.85 \\ 0: otherwise \end{cases} \quad (21)$$

Fourth problem is the single vortex shearing flow. The circular distribution of volume fraction is given with the center of the circle (x_c, y_c)=(0.5, 0.75) with the radius of 0.15. The velocity field is determined by the stream function given by Eq. (22) with the period T=8.0 (e.g. Rider-Kothe configuration[2]).

$$\psi(x_c, y_c, t) = \frac{1}{\pi}\sin^2(\pi x_c)\sin^2(\pi y_c)\cos\left(\frac{\pi t}{T}\right), x_c, y_c \in [0,1] \quad (22)$$

To set initial distribution of ϕ_i for the latter three cases, each cell is divided into 100x100 points prior to the computation following the references[8][9].

3. 2 Computational set up

The computational domain is divided into 120x120 cells (for the first and second problems) or 100x100 cells (for the third and fourth problems) with uniform spacing 0.1. The CFL number for first, second and third problems is defined as

$$CFL = \frac{\Delta t \sum_{faces} CU}{V_i}, CU = \overrightarrow{u_f} \cdot \overrightarrow{s_f} \quad (23)$$

where $\overrightarrow{s_f} = \vec{n}\Delta s$. The CFL for the fourth problem is defined according to Ii et al. (2014)[7]. Notice that the definition by Eq. (23) and the one by Ii et al. (2014)[7] gives similar CFL. The CFL together with the β utilized in the present study are summarized in Table 1. Since there are extensive numbers of combination in CFL, β, the order of interface polynomial and the scheme of time integration, the results present herein are obtained by TVD RK4 with linear/quadratic interface representation.

Table 1 Parameters for the THINC scheme for the present 2D validation

Case	CFL	β	Ref.
Square	0.248	3.5	[3]
Circle	0.248	3.5	[3][9]
Zalesak	0.247	2.3	[5][6][7][8][9][11]
Single vortex	0.149	3.5	[8][9]

3.3 Error definition

To compare the present results with the existing results, the errors in terms of volumetric preservation are defined. For the 2D square and circle advection, the error is defined as

$$E = \frac{1}{N}\sum_{i=1}^{N}\|\phi_i^n - \phi_i^e\| \quad (24)$$

where N is the number of CVs, ϕ_i^n is the calculated solution after n time steps, and ϕ_i^e is the exact analytical solution. For the Zalesak's rotating disk, the error is defined as

$$E = \frac{\sum_{i=1}^{N}\|\phi_i^n - \phi_i^e\|}{\sum_{i=1}^{N}\phi_i^e} \quad (25)$$

For the single vortex shearing flow, the error is defined as

$$E = \sum_{i=1}^{N}\|\phi_i^n - \phi_i^e\|\Delta s \quad (26)$$

In addition to the error defined by Eqs. (24), (25) and/or (26), undershoot/overshoot values of volume fraction during the computation is sometimes evaluated as

$$underest. = \min(\phi_i), i \in [1, N]$$
$$overest. = \max(\phi_i - 1), i \in [1, N] \quad (27)$$

averaged over the iteration count.

4. RESULTS AND DISCUSSIONS

4. 1 2D square advection

Figure 7 shows the contour of advected volume fraction of 2D square together with the reference results[3]. Table 2 summarizes the error in which "Intf.Rep" means the interface representation (lin. or quad.) and the method of evaluating normal vector of the interface. The present method with "node LSQ" evaluation of interface normal vector shows excellent property in interfacial preservation in comparison to the state-of-art compressive scheme (M-CICSAM). Minor wiggle seen in the corner of the interface for "shifted CV, linear" can be removed by evaluating interface normal vector by "node LSQ". Utilizing quadratic surface representation also contributes to improve the accuracy of interfacial preservation, in other words, the effect of curvature tensor is not negligible. The width of the interface lies within three cells. The error of the present method in terms of volumetric preservation are more or less comparable to M-CICSAM and smaller than that of High Resolution Interface Capturing (HRIC) scheme. One concern is that ϕ_i of O(1e-16)~O(1e-9) is observed inside the region bounded by $\phi_i = 0$ iso line, i=imax and j=jmax boundaries, i.e. downwind region with respect to the advected square profile. This phenomenon can be removed by setting larger value of β (β>8.0 in the present case), yet further diagnostics would be necessary to identify the essential reason to cause such behavior.

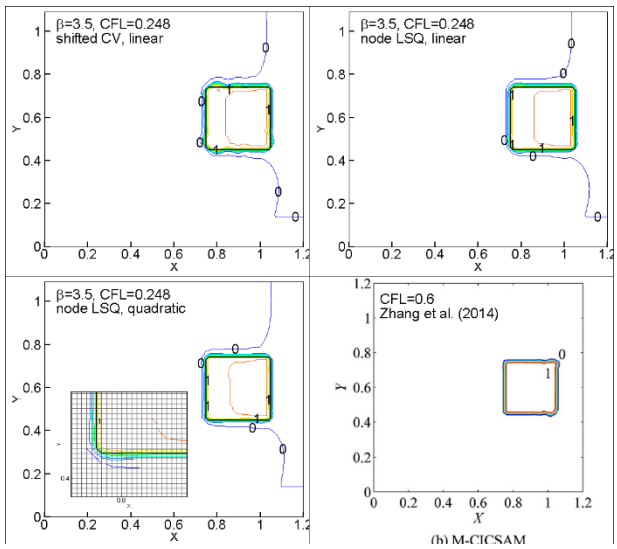

Fig. 7 Computational results of advected square profile

Table 2 Error of 2D square advection

Scheme	Intf.Rep.	*E*
HRIC*	-	5.34e-3
M-CICSAM*	-	1.01e-3
SMTHINC-v0	lin., shifted CV	4.48e-3
	lin., node LSQ	3.72e-3
	quad., node LSQ	3.61e-3

*: CFL=0.2

4. 2 2D circle advection

Figure 8 shows the contour of advected volume fraction of 2D circle together with the reference results[3][9]. Table 3 and Table 4 summarize the error. Similar to the 2D square advection, the present method with "node LSQ" evaluation of interface normal vector shows excellent property in interfacial preservation. The error of the present method in volumetric preservation are comparable to the novel THINC/QQ scheme and smaller than those of HRIC and M-CICSAM. However,

undershoot/overshoot error of the present method are somewhat higher than those of THINC/QQ. As reported in the references[7][9] and partially tested in the present study, the order of undershoot/overshoot errors can easily be changed due to combination of CFL and β. Parametric study will be carried out to investigate quantitative relationship between (CFL, β) and undershoot/overshoot errors. Again, ϕ_i of O(1e-16)~O(1e-9) is observed inside the region bounded by $\phi_i = 0$ iso line, i=imax and j=jmax boundaries, i.e. downwind region with respect to the advected circular profile.

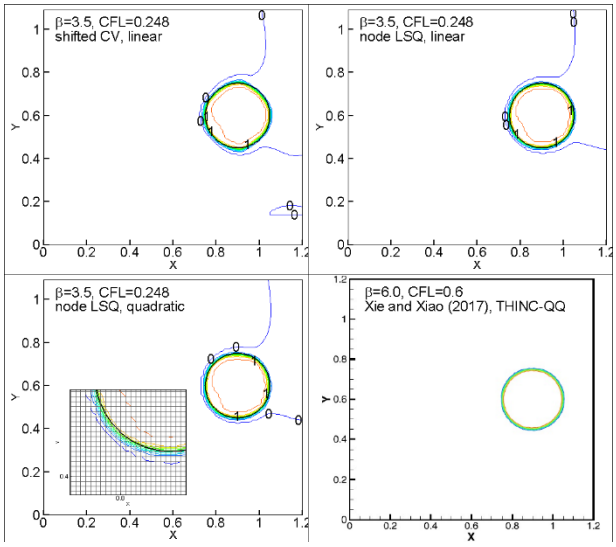

Fig. 8 Computational results of advected circular profile

Table 3 Error of 2D circle advection

Scheme	Intf.Rep.	E
HRIC*	-	5.12e-3
M-CICSAM*	-	3.35e-3
THINC/QQ(12pts)**	quad., node LSQ	1.18e-3
SMTHINC-v0	lin., shifted CV	2.31e-3
	lin., node LSQ	1.58e-3
	quad., node LSQ	1.77e-3

*: CFL=0.2, **: (CFL, β)=(0.2, 3.0)

Table 4 Undershoot/overshoot error of 2D circle advection

Scheme	$\min(\phi_i)$	$\max(\phi_i - 1.0)$
THINC/QQ(12pts)*	0.0	-1.70e-7
SMTHINC-v0, lin., shifted CV	-1.43e-2	1.51e-2
SMTHINC-v0, lin., node LSQ	-1.52e-2	1.48e-2
SMTHINC-v0, quad., node LSQ	-1.51e-2	1.55e-2

*: (CFL, β)=(0.2, 3.0)

4.3 Zalesak's rotating disk

Figure 9 shows the $\phi_i = 0.5$ iso line of Zalesak's rotating disk after 1 and 5 revolutions together with the reference results[6][7]. Table 5 and Table 6 summarize the error. The present computational results show that the shape of disk slot after 5 revolutions is preserved only when quadratic surface representation is adopted. This is an important aspect when propeller cavitation under uniform flow is to be solved by the present scheme. The cavitation extent under uniform flow is, to some extent, steady. If the interfacial representation is linear, the edge of cavity which is analogous to the disk slot of Zalesak may lose its profile as the propeller keeps rotating. The quadratic surface representation may resolve such problem.

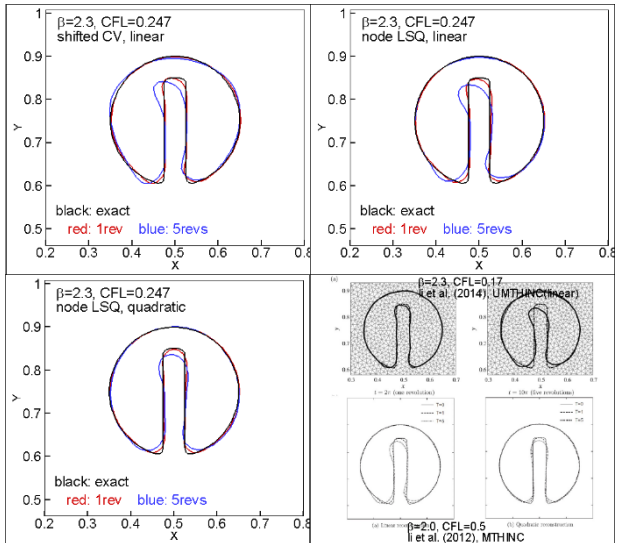

Fig. 9 Computational results of advected disk profile of Zalesak, after 1 rev (red) and 5 revs (blue)

Table 5 Error for Zalesak's rotating disk

Scheme	Intf.Rep.	E
After 1 revolution		
SLIC	-	8.38e-2
PLIC(Youngs)	-	1.09e-2
THINC-WLIC*	linear, cell centered	5.05e-2
MTHINC**	quad, cell centered	1.61e-2
THINC-QHQ***	quad., node LSQ	1.17e-2
THINC/QQ(12pts) ****	quad., node LSQ	3.22e-2
SMTHINC-v0	lin., shifted CV	6.35e-2
	lin., node LSQ	6.59e-2
	quad., node LSQ	6.25e-2
After 5 revolutions		
MTHINC**	quad, cell centered	2.57e-2
SMTHINC-v0	lin., shifted CV	1.26e-1
	lin., node LSQ	1.16e-1
	quad., node LSQ	9.33e-2

*: (CFL,β)=(0.25, 3.5), **: (CFL,β)=(0.5(max), 2.0), ***: (CFL,β)=(0.25(max), 2.3), ****: (CFL,β)=(0.25(max), 6.0)

Table 6 Undershoot/overshoot error of Zalesak's rotating disk

Scheme	$\min(\phi_i)$	$\max(\phi_i - 1.0)$
UMTHINC*	0	-7.11e-9
SMTHINC-v0, lin., shifted CV	-9.22e-8	8.38e-8
SMTHINC-v0, lin., node LSQ	-3.32e-8	2.83e-7
SMTHINC-v0, quad., node LSQ	-7.17e-7	2.27e-6

*: (CFL, β)=(0.2, 3.0)

The error of the present method in volumetric preservation are comparable to SLIC and THINC-WLIC, yet they are larger than those of multidimensional split/unsplit THINC schemes.

Undershoot/overshoot errors of the present method are 4 to 6 orders of magnitude smaller than that of 2D square and circle cases, yet they are still higher than those of UMTHINC. Different to 2D square and circle cases, diffusive behavior of $\phi_i = 0$ iso line does not appear for this problem.

4.4 Single vortex shearing flow (Rider-Kothe[12])

Figure 10 shows the $\phi_i = 0.5$ iso line of single vortex shearing flow after half period and full period together with the reference result[8]. Figure 11 is the close-up view of Fig. 10 (node LSQ, quad.) at the tail of the advected volume fraction at T/2 with additional iso lines of $\phi_i = 0.05$ and 0.95. Table 7 summarizes the error. The results of the present scheme with β=3.5 are presented herein since the results of β=8.0 shows unnatural flotsams in ϕ_i.

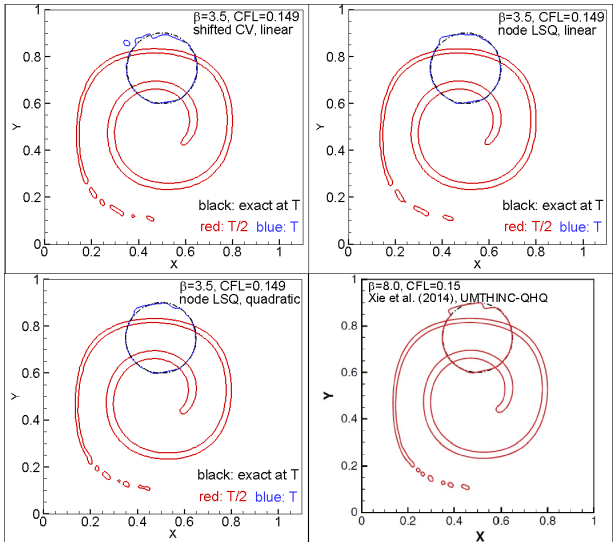

Fig. 10 Computational results of advected profile under time-reversed velocity field after 2/T and T, T=8.0.

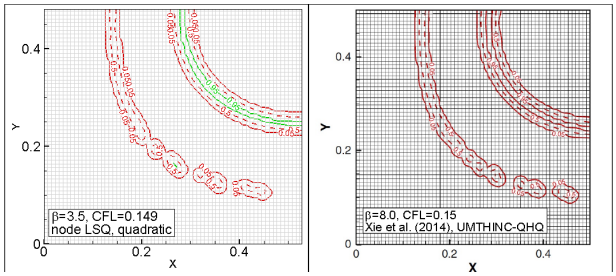

Fig. 11 Same as Fig. 10 but close-up view of the tail with $\phi_i = 0.05, 0.5\ and\ 0.95$ iso lines

Table 7 Error for single vortex shearing flow

Scheme	Intf.Rep.	*E*
PLIC(Youngs)	-	2.16e-3
THINC-QHQ*	quad., node LSQ	3.23e-3
THINC/QQ(12pts)**	quad., node LSQ	3.06e-3
SMTHINC-v0	lin., shifted CV	4.53e-3
	lin., node LSQ	2.85e-3
	quad., node LSQ	2.51e-3

*: (CFL,β)=(0.15(max), 8.0), **: (CFL,β)=(0.25(max), 6.0)

Similar to the other three cases, the quadratic surface representation shows the best performance in interfacial and volumetric preservation. The tail profile shown in Fig. 11 is almost identical to the reference result by Xie et al. (2014)[9]. It is encouraging that the present scheme shows the smallest level of error compared to the novel THINC schemes, and even similar level to the result by PLIC.

5. CONCLUDING REMARKS

The THINC-type VoF advection scheme "SMTHINC-v0" is formulated for structured grid based FVM solver, and is validated throughout four of 2D numerical benchmark cases. Prior to couple the present scheme with NMRI in-house CFD code "NAGISA" with appropriate cavitation models, rigorous verification and validation must be made, e.g. carrying out numerical tests using 1) the grid with non-orthogonal and/or high aspect ratio, and 2) several 3D benchmark cases. Checking the compatibility with overset grid will also be crucial.

ACKNOWLEDGMENT

Fruitful discussion with Prof. Hu at Kyushu University RIAM about THINC scheme will greatly be acknowledged.

REFERENCES

[1] Mirjalili et al., 2017, Interface-capturing methods for tw-phase flows: An overview and recent developments, Center for Turbulence Research Annual Research Briefs.

[2] Rider and Kothe, 1998, Reconstructing volume tracking, Journal of Computational Physics, Vol. 141, pp. 112-152.

[3] Zhang et al., 2014, A refined volume-of-fluid algorithm for capturing fluid interfaces on arbitrary meshes, Journal of Computational Physics, Vol. 274, pp. 709-736.

[4] Xiao et al., 2005, A simple algebraic interface capturing scheme using hyperbolic tangent function, International Journal for Numerical Methods in Fluids, Vol. 48, pp. 1023-1040.

[5] Yokoi, 2007, Efficient implementation of THINC scheme: A simple and practical smoothed VOF algorithm, Journal of Computational Physics, Vol. 226, pp. 1985-2002.

[6] Ii et al., 2012, An interface capturing method with a continuous function: The THINC method with multi-dimensional reconstruction, Journal of Computational Physics, Vol. 231, pp. 2328-2358.

[7] Ii et al., 2014, An interface capturing method with a continuous function: The THINC method on unstructured triangular and tetrahedral meshes, Journal of Computational Physics, Vol. 259, pp. 260-269.

[8] Xie et al., 2014, An efficient and accurate algebraic interface capturing method for unstructured grids in 2 and 3 dimensions: The THINC method with quadratic surface representation, International Journal for Numerical Methods in Fluids, Vol. 76, pp. 1025-1042.

[9] Xie and Xiao, 2017, Toward efficient and accurate interface capturing on arbitrary hybrid unstructured grids: The THINC method with quadratic surface representation and Gaussian quadrature, Journal of Computational Physics, Vol. 349, pp. 415-440.

[10] Morinishi, 2009, Lecture notes on CFD (in-Japanese), Midland Japan CAE Forum. (http://www.cae21.org/)

[11] Rudman, 1997, Volume-tracking methods for interfacial flow calculations, International Journal for Numerical Methods in Fluids, Vol. 24, pp. 671-691.

Aerodynamics of Britain's new polar research ship

Lars-Uve Schrader[1]*, Jan-Patrick Voß[1], Erik Leenders[2], and John Nicholson[3]
[1]HSVA Hamburg Ship Model Basin, Hamburg/Germany,
[2]Rolls-Royce Marine AS, Aalesund/Norway, [3]British Antarctic Survey, Cambridge/UK
*schrader@hsva.de

1 Introduction

Earth's polar regions play a crucial role in the global climate. There is hence a need of environmental science activities in Antarctica and the Arctic – and of modern ice-breaking ships for this purpose. To secure Great Britain's leading position in this field, the Natural Environment Research Council (NERC) commissioned a new research vessel – *RRS Sir David Attenborough* – which will be operated by the British Antarctic Survey (BAS) from 2019. This innovative ship (Fig. 1, Tab. 1), a design by Rolls-Royce Marine AS, features among others a flight deck, a helicopter hangar, a moon pool, two aviation fuel tanks and a foldable foremast carrying the meteorologic instruments, see Leenders & de Jongh (2017). In order to assess the aerodynamic characteristics of the vessel, Rolls-Royce engaged the Hamburg Ship Model Basin (HSVA) in performing a CFD analysis of the wind field around the ship.

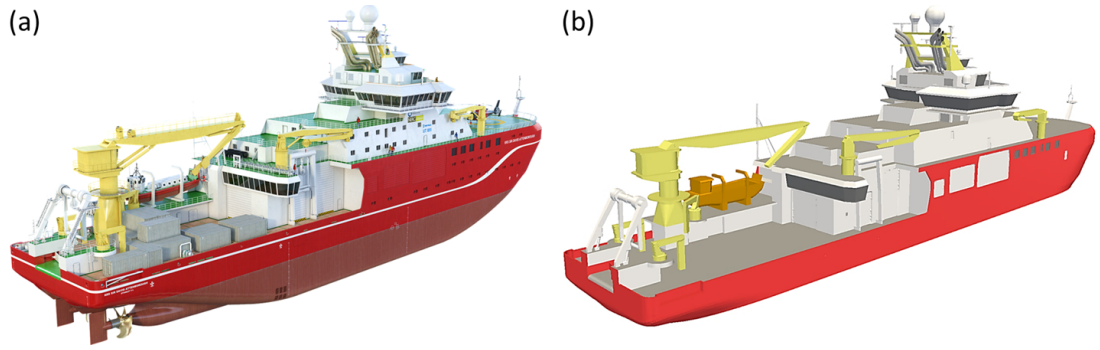

Fig. 1: Polar research ship *RRS Sir David Attenborough*. (a) Detailed CAD model by Rolls-Royce Marine AS. (b) Simplified CFD model for Detached Eddy Simulation

Table 1: Principal dimensions of *RRS Sir David Attenborough* and additional measures with relevance for aerodynamics (T_{air} denotes the air draft of the ship)

L_{pp} [m]	B_{wl} [m]	T_{des} [m]	L_{oa} [m]	B_{oa} [m]	T_{air} [m]
120.28	24.00	7.00	132.33	28.90	40.55

Wind-tunnel testing at model scale is the traditional means of specifying the aerodynamics of a ship. In recent years, CFD has become an alternative thanks to major advancements in turbulence modelling and computer performance. Traditional URANS simulations are more and more replaced by high-fidelity methods which are able to capture turbulent events on small-to-medium spatial and temporal scales. While LES is mostly infeasible in industrial aerodynamics owing the the high computational cost, hybrid URANS-LES approaches represent an attractive compromise between accuracy and efficiency. Detached-Eddy Simulation (DES), cf. Spalart (2009), is a popular variety of such hybrid methods.

2 Virtual wind tunnel

The CFD-based "virtual wind tunnel" offers the possibility of testing the full-scale ship in a very large computational domain ("virtual test section") with minimal boundary effects. Here, the horizontal dimensions are roughly ten times the vessel length while the height is more than four times the air draft of the ship (Fig. 2a). Velocity boundary conditions of Dirichlet type are prescribed at the four vertical boundaries, allowing for a straightforward adjustment of different wind speeds and headings (see Fig. 2b for a definition of the wind parameters). The atmospheric boundary layer over the ocean is modelled by

the following true wind-speed profile $TWS(z)$,

$$TWS = TWS_0 \left(\frac{z}{z_0} \right)^{0.11} . \tag{1}$$

The vertical coordinate z is zero at sea level, and $z_0 = 10$ m is the reference level where the nominal wind speed TWS_0 is attained. A slip-wall condition at the bottom ensures correct behaviour at non-zero ship speed while a pressure condition at the top boundary reduces blockage effects in the virtual test section.

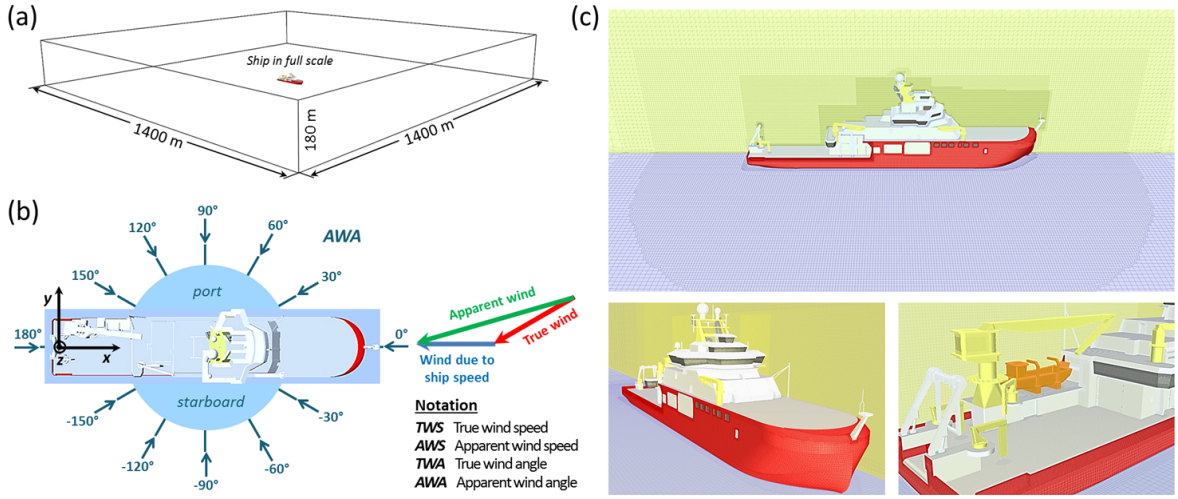

Fig. 2: (a) "Test section" dimensions of the "virtual wind tunnel". (b) Coordinate system and definition of wind parameters. (c) CFD mesh for DES: ship surface mesh and two planes through the volume mesh

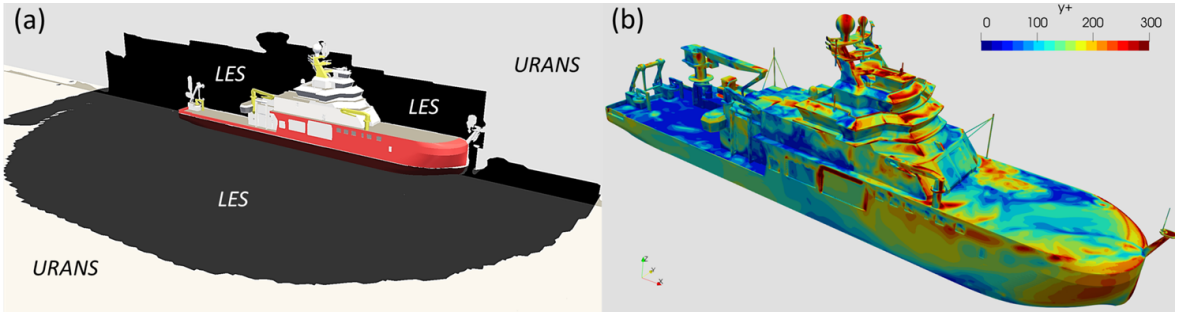

Fig. 3: DDES for wind conditions $AWS = 25$ kn and $AWA = 30°$, snapshot ($t = 115$ s). (a) Regions in LES mode (dark) and URANS mode (light) of the DES turbulence model shown in two planes. (b) Boundary-layer resolution in terms of wall units y^+

The simulations have been carried out using the finite-volume code FreSCo$^+$, see Rung et al. (2009). Key to a successful DES computation is a meaningful domain discretisation. The present CFD mesh comprises cubic finite-volume cells with fine resolution in regions of vortex generation ("source", e.g. deckhouse) and of particular interest ("target", e.g. helideck, see Fig. 2c), activating the LES mode of the hybrid DES model. On the contrary, LES behaviour must be avoided in under-resolved boundary layers to prevent nonphysical "grid-induced separation" (GIS), cf. Spalart (2009). The "Delayed DES" (DDES) approach after Gritskevich et al. (2012) implemented in FreSCo$^+$ offers additional protection against GIS. In practice, the division of the flow domain into LES and URANS regions is time dependent (snapshot in Fig. 3a) – as is the wall-normal boundary-layer resolution in y^+ units (Fig. 3b), adapted here to the use of wall functions. Finally, the DDES turbulence treatment is combined with a volume-of-fluid approach for the simulation of exhaust dispersion in the flow field.

3 Statistical data evaluation

The turbulent airflow around a ship comprises a multitude of randomly interacting spatial and temporal scales, calling for a statistical analysis. To obtain convergence and good accuracy of the statistical quantities, averaging should not start before a sufficient time T_{trs} for the decay of the initial transients has passed; also, the sampling time T_{smp} for averaging should be long enough. The demands on T_{trs} and T_{smp} have been investigated considering local wind speeds around a container-feeder ship (Fig 4a; results from the project *AERONAUT*, www.aeronaut-project.eu). Although the vessel differs from *RRS Sir David Attenborough*, the findings can be transferred to the present case as the ship size, the wind speed and the simulation setup are nearly the same. T_{smp} and T_{trs} have been evaluated in zones of low speed (Fig 4b) and high speed (Fig 4c), with the former zone being more challenging due to the high level of turbulent fluctuations. The investigation reveals that $T_{trs} \geq 40$ s and $T_{smp} \geq 50$ s should be observed to obtain an accuracy of at least ±5% in the local wind speed (red dots in Figs. 4b,c). A much higher statistical accuracy is usually achieved for integral quantities such as the mean wind loads on the vessel.

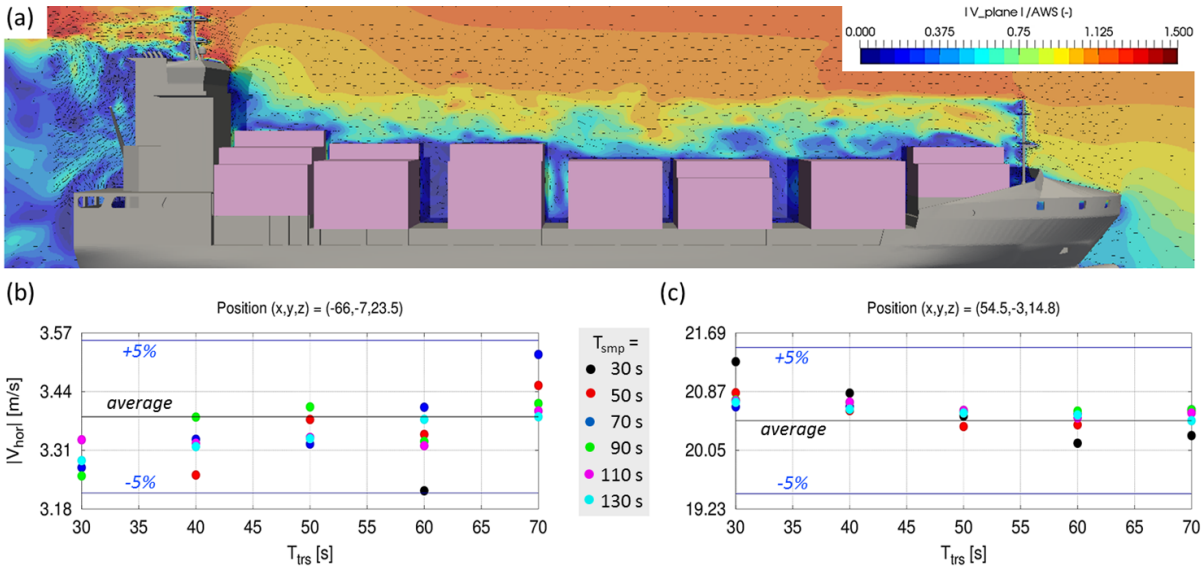

Fig. 4: (a) In-plane velocity amidships of *AERONAUT* vessel ($TWS_0 = 25$ kn, $AWA = 0°$). (b,c) Statistical convergence upon variation of averaging start time T_{trs} (abscissa) and duration T_{smp} (symbols) for mean horizontal wind speed (b) downstream of the bridge and (c) above the foremost container stack

4 Wind measurement

Like many other research ships, *RRS Sir David Attenborough* features a foremast carrying the meteorologic instruments. The helideck at the bow calls for a foldable construction, setting a limit to the mast length; at the same time, the foremast should be tall enough to reduce negative effects on the anemometer accuracy owing to airflow distortion by the deckhouse (Figs. 5a,b for headwind), see also Moat et al. (2006a,b). According to the meteorologists from BAS and their research collaboration partners, errors in wind speed of ±5% are acceptable in upwind conditions as these can be compensated by established correction methods. The simulations reveal that this error level is achieved only when observing a sufficient distance to the mast platform (Fig. 5c).

Vertical profiles of wind speed and angle above the foremast have been evaluated so as to establish a suitable position for anemometer and wind-vane installation. As expected, the deviation of the measured signals from the undisturbed target values diminishes with increasing height (example in Fig. 6a for $AWA = 60°$). A closer look at two levels, $z = 19.1$ m and $z = 25$ m above the water line (Figs. 6b,c), reveals that the accuracy requirement by BAS in upwind conditions is largely fulfilled when installing the wind gauges in a height of $z \geq 25$ m. For wind from the stern, in contrast, the deckhouse shades the foremast, preventing meaningful wind measurements.

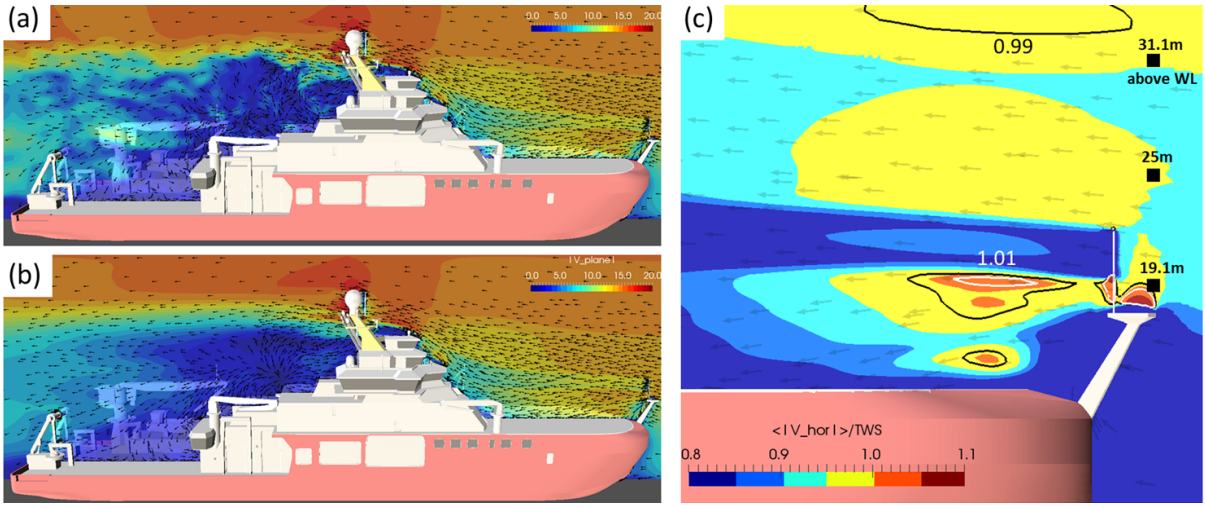

Fig. 5: In-plane wind field around *RRS Sir David Attenborough* for headwind of $TWS_0 = 25$ kn: (a) snapshot, (b) time average. (c) Mean normalised wind speed at the foremast presented in 5% intervals

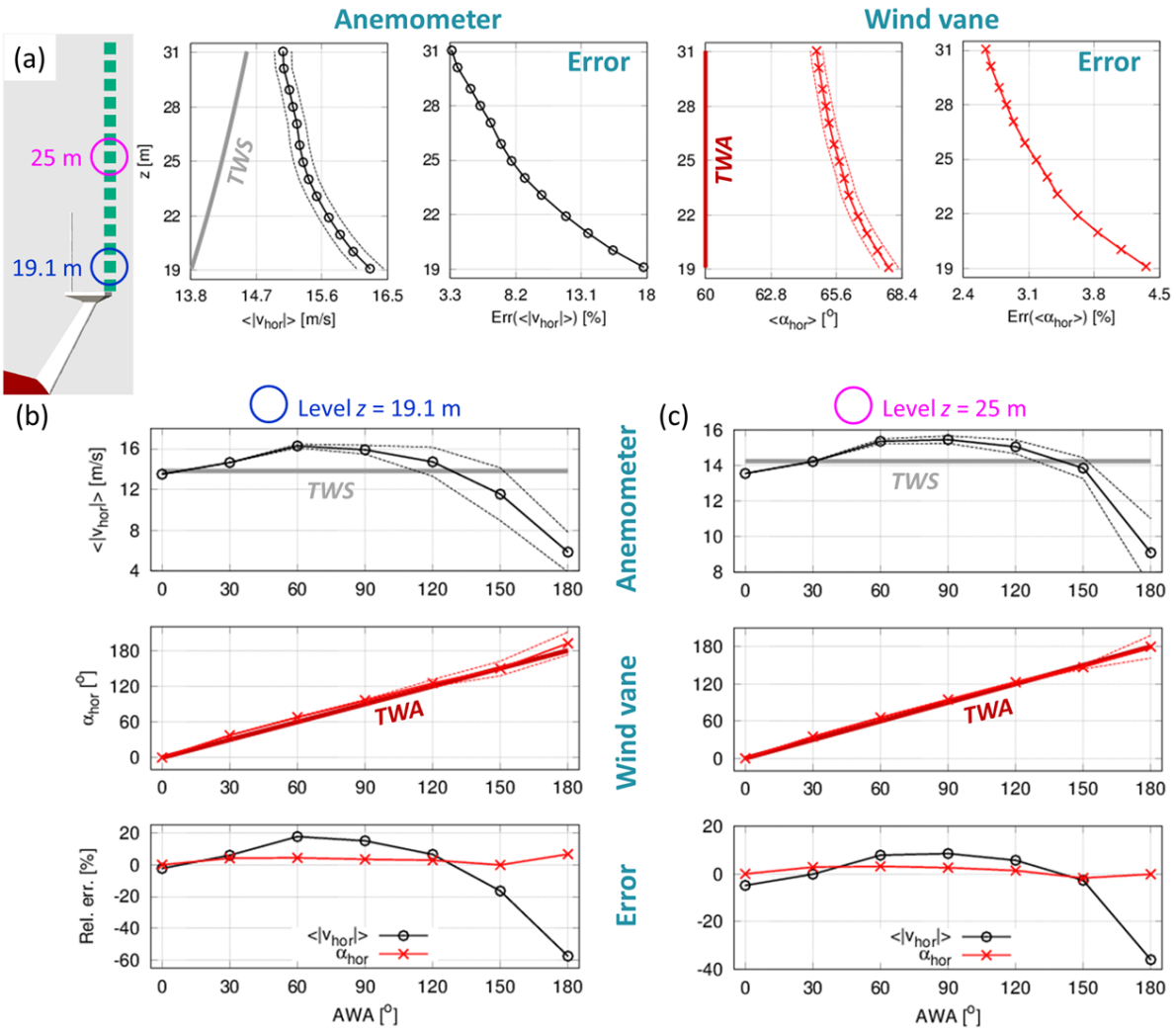

Fig. 6: (a) Wind profile above the foremast ($TWS_0 = 25$ kn, $AWA = 60°$): wind speed (anemometer, black line with symbols) and angle (wind vane, red line with symbols) compared to the undisturbed freestream (thick lines); thin dotted lines depict r.m.s. bands. Errors in TWS and TWA are also shown. (b,c) Signals of wind speed and angle versus AWA (b) 19.1 m and (c) 25 m above the water line

5 Exhaust dispersion

Simulations of exhaust-gas transport in the airstream have been carried out to identify potential risks of pollution at the air intakes towards the main-engine rooms. Two design variants of the exhaust system have been considered, differing in the length and diameter of the exhaust pipes and the arrangement of the radoms and radars next to the pipes. For $AWA = 30°$ – the most critical wind angle studied – the exhaust plumes generated by design 1 (Fig. 7a) are more dispersed than those of design 2 (Fig. 7b). As a result, design 1 violates the odour criterion based on a limit of 300 ppm at the two windward air inlets (Fig. 8a) while design 2 – the final choice – marginally complies with this criterion (Fig. 8b).

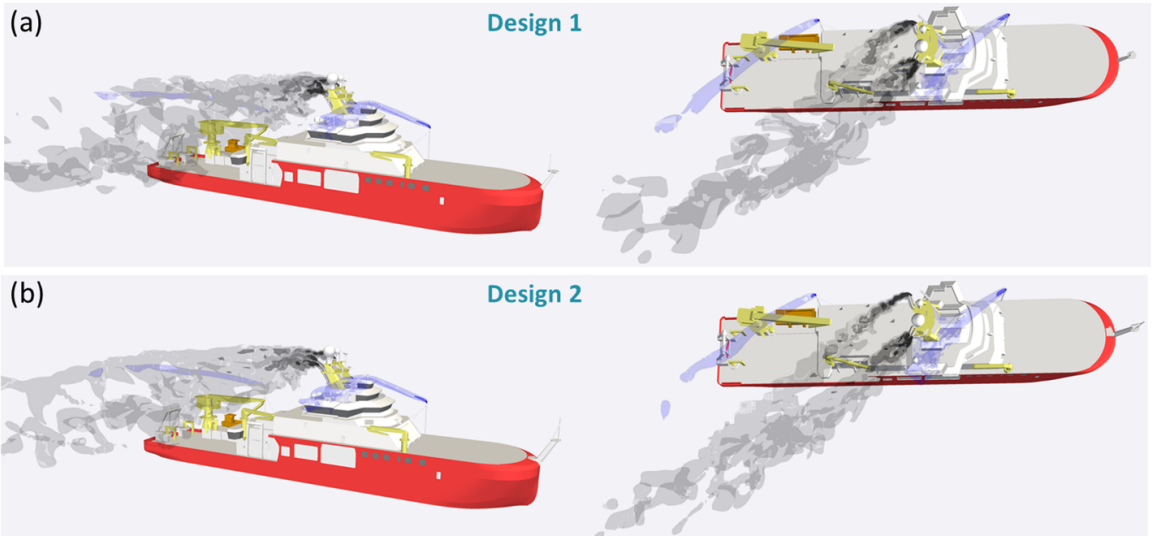

Fig. 7: Exhaust dispersion for $TWS_0 = 25$ kn and $AWA = 30°$. Comparison between two design variants of the exhaust system: (a) design 1, (b) design 2 (cf. text for differences). The blue traces show blow-off gas from the vents of the aviation-fuel tanks

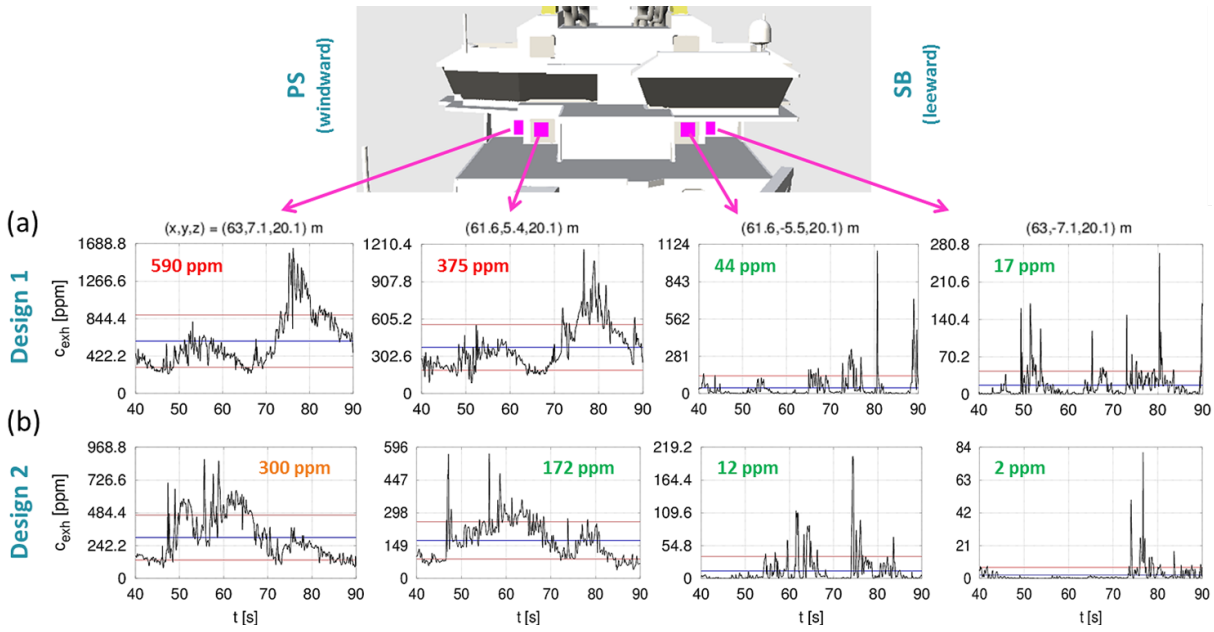

Fig. 8: Exhaust concentration at the intakes to the main-engine room – instantaneous signals and time averages compared to the odour limit of 300 ppm for (a) design 1 and (b) design 2 of the exhaust system

6 Helideck safety

The UK Civil Aviation Authority (CAA) provides two safety limits for helidecks, see CAA (2009): (i) the standard deviation of the vertical turbulent fluctuations should stay below 1.75 m/s; (ii) the 3-second average temperature rise above the ambient due to the exhaust plumes of the ship should not exceed 2°C. In 25-knot upwind conditions, both criteria are largely fulfilled within the helideck aiming circle. If $AWA = 30°$, for instance, the wind is fairly uniform and steady in the forward part of the helideck whereas an unsteady low-speed zone is created near the deckhouse (Fig. 9a). This is reflected in the distribution of "safe" and "unsafe" areas across the helideck as per the CAA guidelines (Fig. 9b). In the simulations, the foremast has been in the upright position for simplicity whereas it will be folded down in practical operation, which further improves the helideck safety in terms of the CAA criteria.

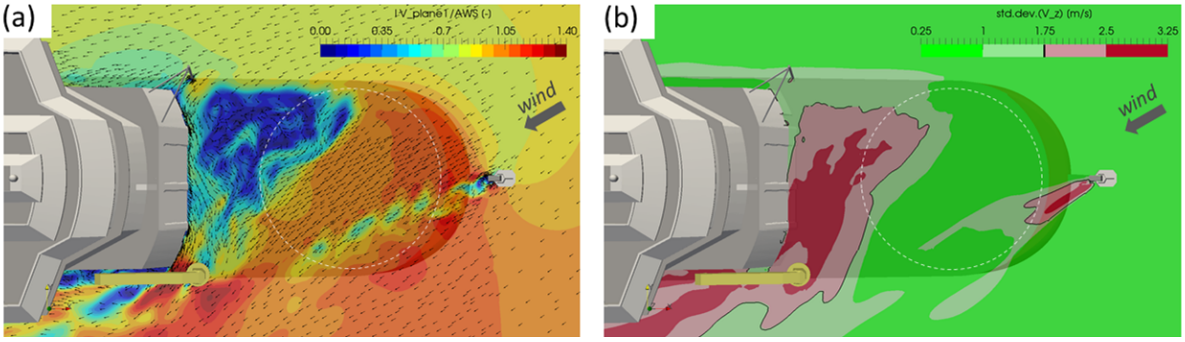

Fig. 9: Turbulence above the helideck for $TWS_0 = 25$ kn and $AWA = 30°$: (a) snapshot of normalised wind speed (colours) and direction (arrows) in a plane 2 m above the deck. (b) Evaluation of the CAA safety limit on the vertical turbulent fluctuation level (green/red: criterion fulfilled/violated)

7 Summary

The present paper reports on a selection of results for Britain's new polar research ship *RRS Sir David Attenborough* which have been obtained in HSVA's CFD-based "virtual wind tunnel". The purpose is to demonstrate the capabilities of modern unsteady scale-resolving simulations such as DDES. Compared to traditional URANS computations, these simulations represent substantial progress in terms of accuracy and confidence level. Here, HSVA has applied DDES in a fruitful collaboration with Rolls-Royce and BAS to verify and improve the aerodynamic performance of *RRS Sir David Attenborough*.

Acknowledgements

The results in §3 have been obtained in the research project *AERONAUT* funded by the Ministry for Economic Affairs and Energy (BMWi), Germany.

References

E. Leenders, M. de Jongh (2017). Planet ice and the dual-functional Attenborough. The Naval Architect, Jan. 2017, p. 37–38.

P. Spalart (2009). Detached-Eddy Simulation. Annu. Rev. Fluid Mech. **41**, p. 181–202.

M.S. Gritskevich, A.V. Garbaruk, J. Schütze, F. Menter (2009). Development of DDES and IDDES Formulations for the k-ω Shear Stress Transport Model. Flow, Turbulence and Combustion **88**(3), p. 431–449.

T. Rung, K. Wöckner, M. Manzke, J. Brunswig, A. Stück, C. Ulrich (2009). Challenges and Perspectives for Maritime CFD Applications. Jahrbuch der Schiffbautechnischen Gesellschaft **103**, p. 127–139.

B.I. Moat, M.J. Yelland, R.W. Pascal, A.F. Molland (2006a). Quantifying the Airflow Distortion over Merchant Ships. Part I: Validation of a CFD Model. J. Atmos. Oceanic Technol. **23**, p. 341–350.

B.I. Moat, M.J. Yelland, R.W. Pascal, A.F. Molland (2006b). Quantifying the Airflow Distortion over Merchant Ships. Part II: Application of the Model Results. J. Atmos. Oceanic Technol. **23**, p. 351–360.

Civil Aviation Authority (2009). Helideck Design Considerations – Environmental Effects. CAA Paper 2008/03.

Simplified CFD Approach for Simulating Propeller Flows in Ship Wake Fields

Keun Woo Shin (keun.shin@man-es.com)[1] and Poul Andersen (pa@mek.dtu.dk)[2]

[1]Propeller & Aftship R&D Department, MAN Energy Solutions, Frederikshavn, Denmark,
[2]Department of Mechanical Engineering (MEK), Technical University of Denmark (DTU), Kgs.Lyngby, Denmark,

1 Introduction

CFD becomes a practical tool to optimize ship propellers for high propulsive efficiency and acceptable cavitation safety in the design stage. As propellers operate behind the hull, it is important to take into account non-uniform hull wake in simulating propeller flows. But CFD simulations on ship and propeller in self-propulsion condition are CPU-intensive. Coupled methods, that the propeller flow solved by a potential flow method is applied to the viscous flow solution around the hull by body forces, are efficient in terms of computational effort, but it has inherent limitations in considering turbulent viscous flows around the propeller.

In CFD used for propeller designs, nominal wake obtained from model-test measurements or bare-hull CFD simulations is applied to the propeller inflow by using an inlet boundary condition and body forces instead of including a hull model (Shin et al 2015). Computational effort can be saved by excluding the hull model, but it still requires considerable computational effort, because reliable CFD simulations on ship propellers require resolving the wall boundary layer and refining the blade edges (Shin & Andersen 2017). CFD with non-uniform hull wake also needs to be made by unsteady simulations on all propeller blades for 4 – 5 propeller revolutions.

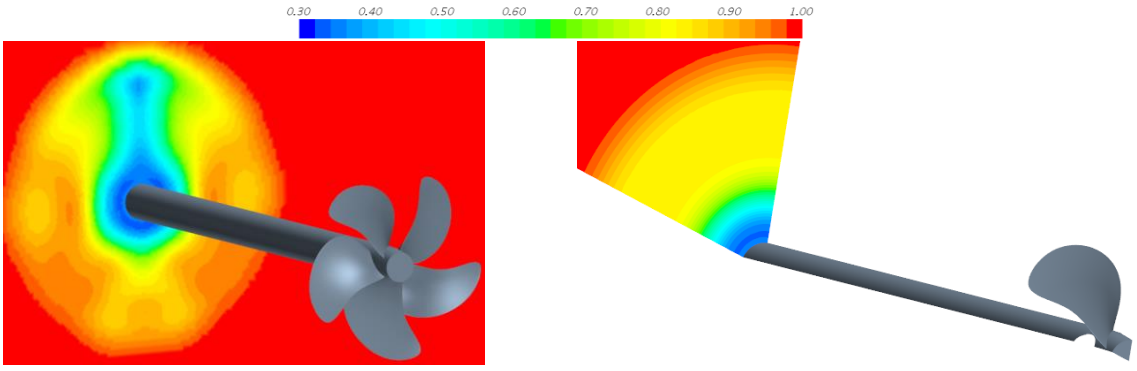

(a) (b)

Figure 1. Propeller model in CFD with (a) full axial wake and (b) simplified hull wake: color contour is for v_a/V_S

In this work, hull wake is simplified to be circumferentially uniform and to vary only along the radial direction for representing a specific blade position and CFD is made only on a single blade with periodic boundary conditions, as shown in Figure 1(b). The reliability and computational efficiency of CFD with the simplified wake are evaluated by examining its possibility to simulate propeller flows at characteristic blade positions. It is also investigated how CFD with the simplified wake can be correlated to that with the full non-uniform wake by looking into single-blade loads and pressure distributions.

KP505 5-blade propeller designed for KCS container ship is considered, because model test results including nominal hull wake measurements are available and CFD validation studies have been made in the self-propulsion condition (Larsson et al 2015). First, CFD results are validated against open-water propeller test results. Next, the hull wake model is prepared to reproduce all three components of the wake field on the propeller plane in CFD without the propeller model and propeller simulation is made with the full hull wake field for validation against self-propulsion test results. The variations of single-blade load and pressure distribution on the suction side of the blade are investigated along a propeller rotation in non-uniform hull wake. Lastly, CFD is made with simplified hull wake corresponding to blade positions of maximum, mean and minimum axial wake.

2 CFD setup

RANS solver in the commercial CFD package StarCCM+ is adopted with the curvature-corrected k-ω SST turbulence model excluding a wall function. Γ-Re_θ transition model is also adopted, because CFD simulations are made at model scale and laminar and transitional boundary layer flows are extensively formed on a model-scale propeller.

For CFD in the open-water condition and with simplified hull wake, a single blade is modelled in a 72-deg cut cylindrical domain with periodic boundary conditions. For CFD with full hull wake, all the 5 blades are modelled in a cylindrical domain. While upstream hubcap and downstream shaft are modelled in open-water CFD, an upstream shaft with the slip-wall boundary condition extending to the inlet is connected to the hub in CFD with hull wake.

The cylindrical domain extends 3·D from the propeller plane to the inlet and 6·D to the outlet with a radius of 4·D, where D is the propeller diameter, D = 0.25 m. An inner domain for modelling propeller rotations has up- and downstream extents of 0.24·D with a radius of 0.6·D. The propeller rotation is modelled by rigid-body motion in unsteady simulations on the whole propeller, whereas the moving reference frame is applied to the rotating domain in steady simulations on a single blade. Since the blade has a high skew of 32 deg, it does not fit in the 72-deg cylinder cut. So a spherical hump is added to a periodic boundary side at the fore-skewed leading edge of 0.3·R – 0.6·R and the other side is dented in the same shape without intersecting the blade surface, as shown in Figure 2(b).

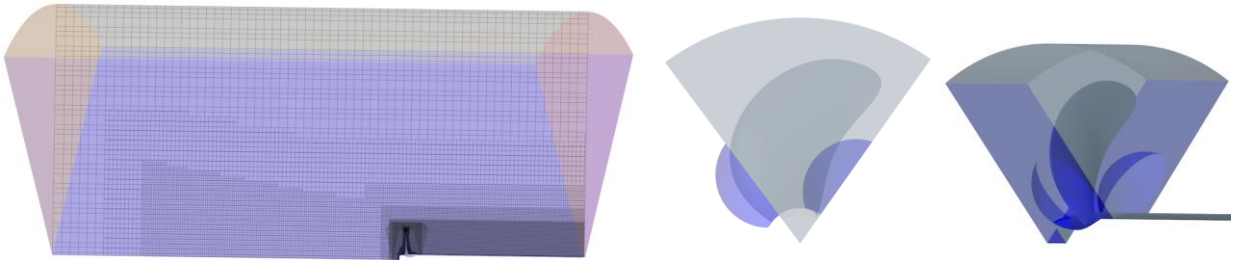

(a) (b)

Figure 2. (a) Computational domain and (b) inner rotating domain around the blade with spherical hump and dent on the periodic boundaries for CFD on a single blade with simplified wake

Unstructured volumetric grid is generated by trimmed hexahedral meshing with prism layers on wall surfaces. The grid size on the overall surface of the blade and hub is $\Delta x = 0.5 – 1.0$ mm and it is refined to $0.5 \cdot \Delta x$ along the blade edges. A consistent grid size of $\Delta x = 4 – 6$ mm is applied to the region around the inner rotating domain and from the inlet to the propeller disk for mapping the periodic boundaries and maintaining the axial hull wake, as shown in Figure 2(a). The grid contains 22.2 mil cells for CFD with full hull wake. It is 4.6 times reduced to 4.8 million cells for CFD on a single blade with simplified wake.

3 Open-water propeller simulation

In open-water CFD, the propeller speed is fixed to N = 12 rps and the inlet flow speed corresponding to the towing speed is varied according to considered values of the advance ratio in the same way as the model test (Fujisawa et al 2000).

Open-water propeller curves are compared between CFD and experiment in Figure 3. CFD shows a good agreement with the experimental results at high loadings and the deviations are less than 3% in K_T, K_Q and η_O at J = 0.1 – 0.5, whereas the underestimations of K_T and K_Q are increased at $J \geq 0.6$ and the deviations are larger than 6% at the design condition of J = 0.728. The model test report mentions that K_T and K_Q are higher than the open-water test results in another model test facility. Another CFD on the same propeller shows 6.5% underestimation at J = 0.7 (Krasilnikov 2013).

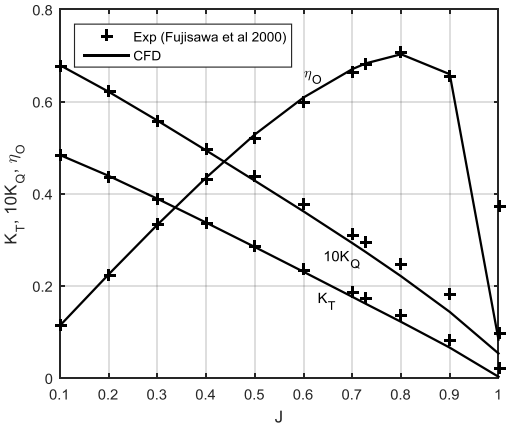

Figure 3. Open-water curves from CFD and model test

4 Propeller simulation in whole non-uniform hull wake

Axial hull wake is applied by using the inlet boundary condition, as shown in Figure 4. Transverse hull wake is modelled by momentum sources applied 0.6·D upstream from the propeller plane. The strengths of radial and tangential momentum sources are basically prepared by multiplying a factor to corresponding velocity components. The multiplication factor is iteratively adjusted by wake model tests made in the same computational grid with excluding the propeller. The velocity field on the propeller plane from CFD with the

final wake model is compared with the wake measurements in Figure 5. The upward flow on the overall propeller disk is weaker in the CFD wake than the measurement and the downward flow at 12 o'clock blade position is exaggerated.

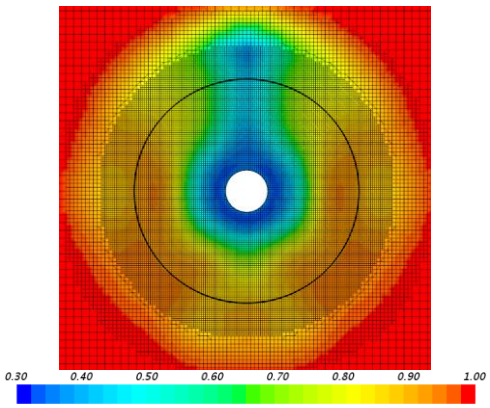

Figure 4. Axial hull wake on the inlet boundary: propeller disk is marked by a thick line

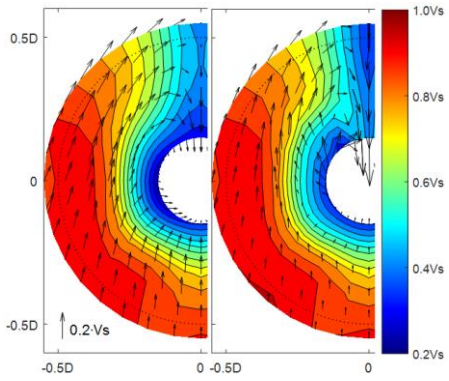

(a) (b)

Figure 5. Hull wake of KCS container ship: (a) experimental measurement, (b) CFD wake model

An unsteady simulation is made on the propeller starting with a relatively large time-step and gradually reducing it to 0.5° propeller rotation per Δt. The axial hull wake is scaled down by the ratio of the effective wake fraction to the nominal one, i.e. $w/w_n = 0.208/0.316$. The nominal wake fraction $w_n = 0.316$ from the wake data manually extracted and interpolated is slightly higher than $w_n = 0.314$ in the model test report. In CFD, the propeller speed is increased from 9.5 rps, which is applied to the self-propulsion test, to 9.75 rps, because K_{TB} and K_{QB} at N = 9.5 rps are around 10% lower than the experimental results, where the subscript B indicates the behind-hull condition.

K_{TB}, K_{QB} and η_B time-averaged over the last revolution are compared with the result from the self-propulsion test in Table 1, where η_B is the behind-hull efficiency, $\eta_B = \eta_O \cdot \eta_R$. K_{TB} and K_{QB} are underestimated like the open-water CFD, but the deviations of K_{TB} and η_B are quite low. Since J is 2.6% lowered from that in the experiment by increasing N, $\Delta\eta_B$ is smaller than $\Delta K_{TB} - \Delta K_{QB} = 3.7\%$.

Table 1. Comparison of propeller performance between CFD with full wake and self-propulsion test

	J	K_{TB}	K_{QB}	η_B	ΔJ	ΔK_{TB}	ΔK_{QB}	$\Delta\eta_B$
Exp	0.728	0.170	0.288	0.690				
CFD (Full wake)	0.709	0.167	0.272	0.693	-2.6%	-2.0%	-5.7%	0.6%

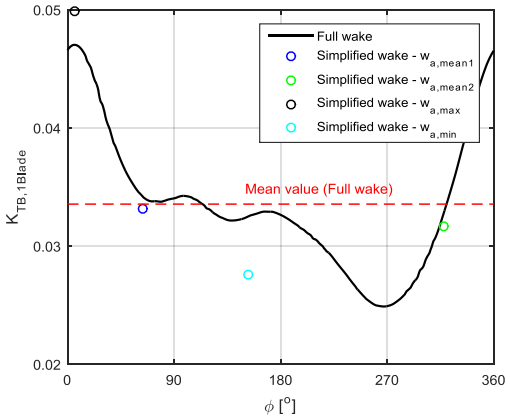

Figure 6. Single-blade thrust in CFD with full wake and simplified wake: φ = 0° is 12 o'clock position

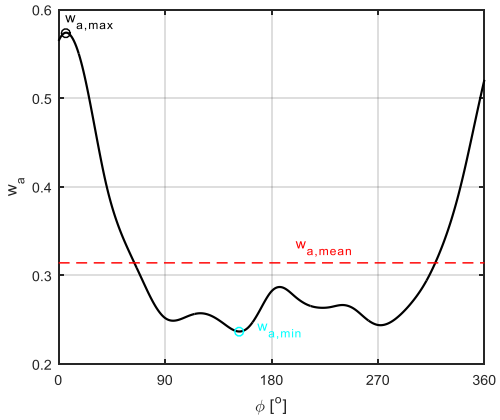

Figure 7. Axial wake averaged along the mid-chord locus at different blade positions

In Figure 6, the variation of single-blade thrust from CFD with full wake over a propeller revolution is presented. In Figure 7, the axial hull wake is averaged with weighting on the radius at each of blade positions. The overall variation of the blade loading is dependent on the axial wake variation. The highest value of $K_{TB,1blade}$ is shown at the same blade position of φ = 6° as the maximum axial wake. While the wake trough is at two blade positions of φ = 150° and 270°, the minimum thrust is shown at only one blade position of φ = 267°, because the thrust on

the starboard side is increased by the tangential wake from the bilge vortex, as the tangential wake is opposite to the downward rotating direction of the blade. The slopes to the maximum value of $K_{TB,1blade}$ are less steep than those of the axial wake due to the tangential wake, which decelerates the increase of $K_{TB,1blade}$ on the port side and the decrease on the starboard side.

In Figure 8, the pressure distribution on the suction side of the blade is shown at different blade positions. As the blade enters the region of high axial wake, low pressure starts to be formed at the leading edge of $0.5 \cdot R - 0.7 \cdot R$ at $\varphi = 330°$ and the low-pressure region is extended at $\varphi = 330° - 30°$. As the blade gets out of the high wake region, the low-pressure region gradually disappears from inner to outer radii at $\varphi = 30° - 60°$, but the low-pressure region at the tip remains up to $\varphi = 120°$, which indicates tip vortex.

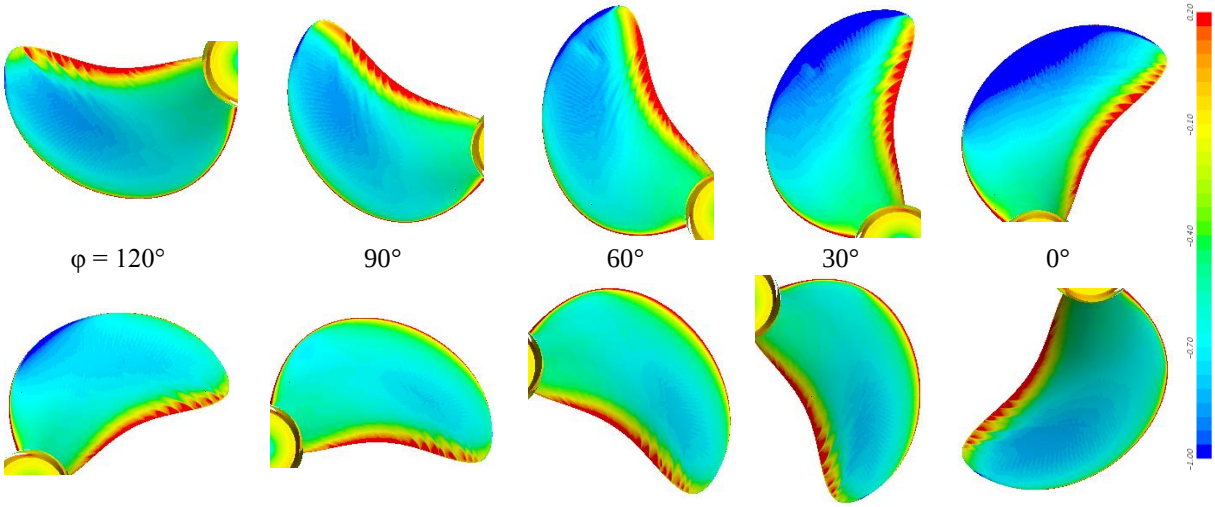

Figure 8. C_P on the suction side of the blade at different blade positions: $C_P = (P - P_\infty) / (0.5 \cdot N^2 \cdot D^2)$

In Figure 9, C_P on constant-radius section of $0.7 \cdot R$ is shown at different blade positions. As the blade enters the region of high axial wake, $|C_P|$ on the both sides of the section increases. As the blade gets out of the high wake region, $|C_P|$ decreases. $|C_P|$ at the leading edge is reversed at $\varphi = 270°$ near the lowest blade loading position. C_P at the leading edge varies according to the blade position, whereas C_P on the region aft of the mid-chord does not vary significantly.

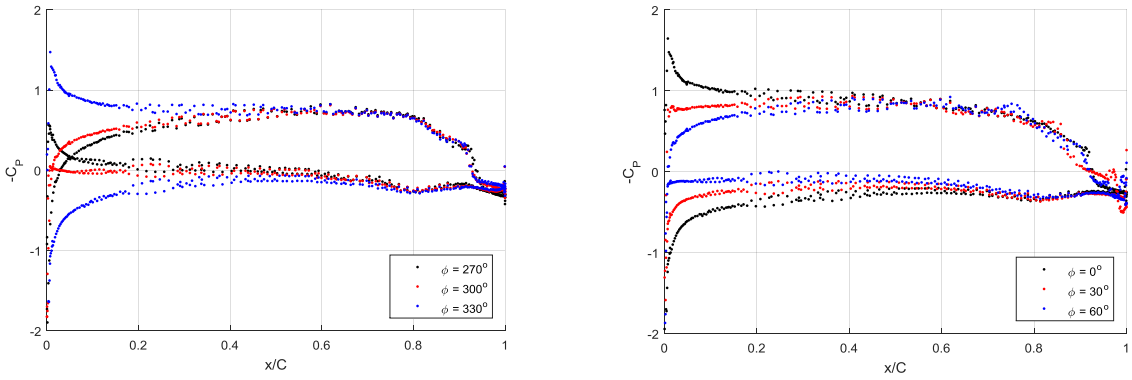

Figure 9. C_P on constant-radius section of $0.7 \cdot R$ at different blade positions

5 Propeller simulation in simplified hull wake

Axial hull wake is simplified to be circumferentially uniform and to vary only along the radial direction. Five different inputs of simplified wake are prepared by considering the distributions of axial wake along the mid-chord locus at 4 blade positions shown in Figure 10(a) and averaging it along the circumferential direction at each of radial points. The five simplified wake inputs are compared in Figure 10(b). The considered 4 blade positions correspond to the maximum, minimum and mean wake in Figure 7, where axial wake is averaged along the mid-chord locus at each of blade positions with weighting on the radius. The mean wake, i.e. the nominal wake fraction is reached at two blade positions, where the blade enters and gets out of the wake peak around 12 o'clock position.

Steady simulations are made on the single-blade model with simplified wake applied to the inlet boundary. J = 0.709 is considered and the wake is scaled down by the ratio of w/w_n = 0.208/0.316 in the same way as CFD with full wake.

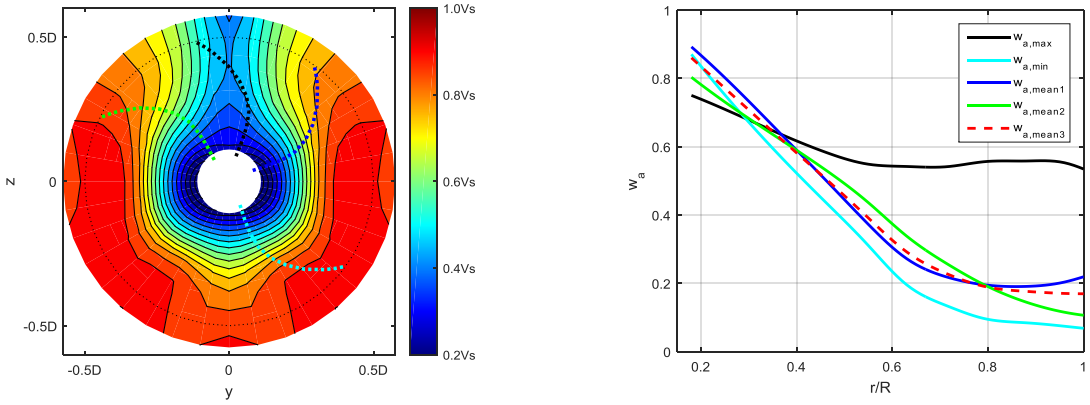

Figure 10. (a) 4 blade positions considered for preparing simplified wake and (b) axial wake distributions along the radial direction: $w_{a,max}$ at φ = 6°, $w_{a,min}$ at φ = 153°, $w_{a,mean1}$ at φ = 64°, $w_{a,mean2}$ at φ = 318° and $w_{a,mean3}$– circumferentially averaged wake

Table 2. Comparison of propeller performance between CFD with simplified wake and self-propulsion test

		K_{TB}	K_{QB}	η_B	ΔK_{TB}	ΔK_{QB}	$\Delta\eta_B$
CFD with simplified wake	Mean wake 1	0.166	0.270	0.710	-2.8	-6.1	2.9
	Mean wake 2	0.158	0.260	0.705	-7.0	-9.7	2.2
	Mean wake 3	0.162	0.265	0.707	-5.1	-8.0	2.5
	Max wake	0.249	0.379	0.762	46.5	31.6	10.6
	Min wake	0.138	0.233	0.685	-19.2	-19.1	-0.7

In Table 2, the results of CFD with simplified wake are compared with the self-propulsion test results. CFD with the three mean wake inputs underestimates K_{TB} and K_{QB} and the deviations in estimating η_B are within 3%. The deviations in K_{TB} and K_{QB} are the smallest for CFD with Mean wake 1. If the tangential wake is considered in CFD with Mean wake 1, K_{TB} and K_{QB} will be increased and the deviations may be reduced. The wake difference between the three mean wake inputs is noticeable at 0.8·R – 1.0·R, which can imply that outer-radii wake is crucial in determining the propeller loading.

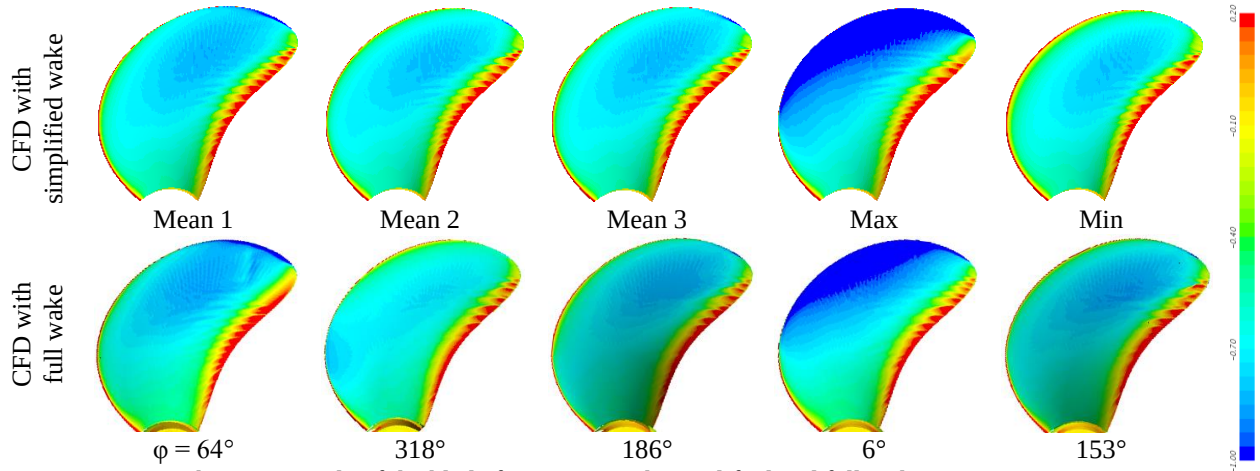

Figure 11. C_P on the suction side of the blade from CFD with simplified and full wake

In Figure 6, $K_{TB,1Blade}$ from CFD with simplified wake is compared with that from CFD with full wake. $K_{TB,1Blade}$ of CFD with Max wake is 6.2% higher than the highest $K_{TB,1Blade}$ of the full-wake CFD, because the maximum axial wake distribution along the mid-chord locus is applied all over the blade. $K_{TB,1Blade}$ of CFD with Min wake is 15.3% lower than that of the full-wake CFD at the minimum axial wake position of φ = 153° and 10.7% higher than the lowest $K_{TB,1Blade}$ of the full-wake CFD at φ = 267°, because the blade loading is increased by the upward tangential wake on the starboard side. $K_{TB,1Blade}$ of CFD with Mean wake 1 and 2 are 2.9% and 3.6%

lower than those of the full-wake CFD at φ = 64° and 318°, respectively. As the error due to the exclusion of tangential wake effects is cancelled out by the over- and underestimation of the loading at 0.8·R – 1.0·R in CFD with Mean wake 1 and 2, respectively, the deviations are less than CFD with Max and Min wake.

In Figure 11, the suction-side surface pressure of the simplified-wake CFD is compared with that of the full-wake CFD at the blade positions considered for preparing simplified wake inputs. C_P of CFD with Mean wake 3 is compared with that of φ = 186°, where $K_{TB,1Blade}$ is the same. The comparison shows overall agreements, but $|C_P|$ at downward blade positions like Mean wake 2 and Min wake is underestimated by the simplified-wake CFD due to the tangential wake effect. The low pressure at the leading edge of 0.5·R – 0.6·R is not reproduced by CFD with Mean wake 2, as the wake is simplified to be uniform along the chordwise direction.

In Figure 12, the comparison of the sectional pressure at 0.7·R between CFD with simplified and full wake also shows overall agreements, but the pressure difference between the two sides of the blade is larger and $|C_P|$ on the suction side is slightly lower at the mid-chord in the full-wake CFD at φ = 318° than the simplified-wake CFD with Mean wake 1 and 2, because the leading edge enters the high-wake region first. The suction peak at the leading edge is higher in CFD with Max wake than the full-wake CFD at φ = 6°, because the maximum axial wake distribution is applied all over the chord in the simplified-wake CFD. CFD with Min wake shows the reversed pressure at the leading edge unlike the full-wake CFD at the corresponding blade position, because the upward tangential wake is not taken into account in the simplified-wake CFD.

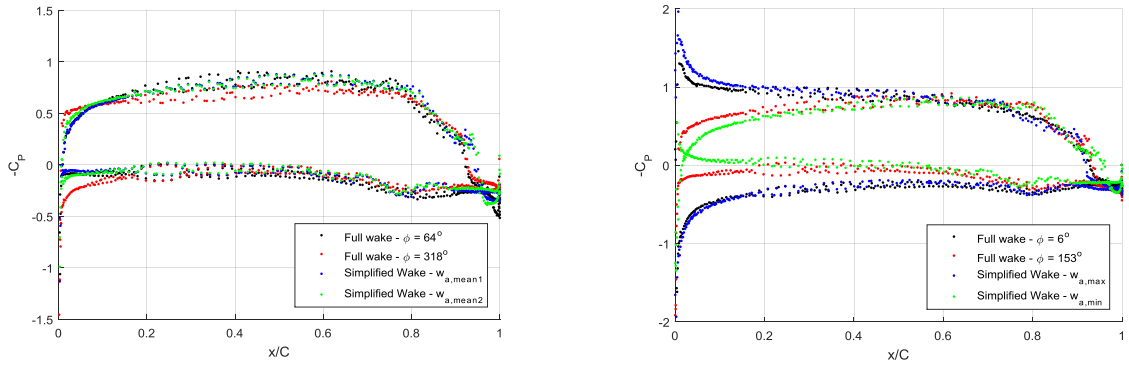

Figure 12. C_P on constant-radius section of 0.7·R in CFD with simplified and full wake

6 Conclusion

CFD with simplified wake has possibility to represent propeller flows at specific blade positions. CFD with simplified wake corresponding to mean wake can be used for high-efficient propeller designs. Suction- and pressure-side cavitation risk can be assessed by considering the maximum and minimum wake in CFD with simplified wake. Considerable computational effort can be saved by running steady CFD with simplified wake instead of unsteady CFD with full wake so that CFD-based propeller optimizations can be conducted more practically.

CFD with simplified wake can be improved by including tangential hull wake effects in the rotating domain. Cavitation is not considered in the current research. When a cavitation model is included in CFD with simplified wake especially for the maximum wake position, it can be a more comprehensive analysis for evaluating propulsive efficiency and cavitation safety in ship propeller designs.

References

Fujisawa, J., Ukon, Y., Kume, K. & Takeshi, H. (2000). Local velocity field measurements around the KCS model. SRI M.S. No. 631

Shin, K.W. & Andersen, P. (2017). CFD analysis of scale effects on conventional and tip-modified propellers. Proc. of SMP'17, Espoo, Finland

Shin, K.W., Regener, P.B. & Andersen, P. (2015). Methods for cavitation prediction on tip-modified propellers in ship wake fields. Proc. of SMP'15, Austin, Texas, USA

Larsson, L., Stern, F., Visonneau, M., Hirata, N., Hino, T. & Kim, J. (Editors) (2015). Proc. of workshop on CFD in ship hydrodynamics (Vol. 2), Tokyo, Japan

Krasilnikov, V.I. (2013). Self-propulsion RANS computations with a single-screw container ship. Proc. of SMP'13, Tasmania, Australia

Demonstration of Propeller Blade Optimization using BEM and CFD

Simon Törnros, Olof Klerebrant Klasson
Caterpillar Propulsion
tornros_simon@cat.com, klasson_olof@cat.com

1 Introduction

The optimum propeller design is a tradeoff between conflicting performance factors such as efficiency, noise and vibrations, and structural strength. Furthermore, there is also a tradeoff due to the conflict between performance in multiple operational conditions, such as high and low speed

Blade design is a time-consuming matter, where a large set of evaluations must be made at every design update. Exploring the design space for a high-end propeller design manually may require weeks of work even for an experienced blade designer, making automatic optimization potentially a vital tool in designing better propellers using less resources.

A propeller blade optimization software called Propart has been developed by MARIN and further developed within the joint industry initiative Cooperative Research Ships (CRS) and the EU funded project MOTOR (Multi-ObjecTive design Optimization of fluid eneRgy machines) [1]. Caterpillar took part in both research projects.

The optimization code is written using MATLAB [2] and the genetic algorithm Non-dominated Sorting Genetic Algorithm II (NSGA-II) [3] will be used in this study. The optimizer evaluates the propeller blade designs using a time efficient low-fidelity tool, based on the Boundary Element Method (BEM). After the optimization, the propellers of interest are analyzed using a high-fidelity tool, based on viscous CFD in open water to validate the optimization results.

The current study aims to analyze the performance of the optimization routine for a realistic test case, and to compare it to a manual state-of-the-art propeller design.

2 Test Case

The propeller chosen for this study is a realistic test case of a twin screw Roll-on/roll-off passenger vessel. There are several off-design conditions with constraints that are contradicting the high requirements on both efficiency and cavitation performance. Four operational conditions were considered for the propeller design.

Design condition

The propeller should be designed with the goal of maximizing the efficiency in the design condition.

- Goal: Maximize efficiency in design condition

Service condition

The service condition includes a sea margin to account for the additional resistance from winds and waves. In this condition, there is a goal to keep the 1st order pressure pulse harmonic on the hull low, below a threshold value, and a constraint is included for minimum margin for K_T with regard to pressure side cavitation. No erosive cavitation is allowed in any condition, introducing a constraint for the service condition.

- Goal: Minimize first order pressure pulse harmonic in service condition
- Constraint: 20% K_T margin against pressure side cavitation in service condition
- Constraint: No erosive cavitation in service condition

MCR condition

In MCR condition the engines are run at maximum continuous rating, meaning that the propellers receive maximum shaft power consequently at a higher pitch setting. The propeller blades must allow lifelong operation at MCR, which gives constraints on the structural integrity and cavitation erosion.

- Constraint: Sufficient structural integrity for lifetime operation in MCR
- Constraint: No erosive cavitation in MCR condition

Slow steam condition

The ship will be operated at slow steam, e.g. during maneuvering. There is a shaft generator on the ship, but since it allows a floating frequency from 60 to 50 Hz, the propeller RPM can be reduced. The pitch will however have to be reduced as well, introducing a constraint for pressure side cavitation.

- Constraint: No pressure side cavitation in slow steam condition

Furthermore, to allow for controllable pitch functionality the blades cannot intersect during pitch setting adjustment which limits the blade area of the propeller. The blade must also fit on the circular blade foot and maintain an area balance around its spindle axis.

- Constraint: No blade intersection during pitch setting adjustment
- Constraint: Blade root must fit on circular blade foot
- Constraint: Maintain balance around the spindle axis

3 Method

The optimization and low-fidelity analysis was run using 10 cores à 3.1GHz with hyper-threading making the total number of logical cores 20. The high-fidelity analysis was run using 48 cores à 2.7GHz without hyper-threading.

Pre-evaluation check

Before an individual enters any evaluation in the optimization routine, a pre-evaluation check takes place to ensure that the blade fulfills the requirements for structural strength and controllable pitch capability.

The propeller blade thickness is explicitly modified to always just fulfill the strength requirement from the DNV-GL rules [4]. To ensure controllable pitch functionality, it is checked so that the blades never intersect during pitch setting adjustment, that the blade is balanced around the spindle axis and that the propeller root can fit on the circular blade foot. Propeller individuals that fail to meet these criteria are rejected immediately, before running any other analysis.

Implementation of goals and constraints

The constraint specifying that no erosive cavitation is allowed is evaluated using two checks. First, by ensuring that the cavity closure line is sufficiently parallel to the incoming flow over the blade sections. Second, by checking so that bubble cavitation does not occur anywhere on the blade. This is done by checking that the minimum pressure downstream the leading edge stays above the vapor pressure. This can be expressed as a safety factor against cavitation $c = \frac{\sigma_n - C_{Pn,min}}{\sigma_n}$ where σ_N is the local cavitation number and $C_{PN,min}$ is the local minimum pressure.

It was found throughout the study that applying a constraint as a goal is necessary to reach convergence of the current optimization setup. Cavitation margin and minimum face side pressure were hence set as goals. The cavitation closure line was set as a hard constraint, which was found

beneficial, since individuals with an unfavorable cavitation behavior were killed, improving the speed of the cavitation simulations for the remaining population.

Low-Fidelity Analysis

The boundary element method based software PROCAL [5] is used in the day-to-day business at Caterpillar for hydrodynamic blade design evaluation, a setup which can be considered industry standard. PROCAL can be used to predict hydrodynamic performance in open water or in-behind condition using an effective wake field (which takes the effect of propeller induced velocity on the wake field into account) with and without cavitation.

High-Fidelity Analysis

A CFD method for numerical analysis of propellers in open water was developed with the purpose of validating the open water results from the low fidelity method. The high-fidelity analysis uses a steady state viscous RANS solver from the finite volume library OpenFOAM v1712 [6]. The simulations were performed using the k-ω SST turbulence model together with wall functions. Only one blade was included in this study, using cyclic boundary condition to reduce the numerical effort.

To allow for a direct comparison with the low-fidelity analysis results, the CFD setup used the same operational condition, was performed in full scale and excluded the blade root fillet. The blade geometry was exported in 3D using a Rhino [7] plugin developed by MARIN [8].

The meshing was performed using the snappyHexMesh utility. The mesh consists of approximately 3.1 million cells mainly of hexahedral shape. Five layers were extruded from the propeller blade, using a growth ratio of 1.2 resulting in an average Y^+ of 350 on the blade.

The total time, including geometry setup, mesh generation, solving and post-processing was 24 minutes on 48 cores, equivalent to less than 20 core hours.

In Figure 1 a comparison of open water results can be seen for experimental results, CFD and BEM. The BEM predicts reasonable thrust and torque close to the design point, but gives increasingly larger discrepancies further from the design point. The CFD based method on the other hand predicts results that are more in line with the experiment for a larger range of advance ratios.

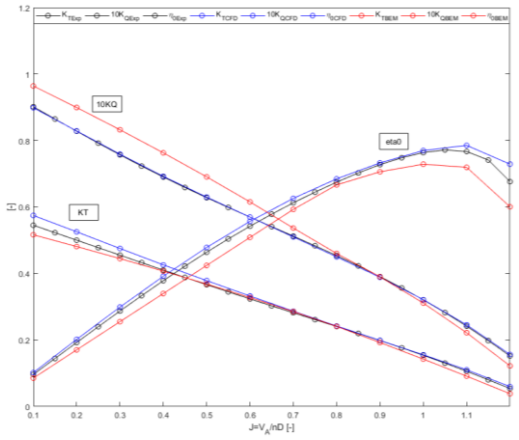

Figure 1 Open water diagram comparison of experiment, CFD and BEM

4 Results

After 44 generations and 8400 (logical) core hours the optimization solution was considered sufficiently converged.

The pareto fronts of all goals with clear tradeoffs are shown in Figure 2. It should be noted that the problem is 4-dimensional, because of the number of goals, so that dense Pareto fronts are not expected. The tradeoffs are in line with expectations:

- High cavitation margin is a tradeoff against high open water efficiency
- Low pressure pulse is a tradeoff against high open water efficiency
- Low pressure pulse is a tradeoff against small amount of pressure side cavitation

Pressure side cavitation is referred to as "Combined pressure 20% K_T and offset pitch". It should be interpreted as the negative min-pressure, so a low value in the plot indicates a higher minimum pressure and hence further away from pressure side cavitation inception.

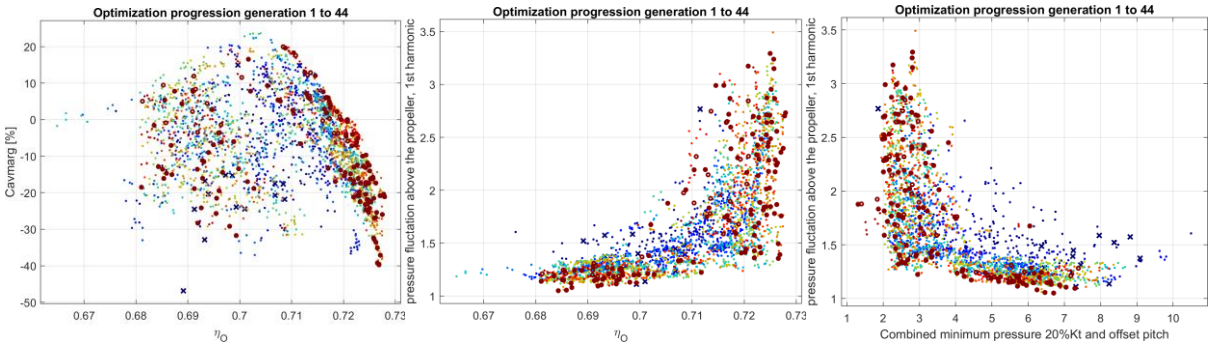

Figure 2: Pareto front results, colored by generation

The constrained pareto front

If we study the goal evolution in Figure 2 and consider that no pressure side cavitation or bubble cavitation is accepted, the final result forms as in Figure 3, where squares and circles are feasible designs and thin dots are violating constraints. The manual design occurs at the pareto front, and the result is encouraging as the tradeoff seem to be well captured.

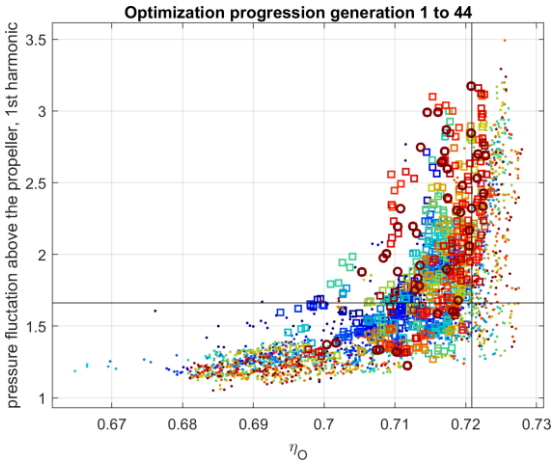

Figure 3: Constrained pareto front of efficiency vs pressure pulses, including the manual design (black lines)

Cavitation pattern results ranging from the propeller with the low pressure pulse and efficiency to the one with high efficiency and pressure pulse on the pareto front can be seen in Figure 4. Evolution has driven the propellers towards high skew and blade area ratio for the low pressure pulse design. The amount of sheet cavitation in tip region has increased significantly for the high efficiency designs.

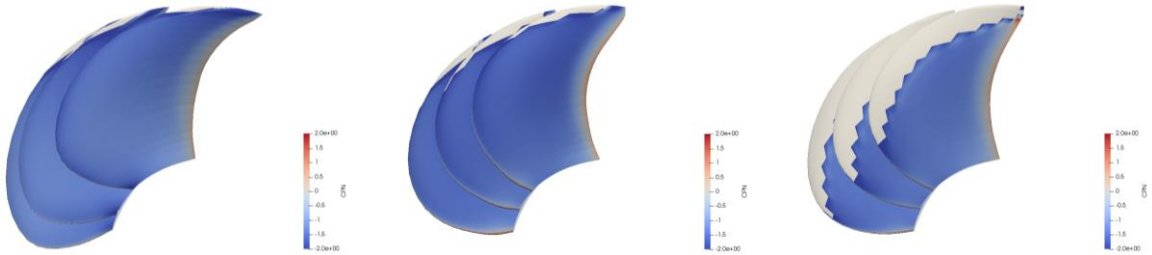

Figure 4: Cavitation pattern and pressure distribution of propellers G31I10 (left), G41I98(middle) and G38I32 (right)

Improvements to manual design

Individual 98 of generation 41 (G41I98) fulfills the same requirement for 1st order harmonic pressure pulse as the manual design with a 0.10 percentage higher open water efficiency. Furthermore, the Pareto front provides understanding of the tradeoff between conflicting performance factors, and shows any margin left unused in the design space.

High-fidelity analysis

Eleven propellers were analyzed using the high-fidelity tool. All propellers give higher thrust, lower torque, and consequently higher efficiency in the high-fidelity analysis compared to the low fidelity analysis. The propeller designs with small first order harmonics pressure pulse tend to give higher thrust, torque and efficiency ratio between CFD and BEM compared to the designs with higher pressure pulse.

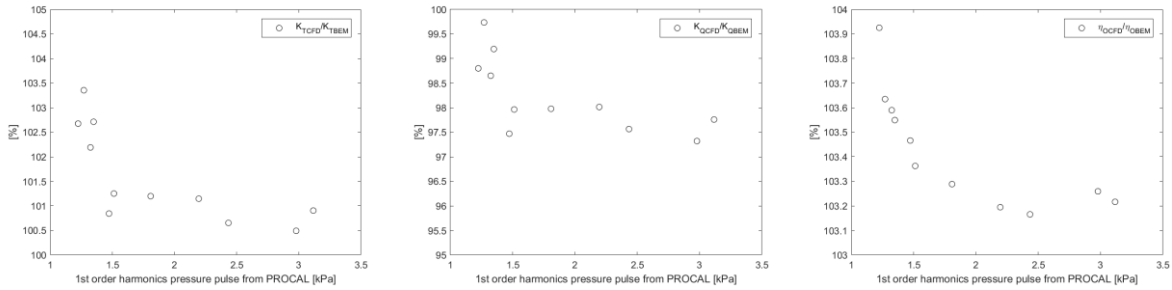

Figure 5 CFD results; thrust coefficient (left), torque coefficient (middle) and efficiency (right)

5 Conclusion

The results from the optimization routine show a Pareto front which includes the manual design. The propeller which just fulfills the requirement for 1st order harmonics pressure pulse has 0.10 percentage higher open water efficiency compared to the manual design. Although this is smaller than the uncertainty of the low-fidelity tool, the optimization design is regarded as highly competitive.

The optimization was considered sufficiently converged after 8400 core hours, meaning that the manual design could be recreated by the optimizer within 2.5 days using 144 cores assuming linear scaling of parallelization. This is a significant cost improvement compared to the one full workweek that was utilized for the manual design.

The high-fidelity tool is fully automated and runs efficiently, requiring less than 20 core-hours per analysis. Analyzing propellers from the open water efficiency – pressure pulse Pareto front show that the high-fidelity tool predicts higher open water efficiencies for all propeller designs. It can also be seen that the difference in predicted open water efficiency increase with decaying pressure pulse.

Research topics that will be investigated further in the future are ways to improve the constraint handling. The inclusion of ducted propeller geometries would be valuable as well as utilizing CFD for more complex off-design conditions and blade root fillet evaluation, which also would require some developments on the FEA side.

Acknowledgements

We thank Evert-Jan Foeth and Douwe Rijpkema at MARIN for all support.

The work leading to these results has received funding from the European Community's Horizon 2020 Programme (2014-2020) under grant agreement n° 678727. The opinions expressed in the document are of the authors only and no way reflect the European Commission's opinions. The European Union is not liable for any use that may be made of the information.

References

[1] "Multi-ObjecTive design Optimization of fluid eneRgy machines," 2018. [Online]. Available: http://motor-project.eu/.

[2] "Matlab R2017b," The Mathworks Inc, Natick, Massachusetts, United States, 2017.

[3] K. Deb, A. Pratap, S. Agarwal and T. Meyarivan, "A fast and elitist multiobjective genetic algorithm: NSGA-II," *IEEE Transactions on Evolutionary Computation,* vol. 6, no. 2, pp. 182-197, 2002.

[4] DNV-GL, Calculation of Marine Propellers, DNVGL-CG-0039, 2015.

[5] PROCAL v.2.325: A Boundary Element Method software developed within CRS.

[6] OpenCFD, "OpenFOAM v1712," 31 12 2017. [Online]. Available: https://www.openfoam.com/releases/openfoam-v1712/.

[7] McNeel, "Rhinoceros v5.0".

[8] MARIN, "MARIN Rhino Plugin v1.5".

Strong quasi-simultaneous coupling for fluid-structure interaction in offshore applications

Arthur E.P. Veldman[a*], Henk Seubers[a], Matin Hosseini Zahraei[b], Peter van der Plas[a], Peter Wellens[b]

[a] Bernoulli Institute for Mathematics, Computer Science and Artificial Intelligence, University of Groningen, The Netherlands

[b] Department of Ship Hydrodynamics, Delft University of Technology, The Netherlands

[*] Corresponding author: a.e.p.veldman@rug.nl

1 Introduction

Simulating the hydrodynamics of deformable, floating structures using a partitioned strategy poses a major challenge when the physical coupling between the fluid and the structure is strong and the ratio of the added mass to the structural mass is considerate. In numerical simulations of such systems with two-way interaction numerical instabilities can occur, which do not occur in systems with inherently one-way interaction. Existing computational procedures for fluid-structure interaction become less efficient or even unstable. In these situations, it is advisable to modify the coupling to allow the fluid to respond better to the body motions. A simultaneous solution of the equations governing fluid and (solid or elastic) body would be a stable choice, but is often not feasible. Usually the numerical problems are taken care of with sub-iterations between fluid and structure, but their convergence can be slow; e.g. [Causin et al., 2005, Forster et al., 2006].

In this paper we present a more powerful, *quasi-simultaneous* approach, which tries to mimic a fully simultaneous coupling in an affordable way as introduced by Veldman for aerodynamic viscous-inviscid boundary-layer interaction [Veldman, 1981, Veldman, 2009]. In our application, the quasi-simultaneous approach makes use of a simple approximation (termed *interaction law*) of the elastic-body dynamics, based on the (6 DOF) solid-body modes and the main elastic modes of the structure.

The fluid solver in this study is the symmetry preserving finite-volume VOF method ComFLOW [Kleefsman et al., 2005, Veldman et al., 2007, Wemmenhove et al., 2015]. A finite element method is used to solve the elastic structure response based on a Euler-Bernoulli beam. Kinematic and dynamic relations couple fluid dynamics to the structural dynamics.

2 Mathematical model

Flow model Incompressible, turbulent fluid flow can be modeled by means of the Navier–Stokes equations

$$M\mathbf{u} = 0, \qquad \frac{\partial \mathbf{u}}{\partial t} + C(\mathbf{u})\mathbf{u} + Gp - V\mathbf{u} = \mathbf{f}. \tag{1}$$

Here M is the divergence operator, which describes conservation of mass. Conservation of momentum is based on the convection operator $C(\mathbf{u})\mathbf{v} \equiv \nabla(\mathbf{u} \otimes \mathbf{v})$, the pressure gradient operator $G = \nabla$, the viscous diffusion operator $V(\mathbf{u}) \equiv \nabla \cdot \nu \nabla \mathbf{u}$ and a forcing term $\mathbf{f}$. The kinematic viscosity is denoted by ν. The flow equations are discretized on a staggered grid with a finite-volume method. The convective terms are discretized in a skew-symmetric energy-preserving way [Verstappen and Veldman, 2003]. Also the discrete pressure gradient G is the negative transpose of the discrete divergence operator M, such that also the pressure does not influence the energy balance.

The free-surface location is indicated by a Volume-of-Fluid [Hirt and Nichols, 1981] function ϕ, and reconstructed by means of Youngs' PLIC method [Youngs, 1987, Düz, 2015].

In this exposition, for simplicity reasons the first-order forward Euler time integration will be used. In the actual calculations, a second-order Adams–Bashforth method is being applied.

The solution of the discrete Navier–Stokes equations is split into two steps. Firstly, an auxiliary variable $\tilde{\mathbf{u}}$ is introduced

$$\Omega \frac{\tilde{\mathbf{u}} - \mathbf{u}^n}{\delta t} = -\mathsf{C}(\mathbf{u}^n)\,\mathbf{u}^n + \mathsf{V}\mathbf{u}^n + \mathbf{f}, \quad \text{such that} \quad \mathbf{u}^{n+1} = \tilde{\mathbf{u}} - \delta t\, \Omega^{-1} \mathsf{G} \mathsf{p}^{n+1}. \tag{2}$$

Secondly, by imposing discrete mass conservation at the new time level, substitution of (2) results in a discrete Poisson equation for the pressure:

$$\delta t \, \mathsf{M}_0 \Omega^{-1} \mathsf{G} \mathsf{p}^{n+1} = \mathsf{M}_0 \tilde{\mathbf{u}} + \mathsf{M}_\Gamma \mathbf{u}_\Gamma^{n+1}, \tag{3}$$

where M_0 and M_Γ represent the discrete continuity operator in the interior and along the boundary, respectively.

Structural model For simplicity, in this study the structure is selected to be a one dimensional Euler–Bernoulli beam. Assuming a constant cross section A for the beam, its equation of motion is

$$\rho_s A \frac{\partial^2 d}{\partial t^2} + EI \frac{\partial^4 d}{\partial s^4} = f, \tag{4}$$

with appropriate initial and boundary conditions. Here, s denotes a coordinate along the beam, d the beam deformation, ρ_s the beam density, E Young's modulus, I the second moment of inertia and f the load per unit length of the beam.

The structural response of the elastic body (eb) is modeled with a finite element method. Omitting the technical details, the resulting discrete set of equations can be written in the form

$$\mathsf{M}_{\text{eb}} \ddot{\mathsf{d}} + \mathsf{K}_{\text{eb}} \mathsf{d} = \mathsf{f}, \tag{5}$$

where M_{eb} is the discrete mass operator and K_{eb} the discrete stiffness operator. These matrices can be simultaneously diagonalized as $\mathsf{Q}^T \mathsf{M}_{\text{eb}} \mathsf{Q} = \mathsf{I}$ and $\mathsf{Q}^T \mathsf{K}_{\text{eb}} \mathsf{Q} = \Lambda$, where Q contains the normalized elastic body eigenvectors (modes) with eigenvalues Λ. In this way, the elastic body dynamics (5) can be rewritten as

$$\mathsf{Q}^{-1} \ddot{\mathsf{d}} + \Lambda \mathsf{Q}^{-1} \mathsf{d} = \mathsf{Q}^T \mathsf{f}. \tag{6}$$

The temporal integration of the structure equations is performed by means of the generalized-α method [Chung and Hulbert, 1992].

Fluid-solid interface The coupling relations along the fluid-solid interface Γ_{FS} consist of two relations: the kinematic and the dynamic conditions. The kinematic condition states that the motion of the interface on both sides matches. The dynamic condition expresses equilibrium of stresses at the fluid-solid interface.

3 Numerical coupling

Time marching with sub-iterations Information has to be exchanged between the two subsystems: the fluid solver provides the loads to the structural solver, whereas in return the latter provides the structural motion to the flow solver. In an explicit, weak coupling this exchange only happens once per time step, but this process is unstable for larger mass ratios. Therefore often per time step sub-iterations with severe under-relaxation (e.g. Aitken [Forster et al., 2006]) are introduced to achieve a strong coupling between the subsystems; Fig. 1(left). The convergence of this process can be rather slow, and each iteration a solid-fluid solve has to be performed. This makes this coupling method inefficient. In the next section we will present a method that shares the strong coupling with the above sub-iterations, but at a limited additional computational effort.

Quasi-simultaneous coupling For two-way coupled problems, a monolithic or simultaneous approach is not always possible, as the sub-domain solvers have to be coupled at a deep iterative level. In this section we will describe an approach that tries to combine the simplicity of a hierarchical coupling approach with the iterative power of a monolithic approach. In the quasi-simultaneous method, an approximation of the body dynamics is solved simultaneously with the fluid. This *interaction law* anticipates the body response in advance of the actual solid dynamics computation. As such, the interaction law (Fig. 1(right)).

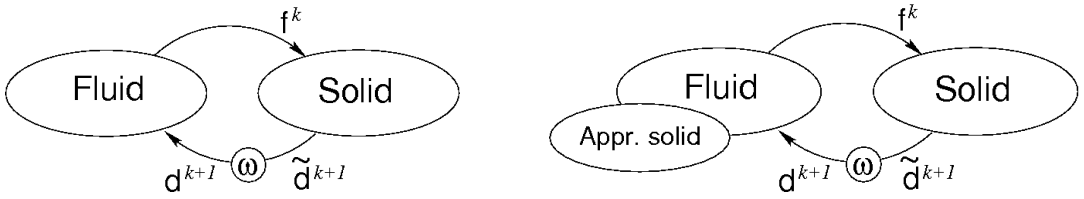

Fig. 1: (Left) Sub-iterative loop of FSI with relaxation within one time step; (right) adding an approximate interaction law. Force f, displacement d, whereas k is iteration level.

To understand the coupling stability, it is useful to formulate the coupling problem in terms of interface variables only: the velocity along the interface $\mathbf{u}_\Gamma$ (related to the displacement d, and the load exerted by the fluid to the structure $\mathbf{f}_\Gamma$ (for an elastic body found from the local stresses, for a solid body found from their integration along the interface).

Elastic body coupling

Because the structural equation (6) contains both $\ddot{\mathsf{d}}$ and d, first a discrete time integration is carried out. Thereafter, the discrete version of the hierarchically coupled problem at the new time level can be denoted as

$$\text{Elastic body } \mathsf{Q}^{-T}\left(\frac{\mathsf{I}}{\delta t^2}+\Lambda\right)\mathsf{Q}^{-1}\mathbf{d}_\Gamma^{k+1}=\mathbf{f}_\Gamma^k, \quad \text{Fluid } \mathbf{f}_\Gamma^{k+1}=-\frac{\mathsf{M}_{\text{ad}}}{\delta t^2}\mathbf{d}_\Gamma^{k+1}. \tag{7}$$

The contribution from the previous time steps is omitted in view of clarity; it is just an inhomogeneous term in the right-hand side, which is not relevant for the convergence of the sub-iterations per time step.

The displacement $\mathbf{d}^{k+1}$ can be eliminated from the system of equations (7), after which the iterative process can be written as

$$\mathbf{f}^{k+1}=-\mathsf{M}_{\text{ad}}\mathsf{Q}(\mathsf{I}+\delta t^2\Lambda)^{-1}\mathsf{Q}^T\mathbf{f}^k. \tag{8}$$

For small enough δt, the amplification factor simplifies to $-\mathsf{M}_{\text{ad}}\mathsf{Q}\mathsf{Q}^T$, where $\mathsf{Q}\mathsf{Q}^T$ has the dimension of $1/kg$. Thus we recognize again an added-mass ratio, leading to divergence when the added mass of the fluid is too large.

In the quasi-simultaneous treatment we approximate the behavior of the elastic body by a simple reduced-order model consisting of a limited number of modes, including the solid-body modes. Let these be collected in the matrix $\tilde{\mathsf{Q}}$. Thus, the proposed interaction law reads

$$\mathbf{d}^{k+1}-\widetilde{\mathsf{Q}}\left(\frac{1}{\delta t^2}+\widetilde{\Lambda}\right)^{-1}\widetilde{\mathsf{Q}}^T\mathbf{f}^{k+1}=\left\{\mathsf{Q}\left(\frac{1}{\delta t^2}+\Lambda\right)^{-1}\mathsf{Q}^T-\widetilde{\mathsf{Q}}\left(\frac{1}{\delta t^2}+\widetilde{\Lambda}\right)^{-1}\widetilde{\mathsf{Q}}^T\right\}\mathbf{f}^k. \tag{9}$$

Letting $\delta t\to 0$, i.e. studying zero-stability, and combining with the fluid-flow model (7), the quasi-simultaneous iterative process reduces to

$$\mathbf{f}^{k+1}=-(\mathsf{M}_{\text{ad}}^{-1}+\widetilde{\mathsf{Q}}\widetilde{\mathsf{Q}}^T)^{-1}(\mathsf{Q}\mathsf{Q}^T-\widetilde{\mathsf{Q}}\widetilde{\mathsf{Q}}^T)\mathbf{f}^k. \tag{10}$$

Clearly, if all of the modes are incorporated into the interaction law, the spectral radius will become zero and the method simultaneously solves the fluid with the ‘exact’ body.

Implementation

The interaction law is a relation between the pressure and the local velocity of the body surface. This relation can be substituted in the right-hand side of the discrete Poisson equation (3) and thus can be considered as a boundary condition. It can be shown that the latter retains its favorable numerical properties (symmetric, negative definite), such that its iterative solution can proceed as before.

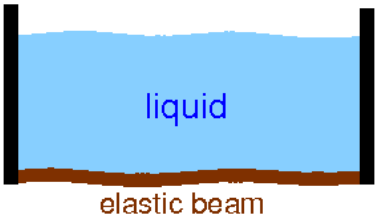

Fig. 2: Schematic of the first test case; the domain with free-surface flow on top and flexible beam at the bottom

4 Examples

Elastic body: tank with membrane bottom

In order to assess the performance of the quasi-simultaneous approach for different mass ratios, a test case has been designed in which this ratio can be varied.

At the bottom of a rectangular container ($1.0 \times 0.1 \times 0.5\,\mathrm{m}^3$) filled with 50 kg of water, a flexible beam is placed as illustrated in Fig.2. The mass of the beam is varied between 1 kg and 50 kg; its module of elasticity is 1 MPa. The interaction law is made out of truncated structural modes; the number of modes dictates its accuracy. The relaxation parameter is adjusted by Aitken's method. Five cases with different mass ratios are solved with and without the interaction law. Also, the effect of the accuracy of the interaction law on the performance is studied.

First, the effect of the added mass ratio is studied. The interaction law is constructed out of the first 10 modes, while the symmetry of the problem cancels out the effect of odd modes. For all the cases the initial relaxation parameter is set to 1, while from the third FSI iteration this value is adjusted by Aitken's method. Fig. 3 shows the convergence of the FSI iterations during the first time step. As shown in Fig. 3(left), higher mass ratios require more computational effort. Plugging in the interaction law, Fig. 3(right) reproduces the same solution while the computational effort is less. It can be observed that the difficult cases with higher mass ratios speed-up a lot more from the quasi-simultaneous approach than the easier cases with modest mass ratios. The difference in convergence rates is clearly visible, with the quasi-simultaneous method hardly needing any under-relaxation.

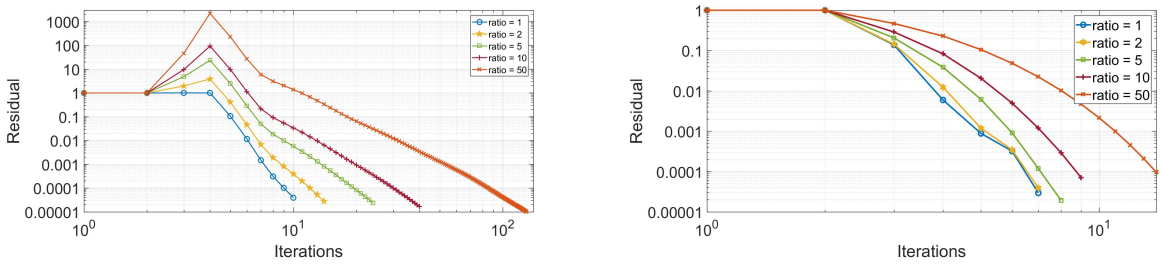

Fig. 3: Convergence history for the first time step for different added mass ratios: (left) without interaction law, (right) with interaction law.

Next, the effect of the number of modes in the interaction law is shown in Fig. 4. Obviously, employing more modes improves the structure response estimation in the interaction law. But there is a trade off, as the gain goes down while making the interaction law itself more expensive. When the mass ratio is low, the number of effective modes is lower than the case when mass ratio is 50.

Rubber gate

The validation test case is an elastic rubber gate placed in front of a bulk of water. This experiment has been performed by Antoci [Antoci et al., 2007]. The gate separating the fluid from the air is partly rigid, but the lower part is elastic. The rubber gate is clamped on the top side and free on the other side. The density of the beam is $\rho_s = 1100$ kg/m^3 and the Young modulus for elasticity is $E = 10$

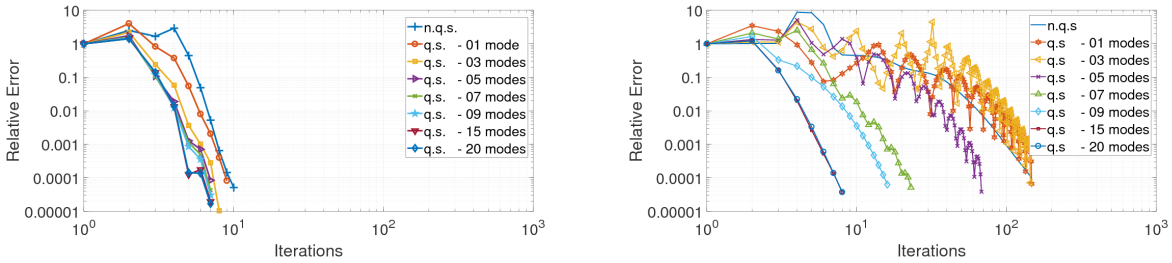

Fig. 4: Convergence history for the first time step for varying accuracy (number of included modes) of the interaction law: (left) mass ratio 1; (right) mass ratio 50.

MPa. According to [Antoci et al., 2007], the problem is mostly two dimensional, so in the current study numerical simulations are performed in 2D. A grid of $250 \times 2 \times 50$ is used. The initial time step is set to be 1×10^{-4}; this value is automatically adjusted during the simulation based on the Courant condition.

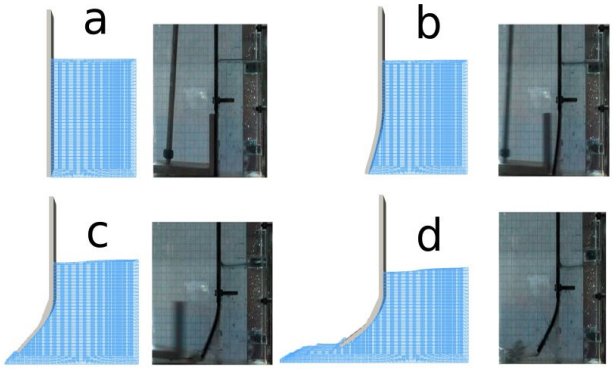

Fig. 5: Snapshots of the simulation past a rubber gate, compared with the experiment of [Antoci et al., 2007]

The results after 0.12 s, with the snapshots from experiment and simulation at time intervals of 0.4 s, are compared in Fig. 5.

5 Conclusion

It has been demonstrated that the ratio of the fluid added mass versus the solid-body mass is an important parameter controlling the (in)stability of a fluid-structure system. Whereas traditional (sub-)iteration methods require severe under-relaxation, a quasi-simultaneous method can handle large added mass ratios more efficiently. An interaction law approximating the structural dynamics is its key ingredient. It is shown that only a couple of dominant modes are needed to achieve a stable method. The stability and resulting efficiency has been demonstrated by comparing the computational effort with and without interaction law on a number of offshore-related applications.

6 Acknowledgments

This work is part of the research programme Maritime2013 with project number 13267 which is (partly) financed by the Netherlands Organization for Scientific Research (NWO).

References

Antoci, C., Gallati, M., and Sibilla, S. (2007). Numerical simulation of fluidstructure interaction by SPH. *J. Comp. Struct.*, 85:879–890.

Causin, P., Gerbau, J. F., and Nobile, F. (2005). Added-mass effect in the design of partitioned algorithms for fluid-structure problems. *Comp. Meth. Appl. Mech. Eng.*, 194:4506–4527.

Chung, J. and Hulbert, G. M. (1992). A time integration algorithm for structural dynamics with improved numerical dissipation: the generalized-α method. *J. Appl. Mech.*, 60(2):371–375.

Düz, B. (2015). *Wave generation, propagation and absorption in CFD simulations of free surface flows*. PhD thesis, Technical University Delft.

Forster, C., Wall, W. A., and Ramm, E. (2006). Artificial added mass instabilities in sequential staggered coupling of nonlinear structures and incompressible viscous flows. *Comp. Meth. Appl. Mech. Eng.*, 196:1278–1293.

Hirt, C. W. and Nichols, B. D. (1981). Volume of fluid (VOF) method for the dynamics of free boundaries. *J. Comput. Phys.*, 39:201–25.

Kleefsman, K. M. T., Fekken, G., Veldman, A. E. P., Iwanowski, B., and Buchner, B. (2005). A Volume-of-Fluid based simulation method for wave impact problems. *J. Comput. Phys.*, 206:363–393.

Veldman, A. E. P. (1981). New, quasi-simultaneous method to calculate interacting boundary layers. *AIAA J.*, 19:79–85.

Veldman, A. E. P. (2009). A simple interaction law for viscous-inviscid interaction. *J. Eng. Math.*, 65:367–383.

Veldman, A. E. P., Gerrits, J., Luppes, R., Helder, J. A., and Vreeburg, J. P. B. (2007). The numerical simulation of liquid sloshing on board spacecraft. *J. Comput. Phys.*, 224:82–99.

Verstappen, R. W. C. P. and Veldman, A. E. P. (2003). Symmetry-preserving discretization of turbulent flow. *J. Comput. Phys.*, 187:343–368.

Wemmenhove, R., Luppes, R., Veldman, A. E. P., and Bunnik, T. (2015). Numerical simulation of hydrodynamic wave loading by a compressible two-phase flow method. *Computers & Fluids*, 114:218–231.

Youngs, D. L. (1987). An interface tracking method for a 3d Eulerian hydrodynamics code. Technical Report AWRE/44/92/35, Atomic Weapons Research Establishment.

Weighted trade-off optimization of a self-propelled passenger ferry using efficient design space analysis techniques and adaptive grid refinement

Kevin Vidal, Benoit Mallol, Charles Hirsch
NUMECA International, Chaussee de la Hulpe, 189 Brussels, Belgium
kevin.vidal@numeca.be, benoit.mallol@numeca.be, charles.hirsch@numeca.be

Abstract

This paper presents an optimization loop of a full scale passengers ferry. The objective is to decrease the delivered power for 4 differents operating conditions by integrating hydrodynamics computations methods and advanced design space analysis. The loop is composed of a parametric design generator, an optimization algorithm and a CFD package for the meshing and the performances evaluation. The optimization is assisted by a surrogate initially created from a design of experiments fitting model. The automatic grid refinement is also used to accelerate the meshing time and enable a low discretization error of the free surface capturing.
Keywords: surrogate-based optimization, CFD-based design, hydrodynamics hull form optimization, surrogate-assisted data mining analysis, powering economic ship design, adaptive grid refinement.

Introduction

Marine engineers and naval architects are facing new challenges involving more efficient and greener ships. The international maritime organization (IMO)'s low carbon shipping and air pollution control regulations states that by 2025, all new ships must be massively 30% more energy efficient than those built in 2014 [1].

Hydrodynamic hull shape optimization is one of the solutions to get a more economic design. But given the ship design loop process, the optimization has to be embedded in the early, but indispensable, design stage. Hence the optimization loop must feature a turnaround time acceptable for industrials.

There are three components used for hydrodynamic optimization: a parametric hull modelling, a performance evaluator using computational fluid dynamic (CFD) and the optimization technologies. The combination of CFD method and optimization algorithm started in the early 2000 with research on parametric optimization of the hull [4,5] and has been recently used for industrial project [6]. With the recent growth of high performance computing, simulation-based design optimization (SBDO) using high fidelity solvers become more affordable at industrial scale [2,3].

The aim of this paper is to present a methodology for exploring and optimizing a full scale passenger ferry with a turnaround time acceptable due to an advanced data mining analysis. The ship is initially designed with a variety of operational profiles requiring several meshes to keep an accurate flow resolution for each loading condition. However the paper uses the adaptive grid refinement to speed up the meshing process, by using only one mesh for all conditions, while keeping a modelization error of the free surface capturing very low.

As the main objective function is the powering, a high fidelity solver is prefered to predict accurately flow field patterns [7]. Moreover the propeller-hull interaction is taken into account by means of a special actuator disk. This CPU time limited self propulsion computation provides accurate informations about the propulsion, which is mandatory to estimate the powering.

Parametric hull design creation

In order to parametrize the hull, the graphical editor, Grasshopper™, is used. On top of Rhino3D, Grasshopper™ has the advantage to provide parametric values for each geometric entity. For example, the passenger ferry is represented by a network of B-Spline curves (cf. Fig. 1) made of cartesian coordinates-defined control points. This strategy leads to a large number of parameters, which requires an important CPU time sampling of the design space.

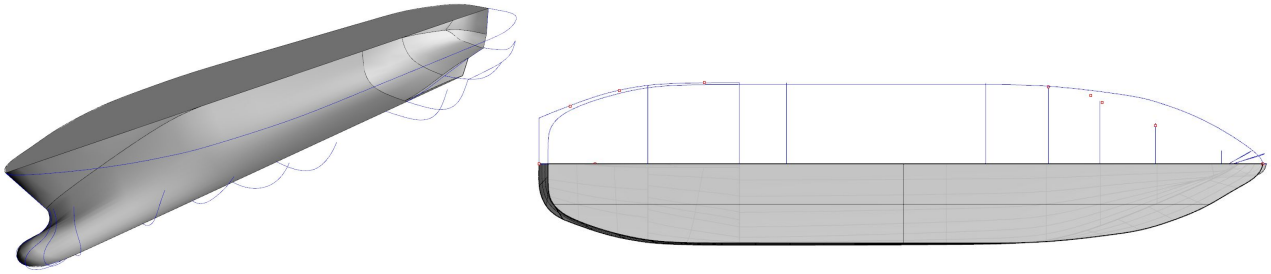

Fig. 1: Hull representation with the B-spline curves network, hardpoints are in red (cf. Chart 2)

In order to reduce the amount of design parameters, the strategy proposed by Guha A [8] is followed. Hence, some parameters are merged together to decrease the design space dimensionality. At the end, the ship hull consists in parametric curves controlled by 15 parameters (Table 1) to change the ferry hull shape. The bounds of each parameter are set to respect hardpoints (fixed points) along the hull.

Parameters	Value	Parameters	Value
Bulb lower length [m]	1.27	Half beam WL [m]	9.071
Bulb upper length [m]	0.32	Propeller clearance [m]	3.62
Bulb lower position [m]	2.41	Deadrise angle [°]	16.38
Bulb height [m]	4.21	Transom inclination [°]	0.5
Half breath bulb [m]	1.05	Transom offset 1 [m]	4.56
Half bottom width [m]	1	Transom offset 2 [m]	4.26
Entry angle [°]	13.51	Bow-Bulb section [m]	6.42
L midship [m]	65.72		

Table 1 : Free design parameters.

Hardpoints	X [m]	Y [m]	Z [m]
Main deck	75.282	8.97	7.589
Vertical guards 1	60.96	10.67	7.47
Vertical guards 2	22.56	10.67	7.47
Vertical guards 3	10.97	9.63	7.47
Vertical guards 4	4.27	7.54	7.47
Tip of bow	100.89	0.0	15.46
Bottom of bow wrapper	96.42	0.0	8.17
Aft CL main deck	7.62	0.0	7.47

Table 2 : Hardpoints locations.

Grid refinement and flow solver

The marine C-Wizard from the FINE™/Marine package is used to automatically prepare the mesh and solver parameters.

	Condition 1	Condition 2	Condition 3	Condition 4
Relative weight	0.35	0.15	0.35	0.15
Δ [tons]	5550	5550	4690	4690
U ship [m/s]	15.0	16.5	15.0	16.5
Initial number of cells	2,447,011			
Number of cells at convergence	2,664,392	2,684,502	2,644,179	2,678,609

Table 3 : Main characteristics of the 4 operational conditions

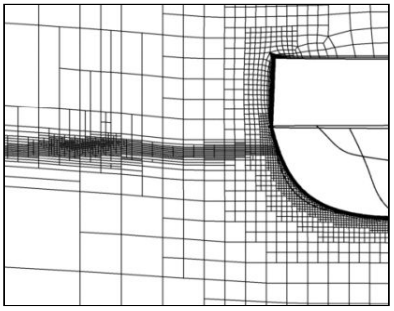

Fig. 2 : AGR refinement

As several loading conditions are studied, a traditional approach is to make a new mesh for each condition, one mesh with a predefined free surface refinement for one hull displacement. To avoid this, the adaptive grid refinement (AGR) [10] technique is used to skip this initial free surface refinement and hereby simplifying the meshing process. For each loading condition, the ship is moved in trim and sink to fulfill iso-displacement constraint. Hence, the free surface refinement and capturing is performed during the computation (Table 3 and Fig. 2). The refinement strategy depends on a matrix tensor-based refinement C_i, computed from the flow solution, and a cell size d_i to calculate a modified size $\widehat{d}_i = C_i d_i$. Eventually the cell is refined when $\widehat{d}_i$ exceeds a given threshold $|\widehat{d}_i| \geq T_r$.

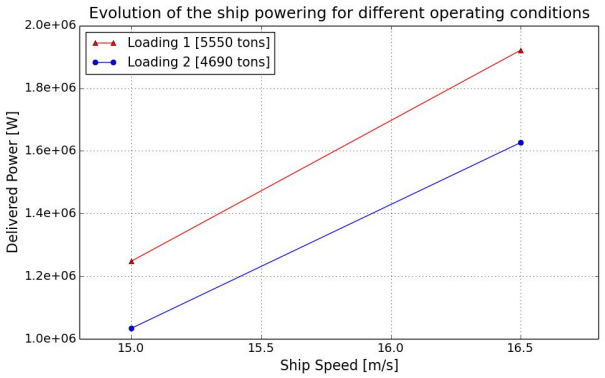

Fig. 3 : Powering evolution

To compute the delivered power, an enriched actuator disk, reading open water data, is applied to model the propulsion system. Based on the trust identity method, the actuator disk mimics the propeller influence by virtually applying a rotational speed to maintain the self-propulsion equilibrium and eventually retrieves the torque from the open water data. The overall power is then computed by summing all conditions with their respecting weight (cf. Table 3). At the end, the computational cost for one individual design and 4 operating points is 480 CPU.hour.

Numerical verification of the adaptive grid refinement

The recent trend of using high fidelity solver needs to be correlated with a rigorous estimation of the numerical errors in order to assess the accuracy of the physical model. It becomes more evident in a optimization framework where the shadow of modelling error can lead to criticism or doubt over the real performances of the final optimum design. That is why, Campana et al [2] has performed a verification analysis of the initial and final designs to validate the optimized solution. The discretization error is assumed to be the most important and the Richardson extrapolation (RE) [9] aims at estimating it. The drawback of the RE method is the need to generate a serie of nested meshes which is engineering time consuming when dealing with several operating conditions. One more advantage of the AGR is to generate rapidly and efficiently different sized meshes.

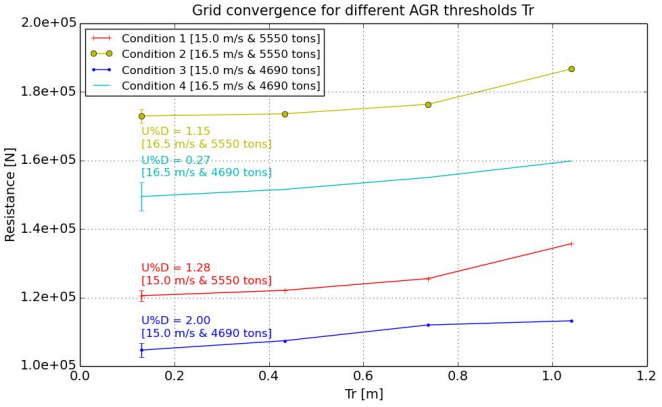

Fig. 4 : Mesh convergence study

The free surface criteria [11] is used to compute the matrix tensor C_i, hence only the discretization error at the free surface is studied. Different thresholds *Tr* are set to get the serie of nested mesh. For this criterion, the threshold directly specifies the mesh size normal to the water surface.

The least-square method proposed by Eça [12] is used to estimate the numerical error onto the finest grid. To eliminate noises, 4 meshes are created and finally show that the maximum error is about 2.00% for the operating point 3 (15 m/s and a displacement of 4690 tons), but all other operating condition were below 1.3%.

To the authors knowledge, an error below 2% is judged satisfactory from an industrial point of view.

Database generation and data-mining investigation

The sampling of the design space or *Design of Experiments* (DoE), is a fundamental step of the optimization process. The sampling defines the surface response model and therefore the convergence rate of the optimization. 24 individuals are selected to populate the design space, using a DoE known as Latinized Centroidal Voronoi Tessellations (LCVT) [13], available in in FINE™/Design3D. The LCVT leads to very good spread of data points compared to other types of DoE. The principle is to maximize the surrogate accuracy over the number of samples.

After populating and computing the design points, an advanced version of a radial basis function network is used as surrogate model. Then a Leave-One-Out (LOO) validation [14] is performed to compute the correlation coefficient *R* which assess the reliability of the surrogate model. In the LOO procedure, the surrogate iteratively fits the *n-1* individuals results with the left out sample, used as validation data. Eventually the weighted sum of all powers shows an acceptable surrogate quality with a *R* equal to 0.729 (*R*=1 means a perfect fit). The *R* coefficient is not meant to be high after the DoE, otherwise it would mean refining the model in areas with low interest in terms of optimal design. Instead the optimization works with an update of the surrogate model, which refines the surrogate close to the interesting regions in terms of optimal design (cf. Optimisation process section).

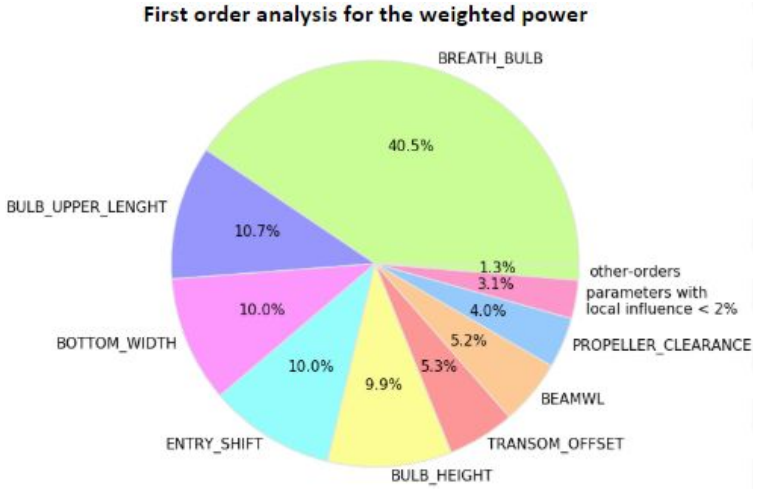

Fig. 5: Global sensitivity analysis of the weighted power

The surrogate model quality is judged satisfactory, and it can be employed in data mining investigations, such as global sensitivity analysis and design space analysis.

The global sensitivity analysis study helps to estimate the global output variability of the surrogate model over the entire range of design parameters. In other words, it identifies the sensibility in the output y due to the input variable change x_i by computing the Sobol's indices [16]. That measure gives the relative importance of the parameters in the output variability.

Only the first order indices S_i are computed by dividing the variance of an y expected value, given x_i, over the total variance Eq.(1). For the weighted power, 61% of the weighted power variance is caused by the variance of 3 bulbous parameters (Fig. 5). The first order indice provides the same information as a "one variable at a time" analysis. In consequence, any coupling effects or errors represented by higher order terms is taken into account by calculating $S_{other-orders} = 1 - \Sigma_{i=1}^{n} S_i$. In our case, $S_{other-orders}$ is equal to 1.3% which proves that the analysis of the first indices is sufficient.

$$S_i = \frac{\int_{x_i} f_i^2(x_i)dx_i}{\int_{R^n} y^2\, dx_1..dx_n - f_0^2} \quad \text{where} \quad y = f(x_1,..,x_n) \quad \text{and} \quad f_i(x_i) = \int_1 .. \int_{n-1} y\, dx_1..dx_{i-1}d_{x+1}..dx_n - f_0 \tag{1}$$

The surrogate technique is also used to analyse the design space. A Self-Organizing Map (SOM) [15], is a type of surrogate assisted data-mining that aims at projecting high dimensional data into lower dimension, typically 2D maps, which therefore eases the identification of correlation and anti-correlation among parameters and responses.

From the initial DoE of 24 samples, the SOM shows a major correlation between all power outputs (for the 4 operating conditions). And it is therefore displayed in the weighted power, where an optimum area is localised in the top left of the map. Indeed Fig.3 shows that the loading condition 2 is just an offset of loading condition 1. In other words, both loadings are correlated, and only optimizing one loading condition will logically influence the other in the same manner. Moreover, for the same loading condition, the ship speed range is small enough such that the influence of one design speed will drive the optimum of the other one into the same direction. This analysis indicates that optimizing a single operating point would have a positive effect on all other conditions.

As a conclusion, it is decided to only optimize the operating point 1 (15m/s and 5550 tons). Because it has a higher weight onto the aggregate power formulation ($w = 0.35$), it displays a very low discretization error and its surrogate for the objective function features an acceptable R coefficient of *0.6*.

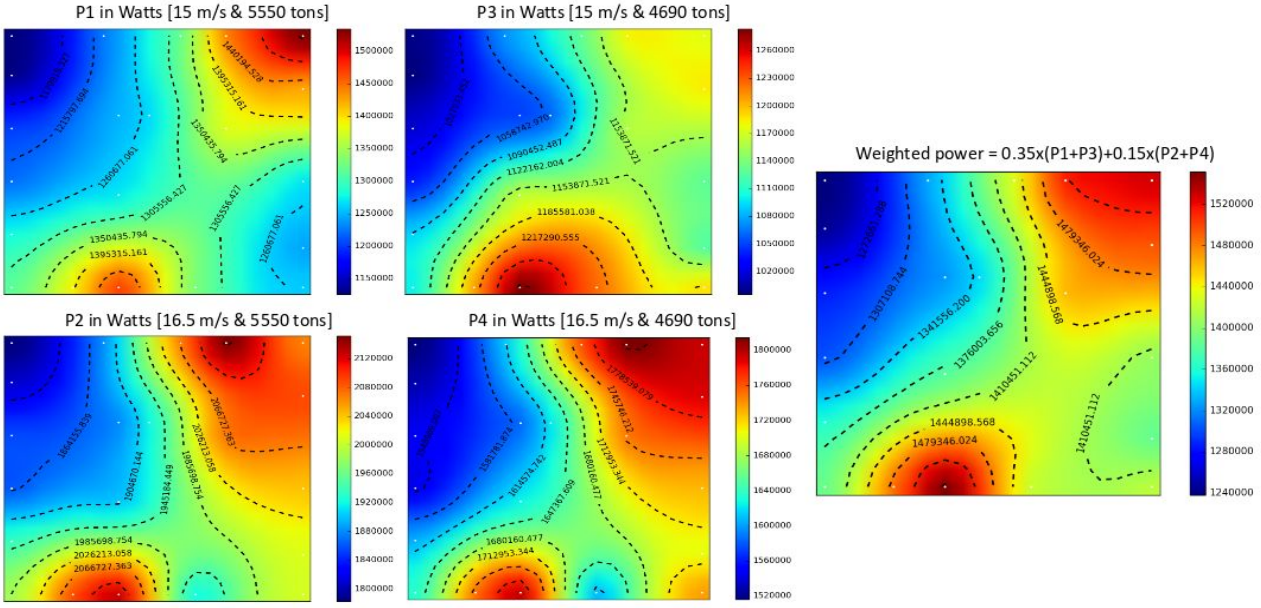

Fig. 6: 2D mapping of differents outputs

Optimisation process

The optimization consists in 2 successive steps, first the optimizer will use genetic algorithm (GA) to find the optimum based on the surrogate evaluation. Then a CFD computation is performed to check the validity of the surrogate optimum search. The new sample is eventually added into the DoE in order to increase the precision of the surrogate model.

GA mimics the process of natural evolution by creating an initial population, then evaluating each individual to extract the strongest candidates, and finally introducing new genetics, from the favorable characteristics of the strongest candidates, into a new set of population. The population, iteratively generated by the GA, are not evaluated through a CFD simulation but by the regression model. The costly high fidelity evaluation is limited at checking the optimizer results whether the model gives a correct optimum or not.

The process, implemented in FINE™/Design3D, converges to an optimum, respecting all constraints, after 10 iterations which represents 1200 CPU.hour, one design point is equal to 120 CPU.hour (cf. Grid refinement and flow solver section).

Afterward, the other operating points of the optimum design are computed in order to check the real overall improvements. As it is expected from the SOM, the main objectives of reducing the power at one operating condition has impacted significantly and positively the other operation points (Table 5). The assumption made with the SOM is thus confirmed. It is possible that using a weighted formulation as main objective function would have lead to a different optimum design, but the overall performance improvement justifies the choice taken.

The same grid refinement study is performed onto the optimum design. And the Fig. 7 shows that the AGR remains consistent in the modelling error. Only the numerical error of the operating condition 4 (16.5m/s and 4690 tons) has doubled. But it could be coming from the initial mesh density, which has not been studied in this paper (cf. Numerical verification of the adaptive grid refinement section) and therefore introduces some uncertainty in this analysis. We can conclude that the optimized design is validated.

To summarize, the methodology proposed is to find an acceptable trade-off design between powering improvement and turnaround time, and the current optimum design matches this requirement.

Constraints	Δ = 4690 tons	Δ = 5550 tons
Draft MAX [m]	5.029	5.029
K_{MT} MIN [m]	10.82	10.06
K_{MT} MAX [m]	11.57	11.69
L_{cb} MIN [m]	46.51	46.17
L_{cb} MAX [m]	47.71	47.37

Table 4: Constraints definition

	Initial	Optimum	Gain [%]
P at 15 m/s & 5550 tons [W]	1248331	1038231	16.8
Weighted power [W]	1331074	1174053	11.8

Tablet 5: Optimization outcome

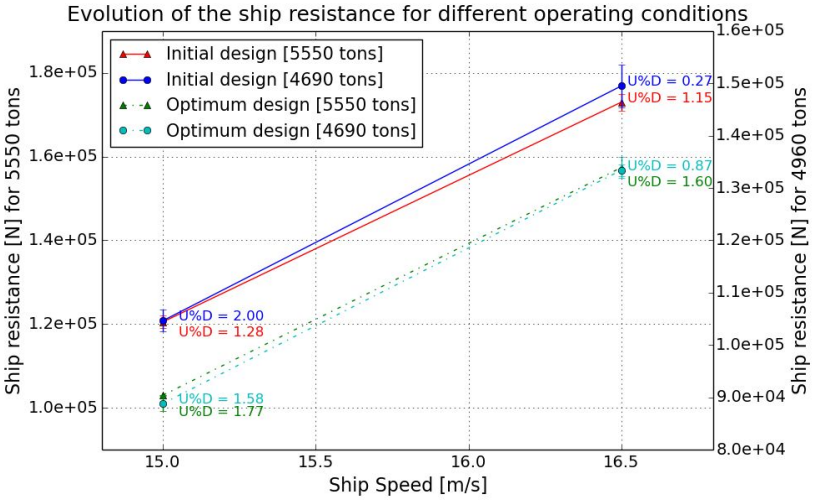

Fig. 7: Power evolution for the initial and optimum design

Conclusion and future work

The paper presents a trade-off optimization study of a full scale passenger ferry. Trade-off study in a sense that the optimization involves several operating points where the engineer does not know if guaranteeing one condition enhancement will induce either improvements or deteriorations on the other conditions.

Thanks to surrogate-assisted data mining, it was possible to quantify the regression model quality, perform a sensibility analysis, and extract correlations between output and input parameters with the Self-Organizing Map (SOM).

The SOM is successfully used to conclude that all operating conditions share a common trend in the powering improvement. In this logic, only one operational condition is optimized and a global enhancement of 12% is finally observed.

The meshing process is reduced to generate a single mesh for all conditions and the adaptive grid refinement (AGR) dynamically resolves the free surface capturing. Moreover the AGR proves to be consistent enough in the modelling error which is a clear advantage in an optimization framework.

The optimization is still CAD-based which implies remeshing the geometry at every new generation. A solution would be to use CAD-free technology, such as morphing or free form deformation (FFD), to directly morph the mesh, and keep the same mesh topology and characteristics.

References

[1] Zhang, Hui. "Towards Global Green Shipping: the Development of International Regulations on Reduction of GHG Emissions from Ships." *International Environmental Agreements: Politics, Law and Economics*, vol. 16, no. 4, Sept. 2014, pp. 561–577.

[2] Campana, Emilio F., et al. "Shape Optimization in Ship Hydrodynamics Using Computational Fluid Dynamics." *Computer Methods in Applied Mechanics and Engineering*, vol. 196, no. 1-3, 2006, pp. 634–651.

[3] Tahara, Yusuke, et al. "CFD-Based Multi-Objective Optimization Method for Ship Design." *International Journal for Numerical Methods in Fluids*, vol. 52, no. 5, 2006, pp. 499–527.

[4] Harries, Stefan. "Parametric Design and Hydrodynamic Optimization of Ship Hull Forms." *Mensch-Und-Buch-Verl.*, 1998.

[5] Janson, Larsson. "A Method for the Optimization of Ship Hulls from a Resistance Point of View" *Twenty-First Symposium on Naval Hydrodynamics*, 1997, pp.680-694.

[6] Lu, Yu, et al. "A Hydrodynamic Optimization Design Methodology for a Ship Bulbous Bow under Multiple Operating Conditions." *Engineering Applications of Computational Fluid Mechanics*, vol. 10, no. 1, 2016, pp. 330–345.

[7] B. J. Guo , G. B. Deng & S. Steen. "Verification and validation of numerical calculation of ship resistance and flow field of a large tanker", *Ships and Offshore Structures*, 8:1, 3-14,2013.

[8] Guha, A., J. Falzaranoa. "Application of Multi Objective Genetic Algorithm in Ship Hull Optimization." *Ocean Systems Engineering*, vol. 5, no. 2, 2015, pp. 91–107.

[9] Richardson, L. F. "On the Approximate Arithmetical Solution by Finite Differences of Physical Problems Involving Differential Equations, with an Application to the Stresses in a Masonry Dam." *Proceedings of the Royal Society A: Mathematical, Physical and Engineering Sciences*, vol. 83, no. 563, Feb. 1910, pp. 335–336.

[10] Wackers, Jeroen, et al. "Adaptive Grid Refinement for Hydrodynamic Flow Simulation." *Ship Technology Research*, vol. 56, no. 4, 2009, pp. 154–160., doi:10.1179/str.2009.56.4.002.

[11] Wackers, Jeroen, et al. "Combined Refinement Criteria for Anisotropic Grid Refinement in Free-Surface Flow Simulation." *Computers & Fluids*, vol. 92, 2014, pp. 209–222

[12] Eça, L., and M. Hoekstra. "A Procedure for the Estimation of the Numerical Uncertainty of CFD Calculations Based on Grid Refinement Studies." *Journal of Computational Physics*, vol. 262, 2014, pp. 104–130

[13] M. Gunzburger Y. Saka and J. Burkardt. , "Latinized, improved lhs, and cvt point sets in hypercubes" , *International Journal of Numerical Analysis and Modeling*, pages 729-743, 2007

[14] Lachenbruch, Peter A., and M. Ray Mickey. "Estimation of Error Rates in Discriminant Analysis." *Technometrics*, vol. 10, no. 1, 1968, p. 1

[15] Kohonen T., "Self-Organizing Maps", *Springer*, Berlin, Heidelberg, 1995

[16] Sobol, I. M., and S. S. Kucherenko. "Global Sensitivity Indices for Nonlinear Mathematical Models. Review." *Wilmott*, vol. 2005, no. 1, 2005, pp. 56–61

Hull shape optimisation using multi-fidelity metamodels and adaptive grid refinement

Jeroen Wackers*, Charles-Edouard Jeanson*, Patrick Queutey*, Michel Visonneau*, Riccardo Pellegrini†, Andrea Serani†, and Matteo Diez†

*LHEEA, Ecole Centrale de Nantes / CNRS-UMR 6598, Nantes/France,

†CNR-INM, National Research Council-Institute of Marine Engineering, Rome/Italy

jeroen.wackers@ec-nantes.fr

1 Introduction

In automatic design optimisation, large numbers of candidate designs need to be evaluated in order to find the best design. If the evaluations are performed with numerical simulation, this may be prohibitively expensive. A way to solve this problem is by using metamodels: a limited number of designs is simulated and a surrogate model for the numerical simulations is created by interpolating between these training points with a suitable technique. The optimisation is then performed over this cheap surrogate model.

The cost of this procedure can be further reduced through multi-fidelity metamodelling. Here, most of the metamodel behaviour is based on relatively cheap, low-fidelity simulations, but these results are corrected with a few expensive high-fidelity simulations. The goal is to obtain a metamodel with the precision of the high-fidelity simulations and the cost of the low-fidelity ones. Different fidelities can be obtained using two separate solvers, such as RANS and potential flow codes. If only RANS is used, the accuracy and cost can be varied by using fine and coarse meshes.

Adaptive grid refinement is a method of creating the mesh during the simulation by locally dividing cells where the flow needs this. By adjusting the global amount of refinement requested, coarse or fine meshes are created in a straightforward manner. Therefore, it is a natural choice to integrate adaptive refinement in an automatic optimisation procedure with multi-fidelity metamodels.

The goal of this paper, a continuation of the work by Pellegrini et al. (2018), is to explore the combination of the multi-fidelity metamodelling techniques developed at CNR-INM with the flow solver ISIS-CFD from ECN – CNRS, which contains adaptive grid refinement. The paper summarises these techniques, focusing on those aspects which are relevant for their combination. Then, a multi-fidelity metamodel-based shape optimisation is presented for the DTMB 5415 destroyer.

2 Adaptive multi-fidelity metamodel

Consider an objective function $f(\mathbf{x})$, i.e. the function to be minimised in the optimisation, where $\mathbf{x} \in \mathbb{R}^N$ is the design variable vector and N the design space dimension. The metamodel prediction $\tilde{f}(\mathbf{x})$ is provided by means of interpolation with stochastic radial basis functions $g(\mathbf{x}, \tau)$, with $\tau \sim \text{unif}[1, 3]$ the stochastic tuning parameter of the metamodel:

$$\widetilde{f}(\mathbf{x}) = \text{EV}\left[g(\mathbf{x}, \tau)\right]_\tau, \quad \text{with} \quad g(\mathbf{x}, \tau) = \sum_{j=1}^{J} w_j \|\mathbf{x} - \mathbf{x}_j\|^\tau, \tag{1}$$

where w_j are unknown coefficients, $\|\cdot\|$ is the Euclidean norm, $\mathbf{x}_j$ are the training points with associated objective function value $f(\mathbf{x}_j)$, and J is the number of training points. The coefficients w_j are determined enforcing the interpolation $g(\mathbf{x}_j, \tau) = f(\mathbf{x}_j)$ by solving $\mathbf{A}\mathbf{w} = \mathbf{f}$, with $\mathbf{w} = \{w_j\}$, $a_{i,j} = \|\mathbf{x} - \mathbf{x}_j\|^\tau$ and $\mathbf{f} = \{f(\mathbf{x}_j)\}$. The uncertainty $U_{\tilde{f}}(\mathbf{x})$ associated with the metamodel prediction is quantified by the 95%-confidence interval of $g(\mathbf{x}, \tau)$, evaluated using a Monte Carlo sampling over τ (Volpi et al., 2015).

The multi-fidelity prediction $\hat{f}(\mathbf{x})$ is defined as a low-fidelity metamodel plus a metamodel of the error between high and low fidelity:

$$\hat{f}(\mathbf{x}) = \tilde{f}_L(\mathbf{x}) + \tilde{\varepsilon}(\mathbf{x}), \quad \text{with} \quad \varepsilon(\mathbf{x}) = f_H(\mathbf{x}) - f_L(\mathbf{x}), \tag{2}$$

where "$\wedge$" indicates the multi-fidelity approximation and f_H and f_L are high- (HF) and low-fidelity (LF) evaluations (Pellegrini et al., 2016). Assuming the uncertainty associated with the low-fidelity and error

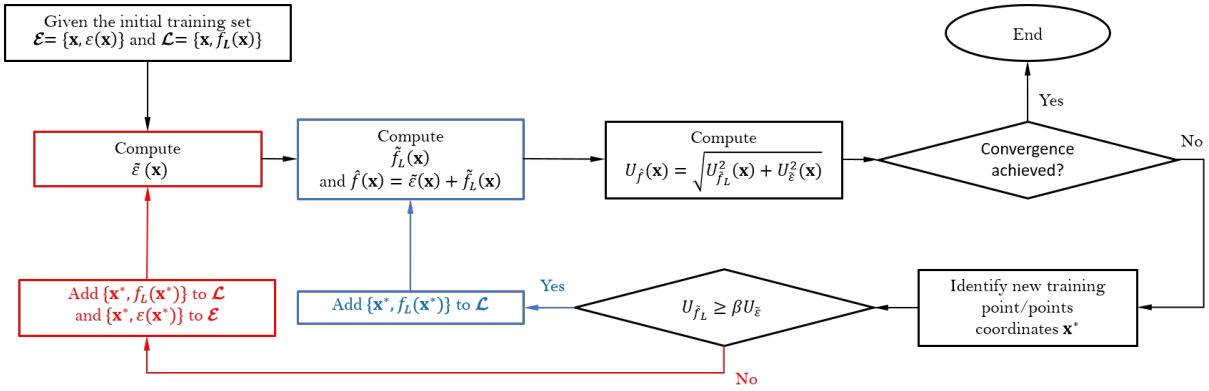

Fig. 1: Adaptive multi-fidelity metamodel updating scheme

metamodels ($U_{\tilde{f}_L}$ and $U_{\tilde{\varepsilon}}$ respectively) as uncorrelated, the uncertainty associated with the multi-fidelity prediction can be defined as:

$$U_{\hat{f}}(\mathbf{x}) = \sqrt{U^2_{\tilde{f}_L}(\mathbf{x}) + U^2_{\tilde{\varepsilon}}(\mathbf{x})}. \tag{3}$$

$\mathcal{L}$ and $\mathcal{E} \subseteq \mathcal{L}$ are the training sets for $\tilde{f}_L$ and $\tilde{\varepsilon}$, respectively. New training points $\mathbf{x}^\star$ for $\mathcal{L}$ and $\mathcal{E}$ are sequentially defined by the adaptive sampling method, as shown in Fig. 1. Once $\mathbf{x}^\star$ is identified, the training sets $\mathcal{L}$ and $\mathcal{E}$ are updated as

$$\begin{cases} \text{If } U_{\tilde{f}_L}(\mathbf{x}^\star) \geq \beta U_{\tilde{\varepsilon}}(\mathbf{x}^\star), & \text{add } \{\mathbf{x}^\star, f_L(\mathbf{x}^\star)\} \text{ to } \mathcal{L}, \\ \text{else}, & \text{add } \{\mathbf{x}^\star, f_L(\mathbf{x}^\star)\} \text{ to } \mathcal{L} \text{ and } \{\mathbf{x}^\star, \varepsilon(\mathbf{x}^\star)\} \text{ to } \mathcal{E}, \end{cases} \tag{4}$$

where $\beta \in [0, 1]$ is the ratio between the LF and HF computational cost. In the first case, only a low-fidelity evaluation is performed, while the second case requires both low- and high-fidelity evaluations for the same $\mathbf{x}^\star$. In this work the aggregate criteria adaptive sampling (ACAS) is applied, it identifies a new training point $\mathbf{x}^\star$ by solving the following single-objective minimization problem:

$$\mathbf{x}^\star = \underset{\mathbf{x}}{\operatorname{argmin}}[\hat{f}(\mathbf{x}) - U_{\hat{f}}(\mathbf{x})]. \tag{5}$$

A deterministic single-objective formulation of the particle swarm optimisation (DPSO) algorithm (Serani et al., 2016) is used for the solution of the minimization problems of Eq. (5). Furthermore, it is used for the multi-fidelity metamodel-based shape optimisation.

3 KLE geometric modeller

The modified geometries ($\mathbf{g}$) are produced by the linear superposition of N orthonormal basis functions ($\boldsymbol{\psi}$) on the original geometry ($\mathbf{g}_0$) as follows

$$\mathbf{g}(\boldsymbol{\xi}, \mathbf{x}) = \mathbf{g}_0(\boldsymbol{\xi}) + \boldsymbol{\delta}(\boldsymbol{\xi}, \mathbf{x}) \qquad \text{with} \qquad \boldsymbol{\delta}(\boldsymbol{\xi}, \mathbf{x}) = \sum_{k=1}^{N} x_k \boldsymbol{\psi}_k(\boldsymbol{\xi}) \tag{6}$$

where $\boldsymbol{\xi}$ are the geometry Cartesian coordinates, whereas $\{x_k\}_{k=1}^N$ and $\{\boldsymbol{\psi}_k\}_{k=1}^N$ are the reduced design variables and the eigenfunctions, respectively, provided by the design-space augmented dimesionality reduction (ADR) procedure described in Serani and Diez (2018). The original design space, formed by $M = 27$ design variables (Serani et al., 2016a), was reduced in dimensionality by the Karhunen-Loève expansion (KLE) (Diez et al. 2015), based on combined geometric and multi-physics/multi-point physical vectors. Design-space ADR by KLE has provided a reduced-order model for the shape modification vector ($\boldsymbol{\delta}$), composed by $N = 14$ reduced design variables ($\mathbf{x}$) retaining at least the 95% of the original design variability. Details about the original design space definition and the ADR method can be found in Serani et al. (2016a) and Serani and Diez (2018), respectively.

4 RANS simulation and meshes for optimisation

Flow simulations are performed with the unstructured finite-volume Navier-Stokes solver ISIS-CFD developed at ECN – CNRS (Queutey and Visonneau, 2007) available in the FINE™/Marine computing suite from NUMECA Int. This section describes the treatment of meshes in this solver, for simulations aimed at shape optimisation.

4.1 Mesh deformation and adaptive refinement

The solver contains an adaptive grid refinement method which adjusts the mesh locally, during the computation, by dividing the cells of an original coarse grid where the solution requires this (Wackers et al., 2017). The decision where to refine comes from a refinement criterion, a tensor field $C(x, y, z)$ computed from the flow. The tensor is based on the water surface position and on second derivatives of pressure and velocity. The mesh is refined until the dimensions $\mathbf{d}_{i,j}$ ($j = 1, 2, 3$) of each hexahedral cell i satisfy:

$$\|C_i \mathbf{d}_{i,j}\| = T_r. \tag{7}$$

As shown in Wackers et al. (2017), if the criterion is not sensitive to grid refinement, then the cell sizes everywhere are proportional to the constant threshold T_r. For multi-fidelity optimisation, this means that high- and low-fidelity results can be obtained by running the same simulations with two different thresholds T_r (Fig. 2), a procedure which is easy to automate in an optimisation loop (Fig. 1).

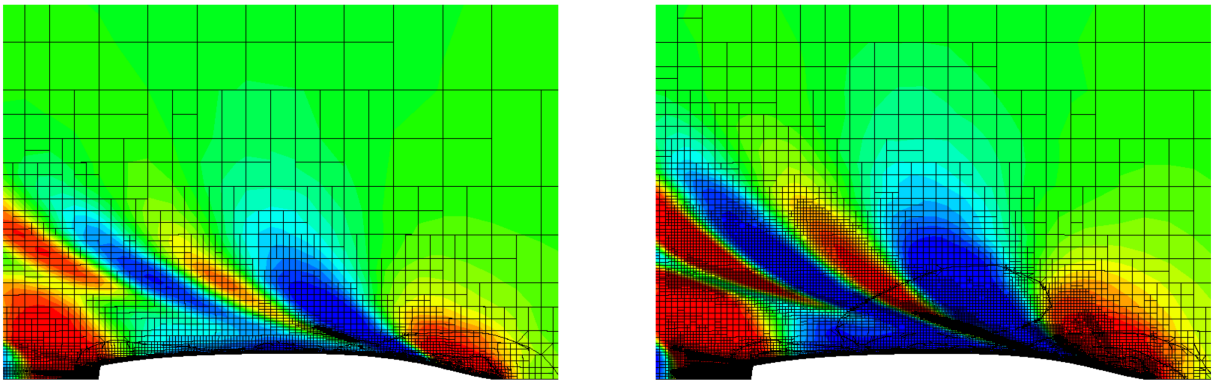

Fig. 2: Fine and coarse meshes are obtained with different thresholds: $T_r = 0.0145$ (left) and $T_r = 0.0072$ (right). Cuts at $z = 0$ coloured with the water volume fraction.

The meshes for the simulation of different geometries in the optimisation process are obtained through mesh deformation. Each simulation starts from the same original mesh (Fig. 3a). The mesh is divided in layers around the hull. For each geometry $\mathbf{g}(\boldsymbol{\xi}, \mathbf{x})$ received from the KLE modeller, the displacement of the hull faces with respect to $\mathbf{g}_0(\boldsymbol{\xi})$ is propagated through these layers (Durand, 2012). The displacements are multiplied with a weighting factor which goes from 1 on the hull to 0 on the outer boundaries, so that the latter are not deformed (Fig. 3b). The original grid is coarse, since deforming these is easier and safer than for fine grids. The final grid, including all the refinement at the free surface, is created using adaptive refinement (Fig. 3c).

4.2 Adaptation for drag computation

A challenge for this work is performing computations with adaptive grid refinement whose sole purpose is the accurate computation of drag. Contrary to simulations meant for studying flow details, locally very fine meshes may not be required. On the other hand, mesh regularity and a low number of cells are essential. Here, some of the ongoing work on improving adaptation for drag computation is shown.

Improving the free-surface meshing To provide adequate surface capturing even on deformed meshes, the fine grid around the free surface is created entirely by adaptive refinement (Fig. 3c). This implies that the original cells have to be divided many times. On undeformed grids (Fig. 4a) this works well: where the surface is at rest, the mesh is refined only in vertical direction and the mesh quality is good. When

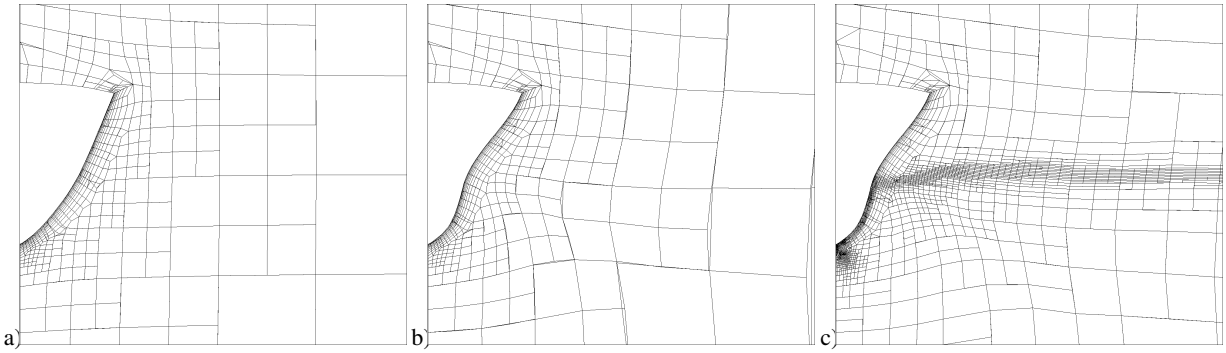

Fig. 3: Mesh creation: original grid (a), after deformation (b), after adaptive refinement (c).

the mesh is deformed (Fig. 4b) the cells are stretched and rotated so they are refined in more than one direction, which leads to unnecessary refinement and mediocre grid quality.

This problem was alleviated by changing the weigting factor. Instead of the Durand (2012) weighting which is based on the distance to the body and this distance squared, a weighting was chosen which is based on the distance to the power 1.6. This induces less deformation of the grid far from the body, which improves the refined mesh (Fig. 4c).

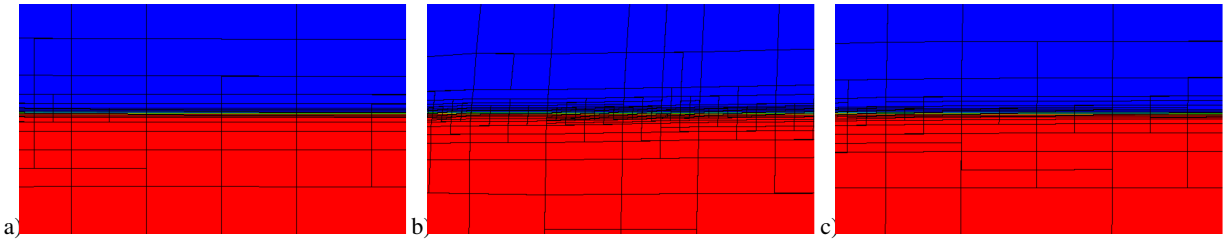

Fig. 4: Undisturbed free-surface mesh detail at $x = 5$: no deformation (a), deformation, old weighting (b) and power 1.6 weighting (c).

Limiting refinement behind the stern Unrestricted application of the velocity / pressure Hessian leads to the accurate resolution of the near and the far wake (Wackers et al., 2017a). This may not be required for drag evaluation. Therefore, tests were run where horizontal refinement is forbidden from a certain distance behind the stern. These results are compared with an estimation of the numerical uncertainty (based on three grids) following Wackers et al. (2017). Fig 5 shows the results for three geometries.

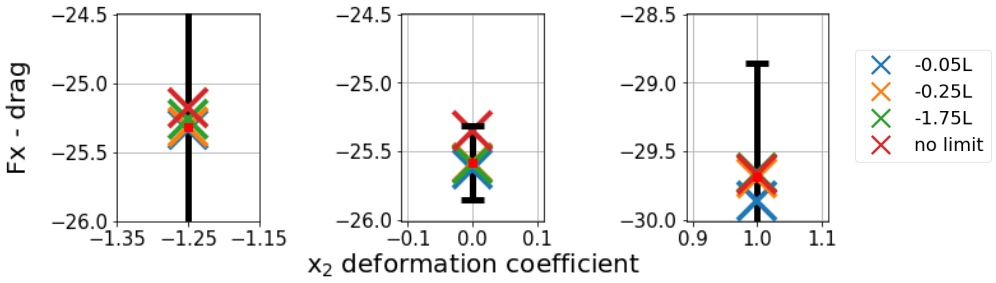

Fig. 5: Drag values when horizontal refinement is forbidden beyond a limit behind the stern, compared with estimated uncertainties on the $-0.25L$ grids, for three geometries.

The uncertainties are bigger for deformed grids than for the undeformed case ($x_2 = 0$). On the other hand, the dependence on the refinement limit position is small, with two exceptions: imposing no limit is a bad idea, since the waves are not damped before the outflow boundary. And the shortest box ($0.05L$) changes the drag when the mesh is deformed. Thus, the resolution of the near wake ($0.25L$) is required for good drag estimation; this also has implications for computations without adaptive refinement.

5 Optimisation of the DTMB 5415 destroyer

5.1 Optimisation settings

The DTMB 5415 is optimised for minimal resistance at even keel, $Fr = 0.30$ and $Re = 1.18 \cdot 10^7$. No constraints apply. The two design variables are the first parameters x_1 and x_2 of the KLE expansion. Initial sensitivity studies showed minimal drag for large negative values of these parameters, so a wide range of $[-1.25, 1.25]$ is used for each parameter. For the initial sample plane, HF and LF simulations were run in the centre of the domain, and with each single parameter at either $+1$ or -1. This results in 5 HF and 5 LF simulations. An optimisation with the ACAS sampling criterion was then run, adding 2 HF and 59 LF points.

5.2 Simulation settings

Simulations are performed on half geometries. The domain runs from $1.5L$ in front of the bow to $3L$ behind the stern, up to $2L$ laterally, and from $-1.5L$ to $0.5L$ vertically. Dirichlet conditions on the velocity are imposed on the inflow and side faces, pressure is imposed on the top, bottom, and outflow side. The hull is treated with a wall law and $y+ = 60$ for the first layer. Turbulence is modelled with $k - \omega$ SST.

The initial mesh has 130k cells; the thresholds for the low- and high-fidelity simulations are $T_r = 0.0145$ and $T_r = 0.0036$ which implies a $4:1$ cell size ratio and results in approximately 260k and 4.3M cells respectively. On a 20-core workstation the computations take about 1.5 and 24 hours each.

5.3 Results

Fig. 6 shows the sampled points and the metamodels at the end of the optimisation. After the initialisation, the adaptive sampler first targets the corners of the design space, then quickly focuses on the region of the optimum. To ensure the correctness of the optimum, a few HF simulations are performed in this region towards the end of the optimisation. The LF simulations appear reliable, since the LF and multifidelity metamodel are similar. However, the error metamodel is not negligible.

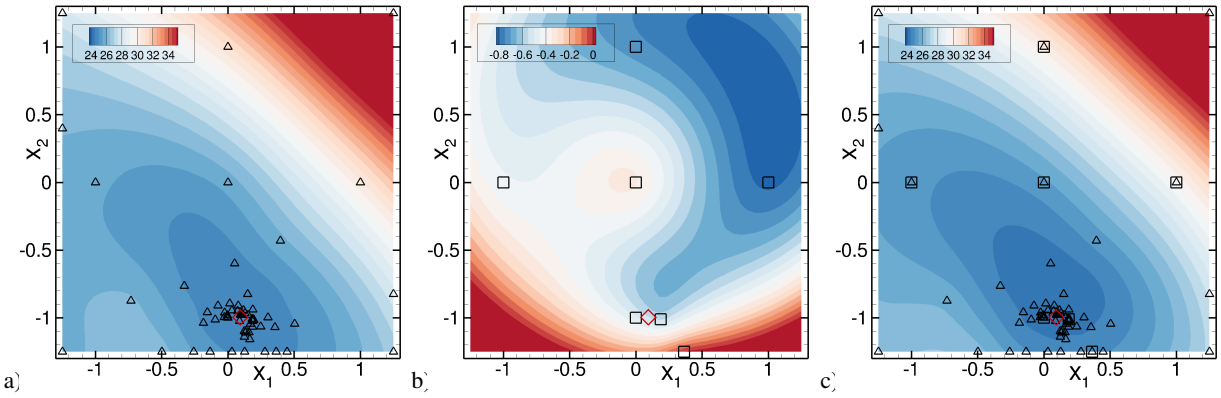

Fig. 6: Low-fidelity $\tilde{f}_L$ (a), error $\tilde{\varepsilon}$ (b) and combined multi-fidelity $\hat{f}$ (c) metamodels. The symbols indicate simulations, Δ: LF, $\square$: HF. The red $\diamond$ is the computed optimum.

The computed optimum is at $x_1 = 0.095$, $x_2 = -0.995$. In this point, the metamodel-predicted drag is 23.98N, the actual drag computed with HF simulation is 24.13N (+0.6%). The original geometry has a HF drag of 25.5412N, which means a gain of 4.9% for the optimisation.

Fig. 7 shows the initial and optimised geometries. The optimum has a more slender aftship which reduces the width of the stern wave, and a slight bulge aft of the bow. This bulge creates a second bow wave out of phase with the first one. These two waves cancel so the total bow wave is reduced. Since this interference depends on the wave lengths, it is expected to be only effective around the target velocity.

6 Conclusions

This work has shown that multi-fidelity metamodelling and adaptive grid refinement function together for the optimisation of realistic ship geometries. Future work will focus on further improving the efficiency of the CFD and on reducing the sensitivity of the metamodel to numerical errors in the simulations.

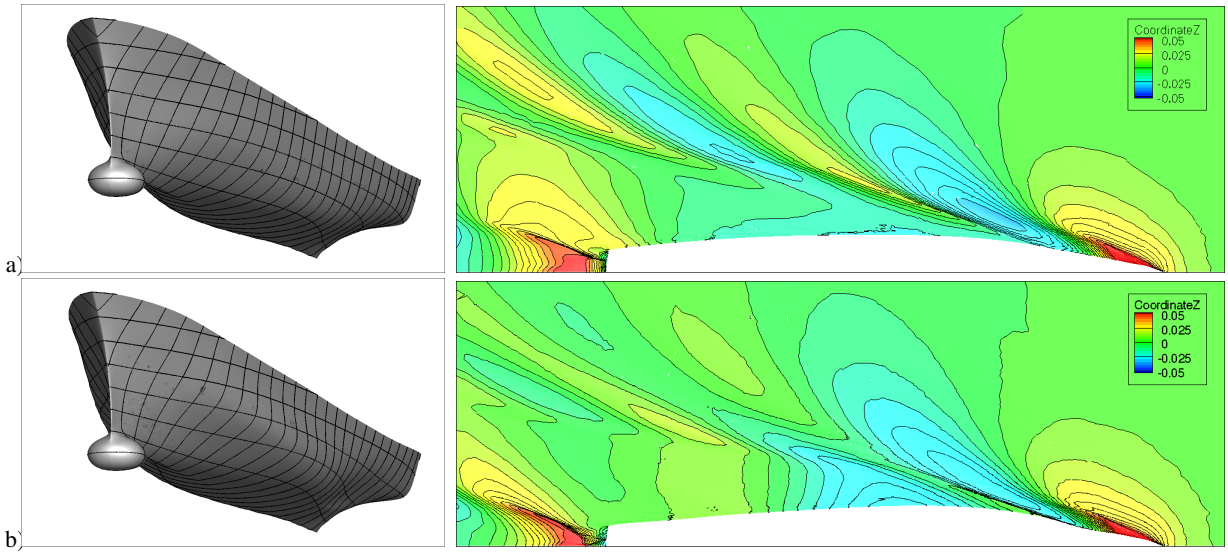

Fig. 7: Initial (a) and optimised (b) geometry and wavepattern.

Acknowledgments

The CNR-INM work is partially supported by the US Department of the Navy Office of Naval Research Global, NICOP grant N62909-15-1-2016 and N62909-18-1-2033, administered by Dr. Woei-Min Lin, Dr. Salahuddin Ahmed, and Dr. Ki-Han Kim, and by the Italian Flagship Project RITMARE, funded by the Italian Ministry of Education. The research is performed within NATO STO Task Group AVT-252 "Stochastic Design Optimization for Naval and Aero Military Vehicles".

References

M. Diez, E.F. Campana and F. Stern (2015). Design-space dimensionality reduction in shape optimization by Karhunen-Loève expansion. *Comput Methods Appl Mech Engrg*, **283**, 1525–1544.

M. Durand (2012). *Interaction fluide-structure souple et légère, application aux voiliers*. Ph.D. thesis, Ecole Centrale de Nantes.

R. Pellegrini, U. Iemma, C. Leotardi, E.F. Campana, and M. Diez (2016). Multi-fidelity adaptive global metamodel of expensive computer simulations. *2016 IEEE Congress on Evolutionary Computation (CEC)*, 4444–4451.

R. Pellegrini, A. Serani, M. Diez, J. Wackers, P. Queutey, and M. Visonneau (2018). Adaptive sampling criteria for multi-fidelity metamodels in CFD-based shape optimization. *ECCM-ECFD*, Glasgow, Scotland.

P. Queutey and M. Visonneau (2007). An interface capturing method for free-surface hydrodynamic flows. *Comput Fluids*, **36**(9), 1481–1510.

A. Serani, C. Leotardi, U. Iemma, E.F. Campana, G. Fasano, and M. Diez (2016). Parameter selection in synchronous and asynchronous deterministic particle swarm optimization for ship hydrodynamics problems. *Applied Soft Computing*, **49**, 313–334.

A. Serani, G. Fasano, G. Liuzzi , S. Lucidi, U. Iemma, E.F. Campana and M. Diez M. (2016a). Ship hydrodynamic optimization by local hybridization of deterministic derivative-free global algorithms. *Applied Ocean Research*, **59**, 115–118.

A. Serani and M. Diez (2018). Shape Optimization under Stochastic Conditions by Design-space Augmented Dimensionality Reduction. *19th AIAA/ISSMO Multidisciplinary Analysis and Optimization Conference*, Atlanta, USA.

S. Volpi, M. Diez, N.J. Gaul, H. Song, U. Iemma, K.K. Choi, E.F. Campana, and F. Stern (2015). Development and validation of a dynamic metamodel based on stochastic radial basis functions and uncertainty quantification. *Structural and Multidisciplinary Optimization*, **51**(2), 347–368.

J. Wackers, G.B. Deng, E. Guilmineau, A. Leroyer, P. Queutey, M. Visonneau, A. Palmieri, and A. Liverani (2017). Can adaptive grid refinement produce grid-independent solutions for incompressible flows? *J Comp Phys*, **344**, 364–380.

J. Wackers, E. Guilmineau, and M. Visonneau (2017a). Unsteady behaviour in RANS simulation of the JBC and KVLCC2. *NuTTS 2017*, Wageningen, The Netherlands.

Experimental and Numerical Hydrodynamic Analysis of Propulsion Factors On R/V Nawigator XXI with a Pre-Swirl Stator Device

Michał Wawrzusiszyn, Marek Kraskowski, Przemysław Król, Tomasz Bugalski, CTO, Gdansk/Poland,
michal.wawrzusiszyn@cto.gda.pl

1. Introduction

The pre-swirl stator (PSS) is a device intended to introduce the swirl into the propeller inflow. The features of PSS make it especially suitable for retrofitting. The PSS designed by means of vortex methods to achieve optimal radial distribution of induced velocities and the propeller marked CP745 cooperating with the PSS designed with use of lifting line algorithm for assumed induced velocity field serve as the subject of extended investigation presented in the following paper. The aims of the work were to improve the propulsive efficiency of the ship at the cost of minor increase of resistance (Król et al., 2017), and to achieve a noticeable net profit in increased speed or reduced power. Radial bound circulation over the stator's blades corresponding to the velocity field that ensures highest propeller efficiency is taken as the design one (Król et al., 2017).

The following paper presents the results of experimental analyses in the towing tank and numerical analyses carried out with the use of the Reynolds Averaged Navier-Stokes equations (RANSE) - CFD analysis of the performance of the vessel equipped with a PSS (Bugalski & Hoffmann, 2010, 2011). Versatility of the RANS solvers allows for final verification of the PSS design quality, taking into account all important phenomena, i.e. free surface, flow viscosity and bodies' interactions. On the other hand, elaborating a computational model of the vessel with rotating propeller presents a substantial challenge due to complexity of the geometry as well as complexity of the motion (propeller rotation embedded in the free motion of the hull).

The CFD results were thus verified by the prediction based on model scale experimental tests carried out in the towing tank. The comparison reveals general agreement between CFD and experiment, showing that the computational predictions of propulsive performance of the vessel is gaining maturity.

The analysed vessel is the training ship of the Maritime University of Szczecin, Nawigator XXI; her geometry was widely used within the EU research project EFFORT, making it a convenient benchmark case (Bugalski & Kraskowski 2006, Bugalski 2007). The hull body lines are presented in Fig. 1.

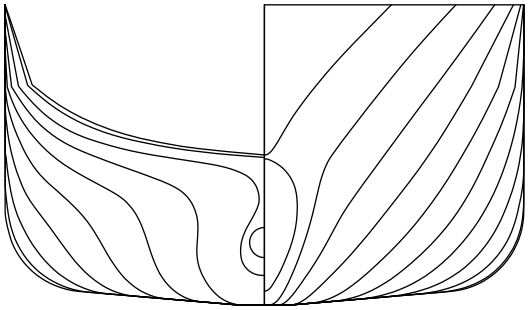

Fig.1 *Body lines of the Nawigator XXI*

Main data of the Nawigator XXI vessel:

Description	Value
Length between perpendiculars L_{PP} [m]	54.00
Length of waterline L_{WL} [m]	55.16
Breadth at waterline B [m]	10.50
Draught: fore T_F [m]	3.15
Draught: aft T_A [m]	3.20
Displacement volume ∇ [m^3]	1128
Area of wetted surface S [m^2]	671
Block coefficient C_B [-]	0.626

2. Model tests

The resistance and self-propulsion tests at model scale 1:10 were carried out in the towing tank of CTO S.A. All tests were done according to the ITTC standards. The hull model was tested with (see Fig. 2) and without the PSS installed. The main aim was to analyse its influence on ship power characteristics.

Fig.2 *Hull model appended for self-propulsion test*

Based on model test results a resistance and propulsion prediction consistent with the ITTC standards was prepared. In Fig. 9 a comparison of resistance model test and CFD results at 13 knots is presented.

3. CFD approach

Performing the CFD computations of ship flow at full scale is now a commonplace. Although the capabilities of numerical analyses theoretically allow solving the problem of Reynolds dissimilitude, the actual accuracy is not fully known, and the validation of full scale computations remains problematic due to lack of full scale reference data. For that reason, the full scale computations presented here were validated based on the extrapolation of model scale laboratory tests.
All computations were carried out with use of the Star-CCM+ solver from SIEMENS, software version 11.02.
The turbulence was solved with the Realizable K-Epsilon model.
The resistance and propulsion analyses were done with the use of the Estimating Hull Performance (EHP) module, which supports the mesh setup and other simulation parameters such a wave damping and time step values. The Superposed DFBI setting for the propeller was used due to consider a pitch and heave motions of the ship (Wawrzusiszyn et al., 2015).
In order to enable direct comparison between the results of experimental model tests and numerical investigation, based on commonly accepted parameters of ship propulsive characteristics, the CFD analyses included all the steps conducted as standard in the towing tank, i.e. open water propeller analysis, resistance and self-propulsion analysis as well as nominal wake computations.

3.1 CFD - Open Water Propeller

The open water propeller computations were carried out at full scale as part of complete propulsion analyses.
The computations were carried out for the following conditions:

- Inlet velocity: 6.0 [m/s]
- Propeller revolutions: 4.4 - 13.3 [rps]
- Temporal discretization: none (steady flow)

The mesh of polyhedral type was used. The number of mesh cells was about 6 616 000 (see Fig. 3). The propeller rotation was simulated using the Moving Reference Frame (MRF) approach. The propeller roughness 30 [μm] (by means of mathematical model implemented in Star-CCM+) was taken into account.
In general, effect of wall roughness is modelled by moving the logarithmic region of the boundary layer closer to the wall (STAR-CCM+, documentation).

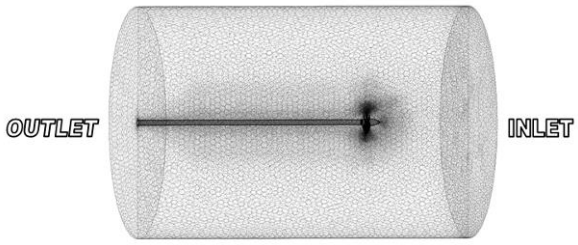

Fig.3 *Domain for the OPW – polyhedral mesh*

In Fig. 4 a vorticity magnitude behind working propeller is presented.

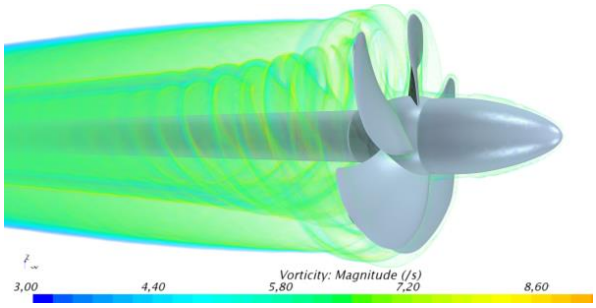

Fig.4 *Visualisation of the vorticity magnitude*

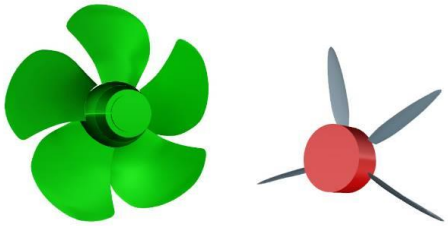

Fig.5. *Propeller CP745 and PSS device*

Propeller CP745	Value
Diameter [m]	2.260
Pitch ratio [-]	0.772
Hub ratio [-]	0.301
Expanded area ratio [-]	0.759

Fig. 6 presents the results of CFD analyses (full scale) in comparison to model propeller (tested at CTO S.A.) results that were recalculated into full scale. CFD analyses and experiments agree well.

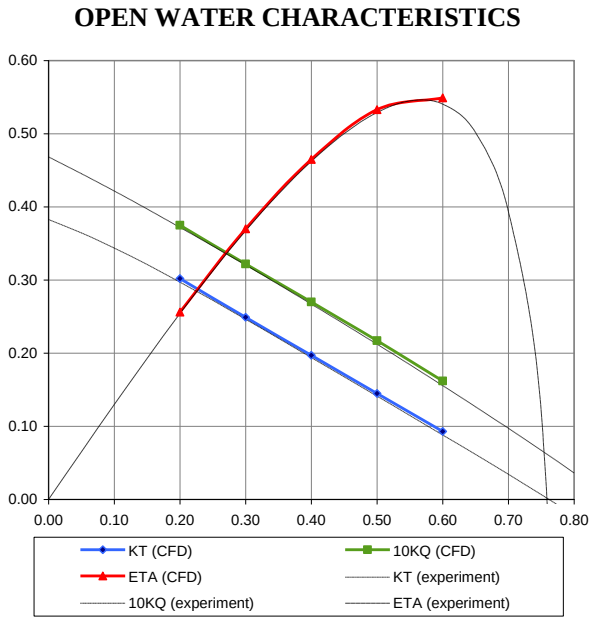

Fig.6. *Open water propeller characteristics – comparison between experiment and CFD*

3.2 CFD - Resistance

The mesh of hexahedral type was used. The number of mesh cells was about 5 700 000 (see Fig. 7). The flow was computed in the rectangular domain of the following dimensions: [6L; 5L; 3L], where L is the hull length (see Fig. 8). The hull was free to move in two degrees of freedom (heave and pitch) during computations of resistance and propulsion.

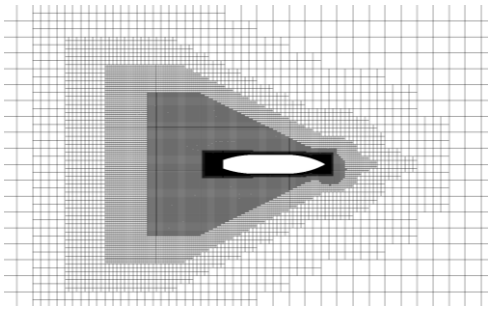

Fig.7 *Mesh density of the free surface*

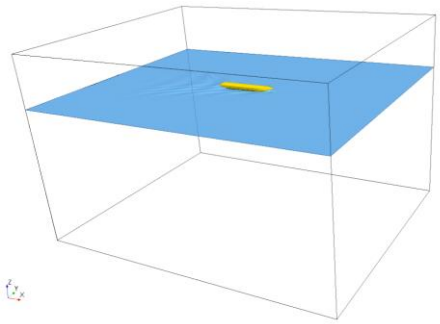

Fig.8 *Computational domain*

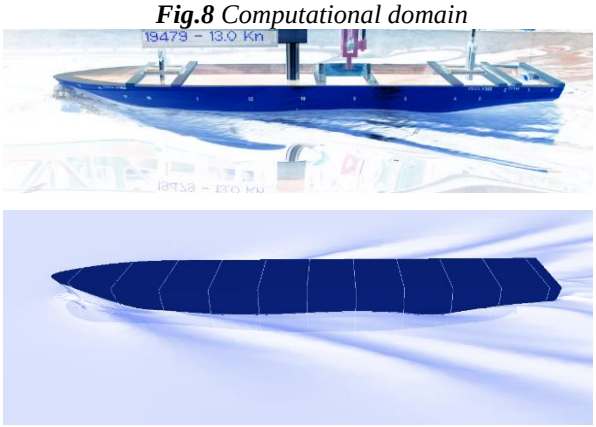

Fig.9 *Resistance model test at CTO S.A. (above) and CFD visualisation wave pattern (below) at speed of 13 knots.*

Comparison of resistance results for vessel speed of 13 knots is presented below.

SHIP RESISTANCE (CFD)

RT_S [kN]	PE_S [kW]	C_R [10^3]	Sinkage [m]	Trim [deg]
96.8	647.0	2.836	0.14	-0.09

SHIP RESISTANCE (EXPERIMENT)

RT_S [kN]	PE_S [kW]	C_R [10^3]	Sinkage [m]	Trim [deg]
95.0	635.0	2.722	0.18	-0.10

RELATIVE COMPARISON [CFD/EXP*100]

RT_S [%]	PE_S [%]	C_R [%]	Sinkage [%]	Trim [%]
102	102	104	78	90

3.3 CFD - Nominal Wake

The nominal wake was determined by post-processing of the resistance computations. There were two cases:

I. Hull with the PSS (see Fig. 11)
II. Hull without the PSS (see Fig. 10)

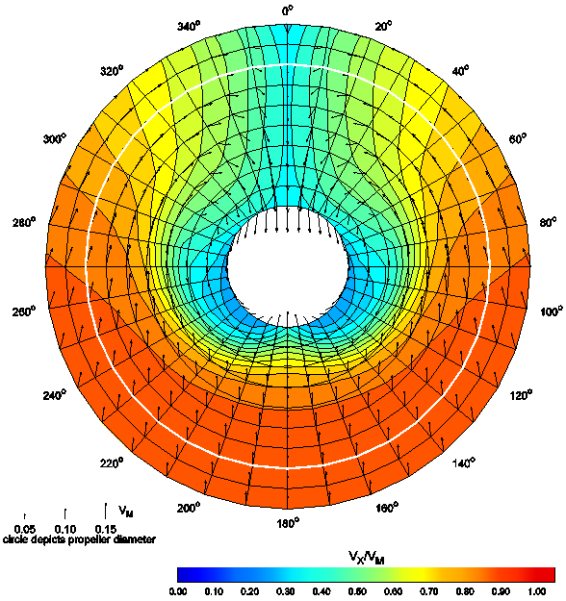

Fig.10 *Nominal wake – hull without the PSS V_S = 13kn*

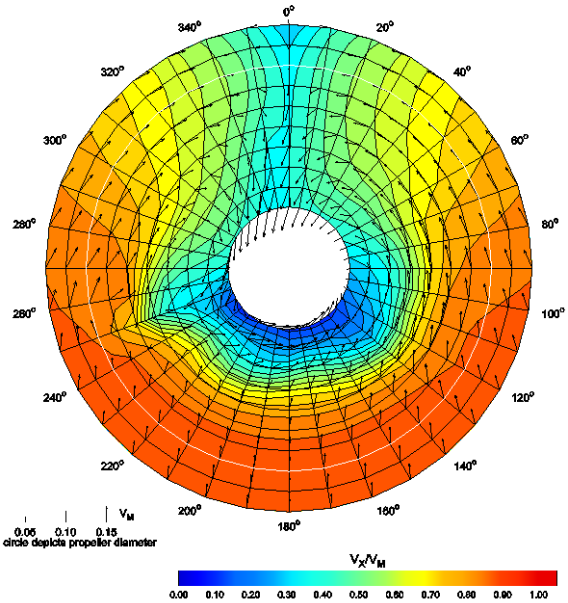

Fig.11 *Nominal wake – hull with the PSS at V_S = 13kn*

In Figs. 10 and 11 the influence of PSS on the nominal wake field is observed. The velocity distribution in the PSS plane is also presented in Fig. 12 for self-propulsion conditions, for propeller revolution rate 289.3 rpm.

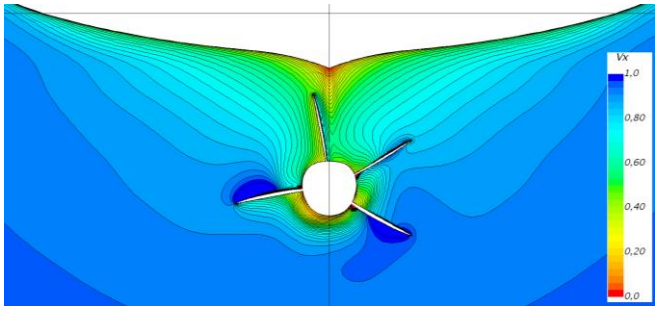

Fig.12 *Velocity distribution in the PSS plane at V_S = 13kn*

3.4 CFD - Self-propulsion

Propulsion computations were carried out with the use of full domain. Simulation of propeller rotation in the domain was solved by MRF approach. Time step was set to 0.001s which corresponds to propeller rotation by about 1.7 degree per each time step. The rudder and the PSS (for particular computation) were included. The mesh of hexahedral and polyhedral type was used. The total number of mesh cells was about 7 000 000 (see Fig. 13).

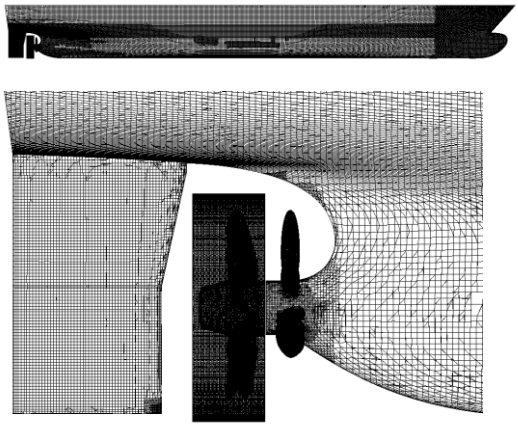

Fig.13 *Hexahedral and polyhedral mesh setup for self-propulsion*

In Fig. 14 a vorticity magnitude behind working propeller is presented.

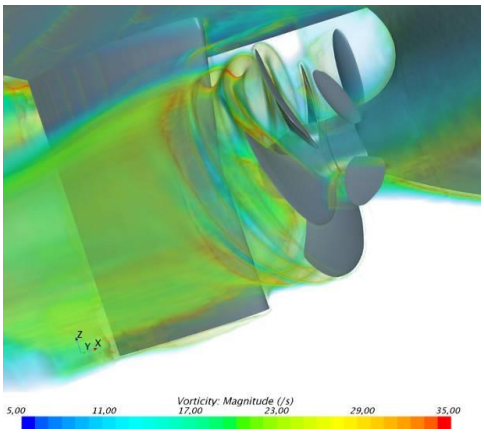

Fig.14 *Visualisation of the vorticity magnitude*

Comparison between CFD and experiment propulsion results for vessel speed of 13 knots is presented below.
Thrust and torque coefficients were determined according to below formulas.

$$K_T = \frac{T}{\rho D^4 n^2}, \quad K_Q = \frac{Q}{\rho D^5 n^2}$$

SELF – PROPULSION (CFD)

PSS	n [RPM]	T [kN]	Q [kNm]	K_T [-]	$10K_Q$ [-]
applied	282.9	125.8	35.6	0.211	0.265
not-applied	289.3	122.2	35.5	0.196	0.253

SELF – PROPULSION (EXPERIMENT)

PSS	n [RPM]	T [kN]	Q [kNm]	K_T [-]	$10K_Q$ [-]
applied	282.9	125.0	36.4	0.210	0.270
not-applied	289.3	124.0	37.1	0.199	0.264

RELATIVE COMPARISON [CFD/EXP*100]

PSS	n [%]	T [%]	Q [%]	K_T [%]	$10K_Q$ [%]
applied	100	101	98	100	98
not-applied	100	99	96	98	96

The propeller revolutions were set constant, exactly the same as in power prediction based on model tests.
The CFD results are in compliance with propulsion prediction based on experiment.

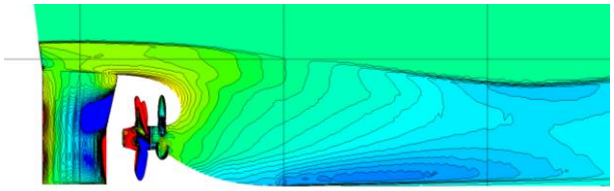

Fig.15 *Pressure distribution at V_S = 13kn – bottom side view, hull with the stator, the propeller is working at 289.3rpm.*

4. Propulsive coefficients

Based on CFD results propulsive coefficients such a thrust deduction fraction *t*, effective wake *w* and propulsive efficiency η_{DS} (according to formulae given below) were determined.

the thrust deduction fraction $t = 1 - \frac{R_{TS}}{T_S}$,

the wake fraction $w = 1 - \frac{J_S D_S n_S}{V_S}$,

the quasi-propulsive efficiency $\eta_D = \frac{P_{ES}}{P_{DS}}$,

the propeller efficiency $\eta_{0TS} = \frac{J_S K_{TS}}{2\pi K_{QS}}$,

the rotative efficiency $\eta_R = K_{QTS} / K_{QS}$

BASED ON CFD

PSS	t	w	η_{DS}	η_R
applied	0.230	0.414	0.614	1.076
not-applied	0.208	0.356	0.602	1.069

BASED ON EXPERIMENT

PSS	t	w	η_{DS}	η_R
applied	0.239	0.418	0.590	1.058
not-applied	0.232	0.371	0.566	1.044

RELATIVE COMPARISON [CFD/EXP*100]

PSS	t [%]	w [%]	η_{DS} [%]	η_R [%]
applied	96	99	104	102
not-applied	90	96	106	102

RELATIVE DIFFERENCES (with vs. without PSS)

	Δt [%]	**Δw [%]**	**$\Delta\eta_{DS}$ [%]**	**$\Delta\eta_{R}$ [%]**
CFD	+9.6	+14.0	+2.0	+0.7
EXP.	+2.9	+11.2	+4.1	+1.3

The most important difference between CFD results and extrapolation of model test results is visible in the evaluation of thrust deduction factor; the difference between the hull with and without PSS is much higher in CFD. However, it can be also seen that the tendency of change is the same in each case, what is encouraging.

5. Conclusions

- Resistance computations are in satisfactory agreement with experiment.
- General tendency in the influence of the pre-swirl stator on the propulsive efficiency is similar in CFD and in prediction based on model scale experiment.
- Thanks to CFD software it is possible to validate energy saving devices such a PSS in early design stage. The potential advantage of CFD is the possibility of full scale analysis and thus to get rid of the scale effect. However, this requires more studies to assure that the full scale flow is evaluated and analysed consciously.
- The open water propeller analyses (full scale) were in very good agreement with experiment (experimental results were extrapolated to full scale).

6. Acknowledgement

The research results presented in this paper come from the European Project INRETRO –ERA-NET MARTEC-2014-2017.

References

1. Król P., Bugalski T., Wawrzusiszyn M., (2017). “Development of numerical methods for marine propeller - pre-swirl stator system design and analysis”, Fifth International Symposium on Marine Propulsion
2. Wawrzusiszyn M., Bugalski T., Hoffmann P., (2015) “Numerical simulations of ship hull-propeller interaction phenomena”, 18th Numerical Towing Tank Symposium
3. STAR-CCM+, Documentation, Version 11.06
4. Bugalski T.: An overview of the selected results of the European Union Project EFFORT, Hydronav07, Archives of Civil and Mechanical Engineering Polish Academy of Sciences,Vol.7, no.3, pp. 55-67, 2007.
5. Bugalski T., Hoffmann P.: Numerical simulation of the interaction between ship hull and rotating propeller. Proceedings of A Workshop on Numerical Ship Hydrodynamics, Goteborg, 8-10 December, 2010, pp.441-446, ISSN 1652-9189.
6. Bugalski T., Kraskowski M.: Validation of the RANSE wake computations for the training vessel Nawigator XXI and the dredger Uilenspiegel, 9th Numerical Towing Tank Symposium, Le Croisic, France 1-3 October 2006, p.6.
7. Bugalski T., Hoffmann P.: Numerical Simulation of the Self-Propulsion Model Tests, SMP'11, Proceeding of 2nd International Symposium on Marine Propulsors, Hamburg, Germany, June 2011.

CALL FOR PAPERS

22nd Numerical Towing Tank Symposium (NuTTS'19)

Tomar, Portugal, 29 September – 1 October 2019

Topics:

- Nonlinear flows around marine structures (LES, RANSE, Euler with or w/o free surface)
- Simulation of ocean renewable energy devices (wave, tidal, floating wind, floating solar)
- Related topics (validation experiments, numerical techniques, grid generation, etc)

Deadlines:

Early feedback (optional):	30 March 2019
Extended Abstracts received:	30 June 2019
Payment received:	15 July 2019

You are invited to participate in the above event. The objective of the event is to provide a forum for informal discussions among experts in the field and to disseminate latest results. Younger workers and Ph.D. students are especially encouraged to participate. The event will be held at the **Hotel dos Templários in Tomar/Portugal**. All participants stay and have meals together to maximize interaction and discussion.

The extended abstracts of the proposed talk will be directly reproduced in pdf proceedings. Work in progress, encountered problems, etc. should be discussed in an open, informal atmosphere (no ties!) among colleagues. The first page of the extended abstract should be headed with the title and authors' names, affiliation and email address in a compact form to economize on space. Academic titles and page numbers shall be omitted. The extended abstract shall neither contain an abstract of the abstract, nor keywords, nor further headers. Font size shall not be less than 10pt Times New Roman. Extended abstracts should be limited to 6 pages in A4 format with 2.5 cm margin. An early reply will help us in organizing the event better. For the early feedback, a tentative title or topic will suffice.

Following the tradition of NuTTS events, the fees will be kept low to allow a maximum number of scientists to attend. The fees including accommodation (3 nights) and all meals during the symposium will be:

350 Euro PhD candidates and students
400 Euro authors
450 Euro other participants

Fees are subject to 19% VAT.

Contact: Luis Eça
luis.eca@ist.upl.pt

Sponsors: WaVEc